

AD-A162 506

PROCEEDINGS OF THE GULF STREAM WORKSHOP HELD AT WEST  
GREENWICH RHODE ISLA (U) RHODE ISLAND UNIV KINGSTON  
GRADUATE SCHOOL OF OCEANOGRAPHY D R WATTS APR 85

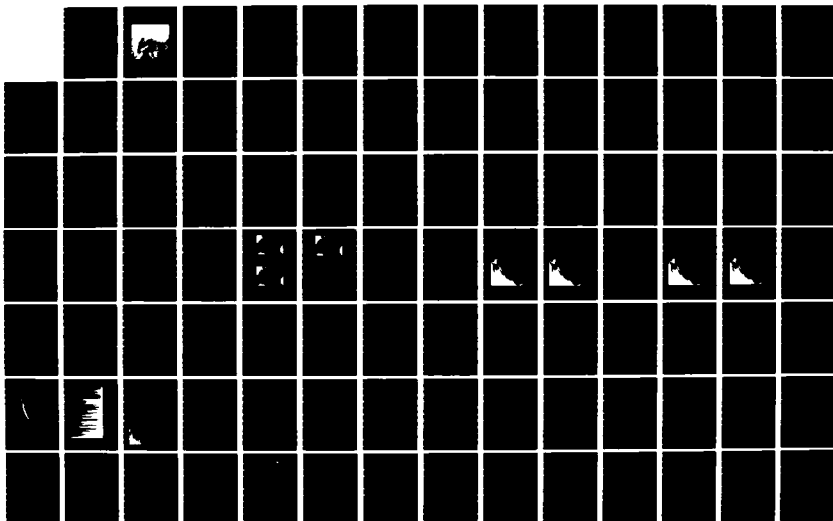
1/7

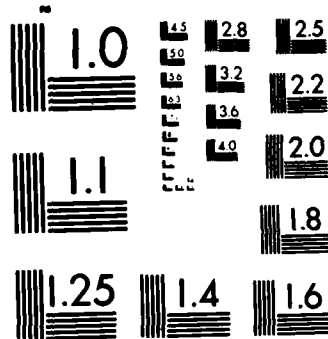
UNCLASSIFIED

N00014-85-G-0322

F/G 8/3

NL





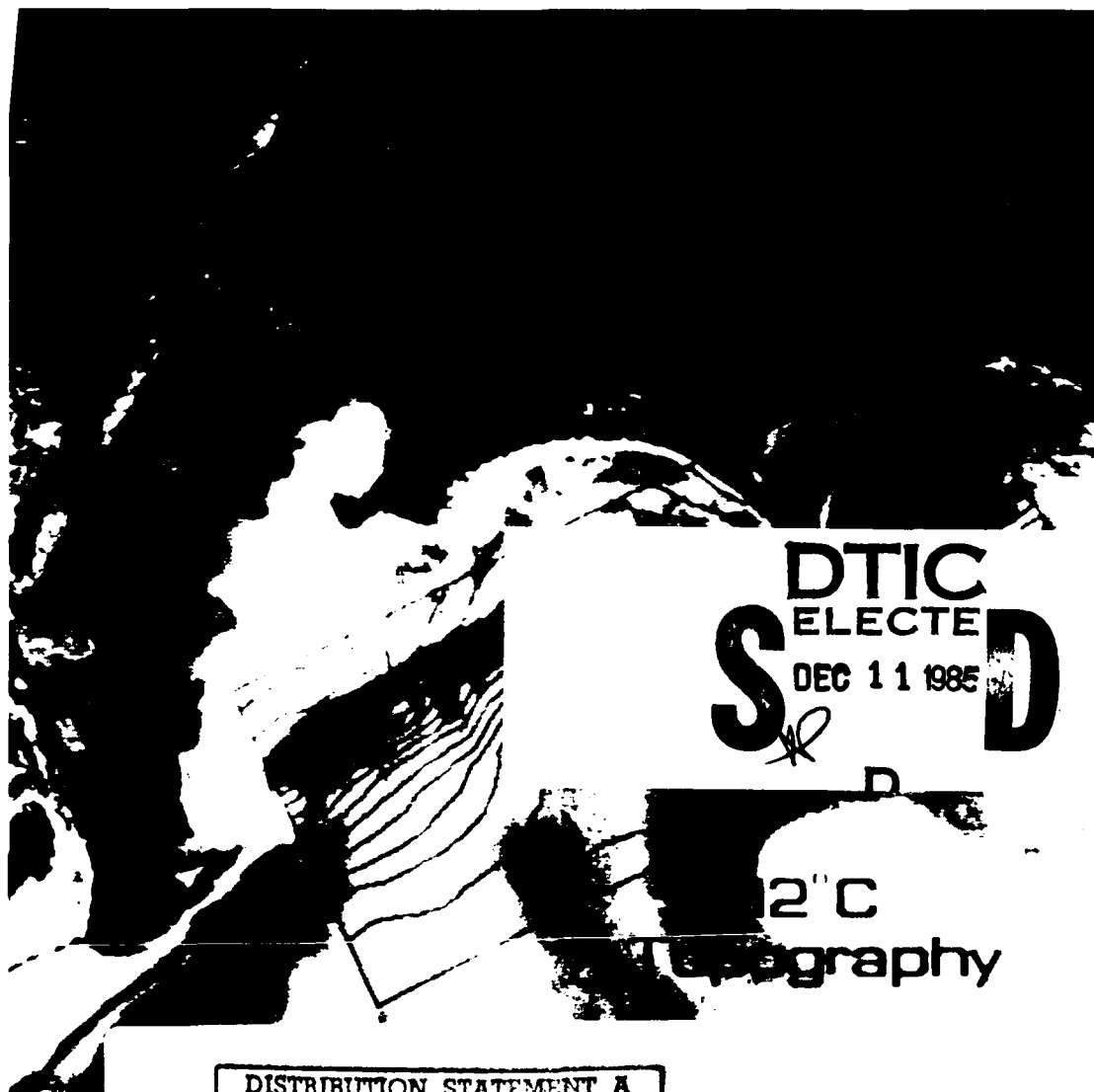
MICROCOPY RESOLUTION TEST CHART  
NATIONAL BUREAU OF STANDARDS-1963-A

# GULF STREAM WORKSHOP

## PROCEEDINGS

AD-A162 506

DTIC FILE COPY



DTIC  
ELECTE  
DEC 11 1985  
S D

2" C  
topography

### DISTRIBUTION STATEMENT A

Approved for public release;  
Distribution Unlimited

23-26 APRIL 1985  
URI ALTON JONES CONFERENCE CENTER  
EXETER, RHODE ISLAND

Host: University of Rhode Island  
Sponsor: U.S. Office of Naval Research  
Convener: D. Randolph Watts

11-21-85-014

GULF STREAM WORKSHOP

- A conference on the fundamental physical processes governing the Gulf Stream circulation and its variability and
- to plan future observations and field studies, and numerical modelling and prediction efforts

PROCEEDINGS

University of Rhode Island  
W. Alton Jones Conference Center  
West Greenwich, Rhode Island  
23-26 April 1985

This work relates to Department of Navy Grant N00014-85-G-0322 issued by the Office of Naval Research. The United States Government has a royalty-free license throughout the world in all copyrightable material contained herein.

Copies available from:

D. Randolph Watts  
Graduate School of Oceanography  
University of Rhode Island  
Kingston, RI 02881



### Cover Photo Description

The results of three independent studies of the Gulf Stream are combined in this illustration to compare the path and structure of the current as observed by a satellite-borne sensor, by a moored array of instruments, and by Lagrangian techniques. All apply to May 20, 1984.

The satellite infrared image shows the Gulf Stream as it flows past Cape Hatteras, NC (lower left) into the deeper waters to the northeast. The false color of the image highlights the sea surface temperature changes from the cooler (blue-to-green) slope water to the warmer (yellow-to-red) waters of the Gulf Stream and Sargasso Sea. Further use of satellite imagery is discussed in a paper by P. Cornillon in these PROCEEDINGS.

In the boxed region superimposed on this image is a contour map of the thermocline depth field as measured by an array of inverted echo sounders. The thermocline, represented by the 12°C isotherm, slopes downward from 150 m in the northwestern portion of the box to deeper than 800 m in the southern section. The contour interval is 50 m. The large Gulf Stream meander crest and trough observed in the satellite image is mapped in the subsurface thermocline topography. The use of inverted echo sounders to produce these objective contour maps is discussed in a paper by R. Watts and K. Tracey in these PROCEEDINGS.

The track of an isopycnal Rafos float is indicated by the solid blue dots. The five positions shown are at daily intervals, with the center one corresponding to 20 May 1984. The float was in 7.5°C water at a depth of 780 m. Through the meander crest it follows a path which is very similar to the 450 m contour of the 12°C isotherm. Further studies using Rafos float trajectories are presented in papers by T. Rossby and by A. Bower in these PROCEEDINGS.

This photo has been produced at the Remote Sensing Center of the University of Rhode Island using software developed at the University of Miami.

## PREFACE

In recent years, studies of the fundamental physical processes governing the Gulf Stream structure and variability have benefited from great advances in observational and theoretical techniques. New observational technology includes (a) instrumentation employed in ship and aircraft surveys, (b) high performance current meter moorings, inverted echo sounders, and acoustic tomographic transceivers, all now capable of sampling within the strong current, (c) Lagrangian drifters and floats capable of tracking water parcel trajectories at various depths within the current, and (d) satellite remote sensing capabilities in infrared imagery processing and improved accuracy in radar altimetry. Theoretical approaches have been advanced with, for example, (a) new finite-amplitude instability models, thin-jet time-dependent stream path models, and the method of contour dynamics, (b) improved numerical techniques both in large-scale eddy-resolving general circulation models and in detailed regional process models, and (c) larger, faster computers.

By combining these new methodologies to best advantage, scientists now feel that a new plateau of understanding of Gulf Stream dynamics is attainable, and that accurate predictive capabilities may be developed for the meandering path of the Gulf Stream. A cooperative research program is being developed to focus efforts on the region northeast of Cape Hatteras, where meanders can grow to large amplitude and the Gulf Stream path frequently interacts with eddies and rings. The problem is complex. We now realize that a correct dynamical description must intrinsically couple the mass-, momentum-, energy-, and vorticity-fluxes of a strong mean current, a strong eddy and ring field, and a moderately strong recirculation region adjacent to each side of the Gulf Stream. Moreover, the studies required to attain this new level of understanding must be extensive, because they must cover interacting phenomena whose spatial and temporal scales span more than two orders of magnitude. With the above technological advances, researchers have demonstrated improved capabilities to study many of the individual constituent parts of the overall Gulf Stream problem, and scientists now feel the time is right for a large collaborative effort, employing the talents, techniques, and energies of researchers from many institutions and specializations to elucidate the fundamental physics of the Gulf Stream.

The U.S. Office of Naval Research is making plans to sponsor a special-focus program entitled "SYNOP" (Synoptic Ocean Prediction) to advance our physical understanding of ocean regions of high synoptic-scale variability and develop predictive capabilities for these phenomena. The Gulf Stream region where meanders grow to exhibit large amplitude is the chosen study area.

In order to exchange ideas among researchers representing the rapidly developing specialties in Gulf Stream studies and to stimulate cooperative research efforts, a Gulf Stream Workshop was hosted by the University of Rhode Island at the Alton Jones Conference Center, on 23-26 April 1985, under U.S. Office of Naval Research sponsorship, Grant N00014-85-G-0322.

The explicit purposes of the conference were:

1. to review the present theoretical and observational knowledge about the Gulf Stream, and
2. to formulate and coordinate future Gulf Stream research efforts among the interested scientists.

The Organizing Committee for the Gulf Stream Workshop consisted of the following members:

D. Randolph Watts,  
Conference Convener  
Nicholas P. Fofonoff  
Nelson Hogg  
Allan Robinson

Valuable organizational advice was also obtained from John Bane, Harry Bryden, Peter Cornillon, Tom Curtin (the responsible ONR Program Director), Dale Haidvogel, and Tom Rossby.

Because the SYNOP program has important observational and theoretical components, the structure of this meeting was designed to bring together participants representative of all the major observational and theoretical interests in Gulf Stream research. We could thus jointly review developments in both specialties and increase communication between the groups. In this respect we followed a pattern which had worked well three years earlier at a "Workshop on Gulf Stream Structure and Variability", convened by John Bane at the University of North Carolina, 1-2 April 1982. That conference was notable for the informative and enthusiastic exchange of information among its participants.

An additional feature which we sought to build into the Workshop structure from the start was a focus on future research plans. In the several weeks before the Workshop some informal contacts were established by distributing one-page statements of individual future research interests among participants, and informal meetings were held at WHOI, URI, and Harvard to discuss research plans.

During the Workshop, sessions were scheduled for observational and theoretical workers to meet jointly to broadly coordinate future research goals and objectives. The Workshop sessions started with short presentations of future plans by individual investigators, followed by plenary discussions. Additionally, two Working Groups, dealing respectively with observational and modeling issues, met separately to make recommendations regarding methods to achieve the goals and objectives.

I would like to thank the other co-chairmen of the Working Groups, Nelson Hogg, Glenn Flierl, and Jim Carton for their efforts in helping to write the Working Group Reports in Part I of these PROCEEDINGS. Lastly, I would like to thank Julie Rahn and Linda Nester for their valuable assistance in organizing and running the conference and in producing these PROCEEDINGS.

D. Randolph Watts  
September, 1985

## TABLE OF CONTENTS

Cover Photo Description	ii
Preface	iii
Table of Contents	v

### PART I: Overview of Workshop Results

1. Introduction	I.1
Table 1.1 SYNOP Scientific Issues and Objectives	I.3
Table 1.2 Summary of Workshop Recommendations for SYNOP	I.4
2. Reports of the Working Groups	
A. Working Group on Observational Issues	I.5
Table 2.A.1. Observational Priorities and Methods	I.6
B. Working Group on Modeling and Prediction	I.9
3. Strawman Observational Plan	I.12
Figure 3.1. Strawman Experiment: Regions of Concentration	I.13
Figure 3.2. Strawman Moored Array Design	I.14
4. General Recommendations	I.15
5. Appendices	
A. Letters of Invitation	I.17
B. SYNOP Program Description (T. Curtin, ONR)	I.20
C. Agenda	I.21
D. List of Participants	I.22

### PART II: Papers and Presentations

A. Keynote Addresses	
GULF STREAM OBSERVATIONS	II.1
N.P. Fofonoff (WHOI)	
RECENT MODELING OF THE GULF STREAM SYSTEM, LOCAL DYNAMICS AND NON-LOCAL EFFECTS	II.21
D.B. Haidvogel (NCAR)	
RECENT GULF STREAM THEORETICAL WORK AND PERTINENT OBSERVATIONS	II.45
N. Hogg (WHOI)	
DATA ASSIMILATION, MESOSCALE DYNAMICS AND DYNAMICAL FORECASTING	II.58
A.R. Robinson (Harvard)	
TWO RECENT VIEWS OF THE GULF STREAM EAST OF CAPE HATTERAS	II.81
H.T. Rossby (URI)	

## B. Oral and Poster Presentations

MODIFICATIONS OF AN INTENSE OCEANIC CURRENT SYSTEM FLOWING INTO A REGION OF COOLING; D. Adamec (Naval Postgrad. School)	II.101
BIMODALITY IN THE GULF STREAM; J.M. Bane, Jr. and W.K. Dewar (UNC)	II.116
RECENT CURRENT MEASUREMENTS IN THE GULF STREAM DOWNSTREAM FROM CAPE HATTERAS J.M. Bane, Jr. (UNC) and D.R. Watts (URI)	II.127
ISOPYCNAL RAFOS FLOATS AND THE DYNAMICS OF GULF STREAM MEANDERS; PRELIMINARY RESULTS A.S. Bower (URI)	II.135
SEA-SURFACE HEIGHT BY GEOSAT-A ALTIMETRY. J. Calman (Johns Hopkins)	II.143
THE STRUCTURE OF THE GULF STREAM AS DERIVED FROM AN EOF ANALYSIS; E.F. Carter (URI)	II.169
GULF STREAM ENVELOPE AND MEAN PATH BETWEEN $75^{\circ}W$ AND $58^{\circ}W$ . P. Cornillon (URI)	II.182
MAXIMUM GRADIENT INVERSE FOR THE GULF STREAM SYSTEM; B.D. Cornuelle (SIO) and P. Malanotte-Rizzoli (MIT)	II.195
FRONTAL GEOSTROPHIC DYNAMICS, B. Cushman-Roisin (FSU)	II.215
AN ANALYSIS OF GULF STREAM MEAN FLOW ENERGETICS OFF CHARLESTON, SOUTH CAROLINA W.K. Dewar and J.M. Bane, Jr. (UNC)	II.256
NONLINEAR WAVES AND COHERENT VORTEX STRUCTURES IN BAROTROPIC $\beta$ -PLANE JETS G. Flierl, P. Malanotte-Rizzoli, N. Zabusky, and S. Meacham (MIT)	II.273
SPATIAL STRUCTURE OF GULF STREAM CURRENT VARIABILITY DOWNSTREAM OF THE NEW ENGLAND SEAMOUNT CHAIN R.M. Hendry (Bedford Institute of Oceanography)	II.281
RECIRCULATION AND THE DEEP GULF STREAM N.G. Hogg (WHOI) and R.S. Pickart (WHOI/MIT)	II.288
EDDY-RESOLVED OCEAN CIRCULATION STUDIES RELATED TO THE GULF STREAM REGION; W.R. Holland and J.C. Evans (NCAR)	II.304

PARTIAL SOLUTIONS FOR INERTIAL WESTERN BOUNDARY CURRENT WITH CONTINUOUS STRATIFICATION R.X. Huang (Princeton)	II.320
TIME SCALES AND STRUCTURE OF TOPOGRAPHIC ROSSBY WAVES AND MEANDERS IN THE DEEP GULF STREAM W.E. Johns (RSMAS) and D.R. Watts (URI)	II.362
BOUNDARY-FORCED NONLINEAR RADIATION: NUMERICAL EXPERIMENTS P. Malanotte-Rizzoli (MIT) and D.B. Haidvogel (NCAR)	II.399
OPTIMAL ESTIMATION AND THE KALMAN FILTER FOR NUMERICAL OCEAN FORECAST MODELING R.N. Miller (Tulane)	II.420
OCEANOGRAPHIC PLANS FOR ANALYSIS OF GEOSAT DATA DURING THE NW ATLANTIC REGIONAL ENERGETICS EXPERIMENT (REX) J.L. Mitchell (NORDA)	II.428
SCALES OF VARIABILITY OF THE GULF STREAM FRONT BASED ON AVHRR IMAGERY AND RELATED TOPICS C.N.K. Mooers (Naval Postgrad School)	II.441
PROTOTYPE DATA ASSIMILATION IN THE GULF STREAM REGION N. Pinardi and M.A. Spall (Harvard)	II.449
THEORETICAL AND NUMERICAL STUDIES OF GULF STREAM RING FORMATION L.J. Pratt (URI)	II.468
GULF STREAM TOMOGRAPHY: PRELIMINARY RESULTS FROM AN EXPERIMENT J.L. Spiesburger and R.C. Spindel (WHOI)	II.479
NUMERICAL MODELLING AND ASSIMILATION OF ALTIMETER DATA IN THE GULF STREAM SYSTEM: RECENT RESULTS J.D. Thompson, H.E. Hurlburt and John Kindle (NORDA)	II.495
OBJECTIVE ANALYSIS OF THE GULF STREAM THERMAL FRONT FROM INVERTED ECHO SOUNDERS D.R. Watts and K.L. Tracey (URI)	II.525

Accession For	
NTIS CRA&I	<input checked="" type="checkbox"/>
DTIC TAB	<input type="checkbox"/>
Unannounced	<input type="checkbox"/>
Justification File	
By	
Distribution	
Availability Codes	
Dist	Available for Special
A-1	



PART I: OVERVIEW OF WORKSHOP RESULTS

1. INTRODUCTION

This workshop brought physical oceanographers together to focus on understanding the large scale meandering of a strong current jet, namely the synoptic scale variability of the Gulf Stream: The goals were to design a research program to elucidate the most relevant dynamics and learn how to predictively model its behavior. The U.S. Office of Naval Research has a special-focus program, "SYNOP", for the purpose of funding such a research program during roughly the next five years, 1986-1991. Appended to these PROCEEDINGS is a SYNOP Program Description written by Dr. Tom Curtin, the cognizant ONR scientific officer, for distribution to workshop invitees.

The timetable which ONR has set for SYNOP was an important practical aspect of the future plans discussed at this Workshop. It is envisioned as a five year program, beginning with (i) a start-up phase with a small amount of funding for "pilot" or preparatory work in FY86, followed by (ii) two years (FY87-88) of substantially increased support for new observational programs and modeling efforts designed to fundamentally improve our understanding of the dynamics of the Gulf Stream, with the goal being to properly model and predict its behavior, and (iii) two more years (FY89-90) in which subsets of the observations will continue to provide information to update and verify predictive models.

Part I of these Gulf Stream Workshop PROCEEDINGS presents a summary overview of the workshop, its discussions, and recommendations for the future. Subjects are presented here in roughly the chronological order in which they occurred.

Background information about the conference is in the Appendix to Part I : (a) the Letters of Invitation, (b) the ONR / SYNOP Program Description written by Tom Curtin preceding the workshop for distribution to the invitees, (c) the Workshop Agenda, and (d) the List of Participants.

As the Agenda shows, plenary sessions were held early in the workshop in order for participants to jointly review new developments and the status of our knowledge about the Gulf Stream. Sessions were scheduled on five Gulf Stream topics, each headed by a Keynote Address and followed by several shorter oral/poster presentations:

SESSION TOPIC	KEYNOTE SPEAKER
Observational Review	Nicholas P. Fofonoff
Theoretical Review	Nelson Hogg
Numerical Modeling Review	Dale Haidvogel
Observations: Emerging Techniques	Thomas Rossby
Modeling: Emerging Techniques	Allan Robinson

Manuscripts of each Keynote Address and all of the shorter presentations are included in Part II of these PROCEEDINGS.



The first of the future plans sessions dealt with Gulf Stream meander modeling and observational work which is already underway at NORDA and JHU/APL in connection with the GEOSAT altimeter. GEOSAT was launched shortly before the Workshop. For the first 18 months it will be in an orbit more expressly suited for geodesy, but beginning about October 1986 it will be shifted to an orbit with repeat tracks specifically chosen for physical oceanography. The detailed presentations of this session (speakers listed in Agenda) are included in Part II.

The next session on Future Plans scheduled researchers to present their individual perspectives and/or more general recommendations on how to understand the synoptic scale variability of the Gulf Stream. Table 1.1 summarizes the SYNOP Scientific Issues and Objectives identified and discussed in these plenary discussion sessions. The first category in this table, "Dynamics", outlines a wide range of phenomena of potential importance to the dynamics of synoptic scale variability; the second category, "Modeling and Prediction", outlines methods and developmental work to be done to numerically replicate and forecast the synoptic Gulf Stream. Modelers and observationalists alike agreed upon the necessity of improving our understanding of fundamental physics of the Gulf Stream, but of course not all of the phenomena and topics listed in Table 1.1 were thought to be of equal importance to the synoptic variability problem.

A "Working Group on Observational Issues" and a "Working Group on Modeling and Prediction" met to discuss their respective specialties in greater detail. The two separate groups assigned remarkably similar priorities to the scientific issues and objectives which should be emphasized in the SYNOP program. The major points of agreement are listed in Table 1.2, a Summary of Workshop Recommendations for SYNOP.

More detailed sets of recommendations, respectively on observational priorities and on modeling objectives, appear in the Reports of the Working Groups presented in Chapter 2.

In Chapter 3 we have attempted to distill a Strawman Observational Plan from the combined recommendations and discussions of the meeting.

Chapter 4 summarizes several General Recommendations from the final plenary discussion regarding funding emphasis, pilot experiments, and scientific management of the SYNOP program.

Table 1.1

SYNOPSIS SCIENTIFIC ISSUES AND OBJECTIVESI Dynamics

1. Local current dynamics and structure (upper and lower layer)
  - a. at Cape Hatteras (inlet conditions)
  - b. Hatteras to Seamounts (increasing transport)
  - c. near Seamounts
  - d. Seamounts to Grand Banks (decreasing transport)
  - e. special processes and statistical/dynamical implications
2. Meanders & stream path dynamics
  - a. baroclinic/barotropic instability
  - b. parcel trajectories
  - c. nodes downstream
3. Eddy and Ring-Stream interactions
  - a. near field/far field
  - b. ring formation/coalescence
  - c. ring dynamics
  - d. eddy radiation (or absorption?)
4. Topographic & bottom boundary interactions
  - a. topographic Rossby waves
  - b. seamounts
  - c. deep western boundary undercurrent
5. General Circulation
  - a. potential vorticity and tracer distributions
  - b. recirculation gyres
  - c. eddy-mean field interactions / fluxes
  - d. separation from western boundary
6. Smaller scales
  - a. shingles, warm outbreaks
  - b. stirring and mixing / intrusions, interleaving
  - c. sub-grid scale parameterizations
7. Air-sea interaction and large-scale forcing
  - a. wind forcing
  - b. thermodynamic forcing

II Modelling and Prediction

1. Dynamical Models
  - a. primitive equations models
  - b. quasi-geostrophic models
  - c. isopycnal-layer models
  - d. embedding (combinations of models)
2. Statistical Models
  - a. multiple scales
  - b. nonstationarity, inhomogeneity, anisotropy
3. Nowcasting & Forecasting - scales, regions, accuracies?
  - a. simulation of data sets and measurement methods
  - b. efficient observational networks & sampling strategies
  - c. data assimilation & updating strategies
  - d. verification & intercomparisons with observations

Table 1.2

SUMMARY OF WORKSHOP RECOMMENDATIONS FOR SYNOPA. Location and timing

1. The study region should extend from Cape Hatteras to the Grand Banks and from the center of the recirculation region to the continental margin.

2. Experiments should simultaneously concentrate moored and other intensive resources within the following spatially separate areas (while linking together the overall region by satellite imagery, float trajectories, and hydrographic surveys):

a. an "inlet conditions" monitoring experiment to specify the stream structure and flow characteristics entering the study region;

b. a "path dynamics and meanders" experiment to the west of the New England seamount chain, and

c. a "path dynamics and meanders" experiment to the east of the New England seamount chain.

The latter two regions both have large amplitude meanders and strong interactions with rings. They are chosen to represent importantly different dynamical regimes within the overall study area inasmuch as they have substantially different relative strengths of barotropic and baroclinic circulations and they represent regions of converging and diverging transport from the recirculation gyres.

3. The longer-term statistical, dynamical, energetics and monitoring components of the experiment (moored instruments, satellite, floats) should run for at least two years.

4. Shorter term (months-long) intensive study periods should make detailed process studies of local dynamics.

B. Processes and phenomena

1. "Inlet conditions" near Cape Hatteras should specify the initial stream path and structure, and the mass- and momentum transport.

2. Meander dynamics "intrinsic" to the Gulf Stream, such as growth and propagation of instabilities, and especially finite amplitude nonlinear processes, must be better described and understood.

3. The "external" field of eddies and rings neighboring the Gulf Stream are inherently and essentially coupled to the meanders; new dynamical observations and models are required for these processes.

4. Interactions with the broader region of recirculation and its eddy variability must be included in the study.

5. Measurements will be required to specify "boundary conditions" sufficient to update the models; the specification of an appropriate distribution of resources for these purposes is an immediate research task.

6. Existing and developing numerical models should be intercompared against each other and with a variety of existing data sets.

7. Numerical simulation studies should be undertaken to suggest the optimal distribution of observations, and the required accuracies and resources for prediction purposes and for model verification.

C. Immediate needs and objectives

1. A pilot experiment is needed to develop efficient techniques to monitor inlet conditions, and model simulations are needed soon to determine the required observational accuracies for these parameters.

2. A workshop on numerical modeling of the Gulf Stream should be held to intercompare models which contain different dynamics and have different ways of specifying boundary conditions, especially for open boundaries.

2A. REPORT OF THE WORKING GROUP ON OBSERVATIONAL ISSUES

Co-chairmen: Nelson Hogg  
D. Randolph Watts

Insufficient knowledge presently exists of the dynamical workings of the Gulf Stream and its nearby recirculation regions. The observational group strongly believes that a major goal of SYNOP should be to extend and improve this understanding of fundamental physical processes. This should be done in concert with the development of better numerical models (predictive and otherwise).

Table 2.A.1 summarizes the deliberations of this working group. The important phenomena as we know them were grouped by length scale as listed down the left side. Across the table, heading the right hand columns are categories representing the host of measurement techniques available to study these phenomena. For simplicity, several types of measurements are lumped together under broad categories, e.g., "ship", as noted at the bottom. We attempted to assign a simple rating (see key in table) regarding how well suited the techniques are for each of the phenomena. It is clear that each measurement technique has its place and that some are more generally applicable than others. It is also clear that no one technique is sufficient - most questions will involve the integration of a variety of techniques and strategies. We also felt that some redundancy and overlap of technique is highly desirable during the intensive observational program.

Discussion followed regarding the relative priorities of the listed phenomena within the context of SYNOP. Highest ranking (A) was given to those items in Table 2.A.1 which were both believed important to the dynamics of the Gulf Stream and realistically measurable within the scope of the program; detailed recommendations on these items are given below. Topics of low priority (C) include the general subtropical gyre circulation in which the Stream is embedded but which clearly demands a scale of measurement that is unattainable with our resources. The Deep Western Boundary Undercurrent was also given low priority, as we have no evidence that its variability influences Gulf Stream meanders. Similarly, topographic effects such as the local influence of seamounts and the explicit investigation of topographic Rossby waves were also downrated as it was believed that these are not central to the problem.

Of somewhat higher ranking (B) was the subject of air-sea interaction through heat exchange and wind stress. These processes may be difficult to measure in situ as it is probably not feasible to set surface moorings in the near field of the Gulf Stream at this time, but every effort should be made to use the routinely collected and analysed data to assess the importance of air-sea interactions. Although the question of how the Stream separates from the coast at Cape Hatteras is very interesting, this was not deemed to be of fundamental importance to SYNOP. Undoubtedly much pertinent information will be collected, but an explicit program designed to attack the separation mechanism was not felt to be appropriate. At the mesoscale, we considered the tracking of rings once they are detached from the stream to be important in that their motions contribute to path fluctuations, but that the detailed

Table 2.A.1.1.

## OBSERVATIONAL PRIORITIES &amp; METHODS

SCALE	PRIORITY	GULF STREAM PHENOMENA/DYNAMICS	PLATFORM		MOORINGS		REMOTE		LAGRANGIAN	
			SHIP	AIR	CM	IES	TOMO	ALT	IR	FLOAT SURF.D.
LARGE SCALE	C	general circulation								
		subtropical gyre	..... 0					0	0	0 .. 0
	B	air-sea interaction (wind stress / thermal)						0	0	
	A	basin bathymetry & large-scale seamount effects	... X	X				X	X	X .. X
	A	volume transport	..... X			X	0	X		
	A	potential vorticity & tracer distributions	..... X	0		X		X		X ..
	A	eddy-mean field interactions	.... X			X	X			
	C	deep western boundary undercurrent	..... X			X				X ..
	A	recirculation gyres	..... X			X	0	X		X .. X
	B	separation physics	..... X	X		X	X	X	X	X .. X
			..... X			X				X ..
MESO- SCALE	A	inlet conditions	..... X			X			X	X ..
	A	meanders / path dynamics / BC & BT instabilities	.... X	X		X	X	X	X	X .. X
	B	rings - detached ring motions	....					X	X	0 .. X
	A	ring/Gulf Stream interactions	.... X	X		0	0	0	X	X .. X
	C	topographic effects - TRWs	.....			X	0	X		
	C	local effects of seamounts	..... X			0	0	0	0	X ..
	A	eddy radiation or inputs (side boundary conditions)	.... 0	X		X	X	0		0 .. 0
	B+	shingles, streamers, outbreaks	... X	X					X	0 ..
	B	intrusions, interleaving, mixing	X	X						0 ..
SMALL SCALE										

suitability of measurement method:

X - major importance

0 - minor importance

o - possible ancillary information

"SHIP" includes: Pegasus, CTD, Ametek, XBT, XCP

## I.7

study of separated rings was outside the SYNOP focus. Small scale processes such as shingles, streamers, warm and cold "outbreaks", intrusions and water mass interleavings are a common feature of surface infrared measurements; some attempt should be made to study their dynamical structure through in situ observations.

Highest priority (A) was given to the following subjects of Table 2.A.1 (listed in no particular order within scales):

a) Basin bathymetry: There is a provocative coincidence between the location of the New England Seamount Chain and the position of largest Gulf Stream transport and largest surface eddy kinetic energy. In addition, numerical model studies suggest a significant influence and there are physical questions as to how much the chain might contribute to the dissipation of momentum through wave and form drag. A general study of the influence of the seamounts seems more appropriate for the theoretical and numerical modeling at this time. However, to the extent that the Seamounts might have an influence on the dynamics of the Gulf Stream at low order it is recommended that detailed measurements be made both upstream and downstream of the New England Seamount chain.

b) Transport: This is the parameter of most fundamental significance to the Stream but is also one with strong spatial variations, changing from some 60 Sverdrups at Cape Hatteras to as much as 200 Sv near the Seamount chain. It is important to characterize the volume or mass transport throughout the region from Cape Hatteras to the Grand Banks. For predictive modeling, the transport of the Stream at the inlet boundary appears to be the most important parameter to be prescribed. The simplest location appears to be near a nodal point at Cape Hatteras. The working group recommends that the Gulf Stream transport be monitored at Cape Hatteras and other representative locations.

c) Tracers including potential vorticity: There are strong water mass contrasts across the Stream especially in and above the thermocline. These give excellent tracers of fluid motions and the direct measurement of the potential vorticity balance is fundamental to the understanding of the dynamics of the Stream and its fluctuations. It is recommended that a shipboard hydrographic program be designed which will measure water mass properties on the regional general circulation scale with adequate resolution of the eddy scale to avoid aliasing.

d) Eddy-mean field interactions: The exchanges of momentum, energy, and vorticity between eddies and the mean field have been a central unresolved issue in physical oceanography for the past two decades. It seems likely that these interactions would be greatest near the Stream where the mean and the fluctuations are both maximum; a signature of this is thought to be the strong recirculation gyres observed in the region. Although it is not presently known how long a measurement program is needed to make significant measurements of these effects it is recommended that such measurements be begun with SYNOP to the extent that they do not seriously drain resources from the shorter time scale problems.

e) Recirculation gyres: The Stream cannot be considered in isolation from its surroundings. Not only is it likely that the recirculations to the north and south of the Stream are forced by the rectification of eddy motions but it is also probable that these westward flows are prone to their own instabilities that can feed back on the Gulf Stream. It is recommended that measurement programs be designed to encompass not only the Stream motions but also those in the recirculations.

f) Inlet conditions: Predictive modeling of the Gulf Stream region requires that conditions be known and specified along the open boundaries of the model. In particular at the inflow region, the position, angle and curvature of the Stream, along with its volume transport and momentum transport have been important parameters in modeling efforts. The simplest experimental strategy is to measure these where the Stream's meandering is at a minimum - namely at Cape Hatteras. It is therefore recommended that the appropriate Stream parameters (accuracy and type to be determined by the numerical working group) be monitored at Cape Hatteras.

g) Path dynamics and meanders: Of highest priority to the synoptic time scale Gulf Stream are the meander processes. In the thermocline these are the dominant mesoscale motions although there also exist strong barotropic motions which dominate the deep water currents. Because these processes are unlikely to be spatially homogeneous and because the largest change appears to take place across the seamount chain it is recommended that two separate (but temporally coincident) experiments be designed one on either side of the Seamount chain, each with adequate resolution of the mesoscale motions. Adequate observation of these phenomena will require periods of intensive measurements and the study of several events or realizations.

h) Ring-Gulf Stream interactions: Rings dominate the thermocline motion field and consequently can have a strong influence on the path of the Stream especially when nearby. It is recommended that some focus be given to this coupling and its dynamic evolution.

i) Eddy radiation: There exist other forms of eddy motions in the vicinity of the Stream which are distinctly different from the ring and meander features. These can be of large amplitude especially beneath the thermocline and may also be important to the problem of Stream path determination. It is recommended that the moored arrays be designed so as to be able to observe possible radiated eddy motions.

2B. REPORT OF THE WORKING GROUP ON MODELING AND PREDICTION

Co-chairmen: Jim Carton  
Glenn Flierl

The discussions of the modeling and prediction working group are briefly summarized in this report. We discussed the objectives of the SYNOP experiment, the theoretical work required, and the steps which need to be taken immediately to prepare for the experiment. The two aspects considered, dynamical and predictive modeling, are closely interconnected: the dynamical findings will be incorporated into the predictive schemes, and, concomitantly, the results from predictive modeling efforts provide data sets which can be used to test dynamical ideas.

1. Region for the SYNOP Experiment

It was felt that the region from Cape Hatteras to the Grand Banks and from the center of the recirculation region to the topography at the north should be regarded as the study region.

2. Times

The experiment should involve two time scales: long-term measurements from satellite, moored instruments and Lagrangian tracers; and, at a more intensified level, several periods of perhaps a few months duration of detailed surveying and profiling activities.

3. Dynamical Objectivesa. Meander Dynamics

The simplest description of meandering as a nonlinear process would be estimates of the propagation and growth as functions of wavelength/amplitude. This may not be adequate in the strongly nonlinear regime, but does seem an informative first step. There are a number of estimates which have used basically linear ideas, but no detailed comparison with linear or nonlinear models has yet been made. Indeed there are discrepancies among the various models themselves which must also be resolved.

b. Signatures of the Stream

To what degree are the surface front or the traditional  $15^{\circ}\text{C}$  at 200 m adequate descriptors of the Stream? How much does the structure vary in the highly curved sections, in different spatial regions at different times?

c. Details of Model Dynamics

As yet, the comparisons between the quasi-geostrophic vs. primitive equation models are incomplete; recent work has suggested noticeable differences when the Rossby number is comparable to those found in the Gulf Stream, but it is not clear to what extent vorticity or energy budgets in an unstable, meandering current will be qualitatively similar for the two models. This type of comparison is underway for general circulation models (GCMs) and should be done for limited area models.



#### d. Ring Formation Scenarios

A number of mechanisms have been suggested as either necessary or greatly enhancing the probability of ring formation: the changes in meander structure due to the seamount chain, pre-existing rings near the Stream, strong nonlinearity, and baroclinicity coupled with beta effects. These mechanisms must be explored in detail, with special attention given to the observational tests which may be able to distinguish different processes.

#### e. Radiation

How strong is eddy radiation from a nonlinear, strongly meandering current? What measurements are necessary to determine the amount of radiation and its importance in the dynamics of the Stream? Analysis of the existing GCM data should be very helpful in understanding the role of this process. In addition, process models of radiation and boundary forcing need to be extended and coupled properly together.

#### f. Recirculation and Intermediate Field

What are the scales of the recirculation region? How much of the reverse flow is contained in intense jets or filaments? What processes maintain the circulation in this region?

We need to explore in more detail the structure of the recirculation regions in the numerical models and to examine the data required to gain an adequate description of the kinematics of this region. The satellite data will cover this region, but may have difficulty with mesoscale filament structure. We feel that data along the southern portion of the region will be helpful in understanding both the radiation processes and the signature of the recirculation. Modelling and objective analysis work is required to determine more precisely what types of data is required and how often it must be gathered.

#### g. Historical Data Analysis Proposal

We suggest that a listing of all available data in the region be gathered and circulated: XBT, AXBT, IES, floats and drifters, SST, sea level, AVHRR, current meter, CTD profiles, etc. From this, a period with relatively frequent observations in the region can be selected and the data gathered and processed to be used in comparisons and testing of the current models of the region.

#### h. Mean Fields

How accurately can the mean fields be determined and what is the required length of time for the measurements? The numerical models indicate that means settle down fairly quickly but that Reynolds fluxes of the type found in the mean vorticity budget may require times on the order of 10 years to give stable estimates. We thus were led to suggest that the focus of the experiment be upon measuring the variability of the Gulf Stream system, rather than attempting at this time to do complete mean budgets. Obviously, the data will also be of use in the latter process, but we did not think that it would be complete enough.

#### i. Secondary Objectives

The modelling and prediction group suggested that several objectives from previous discussions should be regarded as secondary for this experiment (though they may be very important objectives), given the expected duration and level of effort. These included balances of the

mean dynamics, detailed studies of rings as isolated eddies (since the WCR project has a fairly large data set on this topic), smaller scale processes, and longer term air-sea influences.

#### 4. Prediction:

##### a. Data Requirements

Experience with prediction and data assimilation techniques suggests space and time scales for collecting the data necessary to initialize and advance the models in time. Much of this knowledge comes from eddy field models rather than Gulf Stream models, and more experiments are needed to determine the optimal distribution of resources for short-term or longer-term prediction and for the testing and verification of the models.

##### b. Intercomparisons

A number of open-ocean models have been developed or are under development -- e.g. at Harvard, NCAR, and NORDA -- for application to Gulf Stream problems. There are some overlaps as well as some differences between these models, but there have not yet been detailed intercomparison studies which reveal the strengths and limitations of the various dynamics / boundary specification techniques. Planning for such studies is required.

##### c. Workshop on Open Boundary Conditions

We recommend that a workshop be held to explore and evaluate the methods currently in use or new procedures for specifying and solving open boundary condition models.

##### d. Design of Initialization and Verification Data Sets

From the currently available data, and the data gathered from the historical data analysis efforts, sample initialization and boundary condition fields should be constructed to be used for intercomparison and also for model verification exercises.

##### e. Standard Stream structures

One method for initialization involves the use of standardized structures for the Gulf Stream with a few degrees of freedom which can then be determined from a relatively small data set. For example, one could use standardized shapes and simply calibrate the amplitude by a measurement of transport. Studies are required to determine what structures are best and what parameters must be measured to characterize the Gulf Stream inflow or initial flow field.

##### f. Objective Analysis and Statistical Issues

Straightforward objective analysis methods will require special adaptations for Gulf Stream application, since the flow field is anisotropic and the eddy field may be inhomogeneous and nonstationary. Methods to deal with these problems must be developed and then applied to the problem of assimilating data into models. From both the objectively analyzed fields and the output of predictive models, we can obtain data sets of great use in dynamical and forecasting studies. Further work is required on the analysis of error statistics, the effects of removing simple model structures, and updating procedures.

### 3. STRAWMAN OBSERVATIONAL PLAN

Relatively little progress was made within the time limitations of this Workshop toward the design of a complete experiment; however, three important guidelines were adopted.

Firstly, the region of consideration is that bounded by Cape Hatteras on the west, the Grand Banks on the east, and roughly the centers of the recirculation gyres to the north and south (shown in Figure 3.1 by the dotted line).

Secondly, this large area can be covered by satellite measurement systems but cannot be uniformly covered by experiments aimed at the intermediate scale dynamical properties of the Gulf Stream. Therefore, two focused experiments should be carried out in smaller areas, one on either side of the seamount chain, as indicated by the stippled squares in Figure 3.1. These two regions are characterized respectively by converging and diverging transport from the recirculation gyres; both regions have large amplitude meanders and strong interactions with rings, but the relative strengths of the barotropic and baroclinic circulations and eddy fields are thought to differ considerably between them. Additional regions of concentration indicated in Figure 3.1 are at Cape Hatteras and along the southern open boundary of the region, in order to obtain appropriate inlet and boundary conditions. Some effort should be made toward linking these intensively sampled regions with more sparsely spaced instrument systems. A natural coupling will be provided by satellite measurements, the Lagrangian floats, the large scale hydrographic program, and the numerical models themselves.

A third important constraint, provided by ONR, is that the main field program should occur in a two-year period beginning with FY87. Discussions at the Workshop indicated that this duration is certainly a minimal requirement for several of the SYNOP objectives, such as are listed in the Working Group Reports.

A framework for the shipboard programs will be provided by the moored systems, in particular the inverted echo sounders, current meters and tomographic transceivers. It seems especially important, therefore, to first attack the problem of array design. At this time there is no compelling reason to differentiate between the two proposed intensive areas for these design purposes. As discussed above, it is important that these arrays be capable of coherently observing the important mesoscale fluctuations both in the Gulf Stream and the neighboring recirculations to the north and south. A tentative design for such an array is given in Figure 3.2. The current meter moorings are set in 3 groups of five moorings spanning the mean Gulf Stream so as to observe horizontal and vertical structure both in and away from it. The inverted echo sounders are deployed so as to extend the spatial sampling significantly in the alongstream direction, thereby giving far better coverage of meander processes.

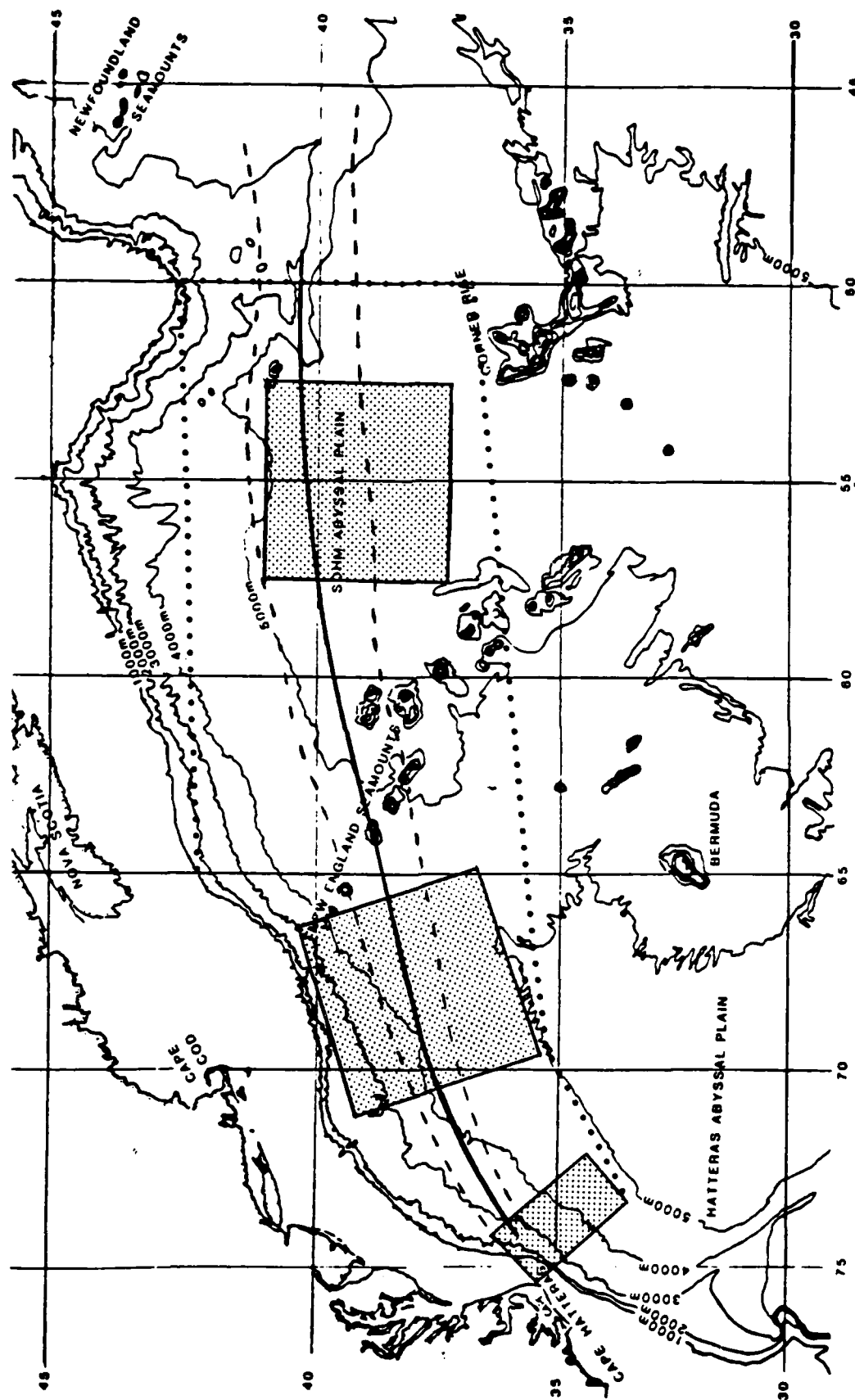


Figure 3.1. Strawman Experiment: Regions of Concentration.

The Gulf Stream north wall (bold line)  $\pm 1\sigma$  (dashed) is indicated.

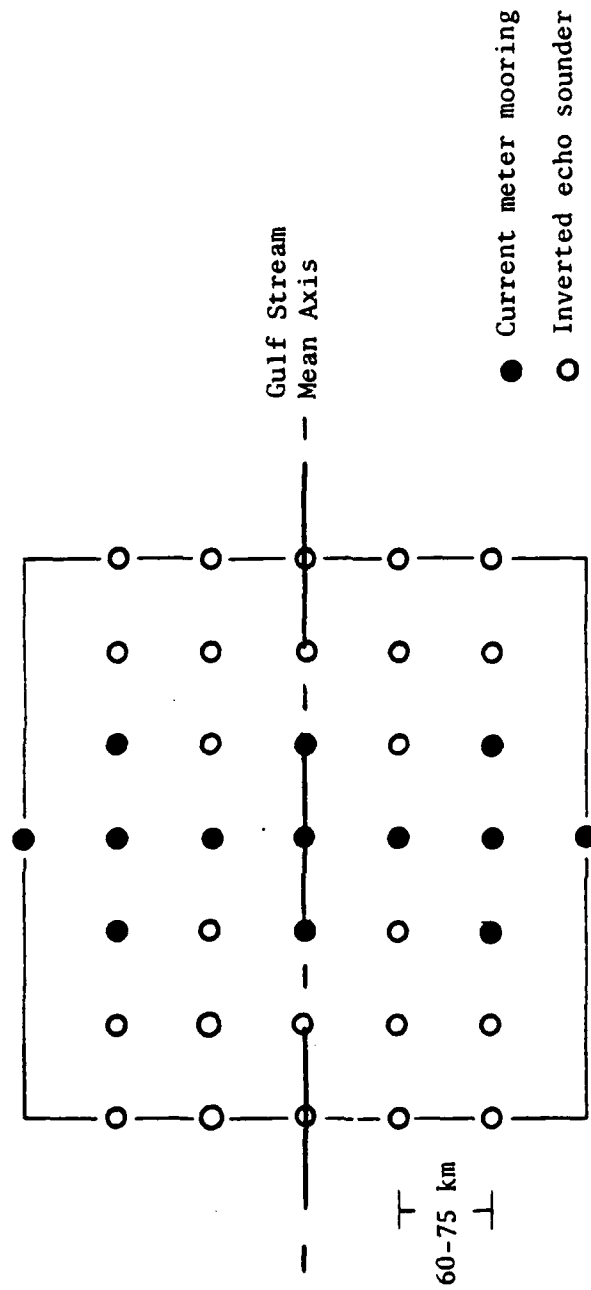


Figure 3.2. Strawman Moored Array Design

#### 4. GENERAL RECOMMENDATIONS

Specific recommendations regarding observational and theoretical plans have been given in the working group reports. In addition to these, the following recommendations were agreed upon in plenary discussion regarding SYNOP experimental design and management.

a) Data Telemetry: In the long run it will be vitally important to be able to telemeter suitable information on a near real time basis in order to update predictive models. However, it is not clear what types of data will be most useful, and we have not yet reached a level of understanding of the basic physical processes in the ocean or the models. Consequently, the incorporation of telemetering moored systems into the experimental plan does not seem crucial. A consensus of the group was that such technology should be developed but not at the expense of draining effort or resources from the scientific issues.

b) Pilot experiments: Some discussion of the workshop was devoted to the possibility that preliminary observational work should be conducted before the main experimental period. One recommendation was that a measurement program for the critical inlet conditions at Cape Hatteras be designed for the coming year, in order that a resource-efficient monitoring program of sufficient accuracy be in place during SYNOP.

c) Management: A scientific organizing committee should be established which is representative of the various efforts within SYNOP. This committee would not attempt to prefilter proposal submissions to ONR (or other agencies). It would coordinate activities such as planning meetings and the field experiment, disseminate information among the participants and serve as a point of contact between the funding agencies and the larger group. On an interim basis this committee will be the ad hoc workshop organizing committee with the addition of the working group chairmen.

d) Meetings: It is expected that smaller meetings will be needed in the near future to focus on specific issues, both modeling and experimental. For example the design of a pilot experiment, array design for the larger experiment, and open boundary conditions in numerical models are all subjects that require timely discussions. There is a special session on meanders at the January 1986 ASLO meeting in New Orleans. It is suggested that it may be appropriate to hold a general meeting of the SYNOP group following that meeting.

e) Telemail drop: In order to facilitate communication and the exchange of ideas it is recommended that a telemail drop (perhaps a "GULF.STREAM" mailing list) be set up as soon as possible.

5. APPENDICES

- A. Letters of Invitation
- B. SYNOP Program Description (T. Curtin, ONR)
- C. Agenda
- D. List of Participants



## LETTER OF INVITATION

February 25, 1985

TO: GULF STREAM WORKSHOP PARTICIPANTS

This letter is to request your participation in a workshop planned for April 23-26, 1985 at the URI Alton Jones Conference Center, West Greenwich, Rhode Island hosted by the University of Rhode Island with Office of Naval Research support. The primary purposes of the workshop are:

1. to review the present theoretical and observational knowledge about the Gulf Stream, and
2. to formulate and coordinate future Gulf Stream research efforts among the interested scientists.

### PROGRAM

Present plans call for discussion sessions on observations (in situ and remote sensing), and theoretical and numerical modeling results. In each category, a balance of presentations will be sought to review past results, introduce developmental techniques, and present strawman research plans for the future. The format will feature a few invited "keynote" speakers, with poster and short oral presentations for most other participants. Open workshop sessions are planned for various working groups to draft improvements on the strawman research plans, for plenary session discussion and iteration.

The list of invitees is given in Appendix I; the tentative agenda is in Appendix II.

### PAPERS/ABSTRACTS

Appendix IV, to be returned by 11 March 1985, polls your preferences regarding poster or oral (with time estimate) presentation, and asks for a tentative title/topic. The intention is to make posters the preferred mode of presentation at this workshop; they will remain up the entire meeting period, and have a scheduled time for individual attention and short verbal summary by the author.

Abstracts from persons interested in making a poster or oral presentation must be returned by 1 April 1985, to be distributed prior to the conference. Appendix III gives the format.

Each author will be requested to bring a written version of his/her presentation to the Workshop for publication in a PROCEEDINGS volume within a few weeks following the Workshop.

### REGISTRATION & HOUSING

Pre-registration deadline is 1 April 1985. A REGISTRATION FORM is enclosed, to be returned by this date. All rooms are doubles with twin beds. You may designate roommates, or our plan is to put attendees into



appropriate shared rooms. Room reservations cannot be guaranteed after 1 April.

We have requested funding for this workshop from the Office of Naval Research, to cover the conference facilities and the meals and lodgings at the conference center for all participants. Additionally, a limited amount of travel support may be provided, but please only request this if you absolutely need the support.

Please send replies to: Conference coordinator, c/o D.R. Watts  
Graduate School of Oceanography  
South Ferry Road  
Narragansett, RI 02882

Sincerely,

*Randy Watts*

D. Randolph Watts, Convenor

INVITATION LETTER FOLLOWUP

March 8, 1985

TO: GULF STREAM WORKSHOP PARTICIPANTS

This letter is to give you more news about the Gulf Stream Workshop planned for April 23-26, 1985 at the URI Alton Jones Conference Center, West Greenwich, Rhode Island.

A reminder: your "Plans for Presentations" (an appendix to the 25 February invitation letter) should already be returned to me to assist with scheduling.

I met with Bryden, Hogg, Fofonoff, and Robinson this week to discuss the workshop plans. We felt that some advance exchange of ideas would be beneficial before attempting to reach a consensus at the Workshop regarding Gulf Stream research plans.

As a product of the workshop, it is hoped to draft a "cover document" describing a coherent research plan, around which proposals from individual investigators could be structured. In preparation for this, some informal correspondence between investigators could be initiated, xeroxed and distributed through my (Watts') office. Among this preparatory distribution of information, Tom Curtin at ONR has sent a short distillation of ONR's objectives in the new SYNOP program (copy enclosed).

All participants are invited to send me a 1-paragraph statement of their individual future research plans -- perhaps an excerpt from your recent ONR planning letter. A strawman list of overall plans and objectives would also be welcome. I will xerox those received by 22 March, and distribute them to the list of invitees.

Additionally, we felt it would be useful to hold two informal gatherings to discuss research plans:

18 March 2:00-5:00pm at URI (GSO), and

1 April 2:00-5:00pm at Harvard (Pierce Hall).

Those interested will go to an early dinner afterward. A check-off sheet is attached for you to reserve some time either of these days to present ideas for future work.

Sincerely,

*Randy Watts*

D. Randolph Watts

## PRELIMINARY PLANNING DISCUSSIONS

I would like to discuss future research plans at the

\_\_\_\_\_ 18 March 2-5pm URI meeting, \_\_\_\_\_ and go to dinner  
 \_\_\_\_\_ 1 April 2-5pm Harvard meeting, \_\_\_\_\_ and go to dinner .

Name: \_\_\_\_\_

return to : Conference coordinator, c/o D.R. Watts  
 Graduate School of Oceanography  
 South Ferry Road  
 Narragansett, RI 02882- 1197

APPENDIX 5B. SYNOP PROGRAM DESCRIPTION (T. Curtin, ONR)

## Synoptic Ocean Prediction (SYNOP)

The overall objective of the Synoptic Ocean Prediction (SYNOP) program is to expand our understanding of synoptic scale ( $\delta t \sim 2-200$  days,  $\delta x, \delta y \sim 6-600$  km,  $\delta z \geq 10$  m) processes within the ocean. A specific goal is to evolve and test this understanding through the development of a predictive capability for synoptic scale features within specific oceanic regions. A central focus in the development is the synthesis of observational and modeling techniques enabling timely predictions. Regions of high synoptic-scale variability are of primary interest.

Initial research efforts will concentrate on model physics and formulation, remote (satellite, tomographic, doppler) and direct (drifter, flow, hydrographic) sensors and data acquisition systems, and assimilation procedures for non-uniform data into models. Field observations during FY87-88 will be in the western North Atlantic, where synoptic-scale processes associated with the Gulf Stream are particularly energetic. Reduced field efforts in FY89 will seek to determine minimum input data requirements for specified prediction skill, and will consider model applicability to other regions. Refinements of models and sampling strategies in FY90 will result in a useful predictive capability for synoptic-scale regional evolution.

This research program is comprehensive, ambitious, and high risk. Real time model-data integration requires synthesis of a broad range of specific investigations. Data density and transmission as well as model size and complexity require state-of-the-art instrumentation, management skill, computational power and algorithms. The degree of success of research into nonlinear processes within high energy regimes cannot be determined a priori. Success depends on the talent and cooperation of a wide spectrum of scientists from universities, laboratories, institutions and agencies.

The SYNOP program has a funding duration from FY86 through FY90. ONR point of contact (Code 422PO): Tom Curtin (202)696-4112.

# I.21

## Gulf Stream Workshop Agenda 23-26 April

TIME	TUESDAY	WEDNESDAY	THURSDAY	FRIDAY
0745-0830	--	Breakfast	Breakfast	Breakfast
0830	--	Obs. New Techn. K4: Rossby	Future Plans (modeling) individual presentations & discussions	Strawman Research Plan & Discussions
0900	--	"	"	"
0930	--	"	"	"
	Obs. Review K1: Fofonoff	O: Cornillon O: Bane	"	"
1000	"	P: Spiesberger etc	"	"
	"	P: Rizzoli	"	"
	"	P: Watts&Tracey	"	"
1030	coffee	coffee	coffee	coffee
1100	Theor. Review K2: Hogg	Models New Techn. K5: Robinson	Plenary discussion of purpose & objectives	Final discussion & reach agreement
1130	"	"	"	"
	O: Flierl et al.	P: Spall&Pinardi	"	"
1200	P: Cushman-Roisin	P: Miller	"	"
	P: Huang	P: Holland&Evans	"	"
1215-0115	Lunch	Lunch	Lunch	Lunch
0115	Modeling Review	Observations	Working Group	--
0130	K3: Haidvogel	P: Mooers	meetings	--
	"	P: Johns&Watts	"	--
0200	"	O: Carter	"	--
	O: Adamec	P: Pickart&Hogg	"	--
0230	P: Pratt	P: Bane&Watts	"	--
	P: Rizzoli et al.	P: Dewar&Bane	"	--
		P: Bower	"	--
		P: Hendry	"	--
0315	coffee	coffee	coffee	--
0330	Forecasting & Future Plans	no meeting	Plenary Reports from Working Groups	--
0400	O: Thompson	"	"	--
	O: Mitchell	"	"	--
0430	P: Hallock	"	"	--
	P: Calman	"	"	--
0500-0600	Social Hour	Refreshments	Refreshments	--
0600-0700	Dinner	Dinner	Dinner	--
0700	--	Future Plans (observations) individual presentations & discussions	Iteration of Plans by Working Group Chairmen	--
0730	--	"	"	--
0800	--	"	"	--
0830	--	"	"	--

## Gulf Stream Workshop

W. Alton Jones Conference Center  
West Greenwich, Rhode Island

23-26 April 1985

PARTICIPANTS

Dr. David Adamec  
Department of Meteorology, Code 63Ac  
Naval Postgraduate School  
Monterey, CA 93943

Dr. John M. Bane  
Marine Sciences Program  
Venable Hall 045A  
University of North Carolina  
Chapel Hill, NC 27514

Ms. Amy S. Bower  
Graduate School of Oceanography  
University of Rhode Island  
Narragansett, RI 02882

Dr. Jack Calman  
Applied Physics Lab  
John Hopkins University  
Laurel, MD 20810

Dr. Everett F. Carter  
Graduate School of Oceanography  
University of Rhode Island  
Narragansett, RI 02882

Dr. Jim Carton  
Pierce Hall 100-C  
Harvard University  
29 Oxford Street  
Cambridge, MA 02138

Dr. Peter Cornillon  
University of Rhode Island  
Graduate School of Oceanography  
Narragansett, RI 02882

Dr. Thomas B. Curtin  
Code 422 P.O.  
Office of Naval Research  
800 North Quincy  
Arlington, VA 22217

Dr. Benoit Cushman-Roisin  
Mesoscale Air-Sea Interaction Group  
Florida State University  
Tallahassee, FL 32306

Dr. William Dewar  
12-5 Venable Hall  
University of North Carolina  
Chapel Hill, NC 27514

Dr. J. Chris Evans  
NCAR  
P.O. Box 3000  
Boulder, CO 80307

Dr. Glenn Flierl  
Building 54-1420  
Massachusetts Institute of Technology  
Cambridge, MA 02139

Dr. Nick Fofonoff  
Woods Hole Oceanographic Institution  
Woods Hole, MA 02543

Mr. Craig Gilman  
Graduate School of Oceanography  
University of Rhode Island  
Narragansett, RI 02882

Dr. Dale V. Haidvogel  
NCAR  
P.O. Box 3000  
Boulder, CO 80307

Dr. Zack Hallock  
NORDA  
Code 331  
NSTL Station, MS 39529

Dr. Ross M. Hendry  
Atlantic Ocean Lab  
Bedford Inst. Oceanography  
Dartmouth, Nova Scotia, Canada B2Y 4A2

Dr. Nelson Hogg  
Woods Hole Oceanographic Institution  
Woods Hole, MA 02543

Dr. William Holland  
NCAR  
P.O. Box 3000  
Boulder, CO 80307

Dr. Rui Xin Huang  
GFD Program  
POB 308  
Princeton University  
Princeton, NJ 08542

Dr. William E. Johns  
RSMAS  
University of Miami  
4600 Rickenbacker Causeway  
Miami, FL 33149

Dr. Richard Lambert  
National Science Foundation  
Physical Oceanography Program  
Room 606  
Washington, DC 20550

Dr. Kevin Leaman  
RSMAS  
University of Miami  
4600 Rickenbacker Causeway  
Miami, FL 33149

Dr. Paola Malanotte-Rizzoli  
Room 54-920  
Department of Earth, Atmospheric  
and Planetary Sciences  
Massachusetts Institute of Technology  
Cambridge, MA 02139

Dr. Robert N. Miller  
Tulane University  
Mathematics Department  
New Orleans, LA 70118

Dr. Jim Mitchell  
NORDA Code 321  
NSTL Station, MS 39529

Dr. Chris N.K. Mooers  
Dept. of Oceanography  
Naval Postgraduate School  
Monterey, CA 93946

Ms. Lucy O'Keefe  
12-5 Venable Hall  
University of North Carolina  
Chapel Hill, NC 27514

Mr. Robert S. Pickart  
WHOI/MIT Joint Program  
Woods Hole, MA 02543

Dr. Larry Pratt  
University of Rhode Island  
Graduate School of Oceanography  
Narragansett, RI 02882

Dr. Allan Robinson  
Pierce Hall 100-C  
Harvard University  
29 Oxford Street  
Cambridge, MA 02138

Dr. Thomas Rossby  
University of Rhode Island  
Graduate School of Oceanography  
Narragansett, RI 02882

Mr. John Schultz  
12-5 Venable Hall  
University of North Carolina  
Chapel Hill, NC 27514

Mr. Michael A. Spall  
Dept. Applied Sciences  
Pierce Hall  
Harvard University  
29 Oxford Street  
Cambridge, MA 02138

Dr. John Spiesburger  
Woods Hole Oceanographic Institution  
Woods Hole, MA 02543

Dr. J. Dana Thompson  
Bldg. 1100, Code 323  
NORDA  
NSTL Station, MS 39529

Mrs. Karen L. Tracey  
Graduate School of Oceanography  
University of Rhode Island  
Narragansett, RI 02882

Dr. Randolph Watts  
University of Rhode Island  
Graduate School of Oceanography  
Narragansett, RI 02882

CMDR. Robert Willems  
Office of Naval Research, Code 422PO  
Ocean Science and Technology Detachment  
NSTL Station, MS 39529

PART II: PAPERS AND PRESENTATIONS

## Gulf Stream Observations

N. P. Fofonoff

Woods Hole Oceanographic Institution

Woods Hole MA 02543

## Abstract

Statistical characteristics of the Gulf Stream region have been described from ship drift records (Wyrski *et al.*, 1976), hydrographic and BT records (Dantzler, 1977), surface drifters (Richardson, 1983) and satellite observations (Cheney *et al.*, 1982; Menard, 1983). More recently, inverted echo sounders, neutrally buoyant floats and moored current meters have augmented the descriptions, particularly of the deeper layers. The general spatial distribution of eddy kinetic energy is now reasonably well known, although the intensities are poorly estimated by some of the techniques used and are likely to be uncertain within a factor of two or more in some areas.

The time scales associated with the Gulf Stream variability are less well known because few time-series measurements are yet available for their estimation. Estimates from current meter records show that half of the eddy energy is at periods of 50 days or less within the Gulf Stream region compared to 100 days or more for the half-energy period in the Sargasso. Time scales in the deeper layers tend to be shorter, particularly where bottom slopes are encountered.

The range of phenomena present in the Gulf Stream is poorly known. Most of the observed events, such as meander and ring formation, are highly nonlinear and yet to be described quantitatively. The interactions of the Gulf Stream with the surrounding waters of the Sargasso and Slope Water regions are unknown. Few experiments to date have matched the temporal and spatial sampling criteria required to resolve the most energetic mesoscale variations of the Gulf Stream. The possibility of combining several techniques of measurement coupled with numerical models for data interpretation holds the prospect of a significant advance in our understanding of the dynamics of the Gulf Stream.



Our present conceptual models of the Gulf Stream are constructed as composites of descriptions based on many observations and dynamical interpretations. The rather simple picture sketched by Iselin (1936), shown in Figure 1, has been greatly elaborated in the past 50 years. Iselin and Fuglister (1948) in reviewing recent developments in the study of the Gulf Stream described a surprisingly modern view of a meandering stream of increasing amplitude from Cape Hatteras (Church, 1937), developing eddies of small scale (Spilhaus, 1940) as well as large scale that appear as meanders and loops of current that have broken off from the main stream. These descriptions coincided with new theoretical ideas about the dynamics of western boundary currents (Stommel, 1948). A major multiple-ship survey "Operation Cabot" carried out in 1950 (Fuglister and Worthington, 1951) provided detail about variations of the path of the Gulf Stream and formation of rings. Although much was learned about the Gulf Stream in the subsequent decade (Stommel, 1958), the next major step in observations was not made until the GULF STREAM '60 program (Fuglister, 1963). This program represented the first systematic multiple-ship survey of the Gulf Stream between Cape Hatteras and the Grand Banks. Eleven meridional hydrographic sections were made at  $2^\circ$  intervals between  $48^\circ\text{W}$  and  $68^\circ\text{W}$  extending from  $33^\circ\text{N}$  across the Gulf Stream to the continental shelf. In addition to the grid of stations, direct measurements in the Stream at 700 and 2000 m were made with neutrally buoyant floats.

Fofonoff and Hall (1983) computed transports of mass, momentum and kinetic energy for each of the sections obtained during GULF STREAM '60 to examine the downstream changes in the transports. An objective of the study was to estimate the magnitude of the downstream pressure gradient and the energy conversion accompanying the gradient. Several features of the Gulf Stream are evident from these data. The transport potential, contoured from nine of the sections, is shown in Figure 2. Although the mass transport remains relatively constant downstream, both the momentum and kinetic energy transports decrease as the Stream broadens and peak currents weaken (Figure 3). There is a well-defined high-velocity core (Figure 4) throughout the survey region with cross-stream scales approximating the Rossby radius of deformation ( $\sim 40$  km). There is a noticeable downstream slope along the northern edge of the stream, indicating detrainment of water into the Slope region. Fofonoff and Hall estimate the transport into the

slope Water region to be about  $9.4 \times 10^9 \text{ kg/m}^3$ . There is also flow in and out of the Sargasso, although the presence of eddies and rings south of the Gulf Stream complicates the flow pattern making it difficult to resolve.

Fuglister and Voorhis (1965) and Hansen (1970) studied meanders of the Gulf Stream by towing a thermistor submerged by a V-fin depressor along the Stream axis. These studies showed clearly the presence and downstream movement of the large meanders at phase speeds of 5-10 cm/s and wavelengths of 200-400 km (Figure 5). The mean values were 320 km and 8 cm/s, for about a 46-day period. The thermal pattern was, at times, very complicated and not easily obtained from shipboard.

Historical archives have been sources for several statistical investigations of currents and temperature variability in the Gulf Stream region. Wyrski *et al.*, (1976) compiled surface eddy kinetic energy (EKE) maps on a  $1^\circ$  grid from ship drift observations. East of Cape Hatteras, the eddy energies decreased from about  $2000 \text{ cm}^2/\text{s}^2$  to about  $600 \text{ cm}^2/\text{s}^2$  south of the Grand Banks of Newfoundland (Figure 6a). These energies correspond to rms speeds of 63 to 35 cm/s. Richardson (1983) computed surface eddy kinetic energies from surface drifters (Figure 6b). Peak energies exceeded  $2000 \text{ cm}^2/\text{s}^2$  between  $70^\circ\text{W}$  and  $60^\circ\text{W}$  downstream from Cape Hatteras. The diminishing energies in the surface layers downstream from about  $70^\circ\text{W}$  agrees with the estimates based on GULF STREAM '60 data. Dantzler (1977) estimated the distribution of eddy potential energy (EPE) from the fluctuations of the  $15^\circ\text{C}$  isotherm surface as measured by XBT's. The distribution on a  $2^\circ$  grid is shown in Figure 6c. The spatial distribution of EPE agrees remarkably well with eddy kinetic energies determined from current measurements along  $55^\circ\text{W}$  (Schmitz, 1977). The meridional variation of EKE at 600 and 4000 m is compared in Figure 7a with the rms variability of the  $15^\circ\text{C}$  isotherm. Recent comparisons of the eddy energies inferred from neutrally buoyant floats (Owens, 1984) with current meter data along  $55^\circ\text{W}$  show that the spatial distributions agrees quite well with each other (Figure 7b) and with the distribution obtained from XBT data. East-west and North-south sections of rms variability of depth of the  $15^\circ\text{C}$  isotherm through the Gulf Stream regions are given in Figure 8 to show the spatial distribution of variability of the  $15^\circ\text{C}$  surface. The agreement with direct current measurements provides some confidence that the spatial extent of the eddy field associated with the Gulf Stream is reasonably well known. The maps

obtained from SEASAT altimeter data (Menard, 1983) are based on one month of tracks and are not comparable statistically with the previous estimates. Yet the pattern and the magnitude of the rms surface topography (Figure 6d) agree surprisingly well with Dantzler's estimates of EPE.

The subsurface distribution of EKE is shown in Figure 9 for 500-600 m level and Figure 10 for the 4000 m level based on about 50 moorings deployed in several experiments in the Gulf Stream and adjoining regions. The Figures show rms eddy velocities as ellipses and mean velocity vectors computed from record lengths varying from about 9 months to 2 years against a background of surface drifter tracks (Richardson, 1983) depicting the meander envelope of the Gulf Stream. Most estimates are based on one year record lengths. The major and minor axes of the eddy ellipses are drawn to the same scale as the mean velocity and are proportional to the rms eddy components. Only recently have measurements been obtained in the upper 500 m within range of the Gulf Stream core (Hall and Bryden, 1985). Figure 9 contains a prominent gap between  $45^{\circ}\text{W}$  and  $60^{\circ}\text{W}$  where current measurements are yet to be made above the main thermocline in the Gulf Stream. The spatial pattern appears consistent with previous studies with the highest speeds near  $70^{\circ}\text{W}$ . The pattern at 4000 m is significantly different in that the highest speeds appear at  $55^{\circ}\text{W}$  over the Sohms abyssal plain.

In addition to the magnitude of the eddy velocity fluctuations, a representative frequency or period of the variations can be used to characterize the eddy field (Fofonoff and Hendry, 1985). As noted earlier, the phase speed of Gulf Stream meanders and their wavelength inferred from path determinations indicated a period of 40-50 days. A comparable time scale can be obtained from the kinetic energy spectra using the midpoint frequency  $f_{0.5}$  or period  $T_{0.5}$  separating the mesoscale energy into equal parts. The relationship of the midpoint frequency to the energy containing scales is illustrated in Figure 11. The kinetic energy spectrum is integrated to yield the cumulative kinetic energy distribution and is normalized by the total eddy kinetic energy to show the relative energy content of the current meter record as a function of frequency. The time scale  $T_{0.5}$  for the 500-600 m level is shown in Figure 12 and for the 4000 m level in Figure 13. The record durations are too short to yield stable estimates of  $T_{0.5}$ . However, some general features are evident. The longer periods are found above the main thermocline and outside of the Gulf Stream

## II.5

region. The periods at 4000 m level were shorter than the shallower levels except over the Sohm abyssal plain. Here, the deep time scales tended to be longer presumably because of the absence of bottom slopes to allow topographic modes.

Except for the surface layers where measurements are difficult to obtain, the intensities and time scales of Gulf Stream velocities have been sampled and estimates of statistical properties describing the flow field are now available over most of the region. The dynamics are still poorly understood. The sequence of events leading to ring formation has been not been described dynamically. The interactions of rings and eddies with the Gulf Stream are not understood. A coordinated experiment sampling the energetic mesoscale meander and eddy field of the Gulf Stream combined with numerical models to assimilate and interpret the data promises to provide a significant advance in our capability to understand and predict major features of Gulf Stream behaviour.

## References

- Cheney, R. E., and J. G. Marsh, 1981: SEASAT altimeter observations of dynamic ocean topography in the Gulf Stream region. J. Geophys. Res., 84, C1, 473-483.
- Cheney, R. E., J. D. Marsh and B. D. Beckley, 1983: Global mesoscale variability from collinear tracks of SEASAT altimeter data. J. Geophys. Res., 88, C7, 4343-4354.
- Church, P. E., 1937: Temperatures of the western North Atlantic from thermograph records. Publ. Sci. Ass. Oceanogr. Phys., No. 4, 1-32.
- Dantzler, H. L., Jr., 1977: Potential energy maxima in the tropical and subtropical North Atlantic. J. Phys. Oceanogr., 7, 512-519.
- Fofonoff, N. P., and M. M. Hall, 1983: Estimates of mass, momentum and kinetic energy fluxes of the Gulf Stream. J. Phys. Oceanogr., 13, 1868-1877.
- Fofonoff, N. P., and R. M. Hendry, 1985: Current variability near the southeast Newfoundland Ridge. J. Phys. Oceanogr. (in press).
- Fuglister, F. C., 1963: Gulf Stream '60. Progress in Oceanography, 1, 265-373.
- Fuglister, F. C. and L. V. Worthington, 1951: Some results of a multiple ship survey of the Gulf Stream. Tellus, 3, 1-14.
- Fuglister, F. C. and A. D. Voorhis, 1965: A new method of tracking the Gulf Stream. Limnol. and Oceanogr., 10 (Suppl.), R115-R124.
- Hall, M. M. and H. L. Bryden, 1985: Profiling the Gulf Stream with a current meter mooring. Geophys. Res. Letters, 12, 203-206.
- Hansen, D. V., 1970: Gulf Stream meanders between Cape Hatteras and the Grand Banks. Deep-Sea Res., 17, 495-511.
- Iselin, C. O'D., 1936: A study of the circulation of the western North Atlantic. Pap. Phys. Oceanogr. Meteorol., 4, 101 pp.
- Iselin, C. O'D. and F. C. Fuglister, 1948: Some recent developments in the study of the Gulf Stream. J. Mar. Res., 7, 317-329.
- Menard, Y., 1983: Observations of eddy fields in the northwest Atlantic and northwest Pacific by SEASAT altimeter data. J. Geophys. Res., 88, C3, 1853-1866.
- Owens, W. B., 1984: A synoptic and statistical description of the Gulf Stream and subtropical gyre using SOFAR floats. J. Phys.

Oceanogr., 14, 104-113.

- Richardson, P. L., 1983: Eddy kinetic energy in the North Atlantic from surface drifters. J. Geophys. Res., 88, 4355-4367.
- Schmitz, W. J. Jr., 1977: On the deep general circulation in the western North Atlantic. J. Mar. Res., 35, 21-28.
- Schmitz, W. J. Jr., W. H. Holland and J. F. Price, 1983: Mid-latitude mesoscale variability. Rev. Geophys and Space Phys., 21, 1109-1119.
- Spilhaus, A. F., 1940: A detailed study of the surface layers of the ocean in the neighborhood of the Gulf Stream with the aid of rapid measuring hydrographic instruments. J. Mar. Res., 3, 51-75.
- Stommel, H., 1948: The westward intensification of wind-drive ocean currents. Trans. Amer. Geophys. Un., 29, 202-206.
- Stommel, H., 1958: The Gulf Stream: A physical and dynamical description. University of California Press, 202 pp.
- Wyrski, K., L. Magaard, and J. Hager, 1976: Eddy energy in the oceans. J. Geophys. Res., 81, 2641-2646.

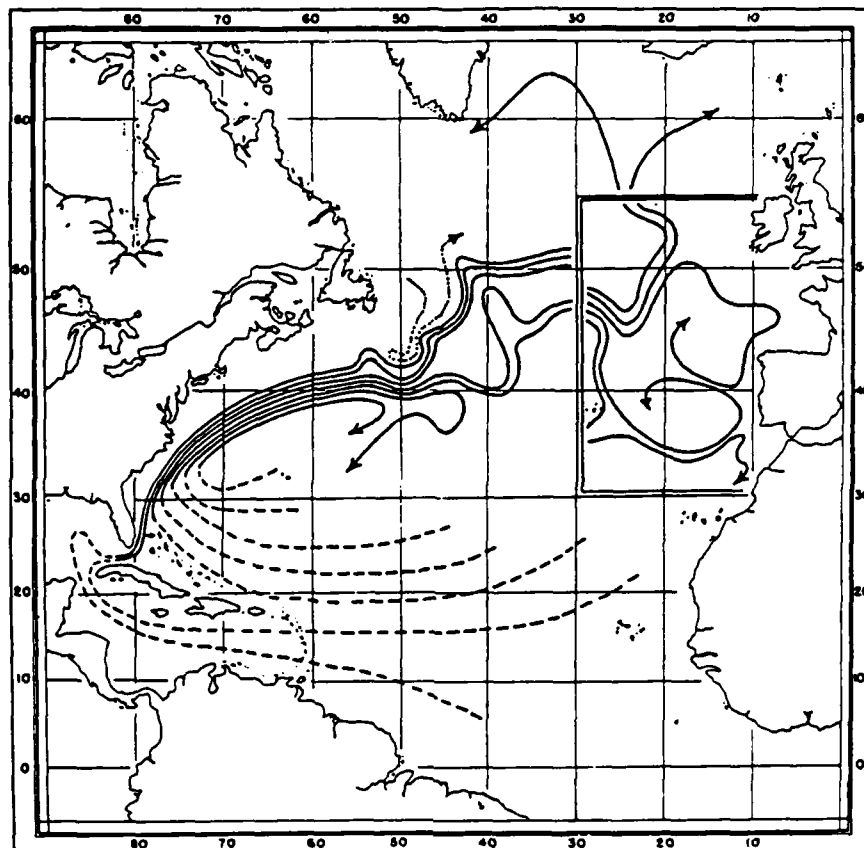


Fig. 1. Iselin's (1936) schematic map of North Atlantic circulation.

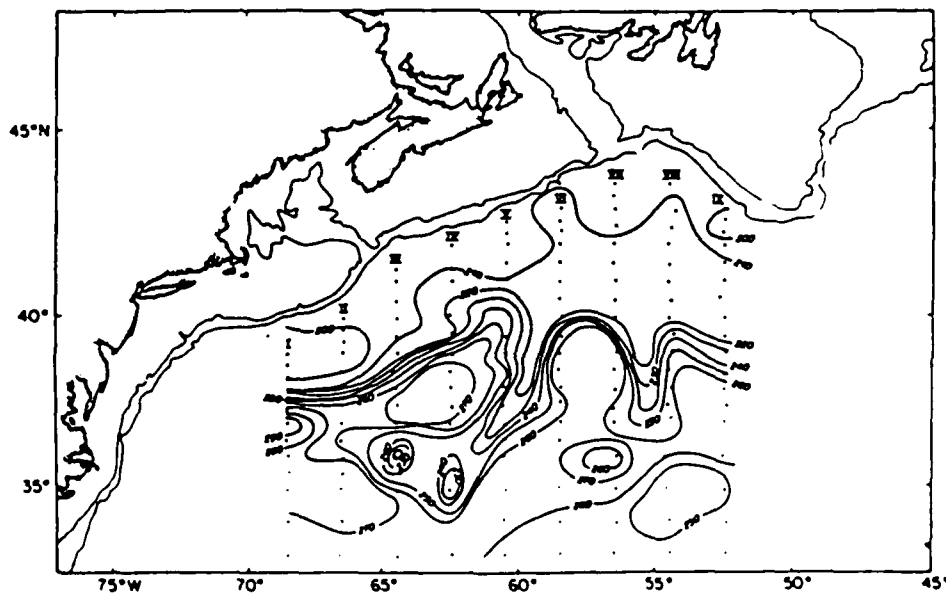


Fig. 2. Transport potential ( $10^5 \text{ J/m}^2$ ) relative to 3000 dbar from GULF STREAM '60 data (Fofonoff and Hall, 1983).

## GULF STREAM '60 SECTIONS

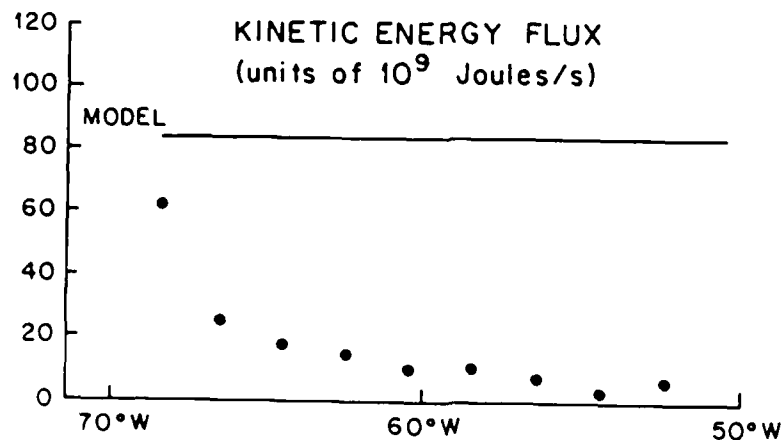
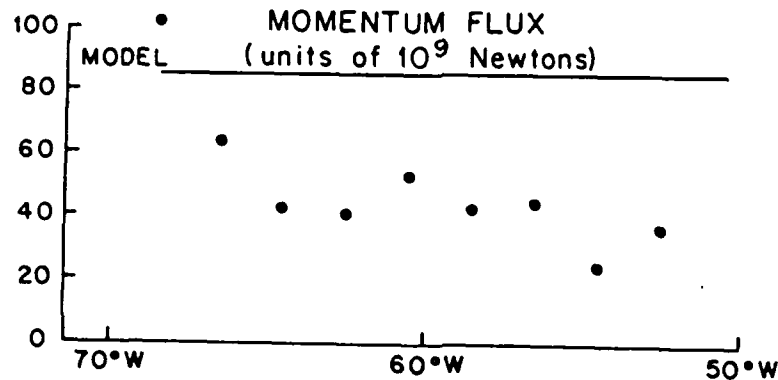
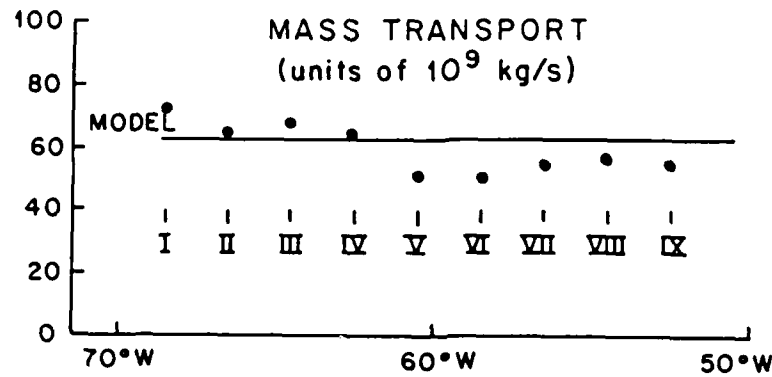


Fig. 3. Mass, momentum and kinetic energy fluxes in the Gulf Stream computed from geostrophic velocities relative to 3000 dbar (Fofonoff and Hall, 1983).



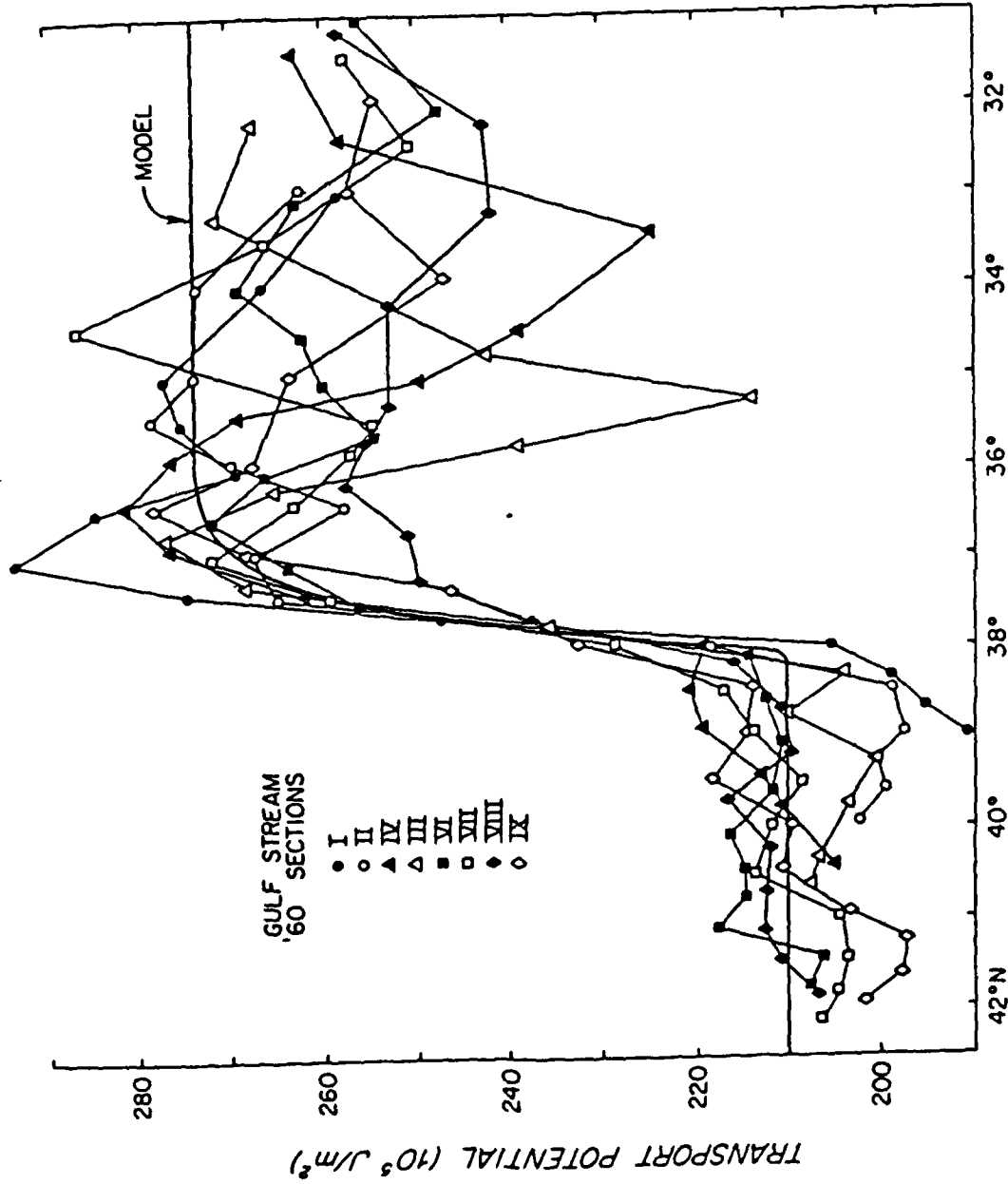


Fig. 4. Cross-stream profiles of transport potential for GULF STREAM '60 sections. The solid line shows transport potential for a two-layer inertial model with 40-km radius of deformation.

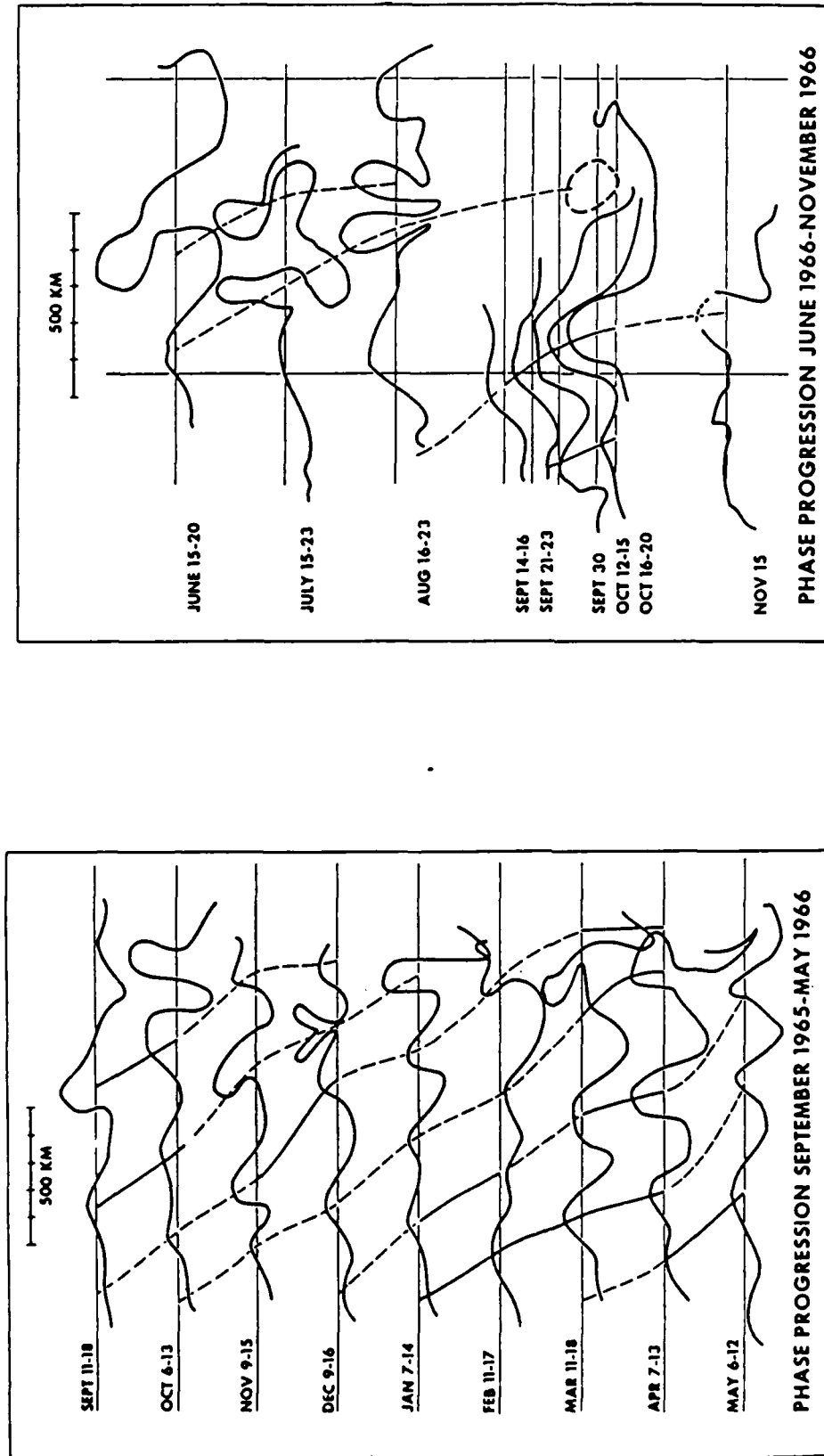


Fig. 5. Gulf Stream paths showing downstream propagation of meanders (Hansen, 1970).

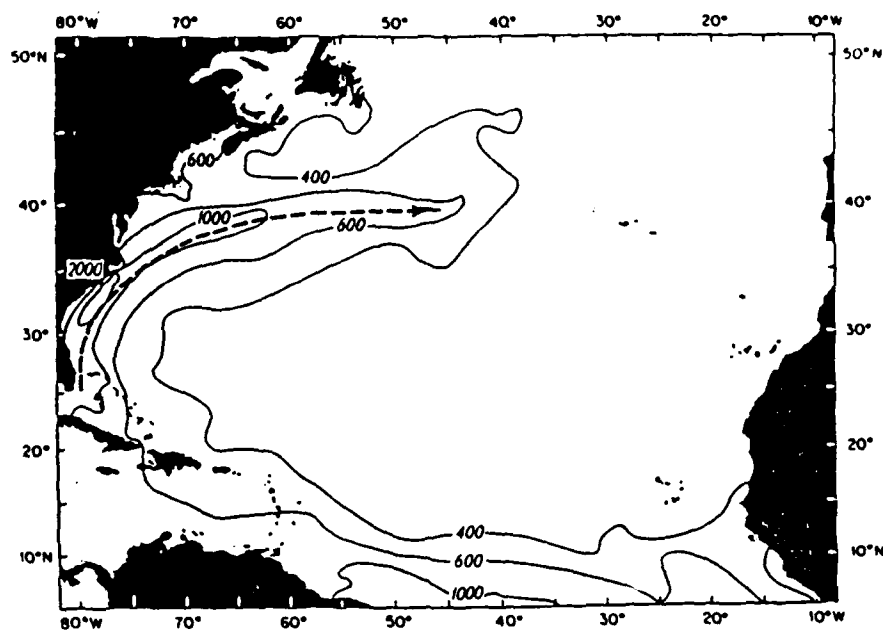


Fig. 6(a). Eddy kinetic energy inferred from ship drift reports in the Gulf Stream (Wyrski *et al.*, 1976, Schmitz *et al.*, 1983).

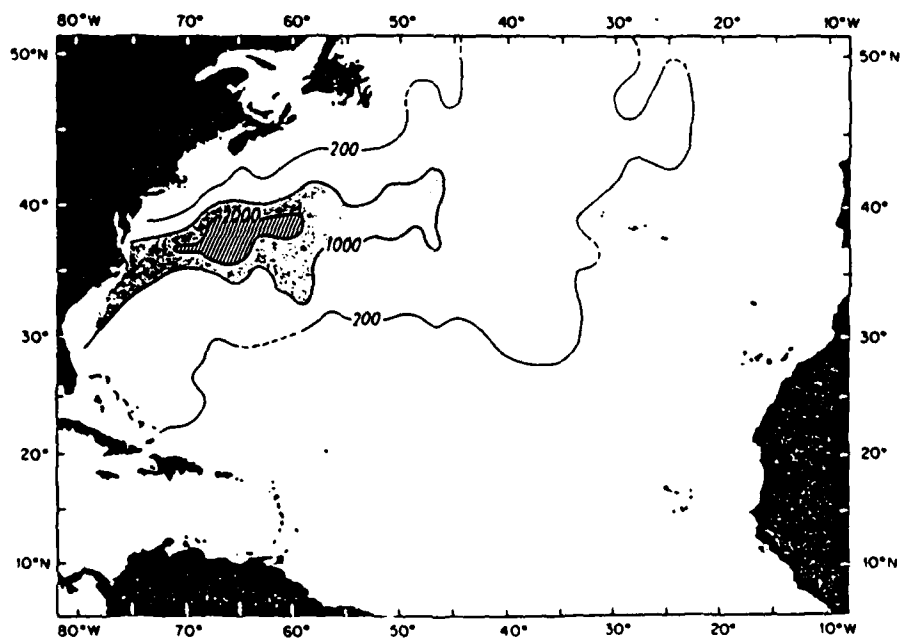


Fig. 6(b). Eddy kinetic energy inferred from surface drifters (Richardson, 1983, Schmitz *et al.*, 1983).

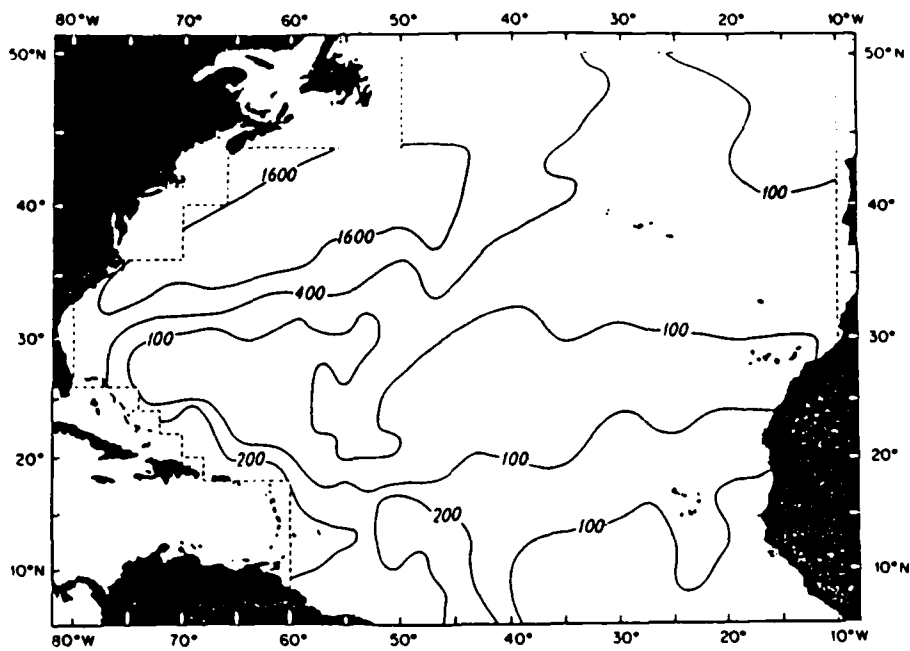


Fig. 6(c). Eddy variance of depth of 15°C isotherm (Dantzler, 1977, Schmitz *et al.*, 1983).

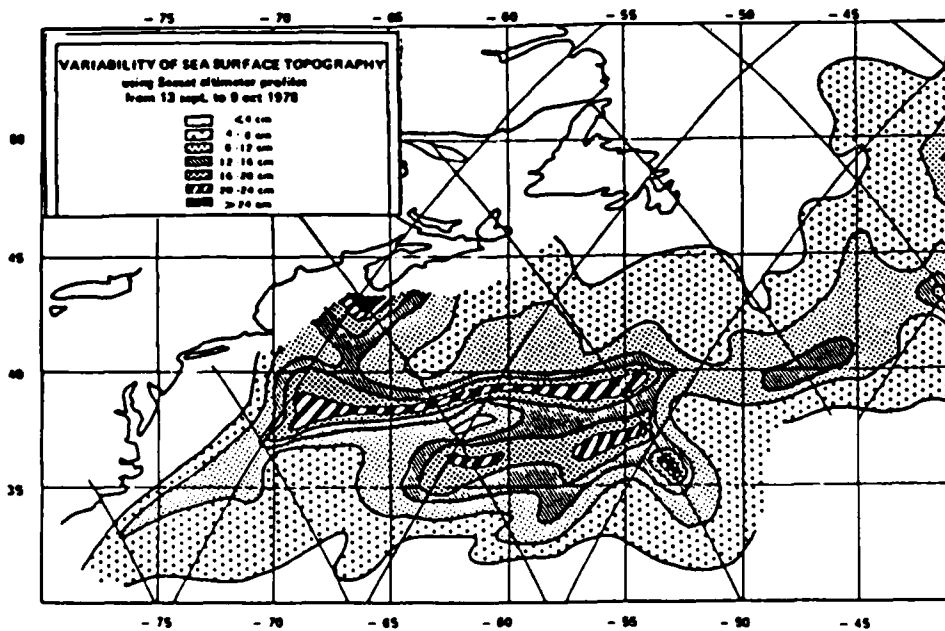


Fig. 6(d). Eddy variance of surface topography from SEASAT altimeter data (Menard, 1983)

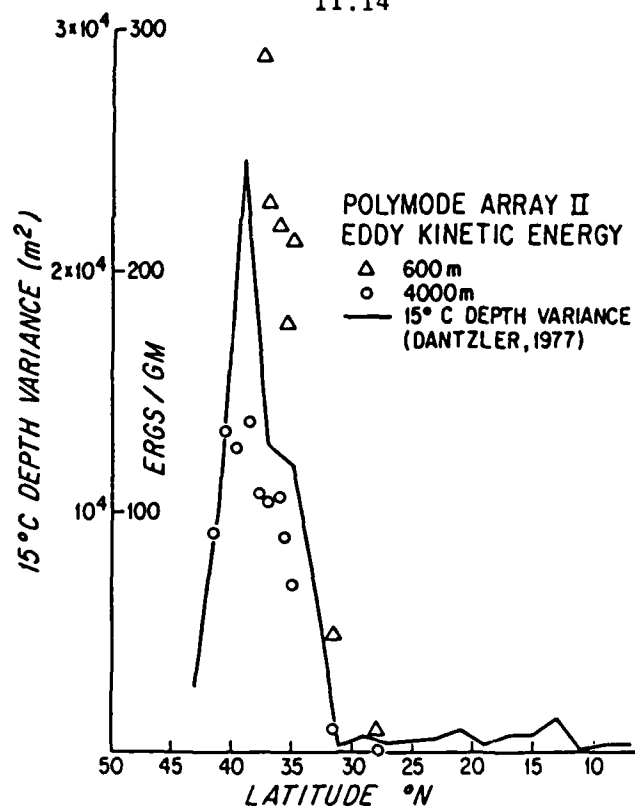


Fig. 7(a). Eddy variance of depth of 15°C isotherm and eddy kinetic energy from moorings along 55°W.

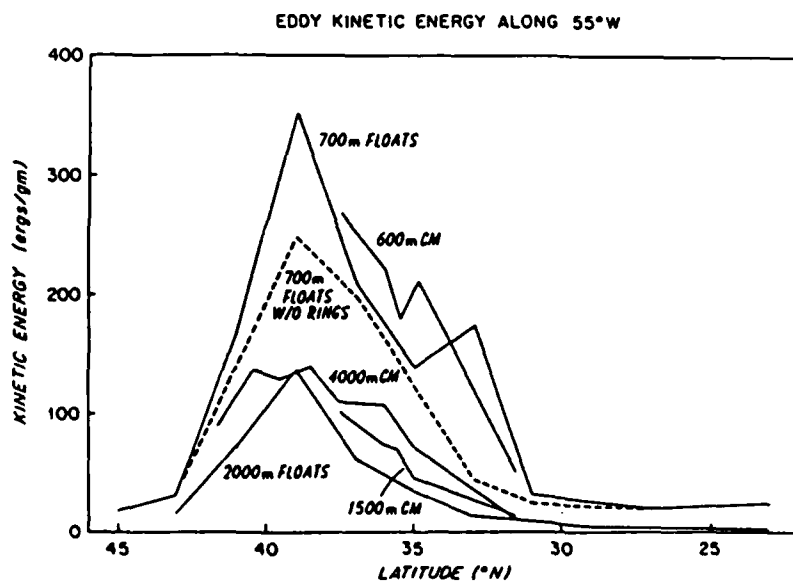


Fig. 7(b). Comparison of eddy kinetic energy from SOFAR floats and moored current meters along 55°W (Owens, 1984).

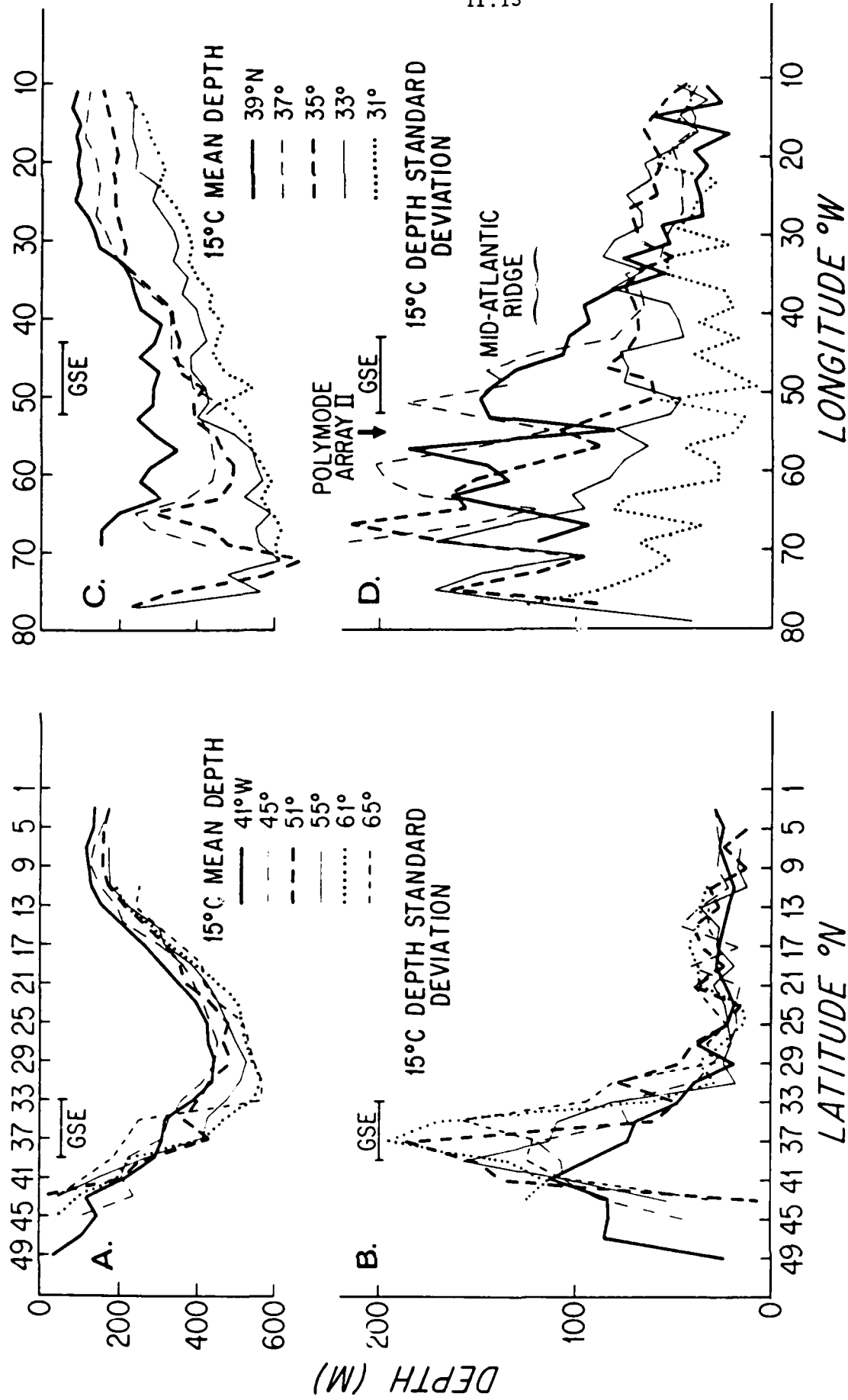


Fig. 8. Mean depth and standard deviation of 15°C isotherm along north-south and east-west sections through the Gulf Stream region.

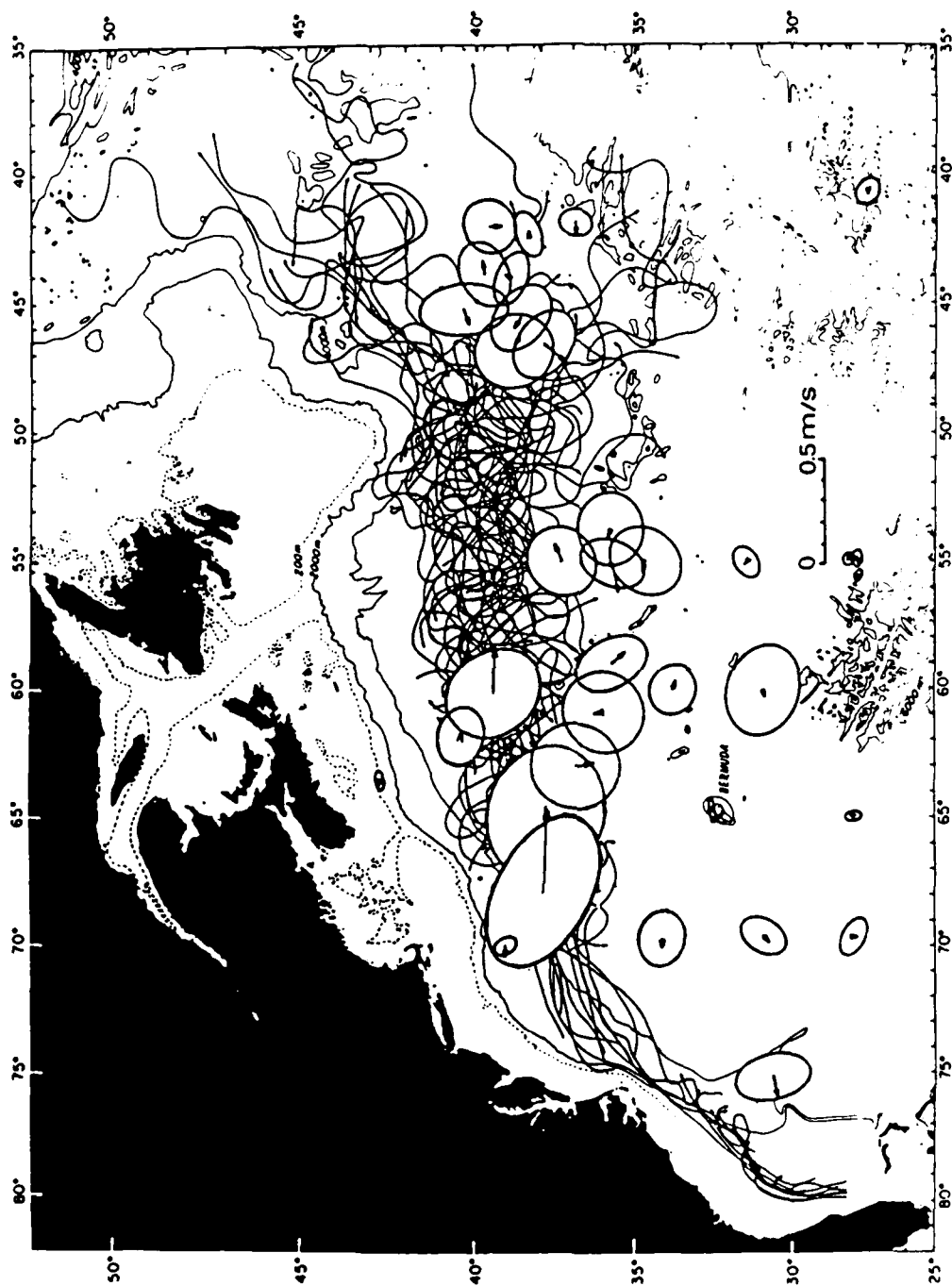


Fig. 9. Rms eddy velocity ellipses and mean velocity vectors at 500-600 m depth from moored current meter records.

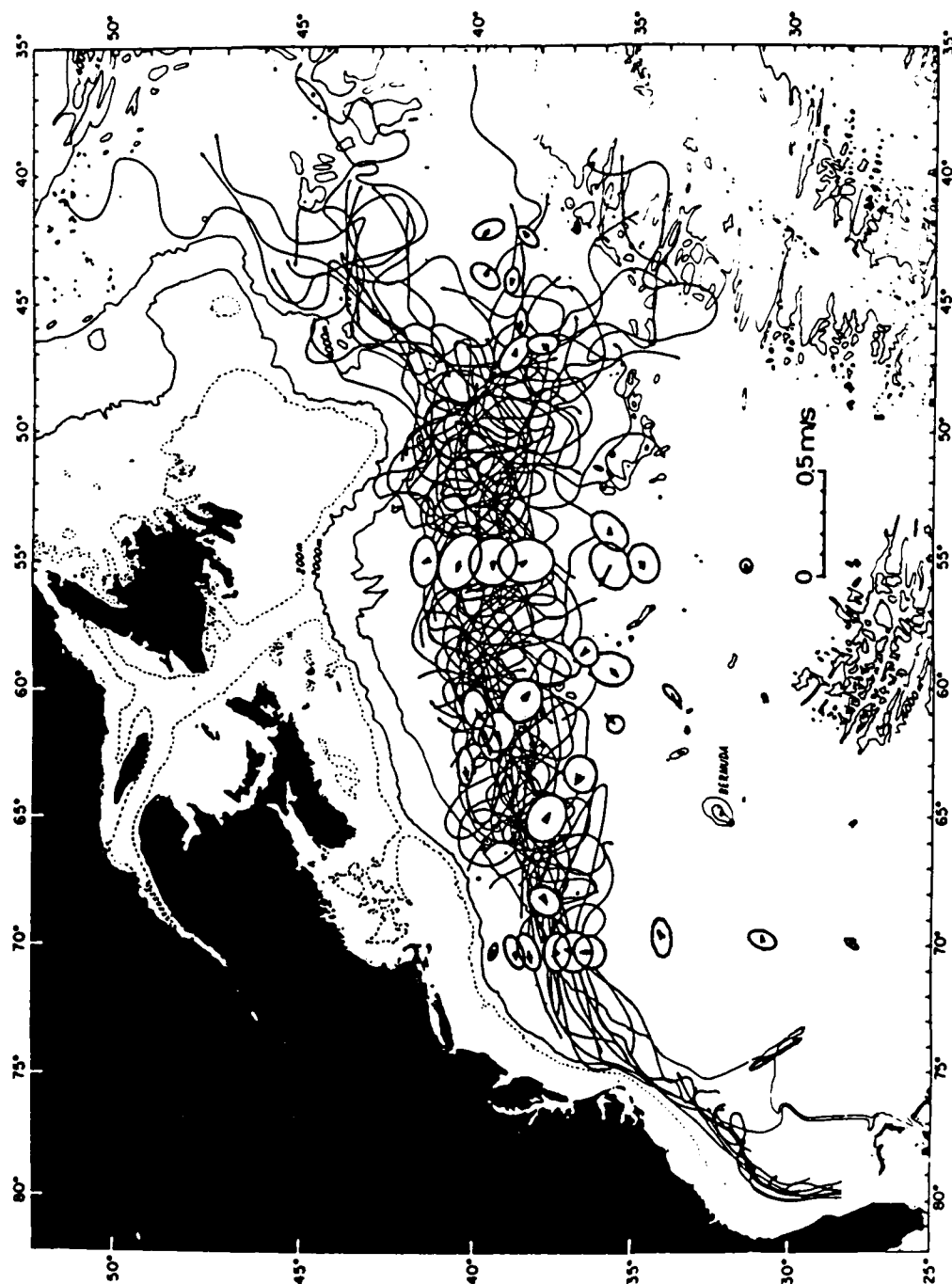


Fig. 10. Rms eddy velocity ellipses and mean velocity vectors at 4000 m depth from moored current meter records.



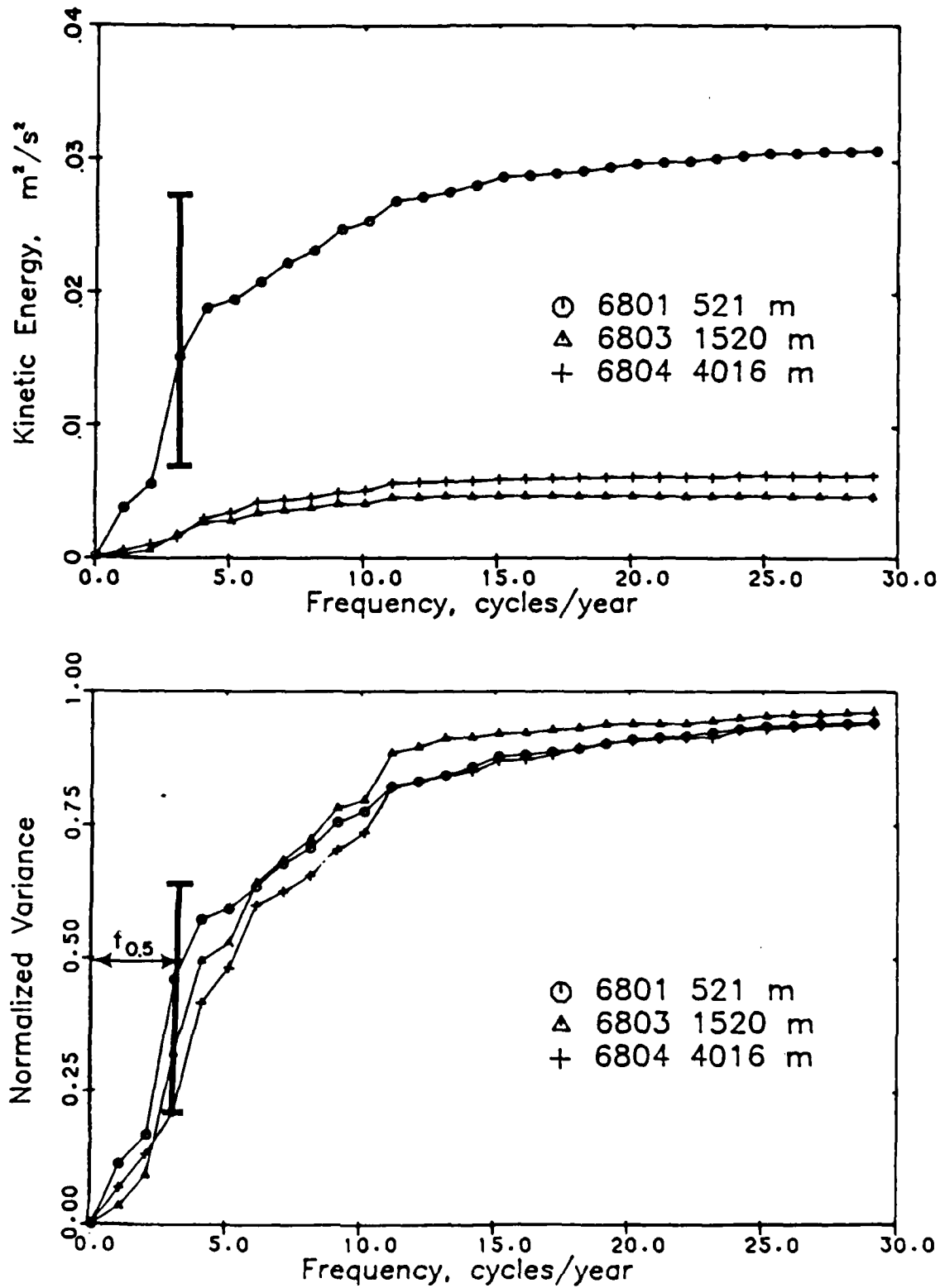


Fig. 11. Example of cumulative kinetic energy spectrum and normalized cumulative spectrum. The midpoint frequency or period is used to characterize the energy distribution.

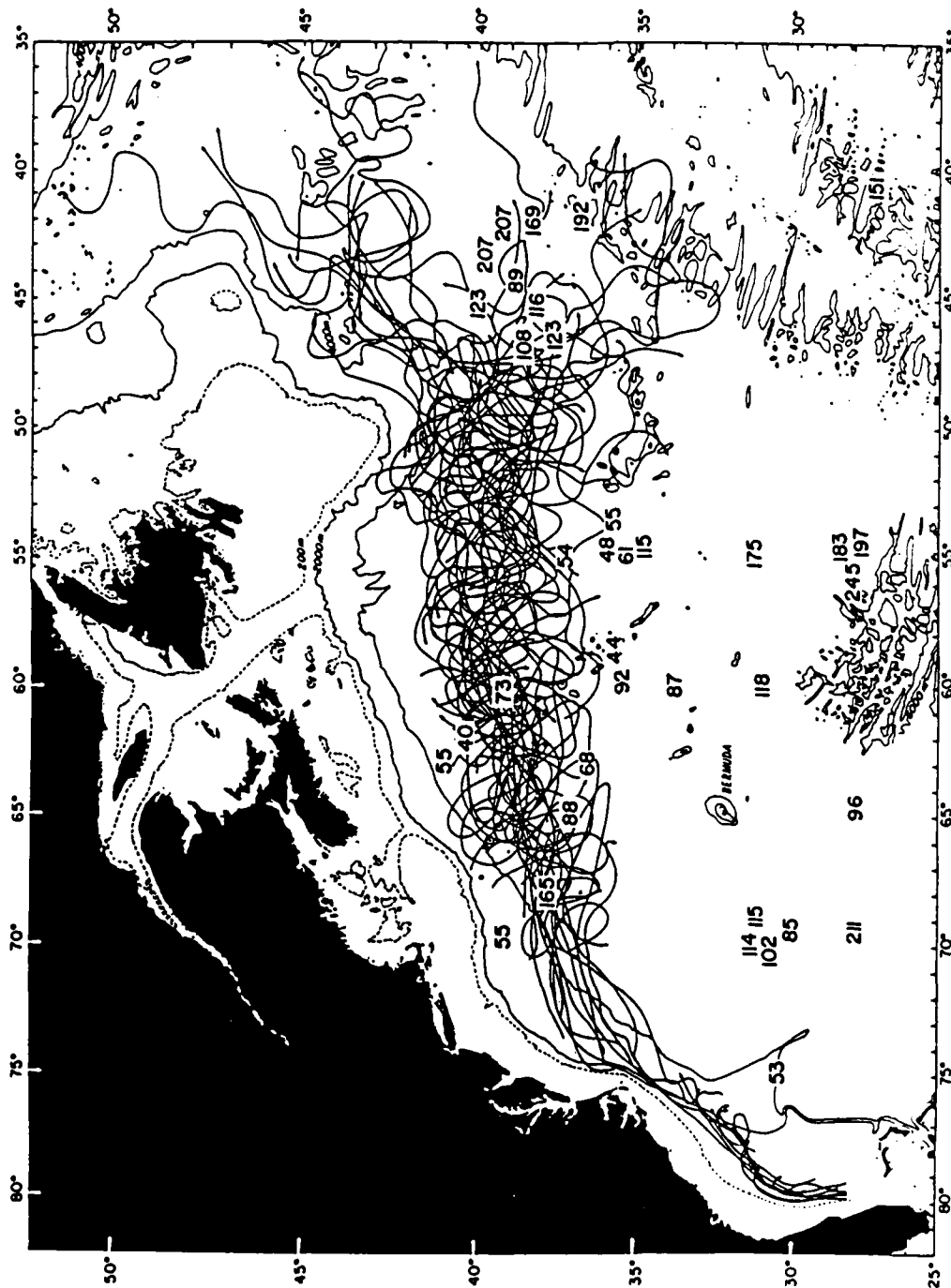
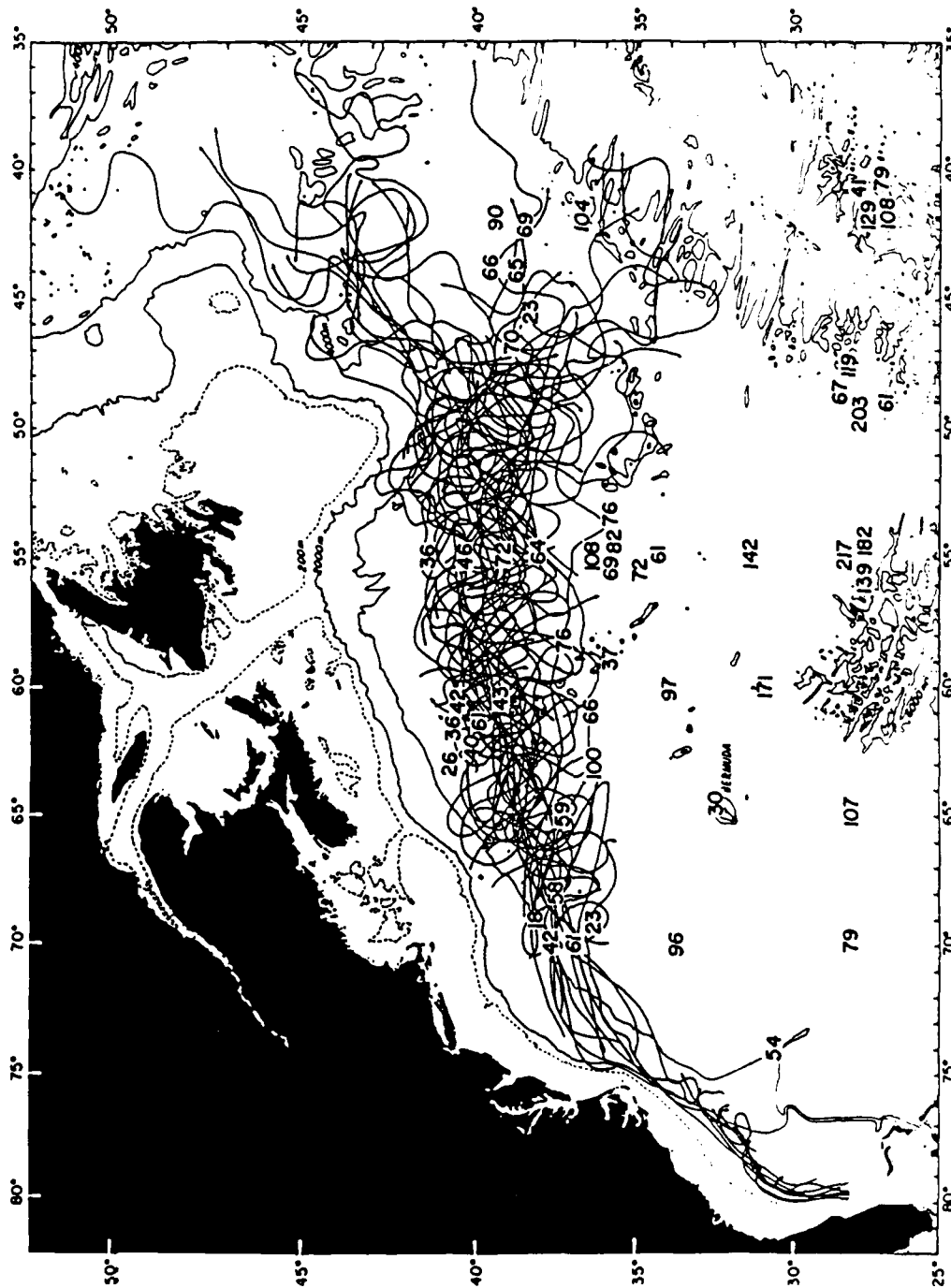


Fig. 12. Distribution of midpoint energy periods  $T_{0.5}$  at 500-600 m from current meter records in the western North Atlantic.



RECENT MODELING OF THE GULF STREAM SYSTEM:  
LOCAL DYNAMICS AND NON-LOCAL EFFECTS

D.B. Haidvogel  
National Center for Atmospheric Research\*  
P.O. Box 3000  
Boulder, CO 80307

May 1985

---

\* The National Center for Atmospheric Research is sponsored by the National Science Foundation.

## Abstract

A variety of theoretical and numerical models are currently being used to explore the dynamic character of the Gulf Stream System (GSS), and its influence on external regions of the North Atlantic. Two questions have received substantial recent attention. The first concerns the local dynamics of the GSS: the origin, statistical properties and inter-relationship of the large-scale mean and mesoscale fields of motion; and the regional influences of topography, stratification and atmospheric coupling. The second relates to the non-local effects of the GSS, and the mechanisms by which transient energy is exported to the mid-ocean.

Here, we briefly review the status of modeling efforts in these two areas. In particular, these results suggest that our dynamical/modeling expertise is presently adequate to undertake detailed "realistic" simulations (both statistical and prognostic) of the Gulf Stream. However, it is noted that substantial enhancement of computer resources and the availability of intensive regional datasets will be needed to fully realize this prospect.

## Introduction

This is a brief (and necessarily limited) review of recent attempts to bring theory and numerical modeling to bear on dynamical issues related to the Gulf Stream System (GSS) and its influence on neighboring mid-ocean regions. The intention is to provide highlights only of recent modeling techniques and results, but to indicate where more detailed information can be found in the refereed literature. Much additional detail is also contained in other papers in this volume.

The following discussion focuses exclusively on the GSS downstream of Cape Hatteras, thereby excluding much theoretical modeling work on the upstream behavior of the Gulf Stream (see, e.g., Dewar and Bane, herein). In addition, only recent work ( $\geq 1980$ ) is explicitly discussed; however, the cited references contain a detailed historical review.

It should be noted that, to date, no dynamically "complete" simulations of the GSS have been carried out. This fact relates not only to the cost of such simulations (see

estimates given later), but to a complex set of operative dynamical processes which includes local hydrodynamic interactions (in situ instabilities, topographic forcing), atmospheric coupling, and two-way feedbacks with the large-scale wind-driven ocean circulation. In the face of this complexity, most modelers of the GSS have opted (quite reasonably) for an examination of at most a few component processes, in isolation from the rest. All the models discussed here fit into this category. However, given appropriate resource availability (observational datasets, computer time and manpower), "realistic" models of the GSS are feasible within the coming few years.

### Local Dynamics

Among the earliest attempts to model the transient character and dynamics of the GSS involved the utilization of full basin, eddy-resolving general circulation models (EGCM's). Their advantage, from the perspective of local GSS modeling, is that the inter-connection of the GSS with the remainder of the North Atlantic gyre is explicitly represented; therefore, recourse to "open" boundary conditions is unnecessary. (Of course, a computational price is paid for this simplicity.) Schmitz and Holland (1982) have examined the mean and eddy statistics associated with the deep Gulf Stream in a two-level EGCM driven by a steady wind stress field (Figure 1). The resulting mean and eddy fields (e.g., Figure 2), when sampled along "dynamically similar" longitude lines, did show promising agreement between the simulated deep mean current structure and that measured along 55W (Figure 3). However, the horizontal penetration length of the simulated GSS was observed to be far too short. More recent work by Holland and Schmitz has explored the relationship of enhanced vertical resolution and bottom topography to the realistic reproduction of the GSS penetration scale. In particular, the need for sufficient vertical resolution has been identified. Eight-level quasigeostrophic EGCM simulations are now available, and are being compared with available data (Figure 4).

A prominent feature of both the simulated and observed GSS circulation pattern is the existence of a strong westward recirculation. The qualitative nature of the recirculation,

and its dynamical origin, can be interpreted using rather simple dynamical arguments [see, e.g., Haidvogel (1983)]. Nonetheless, the resulting recirculation plays a crucial role in many theories and models of the transient behavior of the GSS, as will be emphasized below.

As already noted, formulation of a regional (that is, open) Gulf Stream model involves the significant concern of how to formulate adequate lateral boundary conditions. However, regional models have the advantage of allowing a substantial increase in resolution, given fixed computational cost. Several attempts have in fact been made recently to model and to identify regional dynamical processes in the GSS. Using a flat-bottomed, two-layer QG model having open boundaries (fixed at inflow, radiation at outflow), Ikeda and Apel (1981) studied the mechanisms involved in meander formation and eddy/ring pinch-off. Initialized with a strong eastward-flowing jet plus a small localized perturbation field, their model showed examples of strong downstream meander growth and interaction, and the generation of cut-off rings (Figure 5). Local vorticity budgets were also constructed for the "neck" regions of large-amplitude meanders during the pinch-off of isolated rings (Figure 6). The resulting budgets indicate the predominant importance of lateral advection of relative vorticity during such events, and suggest that the instability-induced westward recirculation is itself closely connected with the process of detachment.

Very recently Robinson, Spall and Pinardi have begun to examine more closely, and with higher resolution QG models, the process of ring formation. Some initial results of their activities are summarized elsewhere in this volume.

It has long been suspected that underlying topography has a substantial impact on the Gulf Stream path and transient behavior. For instance, composites of Gulf Stream path positions indicate enhanced meandering in the neighborhood of the New England Seamount Chain (NESC; Figure 7). Hurlburt and Thompson (1984) have discussed the influence of such small-scale topographic features (e.g., Figure 8) in the context of a two-layer, adiabatic primitive equation (PE) model on a  $\beta$ -plane. The model is applied to the Gulf Stream region (Figure 9); fixed inlet and outlet conditions are used to parameterize the exterior gyre. As a result of their analysis, Hurlburt and Thompson conclude that the NESC can have a substantial influence on the local dynamics of the GSS even when the stream (as in their model) does not directly impact the seamounts. Intense eddy ac-

tivity is noted in the vicinity of the seamounts in these calculations, as is the generation of warm-core rings immediately upstream of the seamounts. Local dynamical budgets are currently being carried out to further characterize the process of small-scale topographic effects on the GSS. The authors also note that a reduced gravity (one baroclinic mode) model severely overestimates ring size and underestimates ring production rate (Figure 9)—another indication of the need for enhanced vertical definition of processes in the GSS.

Adamec (1985) has examined the hypothesis that latitudinal displacements in the Gulf Stream axis can occur when it enters a region of strong cooling (heat loss to the atmosphere). Such cooling effects are known to occur as the Gulf Stream leaves the continental margin at Cape Hatteras (Figure 10). To test the hypothesis, Adamec has adopted a multi-level, non-linear PE model featuring a convective adjustment scheme based on a local gradient Richardson number criterion, and surface heat fluxes proportional to the air-sea temperature difference. The simulations studied the effects on the velocity field of an initial geostrophic jet entering a region of strong cooling (Figure 11). Systematic differential velocities are indeed observed to occur when the surface heating is allowed to act, particularly when momentum mixing due to convective adjustment is included (Figure 12); however, the magnitude of the effect may not be large enough to account for observed wintertime shifts in the Gulf Stream axis. Further dynamical interpretation of these simulations is given by Adamec in these proceedings.

### Non-Local Effects

The foregoing examples indicate that we are beginning to understand the local dynamics of the GSS, including the origin of the energetic variability field and its relationship to the mean flow. Of equal interest is the means by which, once locally generated, the mesoscale energy can be exported to more distant regions of the gyre. Harrison and Robinson (1979) were among the first to address this question in the context of observed EGCM response. They noted, in several simulations, that the mid-ocean eddy field could be ac-



counted for as the barotropic basin response to forcing along the northern boundary of a closed basin. Here, the "forcing" was envisioned as the distribution of time-varying pressure imposed by the meandering Gulf Stream on the fluid to the south. In some smaller basin EGCM runs, this meander-induced forcing mechanism is able to account for a significant amount of the general structure of the mid-ocean eddy field in EGCM simulations (Figure 13). However, in large-basin EGCM studies, the eddy field is much more complex; here, the applicability of this mechanism is less likely due to its reliance on the existence and influence of remote boundaries.

Another prospect for populating the mid-ocean with eddies involves weakly unstable, but radiating, instabilities of the Gulf Stream jet. Talley (1983) has examined this possibility in detail using a linear stability analysis. By adopting piecewise continuous profiles for idealized baroclinic jets (Figure 14), exact dispersion relations and necessary conditions for instability can be found. Two types of instabilities are detected: rapidly growing, but trapped, modes; and more weakly unstable modes capable of radiating (that is, having appreciable amplitude in the far field of the jet). The crucial requirement for the latter modes is that the range of instability phase speeds overlap the phase speeds of freely propagating Rossby waves in the exterior region (see, e.g., Figure 15). In practice, this requirement means that purely eastward flowing jets have no radiating modes, whereas westward jets may have rapidly growing radiating instabilities. Talley (1983) suggests several conditions under which predominantly eastward jets (such as the Gulf Stream) can be made to radiate (Figure 16)—for instance, by allowing vertical shear in the far field, or by including deep westward flow beneath the eastward surface jet. Another likely prospect, given observed Gulf Stream structure, is that the westward-flowing Gulf Stream recirculation is itself unstable to modes which radiate into the interior. However, since the existence of the recirculation is directly related to finite-amplitude dynamic effects in the Gulf Stream, the evaluation of this last prospect awaits close examination of fully non-linear simulations of the GSS. Initial idealized simulations of this type are in fact underway (Talley and Haidvogel).

Additional mechanisms for energy exportation from the GSS to the far field include: the effects of transport due to coherent structures such as Gulf Stream rings, and boundary

forced non-linear planetary radiation. Both prospects deserve increased examination. An initial study of a non-linear boundary forcing problem is described in this volume by Rizzoli and Haidvogel. There it is shown how non-linear effects can circumvent the requirement, in purely linear models, of an eastward phase for the disturbances, and lead to enhanced penetration of the boundary forced signal [see also Malanotte-Rizzoli (1984)].

### In the Future

Although models incorporating a "complete" treatment of Gulf Stream dynamics are feasible, continued application of simple theoretical and/or numerical models of potentially operative processes is essential. In particular, further modeling work is warranted (1) to quantify the effects and importance of radiating instabilities in the finite-amplitude meandering limit; (2) to investigate the transport of momentum, energy and vorticity by coherent features generated within the GSS; and (3) to begin to examine the frontogenetic features of the transient Gulf Stream.

Another important class of experiments involves data assimilation within existing models of the GSS. With the proposed future acquisition of intensive regional datasets in the GSS by (e.g.) hydrographic, altimetric and tomographic means, it will be necessary to determine the best strategies for the insertion of data into existing models, and for the improvement of models (and their forecasts) by appeal to the combined available data sources. Simulations aimed at addressing these questions are intended and/or ongoing at Harvard, NCAR and NORDA.

Lastly, it is now possible to envision a series of high resolution "realistic" simulations of the GSS, for the purposes of both statistical and prognostic comparison with available observations. Such a simulation might, for example, require a 5 km horizontal grid (at least in the cross-stream direction) and as many as ten vertical levels. The inclusion of frontal dynamics, active air-sea exchange and ageostrophic effects (should they be desirable) would call for utilization of a primitive equation model (or perhaps one based on the equations of an intermediate set).

The implementation and application of such a high resolution PE model within a regional domain of (say) 1500 x 1500 km is technically feasible. However, two primary problems exist. First, such a model would be costly to run. Using the Cox (GFDL) PE model as an example, it is estimated that the simulation suggested above would require  $O(100)$  Cray-1 cpu hours per  $O(1)$  model year. Such an investment of resources is not currently feasible. (Of course, a lot can still be accomplished with lower resolution and/or less elaborate physical models.) Second, the success of such realistic regional models is intimately connected with the success of our boundary condition assumptions and parameterizations. While satisfactory treatments of open boundary conditions for (in particular, PE) open ocean models are no doubt possible, substantial work in this area will be necessary.

#### References

- Adamec, D., 1985: *Numerical Simulations of the Response of Intense Ocean Currents to Atmospheric Forcing*. Ph.D. Dissertation, Naval Postgraduate School, 97 pp.
- Haidvogel, D.B., 1983: Periodic and regional models. In: *Eddies in Marine Science*, Springer-Verlag, New York.
- Harrison, D.W. and A.R. Robinson, 1979: Boundary-forced planetary waves: A simple model of mid-ocean response to strong current variability. *J. Phys. Oceanogr.*, 9, 919.
- Hurlburt, H.E. and J.D. Thompson, 1984: Preliminary results from a numerical study of the New England Seamount Chain influence on the Gulf Stream. In: *Predictability of Fluid Motions*, American Institute of Physics, New York.
- Ikeda, M. and J.R. Apel, 1981: Mesoscale eddies detached from spatially growing meanders in an eastward-flowing oceanic jet using a two-layer quasigeostrophic model. *J. Phys. Oceanogr.*, 11, 1638.

Malanotte-Rizzoli, P., 1984: Boundary-forced non-linear planetary radiation. *J. Phys. Oceanogr.*, 14, 1032.

Schmitz, W.J., Jr., and W.R. Holland, 1982: A preliminary comparison of selected numerical eddy-resolving general circulation experiments with observations. *J. Mar. Res.*, 40, 75.

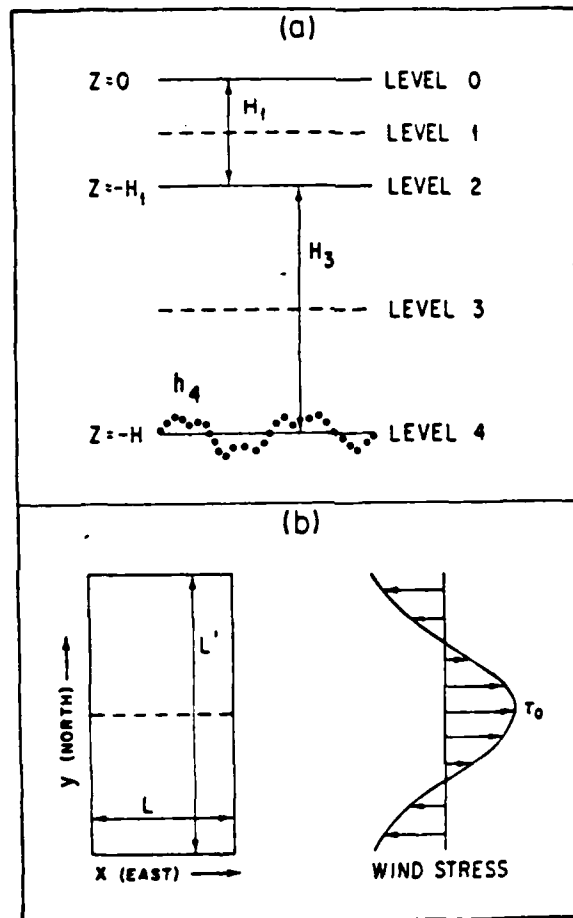


Figure 1. Schematic configuration of the model: (a) vertical structure, (b) horizontal structure. The dashed line in (b, left) denotes mid-basin; the dotted line in (a), labeled  $h_4$ , denotes bottom topographic variations. Notation is defined in the Appendix.

Figure 1. Schmitz and Holland (1982).

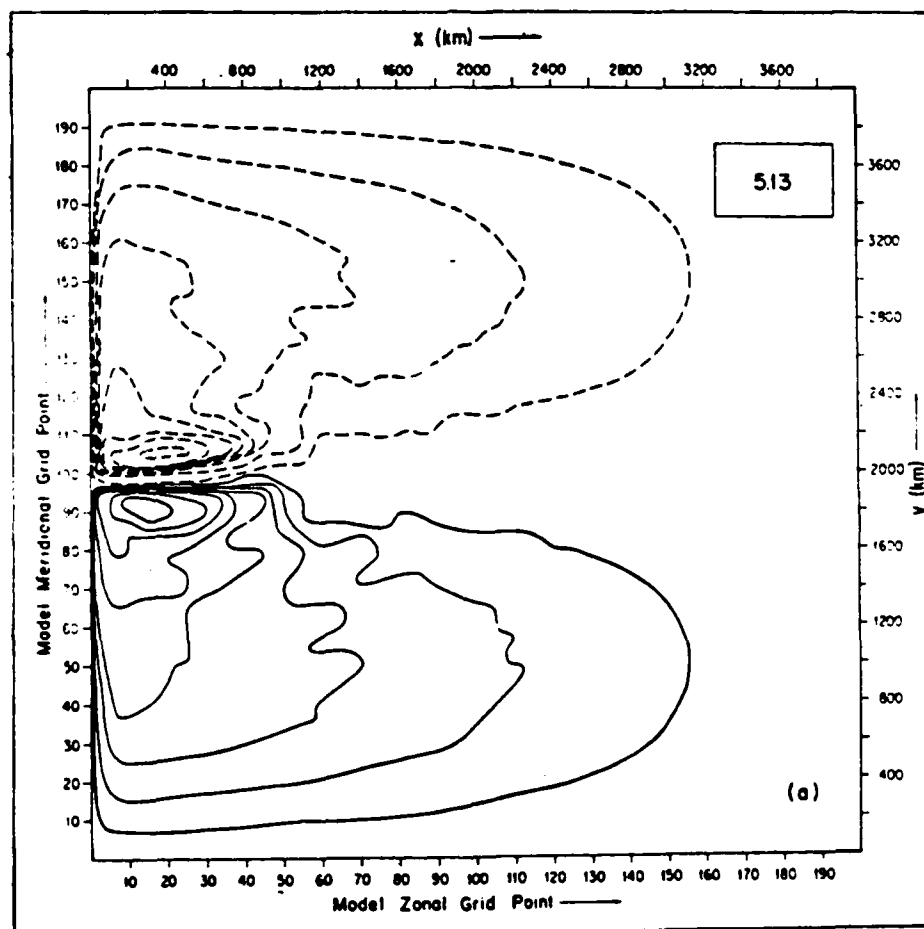


Figure 4. Mean streamline patterns for model run 5.13: contour intervals are variable, being chosen to bring out the major properties of the model general circulation: (a) upper layer, (b) lower layer. Solid lines indicate anticyclonic circulation, dashed lines, cyclonic.

Figure 2a. Schmitz and Holland (1982).

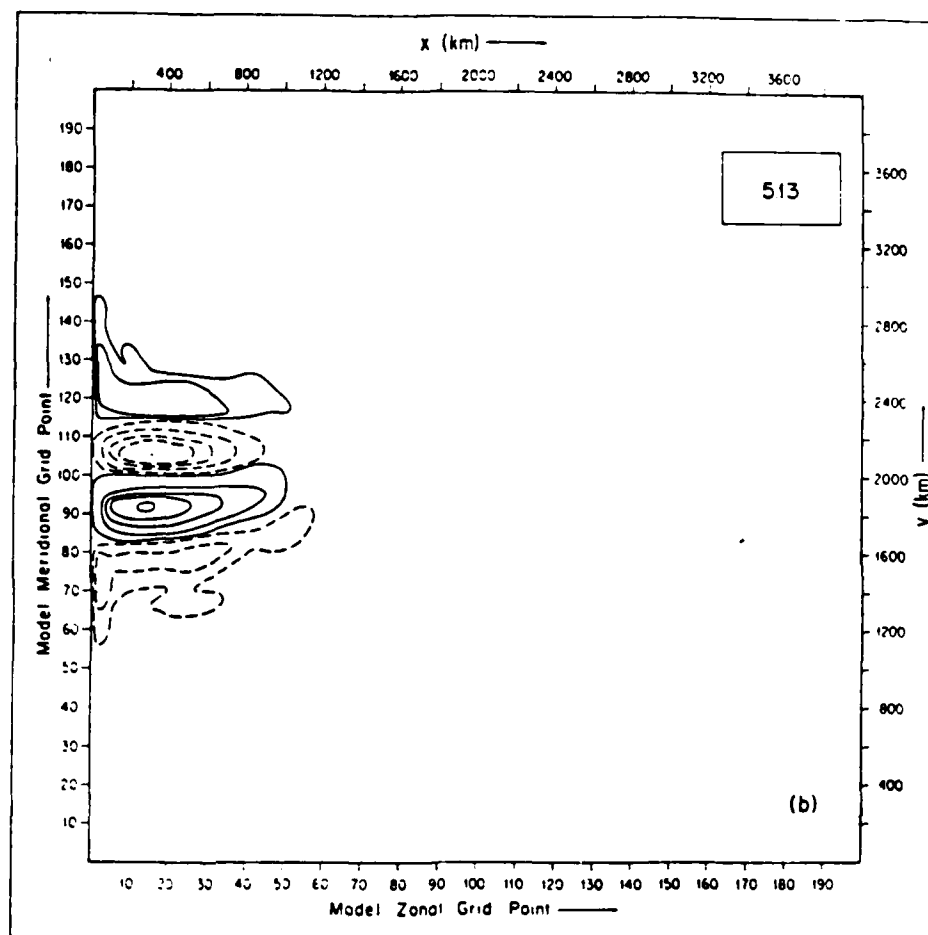


Figure 2b. Schmitz and Holland (1982).

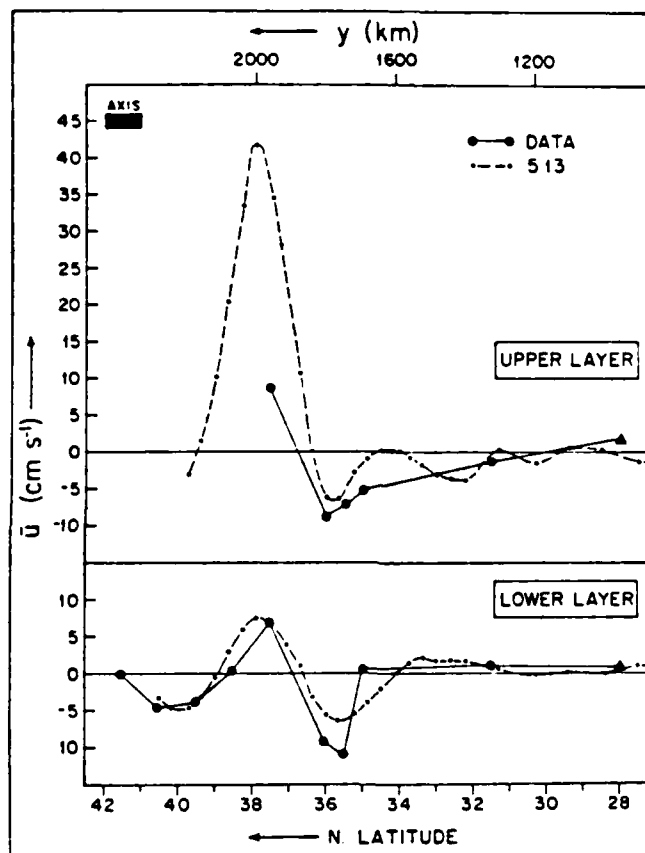


Figure 9. Mean zonal velocity component ( $\bar{u}$ ) for model 5.13 at a distance of 600 km from the west coast, along with observations along 55W. The model latitude ( $y$ ) origin has been arbitrarily chosen to maximize (approximately) the similarity with data. The bar labeled axis denotes the observed climatological range for the Gulf Stream.

Figure 3. Schmitz and Holland (1982).



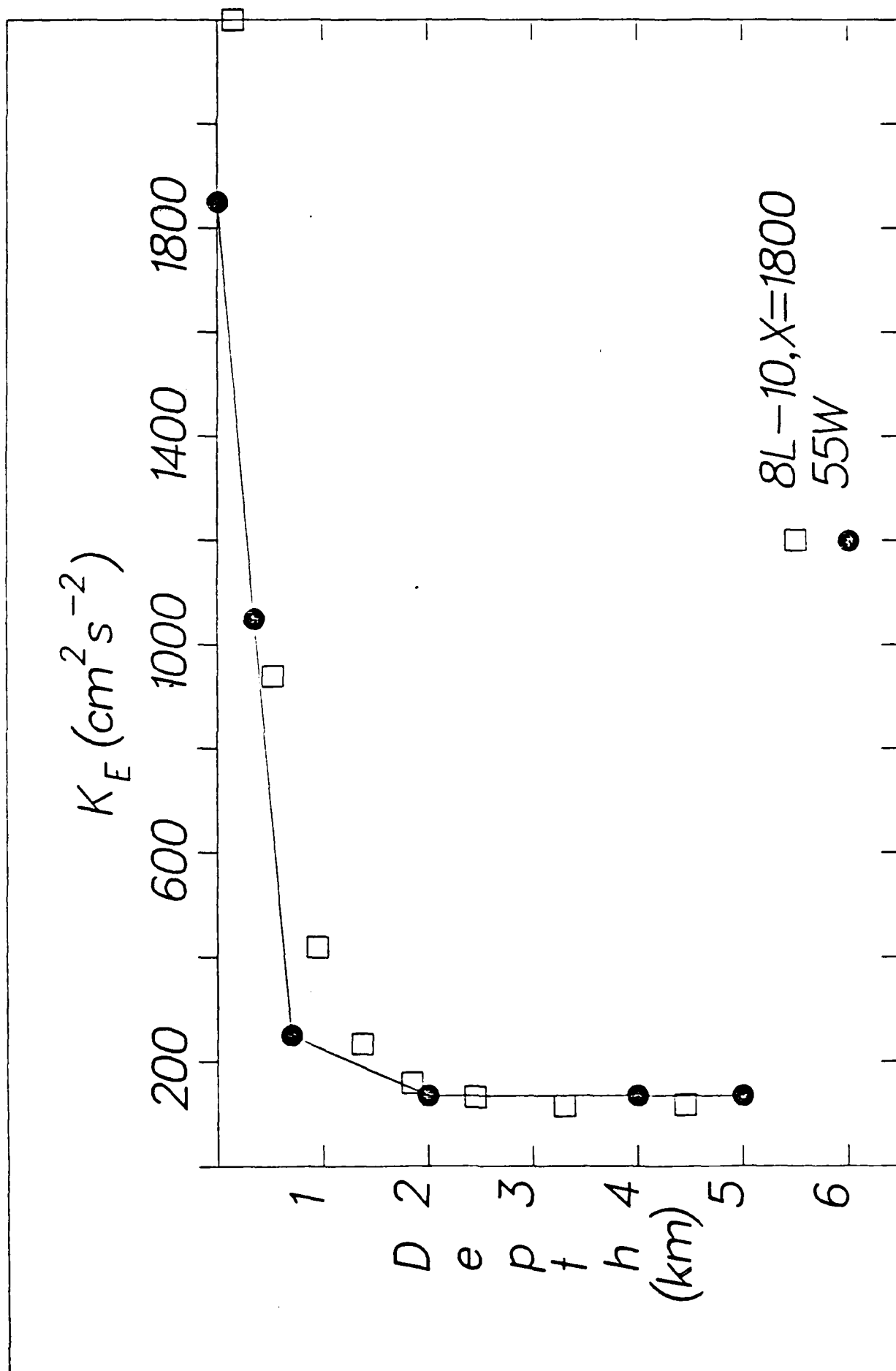


Figure 4. Holland and Schmitz (unpublished).

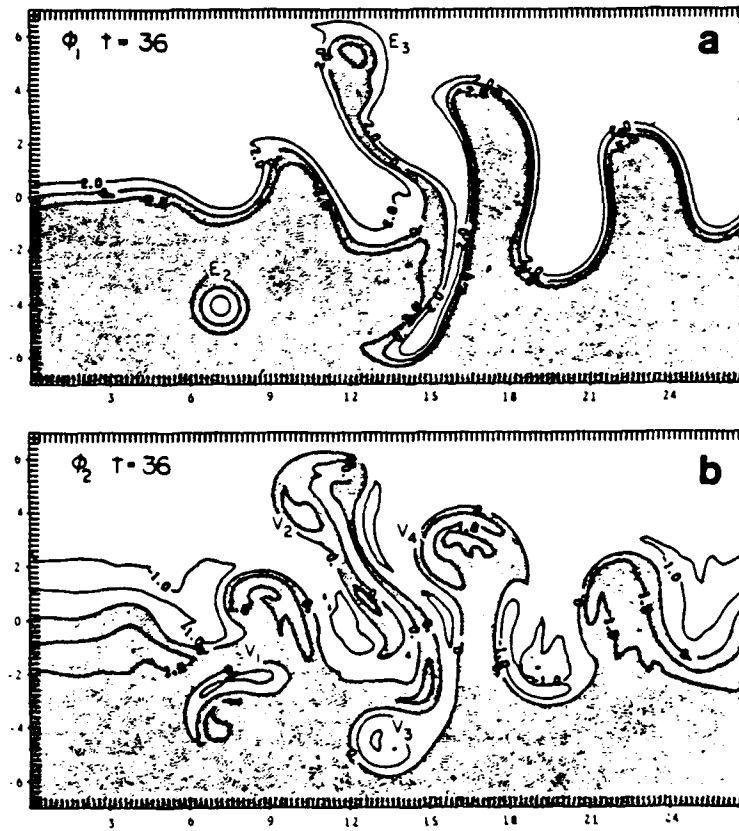


Figure 5.  
Ikeda and  
Apel (1981).

FIG. 5. The potential vorticity at  $t = 36$  in BA1, (a)  $\phi_1$  in the upper layer and (b)  $\phi_2$  in the lower layer. Dotted parts denote southern fluid, and white parts northern fluid.

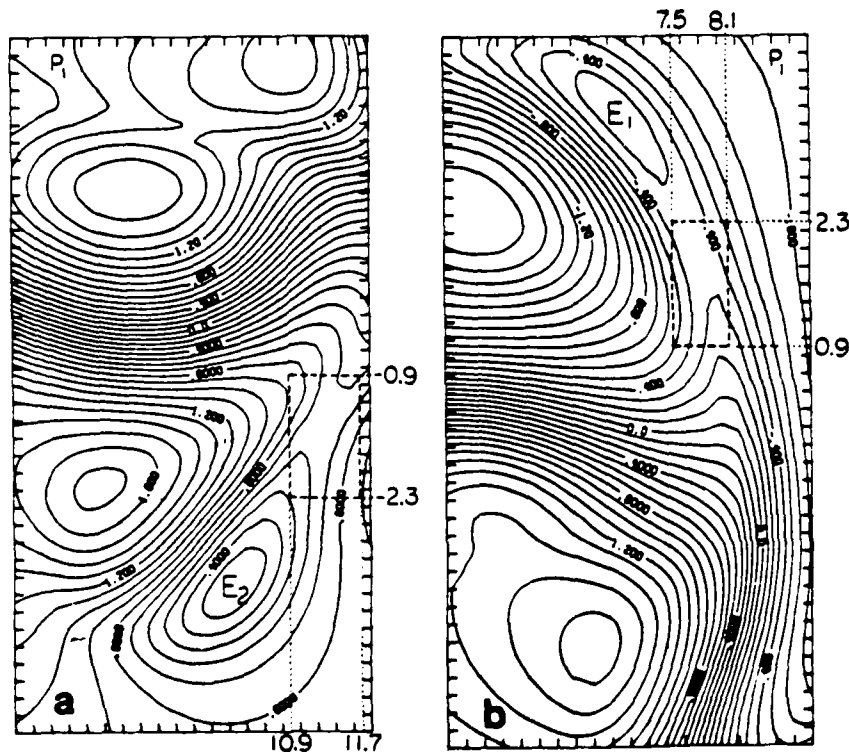


Figure 6.  
Ikeda and  
Apel (1981).

FIG. 12. The upper-layer streamfunction (a) in BA1 at  $t = 27$ , and (b) in BA2 at  $t = 27$ . The rectangles shown by broken lines denote the regions in which potential vorticity budgets are calculated.

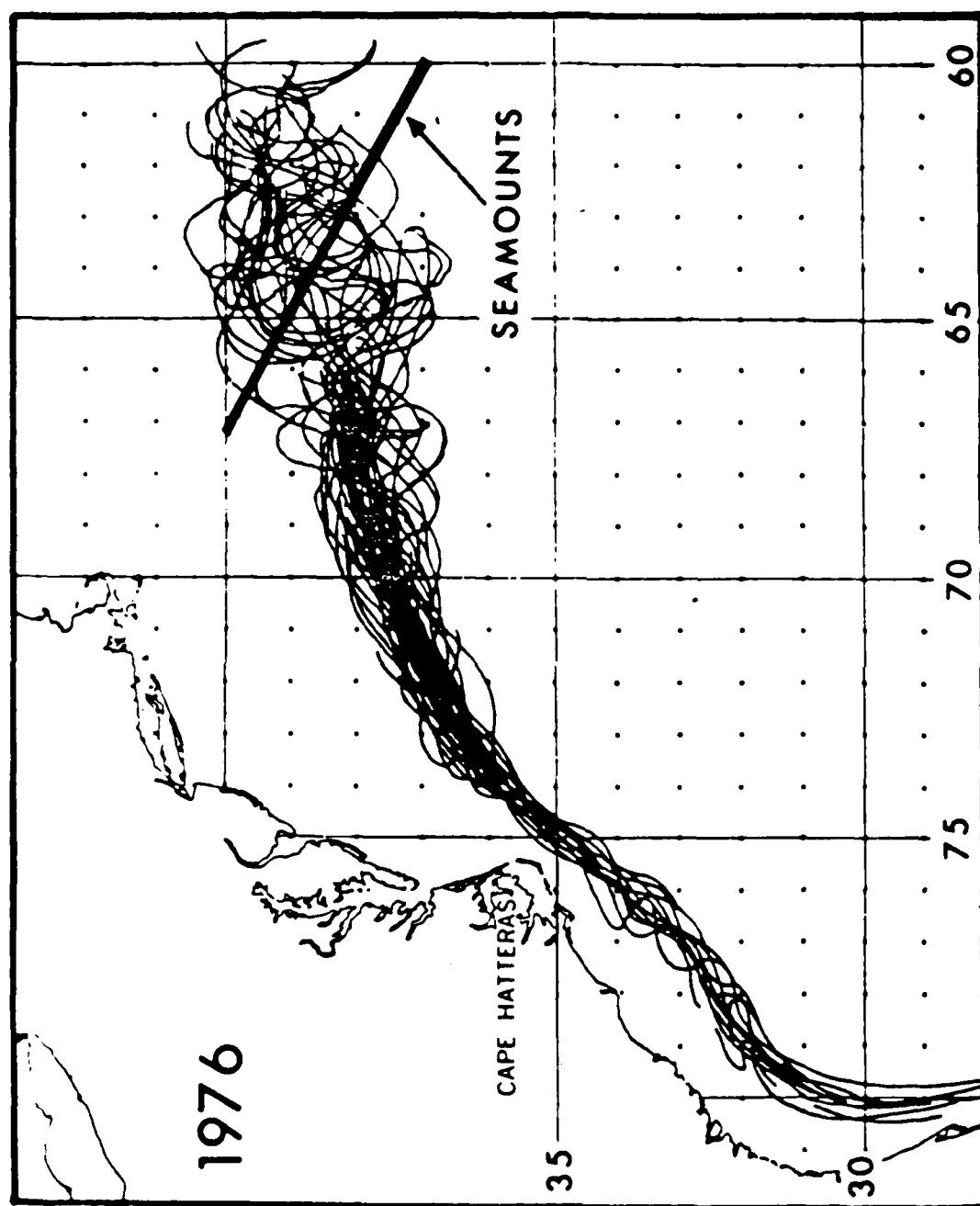


Figure 7. Hurlburt and Thompson (1984).

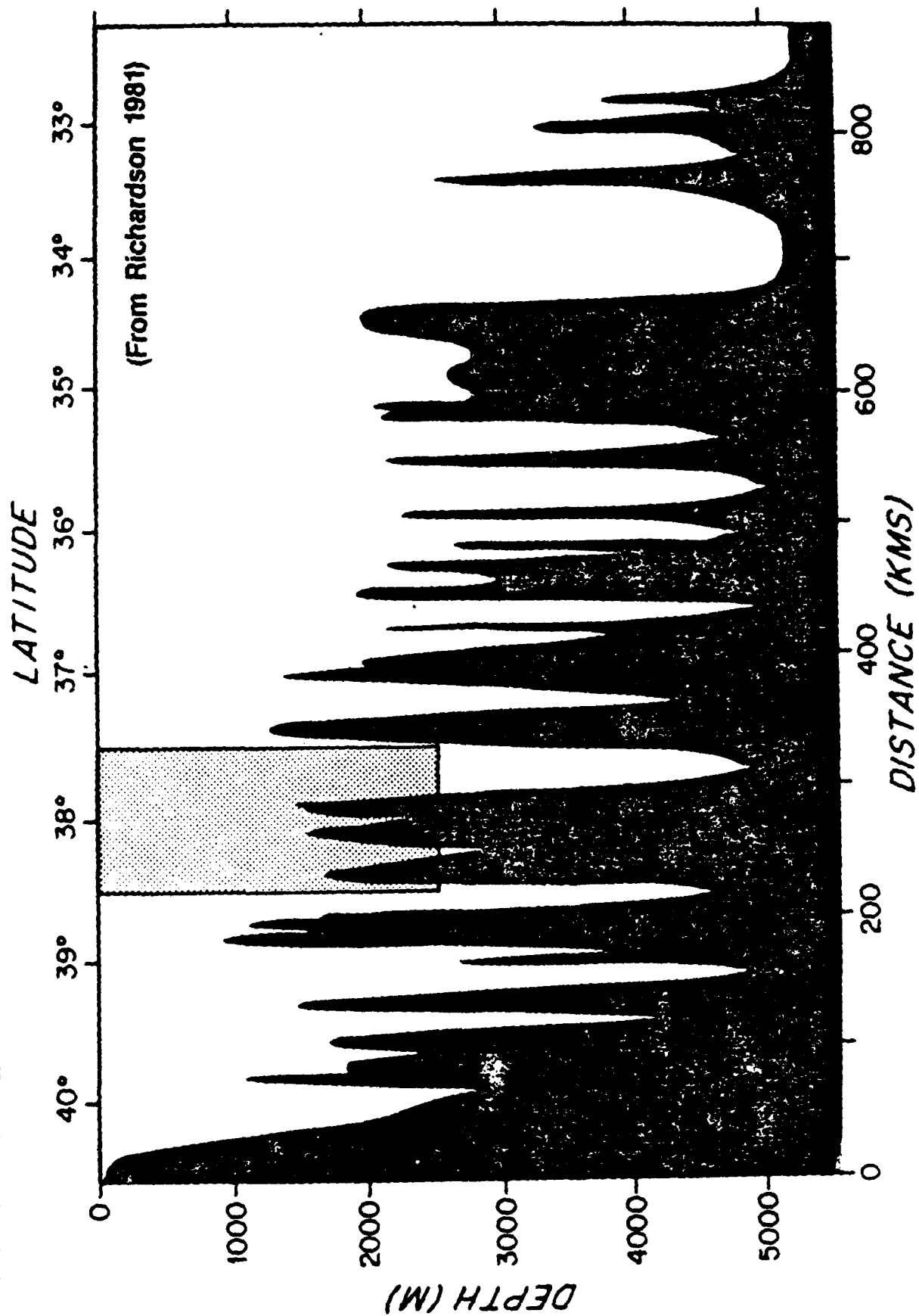


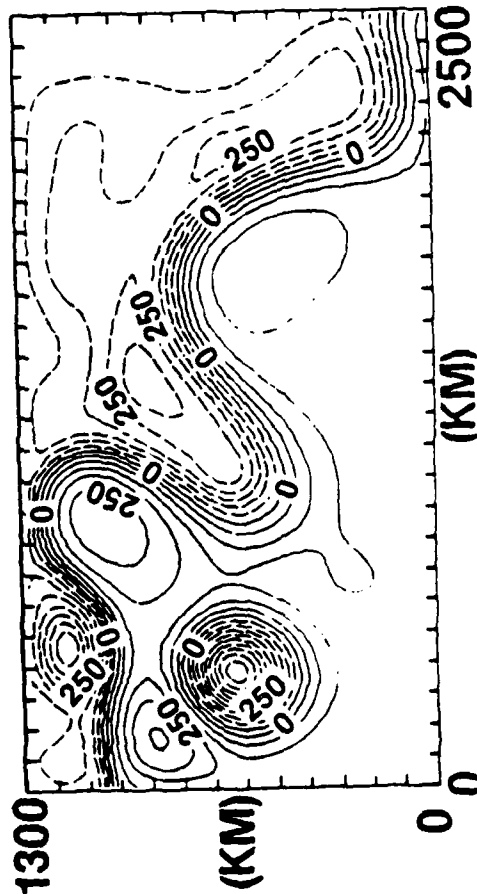
Figure 8. Hurlburt and Thompson (1984).



- SPATIAL SCALE OF RINGS/MEANDERS DECREASE BY FACTOR OF 2.
- FREQUENCY OF RING GENERATION INCREASED BY FACTOR OF 3.  
(BAROTROPIC MODE CRITICAL FOR RING GENESIS.)
- BIFURCATION PHENOMENON OBSERVED.  
(2 BRANCHES OF STREAM ENCLOSING COUNTER-ROTATING VORTEX PAIR.)

— MODEL DOMAIN  
- - - REX REGION

REDUCED GRAVITY—ONE LAYER  
(BAROCLINIC MODE ONLY)  
THERMOCLINE HEIGHT ANOMALY (METERS)



TWO-LAYER MODEL  
(BAROTROPIC AND FIRST BAROCLINIC MODE)  
UPPER LAYER PRESSURE

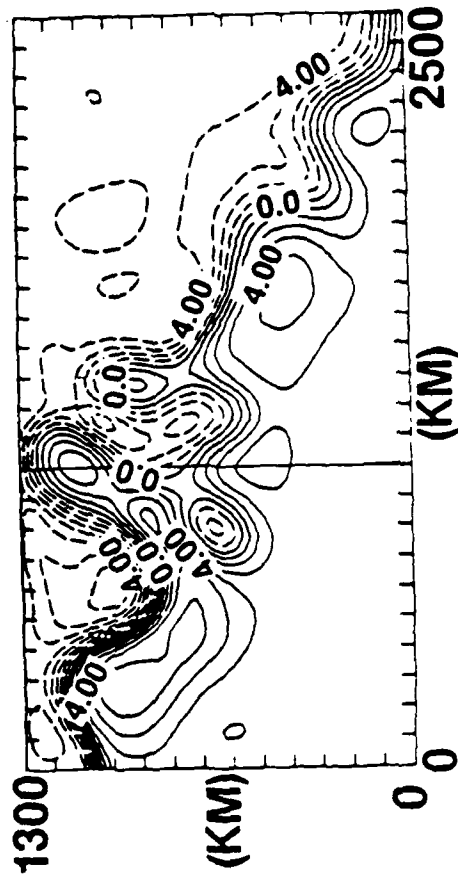


Figure 9. Hurlburt and Thompson (1984).

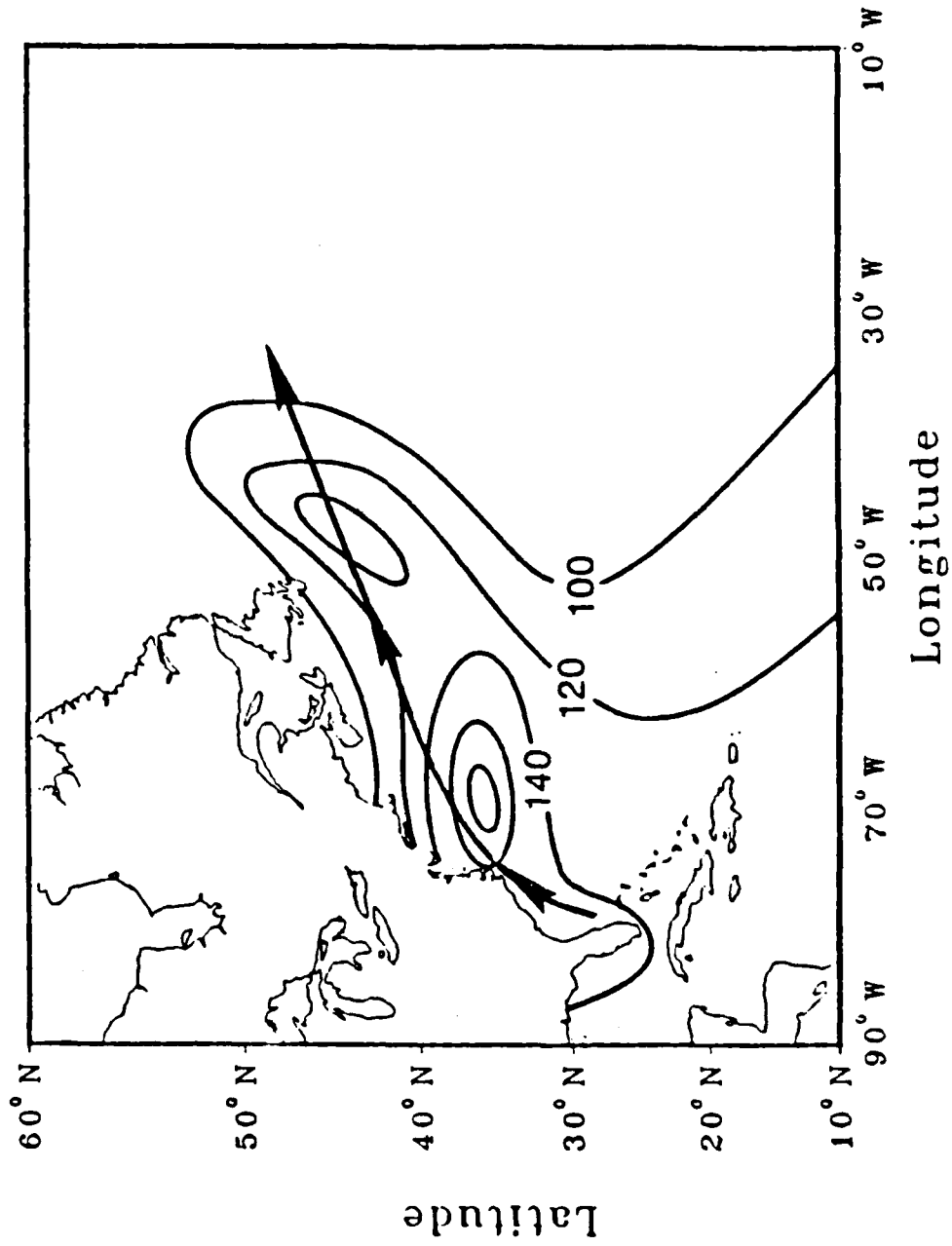


Figure 3. Distribution of the average latent heat flux over the North Atlantic during February (from Gorshkov, 1978). The contour interval is  $20 \text{ W m}^{-2}$ .

Figure 10. Adamec (1985).

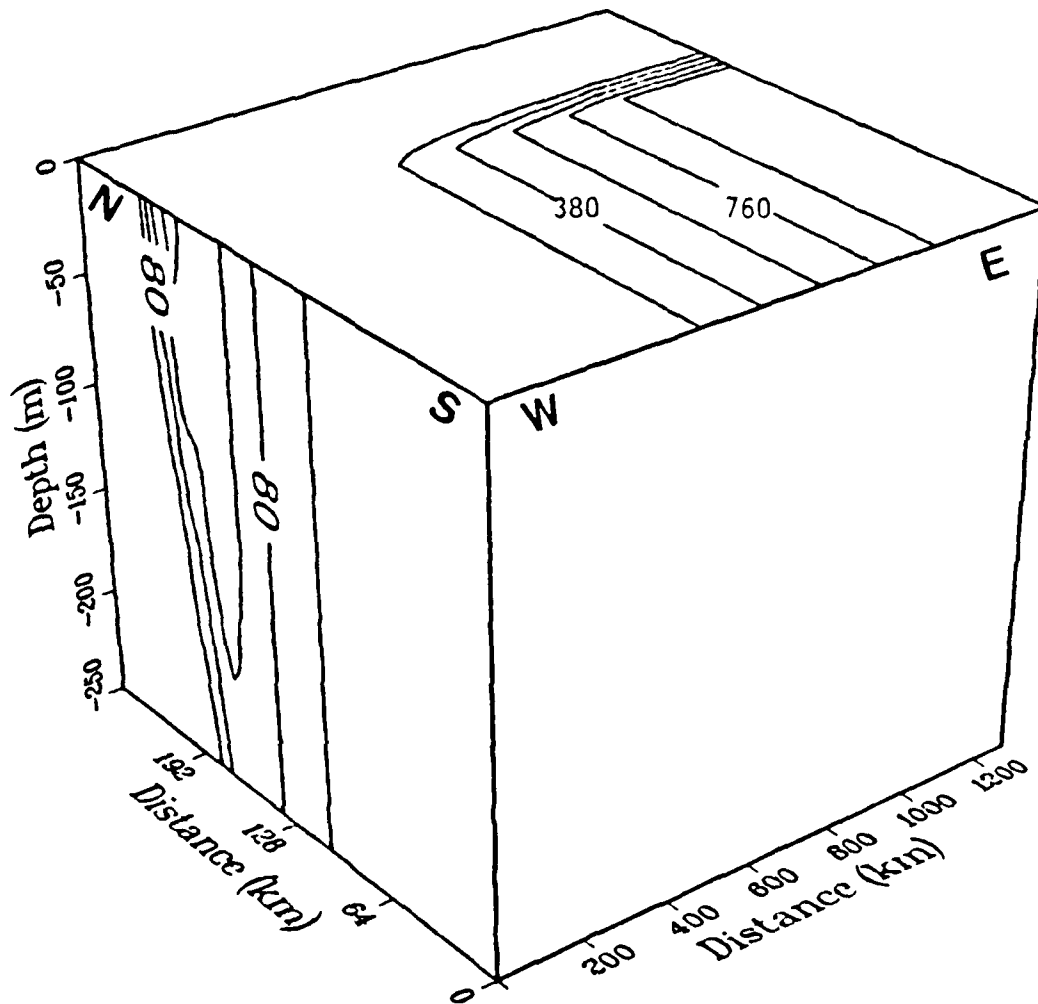


Figure 2. Cross-section of the initial geostrophic velocities of the upper 250 m in the vicinity of the front (side face), and the east-west distribution of the surface cooling (top face). The contour interval for the velocities is  $40 \text{ cm s}^{-1}$ , and the contour interval for the cooling is  $190 \text{ W m}^{-2}$ .

Figure 11. Adamec (1985).

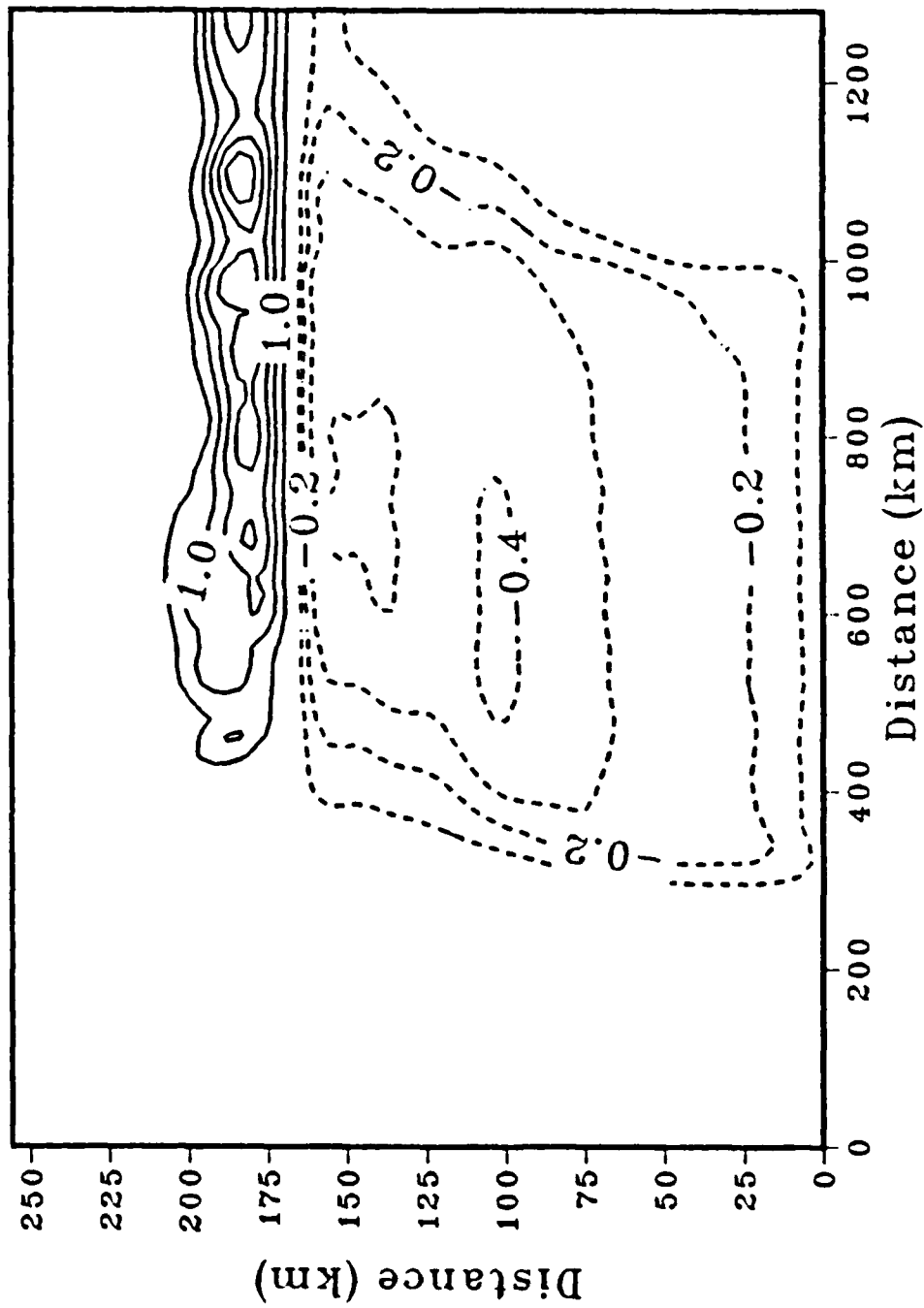


Figure 6. Surface  $v$  component at hour 72 for the simulation with momentum mixing allowed. The contour interval is  $0.5 \text{ cm s}^{-1}$  where the flow is positive (northward), and  $0.1 \text{ cm s}^{-1}$  where the flow is negative (southward).

Figure 12. Adamec (1985).



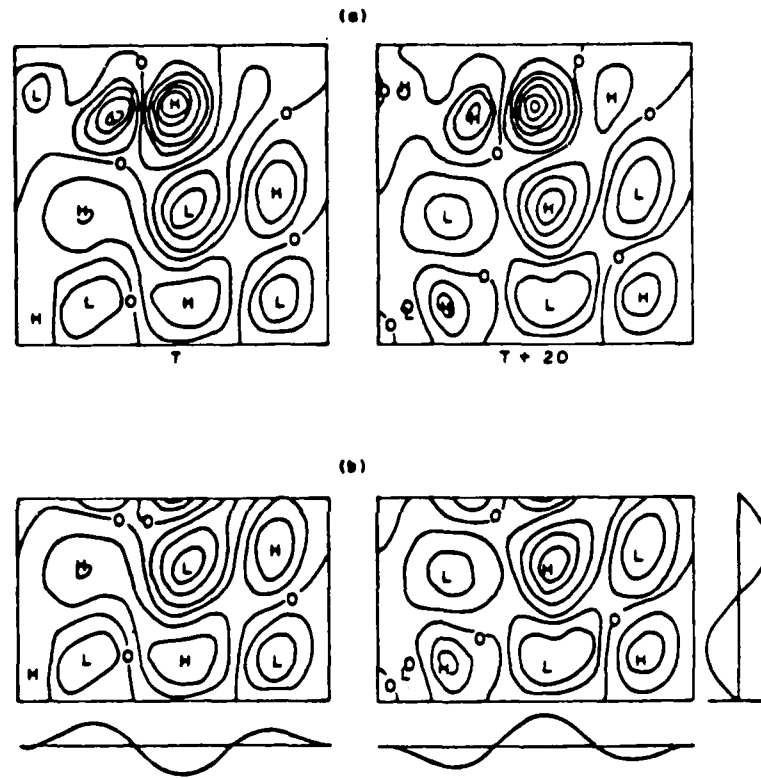


FIG. 1. (a) Eddy streamfunction field snapshots from RHMS, 20 days apart. (b) Comparison of  $m = 1$  MIF term with RHMS eddy streamfunction fields in the MIF basin:  $Y_1(y)$  at far right,  $\cos(M\pi x + t)$   $\sin\pi x$  at bottom.

Figure 13. Harrison and Robinson (1979).

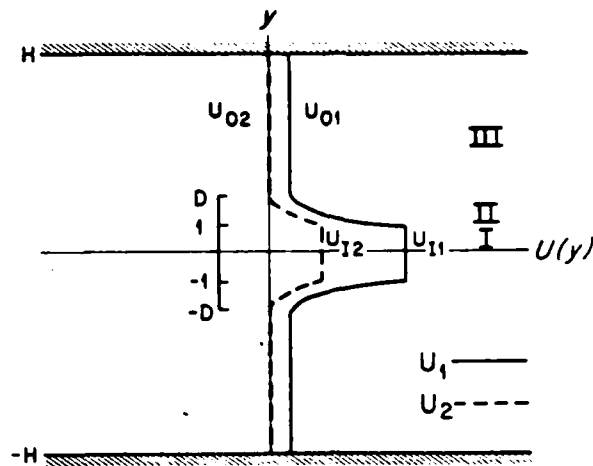


Figure 14.  
Talley (1983).

FIG. 1. Baroclinic jet modeled with two layers and meridional regions of uniform velocity or uniform potential vorticity. In most cases examined, there are no boundaries at  $|y| = H$ .

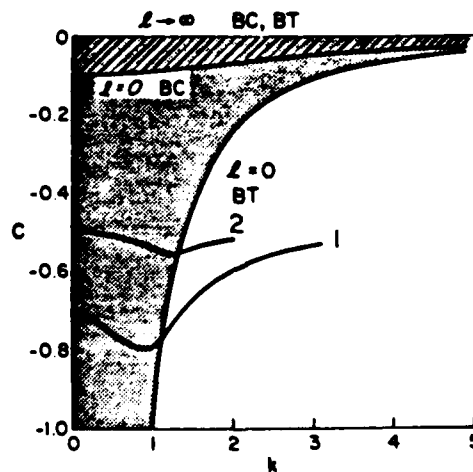


Figure 15.  
Talley (1983).

FIG. 10. Barotropic and baroclinic Rossby wave dispersion relations at  $\beta = 1$  for  $l = 0$  and  $l = \infty$ . The shaded regions indicate where all Rossby waves lie. Superimposed on the diagram is  $c$ , of the westward basic jet ( $\beta = -1$ ) from Fig. 5.

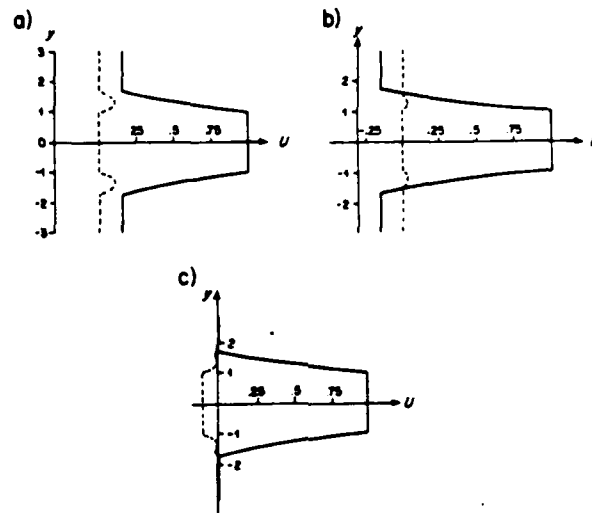


FIG. 11. Three modified eastward jets: (a) with positive vertical shear in Region III, (b) with negative vertical shear in Region III, (c) with a weak, westward undercurrent.

Figure 16. Talley (1983).

Recent Gulf Stream Theoretical Work and Pertinent Observations  
by  
Nelson Hogg

Abstract: Three recent new ideas concerning the dynamics of the Gulf Stream and its relation to the surrounding ocean are discussed and put into the context of new observational information. Luyten and Stommel (1985) have formulated a multi-layered version of the classical inertial boundary layer theory and resolved Blandford's (1965) dilemma of not being able to smoothly continue the solutions from some southern boundary to a more northerly one where all layers separate from the coast. The resolution of this difficulty suggests that the inertial boundary current is hydraulically controlled and that the dynamics of the ocean's interior circulation might not be separable from the dynamics of its western boundary current.

Flierl and Robinson (1984) have updated the thin jet theory for the meandering Gulf Stream. Their important result is a new path equation which explicitly contains the influence of the surrounding ocean on the evolving path of the Stream. The formulation is general (in the thin jet approximation limit) but results in a nonlinear equation coupled to the far field. A solution is given in the small amplitude limit where the far field consists of propagating Rossby waves.

A similar physical problem solved in a more standard manner is the radiating instability model of Talley (1984a,b). Here a piecewise continuous Gulf Stream jet is patched together in such a way that analytic solutions are obtained in each segment and then matched across solution boundaries. Conditions under which instabilities in the jet will radiate energy are emphasized.

### Introduction

Although the Stream is the dominant feature of the North Atlantic general circulation and has been known of for centuries it has been largely ignored by modern physical oceanography. From an observational point of view the swift currents make it difficult to moor sensors in the region and from a theoretical perspective those same swift currents make the dynamical balances inherently nonlinear and, therefore, a difficult challenge for analytic methods. New technology in the form of high speed computers, high performance moorings, neutrally buoyant floats and acoustic tomography to name some examples has put us in the position where new understandings can be made of this difficult and challenging dynamical feature.

The nonlinear nature of the Stream has severely restricted purely theoretical investigations. These have followed three different paths from which the latest ideas will be discussed below.

### Inertial Boundary Layers

a) Steady state: The first modern theoretical representation of the Gulf Stream was in Stommel's (1948) wind driven frictional closed gyre model. Here, a frictional western boundary layer permitted the vorticity input from the wind to be dissipated such that the interior southward Sverdrup transport could be returned

to the north in a (relatively) narrow current. It was soon realized that the nonlinear advective terms in the vorticity balance were more important than friction in the boundary layer and there followed a flurry of inertial boundary layer models of the Stream all pivoted around some convenient linearization.

For example, the steady nonlinear equations of motion for the upper layer of a reduced gravity problem (only the upper layer in motion) can be manipulated to show that the following quantities are conserved:

$$\text{potential vorticity; } \frac{f + \zeta}{D} = Q(\psi)$$

$$\text{Bernoulli potential; } \frac{u^2 + v^2}{2} + g'D = B(\psi)$$

where  $g'$  is the reduced gravity. The integrated mass continuity equation allows the definition of the transport function,  $\psi$ , and Charney (1955) showed that that the two functions above were related:

$$Q(\psi) = \frac{\partial B}{\partial \psi}$$

The most usual assumption is take the potential vorticity distribution to be uniform, i.e.

$$Q(\psi) = Q = \text{constant}$$

One then presumes the situation schematically outlined in Figure 1. A broad interior flow is incident on the western boundary where a narrow current develops in order to return this flow to the north. In doing this, vorticity is conserved so it is left to some other dynamical regime further to the north to dissipate this vorticity in such a way that the water can return to the interior with potential vorticity values appropriate to a more northern latitude. In the upstream region far to the east there is assumed to be no boundary current and, consequently, the westward drift is in geostrophic balance and the potential vorticity is just the local coriolis parameter divided by the upper layer thickness. The transport between the southern boundary and a more northern latitude,  $y$ , is given simply by:



The upper layer thickness is finite for values of the latitude such that  $f(y) < 2f(0)$  but vanishes where  $f(y) = 2f(0)$ . For example if the southern boundary is taken to be at  $20^\circ\text{N}$  then the latitude where  $D(0,y)$  vanishes is  $43^\circ\text{N}$ . Beyond this point there does not exist a solution to the problem, as posed, with a current against the western boundary: it is supposed that the current must exist as a free separated jet beyond this latitude.

b) Wave perturbations: Taking the solution for the mean flow outlined above it is possible to derive the dispersion characteristics of small amplitude motions included as a perturbation. The same semigeostrophic dynamics are assumed and because the basic state has uniform potential vorticity the only wave modes available are generalized Kelvin waves. Taking a separable form according to:

$$v'(x,y,t) = g(x)f(y-ct)$$

where  $c$  is the phase velocity it is possible to show that:

$$c = -(g'Q/f)^{1/2} D(0,y).$$

In other words, the phase velocity of the Kelvin waves is toward the south provided that the upper layer has finite thickness at the wall and vanishes where  $D(0,y)$  vanishes.

This aspect of the dispersion properties is reminiscent of what is found in hydraulic control. For example, consider the situation when water pours over a dam from a resting reservoir. Upstream of the dam the long gravity waves can propagate in either direction whereas downstream the flow is supercritical and waves can only travel away from the dam until the flow is returned to a subcritical state through the formation of a hydraulic jump. At the dam, itself, the phase velocity for the waves endeavoring to travel in the upstream direction vanishes: this is the control point. It would seem that the separation of the Stream from the coast could be considered a natural control induced by the combined effects of the variation of the Coriolis parameter with latitude and the converging transport south of the separation point. The former effect causes the Rossby radius of deformation to decrease toward the north. The ever increasing transport must be carried by an increasingly narrow current until the induced shear causes the interface to (geostrophically) surface. At this point the analogy with the weir problem breaks down for there is no extremum to the hypothesized Gulf Stream control mechanism. However, one could conjecture that the downstream region is one in which the flow must go through a

transition to a subcritical state and the violent meandering may be some indication of this process.

c) Stratification: Blandford (1965) attempted to solve the classical inertial boundary problem for the reduced gravity case with two moving layers (three in all with the bottom one at rest). He discovered an apparent inconsistency in his solution in that thickness of the lower moving layer would vanish well south of the final separation point where the upper interface separates from the wall in a manner analogous to the one moving layer problem. He could find no way of determining a continuous solution all the way from the southern boundary to the final separation point.

Luyten and Stommel (1985) have recently reworked this problem with the hydraulic analogy firmly in mind. When two layers of fluid flow over a weir it is known that there exist two different control points, one at the weir itself - the physical control, and the other further upstream - known as a "virtual control" (Wood, 1968) where the phase velocity for the slower internal gravity wave mode is stopped. Between the two points the flow is supercritical with respect to the slower mode while downstream of the physical control it is supercritical with respect to both modes. The specification that the flow is continuous at this virtual control point further constrains the flow so that the potential vorticity of only one of the layers can be specified a priori: the other must be chosen to give a continuous solution. Blandford (1965) attempted to specify the potential vorticities of both layers and, consequently, his solutions were discontinuous at the virtual control point. Luyten and Stommel (1985) have solved an example calculation for a western boundary current flowing north from the equator (zero potential vorticity).

The possibility that the Gulf Stream is hydraulically controlled suggests that its dynamics controls that of the ocean interior and the two cannot be considered in isolation.

#### Thin Jet Models

Since the pioneering work of Warren (1963) there has been continued interest in the possibilities of predicting the path of the Gulf Stream given specific knowledge of only the state at Cape Hatteras. This work has been carried forth by Allan Robinson and various collaborators and has been put to test at least once in the field. The most recent contribution is that of Flierl and Robinson (1984) which is concerned with the influence of the external motion field on the Stream itself. Contrary to previous work they find that for parameter values appropriate to the Stream that the external field cannot be ignored.

The derivation of a path equation involves a number of specific assumptions about the character of the Stream. With reference to Figure 2 the most important are that 1) the Stream width is small compared to any along stream length scale,  $L$ , 2) the Rossby number based on  $L$  is small (that based on the width can be order 1), 3) the perturbing velocities of the meandering motions are small relative to the downstream jet velocity and 4) that the jet is inextensible; that is, the Stream moves without changing its velocity profile which is further assumed to be only



a function of a cross-stream coordinate and depth. The coordinate system is transformed into a time dependent curvilinear one aligned with the instantaneous Stream as is shown in Figure 2. After separating the velocity into three contributions; that of the inextensible jet, that due to barotropic translations of the jet axis and that of the residual meandering motions a complicated differential equation for the jet axis is developed. This is integrated both in depth and across the Stream to finally derive the equation:

$$F_0(X,t)d + \bar{F}_1(X,t) \langle v \rangle + F_2(X,t) \langle v^2 \rangle \\ = -a \left[ \frac{\partial}{\partial t} + \psi \cos \theta \frac{\partial}{\partial X} \right] \int_{\text{bottom}}^{\text{top}} \mu_m dz \int_{\eta = -d/2}^{\eta = d/2}$$

where the  $F_i(X,t)$  are differential functionals of the axis position, the " $\langle \rangle$ " indicate the integration of the enclosed quantity in depth and across the Stream, and  $\mu$  is the along stream component of the residual meandering velocity evaluated at the inshore and offshore edges of the jet.

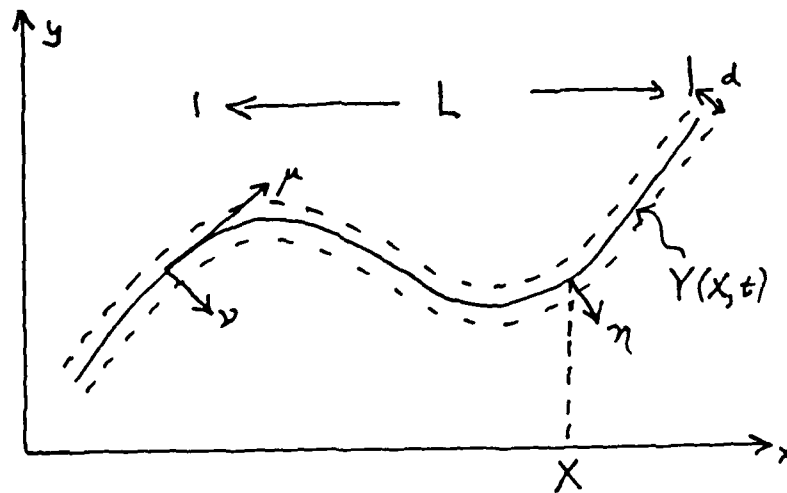


Figure 2. Schematic representation with parameter definitions of a thin jet model for the Gulf Stream.

The important new result of Flierl and Robinson (1984) is the derivation of the RHS of the above equation. Previously this contribution was neglected through inappropriate choice of parameters. Although the equation cannot be simply solved the conclusion is that no solution is valid that is not properly matched to the dynamics of the exterior field. It is also apparent that motions in the recirculations that arise independently through, for example, local instability processes

can influence the path of the Stream.

Flierl and Robinson (1984) have not been able to solve the full finite amplitude problem expressed above but do give a linearized small amplitude result where jet motions are matched to Rossby waves in the far field. They find the following dispersion relation:

$$2c^2 \left( \frac{\beta}{c} \right)^{1/2} + k^2 \langle v^2 \rangle - \beta \langle v \rangle = 0$$

with  $k$  being the zonal wavenumber. For values of the integrated fluxes appropriate to the Stream the solution to this equation is presented in Figure 3. Waves with scales less than about 150 km

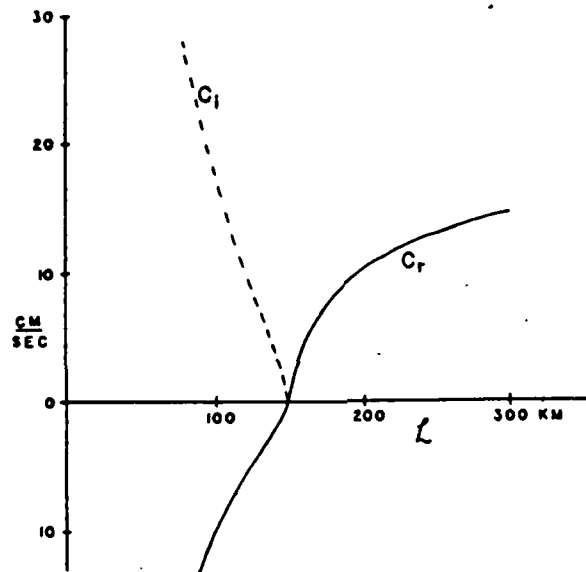


Figure 3. Dispersion relation for small amplitude motions on a thin jet from Flierl and Robinson (1984).

( 900 km wavelengths ) are unstable. A particular shortcoming of this model is that these waves propagate in the retrograde direction contrary to the more traditional instability results and the semi-circle theorem. It is believed that this is an artifact of the thin jet approximation.

The important results of the thin jet analysis are:

1) Stream path variations can force motions in the far field, and

2) Stream path variations can be forced by motions in the far field.

### Conventional Jet Instability

A more classical approach to the problem of unstable motions is to investigate the behavior of small amplitude motions on a steady, geostrophically balanced background flow. The difficulty lies in specifying the background flow such that it is both geophysically interesting and permits a tractable problem for the perturbations. Talley (1983a,b) has investigated jets which are pieced together from regions in which the meridional gradient of the potential vorticity takes on different constant values by supposing that the zonal velocity is either constant or a parabolic function of latitude. We shall confine our attention to her second paper (Talley, 1984b) which deals with the baroclinic problem. Somewhat analogous to the Flierl and Robinson work she is most interested in investigating the linkage between the jet motions and the exterior and finding conditions under which instabilities can radiate energy into the interior. This is a more traditional approach in which the coupling to the far field is conceptually simpler.

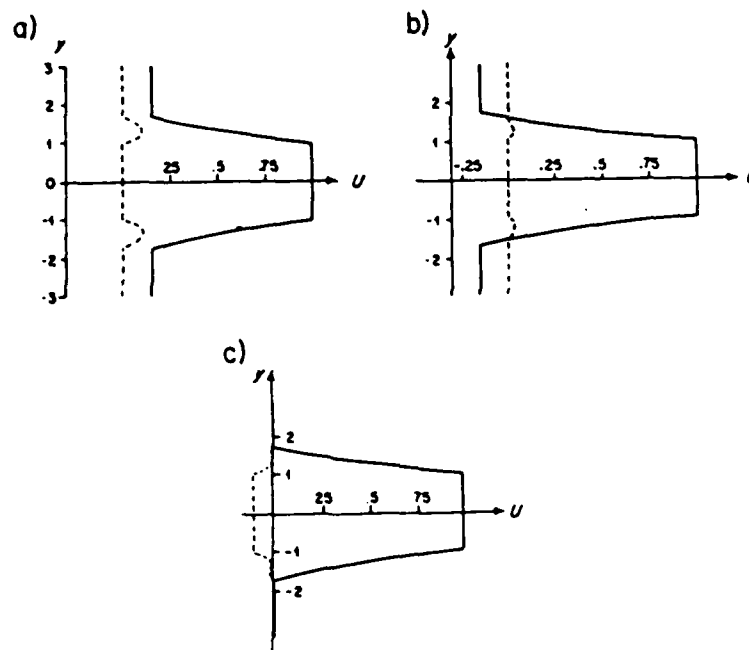


Figure 4. Possible two layer jet configurations which will radiate to the interior when the upper layer jet velocity is eastward.

For far fields which are quiescent in their undisturbed state the small amplitude motions must be planetary Rossby waves whose phase velocity is westward. It is, therefore, relatively easy for instabilities in a westward jet to couple to the forced waves in the exterior as their phase velocities are also westward. However, it is more difficult to find situations in which an eastward jet such as the Gulf Stream will radiate. Shown in Figure 4 are three such configurations that are discussed in detail by Talley. In each case radiation is possible because the

an eastward component has been added to the phase velocity of the exterior motions or a westward component has been added to the jet instabilities.

The Talley study reaches the following set of conclusions:

1) In general both trapped and radiating modes are possible but the latter can occur only if;

a) the jet has a westward part, or

b) there exists an eastward recirculation,

2) Trapped instabilities dominate the near field of the Stream and are barotropic away from the jet,

3) The usual source of energy is potential,

4) The radiating waves are also usually barotropic but can be baroclinic at very low frequencies,

5) The trapped waves can explain the observed meridional distributions of  $u'v'$  but, because they are barotropic they do not explain the observed southward thermocline heat flux,

6) For parameters appropriate to the Gulf Stream region the recirculations are also baroclinically unstable and this gives an alternate, independent source of energy.

### Relevant Observations

The principal conclusion of the recent theoretical studies described above is that the Gulf Stream cannot be studied in isolation from its surroundings. Both the Flierl and Robinson (1984) and the Talley (1985) problems suggest that motions in the recirculations of the Stream will have an impact on the Stream itself. In Figure 6 are shown time series of horizontal velocity

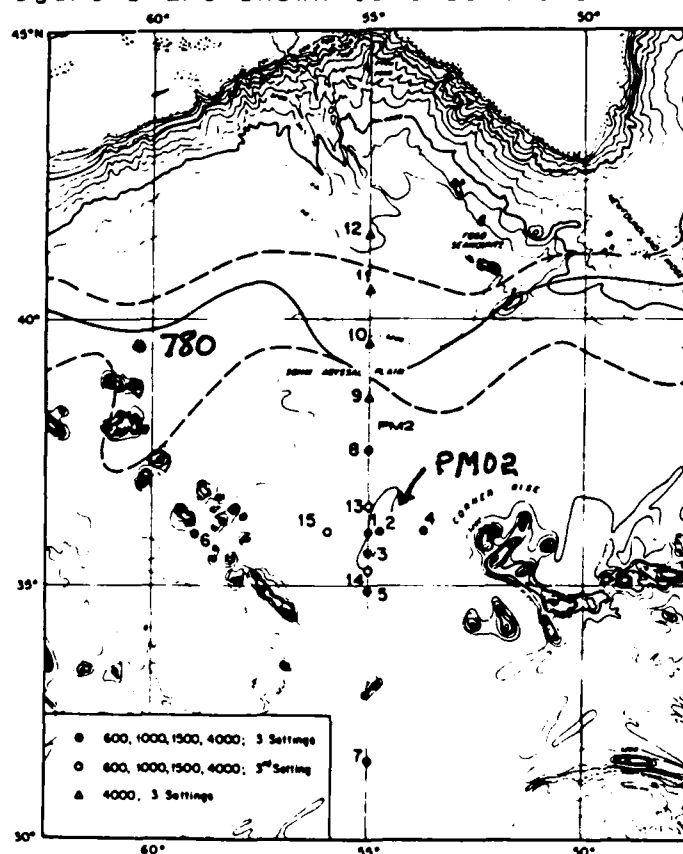
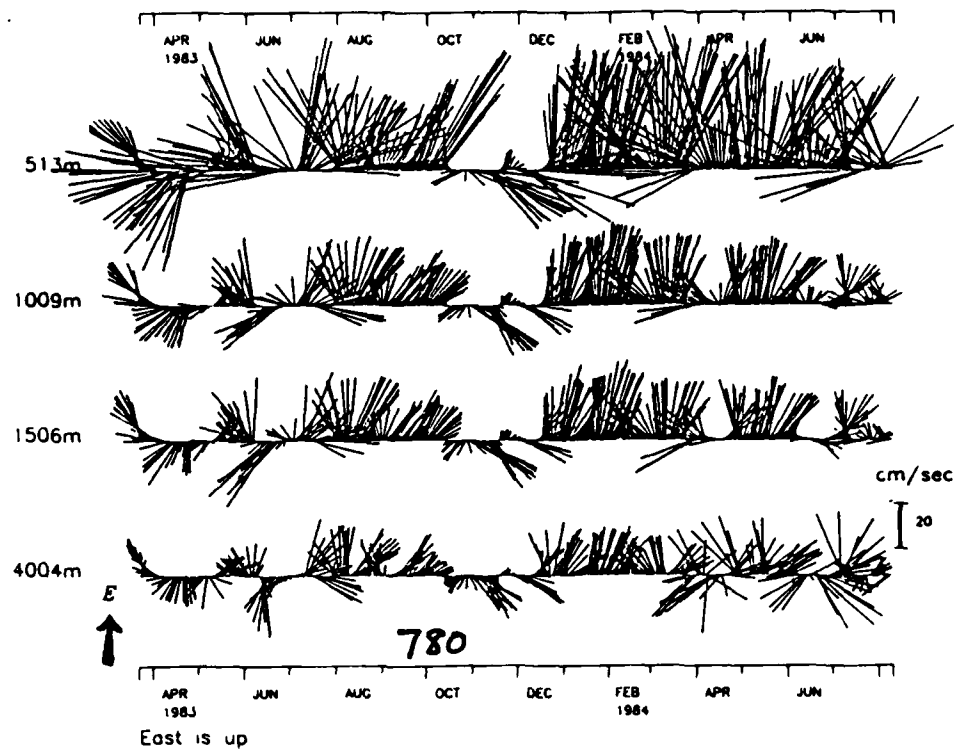


Figure 5. Positions of the moorings whose time series of velocity are shown in Figure 6.



## PM02

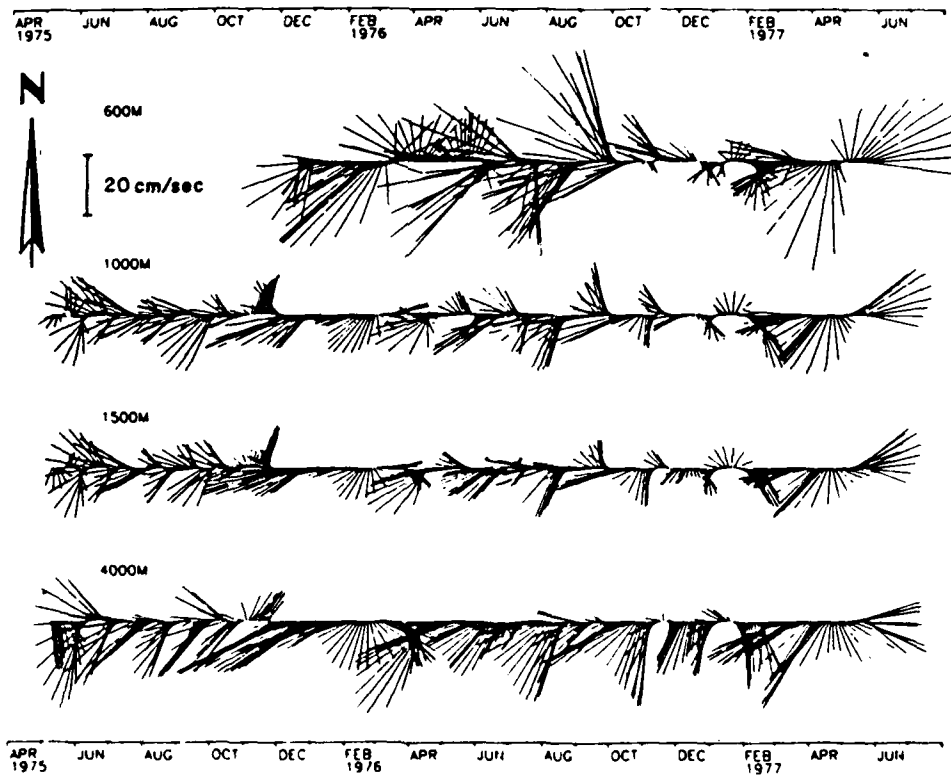


Figure 6. Time series of horizontal velocity at various depths from the two moorings located in the Stream and the southern recirculation, as shown in Figure 5.

from two moorings, one in the Gulf Stream for most of the time and the other primarily in the "Worthington Gyre" the recirculation to the south of the Stream. Precise locations are shown in Figure 5. Although the records are not simultaneous, note their similar character: both exhibit strong almost depth independent low frequency motions. Could this be the barotropic trapped mode of Talley (1984b)?

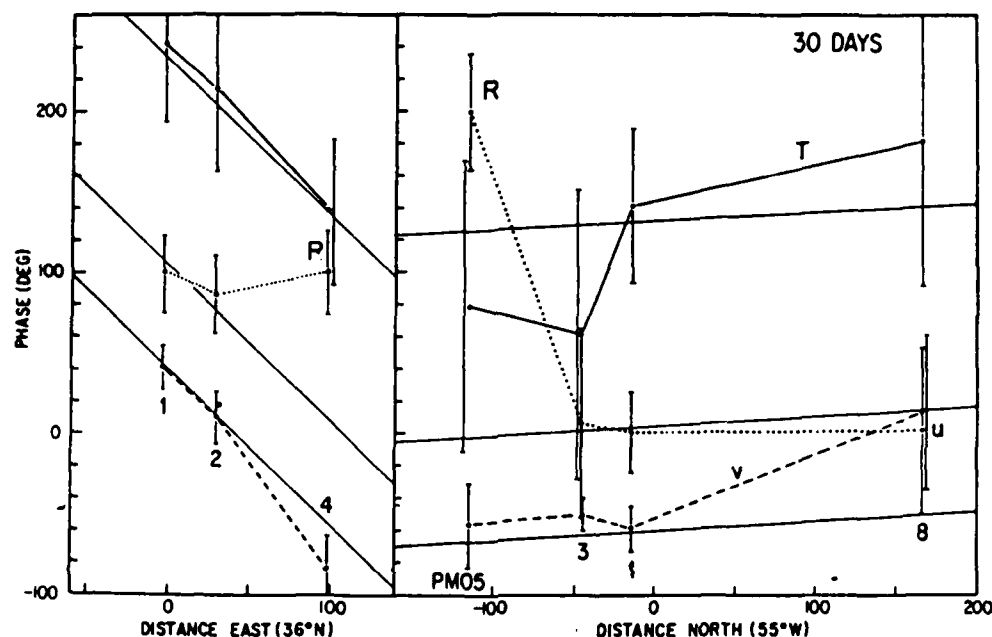


Figure 7. Meridional and zonal phase variations determined from the array of moorings near 36°N, 55°W on Figure 5. These indicate a northwestward propagation for both bands shown.

Shown in Figure 7 are meridional and zonal phase plots from an empirical orthogonal function study (in the cross-spectral domain) of motions in the indicated frequency bands at the moorings indicated. There is both westward and northward phase propagation consistent with the idea that these are a planetary wave forced by the Stream to the north. A similar study of the vertical structure is shown in Figure 8. Here there is a consistent trend in phase upwards (as well as horizontally) such that deep motions lead shallow motions - a strong signature of in situ baroclinic instability. In fact, Hogg (1985) has shown that these motions closely resemble those predicted by the Gill, Green and Simmons (1974) study for reasonable mean flows. concomitant with these kind of motions is a release of available potential energy which produces a southward heat flux in the main thermocline.

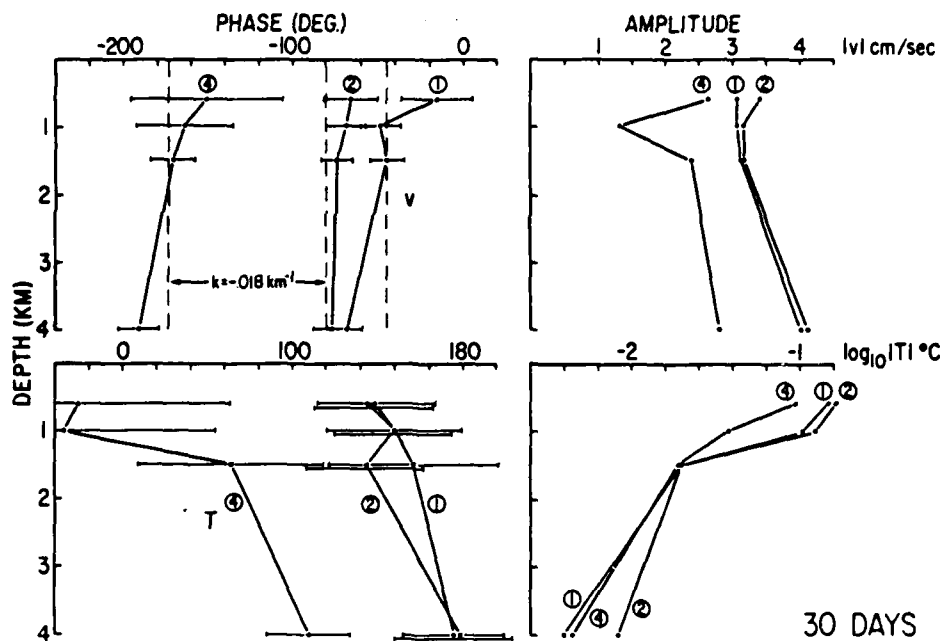


Figure 8. Vertical phase variations for a selected set of moorings from the group used in Figure 7 showing upward phase propagation.

This suggests that Gulf Stream radiation is not responsible for the energetic motions seen in the nearby recirculation. One has to wonder how much of the motions in the Stream, itself, are instead forced by the instabilities of the recirculations.

References

- Blandford, R. 1965. Inertial flow in the Gulf Stream. *Tellus* 17, 69-76.
- Charney, J.G. 1955. The Gulf Stream as an inertial boundary layer. *Proc. Nat. Ac. Sci.*, Washington, 41, 731-740.
- Flierl, G.R. and A.R. Robinson 1984. On the time-dependent meandering of a thin jet. *J. Phys. Oceanogr.* 14, 412-423.
- Gill, A.E., J.S.A. Green and A.J. Simmons 1974. Energy partition in the large-scale ocean circulation and the production of mid-ocean eddies. *Deep-Sea Res.* 21, 499-528.
- Hogg, N.G. 1985. Evidence for baroclinic instability in the Gulf Stream Recirculation. *Prog. Oceanogr.* 14, 209-229.
- Luyten, J. and H. Stommel 1985. Upstream effects of the Gulf Stream on the Structure of the mid-ocean thermocline. *Prog. Oceanogr.* 14, 387-399.
- Stommel, H. 1948. The westward intensification of wind-driven ocean currents. *Trans. Amer. Geophys. Union* 29, 202-206.
- Talley, L.D. 1983a. Radiating barotropic instability. *J. Phys. Oceanogr.* 13, 972-987.
- Talley, L.D. 1983b. Radiating instabilities of thin baroclinic jets. *J. Phys. Oceanogr.* 13, 2161-2181.
- Warren, B.A. 1963. Topographic influences on the path of the Gulf Stream. *Tellus* 15, 167-183.
- Wood, I.R. 1968. Selective withdrawal from a stably stratified fluid. *J. Fluid Mech.* 32, 209-223.



DATA ASSIMILATION, MESOSCALE DYNAMICS

AND

DYNAMICAL FORECASTING

- . INTRODUCTION
- . MODELS, METHODS AND ISSUES
- . A REAL TIME EXPERIMENT
- . SIMULATIONS, EXPERIMENTAL DESIGN, ASSIMILATION STRATEGIES

by

Allan R. Robinson

Harvard University  
Center for Earth and Planetary Physics  
Cambridge, Massachusetts

## INTRODUCTION

We are carrying out research on the optimal estimation of oceanic fields which involve a central focus on real ocean data assimilation in dynamical ocean models. Our formulation of the conceptual basis is in terms of an Oceanic Descriptive-Predictive System (ODPS) (Figure 1- from Robinson and Leslie, 1985) consisting of i) an observational network, ii) a statistical model, and iii) a dynamical model. Optimal estimation involves the melding of field estimates from the three components of the system; the high order statistics required for this process which are generally not yet known for the ocean are taken now from computer generated data obtained by simulation runs of the dynamical model. The field estimates are useful for physical studies as well as other scientific and practical applications. The "dynamical model" component of the system is in fact a multiscale hierarchy of coupled models developed (Figure 2- from Robinson and Marietta, 1985, and Robinson and Marietta, 1984) by the Harvard group in collaboration with Dr. M.G. Marietta's group at Sandia National Laboratories. The hierarchy is intended for studies of ocean current dynamics and of the general circulation, and for transport and dispersion studies over a wide range of scales. (The application of interest to the SNL group is associated with feasibility studies for subseabed disposal of high level nuclear wastes.) Figure 2 shows the Harvard Open Ocean Model, a Regional Eddy Resolving Model (REM) with attached upper and bottom boundary layers embedded in a coarse resolution General Circulation Model (GCM). Central to our approach and the main topic of this communication, is the assimilation of real and intensive data sets (hydrography, currents, sea-surface height, etc.) in the REM. The purposes are to study local dynamical processes and to verify regional

model components, so as to construct a general circulation model from regional components which are consistent with all available data. The components of the hierarchy and the coupling mechanisms should be iteratively improved. The present GCM is a converged (2055 model years) prognostic Bryan-Semtner model in idealized geometry; the GCM component is being tuned to large scale hydrographic, geochemical and transient tracer fields.

#### MODELS, METHODS, AND ISSUES

The present REM is the Harvard Open Ocean Model, a "portable" baroclinic, quasigeostrophic (q-g) model which is shown schematically in Figure 3 (Robinson and Walstad, 1985). The arbitrary (water-water) boundaries are open, but recent progress (not to be further discussed here) allows partially or totally closed boundaries and interior domain islands (Carton, 1985). The mean stratification and local bottom topography describe the local environment, and the fundamental initial-condition/boundary-condition problem IC/BC requires an initial q-g stream function (geostrophic-pressure) field with its associated vorticity field and the specification of inflow-outflow on the boundaries at every time step and as well as vorticity on the boundary inflow points at each level (Charny-Fjortoft-Von Neumann conditions). Numerically, the model is finite-element in the horizontal (Haidvogel, Robinson and Schulman, 1980) and finite-difference or collocation in the vertical (Miller, Robinson, and Haidvogel, 1983). Since the purposes of data assimilation in the model are optimal field estimations, dynamical interpolation and forecasting, and model verification, it is essential to identify and attribute sources of error. Errors arise from i) computational operations, ii) the quantity and quality of observational data, iii) physical inadequacies of the dynamical and statistical models including: explicitly resolved and sub-grid-scale physics, and the structure

of the statistical model and the evaluation of statistical quantities. The interpretation of the *difference-field* between analyzed observations and dynamical model forecasts/scientific-runs is crucial. The model has been computationally calibrated against some exact (advecting-Rossby wave solutions) and also against simulated data characteristic of real oceanic condition of interest (Miller and Robinson, 1984). In conditions characteristic of the POLYMODE SYNOPTIC-DYNAMIC EXPERIMENTS (P-SDE), the model run in a forecast mode with "true" simulated IC/BC data can maintain a NRMS interior error of only a few percent for longer than a year. Initializing the model with real data generally requires the regular gridding in space and time of irregular, asynoptic and gappy data sets, and the compositing of different data types and sampling schemes. This is accomplished in the horizontal by a multi-variate anisotropic mixing space-time objective-analysis scheme (Carter, 1983; Carter and Robinson, 1985) and in the vertical by projecting onto the q-g dynamical modes or on empirical orthogonal functions (Smith, Mooers, and Robinson, 1985). Jets, fronts, multiple types of eddies etc. in complex oceanic regions require highly anisotropic, nonstationary and inhomogeneous statistical models which we are researching. A real data forecast experiment from the PSDE is shown in Figure 4a, and Figure 4b summarizes the behavior of the model with respect to quality of the boundary condition data made available. An important model development recently completed is the attachment of an upper mixed layer model to the REM for dynamical studies and particularly for the assimilation of satellite IR-SST. L. Walstad (1985) accomplished (Figure 5) a first prototype forecast in real time of the mixed layer in the California Current jet and eddy regime (Mooers and Robinson, 1984). Finally in order to use our system as a tool for learning oceanic physics and dynamics from real ocean data, a self-consistent open-ocean

energy and vorticity analysis scheme (EVA) has been developed. The present version employs consistent quasigeostrophic energy equations (Figure 6), which are evaluated entirely in terms of the zeroth order geostrophic pressure field (Pinardi and Robinson, 1985). Running real data fields through the dynamical model as a quasigeostrophic filtering process allows the evaluation of high derivatives required for consistent energetics.

#### A REAL TIME EXPERIMENT

In the context of the OPTOMA program (Ocean Prediction Through Observation Models and Analysis) conducted by the Harvard group together with Prof. C.N.K. Mooers' group at the Naval Postgraduate School data is being collected and the ODPS developed and verified. Figure 7 shows a successful two-week *real time* forecast (Robinson et al., 1985) in which two eddies merged to form a zonal jet via interval dynamical processes within a 150 km sq. region. An after the fact "forecast experiment" which boundary condition updating (Figure 7) nearly perfectly replicates the verification data and illustrates the power of dynamical model interpolation; the eddy merger could not be described by the two data sets alone. EVA (Figure 8) shows the merger to be a "finite amplitude barotropic instability event (Robinson, Carton, Pinardi, et al., 1985).

#### SIMULATIONS, EXPERIMENTAL DESIGN, ASSIMILATION STRATEGIES

New strategies for realistic simulations of oceanic regions are being studied involving running the dynamical mode backward and forward between connected and disconnected field realizations. Based on such data sets, we have evolved via simulated experiments the modular concept of model initialization for nowcasting and forecasting. This involves i) dynamical

interpolation of boundary data into a data empty module (as large as 75 km for the California Current region), ii) building up a large region out of connected modules, and iii) reinitialization of regions with past data and new boundary conditions before melding forecasts with new data. Taking advantage of hardware miniturization and our growing real time experience, we are initiating "shipcasting", i.e., dynamical forecasting at sea with ship-board computers; including EVA will allow data acquisition in dynamically crucial regions. A prototype shipcast over the Nares Plain in the (Walstad et al., 1985) Northwest Atlantic is shown in Figure 9. DeMey and Robinson (1985) have simulated the assimilation of satellite altimetric data using the PSDE set and demonstrated (Figure 10) the remarkable ability of the dynamical model to generate the correct deep flow after a few days; the procedure involves projecting onto the EOF's. Finally, we have now set-up the Harvard models and the ODPS in the Gulf-Stream region (Robinson, Pinardi, and Spall, 1985). Our strategy involves using "feature models" (Figure 11) for the stream and rings, as well as 2-, 3- or 4-dimensional data sets as available (Rafos floats, AXBT's current meters, etc.). The assimilation procedure and forecast thus involves three steps: i) an initial *dynamical adjustment* of the features, ii) *dynamical interpolation* between the features and then iii) the *dynamical evolution* of the flow. Using NOAA analyzed SST alone, the dynamical model was initialized for November 23, 1984. As shown in Figure 12 the stream developed a deep sock meander and snapped off a cold ring, which was observed to occur in the NOAA analysis of December 1984. This scheme is being developed for research in the ONR sponsored SYNOPS program and will include the assimilation of GEOSAT data in collaboration with researchers at Johns Hopkins/APL (Dr. Jack Kalman) and at Sandia National Laboratories (Dr. M. Marietta).

AD-A162 506

PROCEEDINGS OF THE GULF STREAM WORKSHOP HELD AT WEST  
GREENWICH RHODE ISLA (U) RHODE ISLAND UNIV KINGSTON  
GRADUATE SCHOOL OF OCEANOGRAPHY D R WATTS APR 85

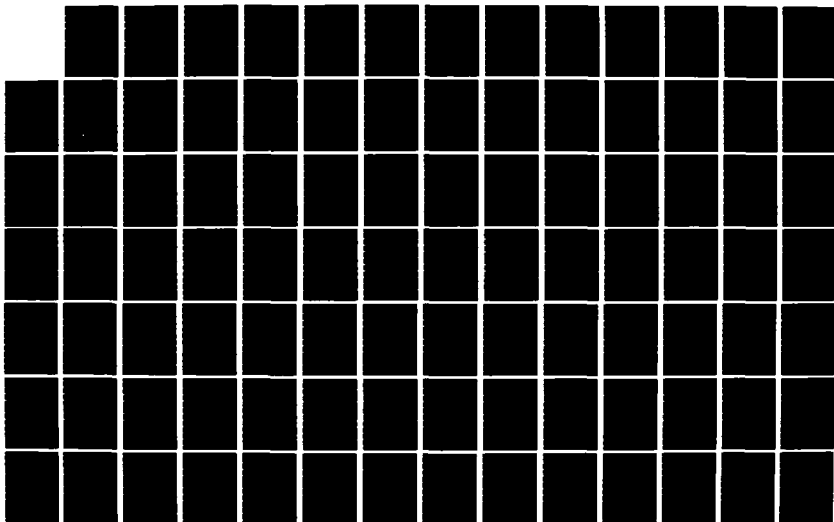
277

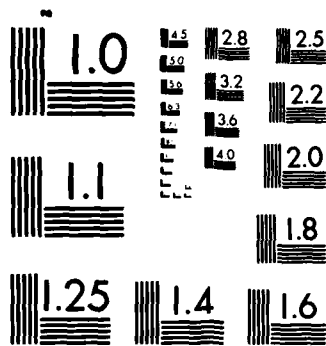
UNCLASSIFIED

N00014-85-G-0322

F/G 8/3

NL





MICROCOPY RESOLUTION TEST CHART  
NATIONAL BUREAU OF STANDARDS-1963-A



DIRECTIONS OF RESEARCH currently in progress include:

- Coupled Upper Mixed Layer Studies (including biology),
- Development of a Primitive Equation Open Ocean Model,
- Development of Inhomogeneous, Non-stationary and Anisotropic Statistical Models,
- Field Melding and Four-Dimensional Assimilation Strategies,
- Shipcasting, Nowcasting and Local Dynamic Methodologies, and
- Embedding Strategies.

## REFERENCES

1. Carter, E.F. (1983). The Statistics and Dynamics of Ocean Eddies, Reports in Meteorology and Oceanography, No. 18, Division of Applied Sciences, Harvard University.
2. Carter, E.F. and A.R. Robinson. (1985). An Analysis Model for the Estimation of Oceanic Fields, Journal of Atmospheric and Oceanic Technology (submitted).
3. Carton, J.S. (1985). private communication.
4. DeMey, P. and A.R. Robinson. (1985). Simulations for the Assimilation of Satellite Altimetric Data at the Oceanic Mesoscale, (in preparation).
5. Haidvogel, D.B., A.R. Robinson, and E.E. Shulman. (1980). The Accuracy, Efficiency and Stability of Three Numerical Models with Application to Open Ocean Problems, Journal of Computational Physics, 34(1), 1-53.
6. Miller, R.N., A.R. Robinson, and D.B. Haidvogel. (1983). A Baroclinic Quasigeostrophic Open Ocean Model, Journal of Computational Physics, 50(1), 38-70.
7. Miller, R.N. and A.R. Robinson. (1984). Dynamical Forecast Experiments With a Baroclinic Quasigeostrophic Open Ocean Model, in "Proceedings of Conference on Predictability of Fluid Motions" (G. Holloway and B. West, eds.), American Inst. of Phys., Proceedings No. 106, AIP, New York.
8. Mooers, C.N.K. and A.R. Robinson. (1984). Turbulent Jets and Eddies in the California Current and Inferred Cross-Shore Transports, Science, 223, 51-53.
9. Pinardi, N. and A.R. Robinson. (1985). Local Quasigeostrophic Energy and Vorticity Analysis of Mesoscale Fields, (in preparation).

10. Robinson, A.R. and M.G. Marietta, editors. (1984). Report of the Second Annual Interim Meeting of the Seabed Working Group, Physical Oceanography Task Group (POTG), Fontainebleau, France, "Research, Progress and the Mark S Box Model for Physical, Biological and Chemical Transport" (in press).
11. Robinson, A.R., J.A. Carton, C.N.K. Mooers, L.J. Walstad, E.F. Carter, M.M. Rienecker, J.A. Smith, and W.G. Leslie. (1984). A Real Time Dynamical Forecast of Ocean Synoptic/Mesoscale Eddies, Nature, 309(5971), 781-783.
12. Robinson, A.R. and W.G. Leslie. (1985). Estimation and Prediction of Oceanic Fields, Progress in Oceanography, 14, 485-510.
13. Robinson, A.R. and M.G. Marietta, editors. (1985). Report of the Third Annual Scientific Workshop meeting of the Seabed Working Group, Physical Oceanography Task Group (POTG), Neuchatel, Switzerland, "Research, Progress and the Description, Modelling Formulation and Dispersal Characteristics of Potential Disposal Sites in the North Atlantic", (in preparation).
14. Robinson, A.R., J.A. Carton, C.N.K. Mooers, N. Pinardi, E.F. Carter, W.G. Leslie, and L.J. Walstad. (1985). An Experiment in Dynamical Forecasting in the California Current, (in preparation).
15. Robinson, A.R. and L.J. Walstad. (1985). Numerical Modelling of Ocean Currents and Circulation, (to appear in Numerical Fluid Dynamics).
16. Robinson, A.R., N. Pinardi, and M.A. Spall. (1985). private communication.
17. Smith, J.A., C.N.K. Mooers, and A.R. Robinson. (1985). Estimation of Baroclinic Quasi-Geostrophic Model Amplitudes from XBT/CTD Survey Data, Journal of Atmospheric and Oceanic Technology, (to appear).
18. Walstad, L.J., A.R. Robinson, S.L. Kupferman, M.G. Marietta, D. Dietrich, J. Garner, and W.G. Leslie. (1985). A Prototype Real Time Forecast Via Shipborn Computer, (in preparation).
19. Walstad, L.J. (1985). Private Communication.

## FIGURE CAPTIONS

1. Schematic of the Descriptive-Predictive System (Robinson and Leslie, 1985).
2. Hierarchy of Coupled Models (Robinson and Marietta, 1985).
3. Harvard Quasigeostrophic Open Ocean Model Schematic.
- 4.a. POLYMODE Synoptic Dynamics Experiment Benchmark Hindcast of 700m Streamfunction.
- 4.b. Model Behavior and Calibration; Tests and Preliminary Experiments.
5. OPTOMA XI Prototype Mixed Layer Forecast (Walstad, 1985).
6. Consistent Quasigeostrophic Energetics - EVA (Pinardi and Robinson).
7. OPTOMA V Forecast and Forecast Experiment (Robinson, Carton, Pinardi, et al).
8. OPTOMA V Vorticity Analysis (Robinson, Carton, Pinardi, et al).
9. Prototype Nares Shipcast (Walstad, Robinson, Kupferman, Marietta, et al).
10. Model Initialization with Altimeter Data (DeMey and Robinson, 1985).
11. Schematic of Stream and Ring Models.
12. Gulf Stream Initialization with IR Data showing Ring Formation.



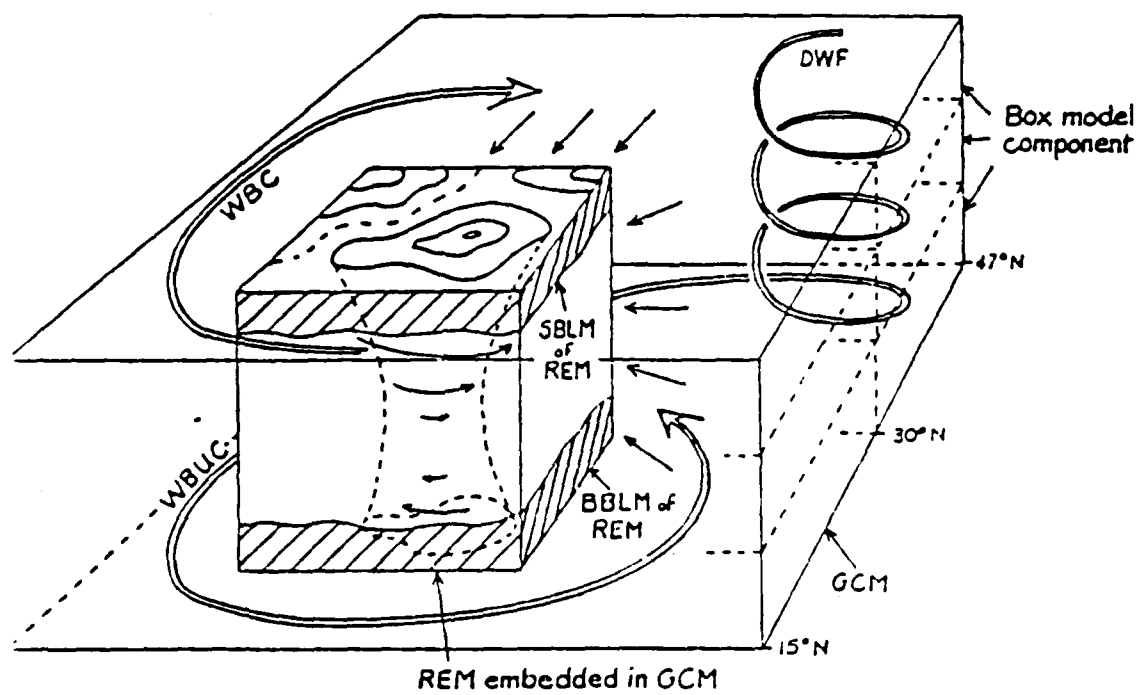


Figure 2

# PORTABLE OPEN OCEAN MODEL

$$\frac{\partial}{\partial t} \left( \nabla^2 \psi + f^2 (\psi_z)_z \right) + \mathcal{J}(\psi, \nabla^2 \psi + f^2 (\psi_z)_z) + \beta \psi_x =$$

IC/BC     $\psi$  inflow/outflow;  $\beta$  inflow     $\frac{f^2}{N^2 H^2}$      $\frac{\partial \psi}{\partial z}$      $\eta, \pi$

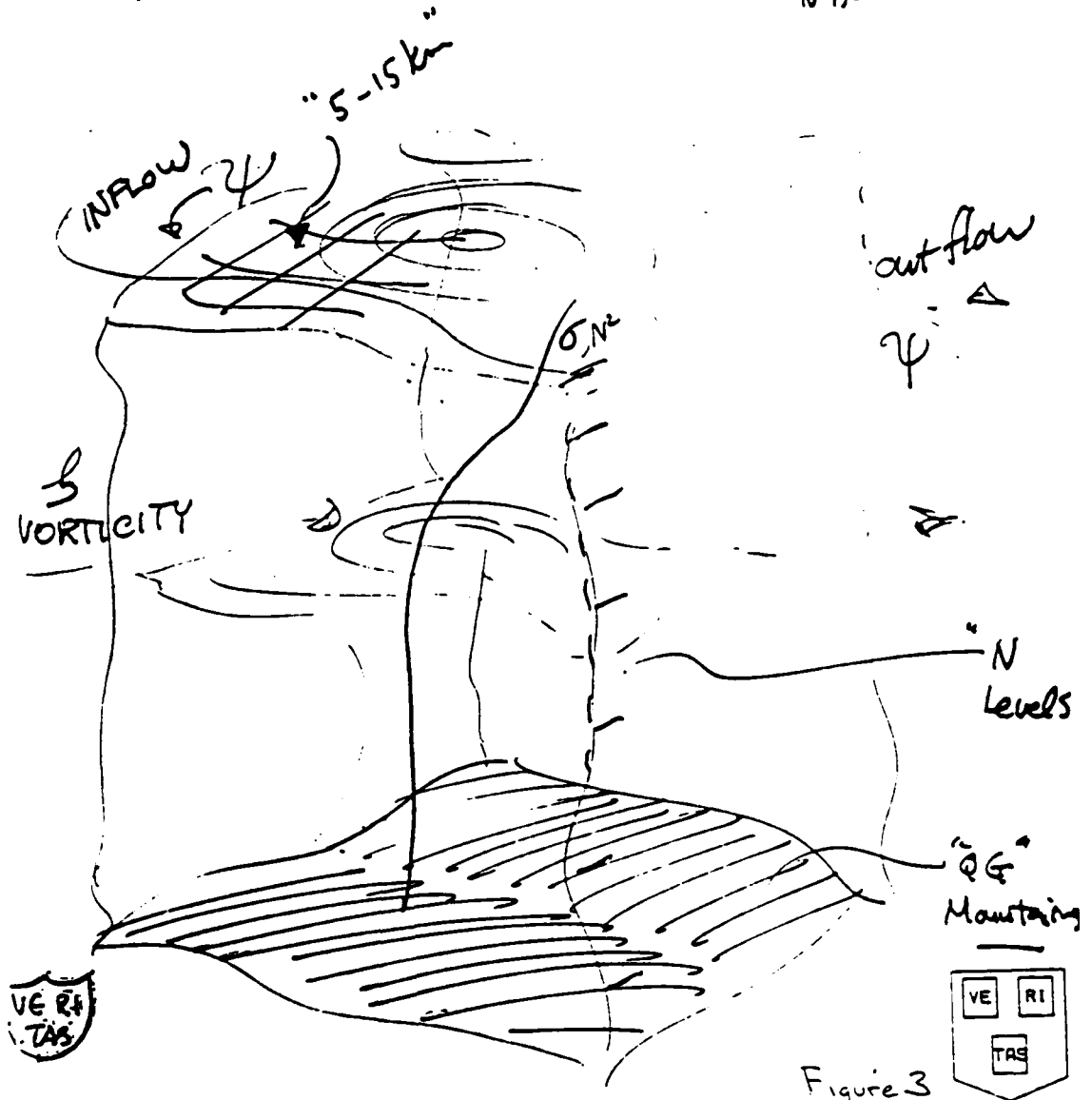
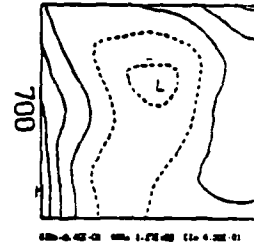


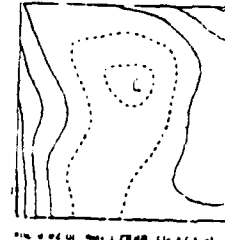
Figure 3

# Polymode Synoptic Dynamics Experiment Benchmark Hindcast

Hindcast STREAMFUNCTION



Data



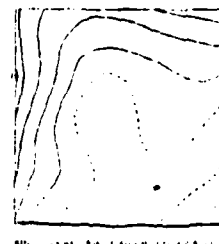
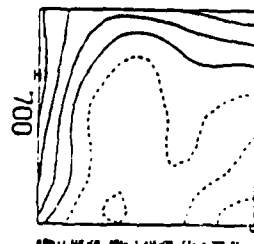
Julian Day

3410

(initialization)

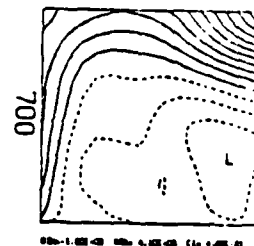
700m Streamfunction

STREAMFUNCTION



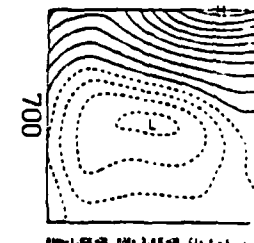
3420

STREAMFUNCTION



3430

STREAMFUNCTION



3440

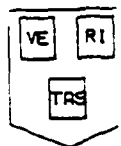
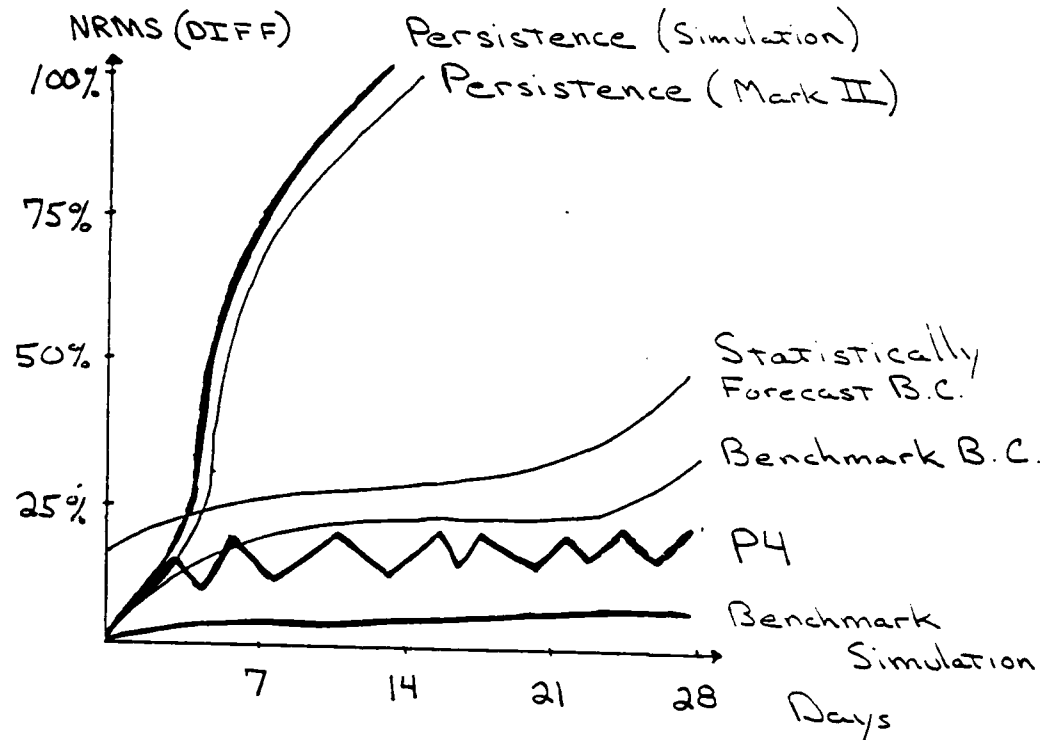


Figure 4a



# Model Behaviour and Calibration Tests and Preliminary Experiments



— Data (Mark II)  
— Simulation

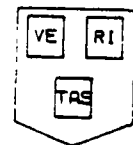


Figure 4b

Prototype  
OPTOMA XI. Mixed Layer Forecast

Initialization  
JULIAN DAY 5860



<30m

Forecast  
JULIAN DAY 5864



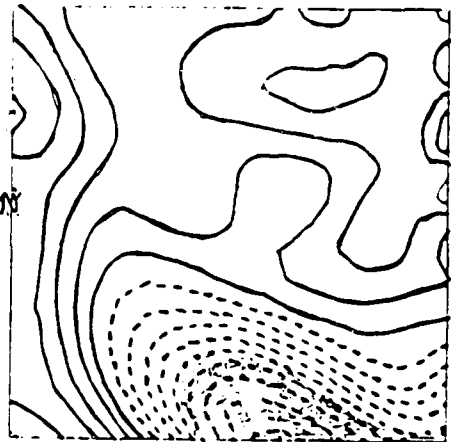
<30m

STREAM FUNCTION



<-

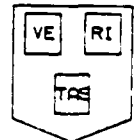
STREAM FUNCTION



<-2.5

(Walstad, 85)

Figure 5



$$\frac{\partial}{\partial t} K_0 = -\alpha \nabla \cdot (\vec{u}_0 K_0) - \nabla_H \cdot [p_1 \vec{u}_0 + p_0 \vec{u}_1] - (p_0 w_1)_z + \beta_0 \psi_1$$

$$\dot{K} = \Delta F_K + \Delta F_\pi + \partial_{T\pi} - b$$

$$\frac{\partial}{\partial t} A_0 = -\alpha \nabla \cdot (\vec{u}_0 A_0) - \beta_0 \psi_1$$

$$\dot{A} = \Delta F_A + b$$

$$\Delta F_\pi = -\nabla \cdot (p_0 \vec{u}_0 \times \hat{k} + p_0 \vec{u}_0 \cdot \nabla (\vec{u}_0 \times \hat{k})) - \beta_0 \vec{u}_0 \cdot \nabla p_0$$

$$\Delta F_\pi^{\text{acc}}$$

pressure work divergence  
due to the acceleration  
of geostrophic fields

$$\Delta F_\pi^{\text{adv}}$$

pressure work divergence  
of advective fluxes

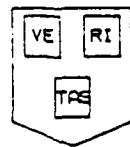
$$\Delta F_\pi^{\beta}$$

→ Due to horizontal gradients of momentum  
fluxes  $\nabla \cdot (\vec{u}_0 \vec{u}_0 \times \hat{k})$

→ In general triplet interaction theory  
this term allows for energy exchange between  
different horizontal wavenumbers since

$$\alpha \nabla \cdot (\vec{u}_0 p_0 q) = -\alpha \nabla \cdot (\vec{u}_0 K_0) + \nabla \cdot (\vec{u}_0 \cdot \nabla (\hat{k} \times \vec{u}_0) p_0)$$

$$q = \nabla^2 p_0$$



(Pinardi and Robinson)

Figure 6

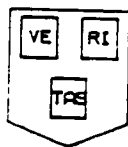
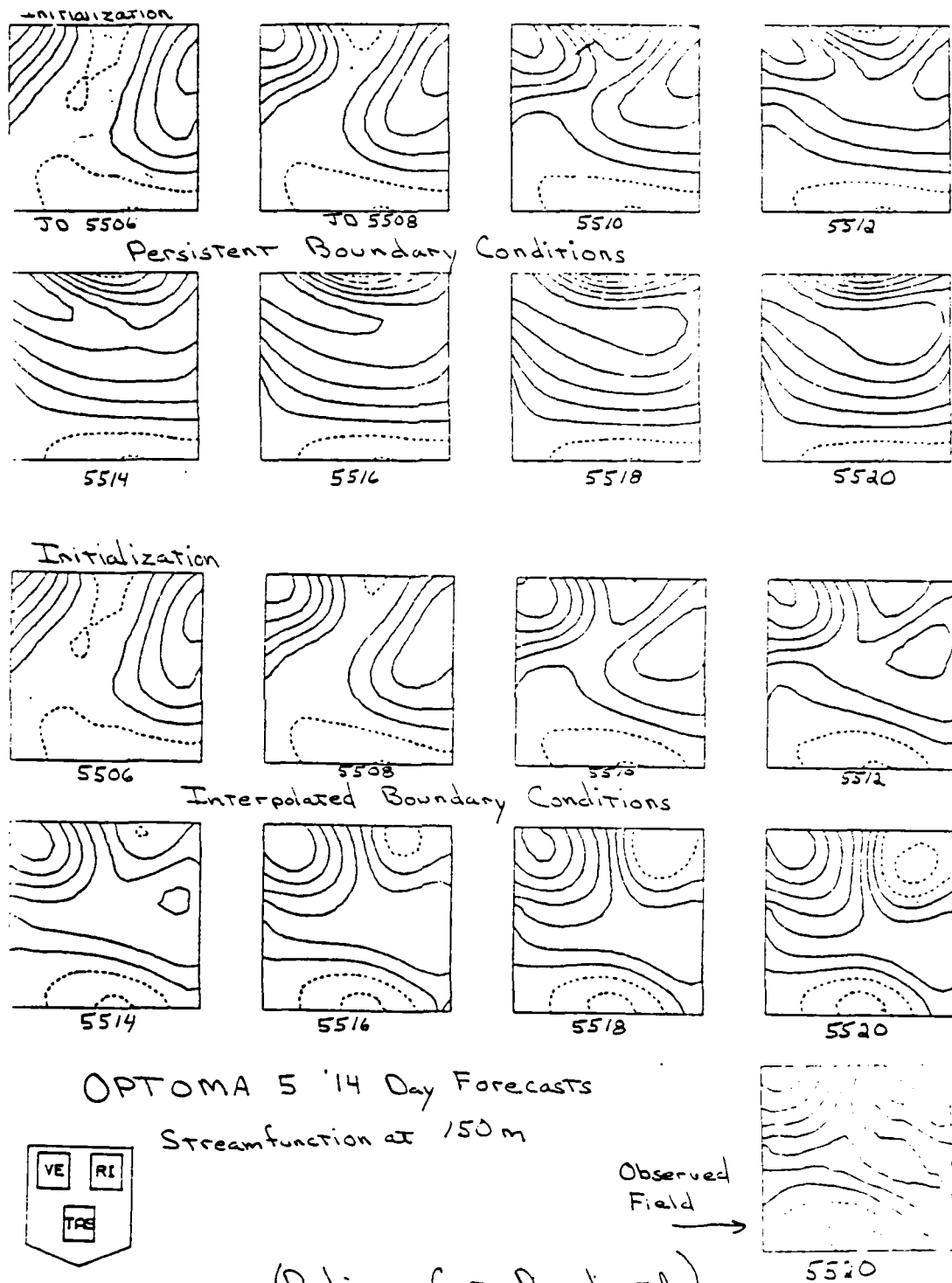
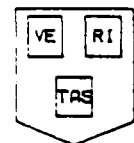
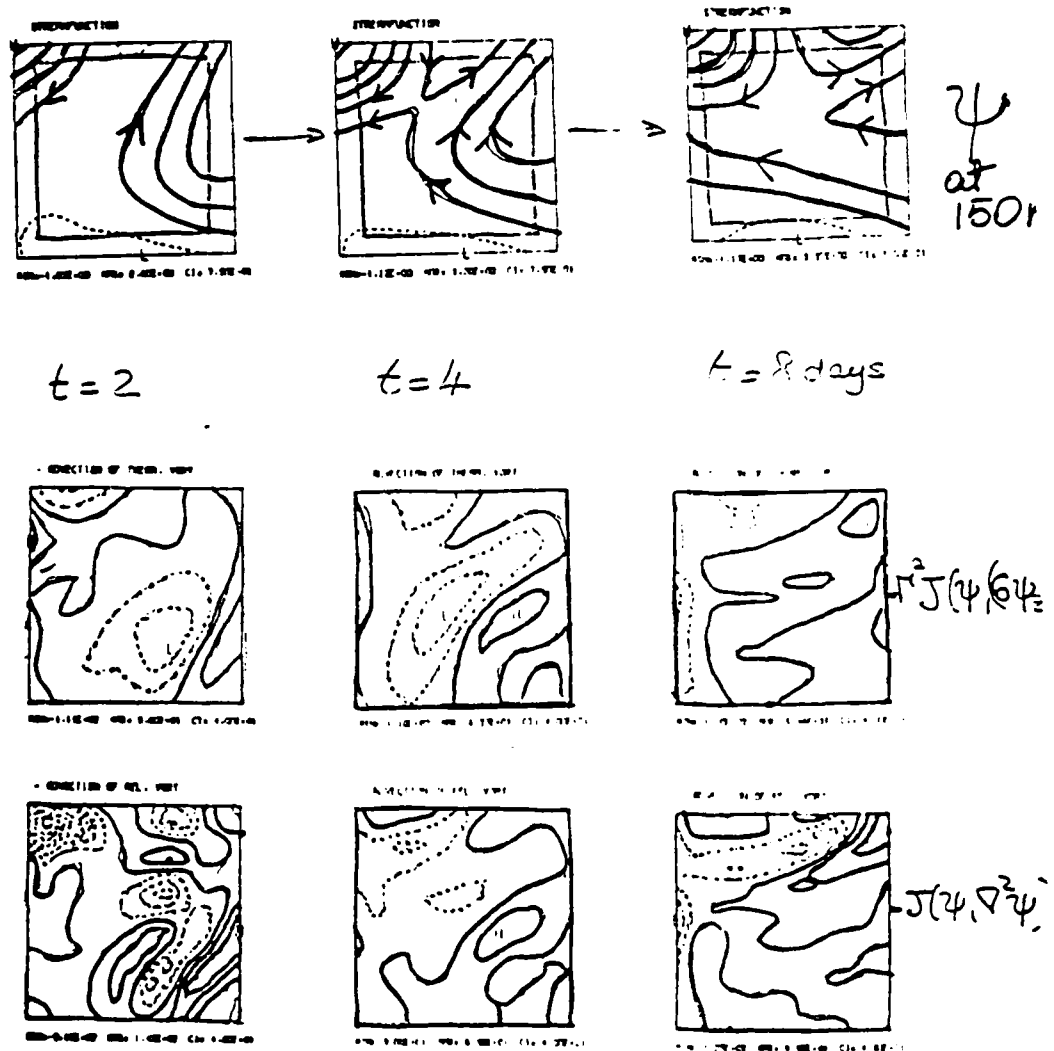


Figure 7

(Robinson, Carton, Pinardi, et al.)

# VORTICITY ANALYSIS OF Case Study 1 CENTRAL EXPERIMENT

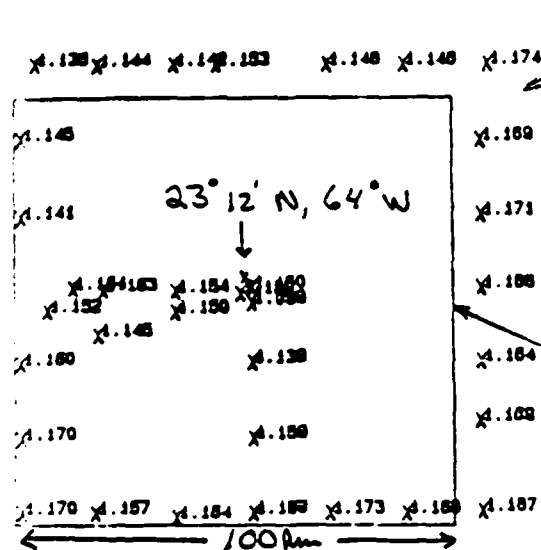


(Robinson, Carton, Pinardi, et al.)

Figure 8

# PROTOTYPE MARES SHIPCAST

Walstad, Robinson, Kupferman,  
Marietta, &



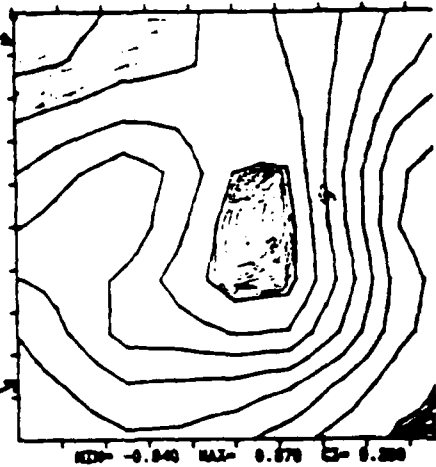
DATA LOCATIONS

30 XBT's, 5 CTD's

(Dynamic Height)

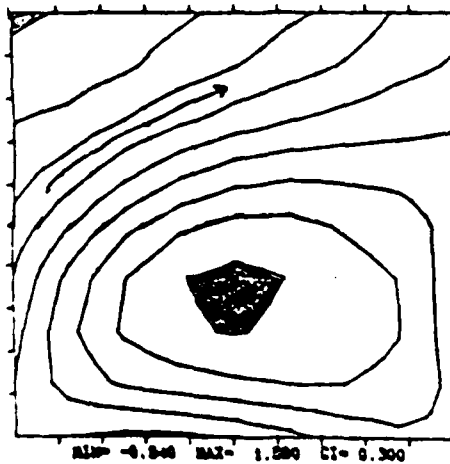
JULIAN DAY = 5967

STREAMFUNCTION



JULIAN DAY = 5977

STREAMFUNCTION

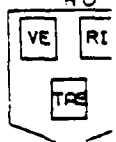


10 Day FORECAST of  
STREAMFUNCTION at 70m

Data to forecast requires  
~ 45 minutes

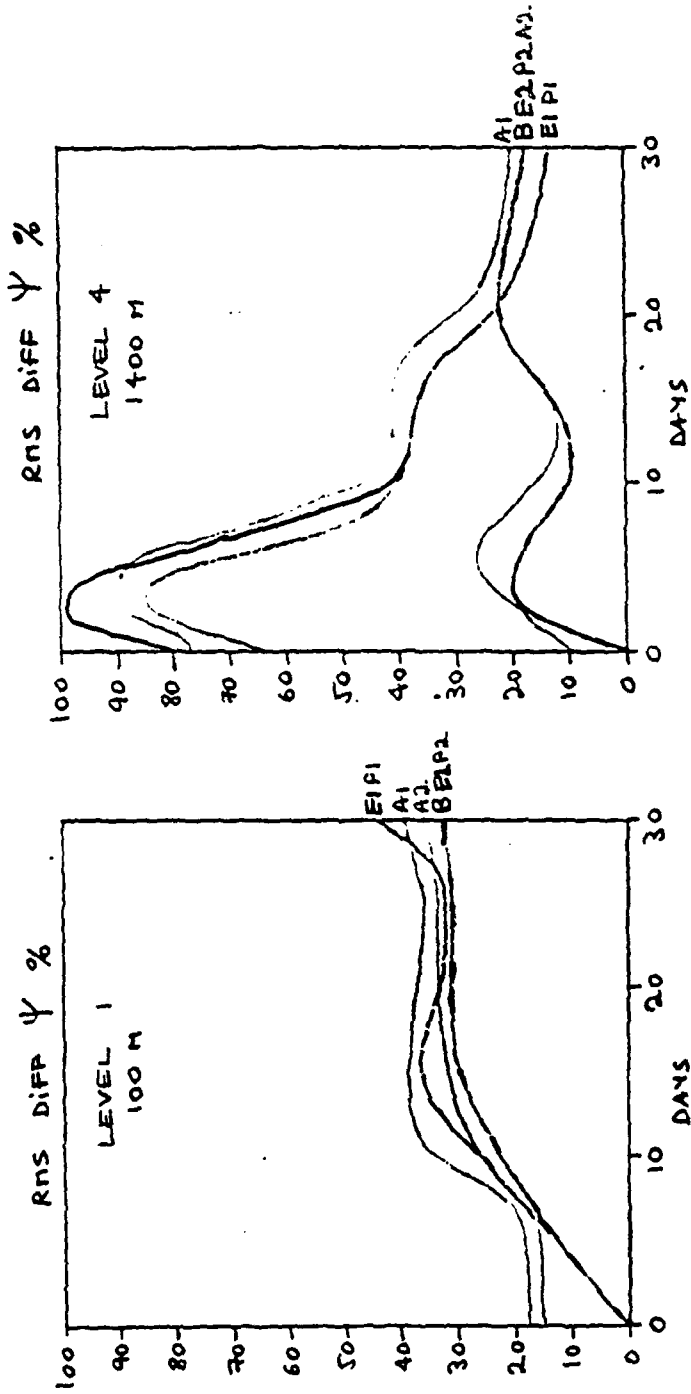


Figure 9



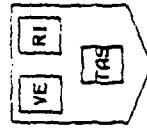
- BENCHMARK
- EXTENSION
- PROJECTION
- ALTI-METER EXTENSION

REFERENCE



3660 - 3690 FORECASTS  
WITH TOPOGRAPHY

INTERIOR FIELD



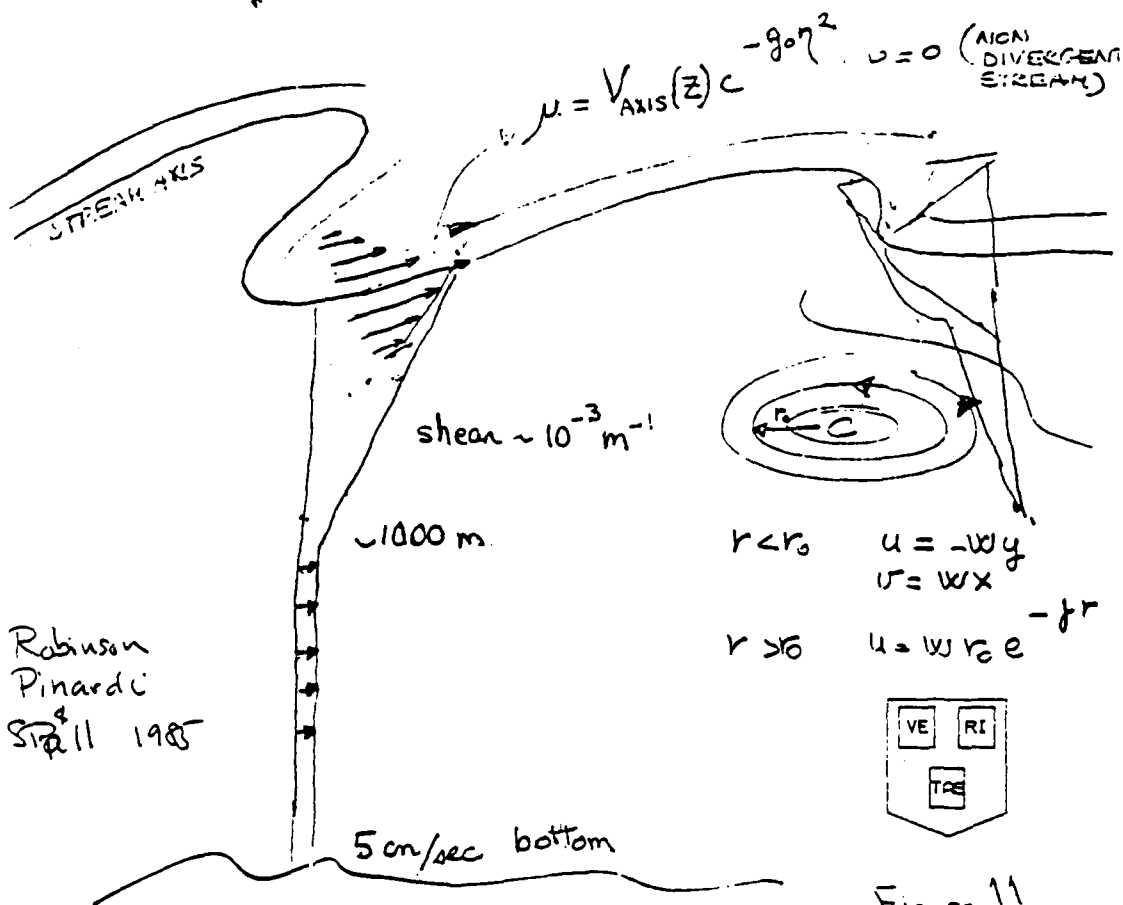
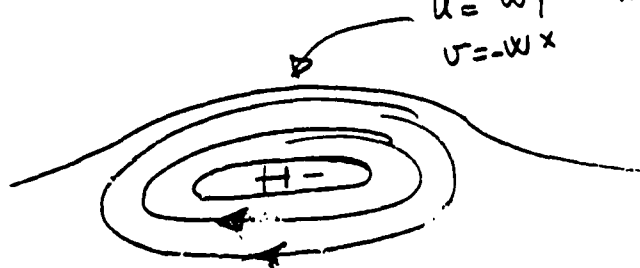
A1 - A2 RUNS: TOPEX NOMINAL 12+7/10

OB MEN AND ROBINSON, 1984

# STREAM + RINGS MODELS & DATA SETS AS AVAILABLE

- DYNAMICAL ADJUSTMENT
- DYNAMICAL INTERPOLATION
- DYNAMICAL EVOLUTION

$$u = wy \quad v = -wx \quad h = 1 - \frac{1}{2} \omega (1 - \omega) r^2$$





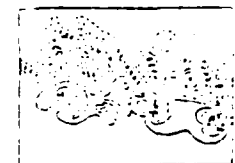
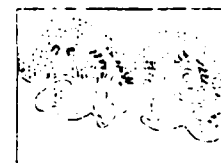
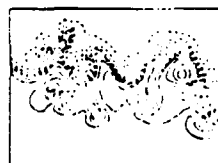
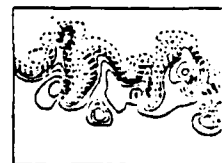
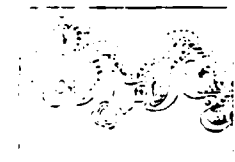
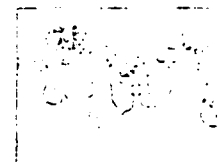
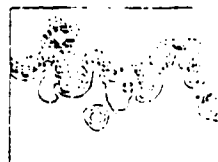
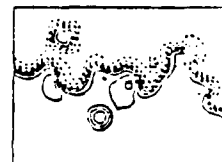
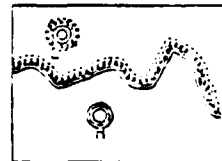
03:46:36 30-MAR-85

0-1 0-100 TO 100

3/28/85 NEW G.S. WITH 200 CM/SEC WINDS FROM 0000Z TO 0600Z  
GAMMA=1.411 AVERAGE BOTTOM DEPTH 4500 METERS UNTIL 1000Z

STREAMFUNCTION AT 300. M  
EVERY 1. DAYS

RING FORMATION

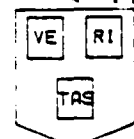


NEW COLD EDDY ~180-200 km DIA

GOOD AGREEMENT WITH IR DATA

Robinson  
Pinardi &  
Spall 1985

Figure 12



## TWO RECENT VIEWS OF THE GULF STREAM EAST OF CAPE HATTERAS

Thomas Rossby

## ABSTRACT

This paper is a summary of two research programs both of which are concerned with the structure of the Gulf Stream east of Cape Hatteras. The first study is an attempt to examine the energetics of the current using a three year data set of bimonthly sections of velocity and temperature. Although the results of this investigation are preliminary and incomplete, it appears from an analysis procedure similar to that employed by Brooks and Niiler (1977) that there is substantial conversion of energy from the mean into the fluctuating field. Of the conversion processes considered thus far, release of mean potential energy is the biggest contributor, followed by the pressure work and lateral shear terms in that order.

The second study is concerned with the Lagrangian properties of the current, i.e. pathways of individual fluid parcels which can be observed using a new class of acoustically-tracked isopycnal floats. A striking yet hoped for characteristic of these float trajectories is the distances over which they remain in the current: from a minimum of 600 km to more than 2000 km with half of them (4 of 8) exceeding 1500 km. In cyclonic curves, floats always shoal and vice versa in anticyclonic turns. The vertical velocities associated with these cross-stream motions are  $O(1 \text{ mm/s})$  and are thus many orders of magnitude greater than in the open ocean. These trajectory data are being used to study the space-time evolution of the path of the current, dispersion from the stream and the mechanisms by which they take place: are they endemic to

the stream or are they triggered by external factors ("expulsion" or "extraction"))?

The paper is concluded with a brief outline for future work in the Gulf Stream.

### Energy Conversion

Following a procedure developed by Brooks and Niiler (1977) (hereafter called BN), we are investigating the energetics of the Gulf Stream at  $73^{\circ}\text{W}$ , about 200 km east of Cape Hatteras in an area where the current is known to be undergoing increasingly large meanders as it flows eastward. Our data consist of seventeen sections gathered on thirteen bimonthly cruises between September 1980 and May 1983 (Halkin and Rossby, 1985). Briefly, the velocity, temperature and computed pressure fields are decomposed into a mean field defined by the ensemble average at each point and a fluctuating component which represents the observed departure of the mean. The pressure field is determined hydrostatically using the observed velocity field at 2000 meters to estimate the pressure fluctuations there geostrophically. The mean fields of velocity in the direction  $62^{\circ}\text{T}$  (mean direction of transport averaged over all sections) and of temperature are shown in Fig. 1. The abscissa denotes the nine locations across the Gulf Stream where the profiles were obtained, the distance between each is about 24 km. Depth is plotted along the ordinate to 2000 meters. Fig. 2 shows the location of the section relative to Cape Hatteras. In order to remove high vertical wavenumber energy (presumably inertial), each velocity profile is first low pass filtered by decomposing it into a set of linear dynamical modes using the local density profile over an assumed flat

bottom and then reconstituting it using only the barotropic and five lowest baroclinic modes. However, the ability of the barotropic and first two baroclinic modes to account for 0(95%) of the kinetic energy suggests that this step may be unnecessary.

The equation which expresses the evolution of the intensity of the fluctuating field following the mean flow is:

$$\frac{d}{dt} \{ \frac{1}{2} (\overline{u'^2} + \overline{v'^2}) + \frac{g}{2} \overline{\rho'^2} / \left| \frac{\partial \bar{\rho}}{\partial z} \right| \rho_0 \} = \quad (1a)$$

$$- \nabla \cdot \{ \overline{\vec{v}' \rho'} / \rho_0 \} \quad (1b)$$

$$- \{ \overline{u'^2} \frac{\partial \bar{u}}{\partial x} + \overline{v'^2} \frac{\partial \bar{v}}{\partial y} + \overline{u'v'} \frac{\partial \bar{v}}{\partial x} \} \quad (1c)$$

$$- \{ \overline{gu' \rho'} \frac{\partial \bar{\rho}}{\partial x} / \rho_0 \left| \frac{\partial \bar{\rho}}{\partial z} \right| + \overline{gv' \rho'} \frac{\partial \bar{\rho}}{\partial y} / \rho_0 \left| \frac{\partial \bar{\rho}}{\partial z} \right| \} \quad (1d)$$

$$- \{ \overline{w'u'} \frac{\partial \bar{u}}{\partial z} + \overline{w'v'} \frac{\partial \bar{v}}{\partial z} \} \quad (1e)$$

The distribution of eddy kinetic and eddy potential energy is shown in Fig. 3. The sharp maximum in the horizontal of EPE is due to the meandering of the density field around its mean position. The bimodal structure of EKE exists for the same reason: there are two regions of large shear, cyclonic and anticyclonic, both of which contribute to the fluctuating field. Had the meandering envelope been larger than the Stream width, these maxima would presumably blur into a single maximum. Note the approximate equipartition of EPE and EKE.

What terms on the right-hand side of equation 1 contribute to either the growth or decay of eddy energy (we can only estimate those with cross-stream derivatives)? The most important term in an area averaged

sense (from 0 to 2000 m and from  $P_0$  to  $P_g$ ) is the baroclinic conversion term (first term in line 1d). It is contoured in Fig. 4 and shows a single maximum coincident with the mean density front where the fluctuations in density are also largest.

The next term in importance is the pressure work term (first term in line 1b). It has a strong dipole structure (see Fig. 5), destabilizing on the cyclonic side and stabilizing on the anticyclonic side. The net contribution of this term to the production of eddy energy is about one-half that from the potential energy. Locally this term can be quite large, but given the rigidity of the velocity structure it is unclear what significance to attribute to this fact. It seems more appropriate to ask what is the net effect of the pressure work field upon the current as a whole.

The third term or process of importance and the one most readily examined in earlier studies is the production of eddy energy due to lateral shear, Fig. 6 (the barotropic term as BN call it even though it is far from depth independent). Its area average is about one-half that of the previous term. It has a pronounced bimodal structure coinciding with regions of strong lateral shear. Note that the contribution by this term, like the others, is substantially limited to the top 500 meters.

The first term of line 1c is smaller yet by two orders of magnitude; and although  $\overline{v'^2}$  is larger than  $\overline{u'^2}$  by a factor 5 or so, we presume that the second term in line 1c is negligible as well since the mean field is horizontally non-divergent. We are presently attempting to estimate indirectly the second terms of 1b and 1d.

In a recently completed study by Halkin and Rossby (1985) it was shown how much of the variability associated with the mean field shown in Fig. 1 can be removed by transforming each of the sections to a "stream" coordinate system defined by a direction of transport, and a "stream" origin. The EKE around this new mean field is reduced by a factor of 3. (That it isn't reduced more than this is due to an omnipresent isotropic eddy velocity field in the deep waters.) Similarly, it can be shown that the lateral scale or width of the current is quite stable exhibiting variations on the order of 10%. Thus the structure of the current itself is very well defined. Much of the eddy variability that has been reported in the past (Dantzler, 1977) reflects therefore the meandering of the current and not structural changes of the current itself. The positive conversion of mean energy into the eddy field is an expression of increased meandering in the downstream direction. Conversely the negative conversions observed by Webster (1961) off Onslow Bay indicate decreased meandering following the mean flow (Hood and Bane, 1983).

These results are very preliminary and the significance of these field estimates has yet to be determined. The degrees of freedom is at least 13 and at most 17.

#### Path Studies

Using a new class of acoustically-tracked isopycnal floats, we are trying to study the Lagrangian properties of fluid motion in the Gulf Stream. By repeatedly seeding the current with floats we can examine (a) the space-time evolution of the path of the current, (b) isopycnal movements within the current and (c) the mechanisms by which dispersion

of water from the Stream takes place. Since July 1984 we have been launching floats in the center of the Gulf Stream off Cape Hatteras. Although weather and high seas have made this a more difficult task than anticipated, numerous trajectories have been obtained to date. The floats are ballasted for  $\sigma_t = 27.0$  ( $T = 12.5$ ,  $S = 35.6$  psu), which at launch is at about 500 meters.

A spaghetti diagram of all trajectories is shown in Fig. 7. Over half of these continue to  $60^\circ\text{W}$ , in excess of 1500 km. Three tracks break off to the south (one in a cold core ring) and one float moves westward in the Slope Water before becoming reentrained. In July-August we obtained four float tracks separated by ten days. Shown in Figs. 8 (a-d) they exhibit quite a range of behavior. The first one in this miniseries, #16, in Fig. 8a moves along until  $66^\circ\text{W}$  where it slows down and enters into a circular orbit, which from satellite IR imagery proved to be a new cold core ring. The next float, #17, follows about the same path 50 km to the north (Fig. 8(b)). Close to where the ring was formed the float escapes northward into the Slope Waters where after a week it is reentrained by a rapidly growing meander and swept downstream at great speed. The third float, #18, Fig. 8(c), crosses the Stream rapidly after a sharp anticyclonic turn and downwells 100 meters/day and escapes to the south shortly thereafter. The fourth float, #20, like many other floats to date, remained in the current for the entire period (Fig. 8(d)).

The pressure record provides important information on the vertical component of motion in the Stream. Inspection of these, Figs. 9(a-d), shows that up- and downwelling nearly always occur in anticyclonic and

cyclonic turns, respectively. Vertical velocities of 0(100 m/day) or 1 mm/s are not that uncommon.\* Clearly the centrifugal acceleration is the major nonlinearity affecting fluid motion in the Gulf Stream.

These remarks on the float program are abbreviated from an article by T. Rossby, A.S. Bower and P-T. Shaw that will appear in the Bulletin of the American Meteorological Society (1985). We will be glad to provide preprints.

### Outline for Future Studies

#### 1) Path Evolution Studies

In this research program we propose to continue our studies of the space-time evolution of the path of the Gulf Stream. The objectives are both descriptive/statistical and dynamical.

#### Descriptive/Statistical

To map out the envelope of pathways of fluid motion - this is in essence a classic dispersion experiment, although for a strongly baroclinic flow rather than homogeneous isotropic systems, for which an interpretative theoretical framework exists. How and where is water removed from the current? Our impression is that loss of water is not stochastic, but strongly coupled to the dynamics of curved flow, but we cannot yet distinguish between internally triggered and externally imposed losses.

---

\* The temperature time series is highly correlated with pressure. This is because the floats are not perfectly isopycnal due to their compressibility being slightly less than seawater.



It will be important to couple the Rafos float path studies with satellite IR imagery for this provides more descriptive information on the eddy activities of the surrounding waters which may be driven by, but at the same time may alter the state or path of the current. The Rafos float trajectory data provide ground truth that should be of considerable help in improving the interpretation of the IR imagery. Together with inverted echo sounder arrays, the floats and IR imagery make a powerful 3-way synoptic, observational capability.

#### Dynamical

The Pegasus sections discussed earlier will provide an accurate description of the potential vorticity field at  $73^{\circ}\text{W}$  and its variability. At the same time potential vorticity should be conserved following a fluid parcel. How is this balance maintained during a float's transit. How can we make better estimates of the various terms in the potential vorticity equation using float data? Amy Bower is looking at these questions and gives a discussion of her work to date elsewhere in the workshop proceedings.

A powerful way to extend the utility of individual (yet repeated) float trajectories is to use these observations together with numerical models of the current. In particular we are cooperating with Dr. A.R. Robinson and his group at Harvard University, which is seeking to develop a predictive capability for the path of the Stream. We hope this kind of cooperative research can be expanded, both computationally and observationally.

## 2) The Anatomy of a Growing Meander

### A Local Dynamical Study

One of the most striking observations to emerge from the Rafos float program is that vertical (lateral) motions are strongly correlated with curvature. This is clearly associated with the centrifugal acceleration and is present whether the meander pattern is steady or not. It is a strong non-linearity, quadratic in speed, so it is large near the surface and weak at depth. How does a meander develop and why? Can we look closely at the dynamical balances and their temporal evolution? We think so.

In an anticyclonic turn, fluid is upwelled to some degree (and vice versa) and shingling (and warm outbreaks?) may occur. The cross-stream motions can be observed and quantified using isopycnal floats at several levels. The temporal evolution of the velocity field can be resolved with successive arrays of Rafos floats which can be seeded upstream of the meander and allowed to drift through the structure. (The floats can be picked up and reused (to economize) if they are programmed appropriately.) Simultaneously, the evolving pressure field can be mapped throughout using a CTD coupled with appropriate velocity measurements to determine the perturbation pressure field at depth. The mapped area should include the region immediately outside the meander in order to study the interaction between the current and the ambient eddy field.

It is reasonable to assume that a growing meander has more Gulf Stream water entering than leaving. This is dictated by mass

conservation. Whether or not a meander will evolve into a ring presumably depends upon whether a mass flux adjustment can be made in time.\* A simultaneous mass flux measurement program using Pegasus may be very desirable.

In summary, the objective of such a program is to obtain a full description of the temporal evolution of velocity, density and pressure in all dimensions from which a complete synthesis of the dynamical evolution of a meander can be achieved.

---

\* One can speculate further on the role of shingling and meandering if one thinks of them as primarily internally triggered. In both cases they are mechanisms for releasing water. Shingles appear to be near surface processes; ring formation involve more of the water column. The Stream can remove a near-surface excess by making relatively sharp bends to enhance the centrifugal acceleration, and broader meanders (and ring formation) to cope with excess flow throughout the (entire) water column. Bower et al. (1985) have argued that some process other than ring formation must be responsible for most cross-frontal exchange in the upper ocean.

References:

- Bower, A.S., H.T. Rossby and J.L. Lillibridge, 1985. The Gulf Stream Barrier or Blender? JPO 15(1), pp. 24-32.
- Brooks, I.H. and P. Niiler, 1977. Energetics of the Florida Current. JMR 35(1), pp. 163-191.
- Dantzler, H.L., 1977. Potential Energy Maxima in the Tropical and Subtropical North Atlantic. JPO 7, pp. 512-519.
- Halkin, D. and T. Rossby, 1985. The Structure and Transport of the Gulf Stream at 73°W. JPO (submitted).
- Hood, C.A. and J.M. Bane, 1983. Subsurface Energetics of the Gulf Stream Cyclonic Frontal Zone off Onslow Bay, North Carolina. JGR 88(8), pp. 4651-4662.
- Rossby, H.T., A.S. Bower and P-T. Shaw, 1985. Particle Pathways in the Gulf Stream. Bull. Amer. Met. Soc. (accepted, Sept. issue).
- Webster, F., 1961. The Effect of Meanders on the Kinetic Energy Balance of the Gulf Stream. Tellus 13, pp. 392-401.

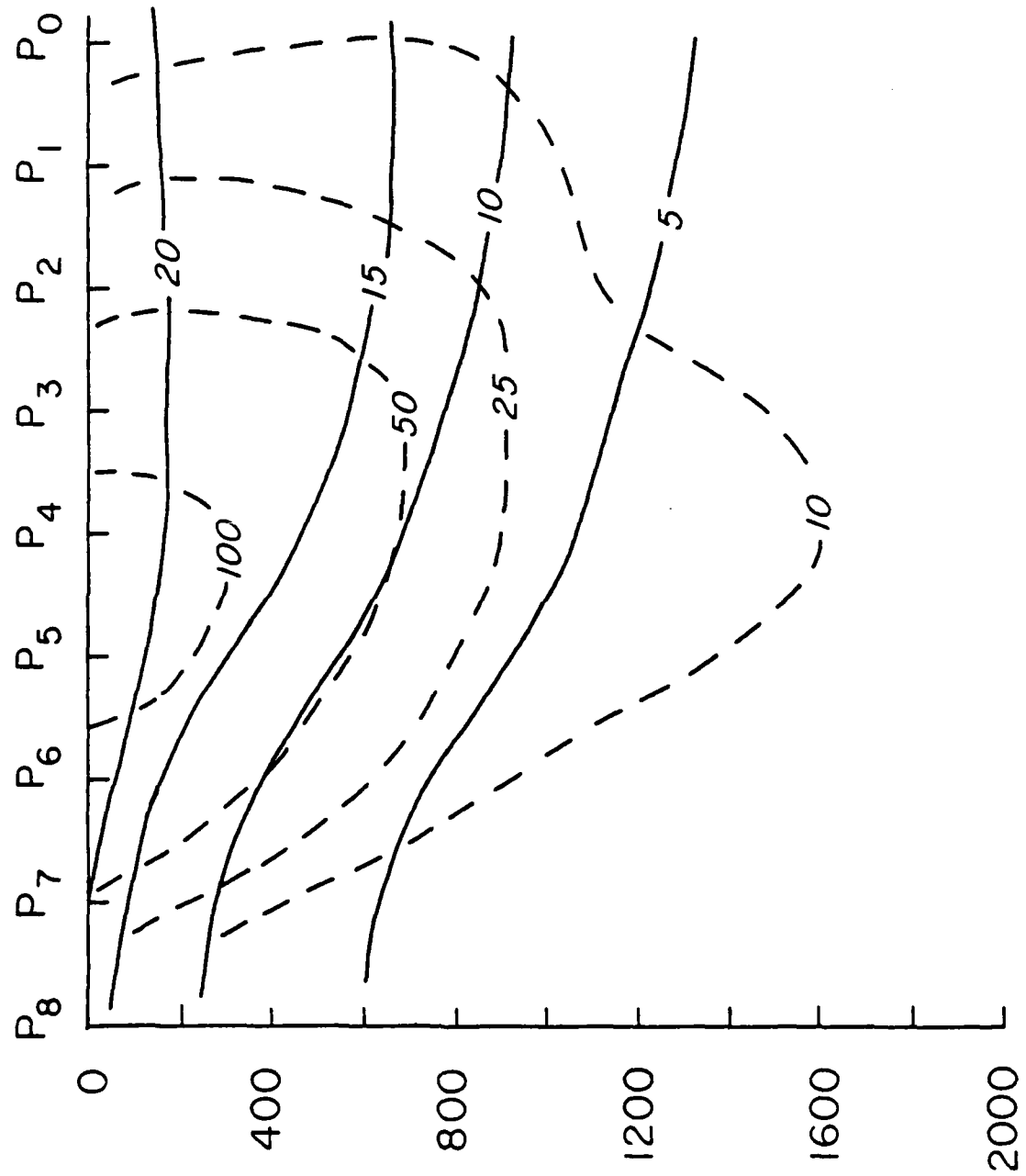


Fig. 1. The mean field of temperature in °C ( — ) and downstream velocity in cm/s ( --- ) at the Pegasus section, 73°W.

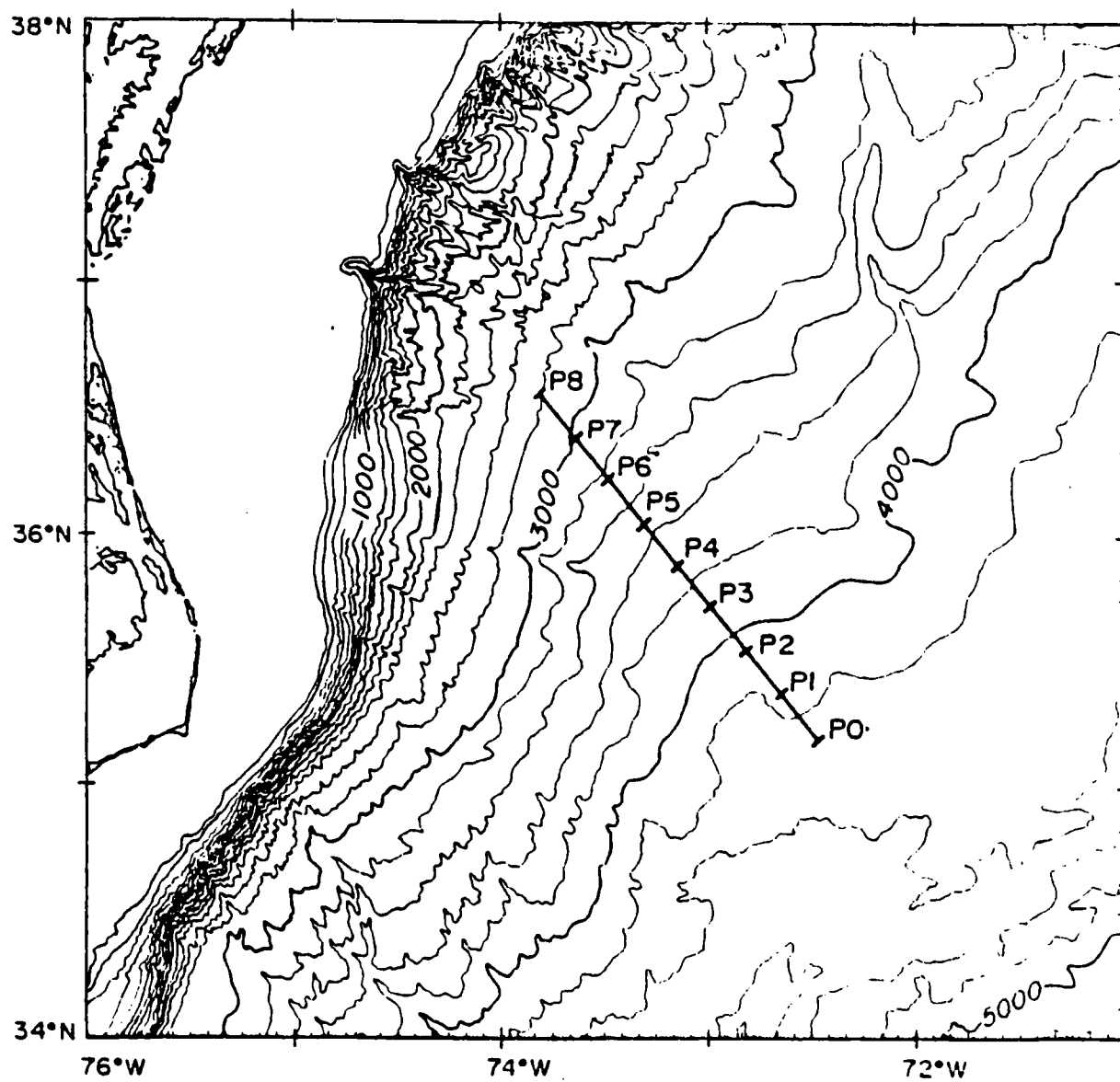


Fig. 2. Location of the nine Pegasus sites relative to Cape Hatteras.

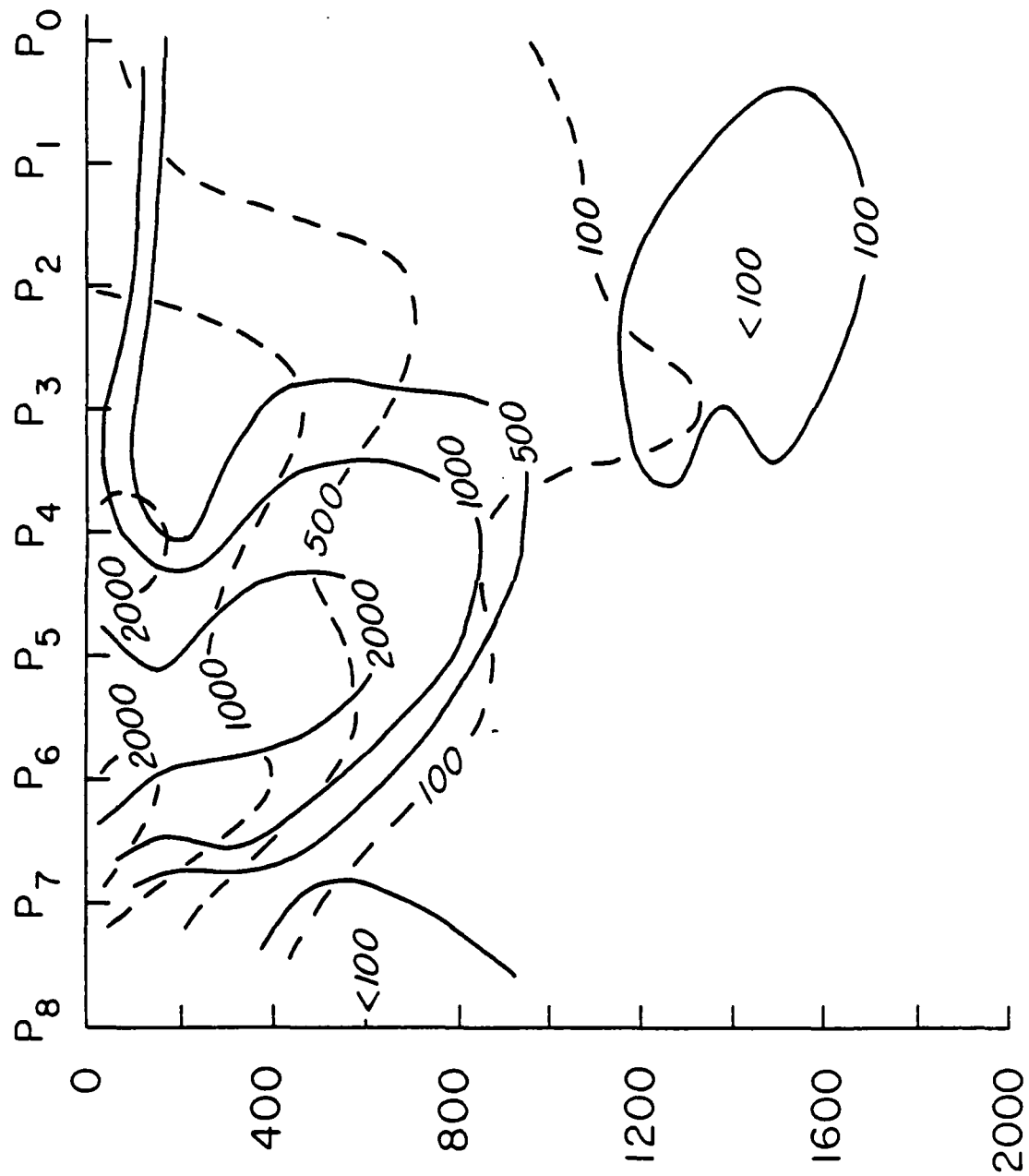


Fig. 3. The distribution of eddy kinetic ( --- ) and eddy potential ( — ) energy along the Pegasus section. The area averaged EKE =  $518 \text{ cm}^2/\text{s}^2$ .

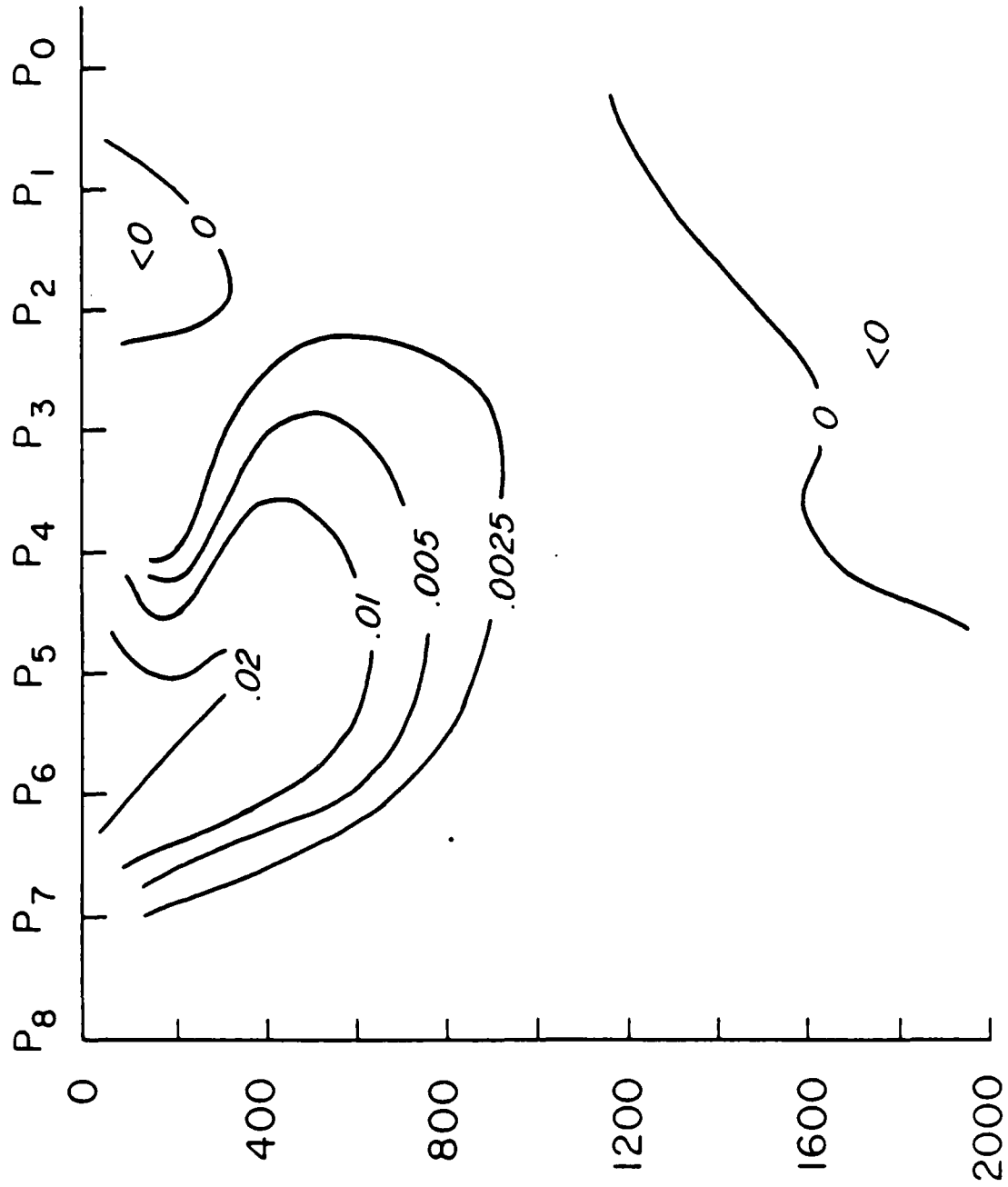


Fig. 4. The distribution of  $-\overline{gu'p'} \frac{\partial \bar{p}}{\partial x} / \rho_0 \left| \frac{\partial \bar{p}}{\partial z} \right|$ . The area average is  $0.0024 \text{ cm}^2/\text{s}^2$ .



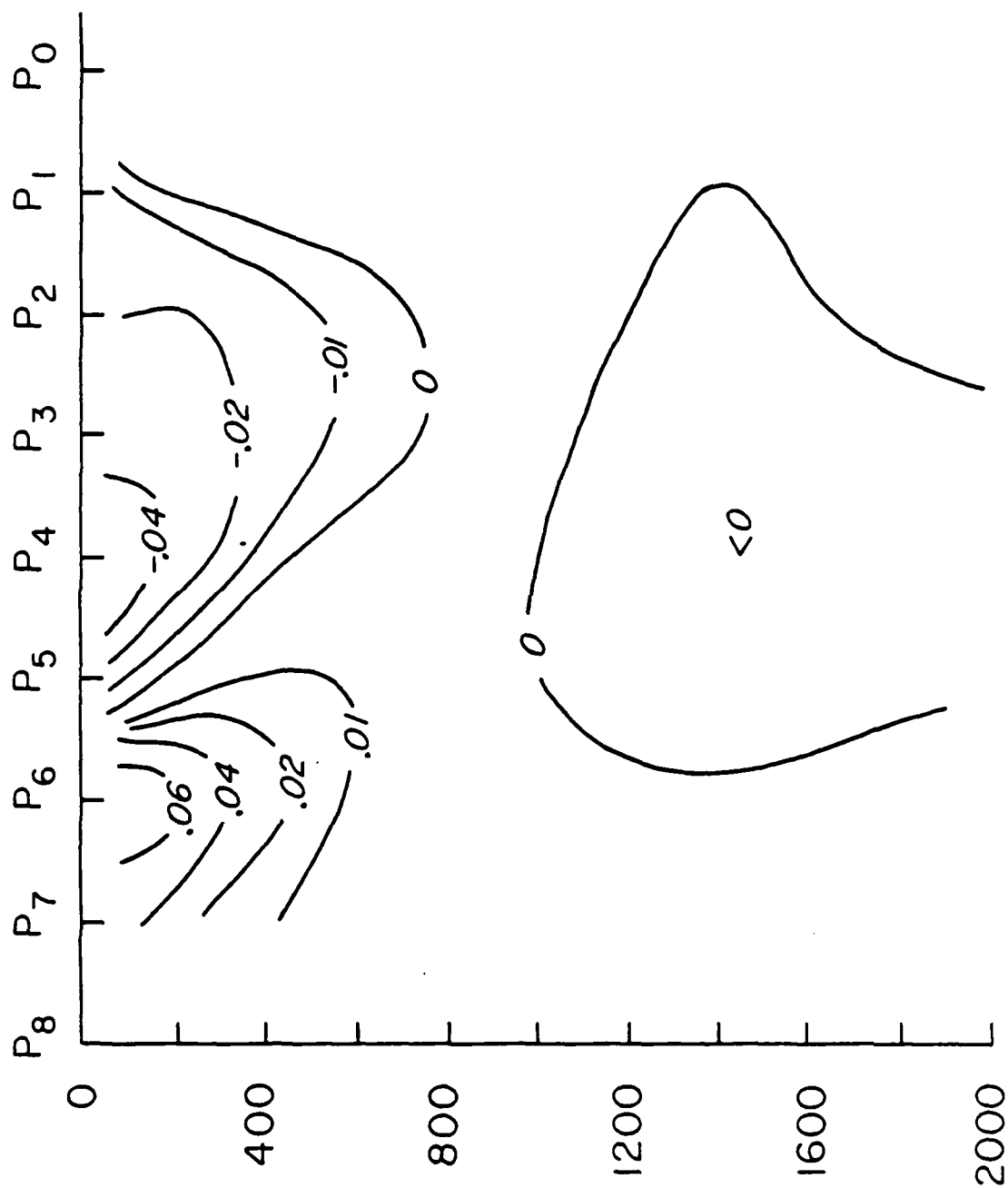


Fig. 5. The distribution of  $\frac{3}{n} \left( \frac{\mu_1^2}{n} \right)$ . The area average is 0.0014 cm<sup>2</sup> (s<sup>3</sup>)

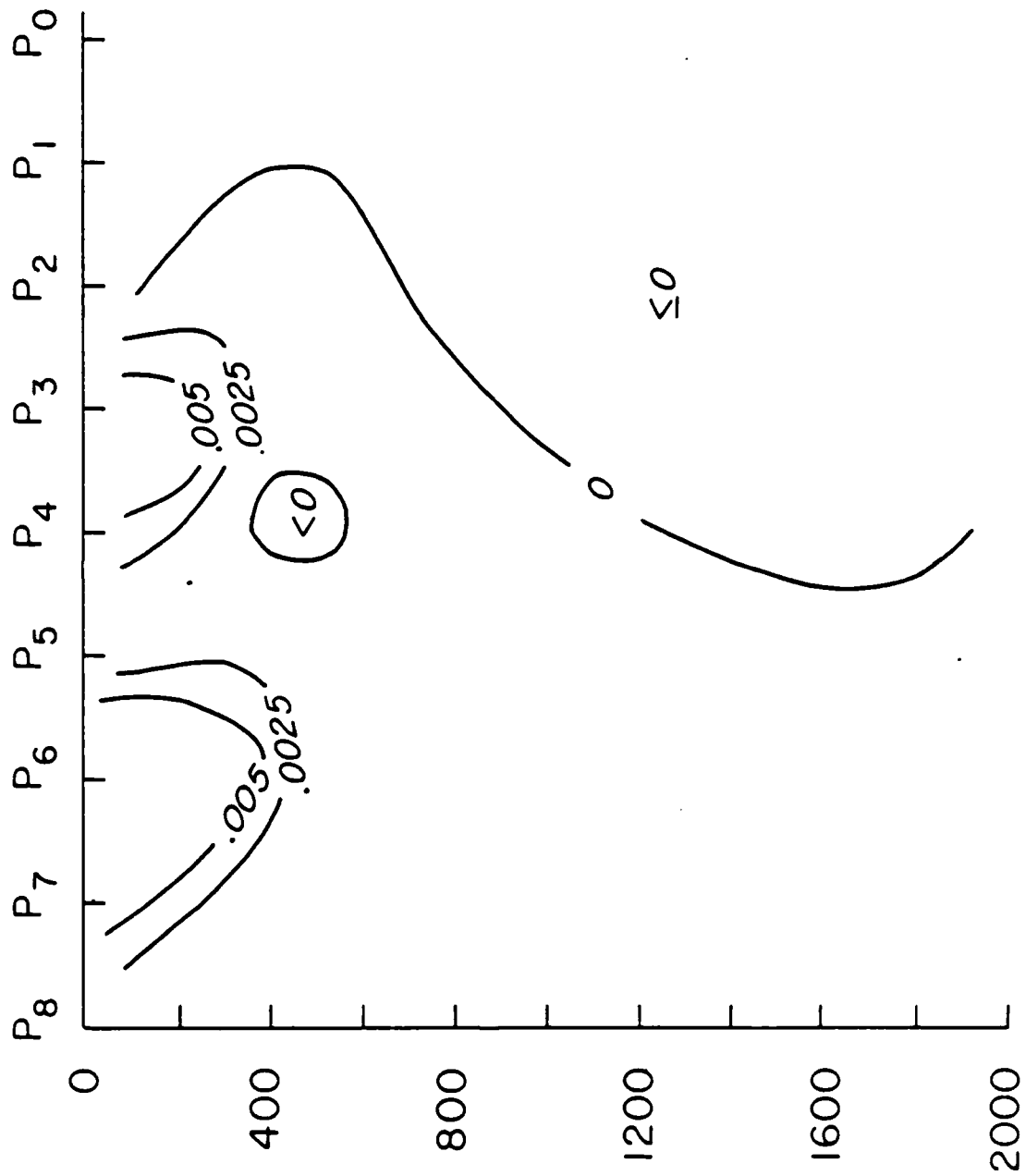


Fig. 6. The distribution of  $-\overline{u'v'}$ . The area average is  $0.00064 \text{ cm}^2/\text{s}^3$ .

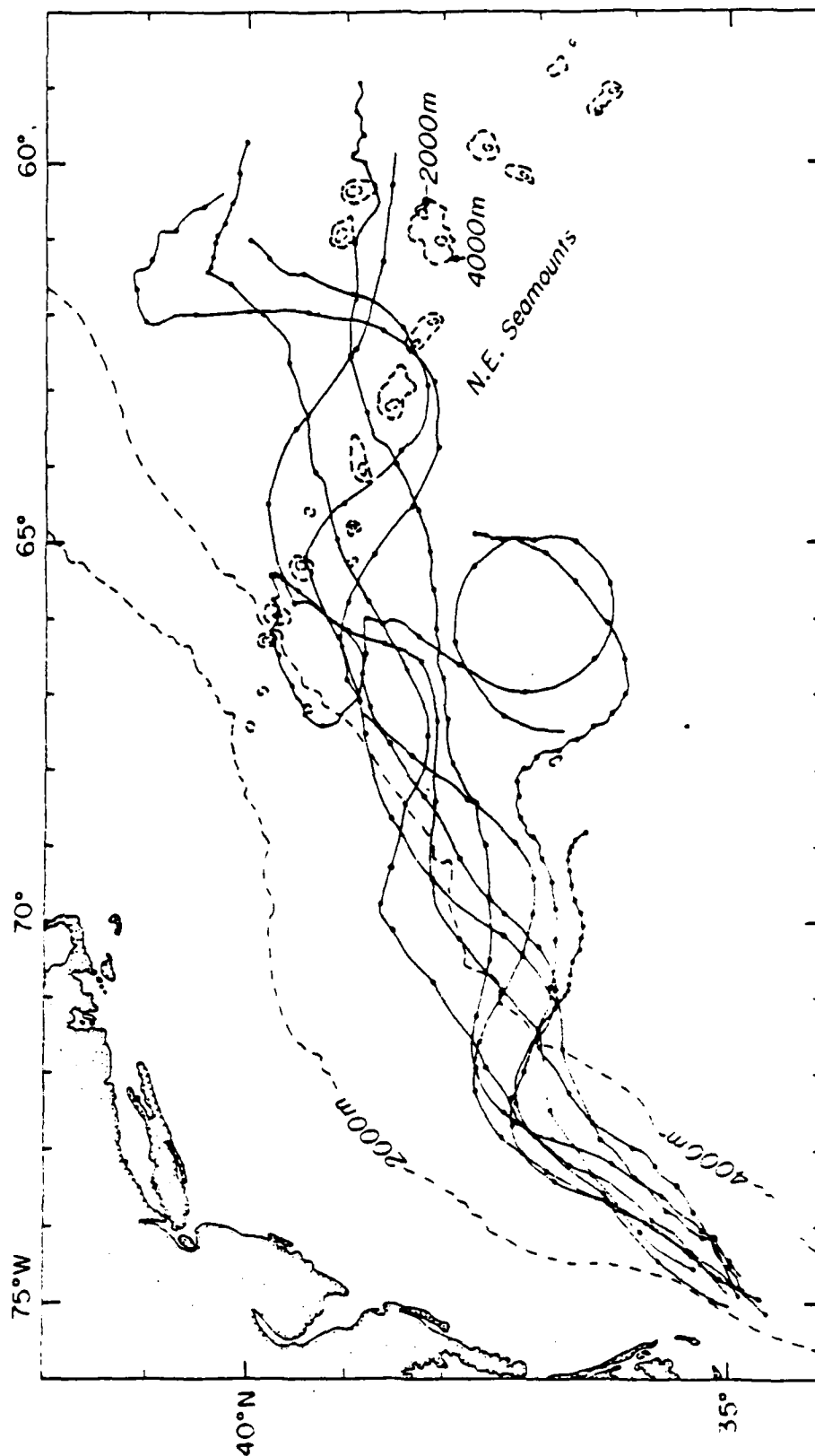


Fig. 7. Spaghetti diagram of eight Rafos trajectories since July, 1984. Dots show daily positions. The 2000 and 4000 bathymetric contours and the New England seamounts are shown.

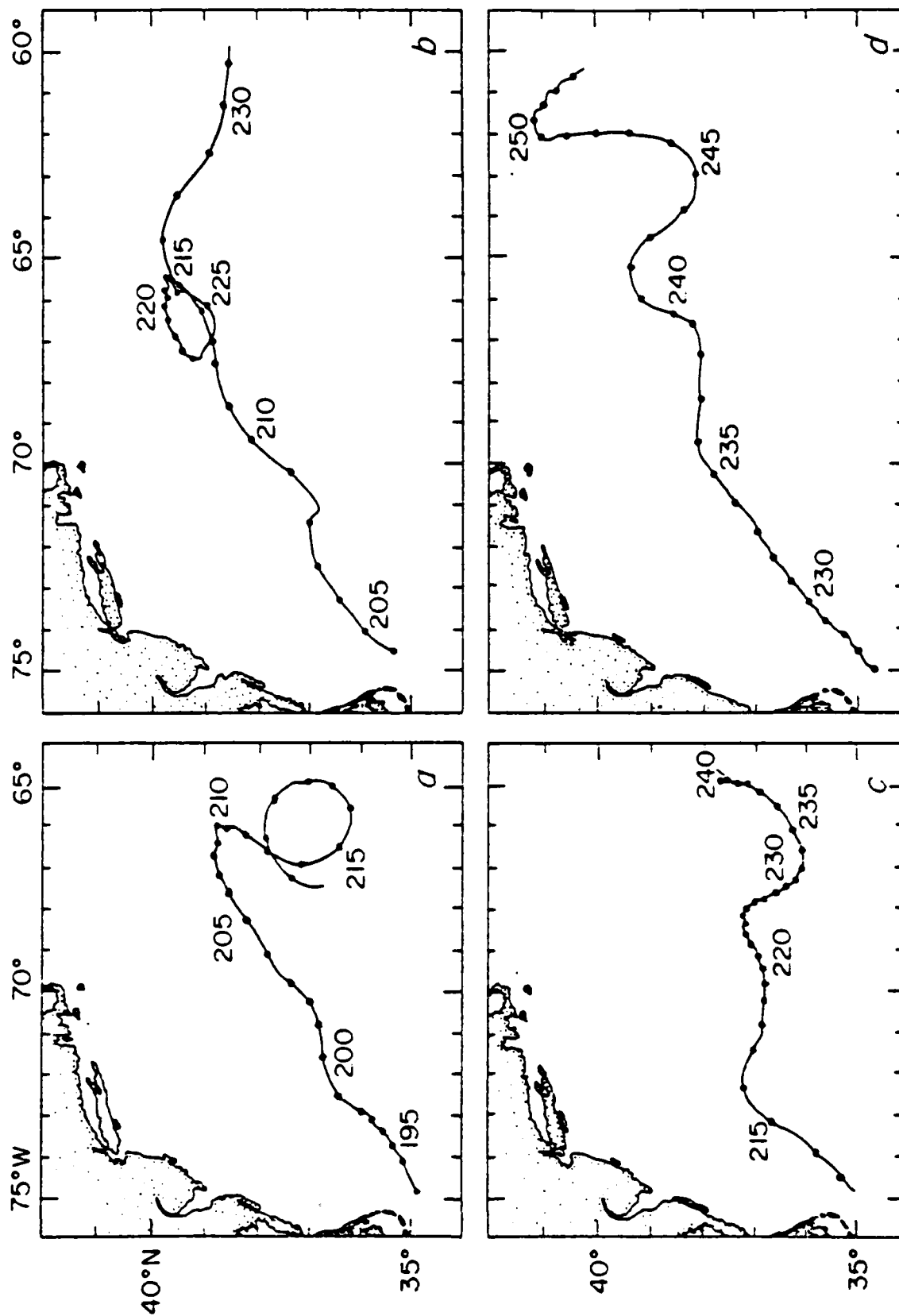
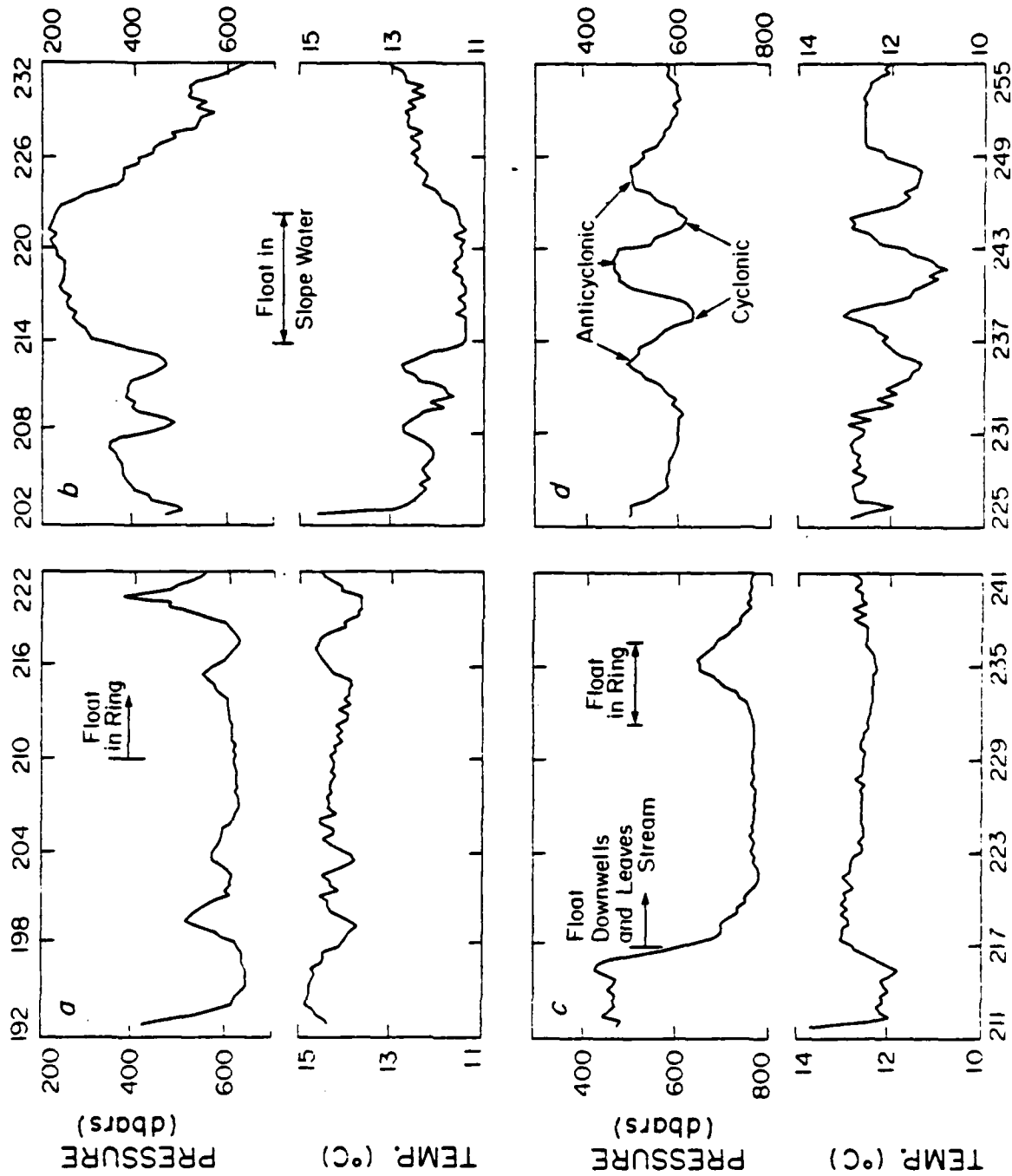


Fig. 8. Trajectories for four Rafos floats launched sequentially in July and August, 1984: (a) #16; (b) #17; (c) #18; and (d) #20. They are 30 days long and the dates are given in year-days. The heavy dots are shown daily; their separation gives a measure of the float's speed. ( $1^\circ$  latitude = 111 km).



## YEARDAYS (1984)

Fig. 9. The pressure and temperature data as a function of yearday for the same four floats: (a) #16; (b) #17; (c) #18; and (d) #20. For an

## MODIFICATIONS OF AN INTENSE OCEANIC CURRENT SYSTEM FLOWING INTO A REGION OF COOLING

David Adamec

Department of Meteorology, Naval Postgraduate School, Monterey, CA 93943

### ABSTRACT

Nof (1983) has proposed that significant latitudinal displacements of an ocean current system and the associated sea-surface temperature gradient may result as the current flows into a region of cooling. In particular, Nof studied the effect of cooling that increases to the east and south on an eastward flowing current. Nof's investigation is extended to include effects due to a time dependent along-front flow, the forced response due to cross-stream cooling gradients and effects due to momentum mixing. Three-dimensional numerical simulations of a current similar to the Gulf Stream extension flowing into a region of cooling show that much of the response in the vicinity of the surface front is due to the cross-stream gradient in the surface cooling, which has been described by Adamec and Elsberry (1985). Part of this response is modified by advection of water from regions where there is no surface cooling. South of the front, an along-stream temperature gradient develops in response to the along-stream cooling gradient and a southward flow occurs which is in thermal wind balance with the along-stream temperature gradient. When momentum mixing is allowed to occur during the convective adjustment forced by the surface cooling, a much stronger cross-stream current directed toward cooler water develops in the immediate vicinity of the initial front.

### 1. Introduction

Nof (1983) has proposed that significant latitudinal displacements of ocean current systems may occur as the flow enters a region of downstream cooling. The response of the Gulf Stream was examined because of the large cooling rates observed east of Cape Hatteras (Budyko, 1963; Worthington, 1976). Nof assumed the density structure could be represented by two layers and that the lower layer was motionless. A density increase of  $1 \times 10^{-3} \text{ gm cm}^{-3}$  over 1200 km in the downstream (eastward) direction was specified to simulate surface cooling of the ocean. Also, surface cooling was allowed to occur south of an  $0.5 \text{ m s}^{-1}$  eastward jet only. A southward cross-stream component developed in response to a zonal pressure gradient which resulted from the along-stream gradient in surface cooling (density increase). A power series solution for a steady state, inviscid, Boussinesq flow yielded cross-stream velocities of  $3 \text{ cm s}^{-1}$ , which could lead to displacements as large as 90 km in a season.

The displacements predicted by Nof appear to be consistent with Fuglister's (1972) isotherm analysis of the Gulf Stream during the 1965-1966 winter, which showed a 100 km north-to-south displacement of the  $5^{\circ}\text{C}$  and  $10^{\circ}\text{C}$  isotherms. Nof's result that a steepening of the frontal interface will occur during winter is consistent with Worthington's (1976) isotherm analyses of the Gulf Stream east of the Grand Banks.

A multi-level, nonlinear primitive equation model is used in these experiments to simulate the Gulf Stream response to atmospheric forcing. The governing equations in flux form for an ocean circulation model which predicts the shear currents in an ocean of uniform depth  $D$  are written in Cartesian coordinates as

$$u_t = - (uu)_x - (vu)_y - (wu)_z + fv + A_M \nabla^2 u + K_M u_{zz} + (\widetilde{uu})_x + (\widetilde{vu})_y - \frac{\hat{P}_x}{\rho_0} \quad (1)$$

$$v_t = - (uv)_x - (vv)_y - (wv)_z - fu + A_M \nabla^2 v + K_M v_{zz} + (\widetilde{uv})_x + (\widetilde{vv})_y - \frac{\hat{P}_y}{\rho_0} \quad (2)$$

$$T_t = - (uT)_x - (vT)_y - (wT)_z + A_T \nabla^2 T + K_T T_{zz} \quad (3)$$

$$u_x + v_y + w_z = 0 \quad (4)$$

$$P_z = - \rho g \quad (5)$$

$$\rho = \rho_0 (1 - \alpha(T - T_0)) \quad (6)$$

where  $\sim$  represents a vertical average over the entire depth and  $\hat{P}$  is  $P - \bar{P}$ , which can be calculated using (5). All calculations in the simulations presented throughout this study are performed on an  $f$  plane at  $36^\circ\text{N}$ .

The model includes a generalized convective adjustment scheme based on a local gradient Richardson number: if the Richardson number falls below a critical value (0 for these simulations), then similar adjustments of heat and momentum occur so that the new adjusted profile will have a local gradient Richardson number slightly larger than the critical value. The details of the adjustment scheme are given in Adamec *et al.* (1981). Zero is used as the critical Richardson number in these simulations to isolate those effects due to convective overturning only in response to the surface cooling.

The horizontal dimensions (resolution) of the domain is 1280 km (20 km) in the east-west direction and 256 km (4 km) in the north-south direction. The vertical extent is 1000 m, and the vertical resolution varies logarithmically from 10 m near the surface to 200 m at 1000 m in 10 levels. The east and west lateral boundaries are open, and are prescribed using a variation of Orlanski's (1976) boundary condition as discussed by Camerlengo and O'Brien (1980).

The initial conditions for temperature are derived from a smoothed version of a hydrographic section across the Gulf Stream at  $38^\circ\text{N}$  during mid-November 1970 (United States Naval Oceanographic Office, 1970) and are shown in Fig. 1. The horizontal sea-surface temperature gradient is  $6^\circ\text{C}$  in 20 km, and is centered along  $y = 192$  km. On the northern side of the front, the temperature is uniform to a depth of 60 m, while the water is well-mixed to a depth of 100 m on the southern side. Notice also that the vertical stability below the mixed layer on the northern side is greater than the vertical stability on the southern side. As a result, the maximum horizontal temperature gradient occurs at a depth of 100 m. Assuming geostrophic balance, the initial zonal velocities (Fig. 2) are eastward with a maximum value at the surface near  $2.0 \text{ m s}^{-1}$ .

The evaporative and sensible heat fluxes are directly proportional to the air-sea temperature difference in the bulk aerodynamic formulation. If the temperature of the air is assumed to be uniform over areas of non-uniform sea-surface temperatures, then the cooling will be largest where the sea-surface temperatures are highest. The choice of a cooling function which increases toward higher sea-surface temperatures seems justified.

The choice of a cooling function which increases in the along-stream direction is more difficult to justify. Observations in the Atlantic support the choice of a cooling function which increases in the downstream direction for seasonal time scales. Gorshkov (1978) presents a monthly average of latent heat flux over the North Atlantic during February (Fig. 3) based on 70 years of ship observations. The maximum values occur off the east coast of the United States and

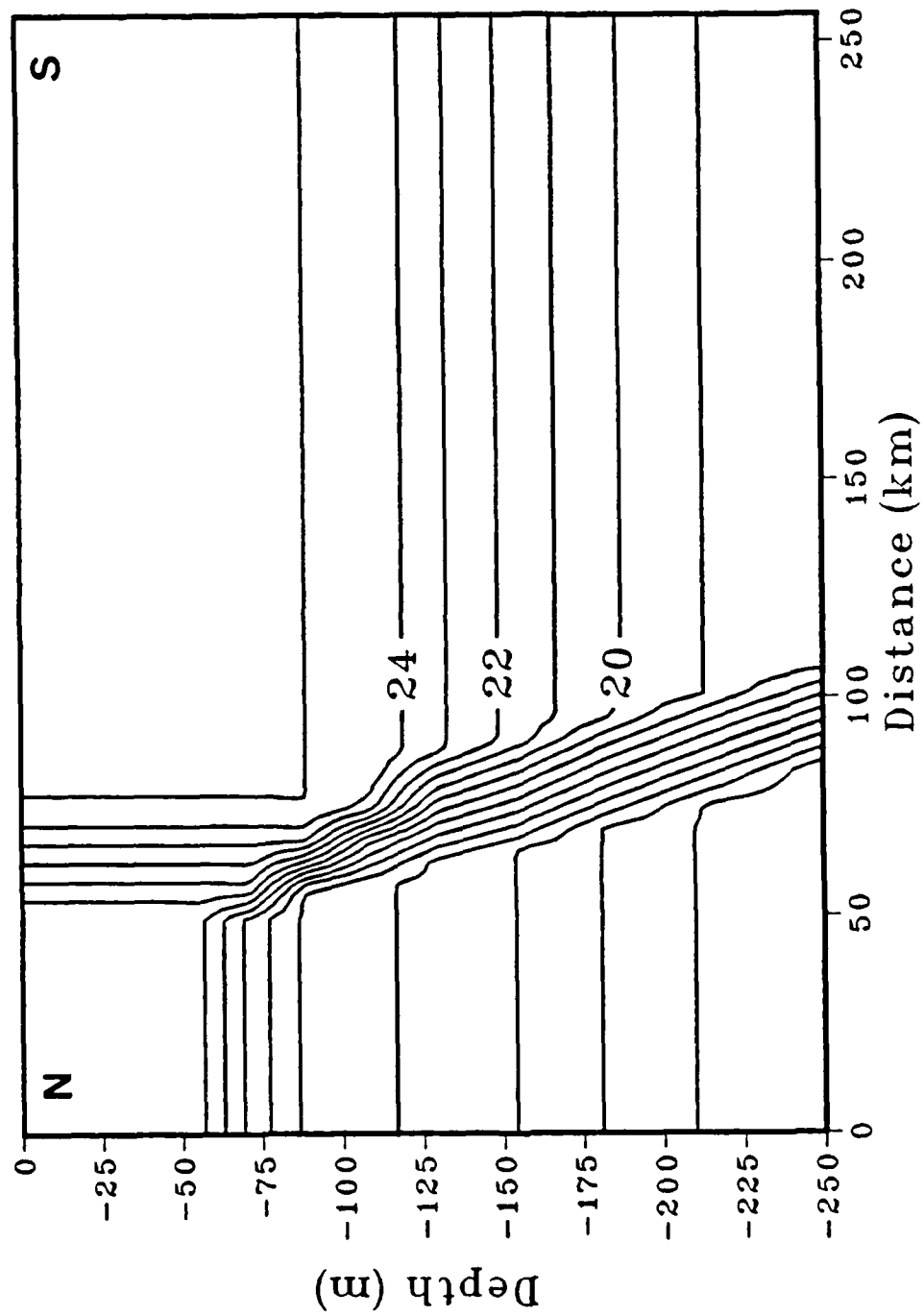


Figure 1. Initial temperature structure of the upper 250 m in the vicinity of the simulated Gulf Stream front. The contour interval is 1.0°C.



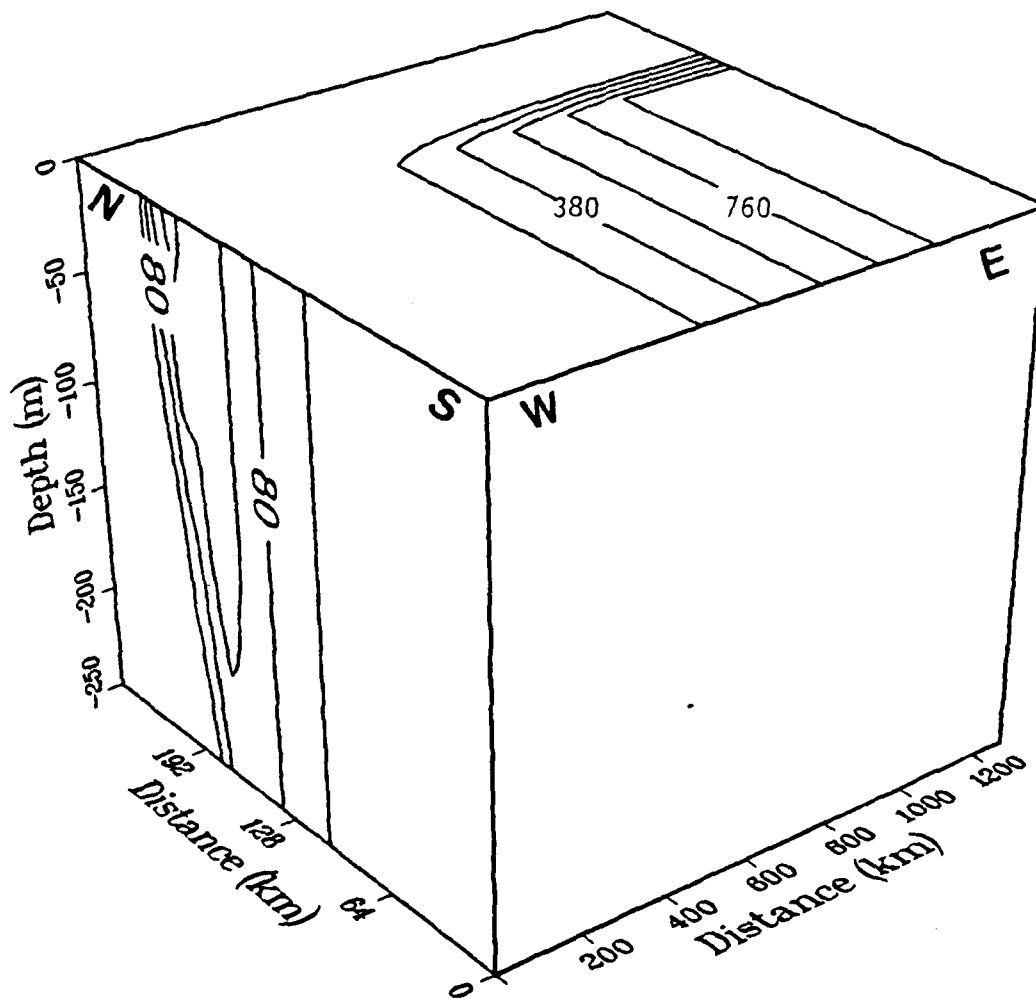


Figure 2. Cross-section of the initial geostrophic velocities of the upper 250 m in the vicinity of the front (side face), and the east-west distribution of the surface cooling (top face). The contour interval for the velocities is  $40 \text{ cm s}^{-1}$ , and the contour interval for the cooling is  $190 \text{ W m}^{-2}$ .

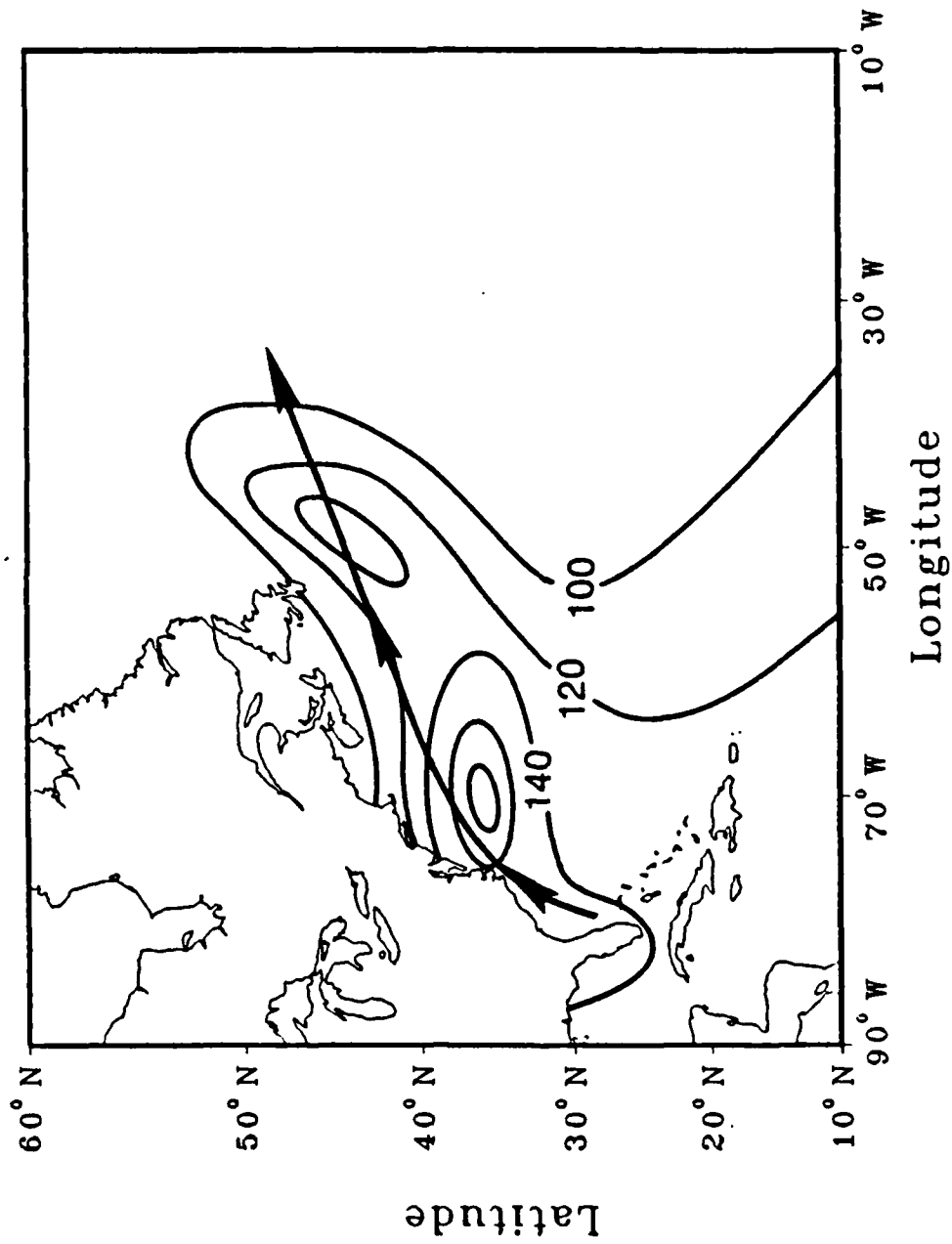


Figure 3. Distribution of the average latent heat flux over the North Atlantic during February (from Gorshkov, 1978). The contour interval is  $20 \text{ W m}^{-2}$ .

are concurrent with the mean position of the Gulf Stream. The Gulf Stream flows from the south toward these maximum values and thus experiences a downstream increase in surface cooling. The maximum value of the average latent heat flux is  $180 \text{ W m}^{-2}$ .

Kondo (1976), from data taken during the Air Mass Transfer Experiment (AMTEX) in 1974, found that maximum values of the heat and momentum fluxes occur to the south of the mean path of the Kuroshio during cold outbreaks. The Kuroshio approaches these maxima from the south, so that both the cooling and wind stress is increasing in the downstream direction. The specification of cooling increases in the downstream direction in the numerical simulations is consistent with these measurements. The maximum total heat flux of  $970 \text{ W m}^{-2}$  is consistent with observations by Agee and Howley (1977) during AMTEX.

## 2. Results

The numerical simulations presented here treat three processes which were not considered in Nof's (1983) original work. Aside from the effects of an along-stream cooling gradient, the numerical simulations also consider: 1) the forced meridional response due to a cross-stream cooling gradient; 2) the effects of momentum mixing during convective adjustment; and 3) the time-dependent response of the zonal flow. These three effects are critical in the simulations since they determine much of the response in the immediate vicinity of the surface front.

Two sets of simulations are presented. The first experiment allows heat only to be mixed during convective adjustment. The second experiment is identical to the first, but also allows momentum to be mixed. All results are presented as deviations from a control run with zero forcing.

### A. EFFECT OF VERTICAL MIXING OF HEAT ONLY

The surface  $v$  components at hour 72 for the simulation with no momentum mixing during convective adjustment are shown in Fig. 4. Within the region where there is a uniform along-stream cooling gradient (Fig. 2), the  $v$  components are negative (southward) with maximum current speeds near  $0.6 \text{ cm s}^{-1}$ . The cross-stream components south of the front are in thermal wind balance as in Nof (1983). The magnitude of the  $v$  components in this simulation are five times smaller than Nof's predictions. Nof used an observed density increase (Gorshkov, 1978) of  $1 \times 10^{-3} \text{ gm cm}^{-3}$  along the Gulf Stream extension. A surface cooling rate of  $2000 \text{ W m}^{-2}$  would have to persist for a period of 10 days to obtain such a density increase in the mixed layer. From the observations by Agee and Howley (1977) and Kondo (1976), such large cooling rates appear to be unrealistic, which implies the density increase used by Nof is not due to surface cooling alone.

There is also a relative maximum in the southward velocity immediately to the south of the initial zonal current maximum. A cross-stream velocity develops at the surface front as the pressure gradient is reduced by the cross-stream cooling gradient without a geostrophically balanced reduction in the zonal flow. The process for the inducement of cross-stream velocities near a jet in the presence of cross-stream cooling is described in detail by Adamec and Elsberry (1985). Most of the cross-stream velocity in the immediate vicinity of the current maximum appears to be due to the two-dimensional effect of cross-stream cooling and not the imposed along-stream cooling gradient. At the current maximum, the cross-stream flow is about half the magnitude of the cross-stream flow further to the south. Thus, displacements of the surface

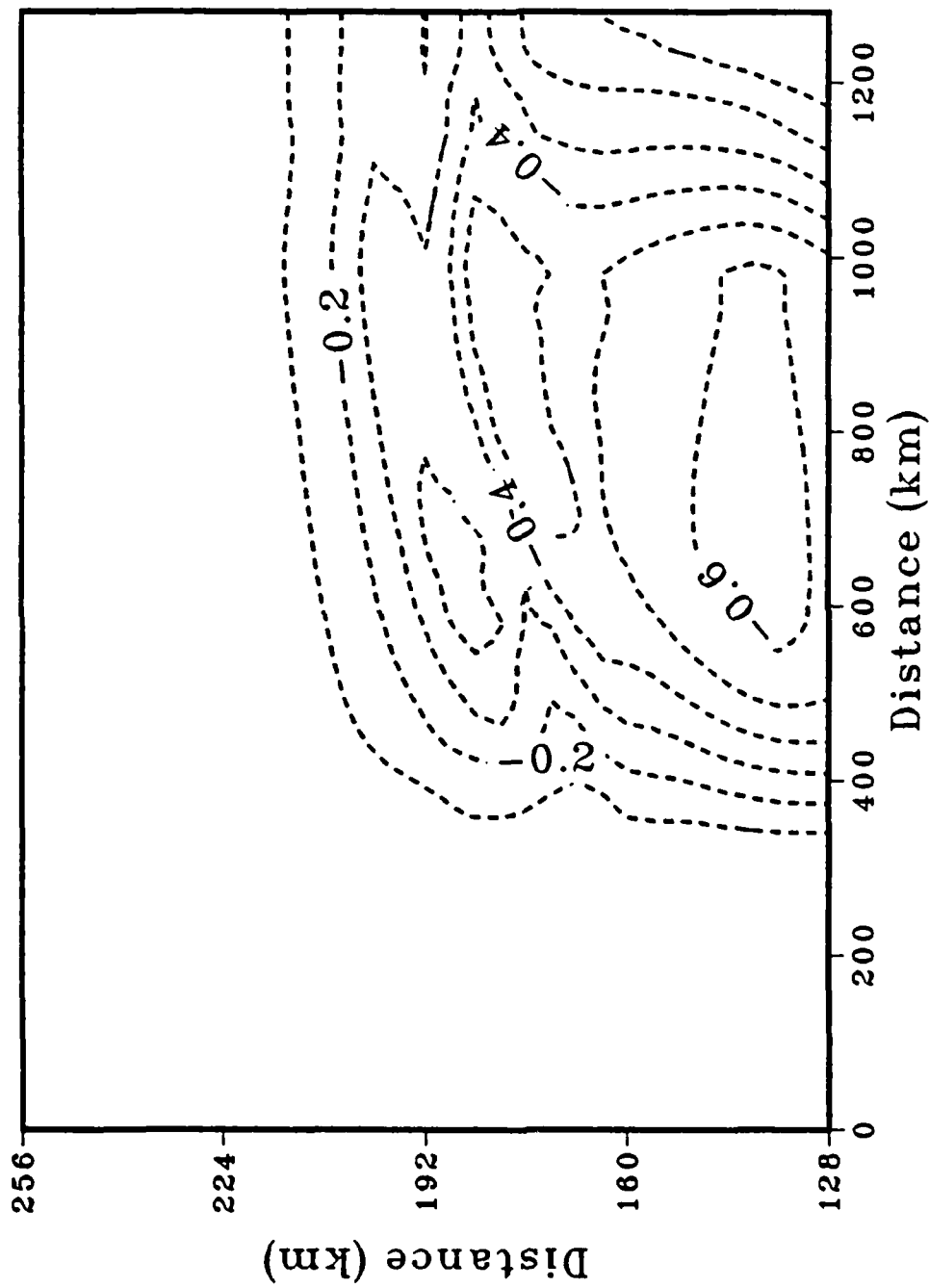


Figure 4. Surface v components at hour 72 for simulation with mixing of heat only. Negative values indicate southward flow, and the contour interval is  $0.1 \text{ cm s}^{-1}$ .

current system would be less than might be inferred from the southward velocities that develop where the zonal gradient in surface cooling is a maximum.

Relatively large zonal gradients in  $v$  occur where the zonal gradient of the cooling changes ( $x = 320$  km and  $x = 1000$  km), especially in the extreme southern portion of the domain where the zonal velocities are small. Between  $y = 100$  and  $190$  km, the zonal gradient in  $v$  is more diffuse. Zonal advection of temperature tends to weaken the zonal temperature gradients near  $x = 320$  km and  $x = 1000$  km. Thus, the southward components, which are in thermal wind balance, are smaller in these areas.

The decreases in the surface temperature field and the change in the surface flow field at 72 hours are shown in Fig. 5. The pattern of the surface temperature changes is very similar to the pattern of the surface cooling (Fig. 2), which indicates that the changes in the surface temperature are due to the surface cooling and not the internal response of the ocean. The temperature changes near the western boundary of the surface cooling are slightly modified by the tendency of zonal advection to restore the temperature field to the initial conditions. As in the case with the velocity components, the maximum temperature change of  $0.8^{\circ}\text{C}$  is very close to the value in two-dimensional simulations by Adamec and Elsberry (1985).

The changes in the surface flow field are consistent with geostrophic adjustments in response to the changes in the surface temperature field. Because the cross-stream cooling gradient reduces the surface horizontal temperature gradient, the surface zonal components are diminished as denoted by the westward pointing arrows in Fig. 5. The maximum reduction in the surface zonal components of  $8.0 \text{ cm s}^{-1}$ , is similar to the maximum decrease in the two-dimensional simulations of Adamec and Elsberry (1985) and occurs along the current maximum at the downstream boundary of the domain. Smaller decreases in the zonal velocity occur to the north and to the south of the front where the cross-stream cooling gradient is smaller. West of  $600$  km, very small decreases in the zonal velocity occur due to the combination of a reduced cross-stream cooling gradient and the tendency of zonal advection to restore both the temperature and zonal velocity to their initial conditions.

In summary, the combined effects of a cross-stream and an along-stream cooling gradient induce a southward flow in these numerical simulations, but the magnitude of that flow is too small to produce displacements of the Gulf Stream of the magnitude suggested by Nof (1983). South of the current maximum the southward velocities are in thermal wind balance with the induced zonal temperature gradient, which is consistent with Nof's (1983) predictions. Near the front, the tendency for the formation of a southward flow is due more to the constant adjustment of the flow fields to the reduced meridional temperature gradient than the along-stream cooling gradient. Much of the change in the magnitude in the initial jet can be explained by the reduced horizontal temperature (pressure) gradient. Because there is no surface forcing on the upstream flow in these simulations, there is a tendency for zonal advection to restore the fields to their initial condition.

#### *B. EFFECT OF MOMENTUM MIXING (EXPERIMENT 4-2)*

It was shown by Adamec and Elsberry (1985) that the inclusion of momentum mixing in the convective adjustment is critical in determining the magnitude and direction of the response of an intense oceanic flow to cross-stream cooling. With momentum mixing, surface cooling causes the relatively high zonal momentum near the surface to be mixed with relatively low zonal momentum immediately below, so that the surface currents decrease relative to their initial values.

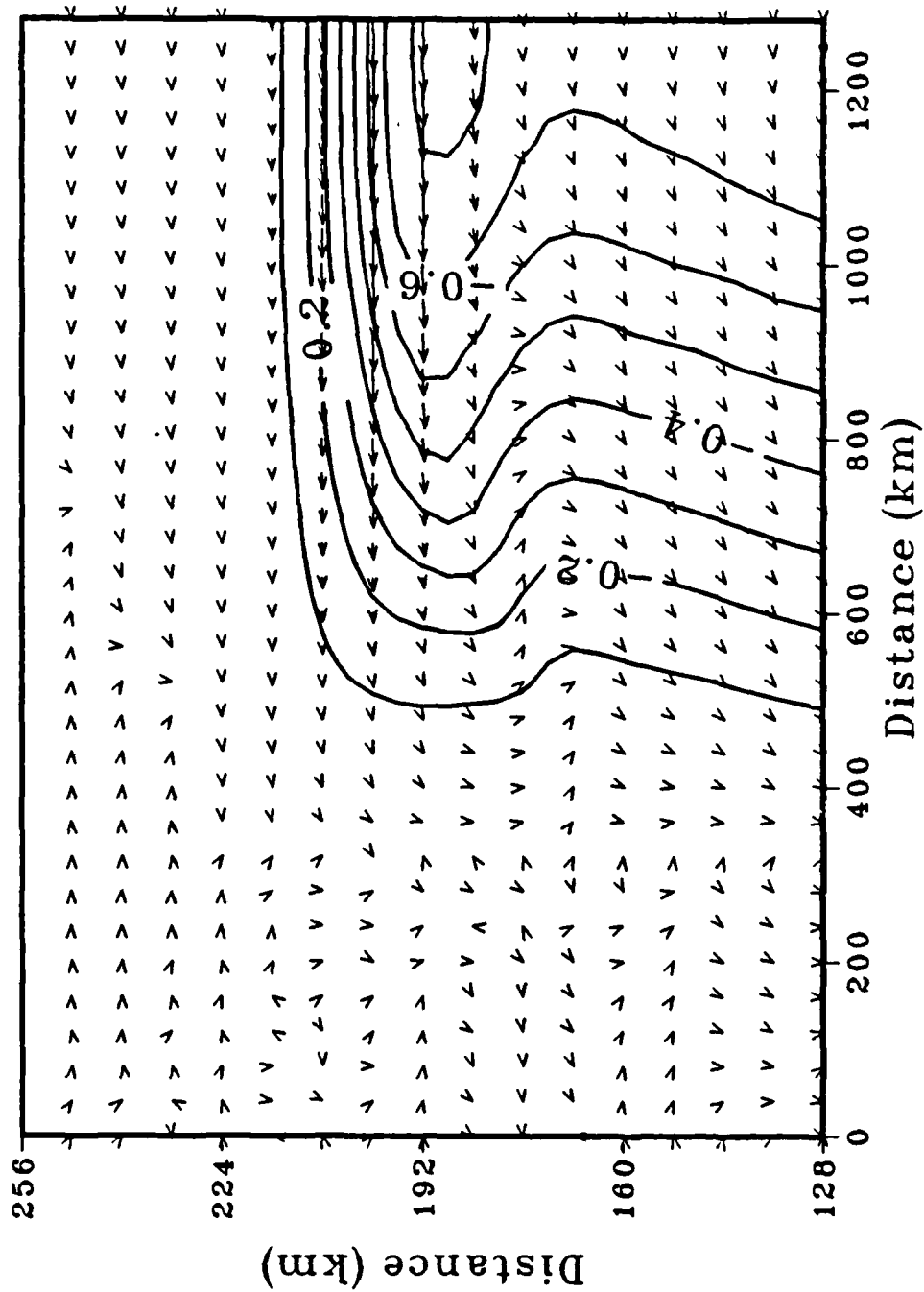


Figure 5. Changes in surface temperature (solid lines) and the velocities (arrows) at hour 72 for the experiment with mixing of heat only. The length of the arrows is proportional to the departure from a control run without forcing. The maximum departure is about  $8 \text{ cm s}^{-1}$ . The contour interval is  $0.1^\circ\text{C}$ .

The horizontal gradient in the surface cooling, and the associated decrease in pressure gradient is not large enough to balance geostrophically the decrease in the momentum. Consequently, the surface flow becomes sub-geostrophic, and positive (northward)  $v$  components occur near the front. This behavior is opposite of that predicted in the previous simulation when momentum mixing was not allowed.

The surface meridional velocities at hour 72 for the simulation that includes convective mixing of momentum are shown in Fig. 6. The maximum cross-stream speeds near the current maximum are now near  $2.5 \text{ cm s}^{-1}$  as opposed to  $-0.3 \text{ cm s}^{-1}$  when momentum mixing is not included. South of the current maximum, the southward flow is only slightly smaller than in the first experiment. The flows in this region are similar in the two experiments because there is little vertical current shear at the initial time, so momentum mixing has almost no effect. Thus, the drastic effect of including or excluding momentum mixing is confined to the region where the initial current has a sizeable vertical shear, i.e. near the front.

The maximum cross-stream component at the front is similar to two-dimensional simulations, but the contribution from the along-stream differences is also noticeable. At the front, the cross-stream velocities near the western boundary of the cooling are only half the magnitude of the cross-stream components farther downstream. Between  $x = 600 \text{ km}$  and  $x = 1000 \text{ km}$ , the surface cross-stream components near the front are nearly constant in  $x$  even though the forcing is a function of  $x$ . The cross-stream response at the front depends more on the initial shear in the zonal velocity than the imposed surface cooling in these simulations. The surface cross-stream components at the front between  $x = 300 \text{ km}$  and  $x = 600 \text{ km}$  are smaller due to the tendency of zonal advection to restore the fields to their initial condition.

The maximum reductions in the zonal components (Fig. 7) near the surface jet are almost twice as large as in the first experiment. The change in the surface zonal components is due to a combination of the adjustment of the flow to a weakened meridional temperature gradient and the reduction of the flow through convective mixing with the sub-surface flow. The reductions in the zonal components extend farther to the south in this simulation than in the first experiment. The larger southward extent of the reductions in the zonal components is due to the divergence of the cross-stream flow south of the front, which tends to weaken the horizontal temperature gradient there. The effect is most noticeable at the eastern boundary of the cooling where there are reductions in the zonal components south of the current maximum, and significantly smaller reductions north of the maximum. Away from areas of meridional cooling gradients and areas of vertical shear, there is little change in the surface zonal flow.

The change in surface temperature after 72 hours (Fig. 8) is similar to the surface temperature changes in the first experiment with only minor differences. As in the first simulation, the temperature changes are primarily due to the surface heat flux rather than the ocean's internal response to the forcing. The maximum temperature decreases are shifted slightly to the north and the west of the decreases that occurred in the previous simulation. The northward shift is due to advection by the positive  $v$  components at the front, and the westward shift is due to the weakened current maximum and thus, weakened tendency for zonal advection to restore the fields to their initial condition.

The changes in the vector flow field after 72 hours (Fig. 8) are also similar to the first experiment, except in the immediate vicinity of the front. There is a noticeable tendency for the vector flow to cross the lines of constant temperature change, indicating that the change in the flow is not as geostrophic as occurred earlier. Away from the immediate vicinity of the surface front, the changes in the flow are parallel to the changes in the temperature.

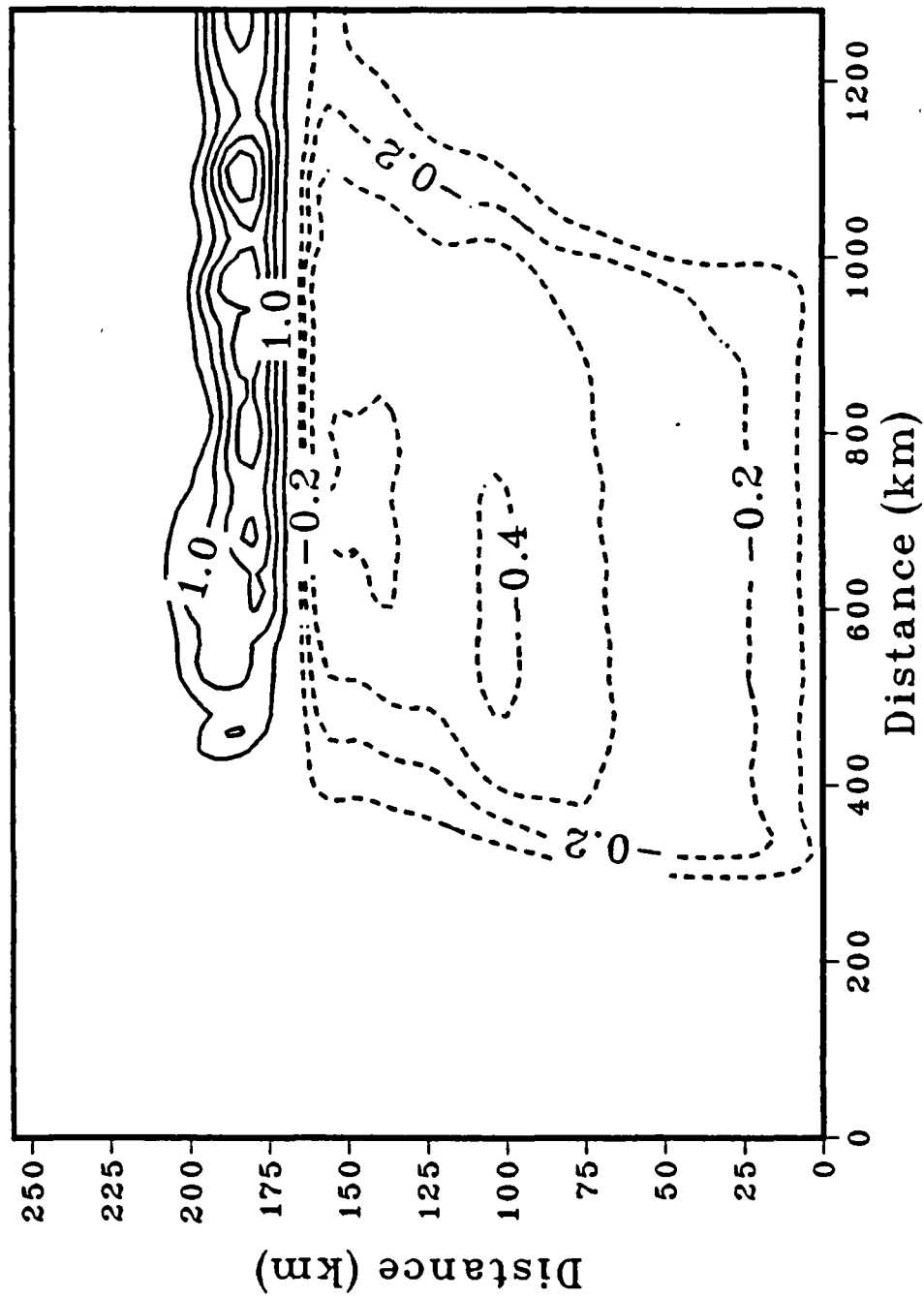


Figure 6. Surface  $v$  component at hour 72 for the simulation with momentum mixing allowed. The contour interval is  $0.5 \text{ cm s}^{-1}$  where the flow is positive (northward), and  $0.1 \text{ cm s}^{-1}$  where the flow is negative (southward).



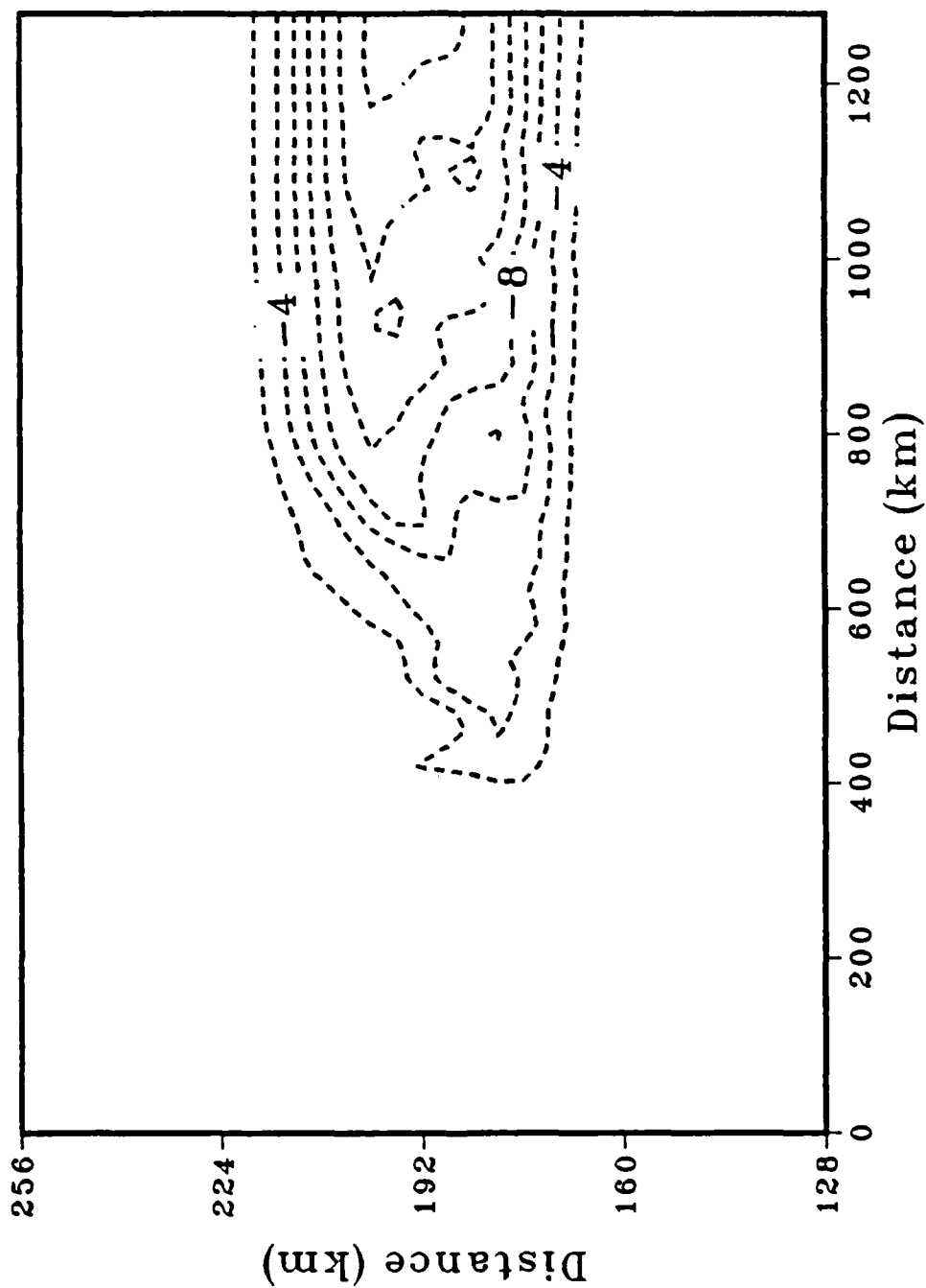


Figure 7. Change in surface u component of velocity at hour 72 for the experiment that allows momentum mixing. Negative values indicate a reduction in the eastward current maximum. The contour interval is  $2.0 \text{ cm s}^{-1}$ .

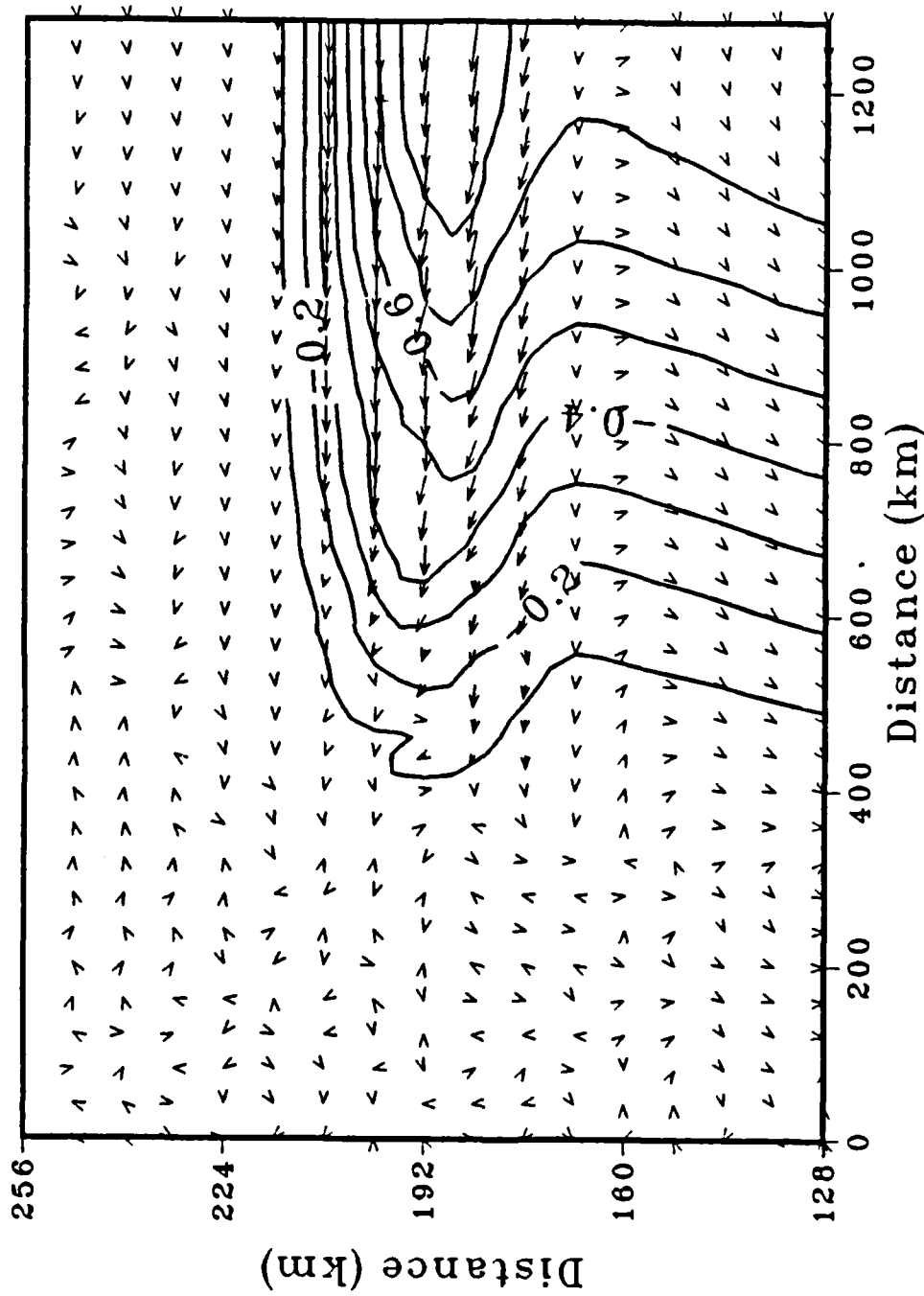


Figure 8. As in Fig.6 except for the simulation with momentum mixing allowed, and the maximum departure is about  $16 \text{ cm s}^{-1}$ .

In summary, the cross-stream components in the immediate vicinity of an ocean front are larger, and in the opposite direction, to the simulation with no momentum mixing during convective adjustment. South of the current maximum, in the region of weak vertical shear, the induced southward flow is only slightly changed by the inclusion of vertical mixing of momentum. The reductions in the zonal component near the current maximum are twice as large as those that occurred in the previous simulation. The changes in temperature are primarily due to the surface forcing rather than an internal adjustment of the ocean. The effects of vertical mixing of momentum dominate the effects of the imposed surface cooling gradients near the current maximum. The tendency to produce northward  $v$  components at the front when momentum mixing is included is large enough to compensate a cross-stream flow of the magnitude predicted by Nof (1983). The above conclusions obviously depend on the assumed initial vertical profile of zonal momentum, and on the assumed form of the vertical mixing of momentum (adjustment based on the value of the local Richardson number). At least for these simulations, strong cooling events alone cannot explain the observed southward shift of the mean position of the Gulf Stream during winter.

#### Acknowledgements

This research was funded by the Office of Naval Research under contract number NR 083-275, program element 61153N. Computer time was supplied by the W.R. Church Computer Center at the Naval Postgraduate School.

#### References

- Adamec, D., R.L. Elsberry, R.W. Garwood Jr., and R.L. Haney, 1981: An embedded mixed layer - ocean circulation model, *Dyn. Atmos. Ocn.*, 6, 69-96.
- Adamec, D., and R.L. Elsberry, 1985: Response of an intense oceanic current system to cross-stream cooling events, to appear in *J. Phys. Oceanogr.*
- Agee, E.M., and R.P. Howley, 1977: Latent and sensible heat flux calculations at the air sea interface during AMTEX 74, *J. App. Meteor.*, 16, 443-447.
- Budyko, M.I., 1963: *Atlas of the heat balance of the earth sphere*, Joint Geophysical Committee, Presidium of the Academy of Sciences, Moscow, 5pp. and 69 plates.
- Camerlengo, A.L., and J.J. O'Brien, 1980: Open boundary conditions in rotating fluids, *J. Comp. Phys.*, 35, 12-35.
- Fuglister, F.C., 1972: Cyclonic rings formed by the Gulf Stream. 1965-1966. In: *Studies in physical oceanography*, vol. 1, A.L. Gordon Ed., Gordon and Breach, N.Y., 194 pp.
- Gorshkov, S.G., 1978: *World ocean atlas*, vol.2, *Atlantic and Indian oceans*, Pergamon Press, N.Y., 306 pp.
- Kondo, J., 1976: Heat balance of the East China Sea during the air mass transformation experiment, *J. Meteor. Soc. Jap.*, 54, 382-398.
- Nof, D., 1983: On the response of ocean currents to atmospheric cooling, *Tellus*, 35A, 60-72.

Orlanski, I., 1976: A simple boundary condition for unbounded hyperbolic flows, *J. Comp. Phys.*, 21, 251-269.

United States Naval Oceanographic Office, 1970: Monthly summary, *The Gulf Stream*, 5, Number 11, 10 pp.

Worthington, L.V., 1976: *On the North Atlantic Circulation*, The Johns Hopkins University Press, Baltimore, MD, 110pp.

BIMODALITY IN THE GULF STREAM?

By

JOHN M. BANE, JR  
and  
WILLIAM K. DEWAR  
Marine Sciences Program  
University of North Carolina  
Chapel Hill, NC 27514

---

Abstract

Currents were measured in the Gulf Stream in the vicinity of the Charleston bump during the period September 1981 through April 1982. Combining these data with satellite sea surface temperature data has provided a description of the major events in the Stream during that period. During roughly the first and last thirds of the time series the Stream was in a configuration which we have called the "weakly deflected state," with its path being affected primarily by the downstream propagation of Gulf Stream meanders and frontal eddies. The dominant periods of Gulf Stream fluctuations during these times range from 2 to 10 days. During the middle three months of the time series the path of the Stream curved considerably offshore near the Charleston Bump, a configuration which we term the "strongly deflected state." During this time the low frequency fluctuations of the Stream changed in character, and exhibited dominant periods near 16 days. It appears likely that the shift from the weakly deflected to the strongly deflected state is accompanied by (and perhaps caused by) a change in the structure of the Stream as it approaches the Charleston bump from the south.

---

1. INTRODUCTION

Understanding of the nature, causes and effects of Gulf Stream variability has increased substantially within the past decade. Numerous observational studies have built a data base that has provided for several detailed descriptions of fluctuation events and processes in the Stream. In particular, wavelike meanders of the Gulf Stream and their attendant frontal eddies are now recognized as the dominant form of mesoscale variability in the Gulf Stream within the South Atlantic Bight (SAB), the region between

Cape Canaveral, Florida and Cape Hatteras, North Carolina. Early views of these features were provided by the pioneering studies of von Arx, et al (1955), who mapped the warm filaments of water which trail southward away from the main body of the Stream and over the outer continental shelf; and of Webster (1961), who successfully observed the progression of a train of four meanders past Onslow Bay, North Carolina, during a 28-day period in 1958. The recent reports by Maul et al (1978), Legeckis (1979), Pietrafesa and Janowitz (1980), Vukovich and Crissman (1980), Bane et al (1981), Brooks and Bane (1981), Lee et al (1981), Pietrafesa (1983), and those contained in the May 30, 1983 special issue of the Journal of Geophysical Research have added considerably to the earlier studies, and yet have paved the way for posing new questions about the dynamics of the Gulf Stream.

One striking feature of the Gulf Stream south of Cape Hatteras is the recurring seaward deflection of its path near 32N latitude. Almost all of the investigators mentioned above have suggested that the deflection process plays a significant role in determining the nature of the Gulf Stream's variability. Legeckis (1976, 1979) has proposed that the deflection process is caused by the flow of the Stream over the "Charleston bump", a topographic feature located on the upper continental slope at about 32N Latitude (see Figure 1). Several studies have shown that the Stream's eddy variability increases downstream of the deflection (see Olson et al, 1983); and Legeckis (1979), Vukovich and Crissman (1980) and Lee et al (1981) have documented individual meander/frontal eddy events propagating through the deflection region, apparently being amplified while doing so. Even with this observational background, the exact nature of the deflection process, how it varies and how it effects the enhanced Gulf Stream variability downstream have yet to be determined.

During the period September 1981 through April 1982, the Gulf Stream Deflection and Meander Energetics Experiment (DAMEX) was conducted in the region of the Stream's seaward deflection. This experiment was designed to study the deflection process and its relationship to subtidal Gulf Stream variability. In this report we describe one aspect of the Gulf Stream's behavior during DAMEX. In particular, we present data which suggest that the deflection of the Stream has a bimodal character, and that the nature of the low frequency variability of the Stream between Charleston and Cape Hatteras varies between the two states of deflection. In another paper in this PROCEEDINGS volume (Dewar and Bane, this volume) we discuss the energetics of the Stream during DAMEX.

## 2. DAMEX

DAMEX was composed of three observational components. Current meters and bottom pressure gauges were moored in seven instrument moorings for a seven month period beginning in September 1981; a CTD survey was made in the deflection region during September, 1981 and four AXBT surveys were conducted along the Stream in an area which encompassed the deflection region during March, 1982. The seven instrument moorings made up the primary DAMEX component, and were grouped into two three-mooring arrays plus one single mooring (Figure 1). The southernmost array, E, consisted of three moorings with two current meters each, and was located about 90 km southwest (upstream) of the center of the Charleston bump. The central array, F, also consisted of 3 moorings supporting two current meters each, and was located roughly 90 km northeast (downstream) of the bump. Two of the F moorings supported the bottom pressure gauges. A single mooring, G, with two current meters was located off Onslow Bay. Arrays E and F were moored in areas

which had not been previously sampled, while G was placed at the site of an earlier mooring that was in place during the Gulf Stream Meanders Experiment, which was conducted during 1979 (cf Brooks and Bane, 1981).

The three moorings in each of the E and F arrays were placed in an 'L'-shaped configuration with one mooring on the 300 m isobath and two on the 400 m isobath. In each array the shallow mooring was identified as the '1' mooring, the mooring downslope from this as the '2' mooring, and the northernmost mooring as the '3' mooring. The top (bottom) instruments at all moorings, including G, were located at a nominal depth of 210 (270) m. We will refer to each instrument by a unique name which denotes its array, mooring and instrument depth; for example, E1T (E1B) where the 'T' ('B') means top (bottom).

The current meters measured velocity, temperature and conductivity at 30 minute intervals from the middle of September 1981 to the middle of April 1982. The data were low pass filtered to remove tides and internal waves by using a modified Lanczos filter with its quarter power point at forty hours. The resulting forty hour low passed (40 HRLP) time series averaged 200 days in length and had an effective sampling interval of six hours. This processing follows that of our earlier experiments in the SAB (cf Brooks et al., 1981). A full documentation of all DAMEX mooring data and processing techniques is given in Bane and Dewar (1983).

Note that significant offshore flows were measured at some of the instruments (Figure 1). To facilitate our discussion in terms of cross-stream and downstream flow, we have rotated the velocity measurements to a frame aligned the the local mean flow direction at each array site (E, F, or G), and we will use this system for this paper. The x(y) axis in each case is oriented to be positive towards the offshore (downstream) direction.



### 3. DAMEX Results: Does the Gulf Stream Path Exhibit a Bimodal Character?

A brief subset of results from DAMEX will be presented here. A more complete report of the observations will be submitted for journal publication at a later date.

Figure 1 shows the seven-month-long mean current vectors at the 270 m level at each of the seven moorings. Also plotted as a dashed line is the mean position of the Stream's shoreward surface thermal front, determined by Olson et al (1983) for a four year period. The moorings were placed along the cyclonic flank of the Stream in a manner that allowed meander and deflection movements of the Stream to be easily detected.

The effects of the deflection of the Stream off Charleston are evident in the array F mean vectors. The directions are consistent with a seaward flow along a cyclonic turn, and the magnitudes are relatively low when compared to E and G vectors. It will be shown below that during a large fraction of the mooring period, the Stream was deflected seaward far enough to reduce the mean velocities at array F to almost zero during that time.

The 40 HRLP time series for downstream speed,  $v$ , cross-stream speed,  $u$ , and temperature,  $T$ , are shown in Figures 2, 3, and 4 for the E2T, F2B and GT instruments, respectively. The central point regarding the bimodal nature of the Stream's deflection is demonstrated in Figure 3. For approximately three months beginning in early November, 1981, the downstream speed decreased and the fluctuation periods increased from those which occurred prior to and following this period. It is during this period that satellite sea surface temperature images show the Stream to be deflected well offshore of its mean position. Images from the earlier and later portions of the mooring period show the Stream to be in a more "typical" state characterized

by the downstream propagation of meander/frontal eddy events of mean weekly periods. Good satellite images during these two different states of the Stream are available for 3 December 1981 and 2 March 1982. These images have been traced and placed side by side in Figure 5 to give an easy comparison. The 3 December image is typical of what we now refer to as the "strongly deflected state" of the Stream, whereas the 2 March image typifies the "weakly deflected state".

The variability which occurs during the strongly deflected state is different from that of the weakly deflected state. As mentioned above, meander/frontal eddy events which progress downstream and have nearly weekly periods occur during the weakly deflected state. The appearance of a deflection near 32N latitude during this state is caused primarily by the rapid amplification of meanders as they pass through the deflection region near the Charleston bump. The apparent deflection during the weakly deflected state is indicated in Figure 5. The dominant variability in the strongly deflected state during DAMEX had periods near 16 days, and had the characteristics of warm anomalies with anticyclonic circulation progressing past array F. The cause of the shift from one deflection state to the other is not presently known.

Acknowledgments. This work was supported by the Office of Naval Research under contract N00014-77-C-0354 to the University of North Carolina at Chapel Hill.

#### References

Bane, J.M., Jr., D.A. Brooks, and K.R. Lorenson, Synoptic observations of the three-dimensional structure and propagation of Gulf Stream meanders along the Carolina continental margin, J. Geophys. Res., 86, 6411-6455, 1981.

- Bane, J.M., Jr., and W.K. Dewar, The deflection and meander energetics experiment, current meter and bottom pressure gauge data report, Rep. CMS-83-2, Univ. of North Carolina, Chapel Hill, 1983.
- Brooks, D.A., and J.M. Bane, Jr., Gulf Stream fluctuations and meanders over the Onslow Bay upper continental slope, J. Phys. Oceanogr., 11, 247-256, 1981.
- Brooks, D.A., J.M. Bane, Jr., R.L. Cohen, and P. Blankinship, The Gulf Stream meanders experiment: Current meter, atmospheric, and sea level data report for the August to November, 1979 mooring period, Rep. 81-3-T, Texas A&M Univ., College Station, 1981.
- Lee, T.N., L.P. Atkinson, and R. Legeckis, Observations of a Gulf Stream frontal eddy on the Georgia continental shelf, April 1977, Deep Sea Res. 28(4), 347-378, 1981.
- Legeckis, R.V., The influence of bottom topography on the path of the Gulf Stream at Latitude 31N from NOAA's satellite imagery. Abstr., EOS Trans. AGU, 57(4), 260, 1976.
- Legeckis, R.V., Satellite observations of the influence of bottom topography on the seaward deflection of the Gulf Stream off Charleston, South Carolina, J. Phys. Oceanogr., 9(3), 483-497, 1979.
- Maul, G.A., P.W. DeWitt, A. Yanaway, and S.R. Baig, Geostationary satellite observations of Gulf Stream meanders: Infrared measurements and time series analysis, J. Geophys. Res., 83(C12), 6123-6135, 1978.
- Olson, D.B., O.B. Brown, and S.R. Emmerson, Gulf Stream frontal statistics from Florida Straits to Cape Hatteras derived from satellite and historical data, J. Geophys. Res., 88(C8), 4569-4577, 1983.
- Pietrafesa, L.J., Shelf break circulation, fronts and physical oceanography: East and west coast perspectives, in Shelf-Slope Boundary: A Critical Interface on Continental Margins, edited by D.J. Stanley and G.J. Moore, Spec. Publ. 33, Society of Economic Paleontologists and Mineralogists, Tulsa, Okla., 1983.
- Von Arx, W.S., D.F. Bumpus, and W.S. Richardson, On the fine-structure of the Gulf Stream front, Deep Sea Res., 3, 46-65, 1955.
- Vukovich, F.M., and B.W. Crissman, Some aspects of Gulf Stream western boundary eddies from satellite and in situ data, J. Phys. Oceanogr., 10, 1792-1813, 1980.
- Webster, F.A., A description of Gulf Stream meanders off Onslow Bay, Deep Sea Res., 8, 130-143, 1961a.

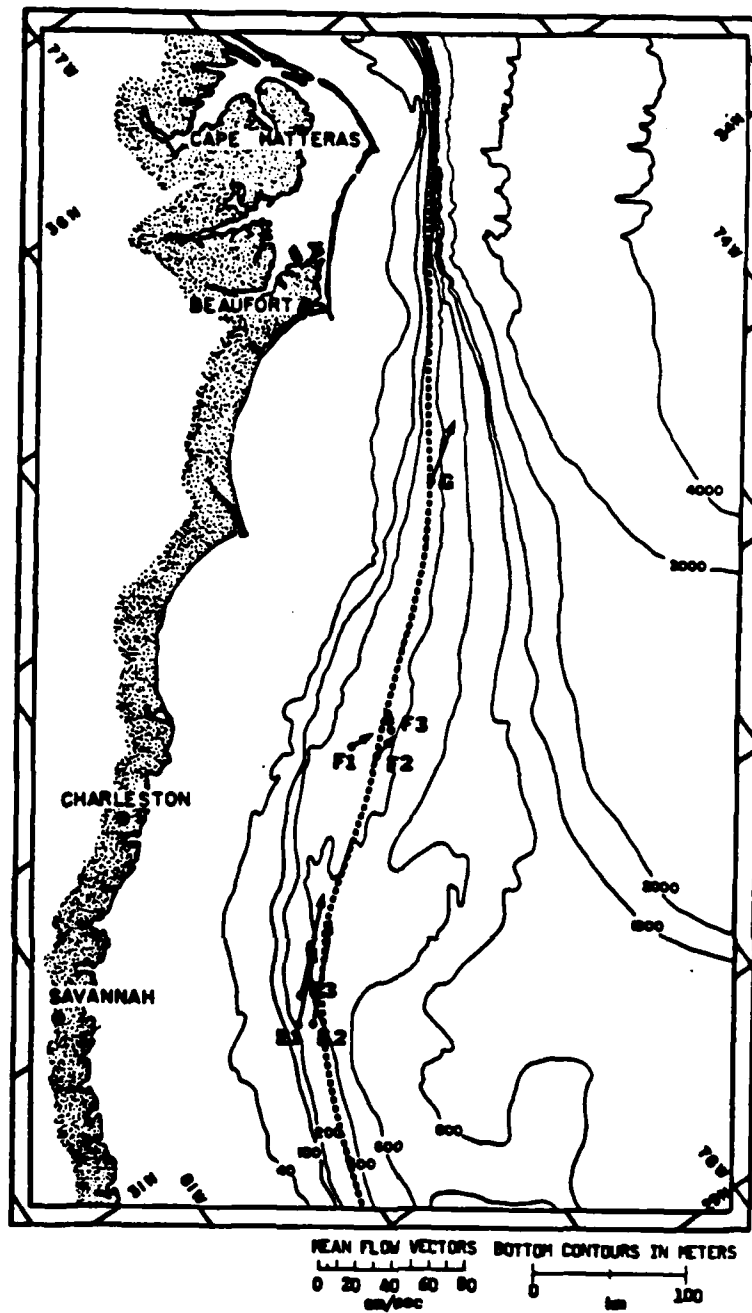


Figure 1. Mean flow vectors for the DAMEX array during the September 1981 through April 1982 period. The dotted line is the mean position of the Gulf Stream's surface thermal front.

## E2T

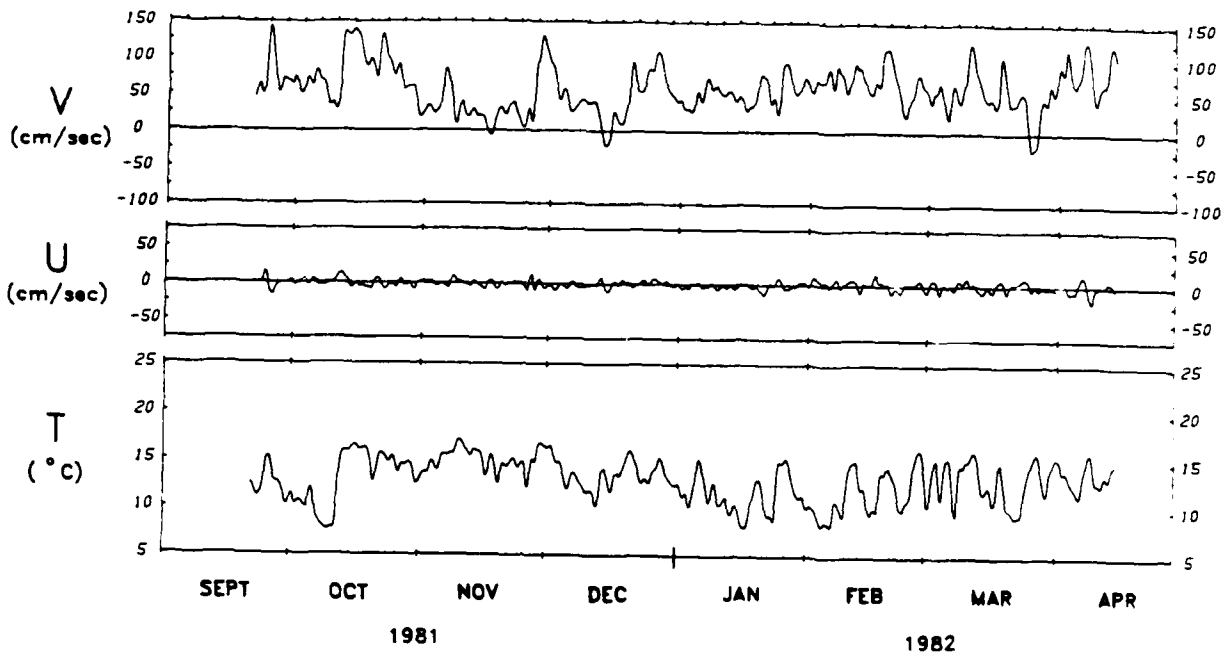


Figure 2. Forty-hour low-passed downstream speed ( $v$ ), cross-stream speed ( $u$ ) and temperature ( $T$ ) from the E2T instrument.

## F2B

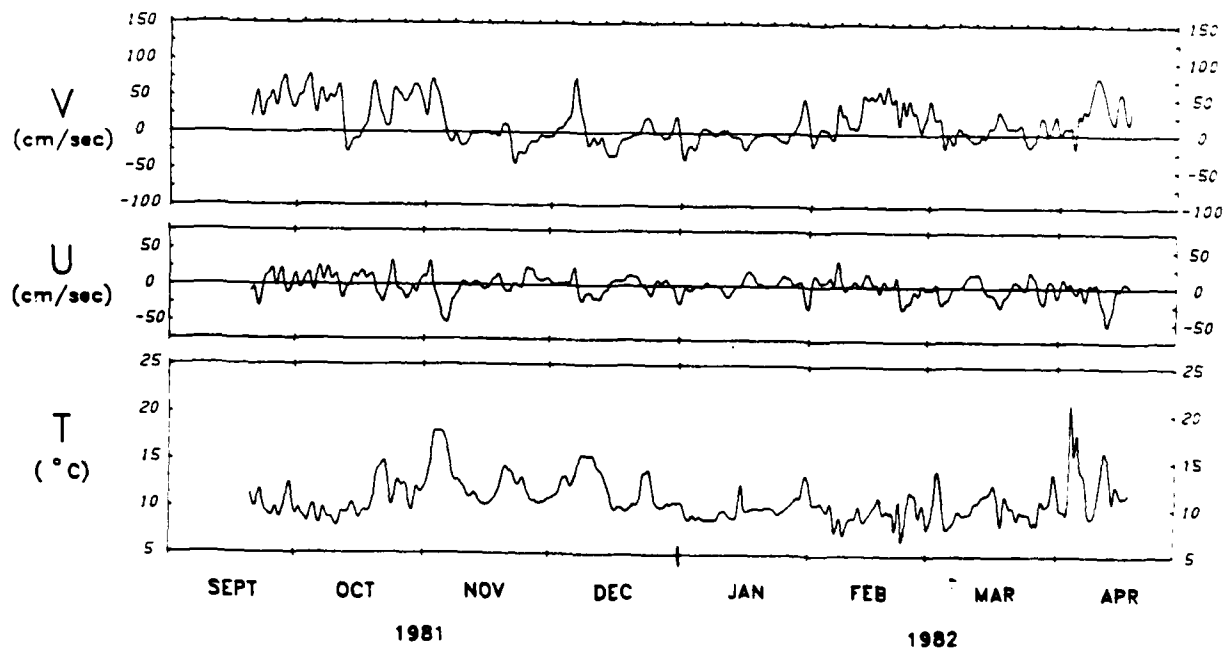


Figure 3. Forty-hour low-passed downstream speed ( $v$ ), cross-stream speed ( $u$ ) and temperature ( $T$ ) from the F2B instrument.

## GT

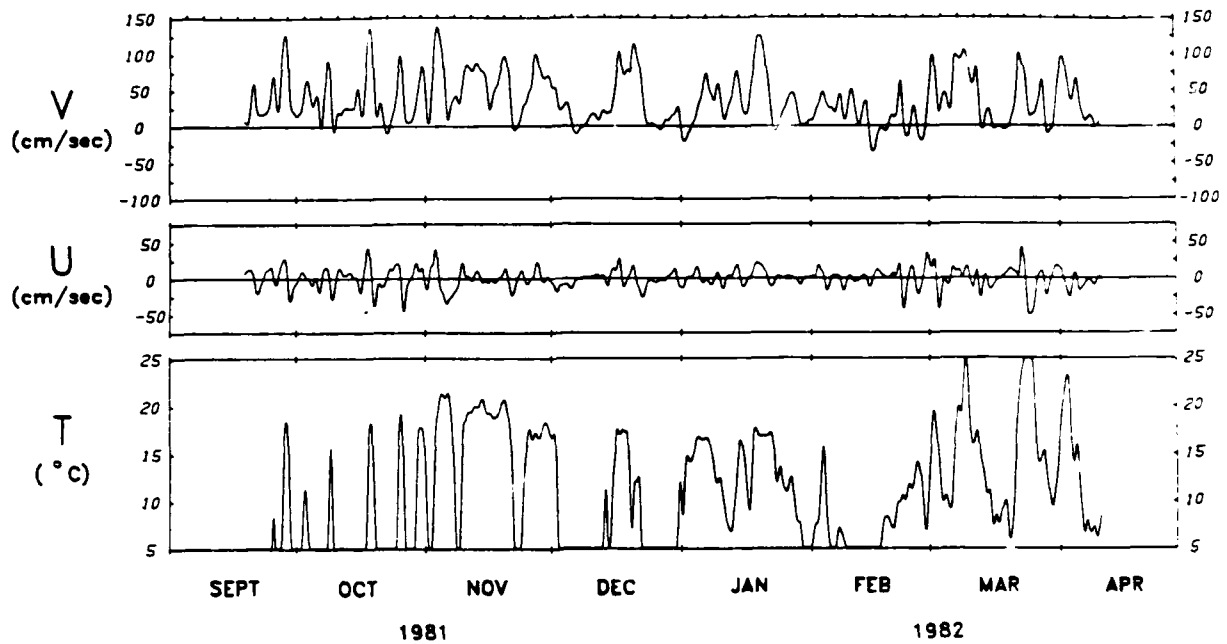
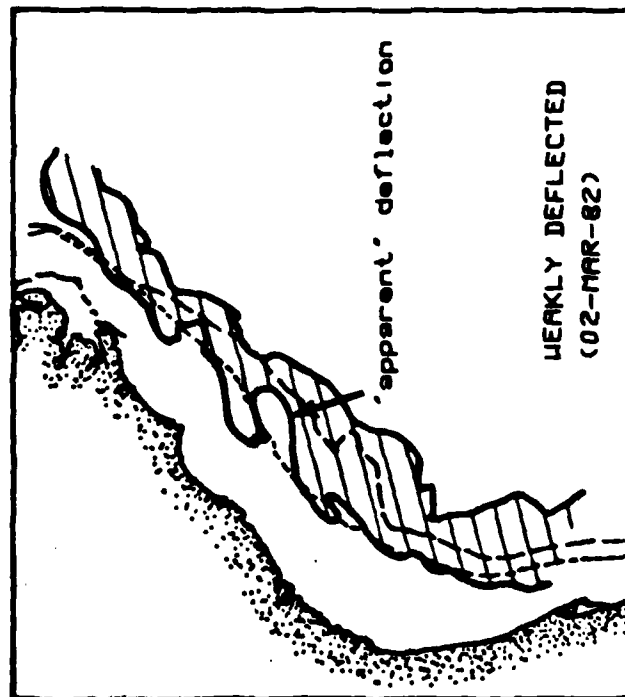
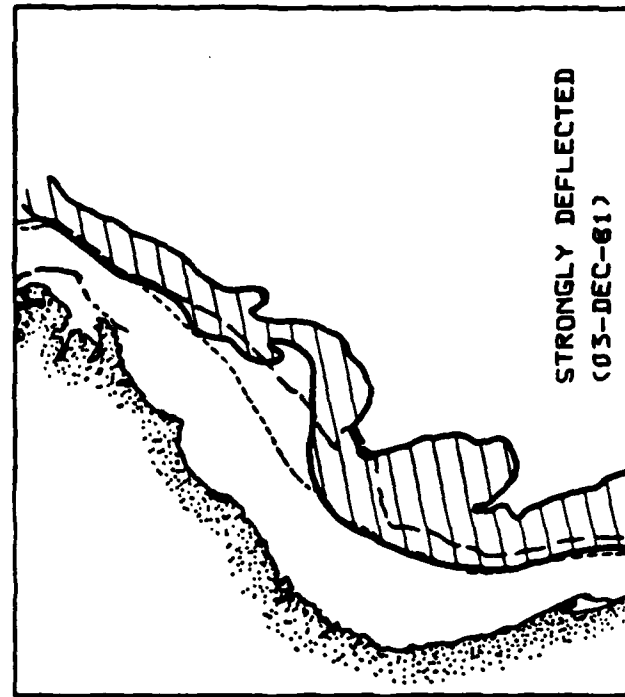


Figure 4. Forty-hour low-passed downstream speed (v), cross-stream speed (u) and temperature (T) from the GT instrument. (The temperature sensor did not function properly on this instrument.)



-----200 meter contour  
 -----600 meter contour

Figure 5. Satellite views of the Gulf Stream for a typical weakly deflected state and a strongly deflected state.

RECENT CURRENT MEASUREMENTS IN THE GULF STREAM  
DOWNSTREAM FROM CAPE HATTERAS

By

JOHN M. BANE, JR.  
Marine Sciences Program  
University of North Carolina  
Chapel Hill, NC 27514

and

D. RANDOLPH WATTS  
Graduate School of Oceanography  
University of Rhode Island  
Narragansett, RI 02882

---

Abstract

An array of five moorings supporting four current meters each was deployed in the Gulf Stream for a one-year period beginning in January 1984. The study area is located 150-250 km northeast ("downstream") of Cape Hatteras, North Carolina, in water depths ranging from about 2800 m to 4000 m. Each mooring had Aanderaa current meters positioned at nominal depths of 500 m, 1000 m, and 2000 m below the surface, and at 500 m above the bottom. The five "tall" moorings were designed to minimize tilting due to the high velocities encountered in this area, and pressure measurements show that vertical excursions of each top current meter were typically  $\pm 50$  meters (standard deviation) about its mean depth.

Velocity and temperature data are presently in an early stage of processing. Subtidal fluctuations in these variables have periods ranging from a few days to 1 year, and show good coherence throughout the array. Good vertical coherence in the long term temperature variations suggests a barotropic nature to the lateral movements of the Stream within the study area. An increase in temperature variance approaching the bottom indicates the presence of bottom intensified motions.

---

Currents were measured in the Gulf Stream for a one-year period beginning in mid-January 1984. The study area, shown in Figure 1, is located about 150-250 km northeast of Cape Hatteras, North Carolina, in a region where Gulf Stream meanders are known to propagate and grow in the



downstream direction. The array was composed of five "tall" moorings supporting four Aanderaa current meters each. Meters were placed at nominal depths of 500 m, 1000 m and 2000 m from the surface and 500 m from the bottom on each mooring, and they recorded current speed, current direction and temperature at one-hour intervals. This array was placed in a fashion that complemented an array of bottom-mounted inverted echo sounders and pressure gauges that was maintained in this area for the duration of the current meter study (Watts and Tracey, 1985). The purpose of this report is to give a preliminary view of the results from this measurement program.

Figures 1a through 1d show the mean flow vectors at the four levels. During 1984 the Stream flowed along a course which was north of its usual path. This condition resulted in our array being positioned within the anticyclonic side of the Stream. This may be clearly seen in the 500 m and 1000 m mean currents shown in Figures 1a and 1b. The near-bottom currents (Figure 1d) show the presence of a deep southwestward mean flow, counter to that of the surface Gulf Stream.

Forty-hour low-passed time series of the downstream speeds ( $u$ ), cross-streams speed ( $v$ ) and temperatures ( $T$ ) measured by the four instruments on mooring B2 are shown in Figures 2a through 2d. Mooring B2 was the westernmost in the array, and was located near 35.8N 73.5W. The depth of the top instrument is also shown in the top panel in Figure 2a, and provides an estimate of the mooring's performance.

Several aspects of the Gulf Stream environment during 1984 may be seen from visual inspection of the Figure 2 time series. The uppermost instrument was south of the Stream during the first and last portions of the period, while from about day 120 to day 350 the Stream had moved far enough south to flow across the array and be detected by mooring B2. A general

decrease in temperature was seen at all B2 instruments during this period, suggesting a barotropic shift of the temperature field to the south along with the Stream as it moved southward.

At least two strong, mid-depth velocity fluctuations may be seen at the 2000 m level (Instrument B2, 3) near days 150 and 220. Little effect was seen at the other three B2 instruments during these events indicating isolated mid-depth eddy motions. Other records from the array (not presented here) clearly show the presence of mid-depth, anticyclonically circulating, warm anomaly eddies moving through the array at other times as well.

The temperature variance on scales of 5-20 days is clearly higher in the B2, 4 record than in the B2, 3 record, suggestive of bottom intensified motions.

Two strong events occurred near day 115 and day 265 in the B2,1 record. Using velocity and temperature signatures at this instrument, plus delay times between instruments within the array, it is possible to interpret these events as cold-core, cyclonic eddies moving to the northeast. Satellite data have confirmed that the events are cold-core Gulf Stream rings travelling in the "downstream" direction with the main current.

This discussion of these data is preliminary. Even so, it is clear that the motions in this area of the ocean are complex and intriguing. Future reports will be made, giving a more complete description of the structure and dynamics of the Stream here.

Acknowledgments. This work was supported by Office of Naval Research Contracts N00014-77-C-0354 to the University of North Carolina and N00014-81-C-0062 to the University of Rhode Island.

References

Watts, D.R., and K.L. Tracey: Objective Analysis of the Gulf Stream Thermal Front from Inverted Echo Sounders, Gulf Stream Workshop April 1985, Proceedings, University of Rhode Island, 1985.

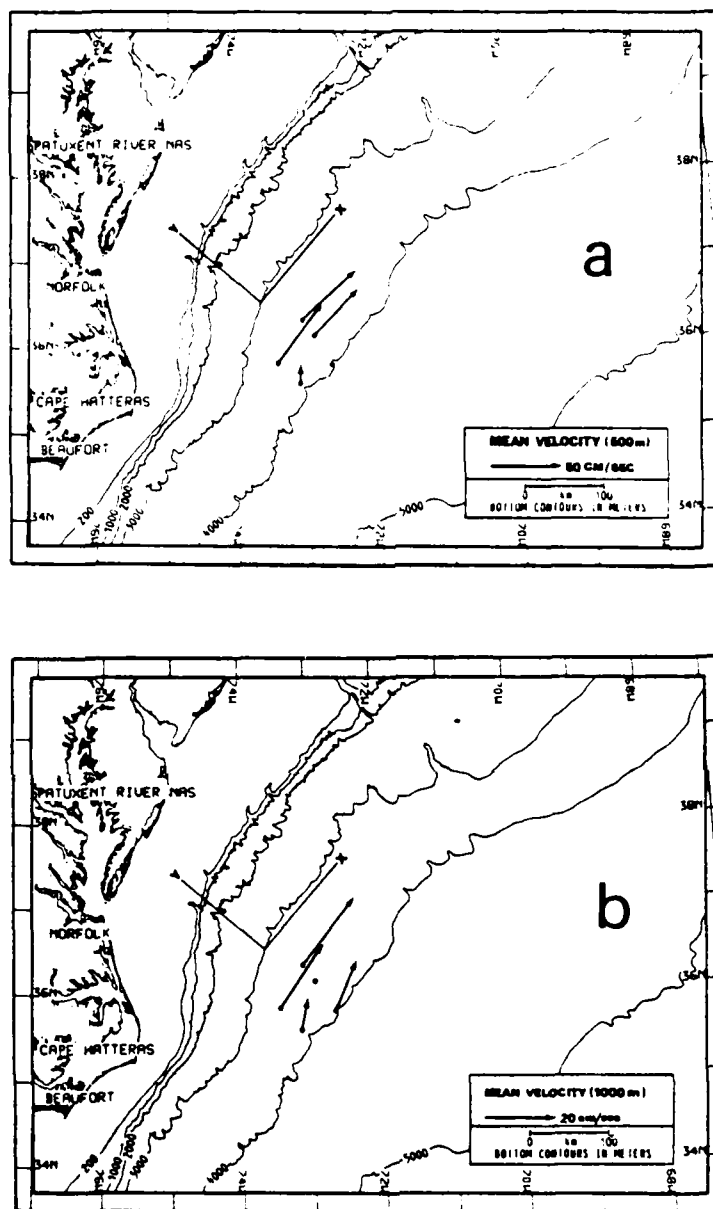


Figure 1. Record long mean velocities in the study area for the instruments moored at nominal depths of 500 m (a), 1000 m (b), 2000 m (c) and total depth minus 500 m (d).

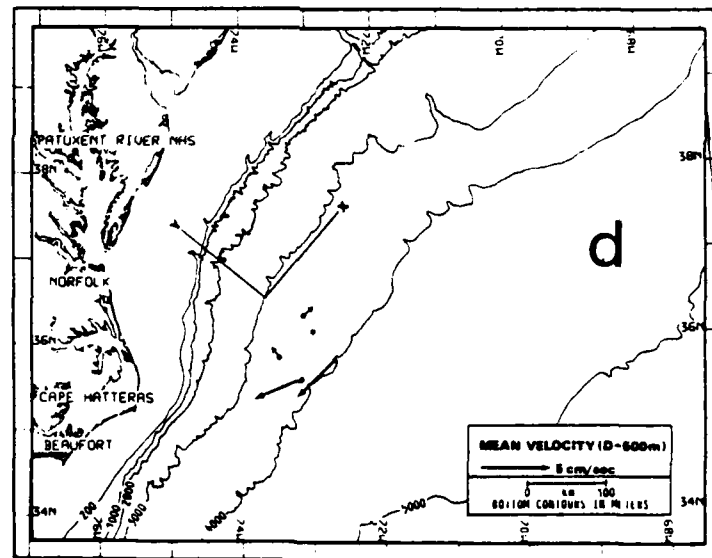
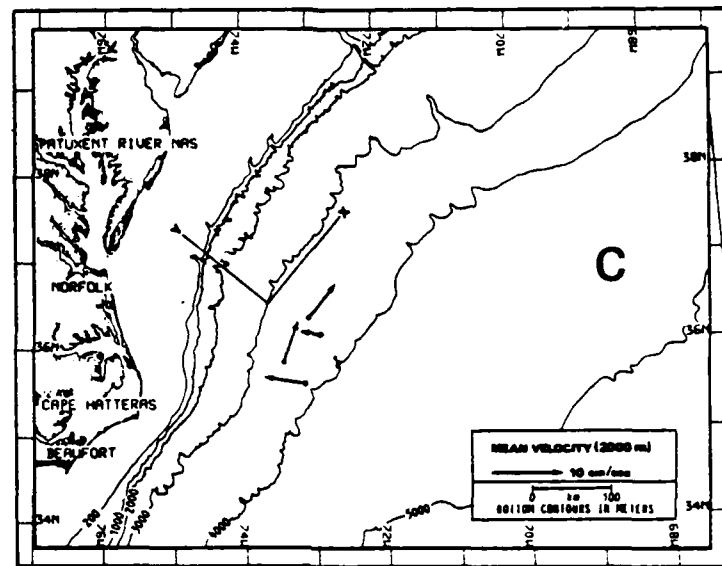


Figure 1 continued.

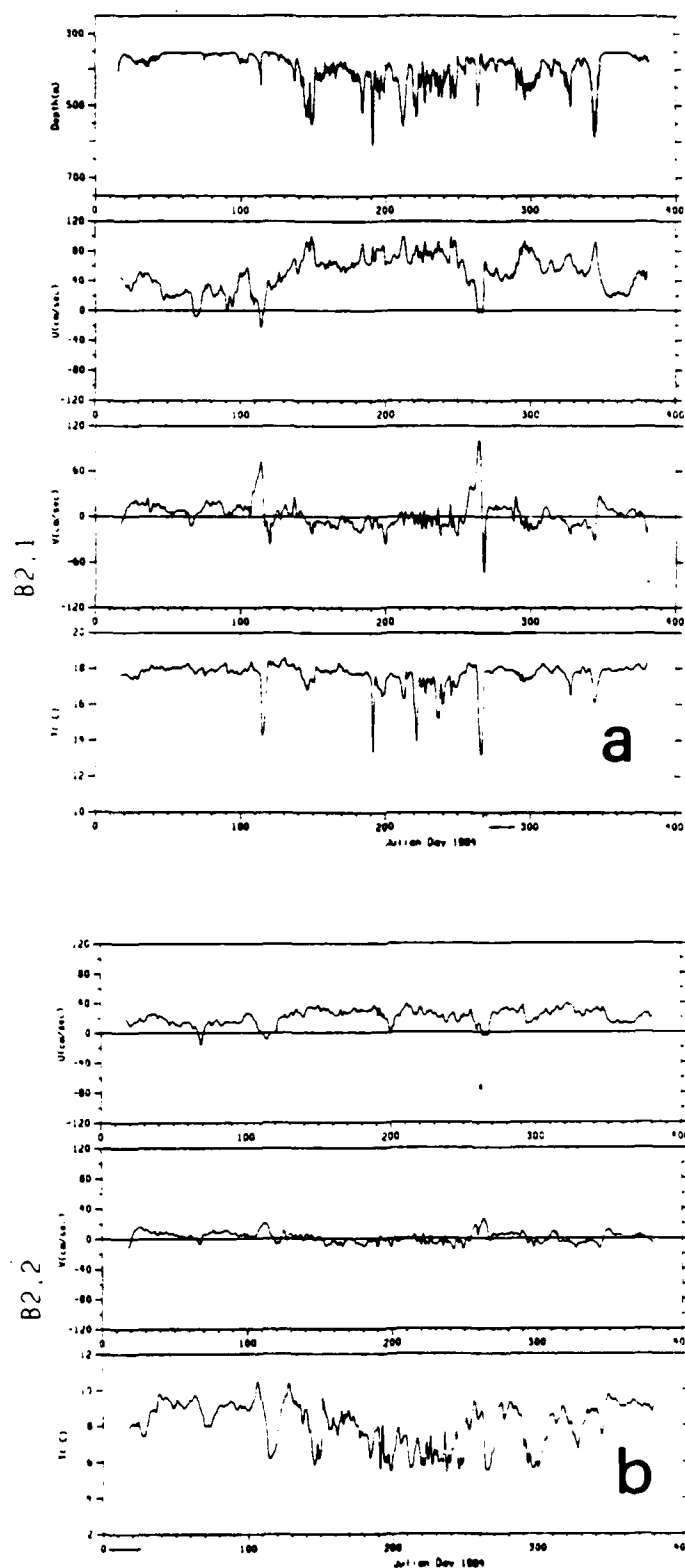


Figure 2. Forty-hour low-passed time series of downstream speed ( $u$ ), cross-stream speed ( $v$ ) and temperature ( $T$ ) from the 4 instruments on the B2 mooring. The records are from the instruments at 500 m (a), 1000 m (b) and 2000 m (c) below the surface, and at 500 m off the bottom (d). All time axes being at 0000 on 1 January 1984.

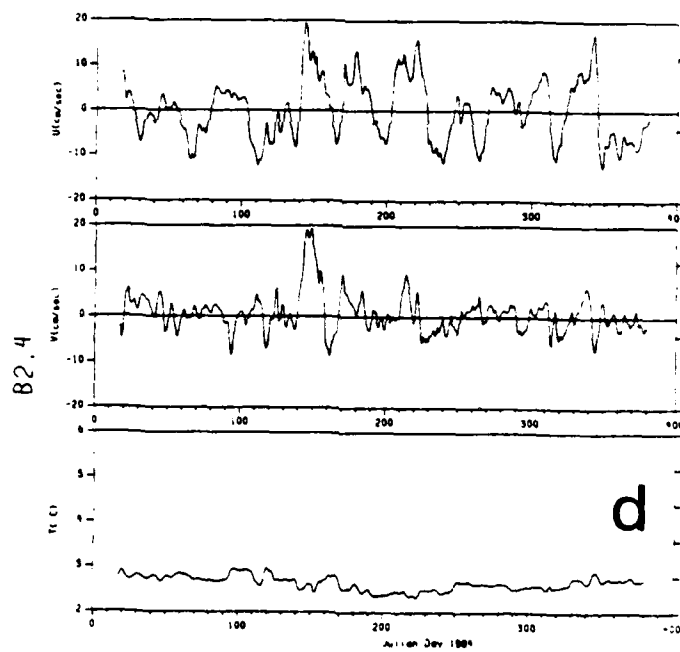
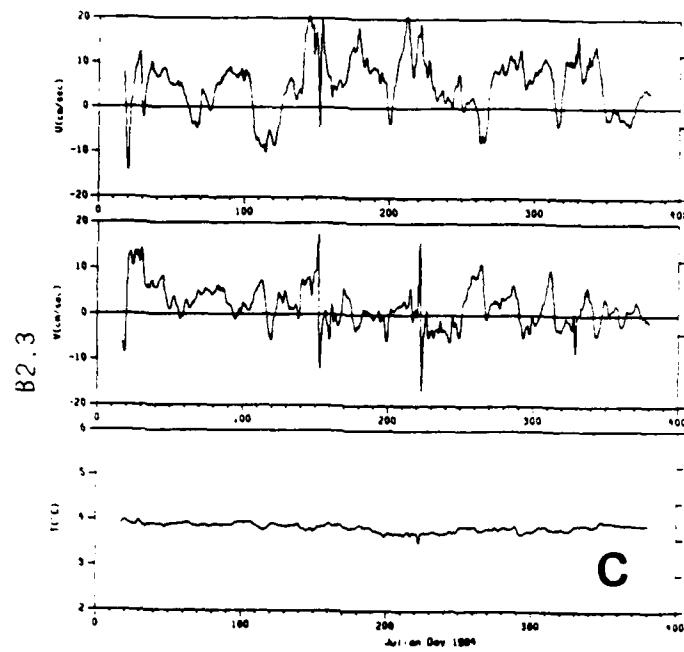


Figure 2 continued.

ISOPYCNAL RAFOS FLOATS AND THE DYNAMICS OF GULF STREAM MEANDERS:  
PRELIMINARY RESULTS

Amy S. Bower

Since July, 1984, Dr. T. Rossby has been launching Rafos floats in the center of the Gulf Stream off Cape Hatteras, North Carolina (details of the program can be found in the article by T. Rossby elsewhere in the workshop proceedings). These floats are isopycnal, acoustically tracked drifters which measure temperature, pressure and position three times daily for 30 days. In this new isopycnal mode, the Rafos floats provide a significant improvement over isobaric Sofar floats in that they can follow isopycnal water parcel motion quite well in the Gulf Stream where density surfaces slope up steeply toward the sea surface as one crosses the current. This characteristic of the Rafos floats renders them ideal for studying the dynamics of Gulf Stream flow.

The most striking features of the Rafos float trajectories are the large cross-stream excursions which appear to be highly correlated with changes in curvature of the Stream path. Floats almost always move toward the Slope Water (and shoal) as they move from meander trough to crest. When the curvature reverses again, the floats usually move across the Stream toward the Sargasso Sea (and deepen) (see Fig. 1a). From a preliminary examination of the data, it appears that the major loss of floats (and water?) occurs when the Stream path curves dramatically and floats downwell or upwell rapidly to the edges of the current and beyond. Since this process may be an important mechanism for cross-stream exchange, dispersion and recirculation of water in the Gulf Stream region, we thought it would be useful to study these isopycnal motions in a dynamical framework.

As a first attempt at understanding the dynamic interactions influencing the motion of the floats, we assume the floats are tracking fluid parcels and are thus conserving potential vorticity along their paths. We consider only the vertical component of potential vorticity (Johns (1984) showed other terms to be small over most of the Gulf Stream). In a



natural, or "stream" coordinate system, the potential vorticity is thus given by,

$$Q_1 = (f + \kappa V - \frac{\partial V}{\partial n}) \times \frac{1}{\rho} \frac{\partial \rho}{\partial z} \quad (1)$$

where  $f$  is the planetary vorticity,  $\kappa$  is the path curvature,  $V$  is the downstream velocity,  $n$  is the cross-stream coordinate (positive to the left of the current) and  $\frac{1}{\rho} \frac{\partial \rho}{\partial z}$  is the vertical stratification. The sum  $\kappa V - \frac{\partial V}{\partial n}$  represents the total relative vorticity, where  $\kappa V$  is the curvature vorticity and  $\frac{\partial V}{\partial n}$  is the lateral shear vorticity. We further assume that the vertical stratification is inversely proportional to the thickness of the layer between the sea surface and the density surface on which the float travels (in other words, consider the water column above the float as a single barotropic layer). With this assumption, we can simplify the potential vorticity as,

$$Q_2 = \frac{(f + \kappa V - \frac{\partial V}{\partial n})}{H} \quad (2)$$

where  $H$  is the depth of the float (see Fig. 1b).

Along a float trajectory,  $f$  changes little, but  $\kappa V$  changes drastically between meander crests and troughs as the sign of  $\kappa$  alternates from negative to positive. We can see from (2) that the large cross-stream motions observed in the float data are somewhat to be expected. As curvature increases (anticyclonic to cyclonic turn),  $H$  must also increase (if  $\frac{\partial V}{\partial n}$  remains unchanged), implying a cross-stream motion toward the Sargasso Sea where the upper layer thickness is greater. Likewise, as curvature decreases along the Stream path,  $H$  must decrease, forcing fluid parcels to move toward the Slope Water region where the upper layer thickness is less.

We are interested in studying the interactions between all the terms in (2), since changes in curvature vorticity must be balanced by changes in  $H$ ,  $\frac{\partial V}{\partial n}$ , or both. For several floats, we have estimated the terms in (2). For a 10-day segment along the trajectory of Float #22 (see Fig. 2),  $f + \kappa V$  was linearly related to  $H$  ( $\frac{\partial V}{\partial n}$  did not change much) and the high correlation between curvature vorticity and vertical stretching is illustrated in Fig. 3. This situation is typical for many floats

which make large cross-stream excursions in response to changes in curvature.

Float #21 (Fig. 4) escaped into the Sargasso Sea, where the potential vorticity is simply given by,

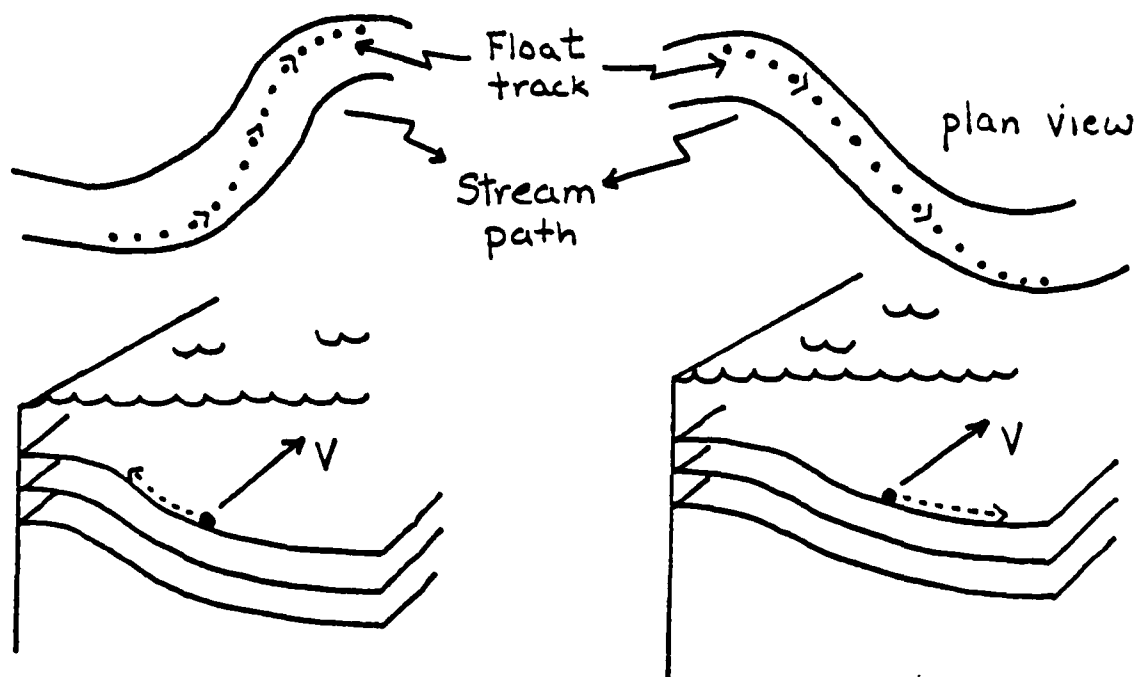
$$Q_2 = \frac{f}{H} \quad (3)$$

due to the slow speeds and weak shear there.  $Q_2$  was estimated directly for this float, and assumed to be conserved all along the float trajectory, even when the float was in the Stream. In this case, all components of (2) can be estimated ( $\frac{\partial v}{\partial n}$  is calculated as a residual since all other quantities in (2) were measured directly). The different components of potential vorticity are plotted in Fig. 5 for a 7-day period when the float was in the Stream. Note the lack of correlation between curvature vorticity and  $H$  in this case, and the relatively high visual correlation between curvature vorticity and lateral shear vorticity. We are still trying to interpret these results in order to determine why some floats (such as #21) escape from the Stream when the current is curving sharply, while others (such as #22) manage to negotiate many meanders and stay in the Stream.

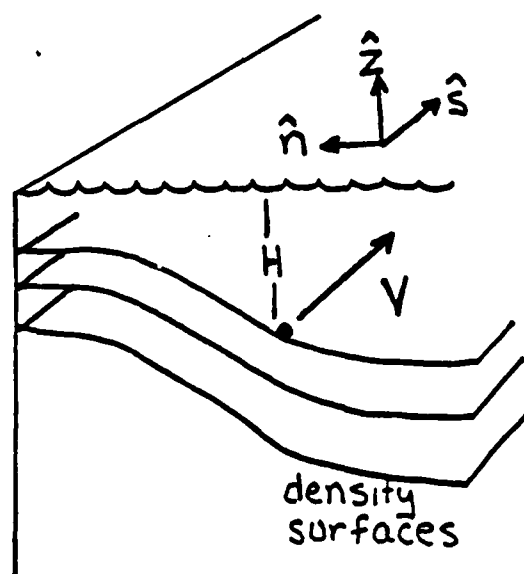
In summary, these observations are the result of the most preliminary exploration of the dynamics of Gulf Stream meanders using constant density Rafoz floats. My future research will involve refining these techniques and developing new strategies for investigating dynamic interactions in the Gulf Stream with Rafoz floats.

#### References:

- Johns, E.M., 1985: Geostrophy and potential vorticity in the Gulf Stream off Cape Hatteras. PhD Thesis, University of Rhode Island, Kingston, RI.



a.



b.

Fig. 1 (a) Two schematic diagrams illustrating how isopycnal floats move shoreward (and shoal) as they travel from meander trough to crest, and move seaward (and deepen) between crest and trough. (b) Schematic diagram showing the layer of thickness,  $H$ , between the float and the sea surface. The natural, or "stream" coordinate system is defined.

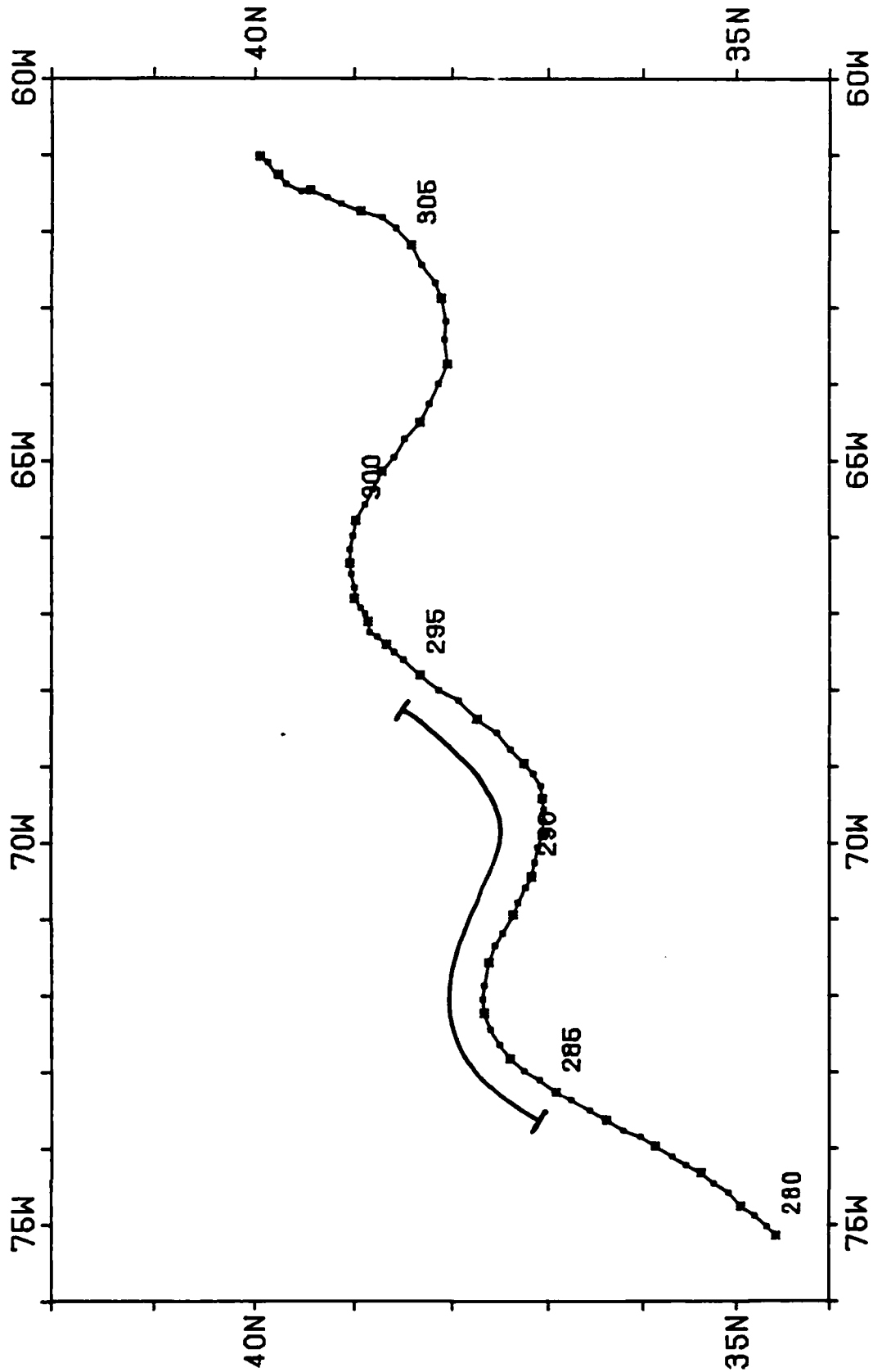


Fig. 2 Trajectory of Float #22. Large dots show daily fixes. Numbers indicate the date in year-days, 1984. Several of the terms in the potential vorticity equation are calculated for the period 285-295.

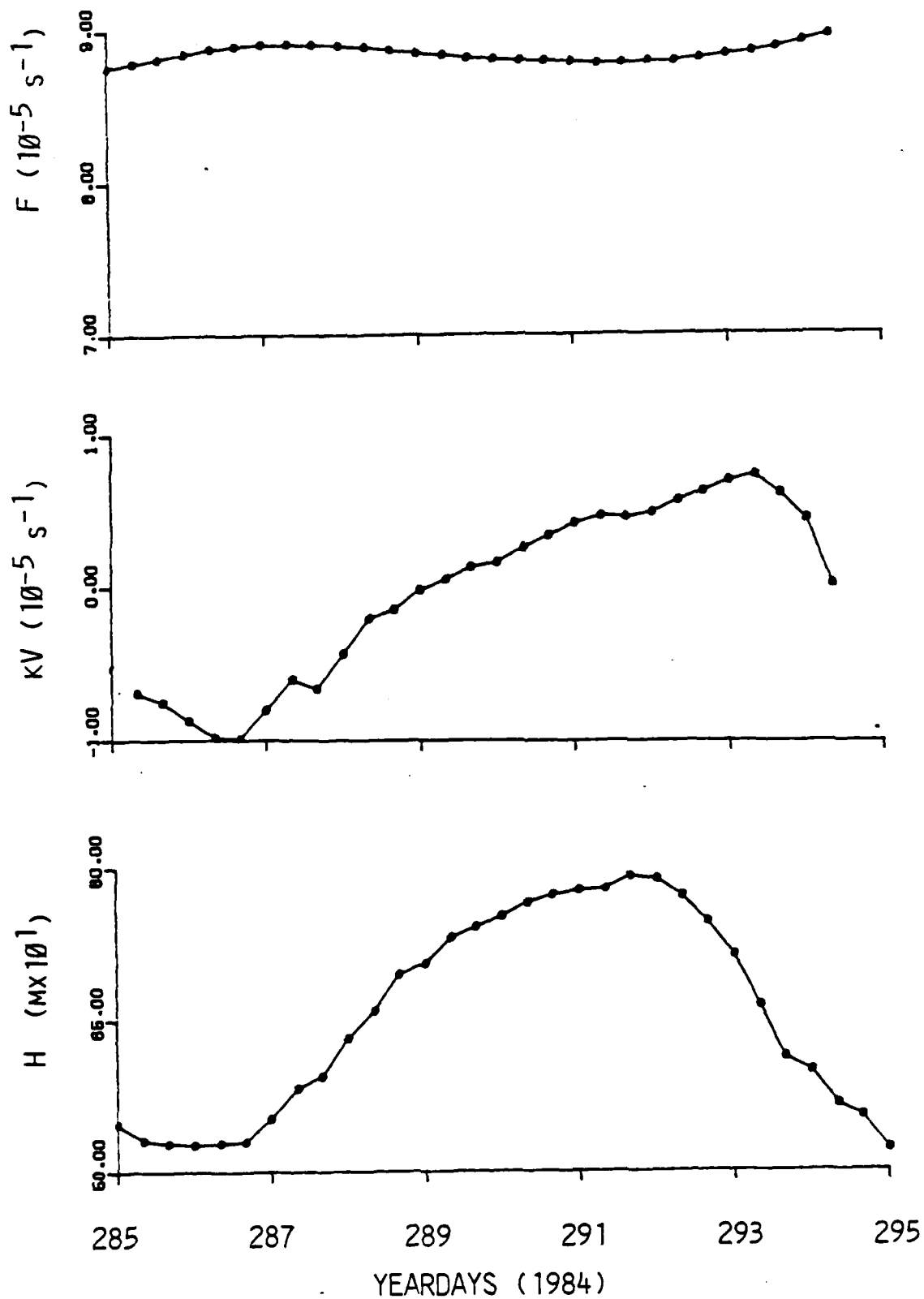


Fig. 3. Potential vorticity components for a 10-day segment of trajectory #22. The water column marked by the float maintains constant potential vorticity by stretching or squashing ( $H$ ) in response to changing curvature vorticity ( $\kappa V$ ). Planetary vorticity ( $F$ ) changes very little.

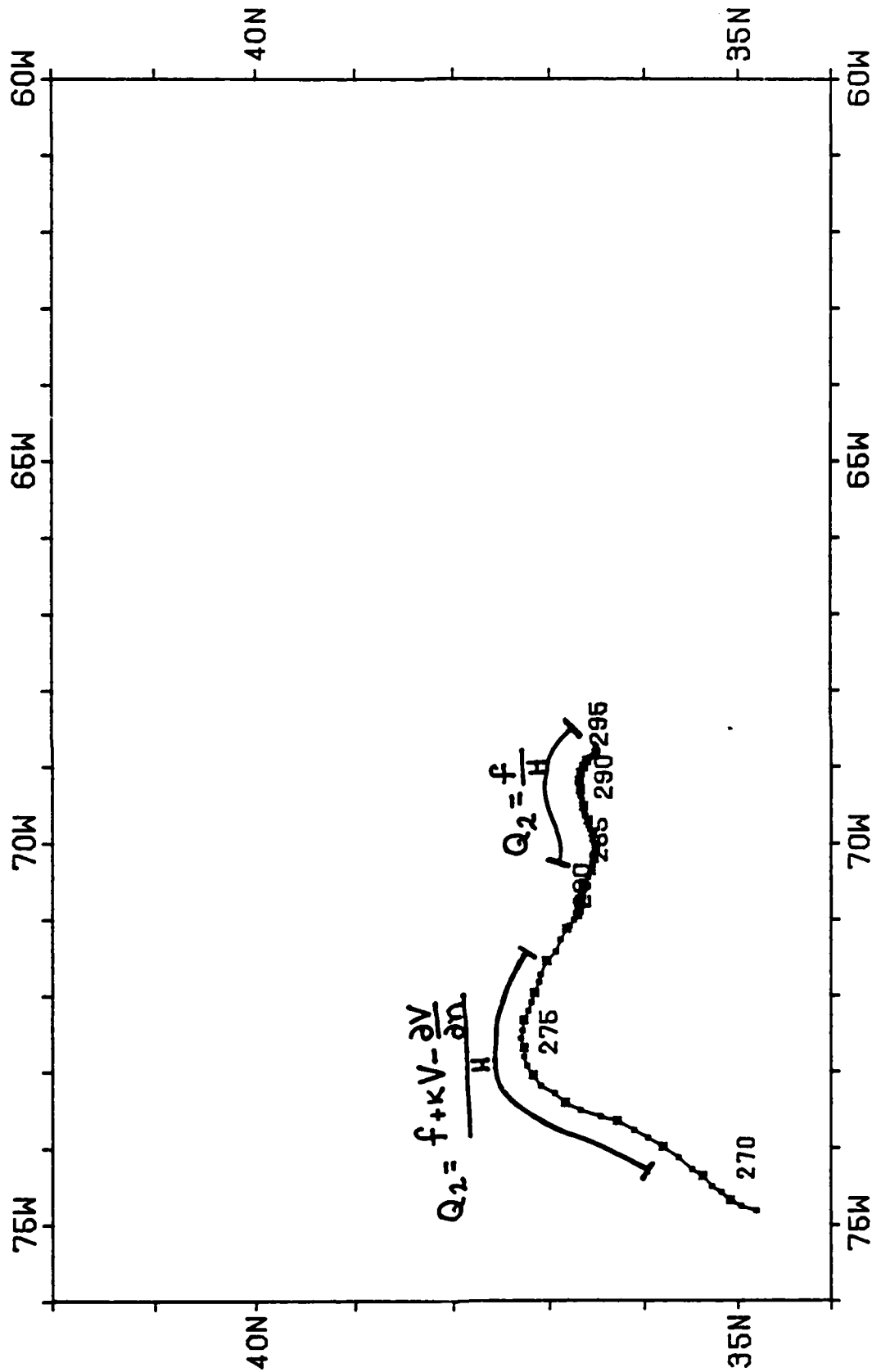


Fig. 4. Trajectory of Float #21, which escaped into the Sargasso Sea. Numbers again indicate date in year-days, 1984. See text for explanation.

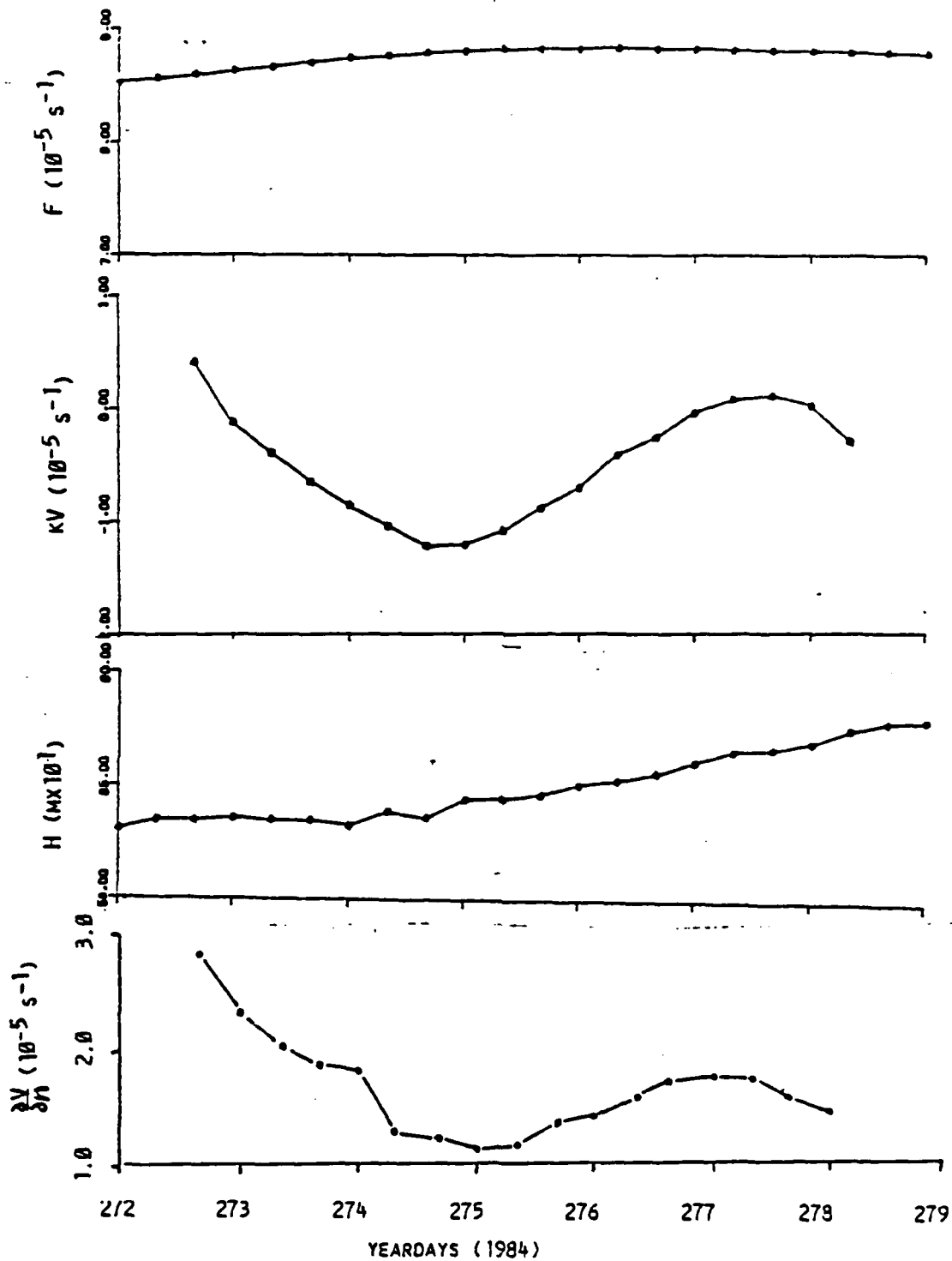


Fig. 5. Potential vorticity components for a week long segment of trajectory #21. In this case, changes in curvature vorticity are compensated for by changes in lateral shear vorticity along the float path.

SEA-SURFACE HEIGHT  
BY  
GEOSAT-A ALTIMETRY

Jack Calman  
Applied Physics Laboratory  
Johns Hopkins University  
Laurel, MD 20707

ABSTRACT

The status of the GEOSAT-A satellite, which was launched March 12, 1985, and of its altimeter data, are presented. A description of the supporting information, including orbit, geoid, atmospheric and other variables, necessary for complete exploitation of the altimeter data is included. An error budget is discussed. A simple example is given of an initial value problem, using a sea surface height displacement and the Harvard mesoscale model. Future plans are summarized.

1. INTRODUCTION

The GEOSAT-A radar altimeter satellite, built by the Applied Physics Laboratory of Johns Hopkins University, was successfully launched March 12, 1985. Its primary mission is to map accurately the global geoid; its secondary mission is to measure sea surface topography. The first phase of the primary mission will be completed in seven months.

It is our intention to use the altimeter data to describe mesoscale ocean variability in the SYNOP region, and to use the data, in conjunction with additional information (to be described below), as part of a predictive-descriptive system in collaboration with the Harvard group.



In this paper, the initial status of the satellite and its data are presented. This is followed by a definition of the altimetry problem which makes explicit all the additional information necessary to exploit the data. There follows a discussion of the orbit, geoid, atmospheric variables, etc., including identification of the sources and classification of some of the data. The problem of error budgets is addressed. A discussion of the length and time scales in the various error terms, which allows access to certain oceanographic problems even when some of the supporting data is unavailable is excluded. A simple example of an initial value problem, using the Harvard mesoscale model and a surface dynamic height field is given. Finally, future plans are summarized.

## 2. GEOSAT-A STATUS

The satellite, Fig. 1, was successfully launched from Vandenburg Air Force Base on March 12, 1985 at 8:00 PM EST. The initial orbit was good. The attitude was determined to be less than 1 degree about 90% of the time.

The altimeter is functioning and constants for the data have been determined. The tracker is operating, but its performance has not been fully evaluated at this time. The system is considered operational and data tapes are being produced routinely. The data tapes are secret, and since the initial evaluation of the data has not been completed, the tapes have not yet been released to approved users.

A summary of the status is given in Table 1.

### 3. ORBIT

The choice of orbit for GEOSAT-A was driven by its primary geodesy mission. At present, the 3-day near repeat orbit creates a grid (at midlatitudes) of size 500 km. After 27 days, the grid spacing is reduced to 60 km. After 72 days, the grid spacing is about 20 km. Finally, after 168 days, the desired 10 km grid has been sampled. A single sampling at this fine grid spacing should be complete near the end of August, 1985. The ground track pattern after 6 days, which shows the 3-day 500 km grid and the start of the 60 km grid is shown in Fig. 2.

The initial orbit parameters (height, eccentricity, inclination, period of revolution, perigee, and apogee) along with the target values, are listed in Table 2.

Daily updates of these orbit elements (which are determined using data from a worldwide tracking network) are sent to APL by NAVSPASUR (Naval Space Surveillance) for purposes of pointing the communications antenna towards the satellite. The orbit computed from these elements is accurate to about 0.6 km in the horizontal and to about 100 m in the vertical. This orbit is unclassified and is available near real time.

The precise orbit is determined by NSWC (Naval Surface Weapons Center) with a time delay of two to four weeks. It is a classified orbit and is available only for certain regions and only to approved users in cleared facilities. It is accurate to about 1.5 m in all directions and is computed at time intervals of 1 minute. APL is in the process of obtaining access to the precise orbit data.

A summary of the orbit sources and accuracies is given in Table 3.

#### 4. SATELLITE ALTIMETRY

In order to exploit fully altimeter measurements for oceanography, additional information about the orbit, geoid, and atmosphere is necessary. The geometry of the basic problem is defined in Fig. 3. When all the vectors are assumed to be parallel, the sea surface height,  $H_s$ , is given by

$$H_s = H_o - H_a - H_g \quad (1)$$

where the orbit height,  $H_o$ , and the geoid height,  $H_g$ , (both above the IUGG reference ellipsoid) must be obtained from other sources. In addition, the height of the altimeter above the sea surface,  $H_a$ , contains corrections for atmospheric effects which depend on data from other sources.

Because the time and space scales of the terms in Equation 1 can be different (and also the classification of and access to the data!), certain problems can be addressed without all of the supporting information. (The mesoscale variability studies using SEASAT data (Reference 1), for example, did not need a precise orbit or geoid). This paper assumes access to all necessary supporting data.

#### 5. THE GEOSAT-A ALTIMETER

The altimeter aboard GEOSAT, operating at a frequency of 13.5 GHz, provides a height measurement 10 times every second. These height measurements are sent down from the satellite with millimeter precision, though the accuracy degrades to about 5 cm after all the corrections have been made. The footprint of the

measurement is about 6 km in diameter, and samples are obtained about every 0.7 km along the ground track of the satellite. The estimates of significant wave height and of surface wind, which can also be obtained from the altimeter signal, are not discussed in this paper.

In order to obtain the true physical height of the altimeter above the sea surface,  $H_a$  (Equation 1), a set of corrections must be applied to the height measured by the altimeter,  $h_a$ . One group of corrections,  $\Delta h_{ins}$ , is associated with the instrumentation and the other group,  $\Delta h_{atm}$ , is associated with atmospheric effects on transmission. The latter are discussed in Section 6. Thus:

$$H_a = h_a + \Delta h_{ins} + \Delta h_{atm} \quad (2)$$

The instrumentation corrections include a calibration,  $\Delta h_c$  (which is updated on board the spacecraft), attitude/waves correction,  $\Delta h_\xi$ , a correction for fm crosstalk,  $\Delta h_f$ , an altimeter word bias correction,  $\Delta h_b$ , and a correction for center of gravity changes due to fuel consumption,  $\Delta h_{cg}$ . These instrumentation corrections are made using data which comes on the data tapes, and can be written as

$$\Delta h_{ins} = \Delta h_c + \Delta h_\xi + \Delta h_f + \Delta h_b + \Delta h_{cg} \quad (3)$$

Some characteristics of these corrections are listed in Table 4.

In addition to the instrumentation height corrections, the time tagging of the data requires some calculation. Because

of a 79 microsecond time tagging bias discovered in the SEASAT data, additional information about the time tagging error budget is being provided for GEOSAT. These time biases are associated with signal processing and transmission delays between the time the radar pulse is emitted and the time the data has a time assigned to it at the ground station UTC (Universal Time Coordinated clock). Schematic definitions of the contributions to the time error budget are shown in Fig. 4. The error budget is shown in Table 5.

## 6. ATMOSPHERE

The atmosphere influences the altimeter height estimate by its effect on the radar propagation characteristics. These effects are due to the dry troposphere,  $\Delta h_{\text{dry}}$ , the wet troposphere,  $\Delta h_{\text{wet}}$ , and to ionization,  $\Delta h_{\text{ion}}$ . The total effect, written as  $\Delta h_{\text{atm}}$  in Equation 1, can be represented as

$$\Delta h_{\text{atm}} = \Delta h_{\text{dry}} + \Delta h_{\text{wet}} + \Delta h_{\text{ion}} \quad (4)$$

In order to correct for these effects, the air temperature,  $T$ , the partial pressure of water vapor,  $e$ , surface barometric pressure,  $P$ , and electron density,  $E$  (number per surface area), must be known. (The surface barometric pressure also has a direct effect due to atmospheric loading, i.e., the "inverse barometer" effect discussed in Section 8).

Some characteristics of the models and data associated with these errors are listed in Table 6.

7. GEOID

When the primary mission is completed, GEOSAT will have significantly improved knowledge of the global geoid. At present, we have obtained four unclassified geoids from NASA (Marsh, Lerch) some of whose characteristics are listed in Table 7. Our plan is to use the Marsh and Chang (Reference 3) 5' X 5' geoid (Fig. 5) because it is the most accurate unclassified geoid available for the SYNOP region.

A formal request has been sent to the Navy to allow NORDA to send us classified sea surface height residuals using a presumably more accurate classified geoid.

8. OCEAN

After all the above corrections have been made, one is left with the sea surface height,  $H_s$  (Equation 1). This sea-surface height contains contributions from the mean sea depth (defined here as the time-independent ocean depth),  $h_m$ , the response to atmospheric pressure (the "inverse barometer" effect),  $h_b$ , tides,  $h_t$ , waves,  $h_w$ , and time dependent currents (defined here as the dynamic height),  $h_d$ , and can be written as

$$H_s = h_m + h_b + h_t + h_w + h_d \quad (5)$$

where it is the dynamic height,  $h_d$ , that is wanted for mesoscale studies in the SYNOP program.

The model for the "inverse barometer" effect is the same one that was used for SEASAT. It requires atmospheric

surface pressure which will be obtained (along with other atmospheric variables discussed in Section 6) from FNOC (Fleet Numerical Oceanography Center). The tidal model is by Schwiderski (Reference 2) and was obtained from NSWC.

The characteristics and sources for the terms in Equation 4 are listed in Table 8.

9.        NUMERICAL MODEL

One of the goals of APL's involvement in the SYNOP program is to provide and assimilate, in near real time, altimeter sea surface height data into numerical mesoscale circulation models (Reference 4). We are at present working with the Harvard group, using their stream function - vorticity model (Reference 5). A simple initial value problem, using a sea surface height field corresponding to a zonal jet has been run at APL. The result for a 30 day two layer run is shown in Fig. 6. We will be running more realistic cases using GEOSAT data in an assimilative scheme as soon as the data is available and techniques are fully developed.

10.       SUMMARY AND FUTURE PLANS

A summary of the corrections used to compute sea surface height, as well as the nature and sources of supporting information, is given in Table 9.

It is our intention to use the altimeter data in several investigations. These include descriptions of mesoscale variability, applications to forecasting acoustic propagation properties, and large scale circulation studies involving a joint study of sea surface topography, hydrography, and geodesy.

REFERENCES

1. Cheney, RE; Marsh, JG, 1983. Global mesoscale Variability from Collinear Tracks of SEASAT Data. JGR, V88, C7, P4343-4354.
2. Schwiderski, EW, 1980. Ocean Tides, Mar Geod, V3, P161-219.
3. Marsh, JG; Chang, ES, 1978. 5' Detailed Gravimetric Geoid in the Northwestern Atlantic Ocean, Mar Geod, V1, N3, P253-261.
4. Robinson, AR; Leslie, WG, 1985. Estimation and Prediction of Oceanic Eddy Fields. Prog Oceanog, V14, P485-510.
5. Miller, RN; Robinson, AR; Haidvogel, DB, 1983. A Baroclinic Quasigeostrophic Open Ocean Model. J Comp Phys, V50, N1, P38-70.



LIST OF TABLES

1. Summary of GEOSAT-A Status as of April 16, 1985.
2. Initial Orbit Parameters for GEOSAT.
3. Sources and Accuracy of Satellite Orbit Data.
4. Altimeter Instrumentation Corrections.
5. Error Budget for Time Tagging Data.
6. Atmospheric Errors and Models.
7. Geoid Characteristics.
8. Contributions to Sea Surface Height.
9. Summary of Corrections and Supporting Data.

II.153

Table 1

SUMMARY OF GEOSAT-A STATUS

April 16, 1985

\*Altimeter functioning, data is being sent down routinely

\*Good orbit achieved

\*Satellite attitude less than 1 degree

\*Ground stations manned and operational

\*Initial data still being evaluated

\*Data classified secret

\*Data not yet released to approved Navy users

Table 2

## GEOSAT ORBIT PARAMETERS

Launched March 12, 1985

Symbol	Name	Present	Target
a	Mean height	788.5 km	800.0 km
e	Eccentricity	0.003158	0.0015
i	Inclination	108.065 deg	108.0 deg
per	Perigee	755 km	
apo	Apogee	842 km	
T	Period	6039.998 s (14.3 rev/day)	6043.855 s

Ground track spacing at midlatitude (km)	Time (days)
500	3
60	24
20	72
10	168

Table 3  
ORBIT SOURCES AND ACCURACY

SOURCE	ACCURACY	TIME DELAY	CLASSIFICATION
NAVSPASUR	x,y = 0.6 km z = 100 m	24 hr	Unclassified
NSWC	x,y,z = 1.5 m	2-4 wks	Secret

Table 4

## ALTIMETER INSTRUMENT CORRECTIONS

$$\Delta h_{ins} = \Delta h_f + \Delta h_{\xi} + \Delta h_c + \Delta h_b + \Delta h_{cg}$$

TERM	MAGNITUDE	RESOLUTION	SOURCE
$\Delta h_f$	1 m	1 mm	fm cross talk
$\Delta h_{\xi}$	10 m	1 mm	attitude, waves
$\Delta h_c$	1 m	1 mm	calibration
$\Delta h_b$	1 m	1 mm	word bias
$\Delta h_{cg}$	10 m	1 mm	center of gravity shift due to fuel consumption

Table 5  
ERROR BUDGET FOR TIME TAGGING DATA

r/t	DESCRIPTION	NOMINAL VALUE	DETERMINED BY	MAX. ERROR	COMMENTS
r <sub>1</sub>	TRANSMISSION TIME DELAY: ALT. ANT. TO SURFACE ( $H_1/c$ )	~2.7 msec.	ALT. MEAS.	$\pm 1 \mu\text{sec.}^1$	NOMINAL VALUE ASSUMES 800 KM ORBIT
r <sub>2</sub>	TRANSMISSION TIME DELAY: SURFACE TO ALT. ANT. ( $H_2/c$ )	~2.7 msec.	ALT. MEAS.	$\pm 1 \mu\text{sec.}$	$\frac{H_1 + H_2}{2}$ = ALTIMETER HEIGHT WORD = H
r <sub>3</sub>	ALTIMETER SIGNAL PROC. DELAY	$(79.38 - \frac{H_1 + H_2}{c})$ msec.	ANALYSIS*	$\pm 10 \mu\text{sec.}$	*DETERMINED BY SEASAT DATA ANALYSIS
r <sub>4</sub>	S/C TLM SYSTEM DELAY	TBS	CALIBRATION	$\pm 9 \mu\text{sec.}$	SYNCH. DATA WINDOW = 9 $\mu\text{sec.}$
r <sub>5</sub>	S/C TX DELAY	$< 1 \mu\text{sec.}^2$	CALIBRATION	$\pm 1 \mu\text{sec.}$	INCLUDES S/C ANT. DELAYS
r <sub>6</sub>	SLANT RANGE TRANSMISSION TIME DELAY (R/c)	~ 2.7 msec @ C.A. <sup>3</sup>	CALCULATION	$\pm 30 \mu\text{sec.}$	CALC. IN SEL BASED ON NAVSPASUR ORBIT
r <sub>7</sub>	GND. STATION RX DELAY	$< 1 \mu\text{sec.}^2$	CALIBRATION	$\pm 1 \mu\text{sec.}$	INCLUDES G.S. ANT. DELAY
r <sub>8</sub>	GND. STATION DIGITAL DELAY	TBS	CALIBRATION	$\pm 1 \mu\text{sec.}$	BIT SYNC DELAYS, ETC.
t <sub>UTC</sub>	UTC TIME CODE (1 $\mu\text{sec.}$ precision)	UTC TIME	CALIBRATION	$\pm 3 \mu\text{sec.}$	CALIB. TO APL TIME STD.

TOTAL MAX. TIME TAG ERROR:  $\pm 56 \mu\text{sec.}$

- NOTES: 1. NOT INCLUDED IN TOTAL MAX. ERROR  
2. ESTIMATE  
3. POINT OF CLOSEST APPROACH (C.A.) @ 800 KM

$$\text{CORRECTED TIME TAG} = t_0 = t_{\text{UTC}} - \sum_{n=1}^8 r_n$$

Table 6

## CONTRIBUTIONS TO SEA SURFACE HEIGHT

$$H_s = h_m + h_b + h_t + h_w + h_d$$

TERM	NAME	SOURCE	MODEL	ACCURACY	MAGNITUDE
$h_m$	mean	GEOSAT	time indep		5 km
$h_b$	barom	FNOC	Seasat	1 cm	10 cm
$h_t$	tide	NSWC	Schwiderski	10 cm	1 m
$h_w$	waves	GEOSAT	lab calib	2%	10 cm?
$h_d$	dynam	GEOSAT	time dep	2-5 cm	30 cm

Table 7

## ATMOSPHERIC CORRECTIONS

$$\Delta h_{\text{atm}} = \Delta h_{\text{dry}} + \Delta h_{\text{wet}} + \Delta h_{\text{ion}}$$

TERM	NAME	SOURCE	MODEL	ACCURACY	MAGNITUDE
$\Delta h_{\text{dry}}$	dry trop	FNOC, P	Seasat <sup>(2)</sup>	5 cm ?	2 m
$\Delta h_{\text{wet}}$	wet trop	FNOC, e, T	Seasat <sup>(1)</sup>	5 cm ?	10-20 cm
$\Delta h_{\text{ion}}$	ion	FNOC, E	Seasat <sup>(3)</sup>	5 % ?	10-20 cm

## key:

P = surface barometric air pressure

e = partial pressure of water vapor

T = surface air temperature

E = electron content (number per surface area)

$$(1) \quad \Delta h_{\text{wet}} = C_1 (C_2 + C_3/T)e$$

$$(2) \quad \Delta h_{\text{dry}} = C_1 (1 + C_3 \cos 2\phi)P, \quad (\phi = \text{latit})$$

$$(3) \quad \Delta h_{\text{ion}} = C_4 E/f^2, \quad (f = \text{transm freq})$$



AD-A162 506

PROCEEDINGS OF THE GULF STREAM WORKSHOP HELD AT WEST  
GREENWICH RHODE ISLA (U) RHODE ISLAND UNIV KINGSTON  
GRADUATE SCHOOL OF OCEANOGRAPHY D R WATTS APR 85

377

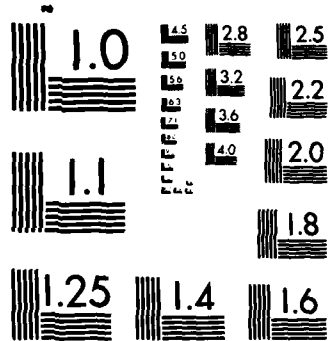
UNCLASSIFIED

N00014-85-G-0322

F/G 8/3

NL





MICROCOPY RESOLUTION TEST CHART  
NATIONAL BUREAU OF STANDARDS-1963-A

Table 8

## GEOID CHARACTERISTICS

NAME	RESOLUTION	ACCURACY	REGION	SOURCE	CLASSIFICATION
M5X5	5 km	1.2 m	SYNOP	NASA (Marsh)	Unclassified
PGSS4			global	NASA (Marsh)	Unclassified
GEM10B	1110 km	1 m	global	NASA (Lerch)	Unclassified
GEML2	2000 km		global	NASA (Lerch)	Unclassified
			global	NORDA (Mitchell)	Secret

Table 9

## SUMMARY OF CORRECTIONS AND SUPPORTING DATA

$$H_s = H_o - H_a - H_g$$

## CORRECTIONS

$$H_s = h_m + h_b + h_t + h_w + h_d$$

$$H_a = h_a + \Delta h_{ins} + \Delta h_{atm}$$

$$\Delta h_{ins} = \Delta h_f + \Delta h_\xi + \Delta h_c + \Delta h_b + \Delta h_{cg}$$

$$\Delta h_{atm} = \Delta h_{dry} + \Delta h_{wet} + \Delta h_{ion}$$

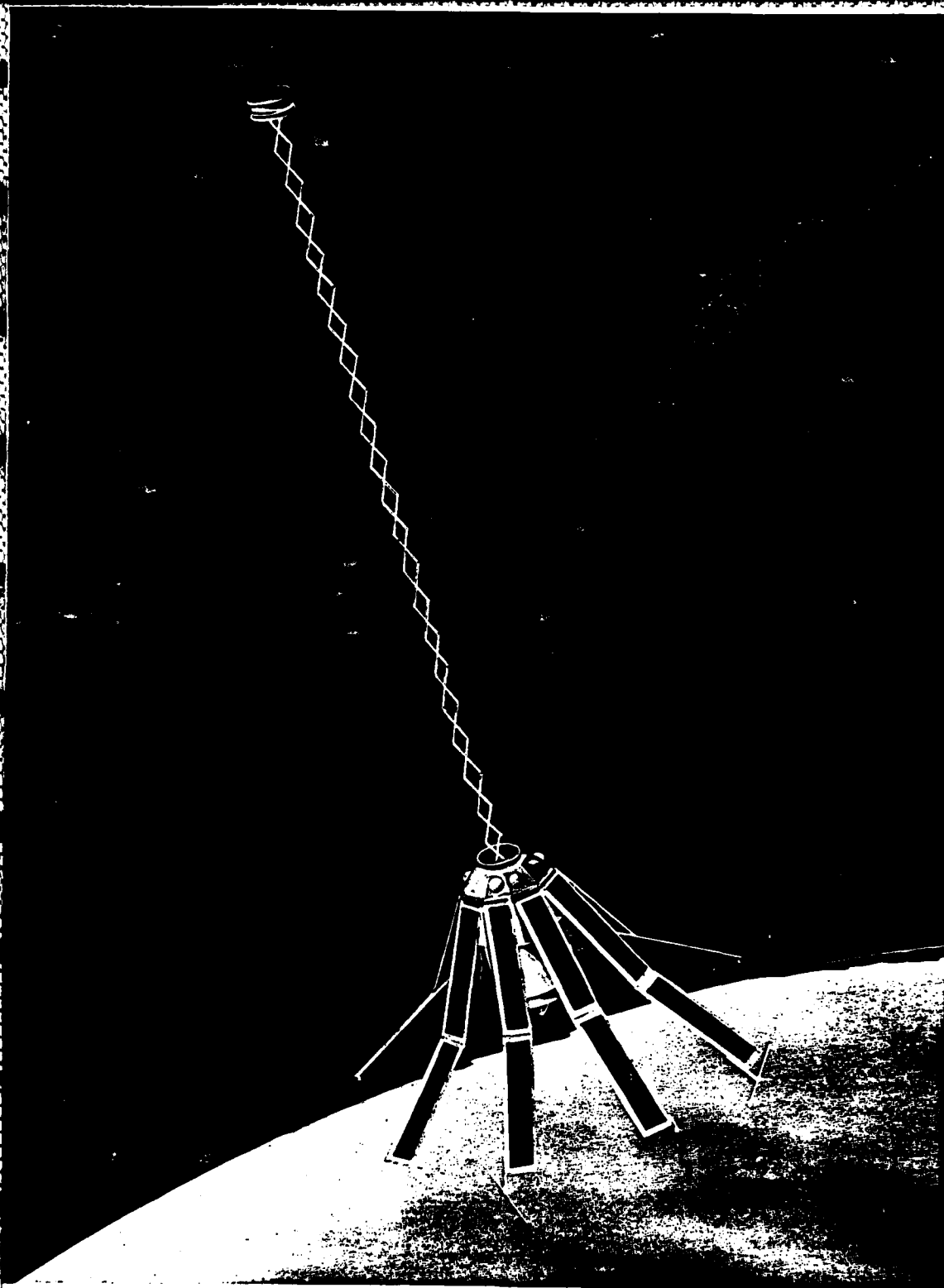
## SUPPORTING DATA

TERM	REQUIRED	SOURCE	CLASSIFICATION
$\Delta h_{atm}$	T , P, e, E	FNOC	Unclassified
$h_t$		NSWC (Schwiderski)	Unclassified
$h_b$	P	FNOC	Unclassified
$H_g$		NASA (Marsh) NORDA	Unclassified Secret
$H_o$		NAVSPASUR NSWC	Unclassified Secret

LIST OF FIGURES

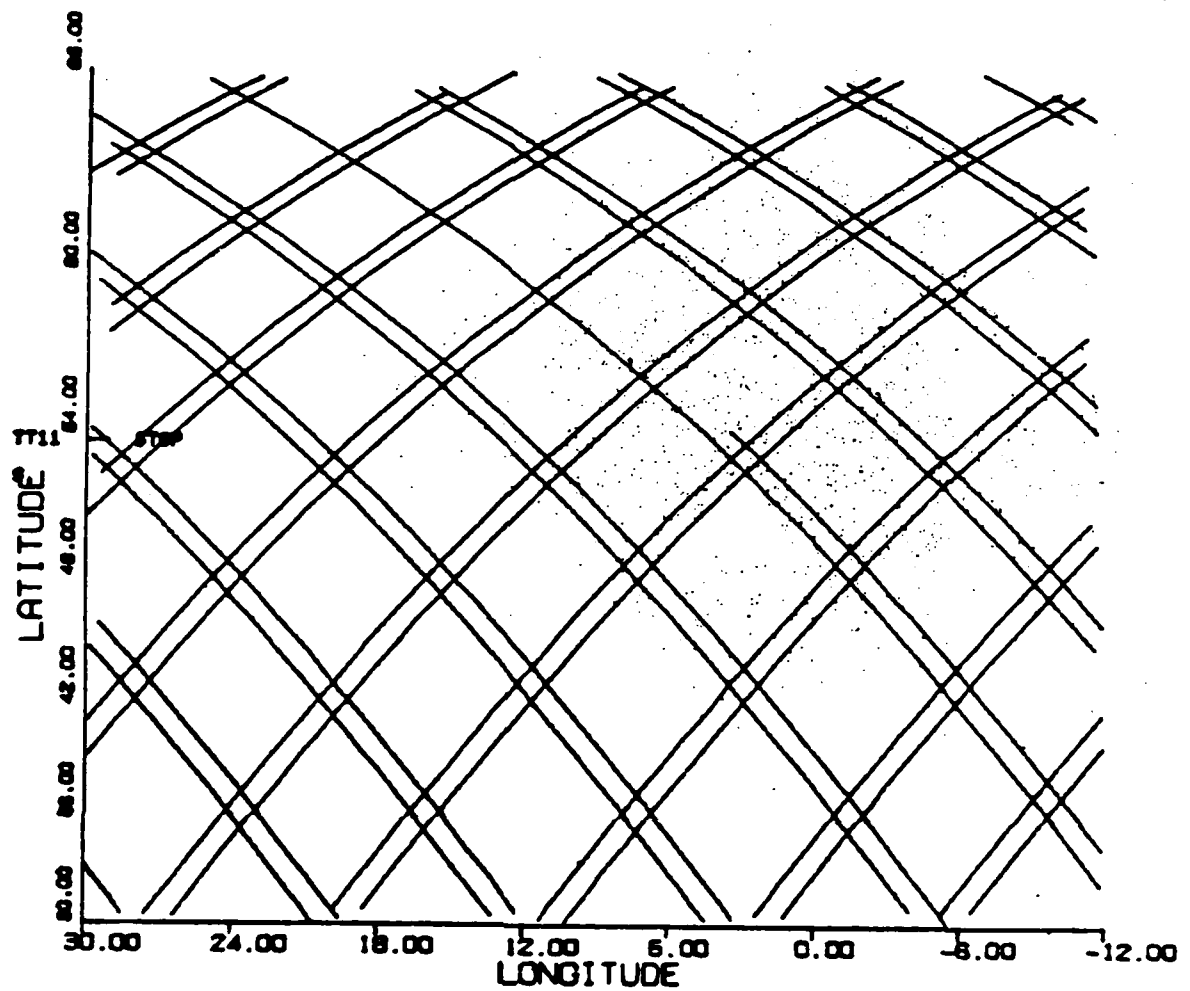
1. The GEOSAT-A Spacecraft in Orbit (Artist's Conception).
2. Ground track accumulation after six days. The larger Squares are about 500 km on a side and are laid down in 3 Days. The smaller squares are about 60 km on a side. after 72 days the grid size is about 20 km.
3. Definition sketch of satellite altimetry geometry.
4. Definition sketch of time tagging corrections.
5. The 5' X 5' gravimetric geoid (NASA/Jim Marsh).
6. Stream function and vorticity fields of a) upper and b) lower layers after 30 days. See text.

II.16

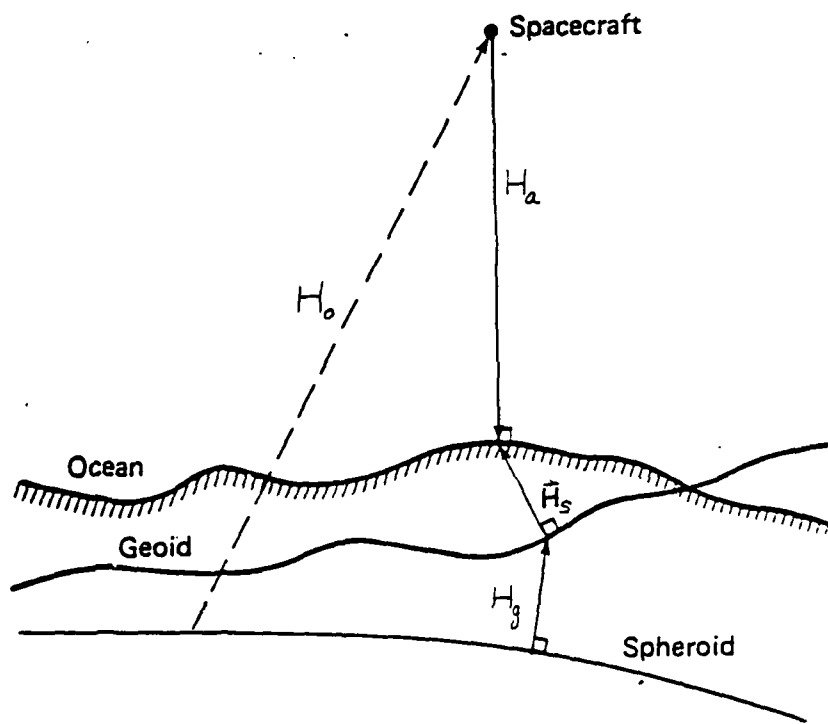


A PAINTING OF THE GEOSAT-A SATELLITE, EXECUTED BY APL ARTIST ROGER SIMMONS

GEOSAT-A RADAR ALTIMETER SPACECRAFT

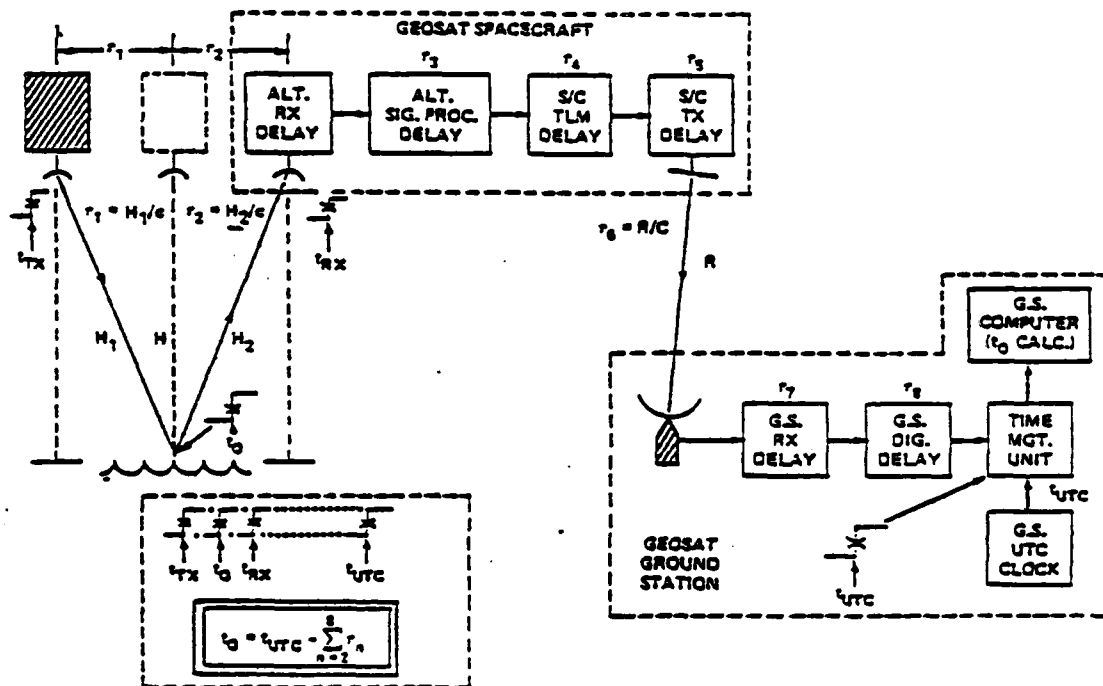


2. Ground track accumulation after six days. The larger Squares are about 500 km on a side and are laid down in 3 Days. The smaller squares are about 60 km on a side. after 72 days the grid size is about 20 km.



3. Definition sketch of satellite altimetry geometry.





#### 4. Definition sketch of time tagging corrections.

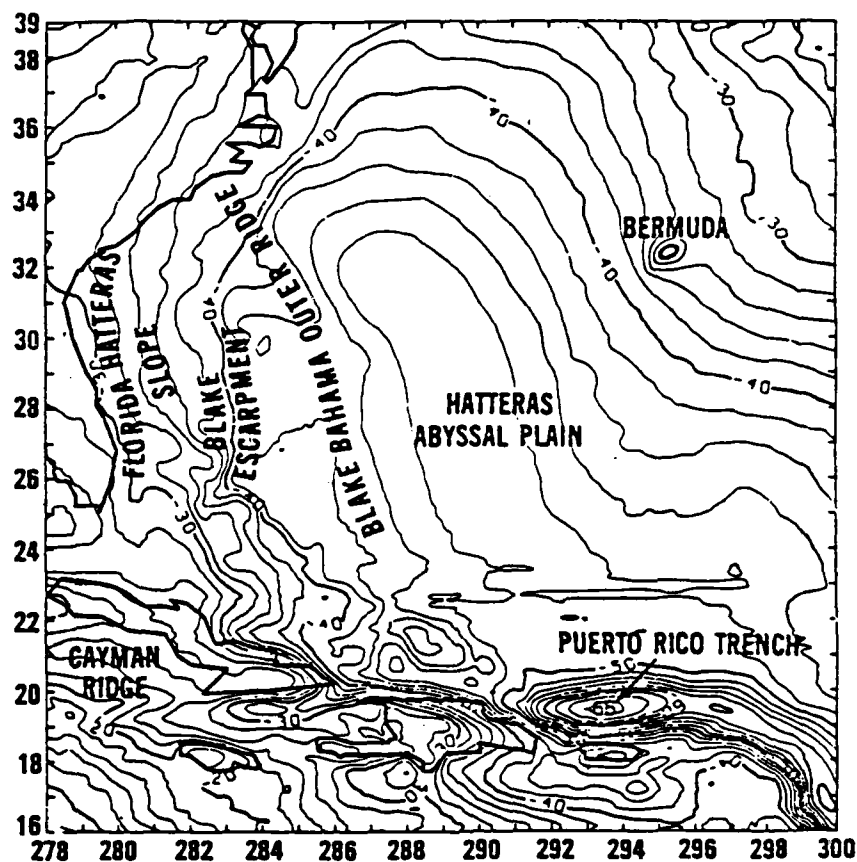
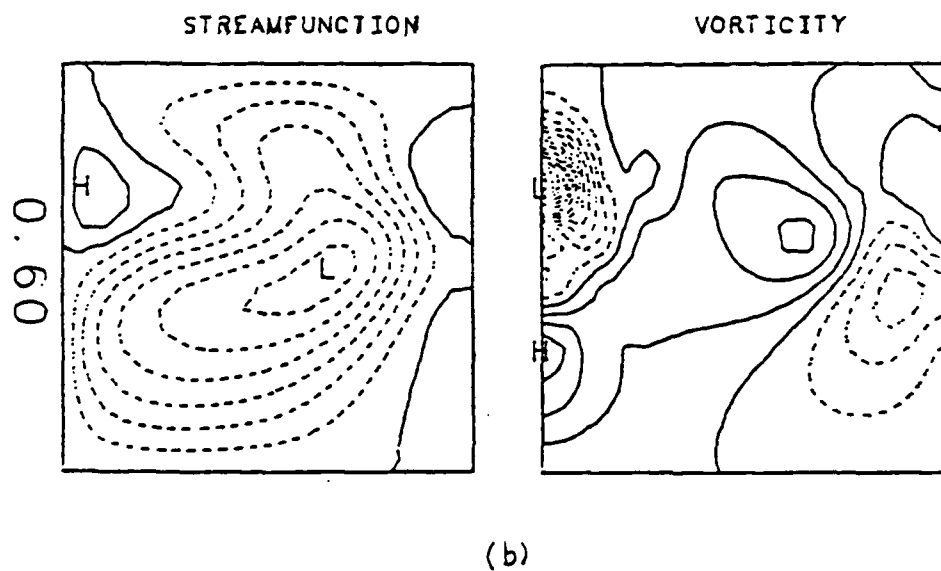
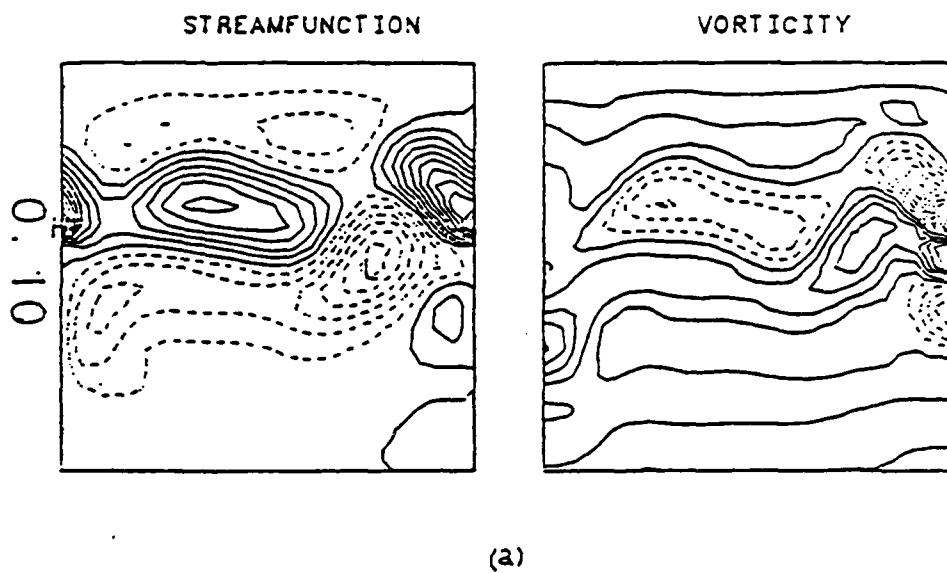


Figure 1. NASA/Goddard Space Flight Center detailed gravimetric geoid for the GEOS-C altimeter calibration area based upon a combination of 5' x 5', 15' x 15', and 1° x 1° surface gravity data and the GSFC GEM-8 Earth model. Contour interval = 2 m.

5. The 5' X 5' gravimetric geoid (NASA/Jim Marsh).



6. Stream function and vorticity fields of a) upper and b) lower layers after 30 days. See text.

The structure of the Gulf Stream  
as derived from an EOF analysis

Everett F. Carter  
University of Rhode Island

In this note we will consider the shape of the Gulf Stream axis as measured from satellites and RAFOS floats, using a complex empirical orthogonal function (EOF) analysis. The stream is variable on several spatial and temporal scales (from order  $10^1$  km to  $10^3$  km, and from days to years). Any statistical analysis of the Gulf Stream is complicated by several factors including: (a) the Gulf Stream is inhomogeneous, (b) it is occasionally multiply valued, and (c) it is possibly not stationary, or at least it contains time scales of several years (see figures 1 to 3). EOFs are attractive for an analysis scheme because they are efficient and can separate out the different scales readily, they can also be applied to multiply valued and inhomogeneous fields. It should be noted that for this analysis, an implicit assumption of stationarity has been made.

Since the use of complex EOFs is not common (see Legler, 1983, for an example of their use in meteorology), they will be explained in some detail. The equations are basically the same as in traditional EOF analysis (e.g. Lorenz, 1956) except that one must take care to keep track

of where complex conjugates occur in the equations. In the matrix operations involved, the Hermitian (complex conjugate transpose) is used where the transpose previously occurred.

First we define:

$$W_j = X_j + iY_j \quad (1)$$

where  $X$  is the longitude of the Gulf Stream axis, and  $Y$  is the latitude. Therefore the modes will be an orthogonal expansion of  $W$ , i.e. the 2-dimensional shape of the stream axis. Then the matrix

$$A_{ij} = \langle W_i W_j^* \rangle \quad (2)$$

is formed.  $\langle \rangle$  is the expectation operator which is applied over the different observations of the axis.  $*$  denotes the complex conjugate.

The observations used in this analysis are of two kinds: (a) RAFOS float tracks for and early subset of 5 floats, and (b) satellite observations of the position of the north edge of the Gulf Stream (Cornillon, 1985). The independent variable, the  $j$  for  $W$  in (1), for the floats is the time relative to the initial time. It is a time series of an observation every 8 hours. For the satellites the independent variable was chosen to be path length along the axis, relative to the initial location. In both cases the

position data was normalized so that the initial point is (1 km, 1 km) with the rest of the track being the corresponding X,Y km distances along the track.

Now the eigenvalues  $\lambda_i$ , and eigenvectors  $E_i$  of the matrix  $A$  are computed. Note that the structure of  $A$  is such that it is symmetric and has complex elements everywhere except along the diagonal, which has real elements. This matrix therefore has complex eigenvectors, but its eigenvalues are real.

For a given observation of an axis, the complex mode coefficients,  $C$ , are given by:

$$C_k = E_k^H W \quad (3)$$

for mode  $k$ .  $E_k^H$  is the Hermitian of the  $k$ -th eigenvector. Conversely, a given axis can be reconstructed from the modes by the equation:

$$W = \sum_{k=1}^n E_k C_k \quad (4)$$

where  $n$  is the number of eigenvalues of  $A$ . If the eigenvectors are sorted in order of decreasing eigenvalue then we can realize one of the important features of EOFs. Since a given eigenvalue represents the amount of variance of the original data that a given eigenvector explains (in the ensemble), we can approximate  $W$  by using a small  $n$

(instead of all the eigenvalues) in (4) and be assured that the incremental addition to  $W$  due to increasing  $n$ , gets smaller each time.

The actual modes for the RAFOS floats are shown in figure 4. Mode 1 represents a mean shape of the axis. It is not necessarily THE mean axis since for any given track the complex coefficient has the effect of stretch (or squeezing) and rotating the shape modes. Mode 2 which represents 1.4% of the ensemble seems to govern the larger scale meandering of the track. Modes 3 and 4 represent an average of 0.5% to 0.2% of the variance each. These two modes are the important modes for the small scale looping and tight meandering of the axis. Mode 5 is very small and is essentially the noise. The amplitude distribution of the modes allows a plot of the mode "spectra" for comparison from float to float. Figure 5 shows example mode "spectra" plots. It shows clearly that individually the meander mode (mode 2) may not necessarily dominate over the looping modes (modes 3 and 4). This variation of the mode "spectra" may provide a basis for the statistical prediction of the axis shape (see below).

The basic results of the EOF analysis of the satellite IR data is similar. Mode 1 is the mean (representing 71.8% of the ensemble variance). Modes 2 and 3 are the meandering (at 11.8% and 7.3%). And the small scale looping is in modes 4 through 7 (at 2.7%, 2.2%, 1.2%, and 0.8% respectively). An important result is that the modes change from year to year

(see figure 6).

The mode amplitudes vary with time; figure 7 shows the mode coefficient amplitudes versus time for the first 15 modes of the satellite observations. The predictability of these changes has not been established at the present time, this question is currently being investigated by the author. Provided the temporal and cross-mode correlations are significant then some predictability is possible. The prediction method that is most suggestive is a multichannel Wiener prediction filter (Robinson, 1967). This technique has been successfully utilized in predicting ocean currents in the California Current region during the OPTOMA experiment (Carter and Robinson, 1985). Because the high modes (the ones with small eigenvalues) can exceed the amplitude of a low mode (one with a larger eigenvalue) during a single realization, the prediction problem may require retaining a relatively large number of EOF modes.

In summary, our preliminary complex EOF analysis for both the RAFOS floats and the satellite IR data gives three groups of significant modes: one mode that represents the mean structure of the axis, a group that describe the large scale meandering, and a third group that describe the smaller looping structures. The variations in the first mode correspond to rotation and expansion of the mean shape. Within the next two groups the second represents the more significant modes in the mean but individually any mode may



be dominant. This means that. (again with the second and third groups) a higher mode can have a larger amplitude than a low one for a particular observation. Finally the predictability of the modes have not as yet been established, and is a concern of current research.

#### References

- Carter, E.F., and A.R. Robinson, 1985; A multiple-scale Objective Analysis method, manuscript in preparation
- Cornillon, P.C., 1985; The Effect of the New England Seamounts on Gulf Stream Meandering, submitted to Science
- Legler, D.M., 1983; Empirical Orthogonal Function Analysis of Wind Vectors over the Tropical Pacific Region, Bull. Amer. Meteorol. Soc., V. 64, No. 3, p 234-241
- Lorenz, E.N., 1956; Empirical Orthogonal Functions and Statistical Weather Prediction, Statistical Forecasting Project Scientific Report No. 1, Dept. of Meteorology, M.I.T., Cambridge, Mass.
- Robinson, E.A., 1967; Multi-channel Time Series Analysis with Digital Computer Programs, Holden-Day, San Francisco, 298 pages

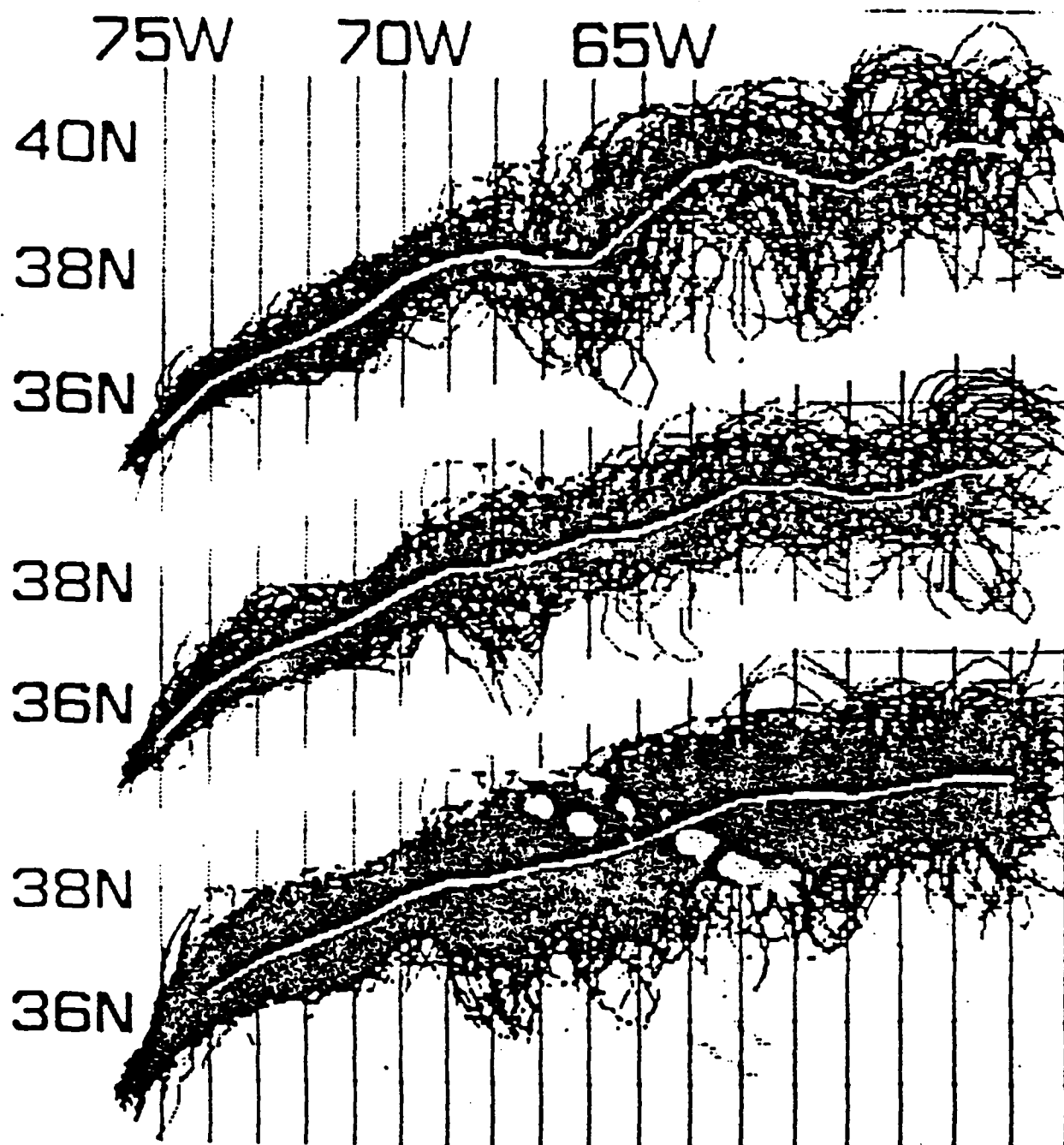


Figure 1: Composite Gulf Stream north edge axes for April to December 1982 (top), for the year 1983 (center), and from April 1982 to Sept 1984 (bottom). The mean axis is shown white for each composite. (From Cornillon, 1985).

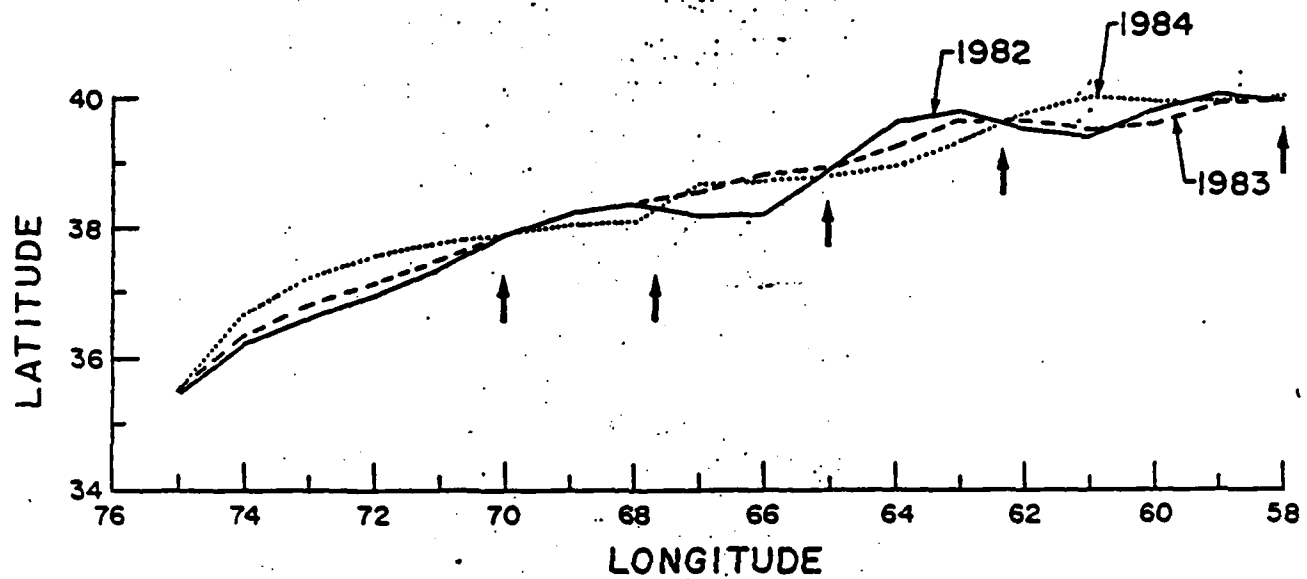
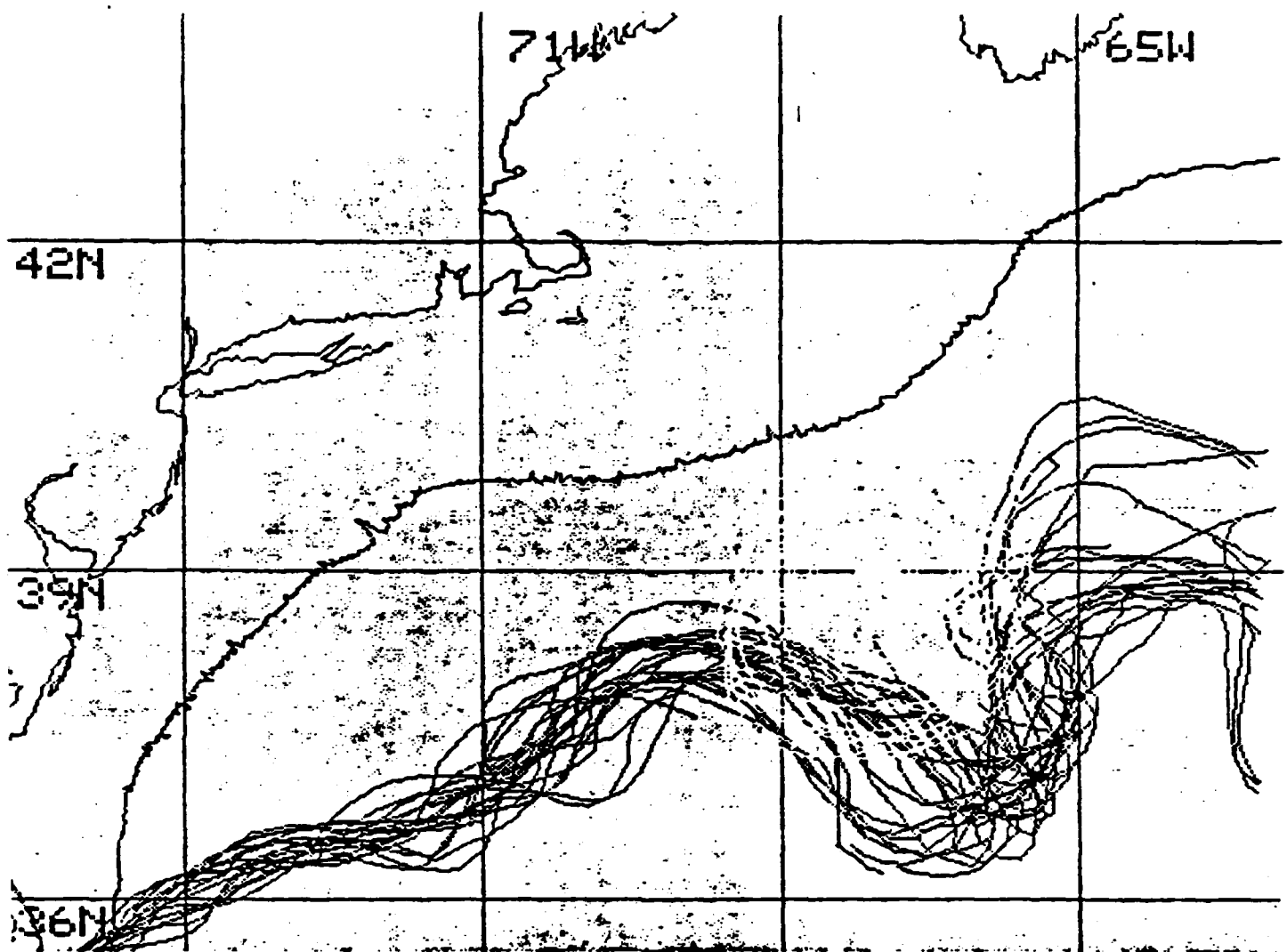


Figure 2: The mean annual Gulf Stream North edge paths for 1982 to 1984. The heavy arrows mark nodal points of the mean paths. (From Cornillon, 1985).



4/12/82 - 5/27/82. North Wall

Figure 3: The Gulf Stream North edge derived from satellite IR for the period 12 April to 27 May 1982, showing relatively slow evolution of the larger scale of the path. (From Cornillon, 1985).

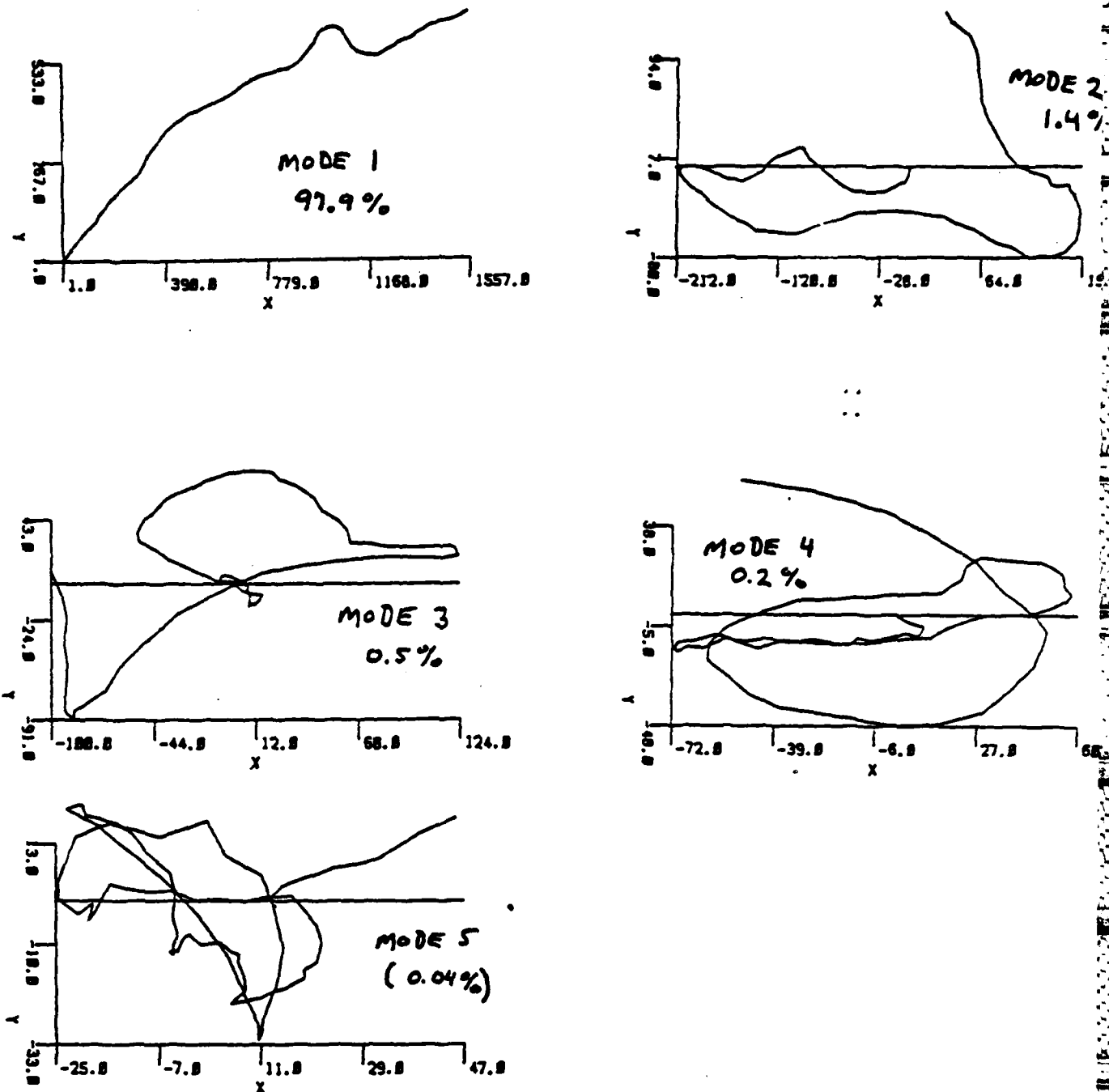


Figure 4: The complex EOF mode shapes derived from 5 early RAFOS floats. For each mode 1 through 5 the ensemble variance explained is given. Individually mode 1 (which describes the mean shape) accounts for 96% upward of the variance, mode 2 (which is the large scale meandering) accounts for as much as 3% to much less than 1%, for modes 3 and 4 (which describes the small looping structures) the variance is sometimes larger than mode 2. Mode 5 is always small, it is essentially the noise and is not statistically significant. These modes were arbitrarily plotted such that the complex coefficient,  $C$ , squared equaled the mode eigenvalue, this allows inferring the typical physical scales of each mode. (X is km east-west, and Y is km north-south).

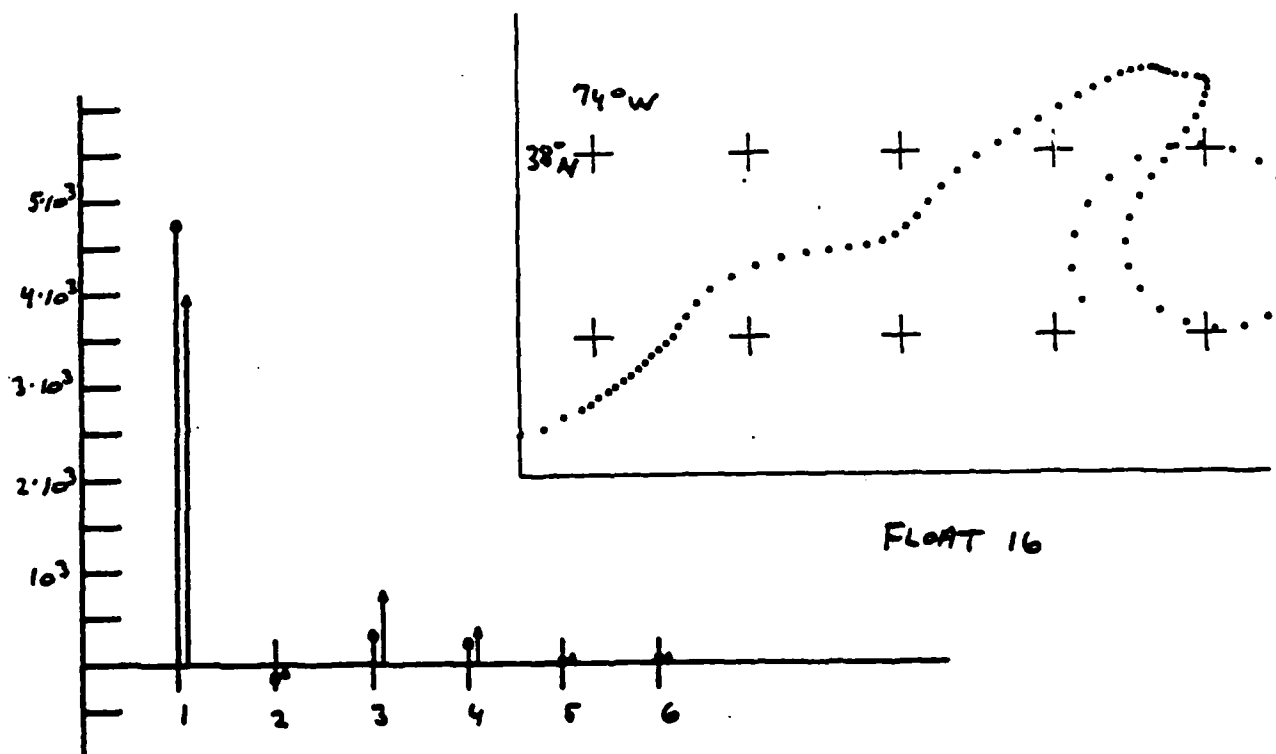
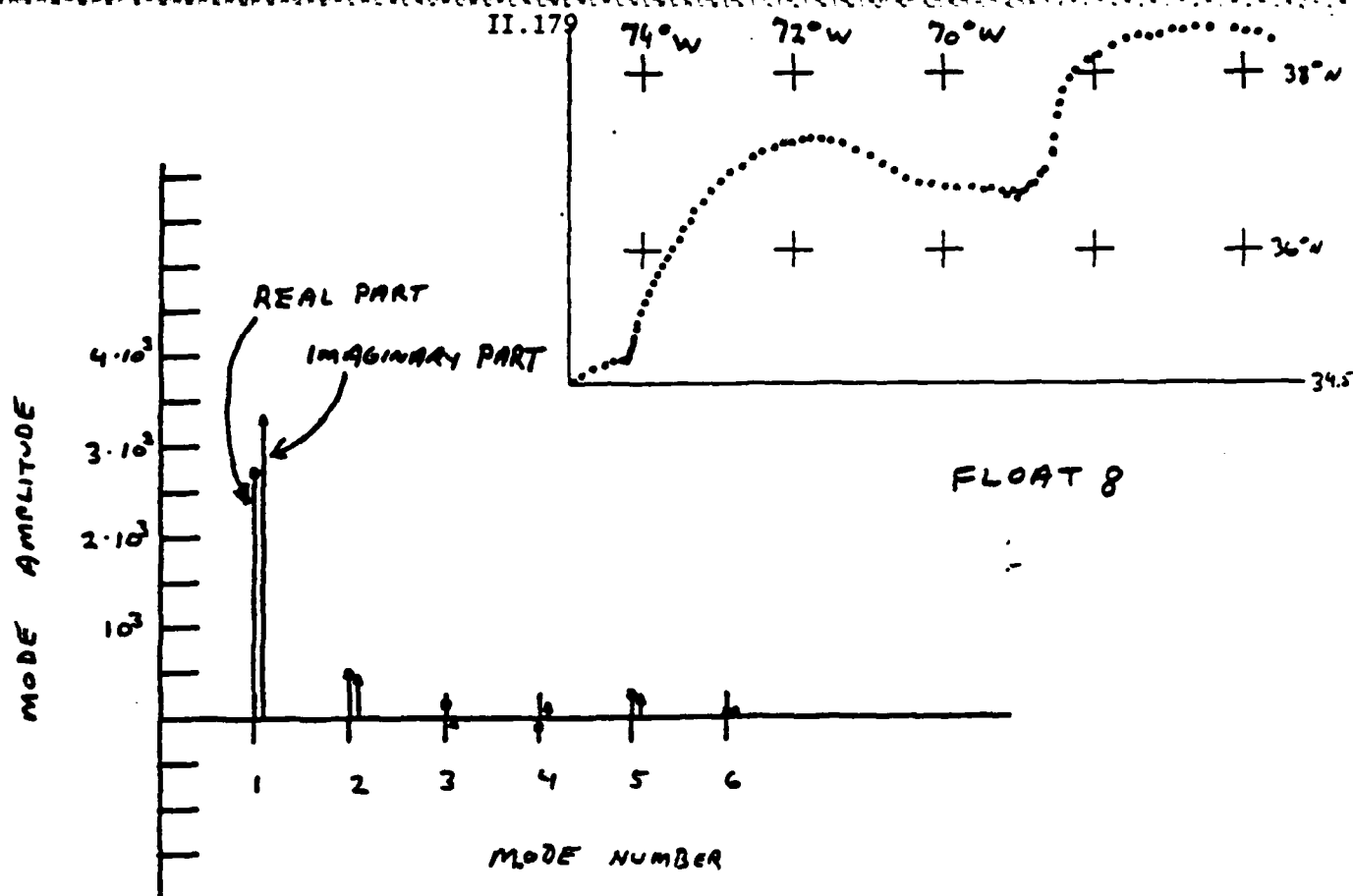


Figure 5: The EOF mode "spectra" for two RAFOS floats, showing the amplitude of each mode versus mode number for each individual track. The actual track for each spectrum is shown as well.

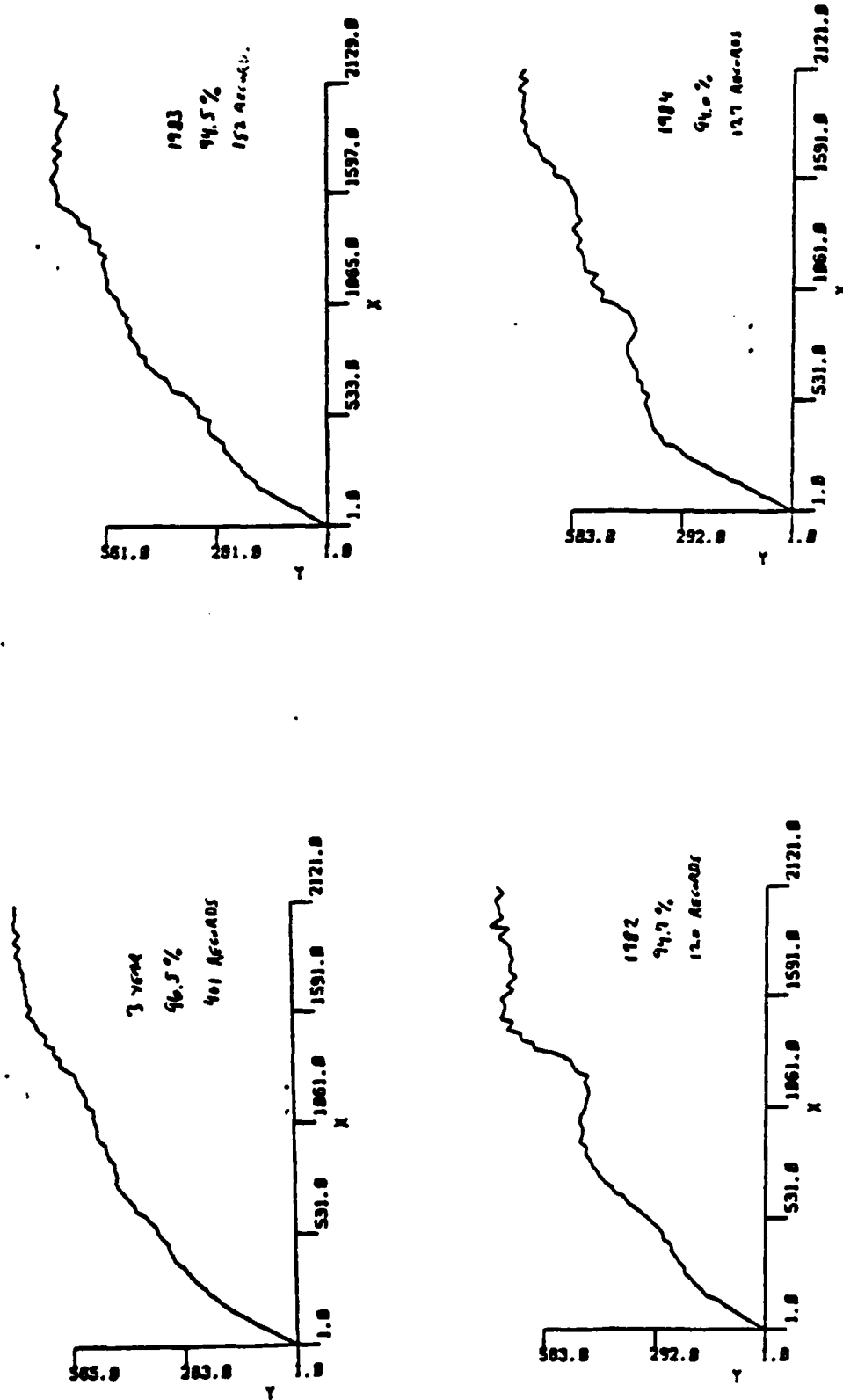


Figure 6: EOF mode 1 for the full satellite data set of observations from April 1982 through September 1984 (upper left). And the same mode using only the 1982 data (lower left), the 1983 data (upper right), and the 1984 data (lower right). The ensemble variance explained is from a preliminary data set that had some data quality problems, subsequent analysis has given similar shapes but the percentage variance explained is about 10% less.

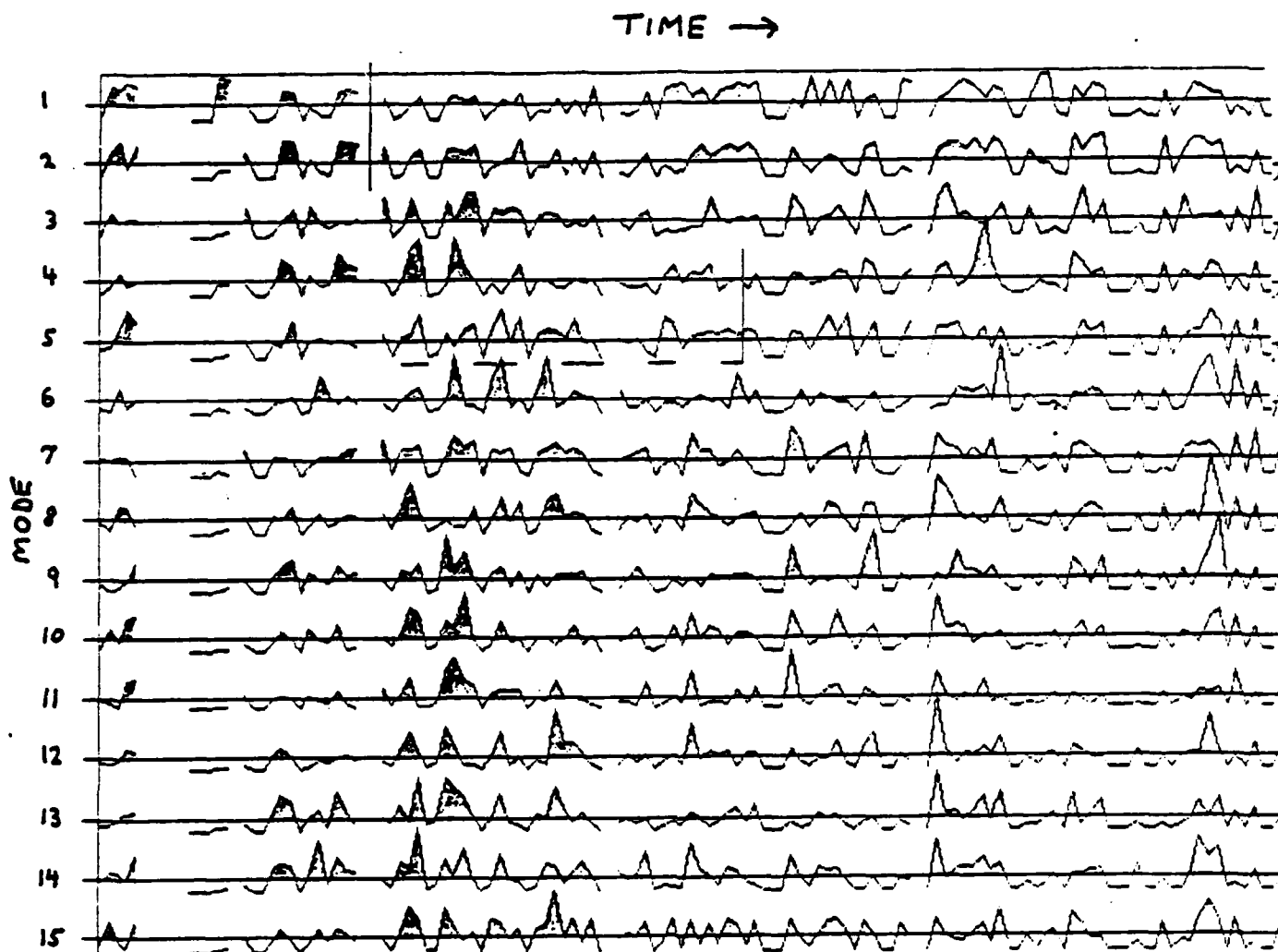


Figure 7: A time series of the first 15 mode coefficients squared versus time for the satellite observations of the north wall. Each horizontal line is a given mode plotted (scaled by its variance in order to keep each curve near the axis), versus time. The horizontal axis for each curve is its mean value.



## Gulf Stream Envelope and Mean Path between 75°W and 58°W

Peter Cornillon

Graduate School of Oceanography  
University of Rhode Island

In the first day of this workshop there were several discussions related to the effect of the New England Seamounts on Gulf Stream meandering. Some numerical models appear to show little impact, while others show a more pronounced effect. Interest in addressing this problem with numerical models stems from the commonly held perception that meandering of the Gulf Stream increase dramatically downstream of the Seamounts. If, in fact, this is true, the results of numerical models should also show such behavior. The difficulty in dealing with the perception of a dramatic increase in the meandering is that the phenomenon is not clearly spelled out in the literature. In fact several different concepts related to meandering appear to be mixed together in previous discussions. It is the confusion resulting from this situation that gives rise to the perception alluded to above. I therefore thought it appropriate to modify the presentation that I had intended to make, to address more specifically this issue. I will begin by categorizing the different concepts that I believe are at issue and then follow this with observations that have been made from satellite thermal IR data.

When one thinks of changes in meandering of the Gulf Stream downstream of the seamounts, three possibilities come to mind. First, the envelope described by the Gulf Stream over a period of time, such as one year, might increase rapidly at the seamounts. This is shown

schematically in Figure 1a. Second, the width of the envelope might change slowly but meandering of individual paths within the envelope might increase dramatically downstream of the seamounts (Figure 1b). Third, both the envelope width and the meandering within the envelope might change gradually, but the mean path of the envelope might make a sharp turn over the seamounts (Figure 1c). This is what was described by D. Thompson as a result of one of his model runs. Finally, any combination of the above is possible. When discussing meandering of the Stream, it is important to try to sort out these three different possibilities.

#### Satellite Thermal IR Data

Over 4000 TIROS-N series AVHRR passes of the western North Atlantic covering the period from April 1982 through September 1984 (Figure 2) were used to study the envelope and the annual mean path. These data were acquired through a joint data collection program of the Graduate School of Oceanography, University of Rhode Island (GSO) and the Rosenstiel School of Marine and Atmospheric Science, University of Miami (RSMAS). These data were: read onto the RSMAS computer; decimated by 4, every fourth element and every fourth scan line being retained, and; SSTs were retrieved from the NOAA-7 data using the NESDIS (1982) algorithm and from the NOAA-6 and NOAA-8 data by simply converting the brightness temperatures to SSTs. At GSO the data were: remapped to a common coordinate system; composited into two-day groups, where the compositing step retains the warmest of the approximately ten pixels of a given location from the ten or so images spanning the two-day interval, and; the northern edge of the Gulf Stream was then digitized

by hand between Cape Hatteras and  $58^{\circ}\text{W}$ . The compositing step resulted in a reduction of the data from over 4000 passes to approximately 400 images.

### Discussion

Figure 3 shows a phase diagram of the northern edge positions of the Gulf Stream plotted relative to the rhumb line  $74^{\circ}\text{W}$ ,  $36^{\circ}\text{N}$  and  $60^{\circ}\text{W}$ ,  $39^{\circ}\text{N}$ . Clear from this plot are the relatively small number of periods during which the northern edge of the Stream was obscured by clouds for the entire two-day compositing interval. Also evident is the downstream decrease in our ability to detect the Gulf Stream. This is due to a combination of factors. First, the downstream cloud cover appears to be higher. Second, the thermal contrast between the stream and surrounding waters decreases downstream. Third, the meandering increases making it more difficult to track the edge. This decrease in our ability to track the Stream to the east is of significance to the use of satellite data downstream of the seamounts. We are currently extending the research described here to  $45^{\circ}\text{W}$  and will better be able to answer the question of the impact of cloud cover, decreased thermal contrast, and increased meandering on such work.

In addition to showing the coverage obtained from this data set, Figure 3 also shows interesting characteristics of the larger meanders in the region. In particular one meander, indicated by the thick solid line, is tracked from  $75^{\circ}\text{W}$  to  $61^{\circ}\text{W}$  between April 1983 and January 1984. The phase speed of this meander decreases from 7.6 cm/s to 2.1 cm/s on June 7 and then increases to 6.1 cm/s on September 3. Most existing models predict a decrease in phase speed with increasing wavelength but

not an increase as observed here.

The envelope of meandering is shown in Figure 4 for April 1982 through December 1982, the upper plot, for 1983, the middle plot and for April 1982 through September 1984, the lower plot. These three plots show several interesting similarities and several differences. Both 1982 and 1983 as well as the three years together show a local minimum in the envelope width at about  $70^{\circ}\text{W}$ . They all show that the envelope is fairly constant from about  $68^{\circ}\text{W}$  to  $58^{\circ}\text{W}$ . This is also shown for the three years together in Figure 5, a plot of the RMS deviation of the envelope with longitude (open circles). The same data extracted from Halliwell and Mooers (1983) are also plotted in Figure 5 (open triangles). The data of Halliwell and Mooers only extends to  $65^{\circ}\text{W}$  but between Cape Hatteras and  $65^{\circ}\text{W}$  agrees well with the 1982-84 data. This is significant in that their study covered a different three-year period, hence the local minimum observed at  $70^{\circ}\text{W}$  persists in all six years of the two studies. The 1982-84 data presented in Figures 4 and 5 show that there is no dramatic increase in the envelope of Gulf Stream paths averaged in one year periods. There is however a large increase in envelope width upstream of the seamounts, beginning at about  $68^{\circ}\text{W}$  that may in fact be related to the seamounts.

The third curve plotted in Figure 5 (solid circles) is a measure of the convolution within the envelope. Figure 6 shows how the points on this curve were obtained. Basically, the integrated path length between integral degrees of longitude was averaged over all paths and then normalized by the integral of the mean path over the same interval of longitude. Although noisier than the RMS width of the envelope, this

curve shows little change in the rate of increase of meandering from Cape Hatteras to 58°W, again with no apparent affect of the seamounts.

Figure 4 shows one major difference from year to year and that is in the mean path of the Stream over a year. In 1982 for example a large meander extending from 68°W to 62°W remained in very nearly the same position for the entire nine-month period observed. The mean paths for each of the three years studied are plotted together in Figure 7. The meander in 1982 is apparent as are other smaller meanders in the same year. Taken together they appear to form a train of waves extending from Cape Hatteras to 58°W. Also apparent are waves of the same wavelength in 1984 but 180° out of phase with those in 1982. In 1983 the same wave pattern is apparent but with a much smaller amplitude. The large arrows in the figure point to nodes in what may be a standing wave pattern. The wavelength is fairly consistent at about 750 km with a period on the order of 48 months. The interval for which we have data is at the limit of being able to resolve waves of this period. We are currently extending our analysis from both ends to see if in fact the relationship holds. The interval does appear to be sufficiently long to show that at least on the average there is no consistent dramatic change in the path of the mean Stream downstream of the New England Seamounts.

#### Summary

Possible changes in the Gulf Stream path downstream of the New England Seamounts, observed with 30 months of satellite IR data have been discussed with three different scenarios in mind: a change in the envelope of path positions; a change in the meandering within the envelope of individual replicates of the Stream; and, a change in the

mean path of the Stream. The satellite data show quite clearly that the envelope does not increase significantly downstream of the seamounts although there is a rapid growth in the RMS size of the envelope immediately upstream of them. The meandering within the envelope does not appear to change much across the seamounts. At least there is not a significant increase in the rate of change. These data are however noisy, possibly hiding smaller effects of the seamounts. Finally, the mean path of the Stream does not change dramatically across the seamounts but does vary significantly over its entire length from year to year.

We are extending these studies in space to  $45^{\circ}\text{W}$  and in time back to January 1982 and forward to the present.

#### REFERENCES:

NOAA/NESDIS, Coefficients presented at the 32nd SST Research Panel

Meeting held by the National Environmental Satellite, Data, and Information Service (NESDIS) of the National Oceanic and Atmospheric Administration (NOAA) at the World Weather Bldg. in Suitland, Maryland, on September 30, 1982.

Halliwell, Jr. G.R. and C.N.K. Mooers, 1983: Meanders of the Gulf Stream downstream from Cape Hatteras 1975-1978. J. Phys. Oceanogr. 13, 1275-1292.

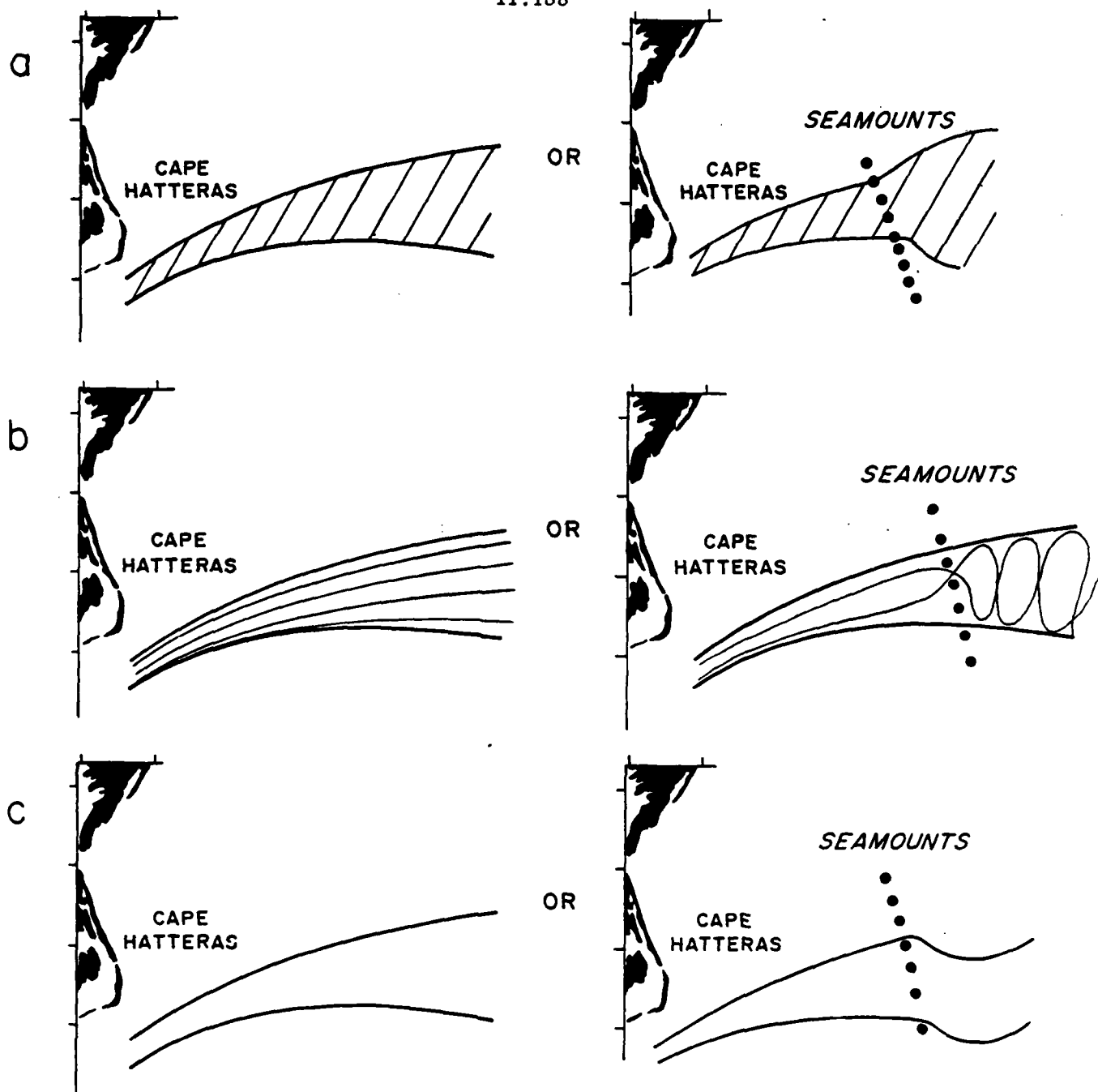


Figure 1. Different effects of the New England Seamounts on Gulf Stream meandering. (Not to scale). a. Increase in the envelope size. b. Increase in convolution within the envelope. c. Change in the mean path of the Stream.

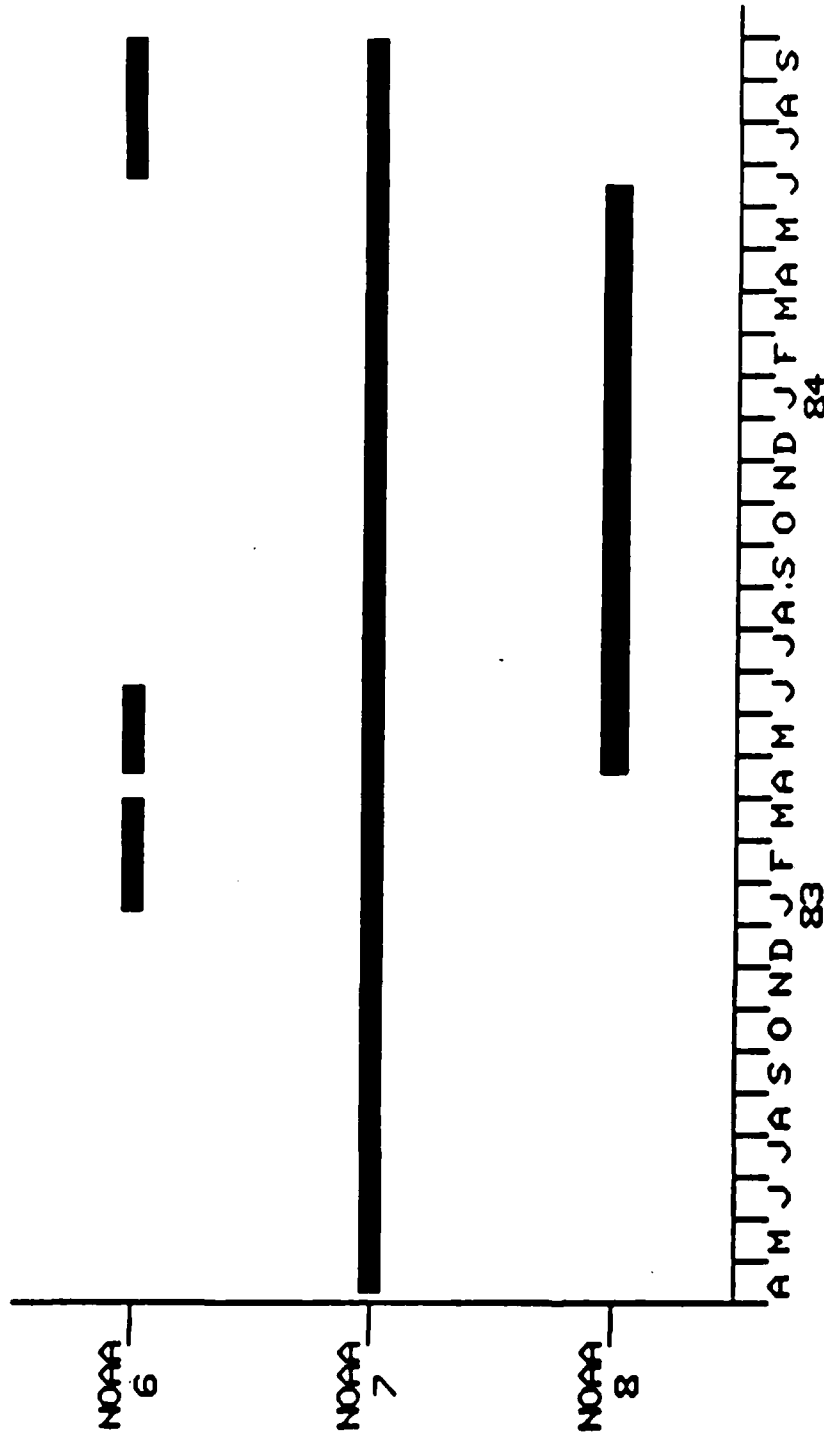


Figure 2. Operational time periods of the NOAA satellites from April 1982 to September 1984.



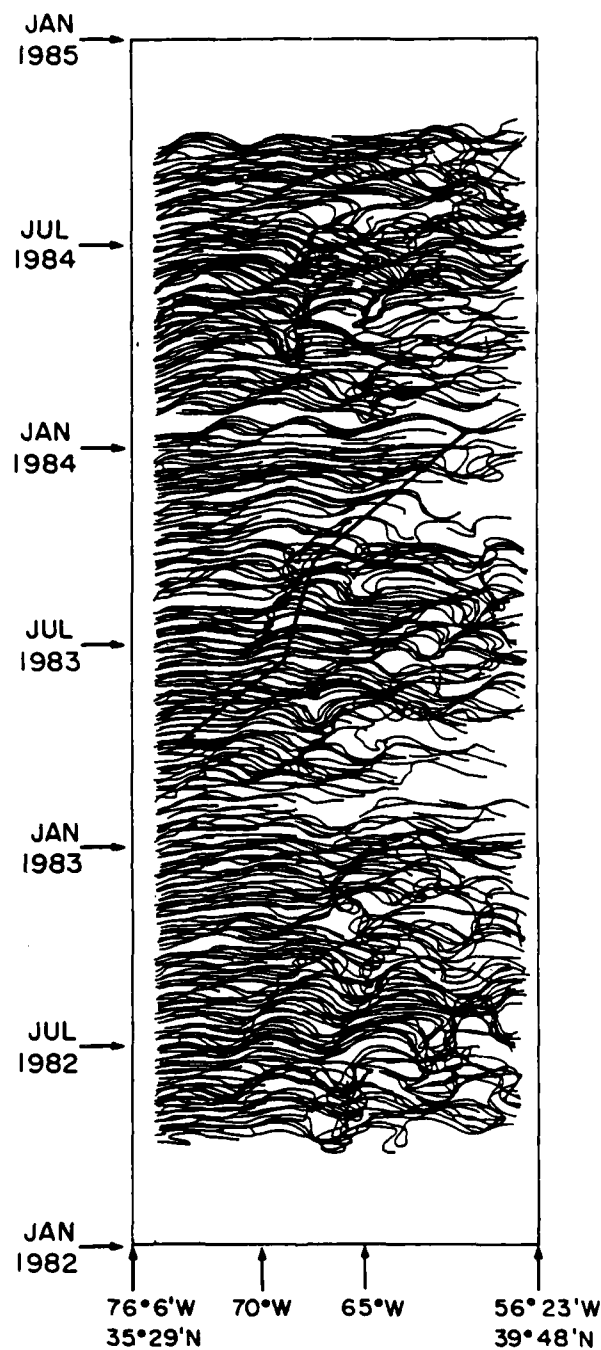


Figure 3. Gulf Stream northern edge displacements relative to the rhumb line through 74°W, 36°N and 60°W, 39°N. One realization is presented for every two days.

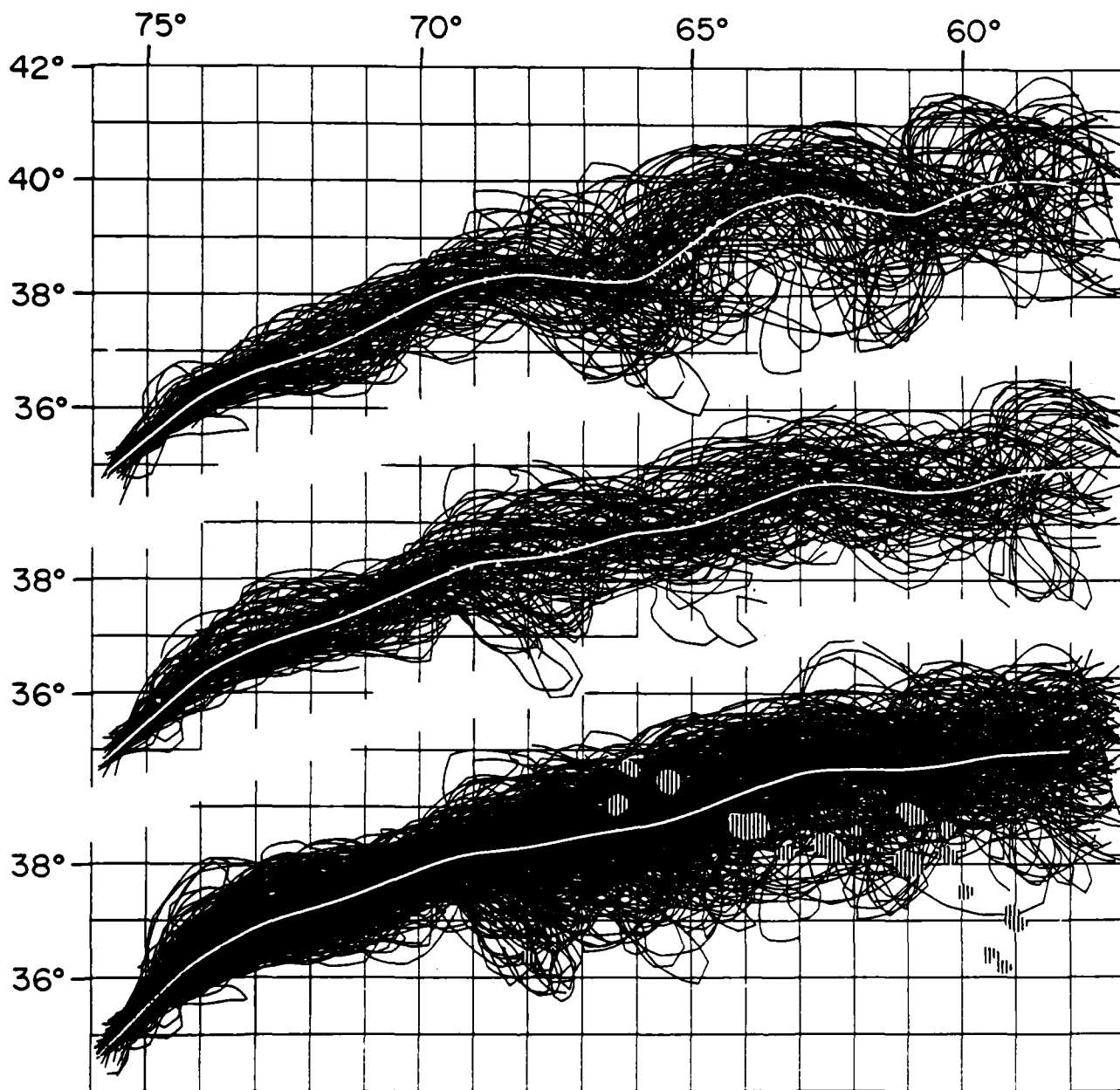


Figure 4. Gulf Stream northern edges superimposed on one another. The upper set is for the period from April 19, 1982, to December 31, 1982. The middle set is for all of 1983. The lower set is for April 19, 1982, to September 30, 1984. The grey spots on the lower plot represent water shallower than 3000 m, the New England Seamounts. The white lines in the middle of each set represent the mean track for that set.

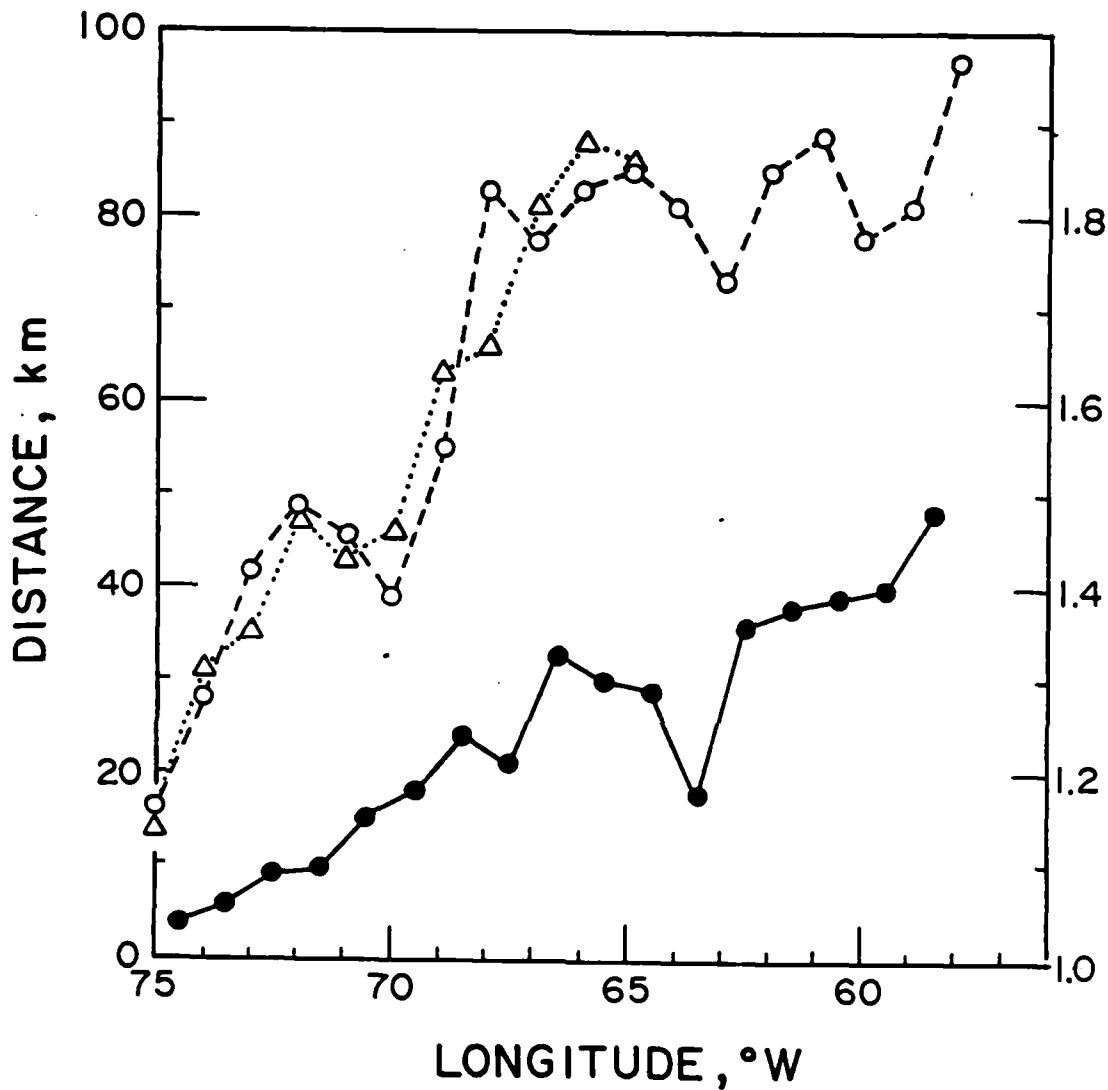
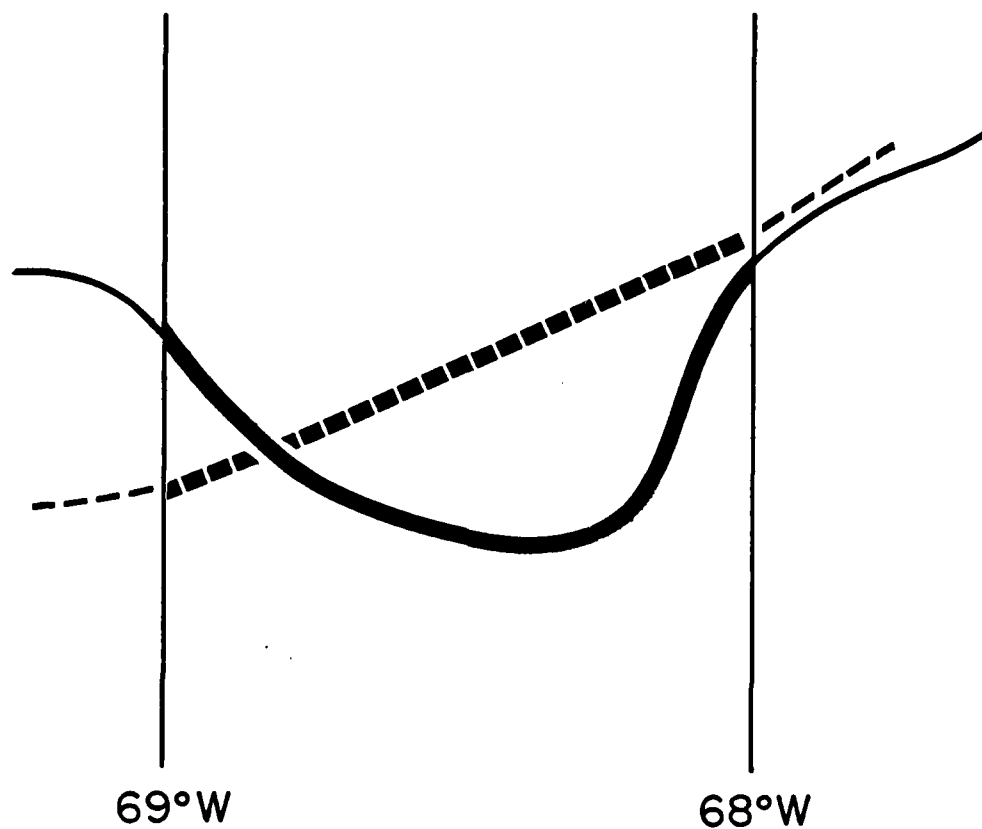


Figure 5. Standard deviation of the Gulf Stream envelope normal to the mean path of the Stream for the thirty month interval shown in Figures 3 and 4: this study, the dashed curve with open circles; Halliwell and Mooers(1983) the dotted curve with open triangles. The scale to the left corresponds to these two curves. The ratio of the mean of the integrated path length to the mean path length between integer degree values of longitude is shown by the solid curve with solid circles. The scale to the right corresponds to this curve.

# GULF STREAM CONVOLUTION



$$\text{CONVOLUTION} = \frac{\frac{1}{N} \sum_{i=1}^N \int_{68^\circ}^{69^\circ} ds_i}{\int_{68^\circ}^{69^\circ} \overline{ds}}$$

Figure 6. Definition of Gulf Stream convolution used for the curve in Figure 5 with solid circles.

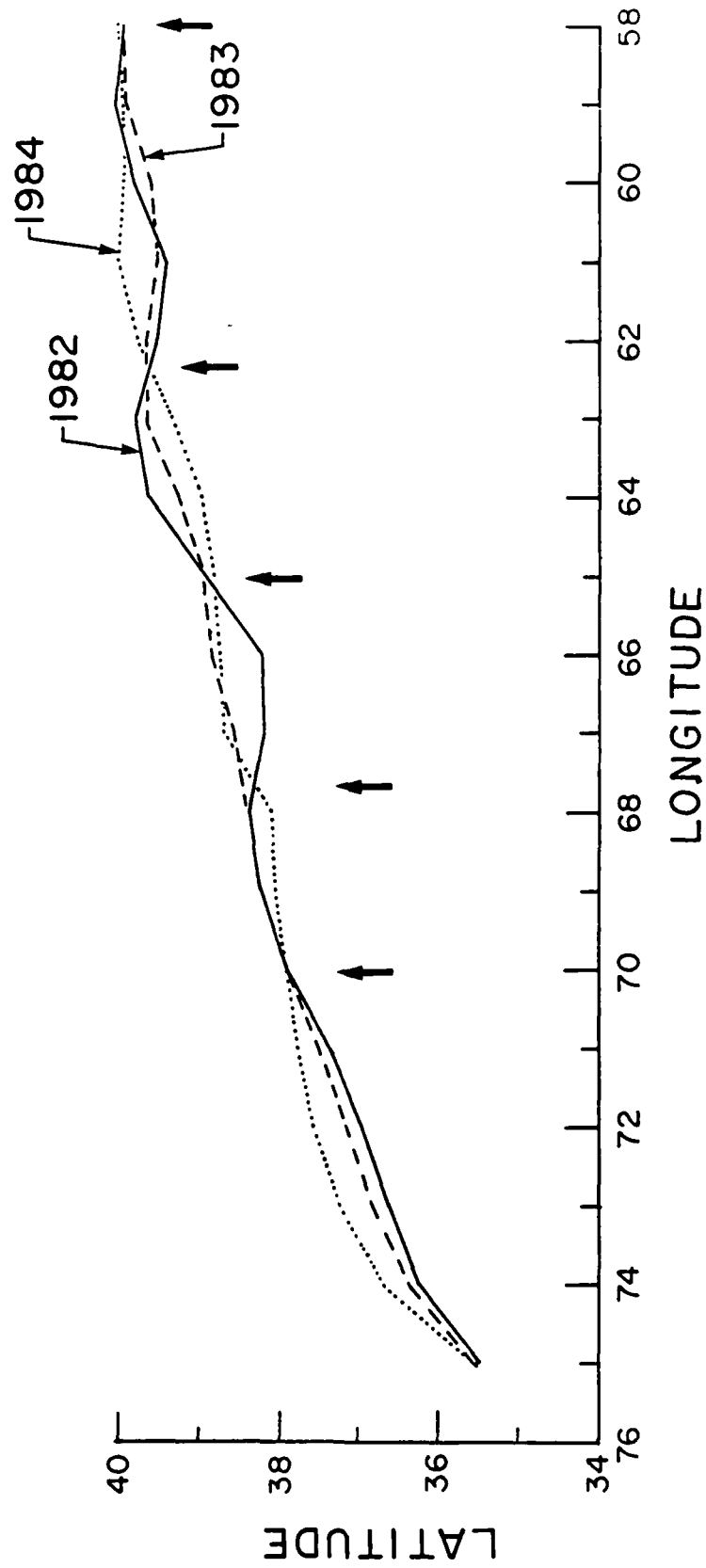


Figure 7. Mean Gulf Stream northern edge for the periods April-December 1982, solid line, 1983, dashed line and January-September 1984, dotted line.

## Maximum Gradient Inverse for the Gulf Stream System

B.D. Cornuelle, SIO, La Jolla, CA 92093

P. Malanotte-Rizzoli, MIT, Cambridge, MA 02139

Introduction: Acoustic tomography uses integrating measurements which require inverse methods to resolve the averages into estimates of spatial structure. In the example considered here, travel times for sound transmitted across the Gulf Stream (called GS hereafter) between a single source and receiver (SR) are to be converted into an estimate of the position and structure of the GS front. The ocean sound channel produces several distinct multipaths along which the rays sample the ocean. In their original paper, Munk & Wunsch (1979) ignored the horizontal information available due to these different ray paths, but in this application it is critical, since we wish to investigate how well acoustic transmission across the GS can determine the true field.

Statistical inverse methods have been used to solve the reconstruction problems (Cornuelle, 1983; Cornuelle et al., 1985; P.M. Rizzoli & W.R. Holland, 1985). These inverse methods require advance estimates of the mean and covariance of the sound speed perturbations and of the errors in the measurements. While it is relatively easy to specify noise statistics, the GS region does not lend itself to this type of statistical characterization (P.M. Rizzoli, J. Spiesberger, M. Chaves, 1985). For this reason we have begun to test a form of inverse which can more easily accomodate the prejudices which we hold for the GS. This inverse solution seeks to minimize the errors in the fit to the data while simultaneously satisfying our expectations that a front exists by maximizing the sum of squares of the gradients observed in the reconstructed section.

Several examples have been run to illustrate the performance of the maximum-gradient inverse techniques on simulated GS acoustic data. The results suggest that the maximum-gradient inverse can reconstruct the GS front with better accuracy than the least-squares inverse but suffers from instability if the gradient constraint is over-emphasized. There are several adjustments for the instability problem, one of which is to limit the maximum sound speed perturbation in accordance with GS data. This inverse method may also have applications to more general regimes where fronts are possible and the smoothing properties of the least-squares statistical inverse are undesirable.

Tomography: Ocean acoustic tomography has been well described in the literature, both in application to mesoscale flows and to the GS region. In the previously quoted references, the stochastic inverse was applied to the following: mapping the mesoscale in the 1981 experiment; single slice geometry and the filtering out of the mesoscale from the estimates of the average quantities for gyre-scale future experiments; and non-linearity in the travel times of the direct problem which may bias the inverse results. Here the small scale structure is at least as important as the large-scale trend; thus the present discussion is quite different from the previous work.

The original studies for the feasibility of GS tomography concentrated on bottom-mounted instruments instead of the mid-depth moorings used in the 1981 experiment. Bottom-mounted instrumentation can be placed directly under the high-speed currents of the GS front, and the surface-reflected rays which make up the dataset are only slightly altered by the shifting front, so that non-linearities due to ray path change are greatly reduced

P.M. Rizzoli, D.D. Cornuelle, D.B. Halverson, 1982. Other advantages of this geometry include the absence of mooring motion and the lower cost of the simpler equipment. On the other hand, the bottom mounting eliminates the multipath arrivals associated with the sound channel, leaving only surface and bottom-reflected rays. Bottom reflected rays depend strongly on local topography which can limit their usefulness as data, so that only one or two rays may be available between each SR pair. In the original design, this drawback was overcome by using seven or more transceivers closely spaced along the bottom, with one source transmitting to several receivers. Given the present cost and availability of tomographic instrumentation, this is difficult to achieve, so it is important to consider alternatives to the original geometry.

Perhaps the most obvious alternative is to return to the geometry employed in the other tomography experiments; mooring the instruments at mid-depth several hundred km apart, so that the multipaths due to the sound channel increase the number of raw data per SR pair. If the instruments are moored outside the range of GS meanders then the strong currents can be avoided while ensuring that the GS front falls within the area surveyed by the array. Because the bottom transceivers must be kept a relatively small distance apart, the wider the range of the meandering, the more advantageous the mid-depth geometry becomes. Any motion of the moorings can be accounted for either by acoustic tracking or by augmenting the inverse problem (Cornuelle, 1985). On the other hand, nonlinearities due to ray path changes under the strong perturbations are very important if the rays are not surface reflected. During the time since the bottom mounting was proposed, these nonlinearities have been studied by several authors (Spiesberger & Worcester, 1983; Spiesberger, 1985; Rizzoli, 1985), and they



been mainly to complicate the problem by requiring iteration in the solution. The inverse proposed herein is already iterative, so the presence of nonlinearities does not fundamentally change the approach. For the purpose of this study, the rays have been assumed to be unchanged by the perturbations, in order to separate questions of horizontal resolution and prior constraints from nonlinear inverse techniques, but the total problem must be addressed as part of a full discussion of the trade-offs between the two alternatives.

Statistical inverse assumptions: The inverse methods used so far in ocean acoustic tomography are linear, least-square methods based on statistical assumptions. The stochastic inverse used with the 1991 experiment requires advance specification of the mean and covariance of both the unknown sound speed field and the observation noise. In the relatively quiet regions far from the GS, the covariances are smooth and more or less homogeneous and isotropic. In the GS region, the statistics are quite different on different sides of the front, and are also anisotropic with respect to distances along the front or perpendicular to it (P.M. Rizzoli, J. Spiesberger and M. Chaves, 1985). The complication of the covariance is an inconvenience, but the covariance is also fundamentally inefficient for constraining the inverse solution to obey the prejudices we have for the GS. The covariance function in fact averages over all possible locations of the GS front, "smearing" it out. The smoothing inherent in the least-squares norm is also contradictory to the expectation of fronts. The least-squares principle encourages equal distribution of parameter values, while the GS perturbation signal is expected to be more concentrated in one place. The same problem can occur whenever moving fronts are expected, and the

alternative inverse method presented below is meant to provide a partial solution to these defects.

Maximum gradient inverse: The easiest way to explain the new method is to compare it with the older, least-squares technique. Given a forward model,  $\underline{G}$ , which relates a set of data,  $\underline{D}$ , to a set of model parameters,  $\underline{M}$ ,

$$\underline{D} = \underline{G}(\underline{M}) \quad (1)$$

the inverse problem is to estimate  $\underline{M}$  given noise-corrupted measurements of  $\underline{D}$ . The stochastic inverse assumes that a model covariance matrix,  $\underline{C}$  and a noise covariance matrix,  $\underline{E}$  are available, and it chooses the solution which minimizes

$$[\underline{D} - \underline{G}(\underline{M})]^T \underline{E}^{-1} [\underline{D} - \underline{G}(\underline{M})] + \underline{M}^T \underline{C}^{-1} \underline{M} \quad (2)$$

The alternative inverse produces an estimate of  $\underline{M}$  which minimizes

$$[\underline{D} - \underline{G}(\underline{M})]^T \underline{E}^{-1} [\underline{D} - \underline{G}(\underline{M})] + \lambda_1 \left[ \sum |M_i|/\sigma_i \right] \quad (3)$$

$$+ \lambda_2 \left[ K - \int \left( \frac{\partial F}{\partial x} \right)^2 dx \right]$$

where  $K$  is a large positive number,  $\sigma_i$  is a scaling value for the  $i$ th model parameter,  $F(x, \underline{M})$  is the physical field of interest, and  $\lambda_1$  and  $\lambda_2$  are weight parameters which determine the relative importance of the minimum norm and maximum gradient constraints.

To understand the practical effect of these constraints, consider a

hypothetical case of an ocean section whose structure is given by a single vertical mode with horizontal amplitude variations limited to six uniform regions. If only one travel time,  $D_1$ , is available for the sections, and the ray has equal, unit length in each region of the section, then  $\underline{M}$  has six elements, each representing 1/6 of the length of the section and specifying the amplitude of the single vertical mode that is the perturbation for that length. Then the forward problem for travel time as a function of  $\underline{M}$  is:

$$D_1 = \sum_{i=1}^6 M_i \quad (4)$$

(4) is the simplified form of (1) if  $\underline{G}^T = 1$ . If each element of  $\underline{M}$  has unit variance then the least-squares inverse minimizes

$$\left(D_1 - \sum_{i=1}^6 M_i\right)^2 / \sigma_N + \sum_{i=1}^6 M_i^2 \quad (5)$$

which is the simplified version of (2); and the new inverse minimizes

$$\left(D_1 - \sum_{i=1}^6 M_i\right)^2 / \sigma_N + \lambda_1 \sum_{i=1}^6 |M_i| + \lambda_2 \left[ k - \int \left( \frac{\partial F}{\partial x} \right)^2 dx \right] \quad (6)$$

the simplified version of (3).

If the measured datum is  $D_1 = 3$ , then many sets of parameters are possible. Let  $M1 = (.5, .5, .5, .5, .5, .5)$ ,  $M2 = (1., 1., 1., 0., 0., 0.)$  and  $M3 = (0., 0., 3., 0., 0., 0.)$ . We can then tabulate the values of each of the penalty functions outlined above for the three vectors. Each inverse will choose the parameter estimate which minimizes its penalty functions.

constraint	M1	M2	M3
$D_1 - G(M)$	0	0	0
$\sum M_i^2$	1.5	3	9
$\sum  M_i $	3	3	3
$K - \int (\frac{dF}{dx})^2 dx$	large	small	very small

(assume finite transition width between blocks)

The least-squares norm will choose case M1 which in fact corresponds to the minimum norm. The absolute value norm will not be able to choose a solution alone between M1, M2 and M3. Further constraints need to be added to the absolute value norm. The gradient constraint chooses M3 which concentrates the perturbation as tightly as possible. This example is pathological, giving only one equation for 6 unknowns so none of the solutions are unique, but they serve to show the tendencies of the constraints. It is particularly important to avoid the smoothing of the square norm if the unknown parameters may be concentrated in one place, since then the prior constraint is at odds with the expectations.

Simulation results: Two simulations were run using the mid-depth geometry and a sound speed profile from an averaged set of GS sections (Figure 1). A model GS section was constructed by superimposing a sound speed perturbation on the basic profile. The vertical structure of the perturbation was given by a single empirical orthogonal function (EOF) from a GS dataset (P.M. Pizzoni, J. Spiesberger, and M. Chages, 1985) and with horizontal amplitude given by piecewise linear segments between 7 horizontal locations at which the mode amplitude was specified. The total length of the section was 300

km, and the bottom depth was assumed to be 3.5 m. A source and a receiver were assumed to be moored at 2 km depth at either end of the section, and rays were traced using the basic sound speed profile. Seven rays were chosen for the model inverses and data were constructed by picking a location for the GS front and giving the EOF unit amplitude to the left of the front and zero amplitude to the right. Because the rays were assumed to be invariant in the presence of the perturbation, the data could be calculated directly from the model given the ray paths,  $Z_i(x)$ , and the sound speed perturbations,  $\delta C(x,z)$ :

$$D_i = \int_{x_s}^{x_R} \frac{\delta C(x, Z_i(x)) \left[ 1 + \left( \frac{dZ_i}{dx} \right)^2 \right]^{1/2} dx}{C_0^2(Z_i(x))} \quad (7)$$

The rays were all assumed to have errors of 0.1 ms, and the mode variances were assumed to be unit  $\sigma_i = 1$ . The least-squares inverse was computed by standard matrix inversion while the maximum gradient inverse was obtained using an iterative Levenberg-Marquardt descent algorithm.

In the first case run, the sound speed perturbation was specified at points located at  $x=0$ , 100km, 125km, 150km, 175km, 200km and 300km (see Figure 2). The model points are shown as boxes at the bottom of the figure, and the vertical structure of the perturbations is shown as vertically spaced horizontal profiles showing the sharp gradient between 150 and 175 km. The linear inverse result is shown as figure 3. The non-linear inverse result is shown in figure 4 for the case where the maximum gradient constraint was weighted at 0.1 of the minimum absolute value constraint ( $\lambda_1 = 1$ ;  $\lambda_2 = 0.1$ ). In figure 5 the maximum gradient constraint was set at  $\lambda_2 = 0.5$  and the absolute value constraint at  $\lambda_1 = 1$ .

Although there are nominally seven equations in seven unknowns, only 3 or 4 of the rays are independent, as indicated by the poor performance of the least square inverse. The smoothing tendency of the standard inverse is apparent in the contrast of figure 3 with figure 4. The destabilizing effect of the gradient constraint is shown in figure 5, in which the tendency to concentrate the perturbation (which was discussed in section 3) distorts the estimate of the profile. The location of the stream axis is still correct, however.

The unequal spacing of the model points provided information to the inverse, as can be seen by examining the second case, where the section was modelled by seven equally spaced points (50 km spacing). Figure 6 shows the actual sound speed perturbation. Figure 7 shows the least square inverse results, and figure 8 the maximum gradient estimate using  $\lambda_1 = 1.0$  and  $\lambda_2 = 0.1$ .

Conclusions: The above inversions across an extremely idealized Gulf Stream section show that it is in principle possible to construct an inverse method which abandons the built-in statistical prejudices which tend to smooth sharp features. Statistical prejudices are central to the stochastic inverses used in the tomographic experiments carried out until now, but that inverse may not be the best for a region as anisotropic and inhomogeneous as the Gulf Stream system.

The maximum gradient inverse instead capitalizes upon physical prejudices, namely the expectation of discontinuities and inhomogeneities, such as sharp fronts in physical space. Obviously, much more study must be done before being able to decide if this new inverse can be successful when

applied to a realistic situation across the Gulf Stream. Instabilities related to excessive weighting of the maximum gradient constraint must be quelled by consistent, objective methods. Note that the structure of the front itself is not well determined here. Other objective criteria must be introduced for the inverse to decide whether the GS front is sharp or diffuse. Realistic cases must be studied, with more than one EOF for the vertical structure; many more travel time data; studying systematically the effect on the inverse estimates of equal versus unequal grid-spacings in the horizontal; and so forth. The final test about the usefulness and efficiency of this new type of inverse will moreover come from the comparison between these inverse results and those obtained from the stochastic type, already available on a routinely working basis. The above idealized examples, however, show that this new approach can produce significantly better results than the old one, and work along the above directions is already under way.

## References

Cornuelle, B.: Inverse methods and results from the 1981 Ocean Acoustic tomography experiment, Ph.D. diss., 359 pp., Mass. Inst. Technol./Woods Hole Oceanogr. Inst., Woods Hole, MA (1983).

Cornuelle, B., C. Wunsch, D. Behringer, T. Birdsall, M. Brown, R. Heinmiller, R. Knox, K. Metzger, W. Munk, J. Spiesberger, R. Spindel, D. Webb, P. Worcester: Tomographic maps of ocean mesoscale, 1, Pure acoustics, J. Phys. Oceanogr., in press, (1985).

Munk, W. and C. Wunsch: Ocean Acoustic Tomography, a scheme for large-scale monitoring, Deep-Sea Res., 26A, 123-161 (1979).

Malanotte-Rizzoli, P., B. Cornuelle, D.B. Haidvogel: Gulf Stream acoustic tomography: Modelling Simulations, Ocean Modelling, 46, pp. 10-11 (1982).

Malanotte-Rizzoli, P., J.L. Spiesberger, M. Chaves: Gulf Stream variability for acoustic tomography, Deep-Sea Res., 32, 237-250 (1985).

Malanotte-Rizzoli, P.: Long-range inversions for ocean acoustic tomography, J. Geophys. Res., in press (1985).

Spiesberger, J.L. and P. Worcester: Perturbations in travel time and ray geometry due to mesoscale disturbances: A comparison of exact and approximate calculations, J. Acoust. Soc. Am., 74, 219-225 (1983).



Schlesinger, J.D.: Ocean acoustic tomography: travel time delays, *J. Geophys. Res.*, 77, 83-100 (1985).

## GULF STREAM TOMOGRAPHY MODELING SIMULATION

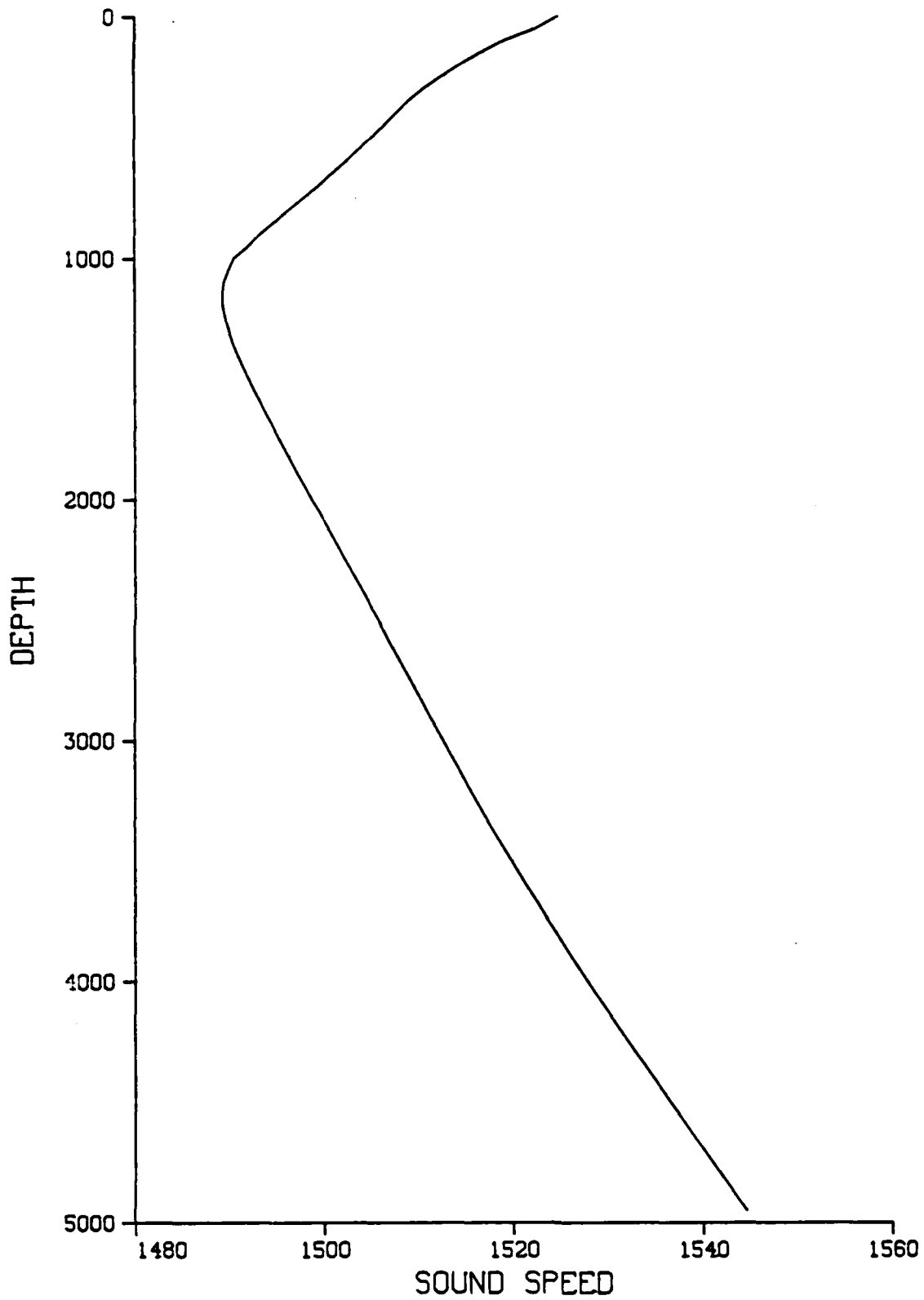


Fig. 1

GULF STREAM TOMOGRAPHY MODELING SIMULATION  
THEORETICAL

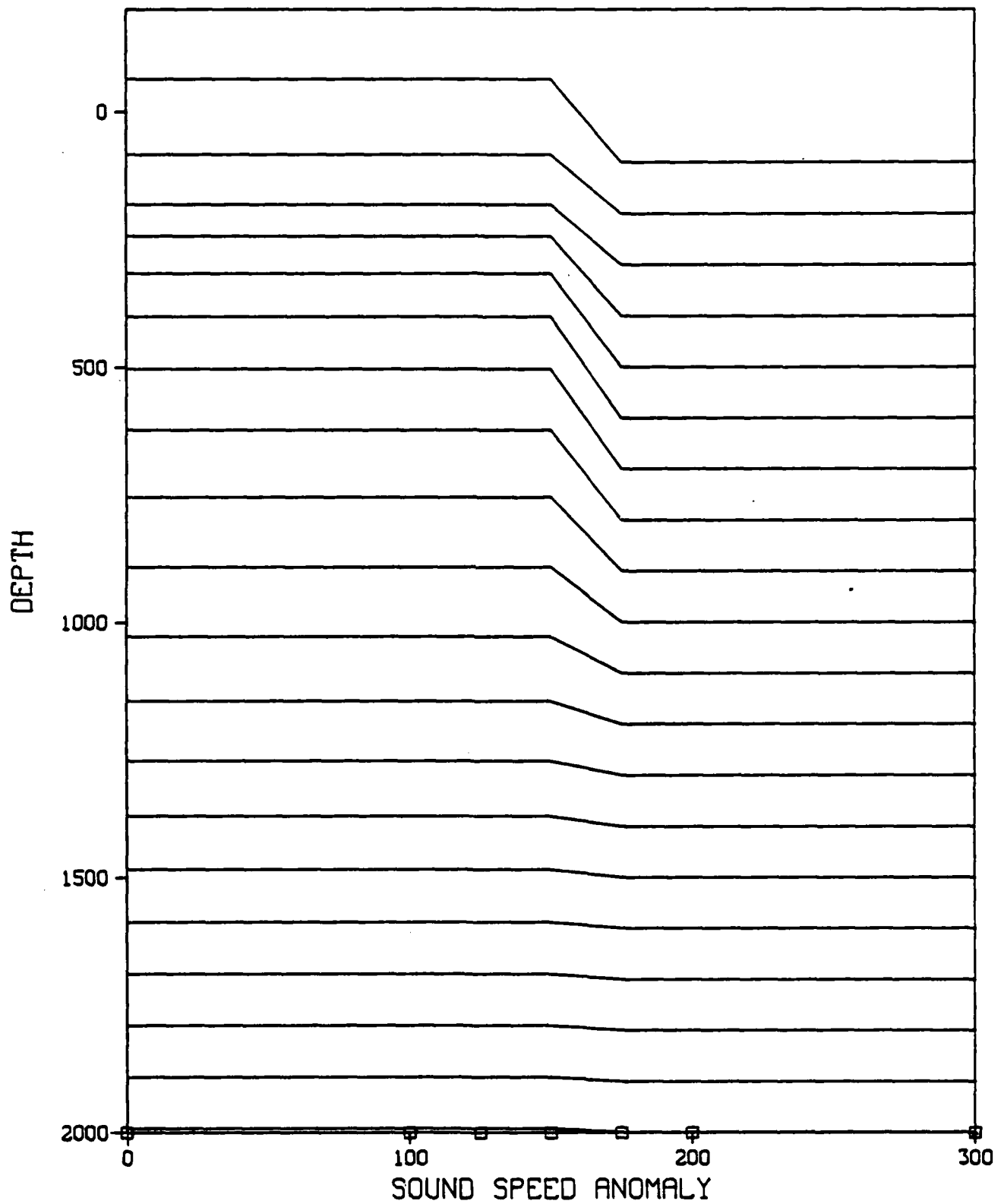


Fig 2

GULF STREAM TOMOGRAPHY MODELING SIMULATION  
WEIGHTED LINEAR INVERSE

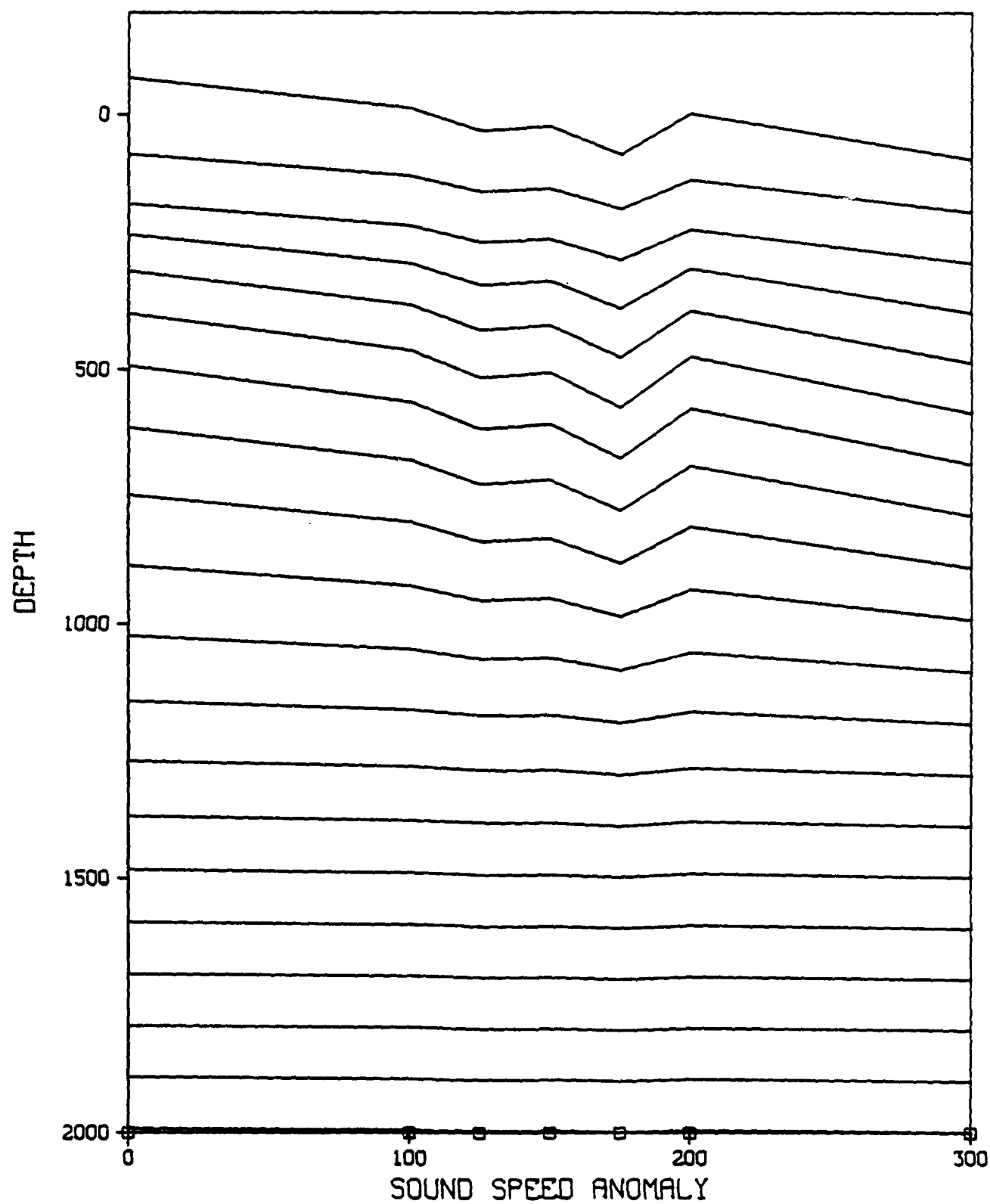


Fig 3

## GULF STREAM TOMOGRAPHY MODELING SIMULATION

WEIGHT FOR GRADIENT CONSTRAINT - 0.1

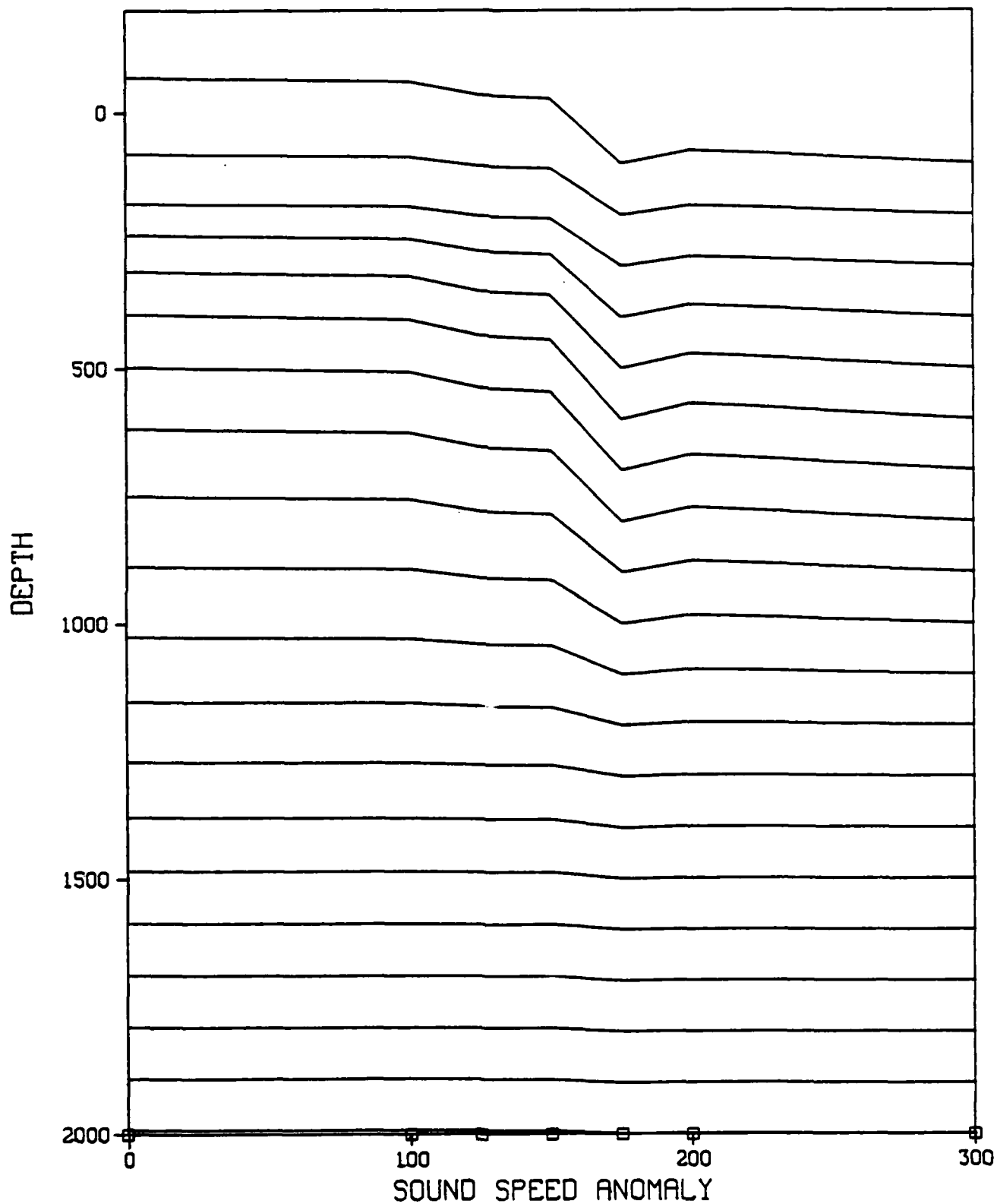


Fig 4

## GULF STREAM TOMOGRAPHY MODELING SIMULATION

WEIGHT FOR GRADIENT CONSTRAINT - 0.5

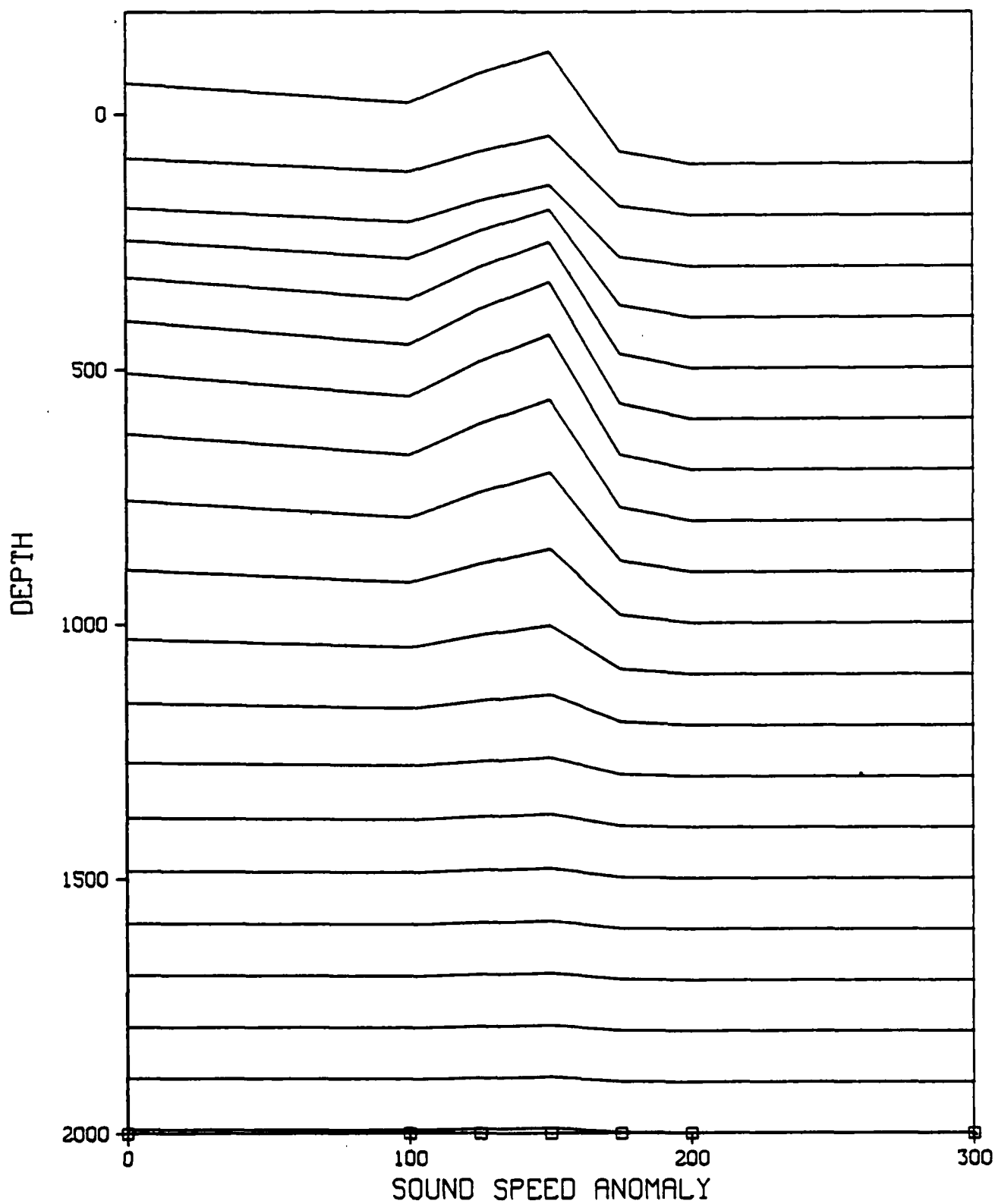


Fig 5

GULF STREAM TOMOGRAPHY MODELING SIMULATION  
THEORETICAL

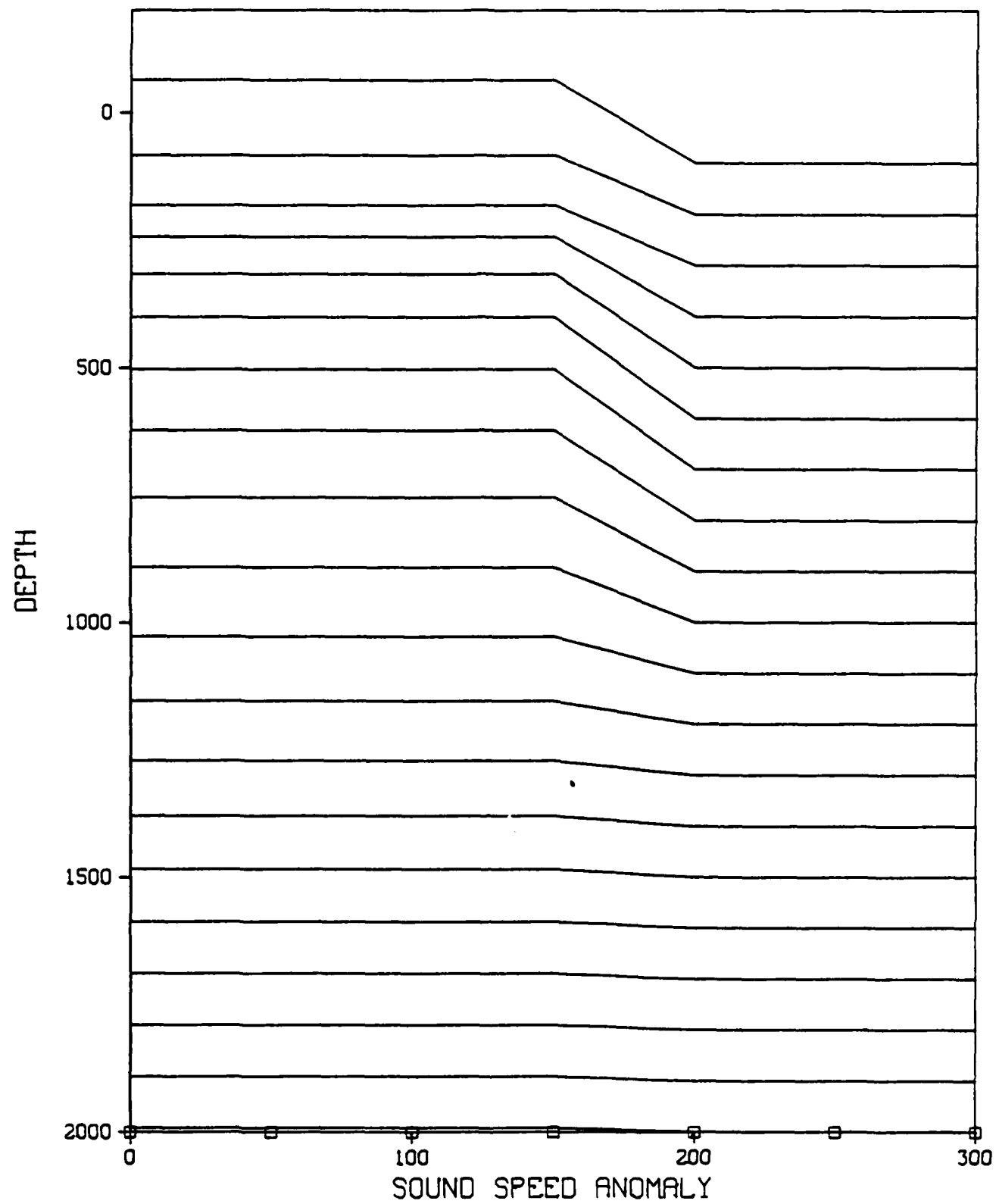


Fig 6

GULF STREAM TOMOGRAPHY MODELING SIMULATION  
WEIGHTED LINEAR INVERSE

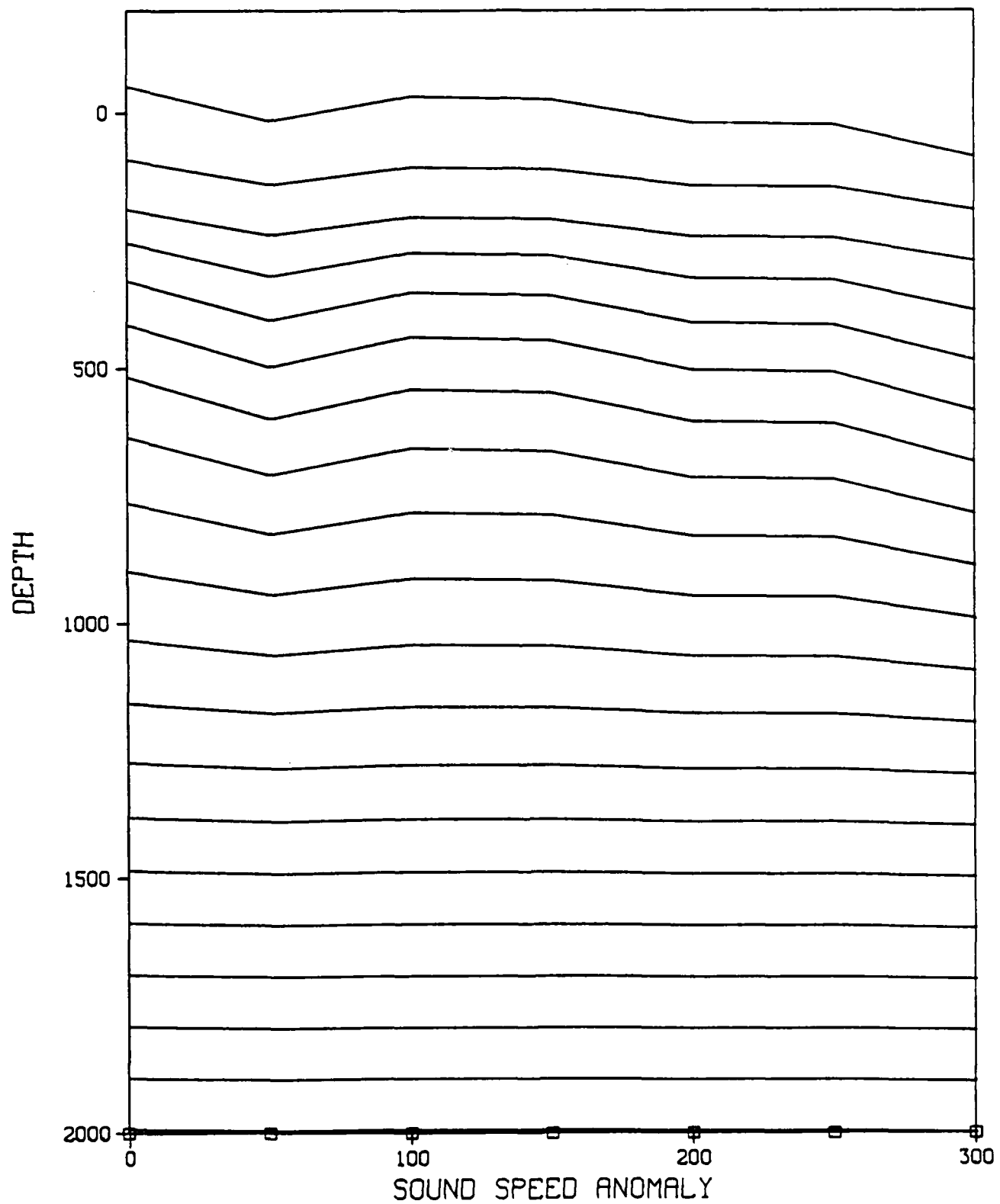


Fig 7



## GULF STREAM TOMOGRAPHY MODELING SIMULATION

WEIGHT FOR GRADIENT CONSTRAINT - 0.1

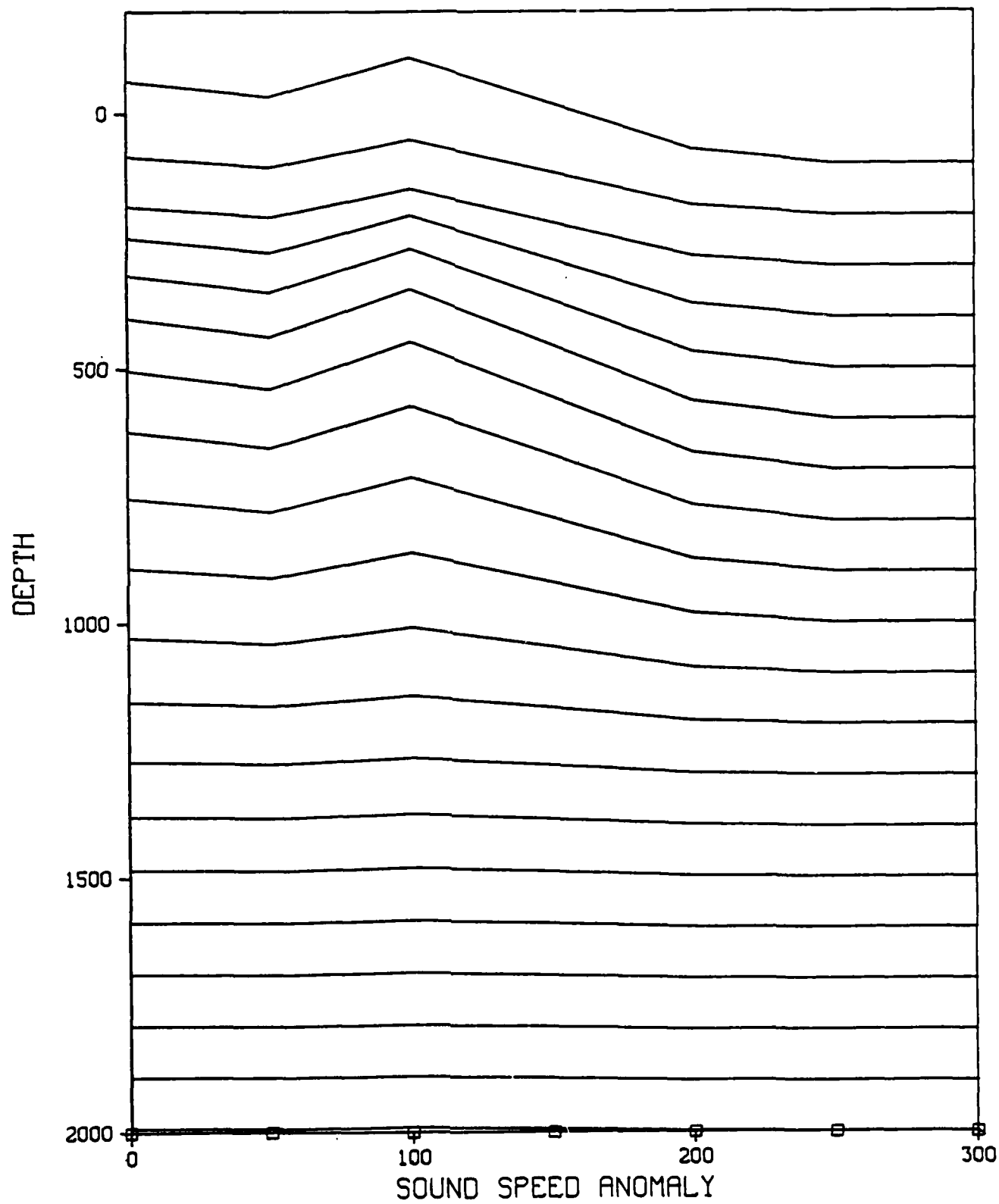


Fig 3

FRONTAL GEOSTROPHIC DYNAMICS

by

Benoit Cushman-Roisin  
Mesoscale Air-Sea Interaction Group  
The Florida State University  
Tallahassee, Florida 32306

April 1985

## ABSTRACT

From the primitive equations, simplified dynamics are derived that apply to frontal situations when interface slopes are important. The formalism, which eliminates inertial motions, is not unlike the derivation of the quasi-geostrophic equation. The difference is two-fold: while quasi-geostrophic dynamics apply for length scales on the order of the deformation radius with limitation to small interface variations, frontal geostrophic dynamics apply for finite interface variations but only at length scales large compared to the deformation radius (three times or more). When the length scale is on the order of the deformation radius and, simultaneously, the interface variations are finite, inertial oscillations cannot be filtered out, and the primitive equations ought to be retained.

In a reduced-gravity context, frontal geostrophic dynamics yield a single equation for the upper-layer depth. Although this equation is cubic in its variable, it is nonetheless considerably simpler than the primitive equations. It is suggested that the use of this equation can further advance the theoretical investigation of dynamical frontal processes.

Some particular solutions have been found. A new breed of waves is discovered. These waves propagate downstream (with the front on their left in the Northern Hemisphere) and are dispersive. They are neither like Kelvin, Rossby nor edge waves. Finally, a solution that corresponds to a time-dependent elliptical warm-core ring is also presented.

## 1. Introduction

Fronts are important natural barriers in the ocean. While they hinder horizontal transfers of heat, momentum and other properties, they play a crucial role in enhancing vertical exchanges. They are also a large reservoir of available potential energy, which often is released in the form of eddies and rings. Observations, especially recent satellite imagery, now document all these aspects in great detail, and the collected facts ask for explanations. For example, when a front shows signs of instability, why does backward wave breaking seem to be the rule (Thomson and Emery, 1985)? And, what governs the slow rotation of elongated rings (Spence and Legeckis, 1981)? There is nowadays a growing motivation to model and understand the physics at play as fronts appear, evolve, distort and break up.

By definition, fronts are regions of large horizontal gradient of certain properties, usually including density. With the superposition of the ubiquitous vertical stratification, fronts are marked by large pycnocline slopes, large in the sense that the depth variation of an isopycnal across a front is typically on the order of the isopycnal depth itself. Multi-layer systems are adequate models for the representation of fronts when interfacial displacements are on the order of the layer depths. In particular, a surface front can be modelled by the surfacing of the uppermost interface(s).

The simplest model of all, yet yielding a wealth of behaviors as illustrated below, is the reduced-gravity system with outcropping interface. In this model, only the uppermost layer is active, and the surface and interface that bound this layer by the top and bottom intersect along one or several lines. Each outcrop line represents a surface front. The present

paper is devoted to the dynamics of such simple frontal models, for there is much to be learned despite the oversimplifications. Thermodynamics do not fall under the scope of this restricted study, and mixing and dissipative mechanisms are therefore absent from the present formalism.

Two situations are possible. Either the outcrop line is open and the front is unidirectional (Example: Gulf Stream front), or the outcrop line is closed onto itself, forming a ring, and the front bounds a finite area (Example: Gulf Stream ring). The ring has a warm or cold core when the light, active layer is inside or outside the front, respectively. It is the author's conviction that rings, given their large thermocline slopes, are better described as such closed fronts rather than quasi-geostrophic features.

Despite its restricted vertical representation, the reduced-gravity model has the advantage of combining adequate horizontal resolution with simple governing equations. For instance, long after the two-layer, pioneering work of Orlanski (1968), most stability studies of frontal systems are now based on a reduced-gravity model. Stern (1980), and later Stern et al. (1982), showed that the coastal front forming the offshore limit of a coastal intrusion can undergo a variety of regimes, such as dispersion, wave steepening, breaking and blocking. On the other hand the open-ocean front where the interface extends from the front to infinity, a model of the Gulf Stream (Stommel, 1966, p. 109) and Kuroshio (Stommel and Yoshida, 1972), is stable to all small-amplitude perturbations (Paldor, 1983a). The double-front structure (band of light water) is unstable to small-amplitude, long-wave perturbations (Griffiths et al., 1982), whereas Paldor (1983b) concluded that the single front along a coast is stable to the same perturbations, arguing that the

double-front instability is caused by resonance. While these studies mentioned above rely on the hypothesis of uniform potential vorticity, Killworth and Stern (1982) demonstrated that the single front in the proximity of a coast is unstable to small-amplitude perturbations when the potential vorticity increases toward the coast. Beside stability of unidirectional fronts, the reduced-gravity model has been applied with success to the description (Csanady, 1979; Flierl, 1979) and evolution (Nof, 1981, 1983 and 1985; Killworth, 1983; Cushman-Roisin et al., 1985) of warm-core rings. All these studies illustrate the wealth of behaviors that are hidden in the yet simple reduced-gravity model with one active layer and demonstrate that this model is an adequate tool for some frontal problems. It simplifies the dynamics to a certain degree while it still retains many physical processes of practical concern.

It is well known, however, that the primitive equations (conservation of momentum, hydrostatic balance and conservation of volume) contain, as subsets, the quasi-geostrophic dynamics (Pedlosky, 1979; Williams and Yamagata, 1984; Cushman-Roisin, 1985) as well as inertial oscillations with a period less than a day in mid-latitudes. The question thus arises of the possibility to simplify further the primitive equations by eliminating the above two physical processes and retaining only the dynamics that specifically pertain to fronts. The hope is to establish even simpler equations which would lead to easier mathematical treatment thus improving our understanding of frontal dynamics and increasing our ability to comprehend observed phenomena. The philosophy is not unlike the one used in the derivation of the quasi-geostrophic formalism. At the onset, an assumption (small Rossby number) is made that

leads to a time scale larger than the inertial period, thus eliminating inertial oscillations. For the establishment of the quasi-geostrophic equation, the Rossby number is made small by requiring that interfacial displacements, and hence the associated geostrophic velocity, be small. On the other side, for the present derivation of a frontal geostrophic equation, when interfacial displacements are finite, the Rossby number is made small by requiring that the length scale be larger than the radius of deformation. In fact, it turns out that the Rossby number is then the square of the ratio of deformation radius over length scale and is thus small enough for practical purposes when the length scale is three times or more the deformation radius. Even typical, intense Gulf Stream rings (Olson et al., 1985) meet this assumption.

The paper is structured as follows. The derivation are presented in Section 2, where the key result is equation (16), called the frontal geostrophic equation. In Section 3, frontal geostrophic dynamics are contrasted with the well-known quasi-geostrophic dynamics. Section 4 is devoted to the integral and invariant properties. Section 5 treats the waves that can be supported by a rectilinear front. Section 6 presents a solution that corresponds to a time-dependent elliptical warm-core ring. Finally, Section 7 outlines less immediate applications of frontal geostrophic dynamics.

### 3. Frontal geostrophic dynamics

The equations that govern a system with one interfacial degree of freedom are those of the shallow-water, reduced-gravity model:

$$u_t + uu_x + vu_y - (f_0 + \tilde{\beta}_y)v = -g'h_x \quad (1)$$

$$v_t + uv_x + vv_y + (f_0 + \tilde{\beta}_y)u = -g'h_y \quad (2)$$

$$h_t + (hu)_x + (hv)_y = 0, \quad (3)$$

where  $x$  and  $y$  are the eastward and northward coordinate, respectively,  $u$  and  $v$  the vertically uniform, upper-layer velocity components along those directions,  $f_0 + \tilde{\beta}_y$  the local Coriolis parameter,  $g'$  the reduced gravity constant (the apparent gravity that a lower-layer particle would have in the upper layer), and  $h$  the upper-layer depth. Derivatives are denoted by subscripts. These equations govern the evolution of a two-layer system where the lower layer is at rest. A line along which  $h(x,y,t) = 0$  is an outcrop, or front, with one active layer on one side and a resting ocean on the other.

Various dynamical behaviors are obtained for various scaling combinations. In a previous paper (Cushman-Roisin, 1985), the author established the various regimes that are possible when the primary balance in equations (1) and (2) is the  $f$ -plane geostrophy, and distinguished twenty such regimes depending on length and velocity scales of the motion. The attention is drawn here on the three regimes that correspond to frontal situations (with beta effect negligible, relevant or dominant). The so-called frontal geostrophic dynamics are re-established here with full description of the consequences that they imply on the velocity field and of the invariant properties.



One first chooses a depth scale,  $H$ , such as a far-field depth or a typical initial depth of the system (the initial, center depth of a ring, for instance). Since fronts are the object of discussion and since they correspond to finite interface depth variations, spatial and temporal variations of  $h$  are also scaled by  $H$ . From the scale  $H$ , a radius of deformation can be constructed  $L_R = (g'H)^{1/2}/f_0$ . One then chooses a length scale,  $L$ , typical of distances over which the layer depth,  $h$ , changes by an order  $H$ . (The radius of the ring, for example). Use of the geostrophic balance in (1) and (2) provides the velocity scale (assumed to be the same in both directions)  $U = g'H/f_0L$ . With such scale, the Rossby number (measure of the nonlinear terms over the Coriolis term) is

$$\epsilon = \frac{U}{f_0L} = \frac{g'H}{f_0^2L^2} = \left(\frac{L_R}{L}\right)^2. \quad (4)$$

On the other side, the relative importance of the beta effect in the Coriolis term is

$$\beta = \frac{\tilde{\beta}L}{f_0} = \frac{L}{L_\beta}, \quad (5)$$

where  $L_\beta$  is the planetary scale, over which the curvature of the Earth should be taken into account. The main assumptions made here are

$$\epsilon \ll 1, \quad \beta \ll 1 \quad (6)$$

which are to say that the length scale of the motion must be somewhat greater than the deformation radius (three times or more) and much less than the planetary scale. In the open ocean, a typical deformation radius is 10km to 50km depending on the feature under study while the planetary scale is about

3500km at 30°N, and such intermediate scale are well possible. On the contrary, atmospheric motions for which the deformation is typically 1000km do not allow scale separation, assumptions (6) cannot be stated concomitantly, and the dynamics exposed in the present paper most likely have no relevance to atmospheric fronts.

A time scale,  $T$ , is also introduced, but will be constrained to meet the natural time scale of evolution of the motion characterized by  $H$  and  $L$ . The ratio of inertial period to motion time scale is written as  $\omega = 1/f_0 T$  and will be found a posteriori to be of order  $\epsilon^2$  or  $\beta\epsilon$ , whichever is greatest. This ratio is thus much less than unity.

With the previously stated scales, equations (1) to (3) are rendered dimensionless

$$\omega u_t + \epsilon(uu_x + vu_y) - v - \beta yv = -h_x \quad (7)$$

$$\omega v_t + \epsilon(uv_x + vv_y) + u + \beta yu = -h_y \quad (8)$$

$$\omega h_t + \epsilon(hu)_x + \epsilon(hv)_y = 0. \quad (9)$$

For  $\omega$ ,  $\epsilon$  and  $\beta$  small compared to unity, the momentum equations (7) and (8) can be expanded about the f-plane geostrophic balance

$$\begin{aligned} u &= -h_y + u_a, & u_a &= O(\omega, \epsilon, \beta) \\ v &= h_x + v_a, & v_a &= O(\omega, \epsilon, \beta) \end{aligned} \quad (10)$$

where the notation  $O(a, b, c, \dots)$  is to be interpreted as "on the order of the maximum of  $a, b, c, \dots$ ." This notation allows for a discussion of terms without a preliminary ranking of the dimensionless numbers. Implementation

of (10) into the continuity equation (9) yields

$$\omega h_t + \epsilon(hu_a)_x + \epsilon(hv_a)_y = 0. \quad (11)$$

This equation is made of two terms of respective orders  $O(\omega)$  and  $O(\epsilon\omega, \epsilon^2, \beta\epsilon)$ . Since the system chooses its time scale so as to match any disbalance among the diagnostic terms, the first term must be among the dominant ones, and  $\omega = O(\epsilon\omega, \epsilon^2, \beta\epsilon)$ . Since furthermore,  $\epsilon\omega \ll \omega$ , it results that  $\omega = O(\epsilon^2, \beta\epsilon)$  and that the time scale is related to the frontal depth and length scales,  $H$  and  $L$ , by

$$T = \frac{1}{f_0} \left(\frac{L}{L_R}\right)^4 \text{ or } \frac{1}{f_0} \frac{LL_g}{L_R^2}, \quad (12)$$

which ever is smallest. Typical numbers will be presented below.

With  $\omega = O(\epsilon^2, \beta\epsilon)$ , i.e. much less than both  $\epsilon$  and  $\beta$ , the time-derivative terms of (7) and (8) are negligible compared to the nonlinear and beta-correction terms. The dropping of these time-derivative terms corresponds to eliminating inertial oscillations from the formalism, and the last remaining time derivative in the continuity equation will correspond to a purely frontal mode.

Estimating the nonlinear and beta-correction terms of (7) and (8) by use of the  $f$ -plane geostrophic balance, one obtains the following expansion for the velocity components

$$\begin{aligned} u &= -h_y - \epsilon J(h, h_x) + \beta y h_y + O(\epsilon^2, \beta\epsilon, \beta^2) \\ v &= h_x - \epsilon J(h, h_y) - \beta y h_x + O(\epsilon^2, \beta\epsilon, \beta^2), \end{aligned} \quad (13)$$

where  $J(a,b) = a_x b_y - a_y b_x$  is the Jacobian operator. These expressions permit elimination of the velocity components in (9) or (11) to yield a single equation for the upper-layer depth,  $h$

$$\omega h_t - \epsilon^2 h J(h, \nabla^2 h) - \epsilon^2 h_x J(h, h_x) - \epsilon^2 h_y J(h, h_y) - \beta \epsilon h h_x = 0(\epsilon^3, \beta \epsilon^2, \beta^2 \epsilon).$$

This equation can be rewritten as

$$h_t - J(h, \frac{\epsilon^2}{\omega} (h \nabla^2 h + \frac{1}{2} \nabla h \cdot \nabla h) + \frac{\beta \epsilon}{\omega} y h) = 0, \quad (14)$$

where the error has now been neglected. Three regimes are possible: (i) the beta effect is negligible ( $\beta \ll \epsilon$  or  $L_R \ll L \ll L_R^{2/3} L_\beta^{1/3}$ ), and the equation is

$$(\omega = \epsilon^2)$$

$$h_t - J(h, h \nabla^2 h + \frac{1}{2} \nabla h \cdot \nabla h) = 0, \quad (15a)$$

or (ii) the beta effect is relevant ( $\beta \sim \epsilon$  or  $L \sim L_R^{2/3} L_\beta^{1/3}$ ), and the equation is

$$(\omega = \epsilon^2)$$

$$h_t - J(h, h \nabla^2 h + \frac{1}{2} \nabla h \cdot \nabla h + \frac{\beta}{\epsilon} y h) = 0, \quad (15b)$$

or (iii) the beta effect is dominant ( $\beta \gg \epsilon$  or  $L_R^{2/3} L_\beta^{1/3} \ll L \ll L_\beta$ ), and the equation is ( $\omega = \beta \epsilon$ )

$$h_t - h h_x = 0. \quad (15c)$$

The last two equations were first established by Williams and Yamagata (1984)

and labeled  $PG_2$  and  $PG_0$ , respectively (PG, standing for Planetary Geostrophic). They overlooked the possibility of negligible beta effect as in (15a) and, apparently, missed to realize the relevance of equations (15b-c) to ocean fronts.

The intermediate scale  $L_I = L_R^{2/3} L_\beta^{1/3}$  is the same as the one discovered by Charney and Flierl (1981) and Yamagata (1982). This is somewhat fortuitous, for the intermediate regime discussed by those authors is not of frontal type but rather is characterized by weak interfacial displacements (much lower Rossby number).

Equation (14), which encompasses all three sub-regimes (beta-effect negligible, relevant or dominant), can be expressed in dimensional variables

$$\frac{\partial h}{\partial t} = J(h, \frac{g'^2}{f_0^3} (h \nabla^2 h + \frac{1}{2} \nabla h \cdot \nabla h) + \frac{g' \tilde{\beta}}{f_0^2} y h). \quad (16)$$

This equation is called the "frontal geostrophic equation." The associated velocity components are

$$\begin{aligned} u &= - \frac{g'}{f_0} h_y - \frac{g'}{f_0^3} J(h, h_x) + \frac{g' \tilde{\beta}}{f_0^2} y h_y \\ v &= \frac{g'}{f_0} h_x - \frac{g'}{f_0^3} J(h, h_y) - \frac{g' \tilde{\beta}}{f_0^2} y h_x. \end{aligned} \quad (17)$$

It is recalled that the above expressions are conditional to assumptions (6), and an examination of the orders of magnitude is in order to determine

the range of applicability to ocean fronts. At  $30^\circ\text{N}$ , the Coriolis parameter  $f_0$  and the planetary scale,  $L_\beta = f_0/\tilde{\beta}$  are  $7 \cdot 10^{-5} \text{ s}^{-1}$  and 3500 km, respectively. For a density contrast of 2% ( $g' \approx 2 \cdot 10^{-2} \text{ ms}^{-2}$ ) and  $H=50 \text{ m}$ , typical values of open-ocean surface fronts, the deformation radius,  $L_R$ , is 14 km and the intermediate scale,  $L_I$ , 90 km. For a density contrast of 1.5% ( $g' \approx 1.5 \cdot 10^{-2} \text{ ms}^{-2}$ ) and  $H=400 \text{ m}$ , typical values for Gulf Stream rings, the deformation radius is 35 km and the intermediate scale is 160 km. The rule is as follows: if the motion length scale,  $L$ , is such that  $L$  is three times  $L_R$  or larger ( $\epsilon = L_R^2/L^2 \ll 1$ ) and much less than  $L_\beta$  ( $\beta = L/L_\beta \ll 1$ ), equation (16) applies. For the above two examples, the requirements are  $42 \text{ km} \lesssim L \ll 3500 \text{ km}$  and  $105 \text{ km} \lesssim L \ll 3500 \text{ km}$ , respectively. The time scale, given by (12), varies greatly with the length scale. For the above two examples, the time scales corresponding to the intermediate length scales are 260 and 76 days, respectively. At half that scale, the time scales are down to 16 and 5 days, respectively.

Equation (16), or its dimensionless version (14), is a single equation for the upper-layer depth, cubic in its variable, first-order in time and third-order in space. It can be integrated numerically by standard techniques. Since it has been constructed so that it retains frontal dynamics but not inertial oscillations, this frontal geostrophic equation is simpler than the primitive equations and is proposed as a new tool that can further advance the theoretical investigation of dynamical frontal processes.

### 3. Contrast with quasi-geostrophic dynamics

It is interesting to compare the previous formalism with the derivation of the quasi-geostrophic equation (Pedlosky, 1979, p. 86) and to stress the complementary aspects. Both formalisms are based on the assumption of a small Rossby number so that the velocity field can be split into an easily calculable geostrophic component and a much smaller ageostrophic correction. Also, in both contexts, the beta contribution in the Coriolis force is small and allowed to be on the order of the Rossby number. It results that the main balance in the momentum equation is the  $f$ -plane geostrophic equilibrium.

If the interfacial-displacement scale is  $\delta H$  (not necessarily equal to the mean depth layer,  $H$ ) and the motion length scale is  $L$  (not necessarily the deformation radius,  $L_R$ ), then, the  $f$ -plane geostrophy requirement provides the velocity scale

$$U = \frac{g' \delta H}{f_0 L}, \quad (18)$$

and it ensues that the Rossby number is

$$\epsilon = \frac{U}{f_0 L} = \frac{g' \delta H}{f_0^2 L^2} = \left( \frac{\delta H}{H} \right) \left( \frac{L_R}{L} \right)^2. \quad (19)$$

The Rossby number thus depends on two scales that characterize the motion:  $\delta H$  and  $L$ . Motions on the scale of the deformation radius ( $L=L_R$ ) are ageostrophic unless the interfacial displacements are small ( $\delta H \ll H$  and thus  $\epsilon \ll 1$ ), in which case the dynamics are quasi-geostrophic. On the other side, frontal motions with finite displacements ( $\delta H=H$ ) are ageostrophic unless the length scale is large compared to the deformation radius ( $L^2 \gg L_R^2$  and thus  $\epsilon \ll 1$ ),

in which case the dynamics are frontal geostrophic as described in the previous section. It is worth noting that the assumption required by frontal geostrophic dynamics is  $L^2 \gg L_R^2$  and not  $L \gg L_R$ . While mathematically these inequalities are equivalent, in practice the former is much less severe, and, with a 10% relative accuracy as it is usually acceptable in oceanography, the required assumption is  $L^2 \geq 10 L_R^2$  or  $L \geq 3.2 L_R$ .

It is instructive to compare the time scales that quasi-geostrophic and frontal-geostrophic dynamics impose. In both formalisms, the time scale is set by the mass-continuity requirement, (3), where the time rate of depth change is the result of divergence or convergence of fluid:

$$h_t \sim H(u_x + v_y),$$

after retention of the main terms. With a scale  $\delta H$  for  $h$  on the left-hand side, a scale given by (18) for  $u$  and  $v$ , and  $L$  for  $x$  and  $y$  on the right-hand side, and noting that  $u_x + v_y$  scales like  $\epsilon$  times the scale of each term separately (the  $f$ -plane geostrophic currents are non-divergent), one immediately determines the time scale:

$$T = \frac{1}{f_0} \left( \frac{\delta H}{H} \right)^{-1} \left( \frac{L_R}{L} \right)^{-2}. \quad (19)$$

For quasi-geostrophic dynamics ( $L = L_R$ ,  $\epsilon = \delta H/H$ ), the time scale is the inertial period divided by the Rossby number ( $T = \epsilon^{-1} f_0^{-1}$ ). For frontal-geostrophic dynamics ( $\delta H = H$ ,  $\epsilon = L_R^2/L^2$ ), the time scale is the inertial period divided by the *square* of the Rossby number, and frontal-geostrophic motions evolve much slower than their quasi-geostrophic counterpart at the



same Rossby number. Furthermore, the acceleration terms,  $u_t$  and  $v_t$  in (1) and (2), are comparable to or much less than the nonlinear advection terms for quasi- and frontal-geostrophic dynamics, respectively. This is the reason why the quasi-geostrophic equation has a dispersion term ( $\nabla^2 h_t$  term) but the frontal-geostrophic equation (16) does not.

Finally, one compares the potential vorticity expressions since both the quasi- and frontal-geostrophic equations are statements of conservation of potential vorticity by water columns. For the primitive-equation system (1) to (3), the expression of the potential vorticity is

$$pV = \frac{v_x - u_y + f_0 + \tilde{\beta}y}{h}.$$

In the quasi-geostrophic formalism, this expression is split into a mean, uniform and steady, value  $f_0/H$  to which corrections due to  $(v_x - u_y)$ ,  $(\tilde{\beta}y)$  and  $(h-H)$  are all small and on the same order. The equation then states the conservancy of the sum of these three corrections as it is carried around by the basic,  $f$ -plane geostrophic flow. On the other side, in the frontal-geostrophic formalism, the potential-vorticity expression is split into a primary, non-uniform and unsteady, contribution  $f_0/h$  to which corrections are brought by  $(v_x - u_y)$  and  $(\tilde{\beta}y)$ . Since the advection of  $f_0/h$  by the  $f$ -plane geostrophic flow is identically zero (there is no effect brought by the advection of a function of  $h$  along a line of constant  $h$ ), the equation then states the conservancy of the sum of two contributions: the first contribution is the advection of the potential-vorticity corrections by the  $f$ -plane geostrophic flow, while the second contribution is the advection of the primary potential-vorticity by the ageostrophic flow.

Overall, it is recognized that the quasi- and frontal-geostrophic formalisms are established by parallel mathematical developments but are based on opposite and complementary physical processes.

#### 4. Integral properties

This section examines, in the context of frontal geostrophic dynamics, integrated quantities and their time evolution. Several invariants are formulated. To simplify the mathematical treatment of integrals, the domain of fluid in motion is assumed to be finite and bounded all around either by rigid vertical walls (no normal velocity) or by fronts ( $h=0$ ).

It must be first realized that the assumption of large length scale, which has led to the geostrophic balance, excludes cases where fronts meet vertical walls. Indeed, along a front  $h$  vanishes, while along a wall  $h$  is uniform (no normal geostrophic flow) and thus also zero by continuity of  $h$ . Such situations cannot persist with time, and motions at the deformation-radius scale develop in the corner where the front meets the wall. These motions include inertial oscillations<sup>and</sup> do not fall in the context of frontal geostrophic dynamics. In summary, frontal geostrophic dynamics can take place if the finite domain is bounded either entirely by walls or by a single, closed front. [Domains of infinite extent are also mathematically acceptable as long as there is no front-wall intersection. Example: an infinitely long band of water contained between a front on one side and a wall on the other.]

For a finite domain, the above consideration leads to the following property. The integral of  $J(h,a)$  over the domain is identically zero for any expression  $a$ . The proof follows from the property  $h = 0$  or  $h = \text{uniform}$  along the closed boundary depending whether the boundary is a front or a wall.

One then defines the Lagrangian derivative

$$\frac{D}{Dt} = \frac{\partial}{\partial t} + \frac{\epsilon}{\omega} \left( u \frac{\partial}{\partial x} + v \frac{\partial}{\partial y} \right) = \frac{\partial}{\partial t} + \frac{1}{\delta} J(h, ) - \frac{\epsilon}{\delta} J(h, \nabla h) \cdot \nabla - \frac{\beta}{\delta} y J(h, ) + O(\delta), \quad (20)$$

where  $\delta = 0(\beta, \epsilon)$  whichever is greatest. Note that this material derivative is expressed in terms of the slow time that governs the overall evolution of the system rather than the geostrophic advection time scale which is much shorter but irrelevant for describing bulk properties. Using (20), one immediately deduces

$$\frac{D}{Dt} = \frac{\partial}{\partial t} - \frac{\epsilon}{\delta} J(h, \nabla h) \cdot \nabla h = J\left(h, \frac{\epsilon}{\delta} h \nabla^2 h + \frac{\beta}{\delta} y h\right) \quad (21)$$

$$\frac{D}{Dt} (dS) = \frac{1}{\delta} (u_x + v_y) dS = - J\left(h, \frac{\epsilon}{\delta} \nabla^2 h + \frac{\beta}{\delta} y\right) dS \quad (22)$$

where  $dS = dx dy$  is the area differential element and where the governing equation (14) has been used. As a result

$$\frac{D}{Dt} (h dS) = 0,$$

which states that volume is conserved as it ought to be. Conservation of volume expressed in this manner leads immediately to the integral result

$$\frac{d}{dt} \iint q h dS = \iint \frac{Dq}{Dt} h dS \quad (23)$$

that holds for any arbitrary expression  $q$ . The double integral covers the entire domain of fluid in motion.

For  $q = 1$ ,  $Dq/Dt = 0$ , and the total volume

$$V = \iint h dS \quad (24)$$

is obviously an invariant. More generally, it can be easily verified that for  $q = h^n$ ,  $hDq/Dt$  can be expressed as a sum of Jacobians each of the type  $J(h,a)$  and thus the integrals

$$I_n = \iint h^n dS,$$

for any exponent  $n$ , are all invariants.

For  $n=0$ , one obtains that the surface area of the fluid in motion is invariant. This result is obvious if all boundaries are rigid walls but is not a-priori evident if the fluid in motion is contained within a closed but deformable front. Cushman-Roisin et al. (1985) found that a pulsation mode for which the surface area shrinks and expands as the vortex deepens and shallows was possible but only at or about the inertial period. For frontal geostrophic dynamics, the time scale is much longer than the inertial period, and such pulsation cannot take place. On the other side, the slow steady rotation of an elliptical vortex, that the same authors obtained and for which area is invariant, is included in the frontal geostrophic dynamics (Section 6). From the conservation of area, it also ensues that infinite spreading of an initial isolated vortex such as a Gulf Stream ring is prohibited, even on a beta plane. In other words, as long as there is no lower-layer motion, there is no Rossby wave dispersion and no outward radiation of energy. Finally, it is noted that conservation of area is nothing but a statement that the leading-order potential vorticity,  $1/h$ , is conserved.

For  $n=2$ , one obtains that the total potential energy is conserved. At low Rossby number and with finite interface displacements, the kinetic energy is negligible, and the conservation of total energy reduces to invariance of potential energy.

Forming all possible linear combinations of the invariants  $I_n$ , one obtains that

$$\iint F(h) dS$$

is also invariant for any function  $F$  of  $h$ .

The coordinates of the center of mass,  $X$  and  $Y$ , are defined by

$$X = \frac{1}{V} \iint x h dS, \quad Y = \frac{1}{V} \iint y h dS, \quad (25)$$

where  $V$  is the volume defined in (24). The mean drift velocity of the vortex is then evaluated

$$\frac{dX}{dt} = \frac{1}{V} \iint \frac{Dx}{Dt} h dS = \frac{\beta}{\delta} \frac{1}{V} \iint y h h_y dS = - \frac{\beta}{2\delta} \frac{\iint h^2 dS}{\iint h dS}$$

$$\frac{dY}{dt} = \frac{1}{V} \iint \frac{Dy}{Dt} h dS = - \frac{\beta}{\delta} \frac{1}{V} \iint y h h_x dS = 0,$$

and one concludes that the center of mass drifts westward at a steady speed. Indeed, all terms entering in the expression for  $dX/dt$  are invariants and can be evaluated from the initial conditions only. Back with dimensions, this westward drift speed is

$$c = \frac{g' \tilde{\beta}}{2 f_0^2} \frac{\iint h^2 dS}{\iint h dS}. \quad (26)$$

This result is identical to the asymptotic expression of the bulk westward drift of an anticyclonic lens as derived by Nof (1981) when the eddy's size is much larger than the deformation radius. The present result is, however, more profound since (i) the drift evaluated here is found to be steady and not assumed to be so, and (ii), as it drifts westward, the vortex is free to evolve and deform around its center of mass unlike in Nof's analysis. Finally, as a

consequence of the large-scale requirement, inertial oscillations are eliminated, unlike in the study of Ball (1963) of contained motion on an f-plane at the deformation radius.

Angular momentum is not conserved on a beta plane. In the present context, the primary contribution to the total angular momentum is due to the f-plane rotating entrainment [Cushman-Roisin, et al. (1985)]:

$$M = \frac{1}{2} \iint [(x - X)^2 + (y - Y)^2] h dS$$

after scaling and is thus half of the moment of inertia,  $I$ . In other words, in the long-scale limit, angular momentum and moment of inertia are proportional and to be discussed together. The time rate of change of angular momentum is found to be

$$\frac{dM}{dt} = - \frac{\beta}{2\delta} \iint (x - X) h^2 dS \quad (27)$$

and is not, in general, a constant. On an f-plane, it is zero, and the angular momentum and moment of inertia are invariants. The mathematical structure of this time rate of change indicates that East-West asymmetries are important in controlling the moment of inertia. In particular, if the vortex is deeper on its eastern side, the integral in (27) is positive, the moment of inertia decreases, and the vortex contracts (inward motion of mass under constant area). This contraction persists until the time evolution of the structure has removed or reversed the asymmetry. Vice-versa, if the vortex is deeper on its western side, mass moves outward until the asymmetry is removed or reversed. The expulsion of mass away from the center is typical of instability and break

up of one initial vortex in or or several smaller ones. The previous result suggests that, on a beta plane, an initial deepening on the western flank may be the perturbation that triggers instability if the eddy is unstable. A thorough stability analysis should verify and document this point.



### 5. Small-amplitude frontal waves

The interfacial slope that is characteristic of a front can support trapped vorticity waves in a manner similar to planetary Rossby waves, topographic Rossby waves and edge waves. The major difference that sets frontal waves apart is the ability of the sloping "bottom" to evolve with the wave.

To study frontal waves in their purest form (i.e. with the minimum of parameters), the following formulation relies on the assumptions of an  $f$ -plane (no planetary vorticity gradient) and of a basic-state front with uniform slope (no intrinsic cross-frontal length). The dimensionless equation that governs the evolution of the interface is

$$h_t = J(h, h\nabla^2 h + \frac{1}{2} \nabla h \cdot h), \quad (28)$$

and the basic state is  $h = x$ , which is obviously a steady solution of (28). The mean position of the front is  $x = 0$ , and the fluid in motion is contained on the positive  $x$ -axis side ( $h > 0$ ). The frontal slope is unity since the arbitrary length and depth scales used to render (28) dimensionless can be so chosen.

A small-amplitude frontal wave is then superimposed:  $h = x + n$ ,  $|n| \ll 1$ . It is governed by the linearized equation

$$\begin{aligned} n_t &= J(x, x\nabla^2 n + n_x) \\ &= x\nabla^2 n_y + n_{xy}, \end{aligned} \quad (29)$$

must be bounded at the front mean position ( $x=0$ ) and ought to decay to zero far away from the front (trapped wave). The most general solution is a superposition of Fourier modes of the type

$$\eta(x,y,t) = \bar{\eta}(x) \exp [ik(y - ct)], \quad (30)$$

where  $\bar{\eta}(x)$  is the cross-front structure to be determined,  $k$  and arbitrary along-front wavenumber that can always be chosen as a real positive constant, and  $c$  the phase speed for that wavenumber. This phase speed is to be determined as a function of  $k$ . Implementation of (30) in (29) yields an eigenvalue problem for  $c$  and  $\bar{\eta}(x)$ :

$$x \frac{d^2 \bar{\eta}}{dx^2} + \frac{d\bar{\eta}}{dx} + (c - k^2 x) \bar{\eta} = 0 \quad (31)$$

$$\lim_{x \rightarrow 0} \bar{\eta} < \infty, \quad \lim_{x \rightarrow \infty} \bar{\eta} = 0.$$

The following change of variable and function

$$\xi = 2kx, \quad \bar{\eta}(x) = \tilde{\eta}(\xi) e^{-\xi/2}$$

turns the equation in the Laguerre type

$$\xi \frac{d^2 \tilde{\eta}}{d\xi^2} + (1 - \xi) \frac{d\tilde{\eta}}{d\xi} + a \tilde{\eta} = 0, \quad a = \frac{c}{2k} - \frac{1}{2}.$$

The first boundary condition eliminates one category of solutions with logarithmic singularity at the front, and all solutions are integer-power series. The other boundary condition requires these series to grow less than  $\exp(\xi/2)$  toward infinity, and constrains the series to be terminated after a finite number of terms. The resulting solutions are the Laguerre polynomials and the constant  $a$  must be a nonnegative integer. The reconstructed solution is

$$\bar{\eta}_n(x) = L_n(2kx) e^{-kx} \quad (32a)$$

$$c_n = (2n + 1)k \quad (32b)$$

where  $L_n$  is the Laguerre polynomial of degree  $n$  ( $n = 0, 1, 2, \dots$ ). In particular the first two modes are

$$c_0 = k \quad \bar{n}_0(x) = e^{-kx}$$

$$c_1 = 3k \quad \bar{n}_1(x) = (1 - 2kx)e^{-kx}.$$

These frontal waves have the following properties. They are trapped waves that decay exponentially away from the front. The e-folding trapping scale is the along-front wavelength (divided by  $2\pi$ ). All waves are stable ( $c$  real) and propagate with the front on their left ( $c$  positive) in the northern Hemisphere. This is also the downstream direction of the geostrophic flow along the front. The waves are also dispersive with the longest and least trapped waves propagating the slowest (Figure 1).

Similar waves were studied and discussed by Paldor (1983a and b). In those studies, inertial motions at the radius of deformation and a less simple frontal structure were included, at the cost of not finding a closed analytical form for the wave cross-frontal structure. Finally, it should be noted that frontal waves are neither edge waves, which propagate with the edge on their right and for which phase speed decreases with wavenumber, nor baroclinic waves, which require at least two layers in motion (Orlanski, 1968). It is, however, anticipated that inclusion of baroclinicity could profoundly affect the stability properties of frontal waves (Killworth et al., 1984).

The above solution perhaps shows the frontal waves in their purest form. The advantage of the simple, analytical expression could now serve as a basis to study the nonlinear evolution of finite-amplitude frontal waves. In particular, it would be interesting to contrast the nonlinear instability and engulfment processes demonstrated by Stern and Pratt (1985) and Stern (1985) in

a quasi-geostrophic context with the corresponding processes in the frontal geostrophic framework. The comparison would be most enlightening, for actual oceanic fronts such as the north wall of the Gulf Stream are neither quasi-geostrophic nor frontal geostrophic but rather in between.

## 6. Elliptical warm-core rings

This section presents another solution on an  $f$ -plane. It consists of a time-dependent lens of water, bordered all around by an outcropping interface. The depth profile is chosen as a quadratic expression of the coordinate variables:

$$h = Ax^2 + 2Bxy + Cy^2 + 2Dx + 2Ey + H \quad (33)$$

with  $A$  and  $C$  negative and  $AC > B^2$  so that the  $h$  contours are closed lines (ellipses) with positive depths inside the frontal line  $h=0$ . Expression (33) is an exact solution of (16), when  $\tilde{\beta}=0$ , provided that the six coefficients  $A$  to  $H$  depend on time. Their time dependence is governed by equations obtained by identifying terms of similar powers of  $x$  and  $y$ . One thus obtains a 6-by-6 nonlinear system of equations.

Initial conditions can always be chosen such that the center of the eddy is at the center of the coordinate axes, and  $D=E=0$  initially. The equations governing time changes of  $D$  and  $E$  (not written here) then show that  $D$  and  $E$  remain zero at subsequent times. Physically, this implies that the eddy's center of mass is a fixed point as it ought to be on an  $f$ -plane (Section 4). Another consequence obtained from the equation governing the change of  $H$  is that  $H$  remains constant. The maximum depth of the eddy at its center is thus invariable.

The remaining equations governing the changes of  $A$ ,  $B$  and  $C$  with time are:

$$\frac{dA}{dt} = 8 \frac{g'^2}{f^3} \Delta B \quad (34a)$$

$$\frac{dB}{dt} = -4 \frac{g'^2}{f^3} \Delta (A - C) \quad (34b)$$

$$\frac{dC}{dt} = -8 \frac{g'^2}{f^2} \Delta B \quad (34c)$$

where  $\Delta = AC - B^2$ . This system is nonlinear. However, one notes that  $d\Delta/dt$  is identically zero,  $\Delta$  is thus a constant with time, and the system takes a linear form. The general solution can be easily found, and the reconstructed height profile is

$$h = H - [A_0 + A_1 \sin(\omega t + \phi)]x^2 - 2[A_1 \cos(\omega t + \phi)]xy - [A_0 - A_1 \sin(\omega t + \phi)]y^2, \quad (35)$$

where  $H$ ,  $A_0$ ,  $A_1$  and  $\phi$  are arbitrary constants, and the frequency  $\omega$  is given by

$$\omega = 8 \frac{g'^2}{f^3} (A_0^2 - A_1^2). \quad (36)$$

A rotation of coordinates shows that the solution corresponds to an elliptical eddy of fixed shape that rotates steadily clockwise at the rate  $\omega/2$ . In terms of the mean radius,  $R$ , of the elliptical outcrop line (square root of product of semi-major and semi-minor axes), the steady rotation rate takes the form

$$\sigma = 4 \frac{g'^2 H^2}{f^3 R^4} = 4f \left( \frac{L_R}{R} \right)^4, \quad (37)$$

where  $L_R$  is the radius of deformation based on the center depth. Since the basic assumption for the basis of frontal geostrophic dynamics in  $R^2 \gg L_R^2$ , it follows that this rotation rate is very slow.

The above solution is the asymptotic expression of the Rodon solution (Cushman-Roisin, et al., 1985) as the size becomes large. However, no

guesswork is evoked here, and the solution for the time-dependent problem is constructed systematically. One notes that the other modes discussed by Cushman-Roisin et al. (1985), viz. inertial oscillation of center of mass, pulsation of a circular vortex and superinertial rotation of an elliptical eddy, are all absent from the present model. The reason lies in the filtering of all inertial and superinertial motions by the long-scale assumption.

How long does the long length scale have to be for the frontal geostrophic dynamics to be applicable is a question that can be answered in the present, particular instance. Figure 2 displays the eddy's clockwise rotation rate as a function of the ratio eddy radius over deformation radius. One curve corresponds to the present solution, (37), while the other is taken from Cushman-Roisin et al. (1985). The agreement is quantitatively good for  $R > 4L_R$  and qualitatively acceptable down to  $R > 3L_R$ . As anticipated in section 2, the length scale of the motion does not need to be much larger than the deformation radius for frontal geostrophic dynamics to reproduce quite correctly the subinertial characteristics of frontal behavior.

An advantage of the present solution, viz. expression (35), is its analytical simplicity. Taking advantage of this simplicity opens the door to further investigations such that stability analysis and inclusion of baroclinicity. Indeed, it is possible that elliptical eddies can be stable or unstable depending on the eccentricities. Kirchoff's vortex (Kirchoff, 1976; Lamb, 1932) of the two-dimensional Euler equations was found unstable if the ratio semi-major axis over semi-minor axis exceeds the value 3 (Love, 1893). It would be of great interest to obtain the corresponding threshold value in the context of the shallow-water equations.

Instability can also be a result of release of potential energy (baroclinic instability mechanism). To include this process, at least a second layer must be set in motion, an addition which may not be too difficult within the present simplified context.



## 7. Conclusions

A simplified equation that governs the height-field evolution near a front has been established under certain limitations. These include the absence of baroclinic-instability mechanism (reduced-gravity model) and a long-scale assumption (length scale at least three times the deformation radius). The momentum balance is mainly geostrophic in both along- and cross-frontal directions, but the evolution critically depends on the small, ageostrophic effects, which are retained in the formalism.

The advantage of the equation is its retention of only subinertial motions that can occur in the vicinity of an outcropping interface (front). The elimination of less relevant processes such as inertial oscillations and quasi-geostrophic dynamics renders the mathematical problem quite simple. It is suggested that new models taking advantage of this simplicity in formalism will further advance our physical understanding of fronts, both open (Gulf Stream front) and closed (Gulf Stream ring, for instance).

Analogies with the quasi-geostrophic formalism are drawn in details, and the complementary aspects of the two approaches are stressed. Invariants are studied as a way of understanding some of the general properties of the governing equations. Finally, some solutions have also been established.

It should be noted that the frontal geostrophic dynamics discussed here (for which the geostrophic balance almost holds in both horizontal directions) are separate from the semi-geostrophic dynamics established by Stern (1980) (where the geostrophic balance almost holds only in the cross-frontal direction). Front modellers thus have at their disposal, in increasing order of mathematical complexity, geostrophic, semi-geostrophic and ageostrophic formalisms.

The implementation of frontal geostrophic dynamics can be used to study a great variety of problems. Two come to mind immediately: (i) the stability study of the elliptical warm-core ring of the exact solution presented here, and (ii) the finite-amplitude evolution and eventual breaking of long waves along an otherwise rectilinear front. On one side, it is anticipated that very elongated eddies will break up into several, more circular ones, and that there is an eccentricity threshold below which the eddy revolves as a whole and beyond which it is unstable and splitting. Indeed, no observations reveal the presence of very elongated, isolated warm-core rings. On the other side, although baroclinic instability processes can initiate the growth of a first disturbance, the further development and eventual separation of the meander as an eddy may well be controlled and described by dynamics more intrinsic to fronts (Stern, 1985). Frontal geostrophic dynamics will not provide definite answers but can guide modellers toward deeper understanding of pinching-off processes. In particular, it is envisioned that the results gleaned separately by the quasi-geostrophic theory, the vorticity-front model (Stern, 1985) and the present frontal geostrophic dynamics, all based on extreme but different assumptions, will bring a clearer picture of what is happening in the real ocean, where none of the assumption truly holds.

A generalization of the frontal geostrophic formalism to two or multiple layers is possible, but not evident. It may be possible, for example, that a two-layer system be governed by frontal dynamics in the upper layer and quasi-geostrophic dynamics in the lower layer. Such extension is now in the works, and is postponed to another article. Also in the works is a numerical

discretization technique that can solve the governing equation for the height field by tracking the trajectories of a limited number of water columns of fixed heights in a way not unlike the point-vortex method.

### Acknowledgements

The author remembers helpful discussions with many colleagues, the list of names of which would be too long to reproduce here. Support for this research was provided by the Office of Naval Research, and this article constitutes contribution No. \_\_\_\_ of the Geophysical Fluid Dynamics Institute at the Florida State University.

## REFERENCES

- Ball, F. K., 1963: "Some general theorems concerning the finite motion of a shallow rotating liquid lying on a paraboloid," J. Fluid Mech., 17, 240-256.
- Charney, J. G., and G. R. Flierl, 1981: "Oceanic analogues of large-scale atmospheric motions," in Evolution of Physical Oceanography, MIT press, 504-548.
- Csanady, G. T., 1979: "The birth and death of a warm core ring," J. Geophys. Res., 84, 777-780.
- Cushman-Roisin, B., 1985: "Toward a unified theory of geostrophic regimes Part 1: Mid-latitude reduced-gravity system," submitted to Geophys. Astrophys. Fluid Dyn.
- Cushman-Roisin, B., W. H. Heil, and D. Nof, 1985: "Oscillations and rotations of elliptical warm-core rings," J. Geophys. Res., in press.
- Flierl, G. R., 1979: "A simple model for the structure of warm and cold core rings," J. Geophys. Res., 84, 781-785.
- Griffiths, R. W., P. D. Killworth, and M. E. Stern, 1982: "Ageostrophic instability of ocean currents," J. Fluid Mech., 117, 343-377.
- Killworth, P. D., 1983: "On the motion of isolated lenses on a beta-plane," J. Phys. Oceanogr., 13, 368-376.
- Killworth, P. D., and M. E. Stern, 1982: "Instabilities on density-driven buoyancy currents and fronts," Geophys. Astrophys. Fluid Dyn., 22, 1-18.
- Killworth, P. D., N. Paldor, and M. E. Stern, 1984: "Wave propagation and growth on a surface front in a two-layer geostrophic current," J. Mar. Res., 42, 761-785.
- Kirchoff, G., 1876: Vorlesungen über Mathematische Physik, Vol. 1, Leipzig: Teubner, 466 pp.
- Lamb, H., 1932: Hydrodynamics, Dover Publ., 6th Ed., 738 pp.
- Love, A. E. H., 1893: "On the stability of certain vortex motions," Proc. London Math. Soc., Ser. 1, 25, 18-43.
- Nof, D., 1981: "On the  $\beta$ -induced movement of isolated baroclinic eddies," J. Phys. Oceanogr., 11, 1662-1672.

- Nof, D., 1983: "On the migration of isolated eddies with application to Gulf Stream rings," J. Mar. Res., 41, 399-425.
- Nof, D., 1985: "On the ellipticity of isolated anticyclonic eddies," Tellus, 37A, 77-86.
- Olson, D. B., R. W. Schmitt, M. Kennelly, and T. M. Joyce, 1985: "A two-layer diagnostic model of the long term physical evolution of warm core ring 82B," J. Geophys. Res., in press.
- Orlanski, I., 1968: "Instability of frontal waves," J. Atm. Sci., 25, 178-200.
- Paldor, N., 1983a: "Linear stability and stable modes of geostrophic fronts," Geophys. Astrophys. Fluid Dyn., 24, 299-326.
- Paldor, N., 1983b: "Stability and stable modes of coastal fronts," Geophys. Astrophys. Fluid Dyn., 27, 217-228.
- Pedlosky, J., 1979: Geophysical Fluid Dynamics, Springer-Verlag, 624 pp.
- Spence, T. W., and R. Legeckis, 1981: "Satellite and hydrographic observations of low-frequency wave motions associated with a cold core Gulf Stream ring," J. Geophys. Res., 86, 1945-1953.
- Stern, M. E., 1980: "Geostrophic fronts, bores, breaking and blocking waves," J. Fluid Mech., 99, 687-703.
- Stern, M. E., 1985: "Lateral wave breaking and 'shingle' formation in large scale shear flow," J. Phys. Oceanogr., in press.
- Stern, M. E., J. A. Whitehead, and B.-L. Hua, 1982: "The intrusion of a density current along the coast of a rotating fluid," J. Fluid Mech., 123, 237-265.
- Stern, M. E., and L. J. Pratt, 1985: "Dynamics of vorticity fronts," J. Fluid Mech., in press.
- Stommel, H., 1966: "The Gulf Stream: A physical and dynamical description, Second Ed., Univ. of California Press and Cambridge Univ. Press, 248 pp.
- Stommel, H., and K. Yoshida, 1972: "Kuroshio. Physical aspects of the Japan current," Univ. of Washington Press, 517pp.
- Thomson, R. E., and W. J. Emery, 1985: EOS, to appear.

Williams, G. P., and T. Yamagata, 1984: "Geostrophic eddies, intermediate solitary vortices and Jovian eddies," J. Atm. Sci., 41, 453-478.

Yamagata, T., 1982: "On nonlinear planetary waves: A class of solutions missed by the quasi-geostrophic approximation," J. Oceanogr. Soc. Japan, 38, 236-244.

## FIGURE LEGENDS

- Figure 1. Plot of the frequency versus wavenumber for waves along a front of uniform slope. These waves propagate with the front on their left (northern hemisphere) and are dispersive with the longest and least trapped waves propagating the slowest.
- Figure 2. Plot of the steady rotation rate of an elliptical eddy versus the ratio eddy radius over deformation radius. One curve corresponds to the present, long-scale approximation, (37), while the other corresponds to the exact analytical solution proposed by Cushman-Roisin et al. (1985).



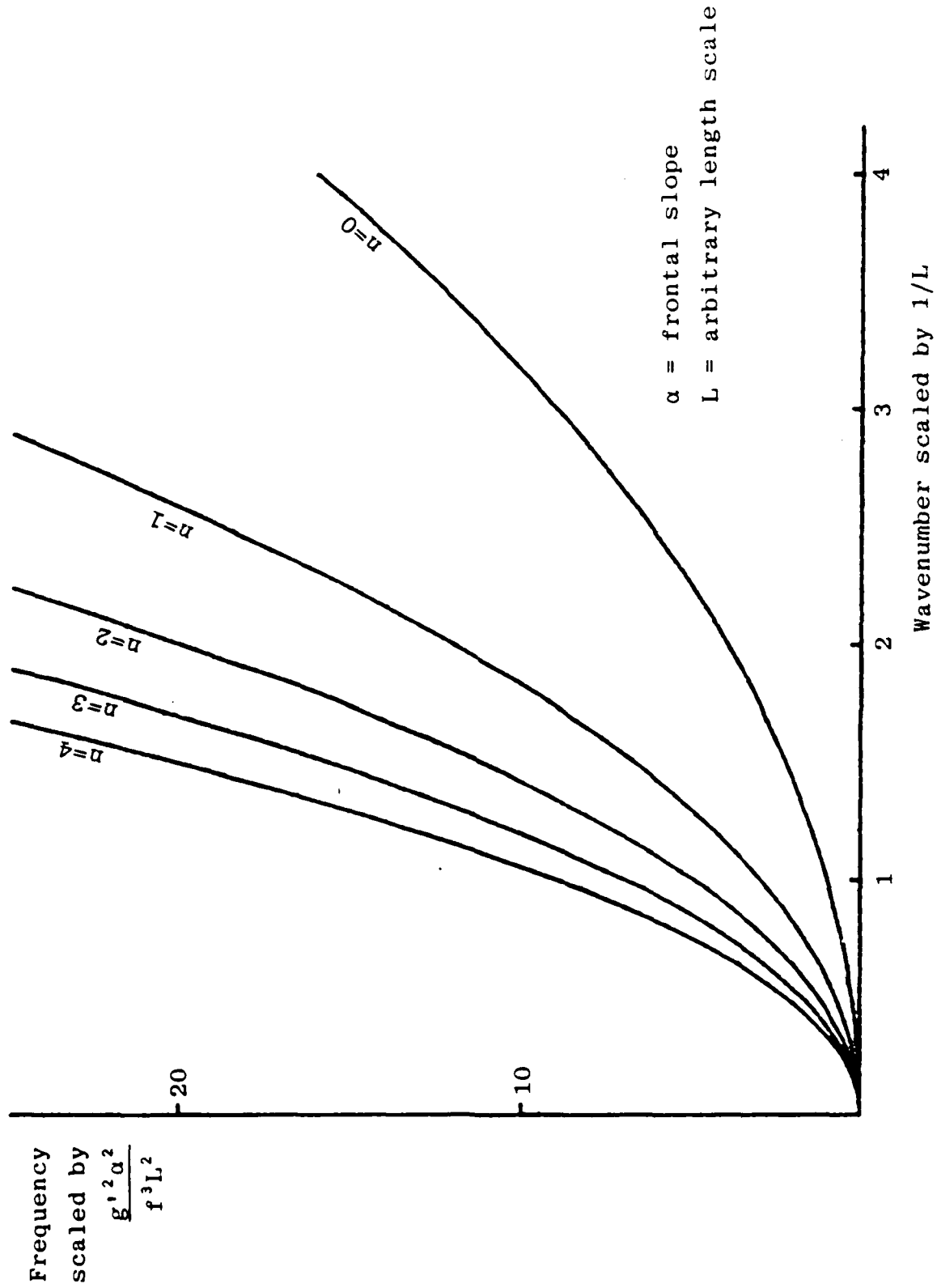


Figure 1. Plot of the frequency versus wavenumber for waves along a front of uniform slope. These waves propagate with the front on their left (northern hemisphere) and are dispersive with the longest and least trapped waves propagating the slowest.

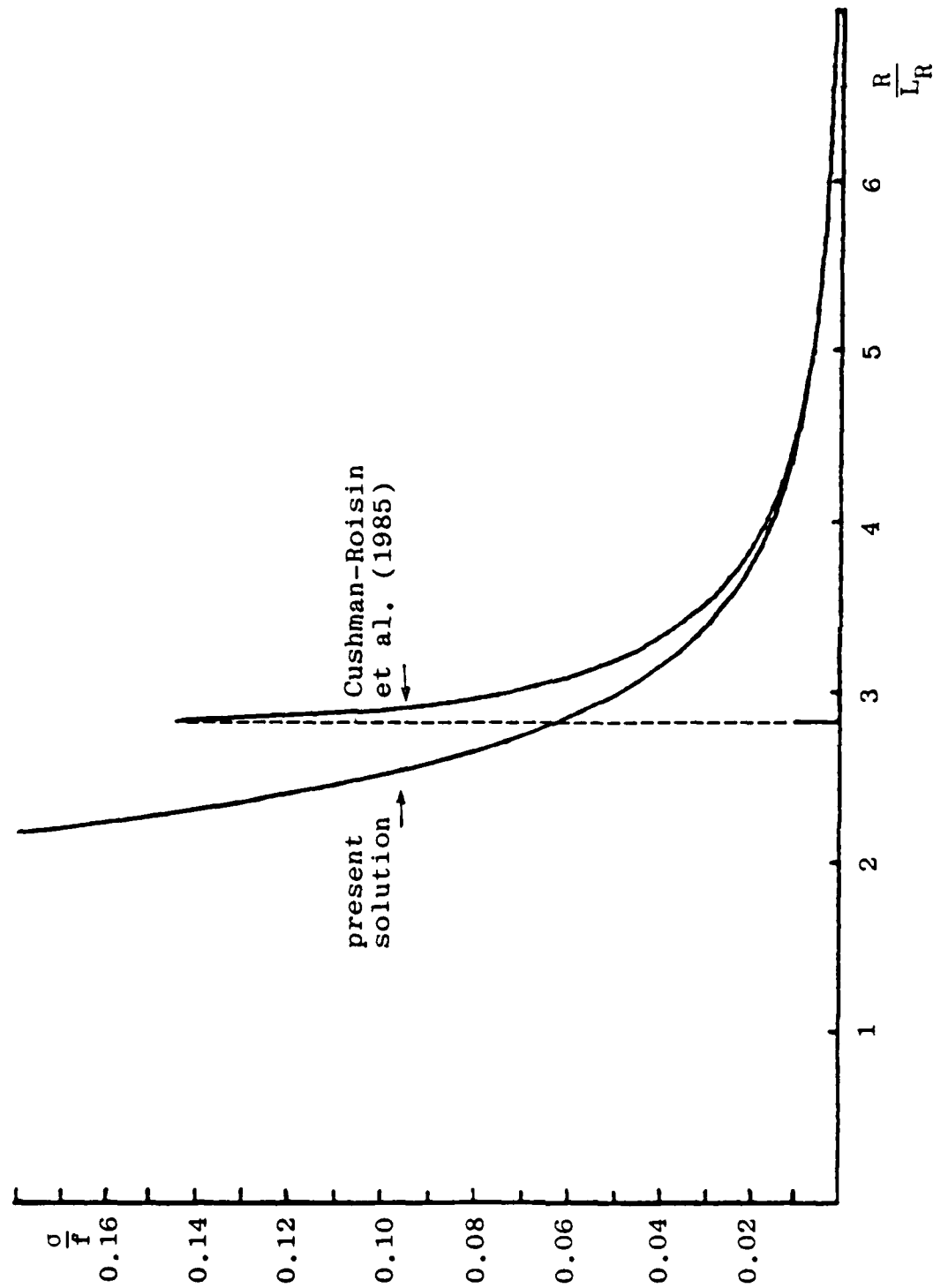


Figure 2. Plot of the steady rotation rate of an elliptical eddy versus the ratio eddy radius over deformation radius. One curve corresponds to the present, long-scale approximation, (37), while the other corresponds to the exact analytical solution proposed by Cushman-Roisin et al. (1985).

AD-A162 506

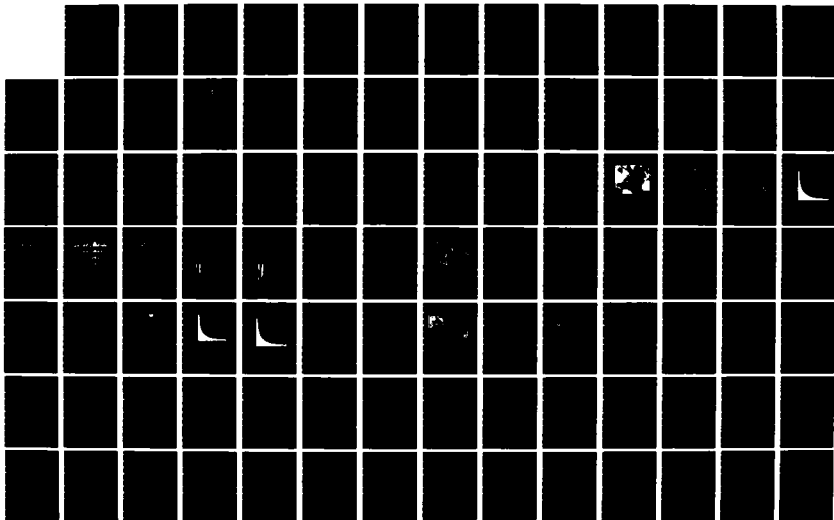
PROCEEDINGS OF THE GULF STREAM WORKSHOP HELD AT WEST  
GREENWICH RHODE ISLA (U) RHODE ISLAND UNIV KINGSTON  
GRADUATE SCHOOL OF OCEANOGRAPHY D R WATTS APR 85  
N00014-85-G-0322

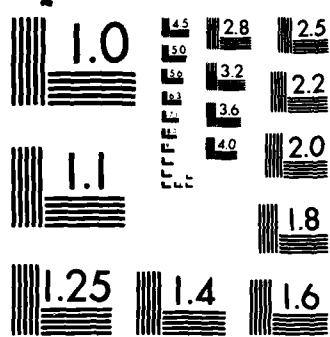
4/7

UNCLASSIFIED

F/G 8/3

NL





MICROCOPY RESOLUTION TEST CHART  
NATIONAL BUREAU OF STANDARDS-1963-A

An Analysis of Gulf Stream Mean Flow Energetics off Charleston, South Carolina

William K. Dewar and John M. Bane, Jr.

Marine Sciences Program  
12-5 Venable Hall 045A  
University of North Carolina at Chapel Hill  
Chapel Hill, N.C. 27514

ABSTRACT

The energy budget of the mean flow in the Gulf Stream off the coast of South Carolina is computed. The results of this analysis are: (1) The mean Gulf Stream kinetic energy flux increases downstream at a rate of  $(2.17 + .98) \times 10^{-2} \text{ ergs cm}^{-3} \text{ sec}^{-1}$ ; (2) The eddies decelerate the mean flow at a rate of  $(-.57 + 1.3) \times 10^{-2} \text{ ergs cm}^{-3} \text{ sec}^{-1}$ ; (3) In order that the mean energy equation be balanced, the Gulf Stream in the South Atlantic Bight (SAB) must be releasing mean potential energy by flowing down a mean pressure gradient. Thus our measurements suggest the Gulf Stream is measurably ageostrophic in the downstream direction. The downstream pressure gradient inferred at our array site is consistent with published estimates of mean alongshore pressure gradients in the SAB; however, the partitioning of the pressure force between mean acceleration and eddy Reynolds stress is most likely local. We also estimate the net loss from the mean potential energy in the SAB using our measured conversion rate and demonstrate that it compares in magnitude but is opposite in sign to that thought to occur downstream of Cape Hatteras. Thus we argue that the Gulf Stream in the SAB is exhibiting some of the properties of the inflow regions of western boundary layers in inviscid inertial models of the circulation. Our measurements, however, also indicate the presence of vigorous eddies whose effects in the mean energy equation are potentially sizeable. Such eddies are, of course, not contained in strictly inviscid, inertial models of the western boundary layer.

INTRODUCTION

Although the potential vorticity dynamics of western boundary layers are now well-known from a theoretical point of view, a comparable understanding of the constraints on western boundary layer energy is just emerging (Fofonoff, 1981; Fofonoff and Hall, 1983). One of the most model dependent characteristics of the western boundary energy concerns the release of mean potential energy by flow down a mean pressure gradient in the boundary layer. If the boundary layer is presumed to be frictional, as in Stommel (1947) or Munk (1949), the energy released in this manner is irreversibly lost. The other extreme is represented by the inviscid, inertial model proposed by Fofonoff (1954). The mean potential energy release in this case is used to intensify the mean kinetic energy on the western boundary. Conversely, the flow proceeds up a mean pressure gradient on the eastern basin boundary and the kinetic energy is reconverted to potential energy. It is a general property of inertial general circulation models that energy is recirculated in this manner.

In the present paper, we use data from the Gulf Stream Deflection and Meander Energetics Experiment (DAMEX, Bane and Dewar, 1983) to examine the mean flow energetics of the Gulf Stream in the South Atlantic Bight (see Fig. 1.). We deduce that the mean kinetic energy equation requires a potential energy release by flow down a mean pressure gradient in order to be balanced. The inferred energy release occurs at a rate comparable in magnitude but opposite in sign to that which apparently occurs further downstream (Fofonoff and Hall, 1983); thus, we support the conjecture of Fofonoff (1981) that the Gulf Stream recirculates energy. The force balance as we measure it appears to be local, however, and possible reasons for this are discussed. The recirculation of energy suggests that the Gulf Stream possesses some inertial characteristics. However, eddies also appear to be non-negligible in their effects in the mean energy equation and thus the comparison of the oceanic Gulf Stream with inviscid, inertial models is not immediate. We end by speculating on how the eddies influence the integrated Gulf Stream force balance.

#### THE DAMEX EXPERIMENT AND DATA PROCESSING

The field phase of DAMEX took place from September 1981 to April 1982, and consisted of current meter mooring deployments, hydrographic surveys, and AXBT surveys. We shall be primarily concerned with a subset of the current meter data. Fourteen Aanderaas RCM-4 current meters on seven moorings were placed in three locations along the continental margin. The study area is shown in Fig. 2 and details about the moorings are provided in Table I. Arrays E and F were located immediately upstream and downstream of the Charleston bump respectively. A single mooring, G, was located off Onslow Bay.

We will discuss the data from array E. Array E consisted of three moorings deployed in an L-shaped configuration (see Fig. 2). Two of the moorings in this array were located on the 400 m isobath and the remaining mooring was located on the 300 m isobath. Two current meters were supported at nominal depths of 210 m and 270 m by each mooring.

The current meters recorded temperature, conductivity, current speed and current direction at 30 minute intervals. The raw data were low-pass filtered in the manner of Hood and Bane (1983) using a Lanczos-type filter (Brooks, 1976) with a quarter power point at 1 cycle/40 hours and an energy rejection factor of  $10^{-6}$  at 1 cycle/12 hours. The resulting time series had an equivalent sampling interval of 6 hours. Complete documentation of the data, processing methods, and related topics are given in Bane and Dewar (1983).

The mean flow energy budget requires estimates of the means and variances of several quantities. The values of such quantities are quite dependent on depth in the DAMEX study area (see Table 2) due to the strong vertical shear of the Gulf Stream. We have attempted to minimize this effect in our calculations at array E by first computing the required means and variances at each current meter and then linearly interpolating them to a standard depth. Failure of the bottom instrument from one of the E

moorings forced us to use the depth of the top meter at that mooring (219 m) as the standard depth.

Errors for the means and variances have been computed as described in Dewar and Bane (1984). Errors for the linearly interpolated quantities and the terms in the energy equations have been calculated using standard formulae for the sums and products of independent quantities (see for example Bevington, 1969).

## RESULTS

In this section we discuss and compare the estimates of the terms in mean kinetic energy equation. We assume throughout that the Boussinesq equations apply. We briefly mention the derivations of the equation; complete analyses are given in Brooks and Niiler (1977) and Szabo and Weatherly (1979).

An analysis of the mean flow kinetic energy equation using current meter data is of necessity incomplete, as not all the terms in those equations can be estimated. In particular, we have no direct measurements of vertical velocity nor reliable measurements of pressure at a fixed depth. Thus, it must be borne in mind when estimates are presented in the following section that some terms might have been omitted. For example, our estimate of the divergence of mean kinetic energy flux does not include vertical advection. Other instances where such omissions occur should be apparent.

### Mean Kinetic Energy at E

The mean kinetic energy equation is obtained by ensemble averaging the horizontal momentum equations and vector multiplying the result by the ensemble averaged horizontal velocity:

$$\frac{\partial}{\partial x_j} \langle u_j \rangle \langle u_\alpha \rangle^2 / 2 = - \frac{\partial}{\partial x_\alpha} \langle p \rangle \langle u_\alpha \rangle - \langle u_\alpha \rangle \frac{\partial}{\partial x_i} \langle u'_i u'_\alpha \rangle \quad (\text{Eq. 1})$$

where Greek indices obtain the values 1 and 2.  $(x_1, x_2, x_3) = (x, y, z)$  are eastward, northward, and vertical position variables and  $(u_1, u_2, u_3) = (u, v, w)$  are the eastward, northward and vertical velocities.  $P$  is pressure. The angle brackets  $\langle \rangle$  denote an ensemble average and the primes denote fluctuations about that average. Eq. (1) relates the divergence of the mean flux of kinetic energy to mean pressure work and the eddy acceleration of the mean flow. Mean potential energy enters implicitly in Eq. (1) through pressure work. Several of the means and covariances listed in Eq. (1) as measured at array E are given in Table 2. Means and covariances interpolated to the standard depth of 219 m are listed in Table 3. We are able to directly estimate two of the three terms on the left hand side of Eq. (1) and four of the six terms in the second quantity on the right hand side of Eq. (1). The values of these estimates using the standard depth quantities are listed in Table 4.

The individual terms involved in the mean flow acceleration by the eddies are at best marginally significant. Their sum:

$$-\langle u_{\alpha} \rangle \frac{\partial}{\partial x_j} \langle u'_{\alpha} u'_j \rangle = [-.57 \pm 1.3] \times 10^{-2} \text{ ergs cm}^{-3} \text{ sec}^{-1}$$

is therefore not significantly different from zero and indicates no measurable eddy effect on the mean. It is worth remarking, however, that the sign of the measured quantity is negative and would otherwise indicate an eddy deceleration of the mean.

The largest contribution to the divergence of the mean advection of mean kinetic energy comes, somewhat surprisingly, from cross-stream advection and is significantly greater than zero. The total divergence:

$$\frac{\partial}{\partial x_j} \langle u_j \rangle \langle u_{\alpha} \rangle^2 / 2 = [2.17 \pm .98] \times 10^{-2} \text{ ergs cm}^{-3} \text{ sec}^{-1}$$

is also significantly positive and is the largest of any estimate we have computed. The above value indicates that more kinetic energy is exiting a control volume surrounding array E than is entering it, or that the mean flow is gaining kinetic energy in the downstream direction.

The two quantities we have estimated from Eq. (1) are not balanced; indeed the residual of the above terms:

$$\frac{\partial}{\partial x_j} \langle u_j \rangle \langle u_{\alpha} \rangle^2 / 2 + \langle u_{\alpha} \rangle \frac{\partial}{\partial x_j} \langle u'_{\alpha} u'_j \rangle = (2.74 \pm 1.7) \times 10^{-2} \text{ ergs cm}^{-3} \text{ sec}^{-1}$$

is significantly greater than zero. Accordingly, the mean flow is gaining in kinetic energy but apparently not at the expense of the eddies, whose most likely effect is to decelerate the flow. The other sources of mean kinetic energy are acceleration by vertical eddy stress, vertical advection of kinetic energy and pressure work. Of these, the most likely candidate for the source is mean pressure work. Scaling arguments in support of this statement will be reviewed later; we mention here that a balance including pressure work requires a downstream drop in pressure. This is interesting for two reasons. First, it suggests the Gulf Stream is measurably ageostrophic in the downstream direction and second, strong downstream pressure gradients are characteristic of inertial Gulf Stream models (Fofonoff, 1962).

#### Export of Eddy Energy at Array E

A detailed analysis of the eddy energy equation was conducted in Dewar and Bane (1984). As a synopsis of these results, their analysis of the eddy kinetic energy equation showed that the eddies are configured so as to transfer energy to the mean, but the analysis of the mean kinetic energy equation presented here suggests that the eddies are acting as a mean energy sink. These apparently contradictory results are resolved by recognizing that the eddy source for the mean energy differs from the eddy sink for the eddy energy. These quantities differ by the divergence of a vector:

$$\frac{\partial}{\partial x_j} \langle u_i \rangle \langle u'_i u'_j \rangle$$

which is perhaps most easily understood as the 'export' of eddy energy (Bryden, 1983). We are able to partially estimate the magnitude of this quantity using the DAMEX data.

The largest terms in the above involve the divergence of the down-



stream mean transport of eddy variance. The sum of all components is significantly greater than zero:

$$\frac{\partial}{\partial x_j} \langle u_i \rangle \langle u_i' u_j' \rangle = [1.58 \pm 1.39] \times 10^{-2} \text{ ergs cm}^{-3} \text{ sec}^{-1}.$$

Its positive value suggests that eddy variance is being removed from the region by mean advection.

Thus, the eddies and the mean flow interact so as to release both eddy and mean flow kinetic energy, but that energy is not used locally. Rather it is exported and can eventually become either mean or eddy energy. Furthermore, as our measurements are unable to detect a significant change in the local eddy energy (Dewar and Bane, 1984) and also suggest an increase in mean kinetic energy, the net energy being exported must be supplied by other sources. Likely candidates are the mean and eddy pressure work, although we have no measurements to directly substantiate these conjectures.

### DISCUSSION

It is interesting to consider the character of the mean flow at array E. Our data suggests a gain in mean kinetic energy flux and an apparent imbalance of mean energy flux divergence and eddy-mean flow interaction. Thus we have inferred that other mean kinetic energy sources, namely vertical advection, vertical eddy Reynolds stress or pressure work, must be important. Unfortunately, we have no measurements which allow us to compute the vertical eddy stress. It is also difficult to estimate the magnitude of this term as it depends critically upon the vertical structure of the covariance of vertical and horizontal velocity, a topic about which little is known. In what follows, we neglect vertical eddy stress ab initio. Our data does suggest that mean vertical kinetic energy advection needs some consideration. The evidence for this includes the presence of less dense water at the standard depth at the downstream E mooring and the general tendency of the mean flow to cross isobaths from shallower to deeper waters. Thus our measurements appear to be consistent with a slight downward velocity, which is possibly topographically induced. The mean flow at E is directed primarily from the mooring on the 300 m isobath to the downstream mooring on the 400 m isobath over a separation of roughly 22 km. An estimate of the topographically induced downwelling is therefore:

$$u_B \cdot \nabla h = -.045 \text{ cm/sec}$$

where we have extrapolated the observed mean velocities to the bottom. An order of magnitude estimate of the effects of vertical energy advection is thus:

$$\frac{\partial}{\partial z} (\langle w \rangle (\langle u \rangle^2 + \langle v \rangle^2)) \sim -10^{-2} \text{ ergs cm}^{-3} \text{ sec}^{-1}$$

where we have used the average of the vertical gradients of mean kinetic energy measured at array E. Although comparable in magnitude to the directly measured quantities, the above is insufficient to provide a balance in Eq. (1). We are left with a residual of

$$[1.74 \pm 1.7] \times 10^{-2} \text{ ergs cm}^{-3} \text{ sec}^{-1}$$

which, without a careful error analysis, appears to be significantly greater than zero and suggests that a balance in Eq. (1) requires net positive pressure work. This corresponds in physical terms to a release of mean potential energy caused by a mean flow down a pressure gradient.

It is possible to estimate the magnitude of the required downstream pressure drop from the above residual:

$$\begin{aligned} -\langle p \rangle_y &= -\langle v \rangle^{-1} (1.77 \pm 1.7) \times 10^{-2} \text{ ergs cm}^{-3} \text{ sec}^{-1} = \\ &= (3 \pm 2.8) \times 10^{-4} \text{ cm/sec}^2, \end{aligned}$$

If vertical energy advection is not included, the pressure gradient estimate is:

$$-\langle p \rangle_y = (4.5 \pm 2.7) \times 10^{-4} \text{ cm/sec}^2$$

Using a combination of hydrographic and surface velocity data, Sturges (1974) has estimated the downstream pressure gradient in the Gulf Stream to be from  $2.0 \times 10^{-4}$  to  $2.5 \times 10^{-4}$  cm/sec<sup>2</sup>. This range of values agrees rather well with the former estimate and is within the error bars of the latter.

The trading of potential and kinetic energy, such as we have inferred, via pressure work in boundary currents is an identifying feature of inertial Gulf Stream models (Fofonoff 1962, 1981) thus our observations are consistent with the premise that the Gulf Stream is an inertial jet. One implication of this is that the Gulf Stream is recirculating energy. Downstream of Cape Hatteras, Fofonoff and Hall (1983) have suggested that the observed decrease in mean momentum flux in the downstream direction is balanced by an increase in pressure. The resulting flow up the mean pressure gradient is thought to reduce the mean kinetic energy of the Gulf Stream by roughly  $50 \times 10^9$  Joules sec<sup>-1</sup>. If we assume the lower estimate of mean potential energy release is typical of the Gulf Stream along the margin, an estimate of the total Gulf Stream potential energy loss in the SAB is roughly  $70 \times 10^9$  Joules sec<sup>-1</sup>, where we have assumed the conversion occurs in a 1000 km long core region one Rossby deformation radius (50 km) wide by 800 m deep. This potential energy loss is clearly comparable to the gain computed by Fofonoff and Hall (1983). Admittedly, we have applied a point estimate all along the SAB; but this is consistent with Sturges (1974) who observed a pressure drop over the inshore edge of the Gulf Stream along the entire southeastern continental margin.

Sturges (1974) also considered the possible dynamical balances within the downstream momentum equation given his estimated pressure force. He determined that the eddy Reynolds stresses measured off Florida by Schmitz and Nifler (1969) provided a downstream momentum balance. It is of interest to compare the force balance inferred from our measurements with those of Sturges (1974). In the direction of the mean flow, the momentum equation reduces to:

$$\langle v \rangle \langle v \rangle_y + \langle w \rangle \langle v \rangle_z = -\langle p \rangle_y - \langle u'v' \rangle_x - \langle v'v' \rangle_y - \langle w'v' \rangle_z$$

Note that this equation applies to a component of the mean flow velocity

vector, and as such direct estimates of the terms from our data are sensitive to small errors in the estimation of mean flow direction. The balance inferred by Sturges (1974) involved the first two terms on the right hand side of the above equation. The balance inferred from our data involves the first term on the left hand side and the third term on the right hand side as well. Our inferred pressure force is consistent with a downstream mean flow acceleration of:

$$\langle v \rangle \langle v \rangle_y \sim 3 \times 10^{-4} \text{ cm/sec}^{-2}.$$

Integration demonstrates that this balance cannot describe the Gulf Stream over much of its extent, for accelerations of this magnitude over distances of a few hundred kilometers result in velocities of roughly 200 cm/sec. Flows of this speed are not characteristic of the mean subsurface Gulf Stream. While the observed potential energy release and inferred pressure gradient appear to be characteristic of the Gulf Stream in the SAB, the particular partitioning of the pressure force observed at array E does not. The obvious candidate for producing this local balance is the Charleston bump. Although the offshore deflection of the mean Gulf Stream path begins to the north of array E, it is known that the Gulf Stream formed a large relatively stationary offshore loop during the DAMEX experiment (Dewar and Bane, 1985). It is felt that the loop formed as a result of the interaction of the Stream with the bump and its effects were observed at E for roughly 3 months of the 7 month mooring period. It is possible that our measured force reflects this structure.

The observational premise which argues against the generality of our momentum balance at E is that the mean flow speeds are not observed to increase in magnitude along the Gulf Stream's track (Schmitz and Niiler, 1969). What is observed, however, is that the Gulf Stream broadens appreciably between Florida and Cape Hatteras. Therefore, some mechanism must exist for accelerating newly entrained water from a state of near rest to the observed 0(100 cm/sec) velocities typical of the Gulf Stream. Given that the force balance proposed by Sturges (1974) is in our opinion more typical of the Gulf Stream inshore edge, it is interesting to speculate on how the acceleration might occur. We have demonstrated that the inshore edge of the Gulf Stream is a region of export of eddy energy. One possible area to which that energy might be exported is the offshore edge of the Stream. The data reported by Schmitz and Niiler (1969) suggests that both the eddy and mean fields in the Gulf Stream anticyclonic zone are obtaining energy in their interactions with each other, and therefore that this must be a region of energy import. A crude estimate of eddy acceleration of the mean from Fig. 1 in Schmitz and Niiler (1969) along with their published estimates of kinetic energy transfer to the eddies (both on the Gulf Stream offshore edge) returns a value of:

$$\int x_j \langle u_i \rangle \langle u_i' u_j' \rangle \sim -1 \times 10^{-2} \text{ ergs cm}^{-3} \text{ sec}^{-1}$$

which is opposite in sign but similar in magnitude to the export we have measured at array E. In the view of Schmitz and Niiler (1969), the net energy transfer to the eddies over the width of the Gulf Stream is negligible; hence, the eddies act primarily to internally redistribute energy and momentum. It is therefore possible that the energy necessary to accelerate the entrained water in the Gulf Stream is released initially by mean pressure work, and distributed laterally by eddies.

Data from several experiments at a variety of locations in the SAB are now available. The primary objectives of the data analyses to date have centered on the time dependent flow. It would be interesting to compare the character of the mean flow at the other sites with that inferred here. On the anticyclonic shear side of the Stream, the sign and magnitude of the export of eddy energy are of particular interest. Are the eddies and mean flow in this region importing energy or are they exporting energy as occurs inshore? Also of interest are a number of questions which can be addressed with any of the SAB data sets. Can a net pressure work and net downstream pressure gradient be inferred elsewhere in the SAB and is there a local divergence of the mean flux of mean kinetic energy? How is the pressure force partitioned between mean flow acceleration and eddy stress?

It appears that the mean Gulf Stream structure involves a complicated interplay between mean and time dependent flow. Among other things, we have taken a few tentative steps in the description of the mean flow dynamics in this paper. It seems advisable to analyze mean Gulf Stream structure elsewhere in the SAB using data already in hand. Such information will undoubtedly be valuable and would aid in the understanding of the Gulf Stream system.

#### REFERENCES

- Bane, J. M. and W. K. Dewar, 1983: The deflection and meander energetics experiment, current meter and bottom pressure gauge data report. University of North Carolina Technical Report #CMS-83-2, Chapel Hill, North Carolina.
- Bevington, P. R., 1969: Data Reduction and Error Analysis for the Physical Sciences, McGraw-Hill Book Co., New York.
- Brooks, D. A. (editor), 1976: Festa at NCSU. Center for Marine and Coastal Studies, North Carolina State University, Raleigh, North Carolina.
- Brooks, I. H. and P. P. Niiler, 1977: Energetics of the Florida Current. J. Mar. Res., 35, 163-191.
- Dewar, W. K. and John M. Bane, 1984: The subsurface energetics of the Gulf Stream near the Charleston bump, accepted, J. Phys. Oceanogr.
- Dewar, W. K. and John M. Bane, 1985 (in prep.): Gulf Stream mean flow and variability near the Charleston Bump.
- Fofonoff, N., 1954: Steady flow in a frictionless, homogenous ocean. J. Mar. Res., 13, 254-263.
- Fofonoff, N., 1962: The dynamics of ocean currents. In: The Sea: Ideas and Observations on Progress in the Study of the Seas, Vol. I. M. N. Hill, ed., Wiley-Interscience, New York, 3-30.
- Fofonoff, N., 1981: The Gulf Stream System, in: Evolution of Physical Oceanography. B. A. Warren and C. I. Wunsch, eds., M.I.T. Press, Cambridge, MA, 112-129.

- Fofonoff, N. and M. M. Hall, 1983: Estimates of mass, momentum, and kinetic energy fluxes of the Gulf Stream. J. Phys. Oceanogr., 13, 10, 1868-1877.
- Knauss, J. A., 1969: A note on the transport of the Gulf Stream. Deep Sea Res., 16 (Suppl.), 117-173.
- Munk, W. H., 1950: On the wind-driven ocean circulation, Jour. Meteor., 7, 79-93.
- Pedlosky, J., 1979: Geophysical Fluid Dynamics. Springer-Verlag, New York and Berlin.
- Richardson, W. S., Schmitz, W. J., and P. P. Niiler, 1969: The velocity structure of the Florida current from the Straits of Florida to Cape Fear. Deep Sea Res., 16, 225-231.
- Schmitz, W. J. and P. P. Niiler, 1969: A note on the kinetic energy exchange between fluctuations and mean flow in the surface layer of the Florida Current. Tellus, 11, 814-819.
- Stommel, H. M., 1947: The westward intensification of wind-driven ocean currents. Transactions of the American Geophysical Union, 29, 202-206.
- Sturges, W., 1974: Sea level slope along continental boundaries. J. Geophys. Res., 79, 6, 825-830.

FIGURE CAPTIONS

- Fig. 1 The continental margin of the eastern U. S. The location of the Gulf Stream surface thermal front as determined by Bane and Brooks (1979) and Olson, Brown and Emmerson (1983) is indicated by the dashed line. Also shown are the 200 m and the 600 m isobaths. The insert encloses the study area and is shown in greater detail in Fig. 2.
- Fig. 2. The study area. The DAMEX experiment employed three arrays, labelled E, F and G in the diagram. Arrays E and F each consisted of three moorings deployed in an L-shaped pattern and were positioned immediately upstream and downstream of the Bump. The mean flow vectors the top current meters in Array E and the current meters which functioned for the duration of the experiment at F and G are also shown.

Table 1

## Mooring Data

Array	#	Location		Deployment	Recovery	Meter	#	Depth (m)
E	1	31	14.7 N 79 40.7 W	9-19-81	4-25-82	T	5705	201
							3424	261
E	2	31	13.8 N 79 38.5 W	9-19-81	4-25-82	T	5707	229
							5708	289
E	3	31	24.7 N 79 33.7 W	9-19-81	4-25-82	T	5706	219
							3427	279
F*	1	32	25.5 N 78 15.3 W	9-18-81	4-22-82	T	3337	206
							3423	266
F*	2	32	16.9 N 78 10.4 W	9-18-81	4-22-82	T	3425	210 <sup>+</sup>
							3344	270 <sup>+</sup>
F	3	32	22.3 N 77 55.7 W	9-18-81	4-22-82	T	3426	212
							3345	272
G	-	33	21.0 N 76 40.7 W	9-17-81	4-21-82	T	3332	210 <sup>+</sup>
							3343	270 <sup>+</sup>

distance E1-E2 = 3.86 km  
 distance E2-E3 = 21.58 km  
 distance E1-E3 = 21.59 km  
 distance F1-F2 = 17.69 km  
 distance F2-F3 = 25.10 km  
 distance F1-F3 = 31.24 km  
 distance E2-F1 = 165 km  
 distance F2-G = 183 km  
 distance E2-G = 354 km

---

\*These moorings supported a bottom pressure gauge.

<sup>+</sup>Nominal depths used.

Table 2  
Statistics at Array E

	$\langle u \rangle$	$\langle v \rangle$	$\langle u^2 v^2 \rangle$	$\langle u^2 u^2 \rangle$	$\langle v^2 v^2 \rangle$	$\langle u^2 E^2 \rangle^{\dagger}$	$\langle v^2 E^2 \rangle^{\dagger}$	$\langle \sigma \rangle^{\dagger}$	$\langle u^2 \rho^2 \rangle$	$\langle v^2 \rho^2 \rangle$	$\langle u^2 \rho^2 \rangle$	$\langle v^2 \rho^2 \rangle$	d
E1T	8.90	41.6	249.9	81.5	1135.0	1485.0	2885.0	26.96	$.966e^{-4}$	$-.118e^{-2}$	$.81e^{-7}$	$.102e^{-7}$	201
	1.5	5.4	53.1	13.1	225.0	2177.0	9563.0	.061	$2.53e^{-4}$	$.104e^{-2}$	$.13e^{-7}$	$.51e^{-7}$	
E1B	1.73	18.7	33.4	19.4	361.0	140.0	-1494.0	27.31	$.126e^{-3}$	$.262e^{-3}$	$.353e^{-7}$	$.333e^{-8}$	261
	.66	3.3	9.0	2.0	82.9	172.0	1871.0	.05	$.089e^{-3}$	$.45e^{-3}$	$.158e^{-7}$	$1.3e^{-8}$	
E2T	8.75	58.6	160.	54.6	984.0	1063.0	3945.0	26.81	$-9.05e^{-5}$	$-1.34e^{-3}$	$.447e^{-7}$	$.442e^{-8}$	229
	.98	5.2	26.5	7.2	184.0	1359.0	7943.0	.043	$.124e^{-3}$	$.608e^{-3}$	$.260e^{-7}$	$2.0e^{-8}$	
E2B	9.53	42.8	99.5	78.3	352.0	140.0	-1364.0	-----	$-.920e^{-3}$	$-.729e^{-3}$	$.923e^{-7}$	$.304e^{-6}$	289
	1.60	2.7	18.8	16.9	90.0	543.0	1973.0		$.51e^{-3}$	$.49e^{-3}$	$.641e^{-7}$	$.306e^{-6}$	
E3T	10.5	56.9	209.0	43.6	1368.0	-1487.0	-8162.0	26.80	$.828e^{-4}$	$.650e^{-3}$	$.467e^{-7}$	$-.174e^{-7}$	219
	1.2	7.4	71.0	14.5	341.0	2369.0	13130.0	.049	$1.53e^{-4}$	$.898e^{-3}$	$.207e^{-7}$	$.209e^{-7}$	
E3B	--	--	--	--	--	--	--	27.28	--	--	--	$.277e^{-7}$	279
								.046				$.120e^{-7}$	

The top number in each bin is the estimate for that statistic. The bottom number is its error. All velocities are in cm sec<sup>-1</sup> and densities in gm cm<sup>-3</sup>. The notation 'e' followed by a superscripted integer signifies 10 raised to that integer power. The depth of each instrument in meters is given in the last column.

$$^{\dagger} E^2 = (u^2 + v^2)/2$$

$$^{\dagger} \sigma = \text{sigma-t} = (\rho - 1) \times 1000.$$



Table 3

## Standard Depth Statistics at Array E

	$\langle u \rangle$	$\langle v \rangle$	$\langle u'v' \rangle$	$\langle u'u' \rangle$	$\langle v'u' \rangle$	$\langle u'E' \rangle^1$	$\langle v'E' \rangle^1$	$\langle \sigma \rangle^+$	$\langle u'p' \rangle$	$\langle v'p' \rangle$	$\langle p'^2 \rangle$	$\langle u'p'^3 \rangle$	$\langle v'p'^3 \rangle$
$E1_s$	6.8	34.7	185.	62.9	903.	1082.	1571.	27.07	.105e <sup>-3</sup>	-.747e <sup>-3</sup>	.672e <sup>-7</sup>	.814e <sup>-8</sup>	-.589e <sup>-7</sup>
	1.0	3.9	37.	9.2	160.	1525.	6717.	.045	.18e <sup>-3</sup>	.74e <sup>-3</sup>	.10e <sup>-7</sup>	3.60e <sup>-8</sup>	1.2e <sup>-7</sup>
$E2_s$	8.6	61.3	170.	50.7	1090.	1216.	4830.	26.75	.478e <sup>-4</sup>	-1.45e <sup>-3</sup>	.367e <sup>-7</sup>	-.455e <sup>-7</sup>	-.504e <sup>-7</sup>
	1.2	6.1	31.	8.8	216.	1590.	9272.	.052	1.7e <sup>-4</sup>	7.1e <sup>-4</sup>	.430e <sup>-7</sup>	.56e <sup>-7</sup>	.97e <sup>-7</sup>
$E3_s$	10.5	56.9	209.	43.6	1368.	-1487.	-8162.	26.80	.828e <sup>-4</sup>	.650e <sup>-3</sup>	.467e <sup>-7</sup>	-.174e <sup>-7</sup>	-.939e <sup>-7</sup>
	1.2	7.4	71.	14.5	341.	2370.	13135.	.049	1.5e <sup>-4</sup>	.9e <sup>-3</sup>	.210e <sup>-7</sup>	.21e <sup>-7</sup>	1.34e <sup>-7</sup>

11.268

As in Table 2, except all statistics have been interpolated to 219 m.

$$^1 E' = (u'^2 + v'^2)/2$$

$$^+ \sigma = \text{sigma-t} = (p - 1) \times 1000.$$

Table 4

## Energy Calculations at Array E

## 1. eddy acceleration of the mean flow:

$$\begin{aligned}
 & -\langle u \rangle \frac{\partial}{\partial x} \langle u' u' \rangle - \langle v \rangle \frac{\partial}{\partial x} \langle u' v' \rangle - \langle u \rangle \frac{\partial}{\partial y} \langle u' v' \rangle - \langle v \rangle \frac{\partial}{\partial y} \langle v' v' \rangle = \\
 & = (.24 + \underline{.25}) \times 10^{-3} + (.19 + \underline{.60}) \times 10^{-2} + (-.17 + \underline{.34}) \times 10^{-3} + (-.76 + \underline{1.1}) \times 10^{-2} = (-.57 + \underline{1.25}) \times 10^{-2}
 \end{aligned}$$

## 2. divergence of the mean flux of mean kinetic energy:

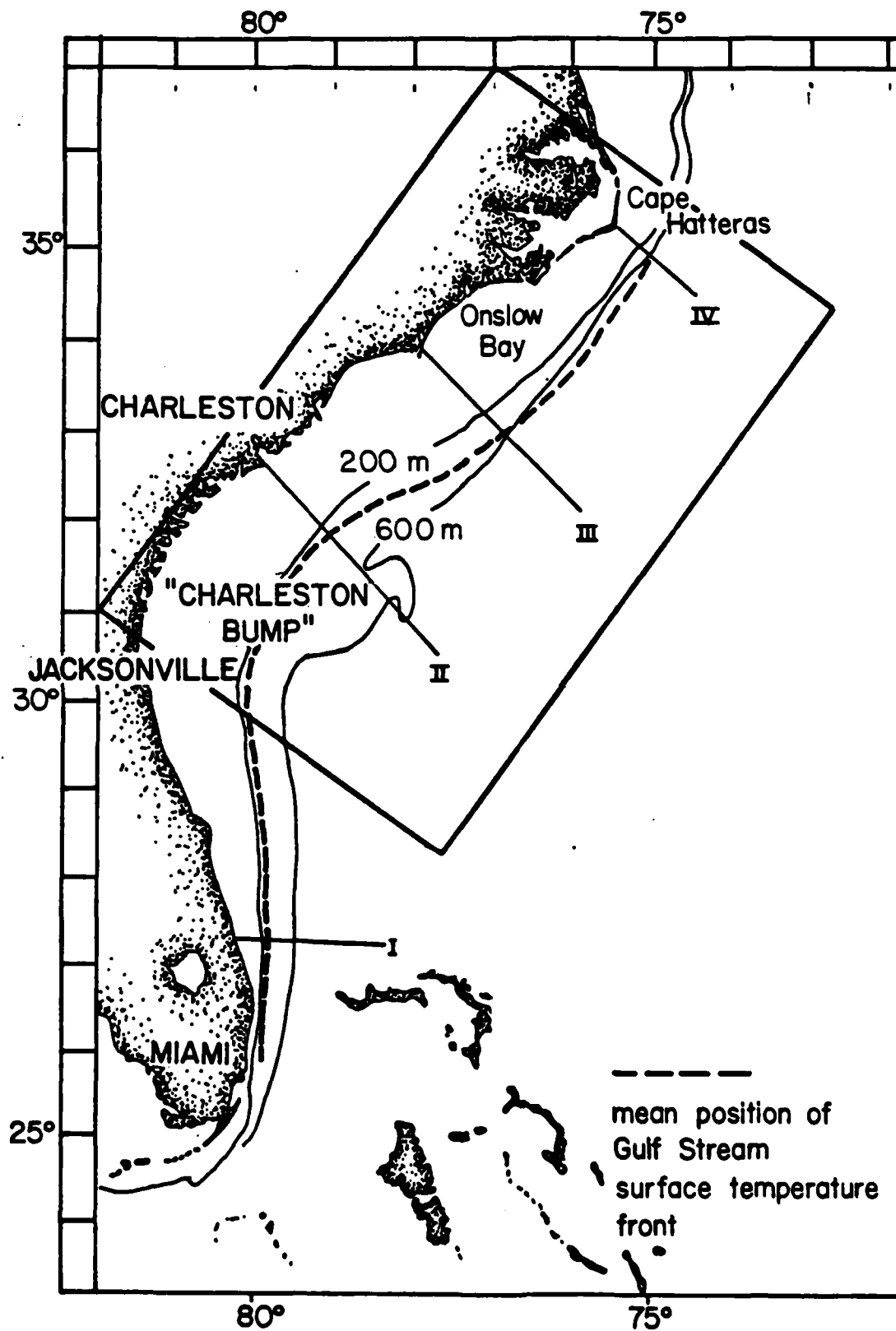
$$\begin{aligned}
 & \frac{\partial}{\partial x} \langle u \rangle \langle u \rangle^2 / 2 + \frac{\partial}{\partial x} \langle u \rangle \langle v \rangle^2 / 2 + \frac{\partial}{\partial y} \langle v \rangle \langle u \rangle^2 / 2 + \frac{\partial}{\partial y} \langle v \rangle \langle v \rangle^2 / 2 = \\
 & = (.43 + \underline{.13}) \times 10^{-3} + (.31 + \underline{.06}) \times 10^{-1} + (.40 + \underline{.22}) \times 10^{-3} + (-.10 + \underline{.076}) \times 10^{-1} = (2.17 + \underline{.98}) \times 10^{-2}
 \end{aligned}$$

## 3. export of eddy energy:

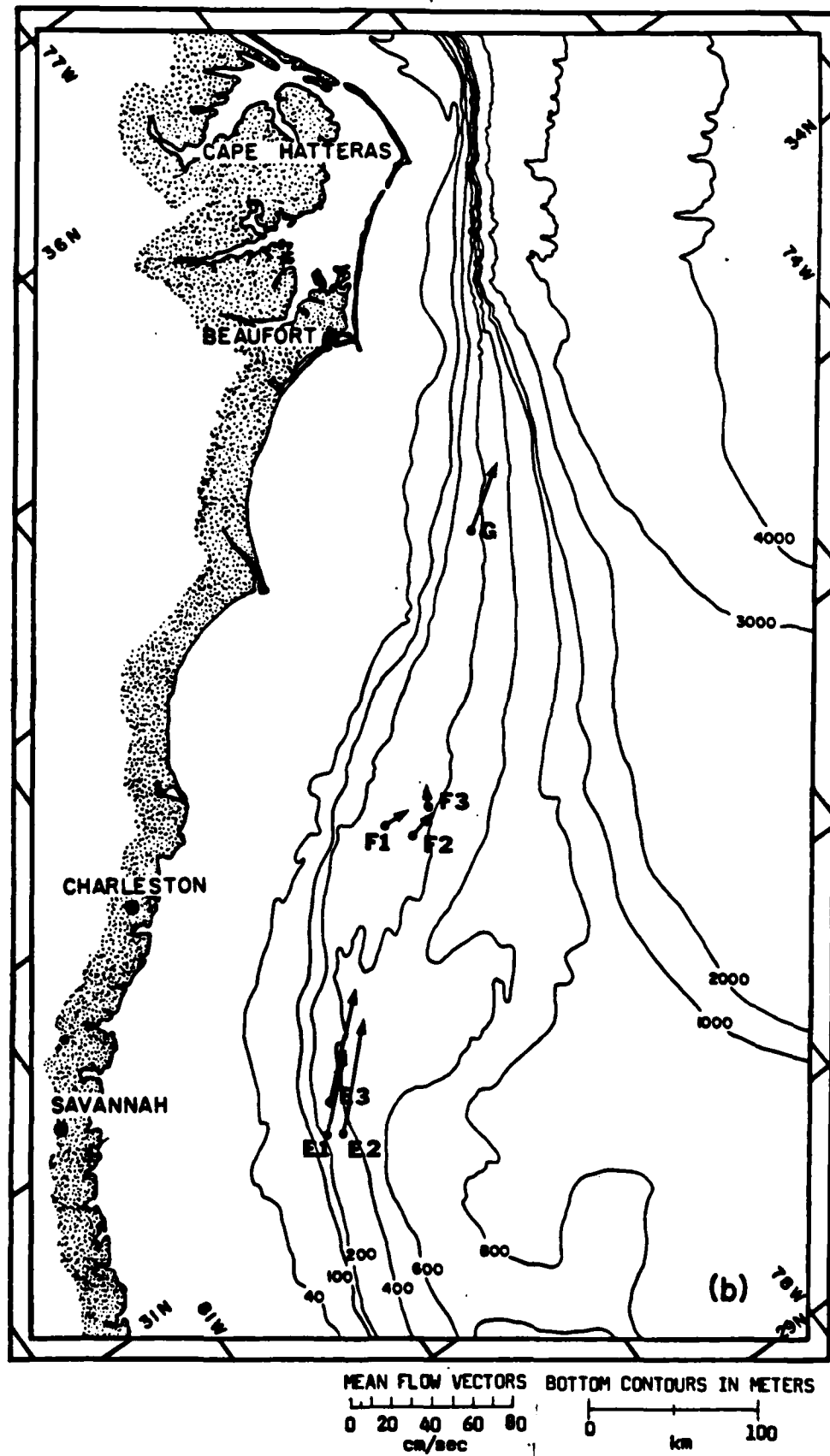
$$\begin{aligned}
 & \frac{\partial}{\partial x} \langle u \rangle \langle u' u' \rangle + \frac{\partial}{\partial x} \langle v \rangle \langle u' v' \rangle + \frac{\partial}{\partial y} \langle u \rangle \langle u' v' \rangle + \frac{\partial}{\partial y} \langle v \rangle \langle v' v' \rangle = \\
 & = (.32 + \underline{3.4}) \times 10^{-4} + (.10 + \underline{.068}) \times 10^{-1} + (.34 + \underline{.40}) \times 10^{-3} + (.052 + \underline{.12}) \times 10^{-1} = (1.58 + \underline{1.39}) \times 10^{-2}
 \end{aligned}$$

ACKNOWLEDGEMENTS

We gratefully acknowledge the support for this research, which was provided by the Office of Naval Research through a renewal of contract number N00014-77-c-0354. In addition, we wish to thank Russell S. Ault and Jean Marie Leech for their many invaluable contributions to this project. The crews of the Research Vessels RESEARCHER (NOAA) and CAPE HATTERAS (UNC/Duke) performed expertly at sea. Marsha D. Jones has patiently endured the typing of several drafts of this manuscript with unfailing good humor.



Dewar and Bane Figure 1.



Dewar and Bane Figure 2.

Nonlinear Waves and Coherent Vortex Structures in Barotropic  $\beta$ -plane Jets

G.R. Flierl, P. Maranotte-Rizzoli, N. Zabusky, and B. Meacham

**Purpose:** We are exploring systematically the instability and evolution to finite amplitude of meanders of a jet. Currently, we have examined the effects of  $\beta$  and the initial wavenumber upon the structure of the final state using a barotropic model.

**Model:** We have solved

$$\frac{\partial}{\partial t} \nabla^2 \psi + J(\psi, \nabla^2 \psi) + \beta \frac{\partial \psi}{\partial x} = -K \nabla^6 \psi$$

on 32x32, 64x64 and 128x128 grids using pseudo-spectral codes. The initial conditions consist of a jet flow with weak inverse flow in the rings

$$-\text{erf}(y) + y/2L$$

and a perturbation of wavenumber  $k$

$$+\delta \exp(-y^2) \sin kx$$

where  $L$  is the domain size. For the Gulf Stream, the parameter  $\beta$  is on the order of .1.

**Linearized instability and nonlinear regime diagram:** The growth rates for linearized sinuous or varicose perturbations are shown in Figure 1 as functions of  $\beta$  and  $k$ . The  $\beta$ -cutoff occurs for  $\beta > .9$ . Figure 1a represents schematically the various regimes observed at finite amplitude. These are described below.

**Dipole regimes:** Long, slowly growing waves, with a small value of  $\beta$ , force second and third harmonics which also extract energy from the jet. The

latter cause a folding of the jet and bring patches of vorticity together, resulting in a pairing of pieces from either side of the jet. These smaller structures then move away from the jet center, breaking the jet quite effectively.

Street regime: Intermediate scale waves break by a different mechanism: the individual vortices roll up to form an alternating vortex street. As  $k$  increases, the street becomes more compact and the area of the rolled up vorticity region becomes smaller. Finally something like a "cat's eye" pattern is obtained near the short wave cutoff. The  $\beta$ -effect tends to decrease the final amplitude of the perturbation and also to make the street much more compact.

Harmonic subcritical instability: Long waves are linearly stable in the presence of  $\beta$  but generate shorter harmonics which extract energy and grow. Because of the energy still existing in long waves, however, vortex pairing occurs and the perturbation energy moves gradually back to longer scales.

Wave-like meanders: For intermediate wavelength perturbations in the  $\beta$ -plane jet, the vorticity collects in the troughs of the pattern and does not roll up significantly. Because of the inverted nature of the resulting vorticity pattern (lows north of the highs), the wave may propagate westward. At the edges of the jet, "shingles" of vorticity being slowly cast off appear where the meander is interacting with the more rapidly propagating Rossby wave field.

A note on perturbations with a full spectrum of initial disturbances: Although the long wave modes are not the most rapidly growing form of disturbance, they still can play a very important role in the development of a perturbation which contains many scales. The vortex streets which form initially rather rapidly transfer this energy into larger scales by merger events. At later stages more chaotic vortex pairing into dipoles occurs.



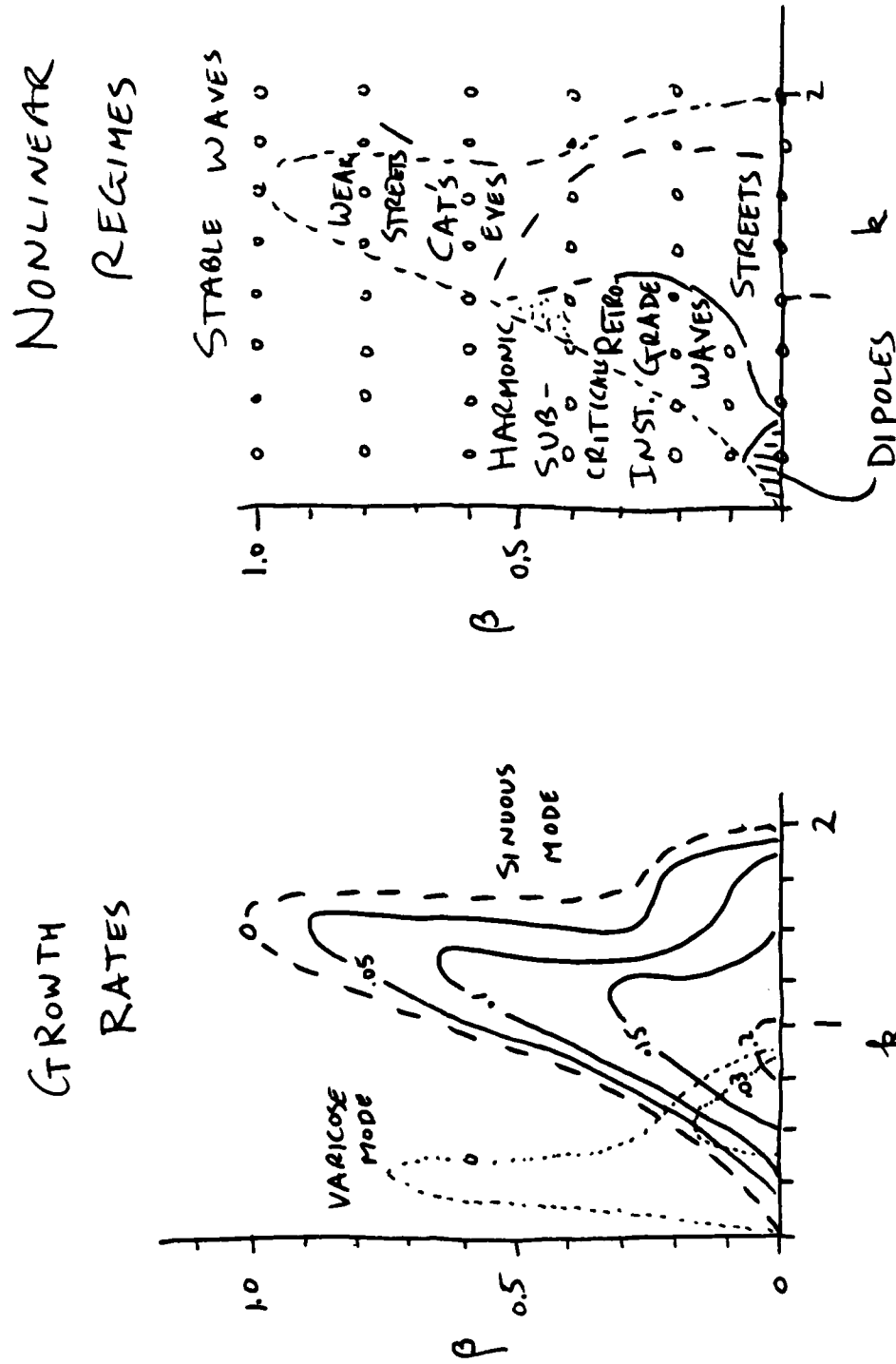
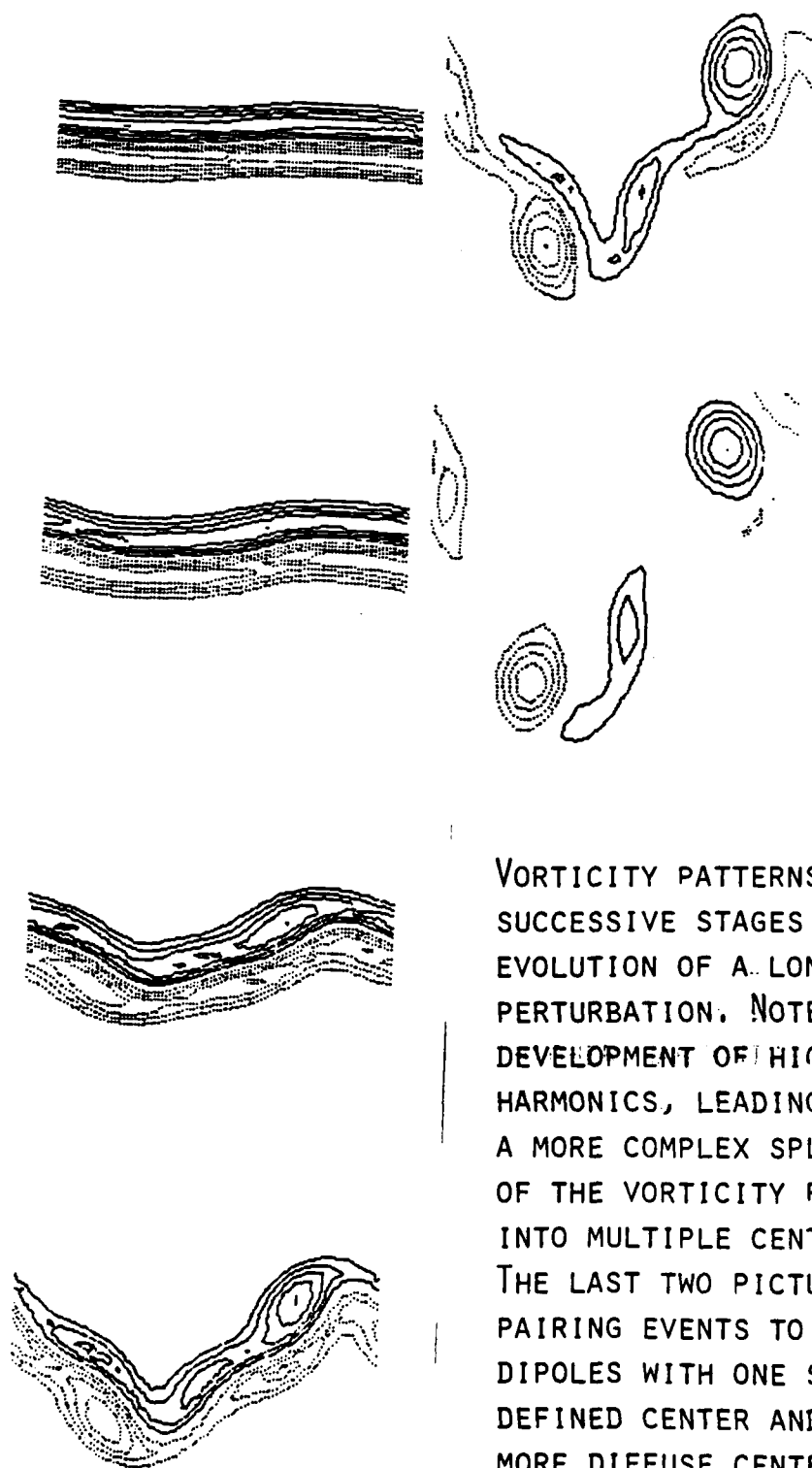


FIGURE 1

# EVOLUTION OF A LONG WAVE PERTURBATION ON A JET - VORTICITY PATTERN

$\beta = 0$  CASE



VORTICITY PATTERNS FOR THE SUCCESSIVE STAGES IN THE EVOLUTION OF A LONG WAVE PERTURBATION. NOTE THE DEVELOPMENT OF HIGHER HARMONICS, LEADING TO A MORE COMPLEX SPLITTING OF THE VORTICITY FIELD INTO MULTIPLE CENTERS. THE LAST TWO PICTURES SHOW PAIRING EVENTS TO FORM DIPOLES WITH ONE SHARPLY DEFINED CENTER AND ONE MORE DIFFUSE CENTER. THESE PROPAGATE OUTWARDS.

# EVOLUTION OF A LONG WAVE PERTURBATION ON A JET - VORTICITY PATTERN

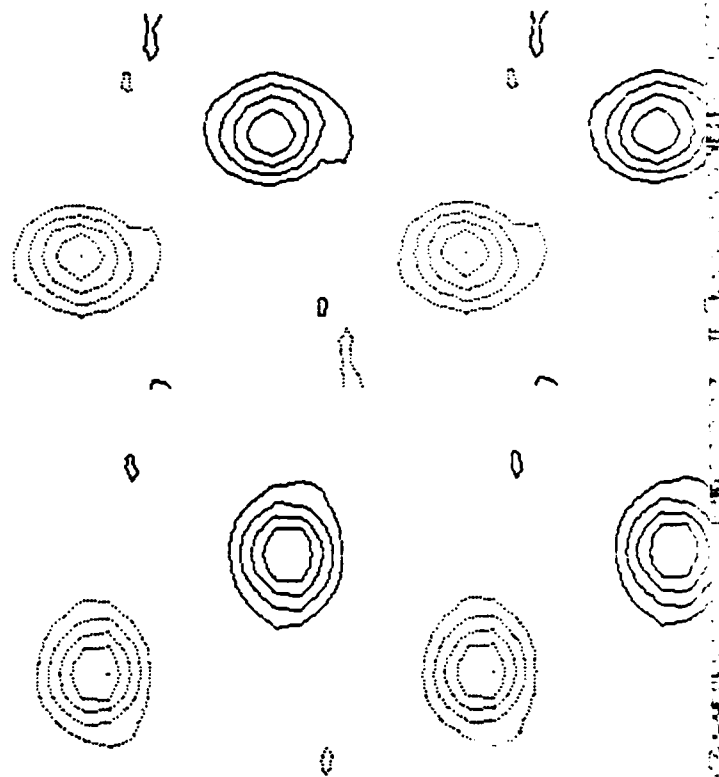
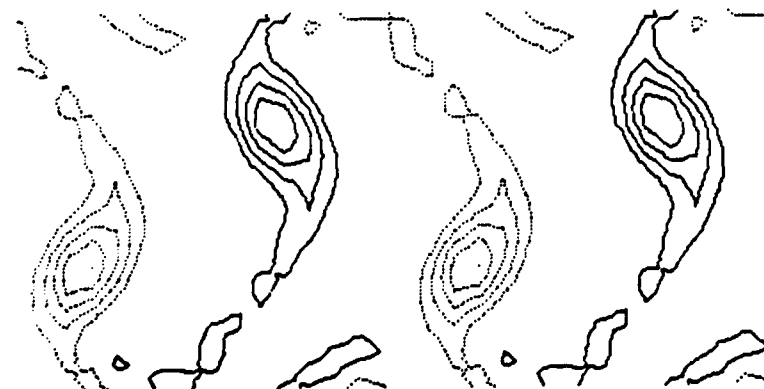
$\beta = 0.4$  CASE



WHEN  $\beta$  IS SUFFICIENTLY STRONG, THE LONG WAVE IS STABLE. THE NON-LINEARITY GENERATES HIGHER HARMONICS (IN THIS CASE, THIRD) AS APPEARING IN THE THIRD FRAME. THIS GROWS TO A FINITE AMPLITUDE. IN THE FINAL FRAME AN ALTERNATING STREET IS SEEN WITH THE VORTICES CLOSE TO THE CENTERLINE AND SOME INDICATIONS OF MERGER WHICH WILL OCCUR SOMEWHAT LATER.

# EVOLUTION OF SHORT WAVE PERTURBATION ON A JET - VORTICITY PATTERN

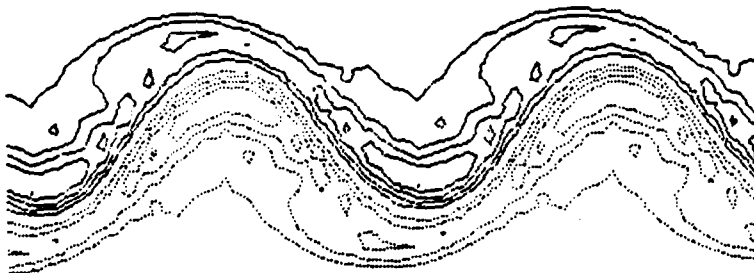
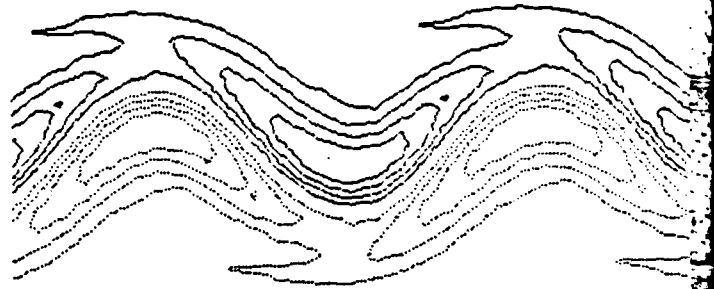
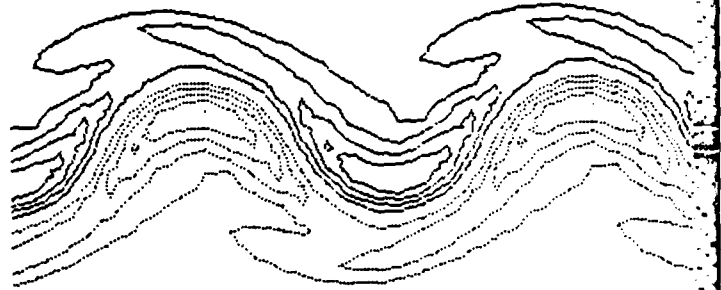
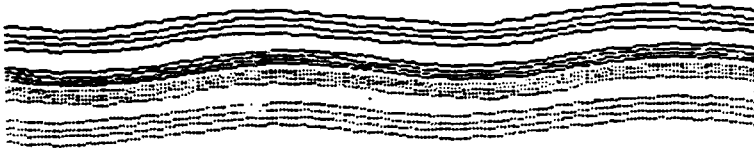
$\beta = 0$  CASE



SUCCESSIVE TIME PICTURES  
SHOW THE GROWTH OF THE  
PERTURBATION, THE BREAK-  
ING OF THE VORTICITY  
CONTOURS INTO ISOLATED  
PATCHES. THESE  
ELLIPTICAL EDDIES THEN  
ROLL UP TO FORM FAIRLY  
CIRCULAR VORTICES  
ARRANGED IN AN  
ALTERNATING STREET  
PATTERN.

# EVOLUTION OF A SHORT WAVE PERTURBATION ON A JET - VORTICITY PATTERN

$\beta = 0.1$  CASE



SUCCESSIVE PICTURES SHOW GROWTH OF THE PERTURBATION TO AN EQUILIBRATED MEANDER. THE VORTICITY BECOMES CONCENTRATED ALONG THE CENTER LINE AND NEVER BREAKS INTO ISOLATED PATCHES. NOTE THE BACKWARDS BREAKING PATCHES NEARS THE CRESTS AND TROUGHS. THE FINAL PATTERN HAS A SLOW RETROGRADE PROPAGATION.

**Spatial Structure of Gulf Stream Current Variability  
downstream of the New England Seamount Chain**

R.M. Hendry  
Atlantic Oceanographic Laboratory  
Fisheries and Oceans Canada

This note presents a preliminary discussion of the vertical and horizontal spatial scales and spatial structure of low-frequency fluctuations of horizontal currents associated with the Gulf Stream near 59° W, downstream of the New England Seamount Chain. An analysis of one year of moored current meter measurements from a five-mooring array shows that an equivalent barotropic mode with unidirectional flow at all depths provides an efficient description of observed current variability at the four measurement levels between 400 and 4000m depths. The dominant horizontal scales of the current fluctuations are at least as large as the 110km maximum horizontal separation provided by the array.

Five subsurface moorings with consecutive Atlantic Oceanographic Laboratory (AOL) designators 557 through 561 were set during 6-10 May, 1983 and recovered during 29 April - 1 May, 1984 to provide the first year of measurements in a planned two-year effort aimed at studying Gulf Stream current structure. Each mooring was instrumented with Aanderaa RCM5 current meters at four vertical levels, nominally 400, 800, and 1300m spanning the main thermocline and 4000m representing the abyssal flow. Total water depth in the area is about 5150m. All instruments recorded speed and direction of the horizontal flow, temperature, and pressure at hourly intervals. The three uppermost current meters were also equipped with conductivity cells. The array configuration and local bathymetry are shown in Fig. 1. The central mooring in the array was located at 39°30'N and 59°00'W near the mean position of the Gulf Stream as defined by the landward surface edge seen in satellite imagery (Auer, 1983). The cross-shaped array gives maximum horizontal separations of approximately 110km in both zonal and meridional directions. Scientific goals of the study included the measurement of the vertical structure of the mean flow and estimates of the total mass transport, the statistical description of flow variability, the horizontal mapping of measured fields over a limited region and the investigation of cross-stream variations in temperature-salinity properties. The purpose of this paper is to provide a statistical overview of the spatial structure of observed low-frequency current variability.

---

Bedford Institute of Oceanography  
P.O. Box 1006  
Dartmouth, Nova Scotia  
CANADA B2Y 4A2

### Vertical Structure

Central Mooring 557 is chosen as representative of the general case for a discussion of vertical structure. The covariances between current fluctuations at the four vertical levels were derived separately for  $u$  (zonal) and  $v$  (meridional) components, and empirical orthogonal eigenfunctions (EOF) were computed. These are normalized to unit mean squared amplitude, and the associated eigenvalue gives the variance represented by the empirical mode. Fig. 2 presents the first two modes for both the  $u$  and  $v$  fluctuations, and the percentage of total current variance accounted for by each mode. A unidirectional equivalent barotropic mode accounts for over 90% of the total variance for both components. A second mode accounts for essentially all the remaining variance in both cases; it shows a reversal in sign of the flow fluctuations between the 400m level and the 800m and deeper levels, reminiscent of a first baroclinic mode in linear flat-bottomed wave theory.

### Horizontal Structure

Two complementary methods are used to discuss the observed horizontal structure. Fig. 3 shows the longitudinal and transverse correlations of velocity fluctuations computed between each horizontally separated pair of instruments at both 400 and 4000m levels. This presentation is appropriate for a horizontally homogeneous and isotropic velocity field, which provides the simplest statistical model for streamfunction mapping using the technique of objective analysis (Bretherton *et al.*, 1976). The results of the correlation calculation as shown in Fig. 3 are superficially consistent with such a model. The longitudinal correlations are positive for all spatial separations available, while the transverse correlations decrease more rapidly with increasing spatial separation as expected for a horizontally non-divergent flow. These results are not much different from similar correlation estimates obtained from zonally-separated measurements at abyssal levels beneath the Gulf Stream near 55°W (Hendry, 1982), and essentially represent a confirmation of the experimental design for the present array.

The second method involves the use of EOF decomposition of a vector field. The full covariance matrix for  $(u,v)$  pairs at each of five horizontal locations at the nominal 800m level was used, giving ten degrees of freedom. The first four eigenvectors are shown in Fig. 4, along with the percentage of the combined current variance accounted for by each mode. The first two modes show nearly collinear flow patterns, with approximately orthogonal directions, and together represent 65% of the total variance in the 800m flow. Modes 3 and 4 show spatial patterns with more structure, suggesting a swirling mode and a deformation mode respectively, but accounting for a relatively minor fraction of the overall variability. Future efforts must include a characterization of the statistical significance of these results.

These rather preliminary calculations provide an overview of the dominant spatial patterns of flow variations in the Gulf Stream downstream of the New England Seamount Chain. The intention is to expand this approach to include the temporal dimension and to try and relate such a statistical description to the meandering of the instantaneous Gulf Stream.

#### Acknowledgement

I wish to thank the U.S. Office of Naval Research for supporting my attendance at the April 1985 U.R.I. Gulf Stream Workshop for the SYNOPS Program.

#### References

- Auer, S.J., 1983 Gulf Stream Landward Surface Edge Statistics. NOAA Tech. Memo. NWS NMC 67.
- Bretherton, F.P., R.E. Davis and C.B.Fandry, 1976. A technique for objective analysis and design of oceanographic experiments applied to MODE. Deep-Sea Res., 23, 559-581.
- Hendry, R.M., 1982. On the structure of the deep Gulf Stream. J. Mar. Res., 40, 110-142.



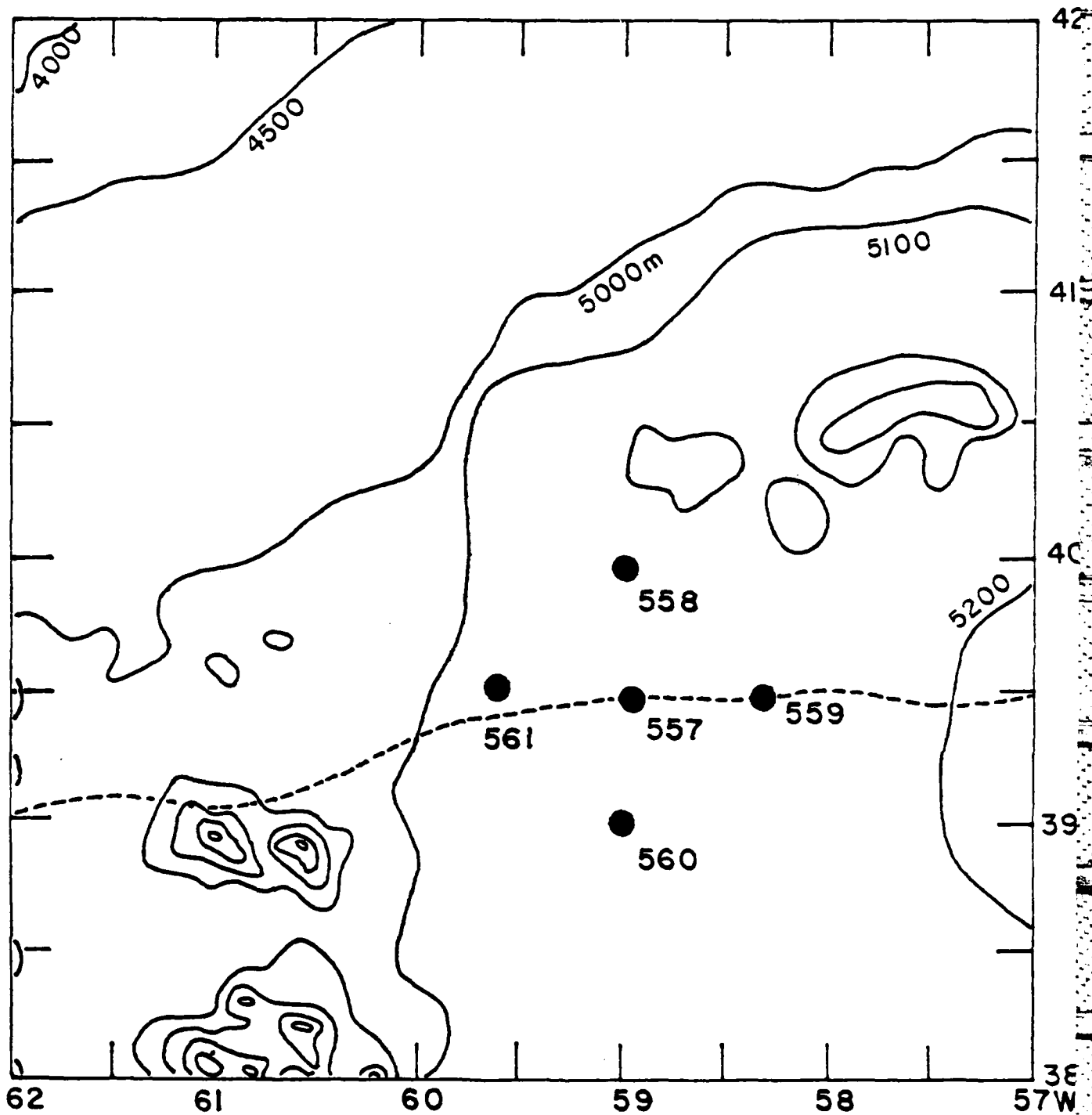


Figure 1 Mooring locations and local bathymetry. The dashed contour gives the mean position of the landward surface edge of the Gulf Stream from mid - 1980 to mid - 1981 according to Auer (1983).

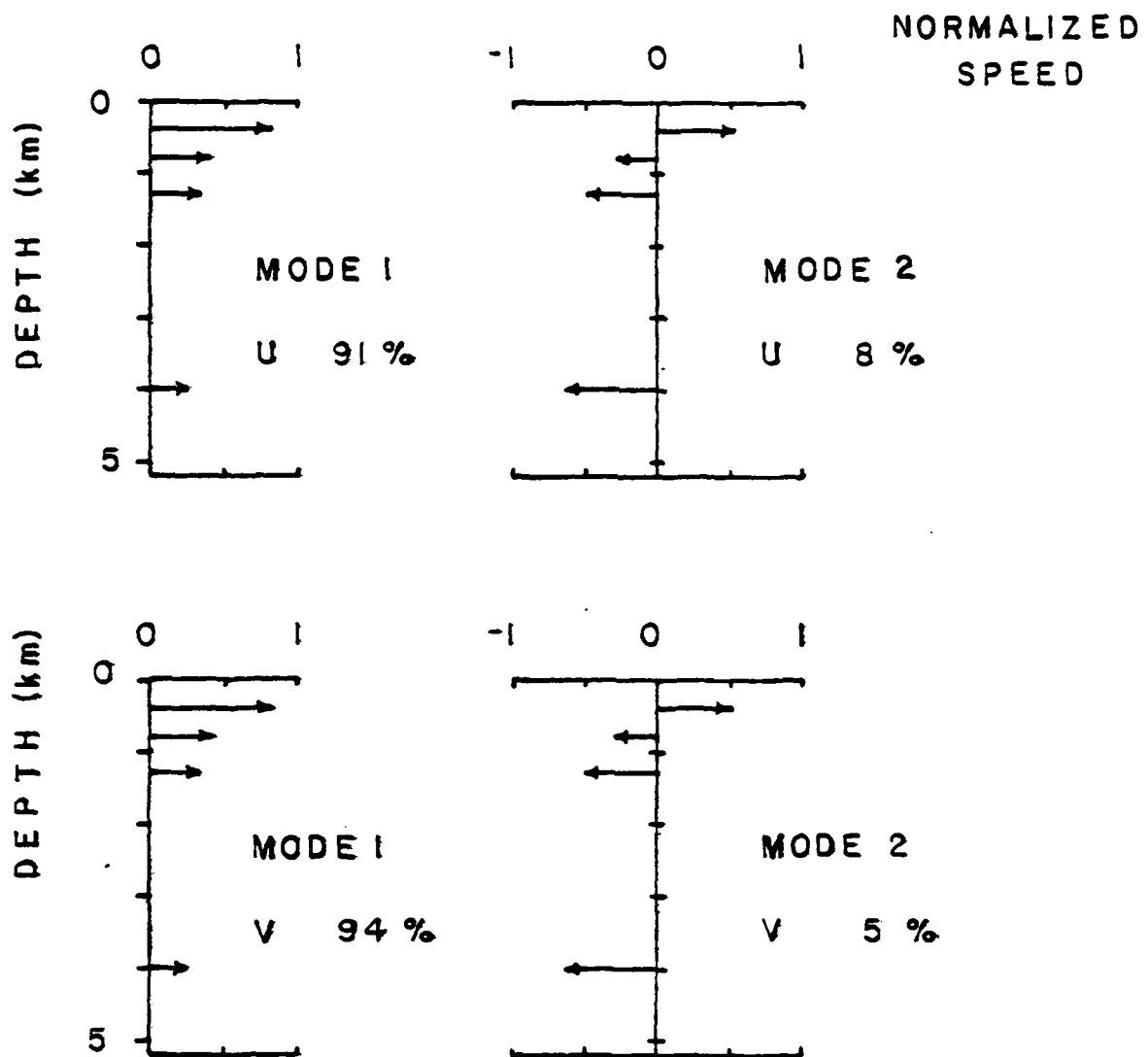


Figure 2 Empirical eigenfunctions of vertical structure of  $u$  (zonal) and  $v$  (meridional) velocity component fluctuations at Mooring 557. The two most energetic modes are shown, along with the percentage of component variance accounted for by each mode.

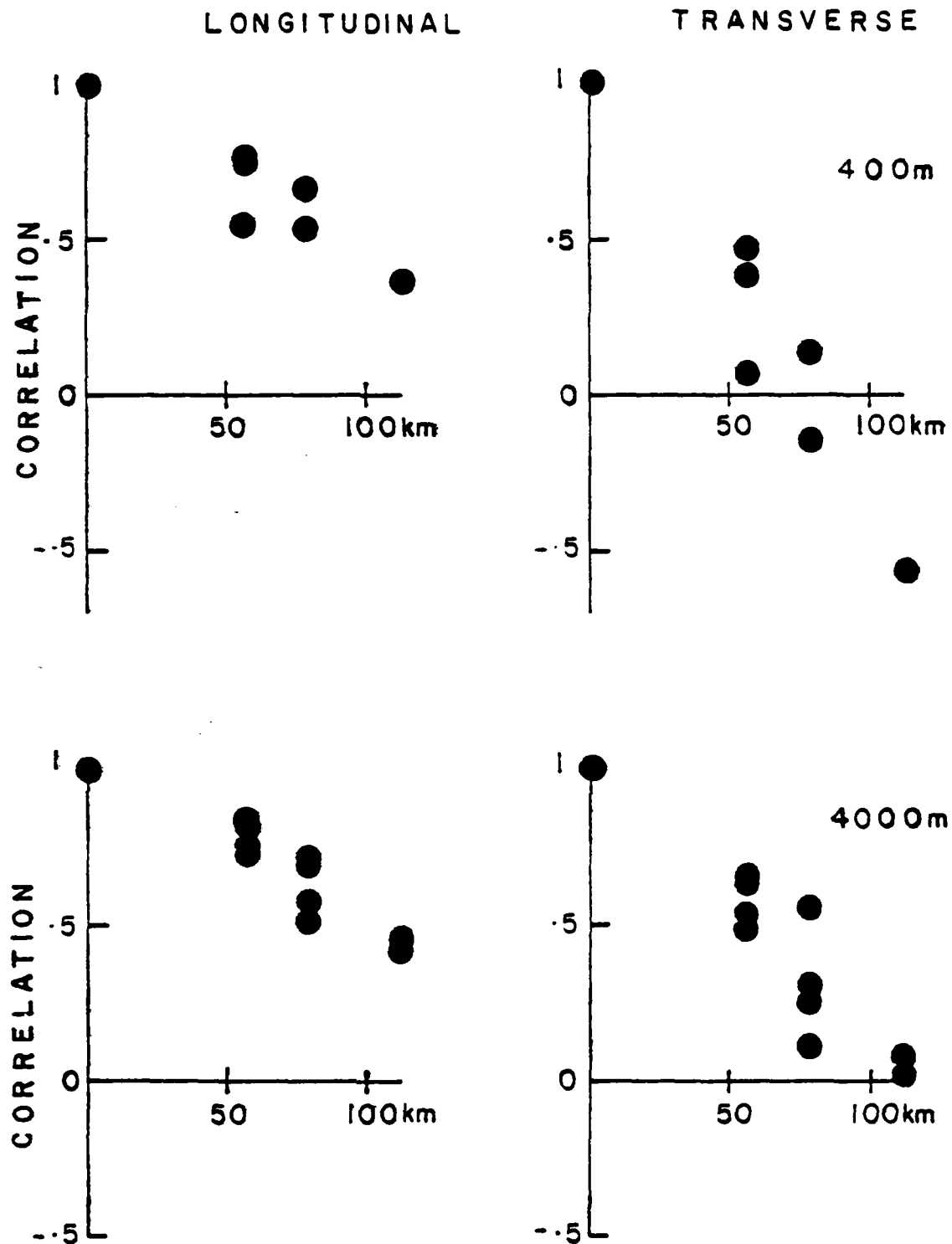


Figure 3 Longitudinal and transverse velocity correlations as a function of spatial lag estimated at nominal 400 and 4000m levels.

0 1 NORMALIZED  
SPEED

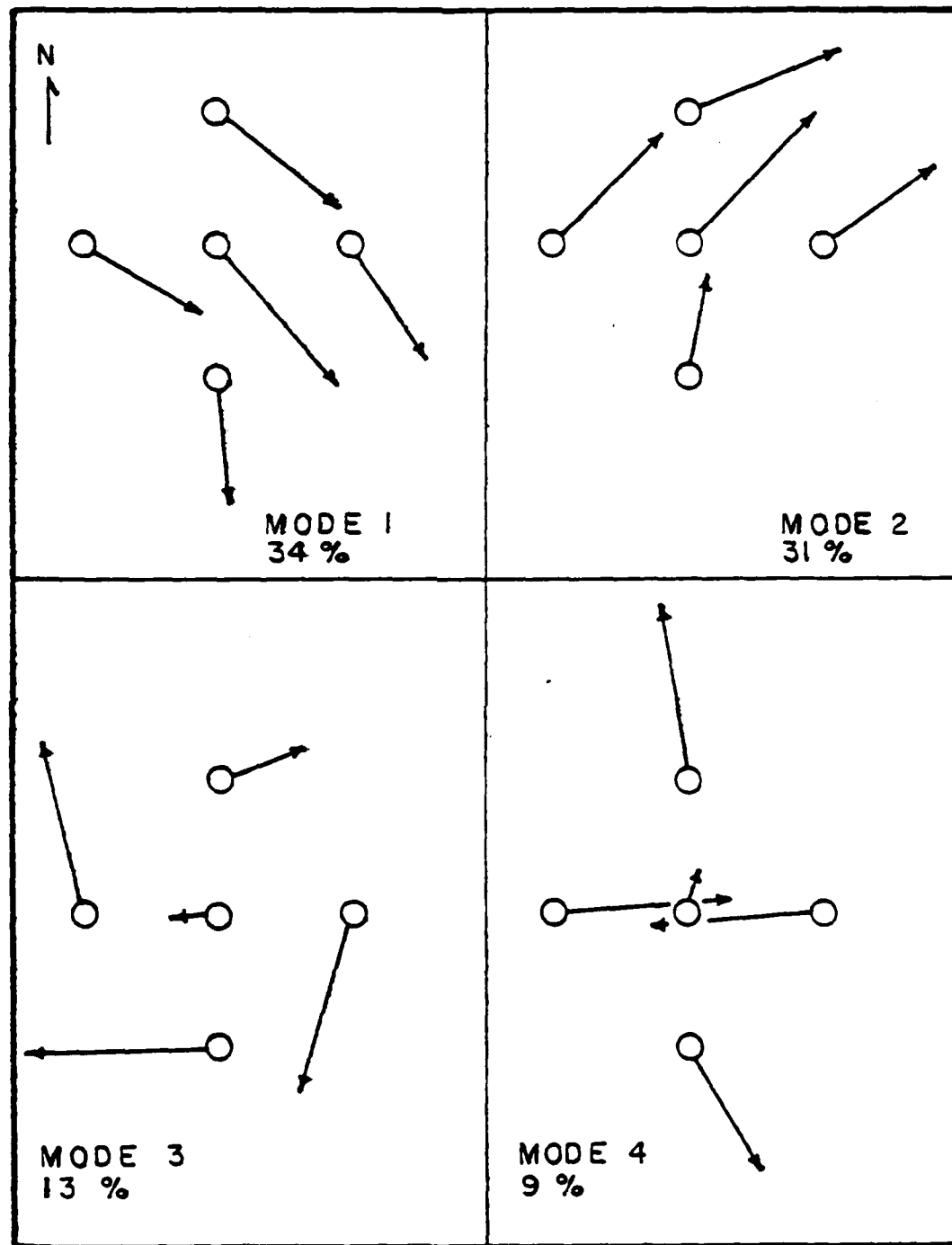



Figure 4

Empirical eigenfunctions of the horizontal structure of horizontal flow fluctuations observed at the nominal 300m level. The four most energetic modes are shown, along with the percentage of overall velocity variance accounted for by each mode.

## RECIRCULATION AND THE DEEP GULF STREAM

N.G. Hogg (Woods Hole Oceanographic Inst., Woods Hole, MA.)

R.S. Pickart (WHOI/MIT joint program, Woods Hole, MA.)

## BACKGROUND

The existence of the deep western boundary current (DWBC) in the North Atlantic, which flows around the grand banks of Newfoundland and onward to Hatteras, is well established. Off shore of this however there is some uncertainty as to the mean abyssal circulation. On the premise that as a fluid parcel circulates its properties remain unchanged, Worthington (1976) postulated the existence of the deep gulf stream system in figure 1a. Applying inverse methods to the same data set, Wunsch and Grant (1982) argued that the deep flow consists primarily of a cyclonic gyre (figure 1b).

Recent theoretical and observational evidence suggests a scheme distinct from these in which there are two (or more) counter rotating gyres. Figure 2 shows the streamline pattern that Hogg (1983) inferred from a synthesis of long term deep current meter data from the region. Consistent with this picture is a section of average zonal velocity along 55W (figure 3) that Richardson (1984) constructed using data from surface drifters, so-far floats, and current meters. Here we refine the streamline pattern using more recent current meter data, and discuss the relationship between the circulation and observed tracer fields with the aid of an advective-diffusive numerical model.

## A MOORED CURRENT METER ARRAY

In 1983 field work was undertaken in the region 35N-45N,

70W-55W to investigate the existence of recirculation. The experiment consisted of an array of moored current meters spanning the gulf stream , and associated hydrographic work. The deployment lasted one year and each mooring had four instruments spread throughout the water column. Figure 4 shows the time series from two of the moorings.

Another moored array, part of the SME experiment (Ross Hendry, Bedford Inst.), was deployed over the same time period a bit further to the east. When the deep mean vectors from these arrays are included in the compilation of figure 2, the associated streamline pattern is somewhat altered. The outstanding feature is that the recirculation of the northern most gyre appears to be tighter than earlier believed (strengthening even further the distinction between the cyclonic gyre here and that in figure 1b).

This means that the flow lines have a sharp southward bend near 57W, as does the mean path of the gulf stream (figure 5). Hogg and Stommel (1985) explain that because the thermocline and bottom depth both deepen offshore of the slope, it is possible to have closed contours of layer thickness for the deep layer in this region. The abrupt deepening of the thermocline across the gulf stream inhibits the southward penetration of one such contour (figure 5), allowing for a recirculating abyssal flow which preserves its thickness and exhibits such a feature near 57W.

## THE TRACER FIELDS

### A) An advective-diffusive numerical model

As seen in figure 2 the northern most gyre is in close contact with the DWBC from 60W-65W before turning off shore. The DWBC represents a

source of low salinity and high oxygen and thus it might be expected that the gyre influences the spreading of these water properties away from the current. To better understand this process a numerical experiment was performed in which the flow field consisted of a gyre alongside a southward flowing current, with a source of tracer imposed at the upstream end of the current. The model was run to steady state, figure 6 represents salinity and figure 7 oxygen (the outer most streamlines are included). The difference between the two is that for oxygen, unlike salt, there are lower concentrations above and below the depth of DWBC which means a net vertical diffusive flux out of the layer. This effect was modeled by including a radioactive decay term in the advective-diffusive equation. As a result less tracer was entrained into the gyre, and within the gyre there exists a minimum, unlike the salt which is homogenized throughout the gyre (figure 8).

#### B) The data

Figures 9 and 10 represent the lateral distributions of salt and oxygen anomaly for the region covered by the hydrographic portion of the 1983 field experiment. In addition to the data from this experiment the maps also include data from other surveys in the area. Each point represents the average value over the depth range of the DWBC. Overlaid on each are the thickness contours of figure 5.

For the oxygen there is a well developed plume extending from the DWBC which encloses a region of lower values. That the plume extends south of where the current turns offshore is supported by the model results. The salt map differs from that for the oxygen, suggesting that different mechanisms influence the two tracers, such as the presence or non-presence of vertical flux.

## REFERENCES

- Hogg, N.G. (1893) A note on the deep circulation of the western North Atlantic: its nature and causes. Deep-Sea Research, 30, 945-961.
- Hogg, N.G., and H. Stommel (1985) On the relation between the deep circulation and the Gulf Stream. Deep-Sea Research, accepted.
- Richardson, P.L. (1984) Average velocity and transport of the Gulf Stream near 55W. Journal of Marine Research, submitted.
- Worthington, L.V. (1976) On the North Atlantic circulation. The Johns Hopkins Oceanographic Studies, 6, 110 pp.
- Wunsch, C., and B. Grant (1982) Towards the general circulation of the North Atlantic Ocean. Progress in Oceanography, 11, 1-59.



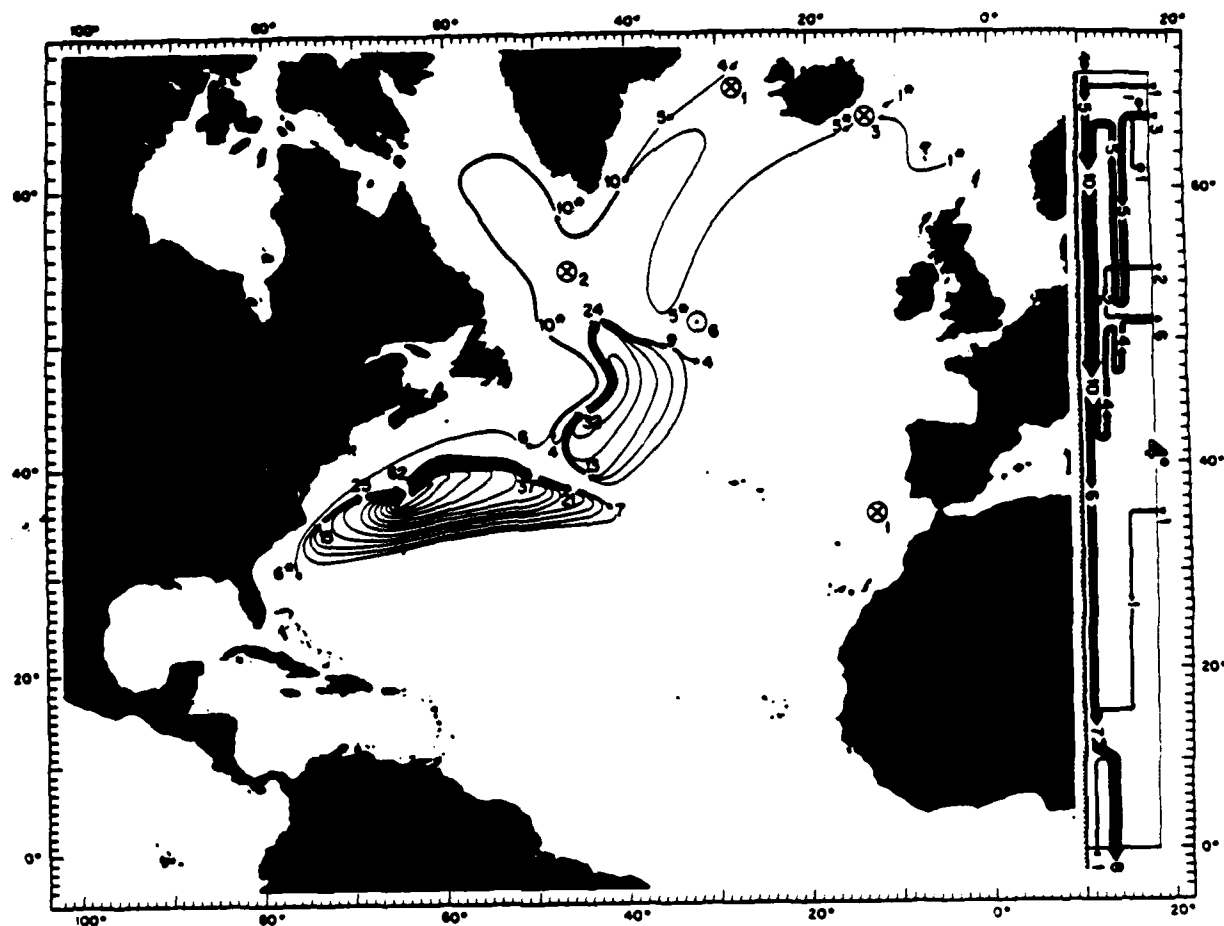


FIGURE 1a

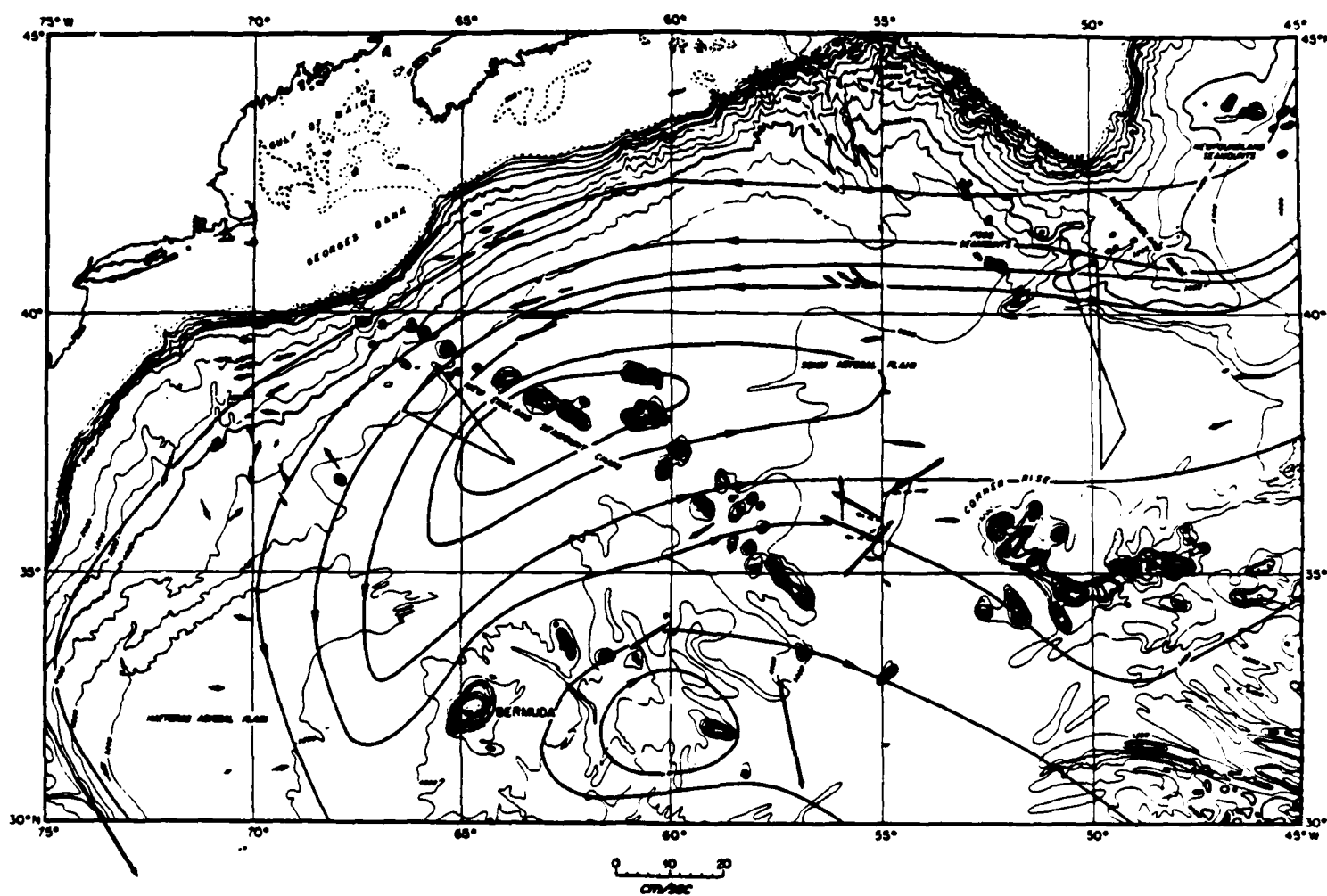


FIGURE 1b

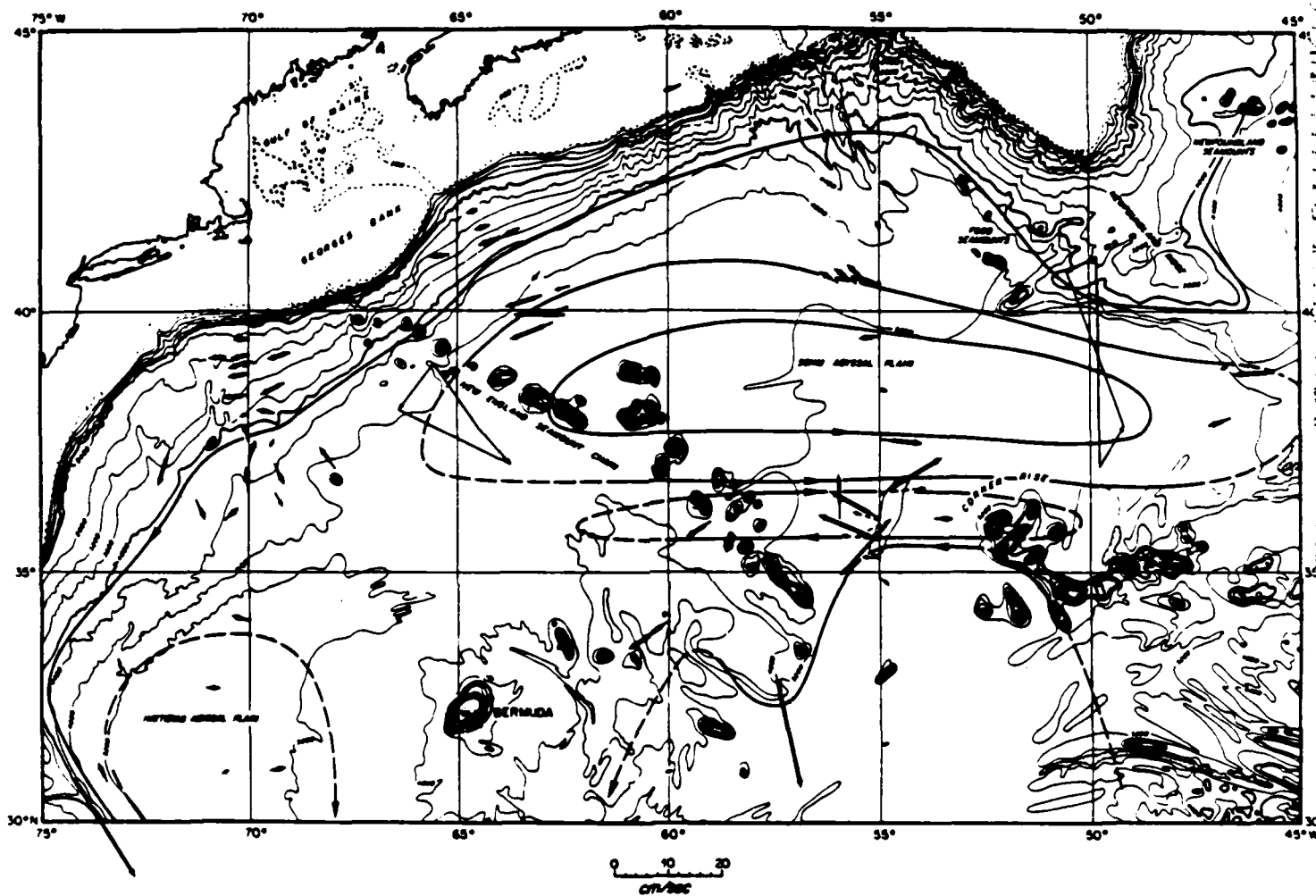


FIGURE 2

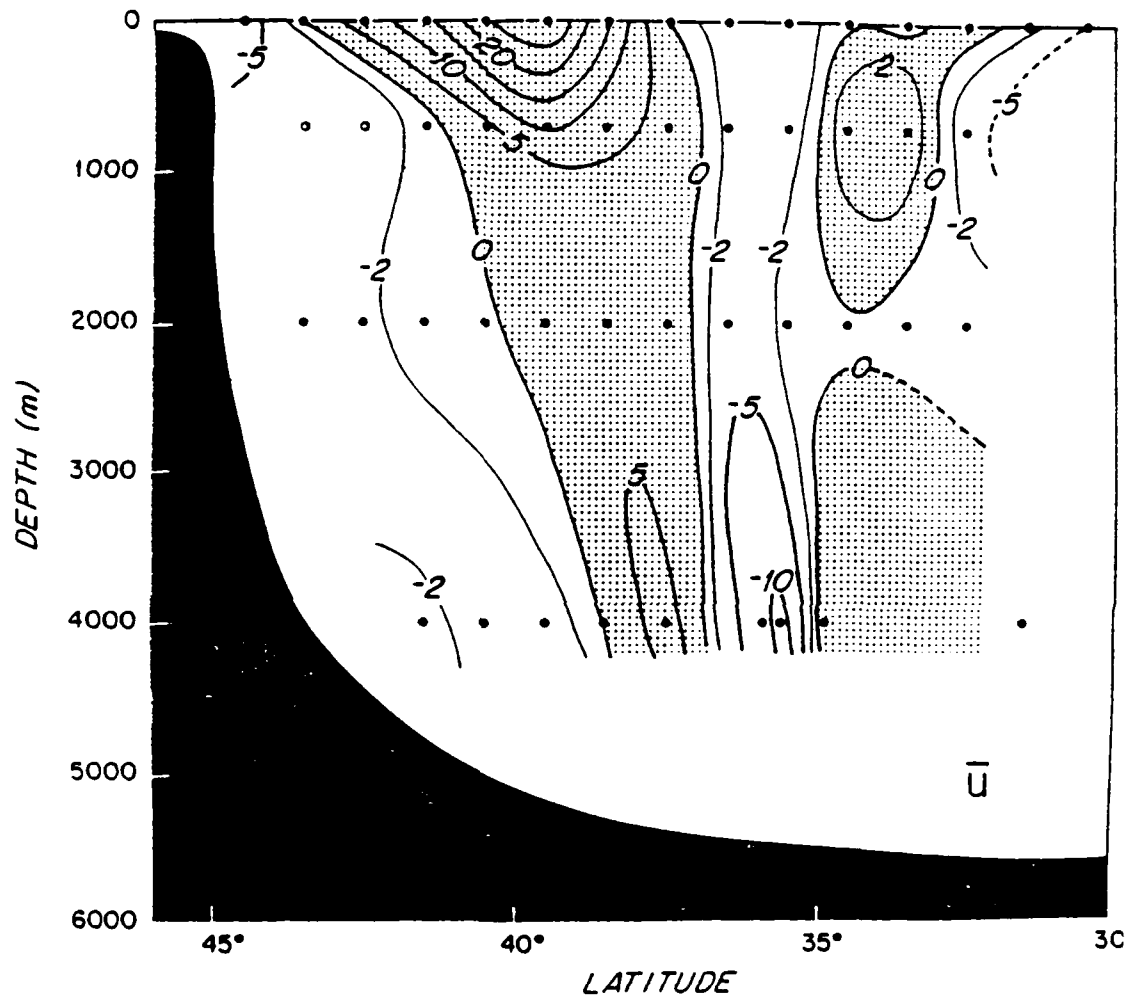


FIGURE 3

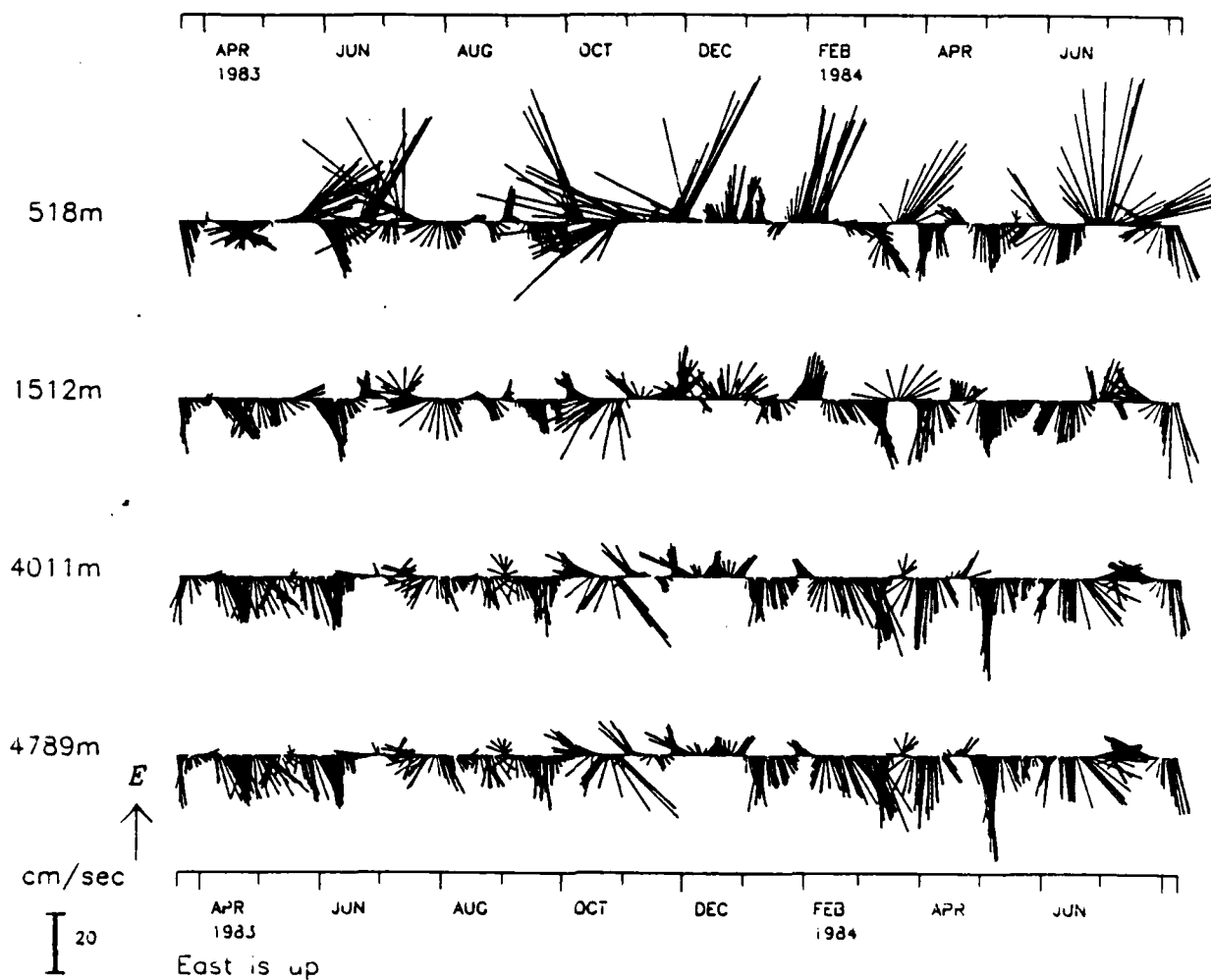


FIGURE 4a Mooring 776

(see figure 5)

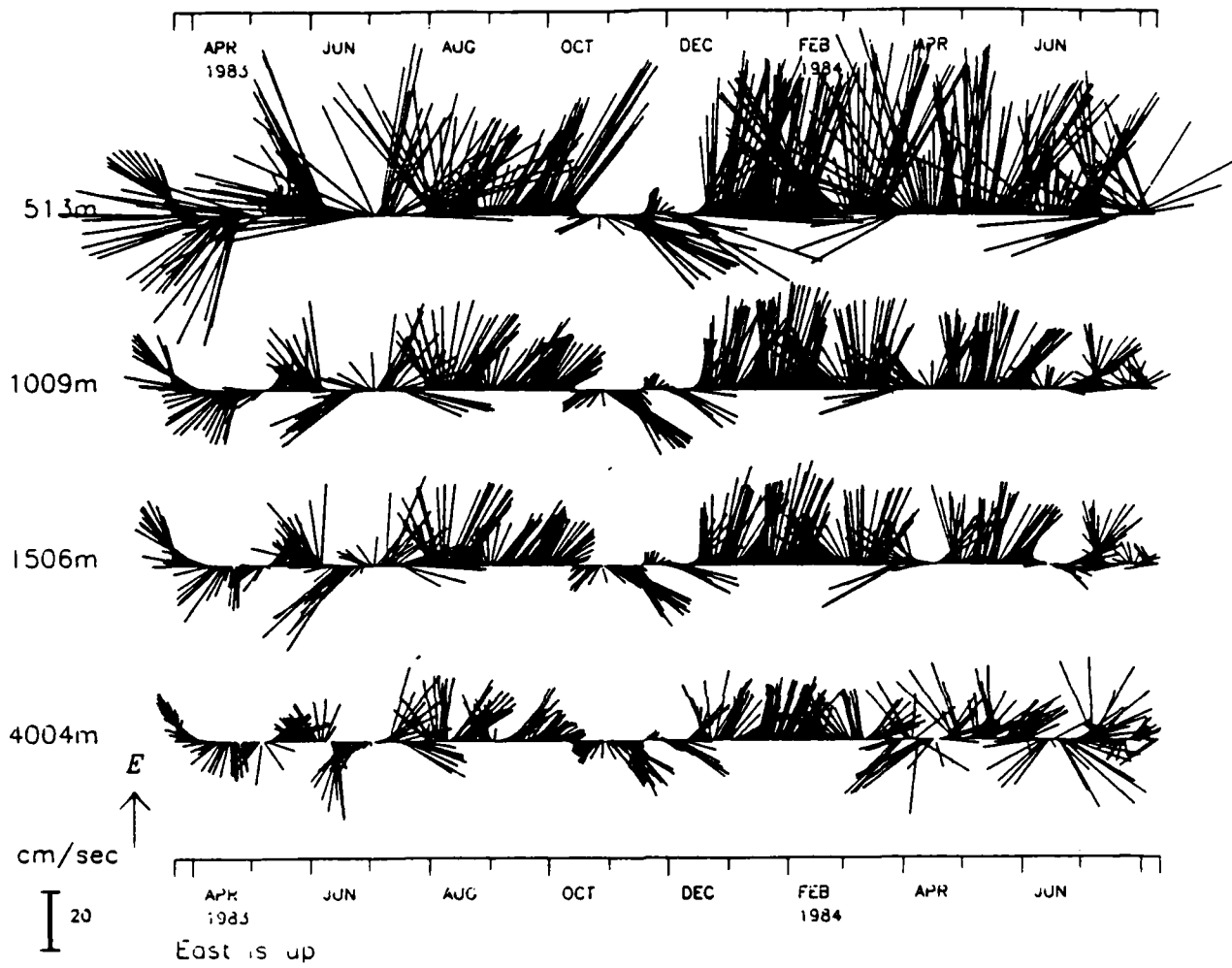


FIGURE 4b Mooring 780

(see figure 5)

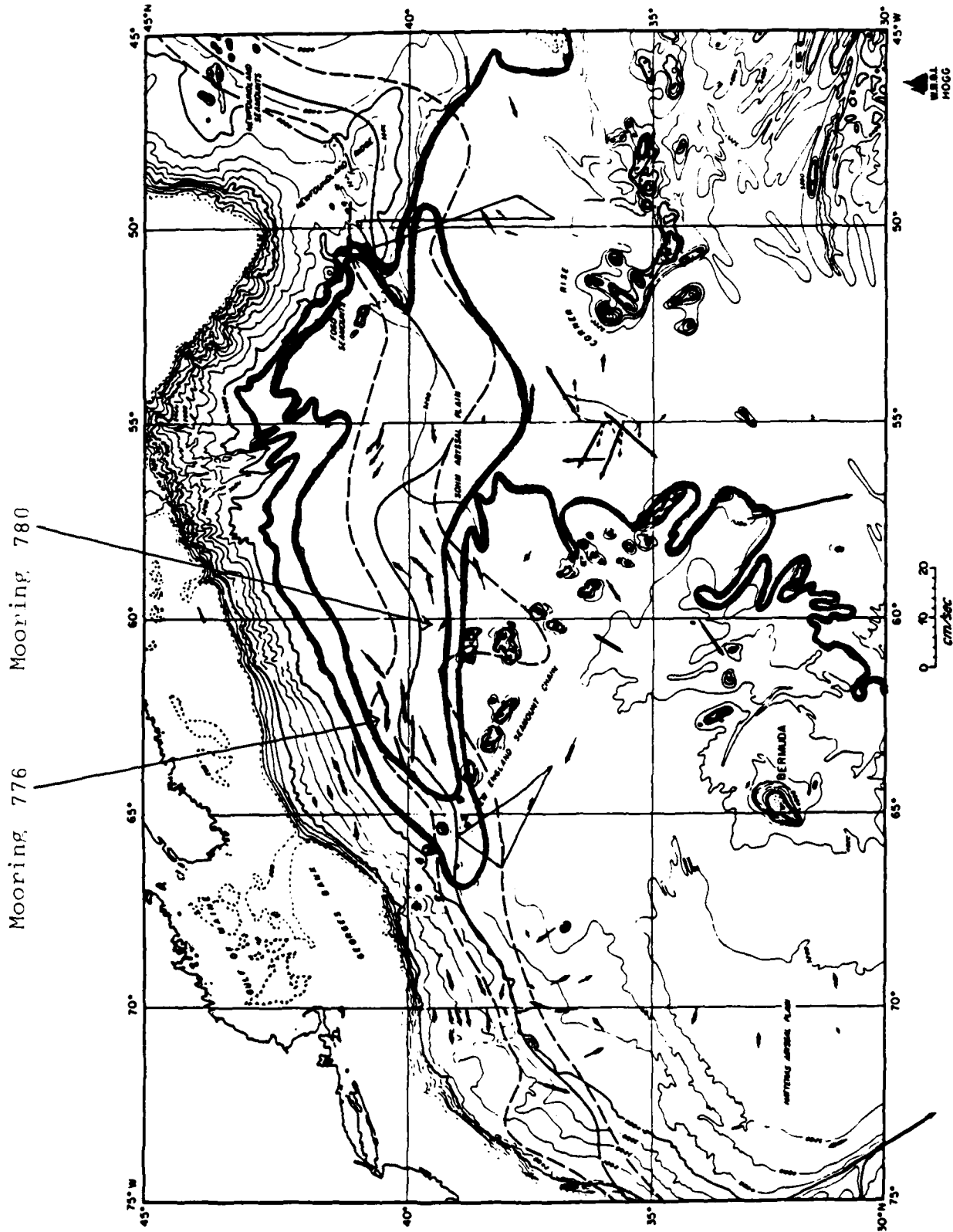


FIGURE 5

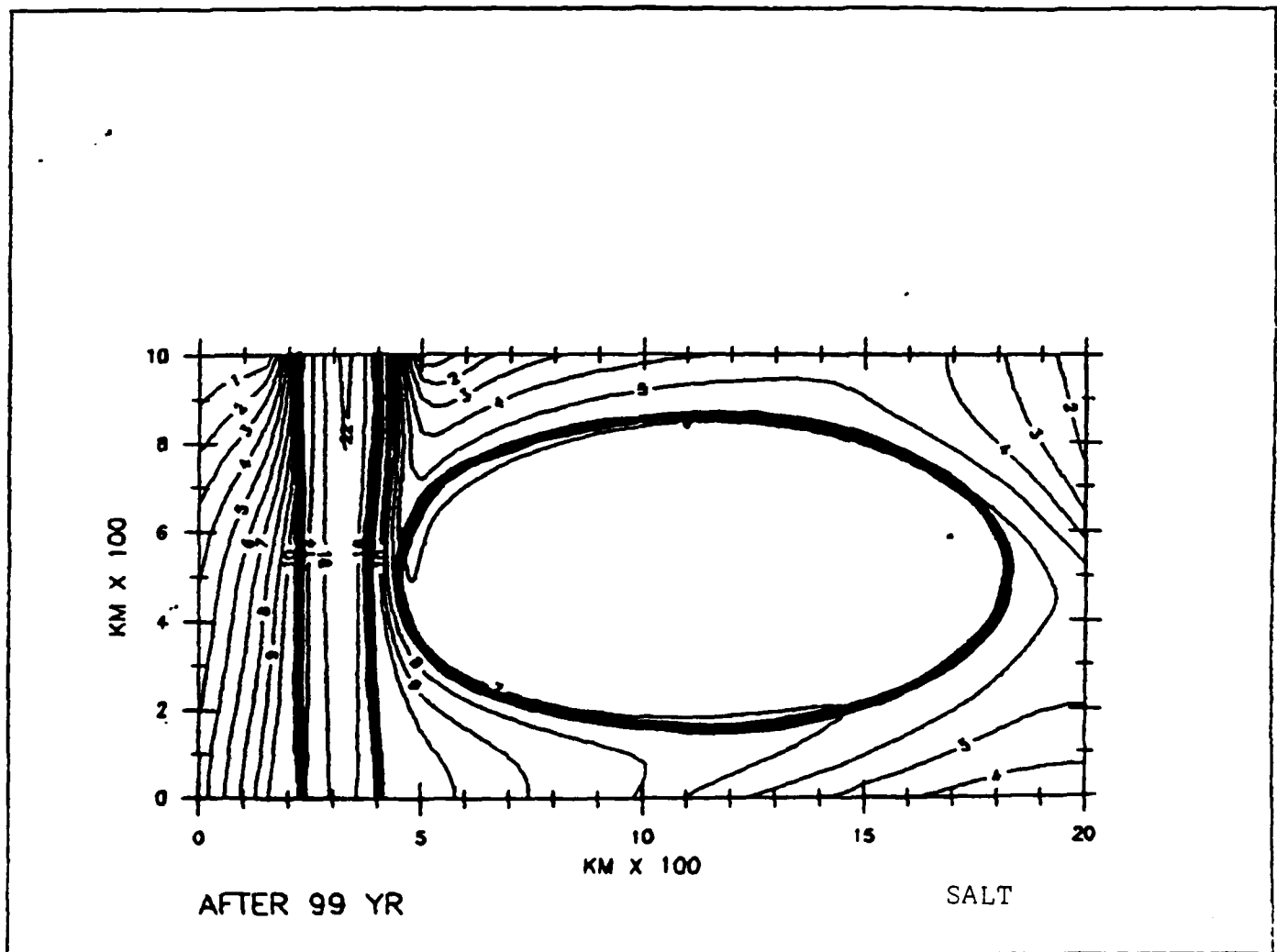


Figure 6



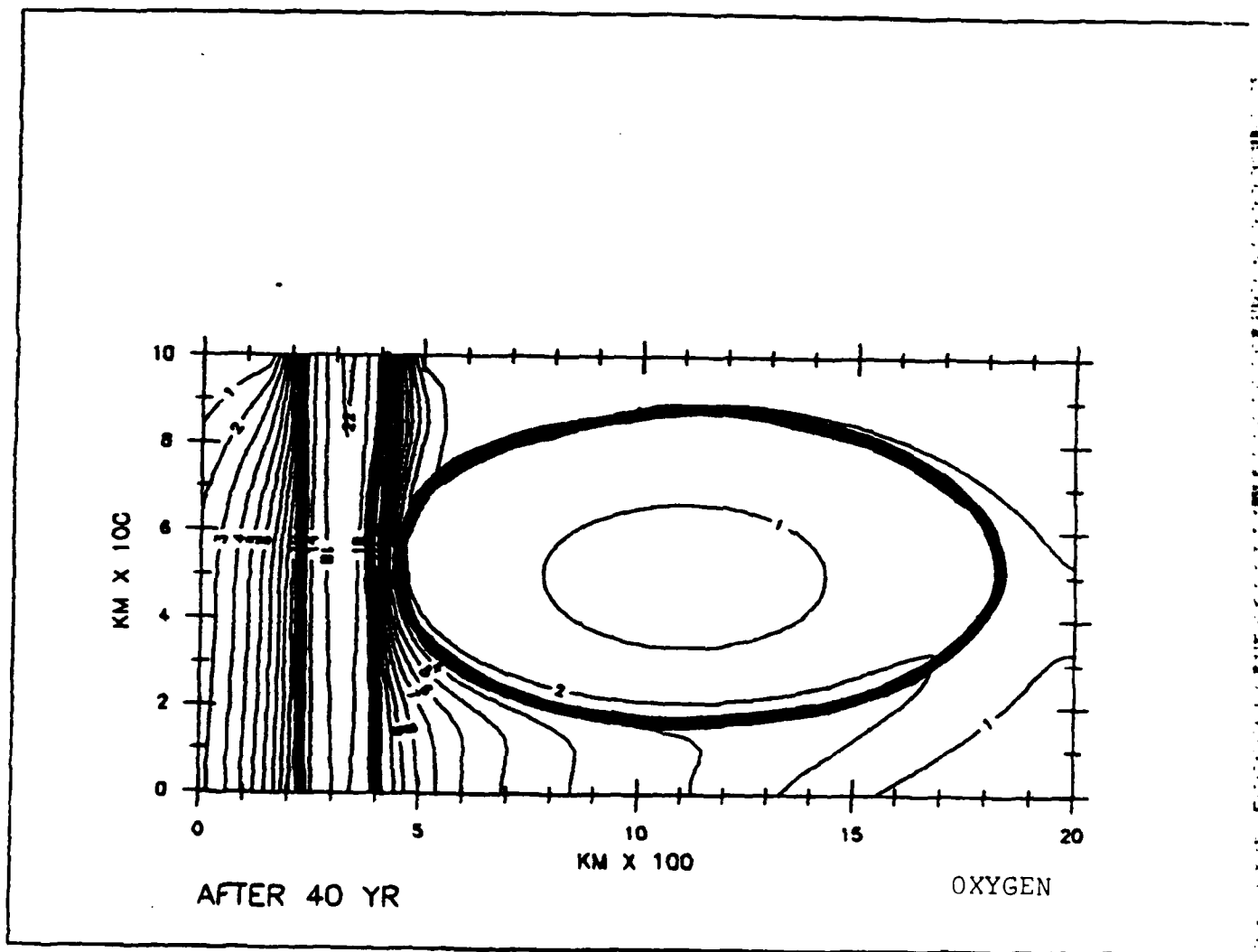
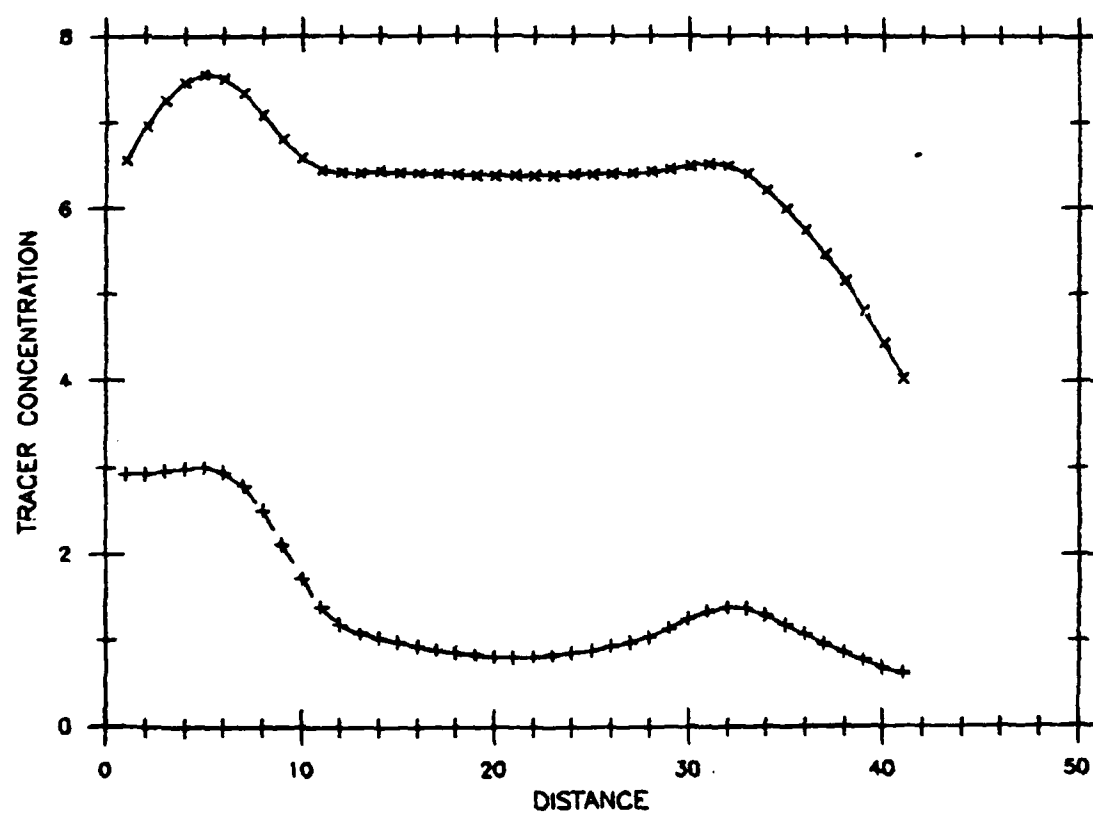
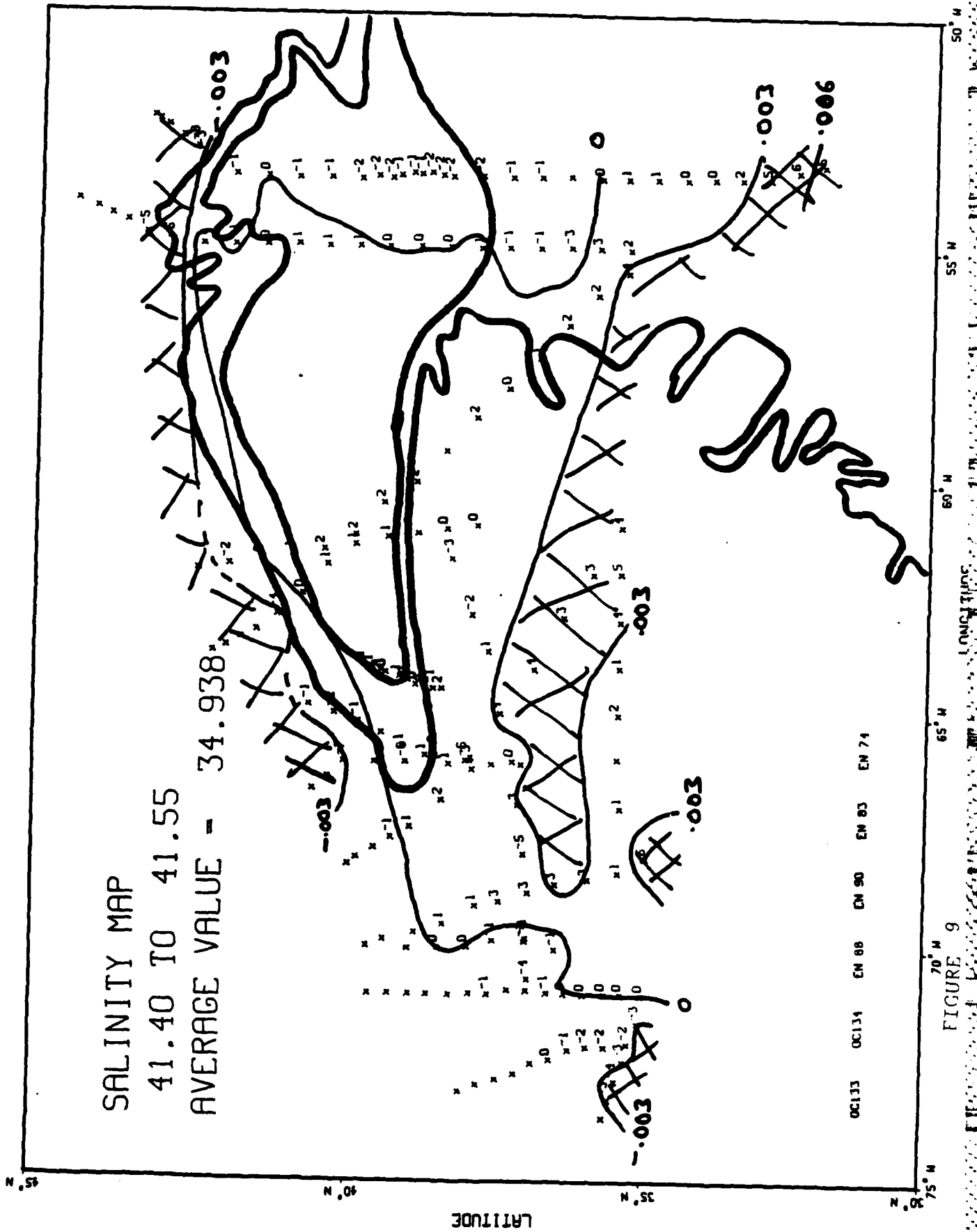


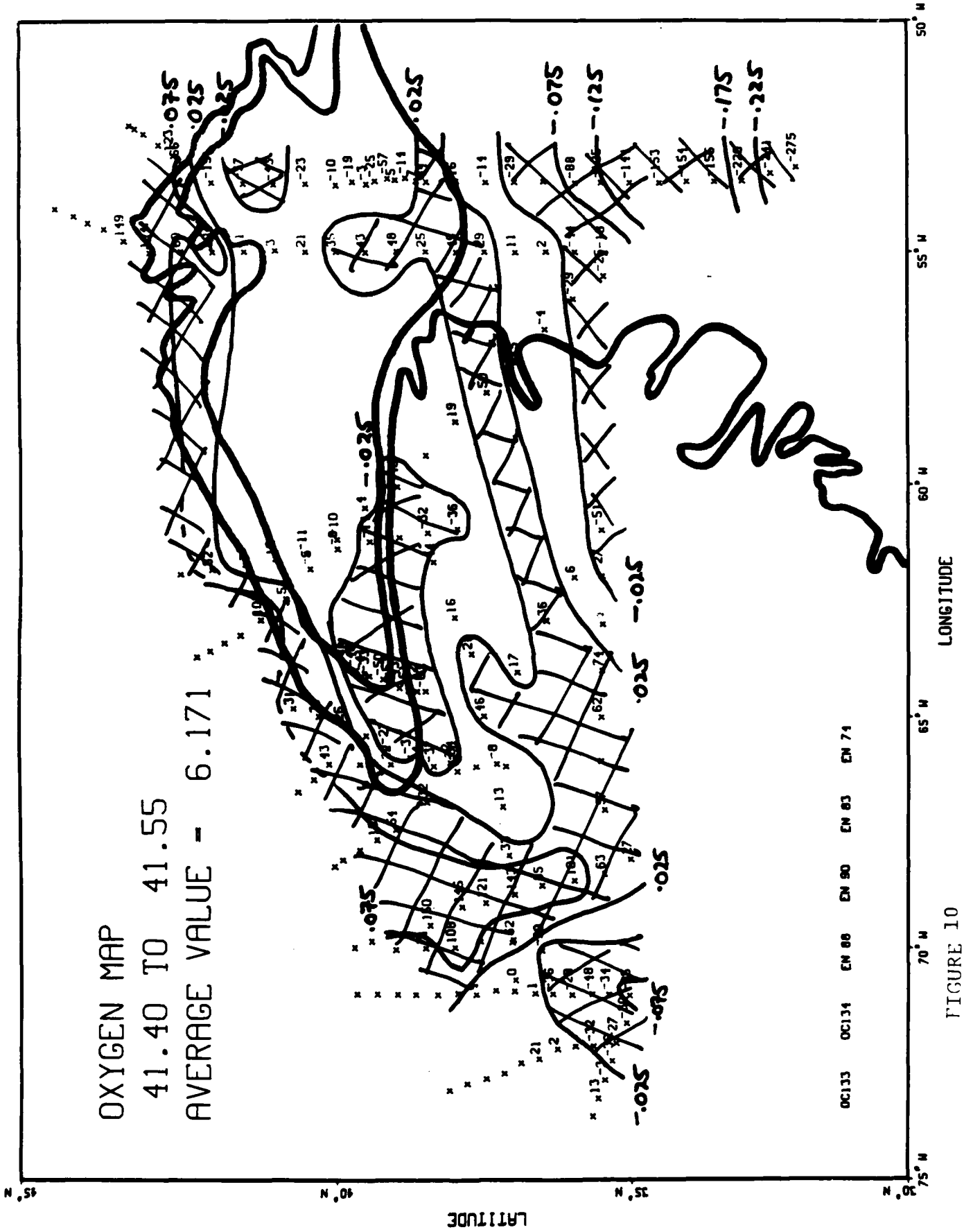
Figure 7



N-S SECTION ACROSS GYRE, SALT x OXYGEN +

FIGURE 8





EDDY-RESOLVED OCEAN CIRCULATION STUDIES RELATED TO THE  
GULF STREAM REGION

William R. Holland and James C. Evans

Introduction

Studies of eddy/mean flow interactions in basin-scale, eddy-resolved numerical models have been carried out for a decade or so. The early work focused upon the origin of mesoscale eddies as a result of baroclinic and barotropic instabilities of the western boundary current and its seaward extension and of the recirculation nearby (Holland and Lin, 1975a,b; Holland, 1978). Recent work has begun to refine the picture and has examined various theoretical issues. These include studies of the homogenization of potential vorticity (Holland, Keffer, and Rhines, 1984), instability mechanisms (Haidvogel and Holland, 1978; Holland and Haidvogel, 1980), eddy mixing and gyre equilibration (Rhines and Holland, 1979; Holland and Rhines, 1980), the dynamics of Gulf Stream Rings (Evans, 1984), and the penetration scale of the Gulf Stream (Holland and Schmitz, 1985).

In addition to these theoretical studies, comparisons of model results with observations have played an important part in model refinement and in identifying important issues regarding the physics of the Gulf Stream system (Schmitz and Holland, 1982; Schmitz et al., 1982; Holland, 1985). This work is currently being extended with models of much higher vertical resolution than heretofore to examine the vertical structure of mean and eddy fields in the Gulf Stream and Kuroshio. As illustrations of this kind of comparison, Figures 1-5 show several

observational/model intercomparisons that are currently being examined. Figures 1 and 2 show meridional sections of mean zonal flow and eddy kinetic energy in an eight layer numerical experiment; Figures 3 and 4 show similar sections (Richardson, 1983, 1984) of mean zonal flow and eddy kinetic energy based upon a whole host of observations along 55°W crossing the Gulf Stream. The correspondence is by no means exact but it is clear that vertical/horizontal structure in the numerical experiment has many features in common with the data in both mean and eddy quantities, including approximately correct ratios of surface to deep mean and eddy currents in the intense flow and similar meridional structure in terms of eastward and westward (recirculating) mean flows. Figure 5 (kindly supplied by W. Schmitz) shows an additional comparison between the data at 55°W (in the Gulf Stream) and a similar point in the intense eastward flow of another eight layer model calculation (with somewhat different parameters than the previous one). In this case the vertical structure of eddy kinetic energy is found to be remarkably similar, suggesting strongly that we are on the right track regarding the eddy/mean flow interactions that give rise to the intense eddy field in the western North Atlantic.

To date, most numerical studies have been highly idealized with respect to the geometry of the ocean basin in question. There are many good reasons for this. For one thing, simpler situations are a vital and necessary part of understanding the more complex ones. When confronting questions about detailed comparisons with observations, however, one must ask whether or where dynamically similar regions of an idealized basin can be found in the western North Atlantic? Or, turning

the question around, where in an idealized basin should one seek to compare observations along 55°W (or any other place)? Thus, as models more faithfully reproduce observed features, we are driven toward more faithful inclusion of basin shape, bottom topography, and boundary conditions (e.g., wind stress, buoyancy flux, inflow and outflow across the boundaries of local domains, etc.) into our models. Such models, with various physical and geometrical factors successively put in or taken out, allow us to ascertain which features are key to understanding the dynamics and which are not.

In the last several years, NCAR oceanographers have begun to develop models of the North Atlantic (and other basins) that have somewhat 'realistic' geometry. For example, Holland (1982) has begun to examine the wind-driven circulation in the North Atlantic basin from 15°N to 65°N using a three layer quasigeostrophic model with 1/4° horizontal resolution. Studies of the role of eddies in the general circulation and studies of the oceanic response to transient wind forcing are underway. Figures 6 and 7 show, for example, the time averaged, upper layer streamfunction for a particular case with steady wind forcing and the mid-thermocline instantaneous interface displacement for another case with purely transient (annual) forcing. The first shows the basic gyres forced by Hellerman wind stress and equilibrated by the eddies while the second shows annual period baroclinic Rossby waves driven by seasonal winds.

Even though these studies can be made with a horizontal resolution of 1/4° latitude and longitude, for some purposes even higher resolution will be needed. Unfortunately given present computers, the above models

cannot effectively be used with much higher resolution--the computational expense is just too high. Therefore, a new generation of limited area models that can successfully handle open boundaries is being developed that will allow us to telescope in on local regions of a larger domain. Figures 8 and 9 show the barotropic flows in two such eddy-resolving limited area models (ELAM's) of the western North Atlantic, one for the Gulf Stream region downstream of Cape Hatteras and one for the formation region of the Gulf Stream system including the Caribbean and Gulf of Mexico. We feel such models used in conjunction with each other and with somewhat coarser resolution basin models, will provide the ability to understand problems requiring much higher resolution ( $1/12^\circ$  resolution models are contemplated).

The inflow and outflow boundary conditions must be given on the open boundaries of limited area models, either from observations or by choosing various hypothesized conditions and varying them. A variety of techniques for treating such boundaries need study to fully understand the influence of these boundary conditions upon interior dynamics and to successfully handle the radiation of energy and the movement of waves and other dynamical features across such boundaries. Such studies are underway. We have recently developed a finite different formulation for the multi-layer quasigeostrophic energy equations that holds promise for improved treatment of radiation through open boundaries, since it allows direct examination of the energy flux impinging upon those boundaries.



### Plans

As part of the modeling component of the Synoptic Ocean Prediction Study (SYNOPS), we plan a long-term (approximately five years in duration) numerical study focusing on that portion of the Gulf Stream between Cape Hatteras and the Grand Banks (the "SYNOPS region"). The first two years of the study will address primarily dynamical issues including, inter alia, the physical mechanisms causing formation of the Recirculation, the vertical structure of the jet and the Recirculation, instability mechanisms, eddy and ring generation and their interactions with the jet and Recirculation, and topographic influence upon the flow. The later years will be devoted to comparisons between models and observations, use of the observations as boundary conditions to drive the models, and data insertion of observations into the model interiors.

Limited area models of the SYNOPS region are central to our plans. Comparisons will be made among the models, including quasigeostrophic, adiabatic primitive equation, and thermodynamic primitive equation models, and between models and observations.

To supplement the area models of the SYNOPS region, basin models will be used to examine the role of the region to the overall gyre-scale circulation of the North Atlantic. In cases where we are interested in mutual feedback between regional and gyre-scale circulations, higher resolution regional models will be embedded in the basin ones having coarser mesh.

Very high resolution local models will also be utilized to study detailed features of the flow, such as the effects of the New England

Seamounts. Embedding techniques will also be useful here to study the interactive effects of local and regional scale flows.

We have begun to look at the archived history files from Holland's prior modeling experiments for information relating to the adequacy for certain theoretical calculations of the planned two-year duration of the observational program. Specifically, we will (i) assess the rate of reduction of the errors in estimates of various terms in the energy and vorticity equations for the mean and eddy fields, (ii) compute the statistics of ring formation in the models, and (iii) describe statistically the time-dependent nature of the structure of the Recirculation.

Also during the next two years we will develop techniques for utilization in the models of the observational data that will be provided by SYNOPS. Methodology will be improved for use of the data to force the models at their open boundaries.

Because of the broad range of models available and the large ocean data sets archived here at the National Center for Atmospheric Research (NCAR), many model/model and model/data comparisons can be conducted in-house. We will continue current efforts to develop acceptable techniques for insertion of observations into numerical models (i.e., not simply changing the model dynamical state suddenly to match the data).

Once the SYNOPS data becomes available, we will examine in detail the correspondence between model results and observations. As our models improve, we will be in a better position to utilize observations as boundary conditions for the models. Comparisons between the model internal flows forced by the observed boundary conditions and the measured internal flows within the observational domain should permit us

to further refine our models. The data insertion techniques we shall have developed will be useful in the assimilation of real data.

### References

- Evans, James C., 1984: On the interaction of cyclonic rings with the Gulf Stream recirculation. Unpublished Ph.D. Thesis, Florida State University, December 1984.
- Haidvogel, Dale B. and William R. Holland, 1978: The stability of ocean currents in eddy-resolving general circulation models. J. Phys. Oceanogr., 8, 393-413.
- Holland, W.R., and L.B. Lin, 1975a: On the generation of mesoscale eddies and their contribution to the oceanic general circulation. I: A preliminary numerical experiment. J. Phys. Oceanogr., 5, 642-657.
- Holland, W.R., and L.B. Lin, 1975b: On the generation of mesoscale eddies and their contribution to the oceanic general circulation. II. A parameter study. J. Phys. Oceanogr., 5, 658-669.
- Holland, W.R., and D.B. Haidvogel, 1980: A parameter study of the mixed instability of idealized ocean currents. Dyn. Atmos. Oceans, 4, 185-215.
- Holland, W.R., and P.B. Rhines, 1980: An example of eddy-induced mean circulation. J. Phys. Oceanogr., 10, 1010-1031.
- Holland, W.R., T. Keffer, and P.R. Rhines, 1984: Dynamics of the oceanic general circulation: the potential vorticity field. Nature, 308, 698-705.
- Holland, W.R., and W.J. Schmitz, Jr., 1985: The penetration scale of the Gulf Stream. J. Phys. Oceanogr., submitted.
- Holland, W.R., 1978: The role of mesoscale eddies in the general circulation of the ocean-numerical experiments using a wind-driven quasigeostrophic model. J. Phys. Oceanogr., 8, 363-392.
- Holland, W.R., 1982: Simulation of North Atlantic variability. In: Proceedings of the Workshop on Gulf Stream Structure and Variability. Editor, John M. Bane, Jr.
- Holland, W.R., 1985: Simulation of mesoscale ocean variability in mid-latitude gyres. In Atmospheric and Oceanic Modeling, Volume XX of Advances in Geophysics, in press.
- Rhines, P.B., and W.R. Holland, 1979: A theoretical discussion of eddy-driven mean flows. Dyn. Atmos. Oceans, 3, 289-325.
- Richardson, P.L., 1983: A vertical section of eddy kinetic energy through the Gulf Stream System. J. Geophys. Res., 88, 2705-2709.
- Richardson, P.L., 1984: Average velocity and transport of the Gulf Stream near 55°W, submitted.
- Schmitz, W.J., Jr., and W.R. Holland, 1982: A preliminary comparison of selected numerical eddy-resolving general circulation experiments with observations. J. Mar. Res., 40, 75-117.
- Schmitz, William J., Jr., P.P. Niiler, R.L. Bernstein, and William R. Holland, 1982: Recent long-term moored instrument observations in the Western North Pacific. J. Geophys. Res., 87, 9425-9440.

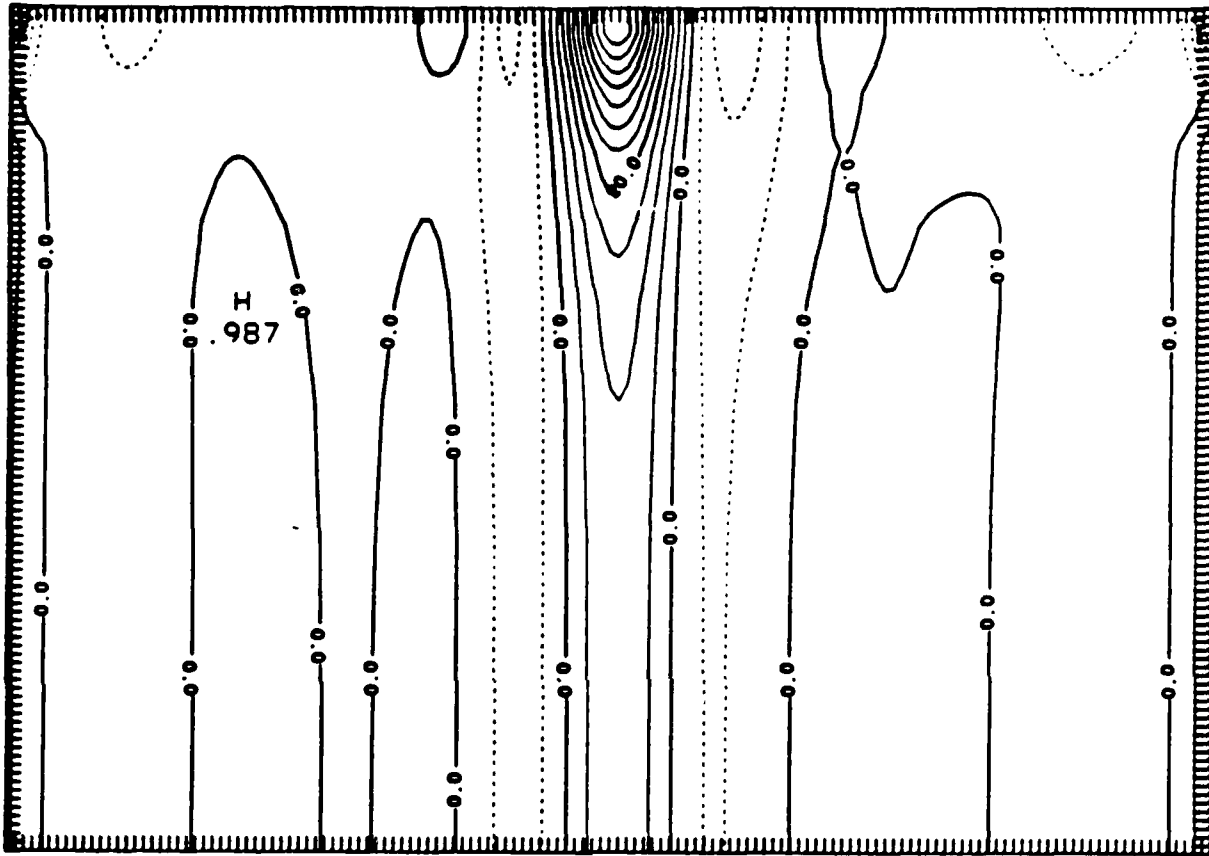


Figure 1. The mean zonal velocity in experiment 8L-2 in a north-south section at a mid-longitude in the basin. The contour interval is  $5 \text{ cm s}^{-1}$ , showing a surface jet maximum of  $55 \text{ cm s}^{-1}$ , a deep eastward flow of about  $8 \text{ cm s}^{-1}$ , and deep westward recirculating flows of  $6 \text{ cm s}^{-1}$ .

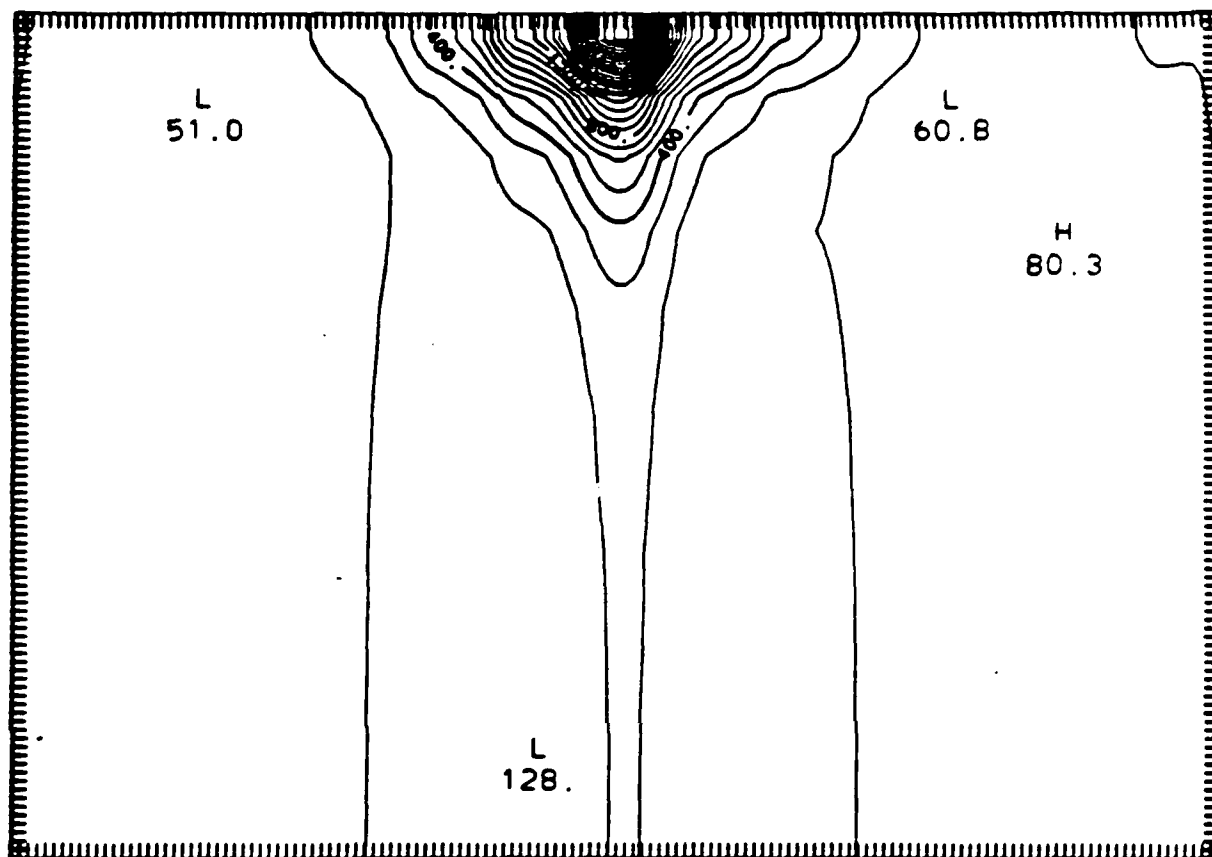


Figure 2. The eddy kinetic energy in experiment 8L-2 in a north-south section at a mid-longitude in the basin. The entire depth range—0 to 5000 m—is shown. The contour interval is  $100 \text{ cm}^2 \text{ s}^{-2}$ , the surface maximum is about  $2900 \text{ cm}^2 \text{ s}^{-2}$ , and the bottom maximum is about  $160 \text{ cm}^2 \text{ s}^{-2}$ .

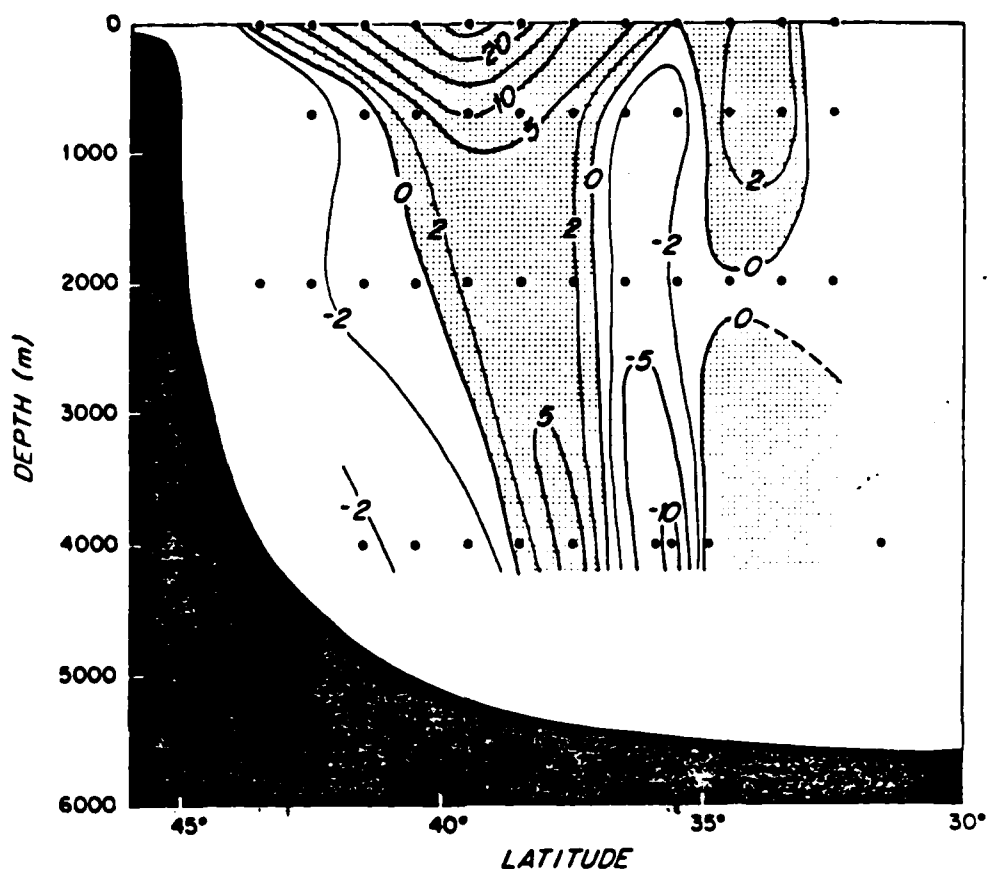


Figure 3. Contoured mean zonal velocity section ( $\text{cm s}^{-1}$ ) along  $55^\circ\text{W}$  and through the Gulf Stream from drifters, floats and current meters. Eastward velocity is shaded. Dots indicate centers of boxes used in calculating velocity except at 4000 m, where they show current meter locations. The bottom profile is from  $55^\circ\text{W}$ ; the average bottom profile between  $50-60^\circ\text{W}$  is shifted southward from this by about one degree in latitude (from Richardson, 1984).

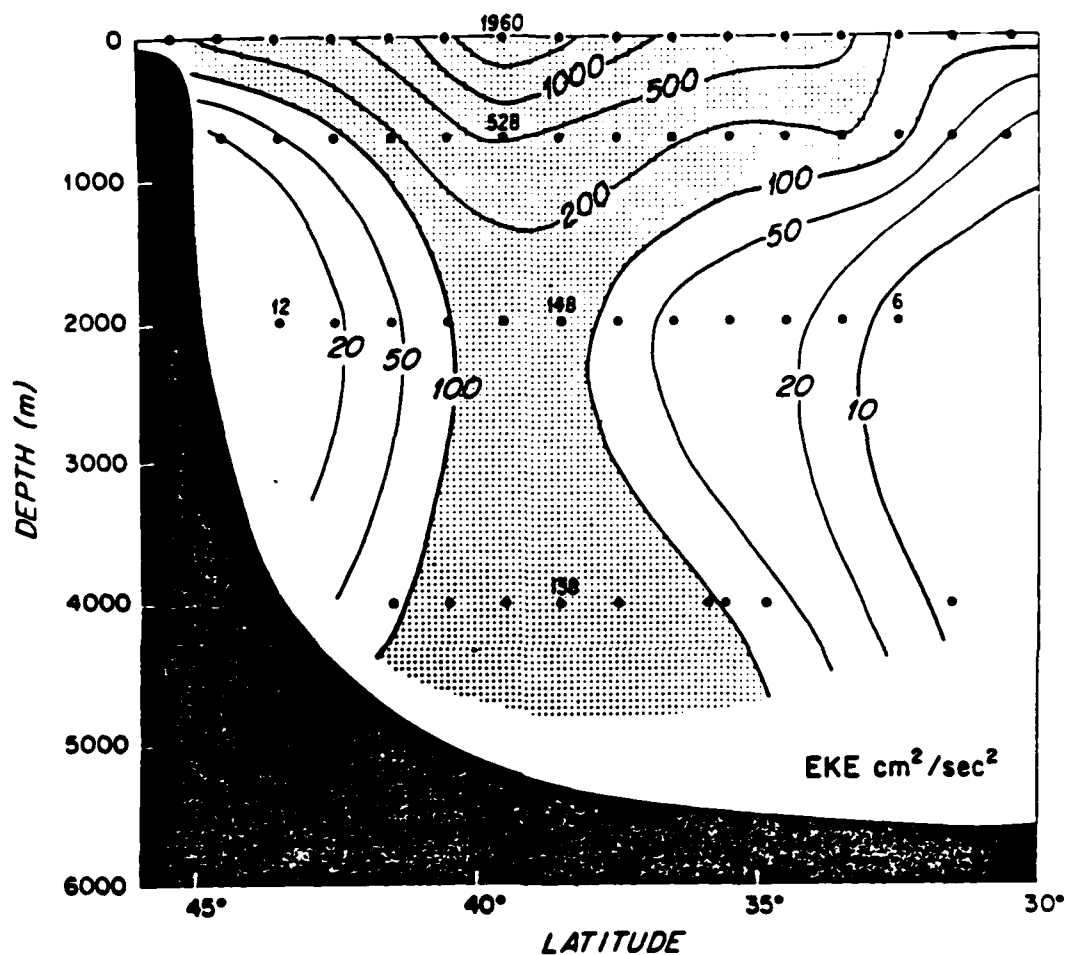


Figure 4. Contoured section along  $55^{\circ}\text{W}$  of eddy kinetic energy (per unit mass). Units are  $\text{cm}^2 \text{ s}^{-2}$ . High eddy kinetic energy and its gradient coincide with the deep mean Gulf Stream and bounding countercurrents (from Richardson, 1983).

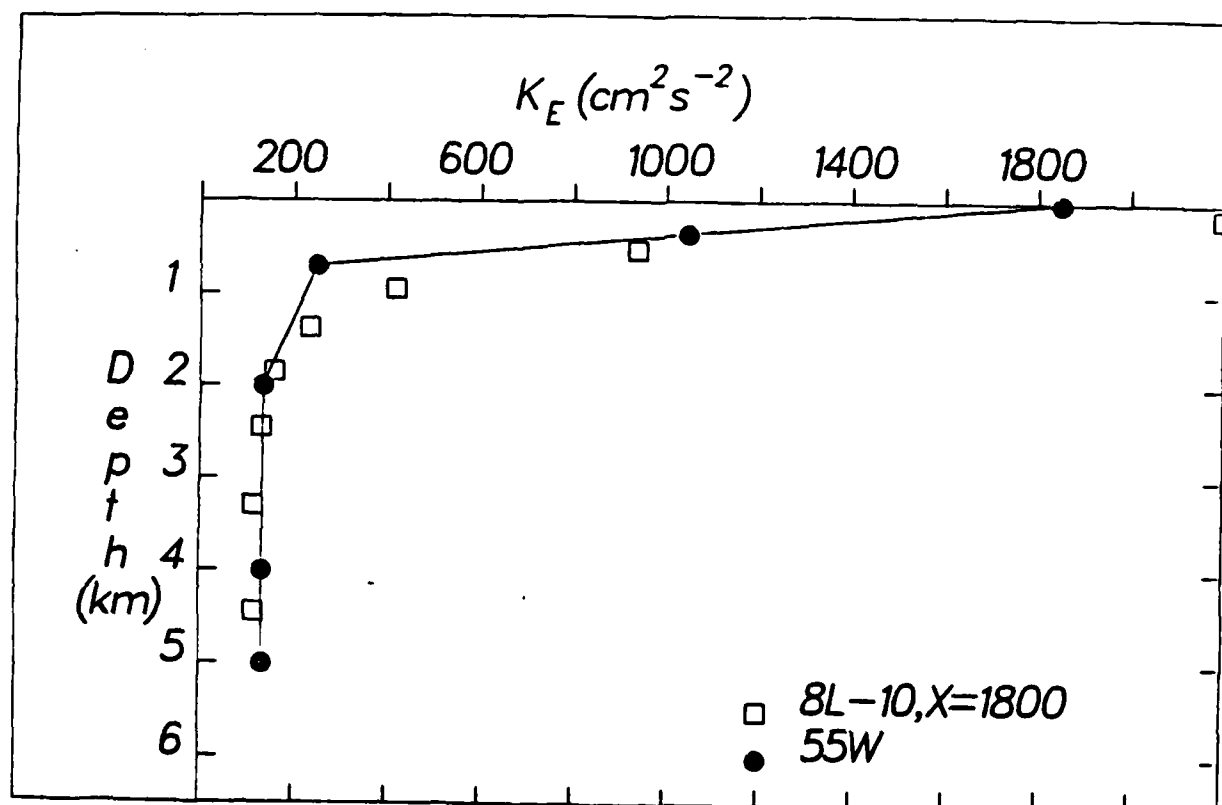


Figure 5. The vertical distribution of eddy kinetic energy. The observations (solid circles) are taken at 55°W at the latitude of the mean Gulf Stream. The model results (open squares) are from an eight layer numerical experiment in the intense eastward jet 1800 kilometers from the western boundary.



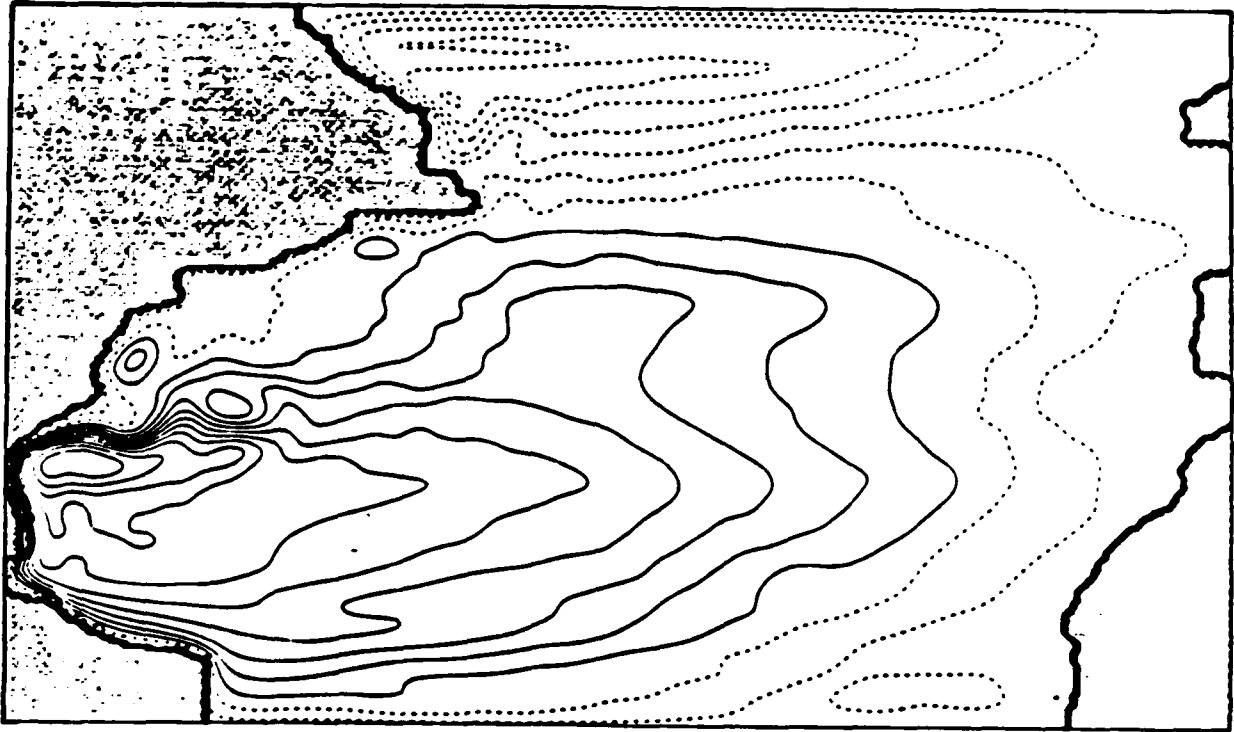


Figure 6. The time averaged, upper layer streamfunction from a three-layer, quasigeostrophic model of the North Atlantic basin. The model ocean is forced with the mean Hellerman wind stress, the horizontal resolution is  $1/4^\circ$ , and the instantaneous model ocean (not shown) is strongly transient with Gulf Stream meandering, ring formation, and mesoscale eddies present.

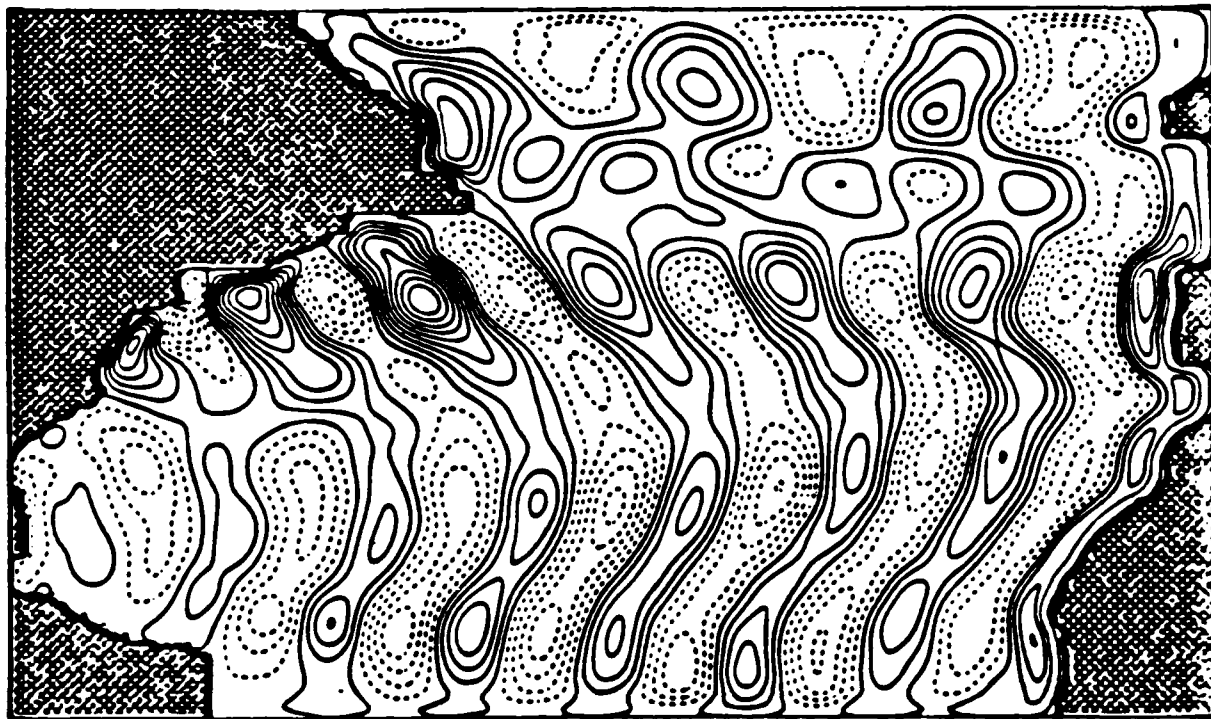


Figure 7. An instantaneous picture of the perturbation of the main thermocline depth for a North Atlantic ocean basin model driven by Hellerman's seasonal winds only (no mean forcing). Annual period, first baroclinic mode Rossby waves make up the primary response.

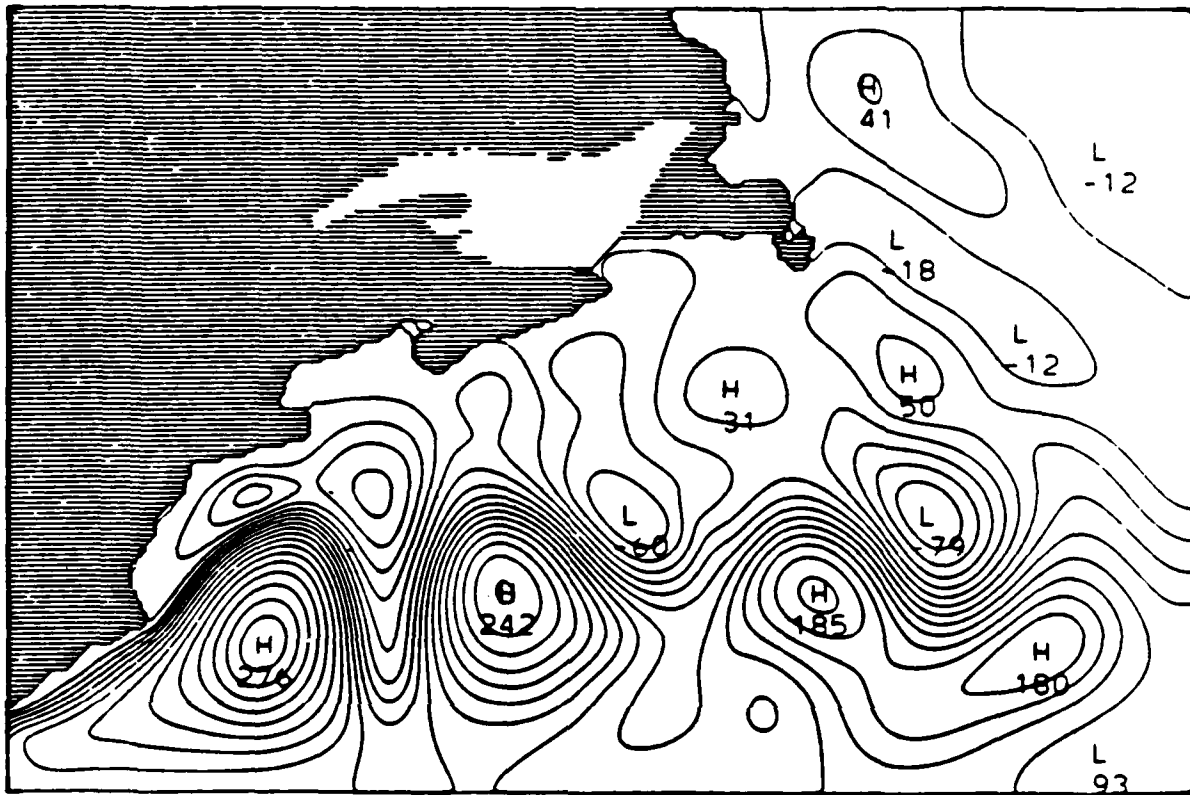


Figure 8. An instantaneous picture of the barotropic streamfunction in a limited area model of the Gulf Stream region. The horizontal resolution is  $1/6^\circ$ . The ocean circulation is driven by inflow in the southwest corner and outflow along the eastern boundary; no wind forcing is present. Separation occurs at the appropriate point near Cape Hatteras. Evidence of a recirculating gyre is apparent to the south of the eastward flowing jet.

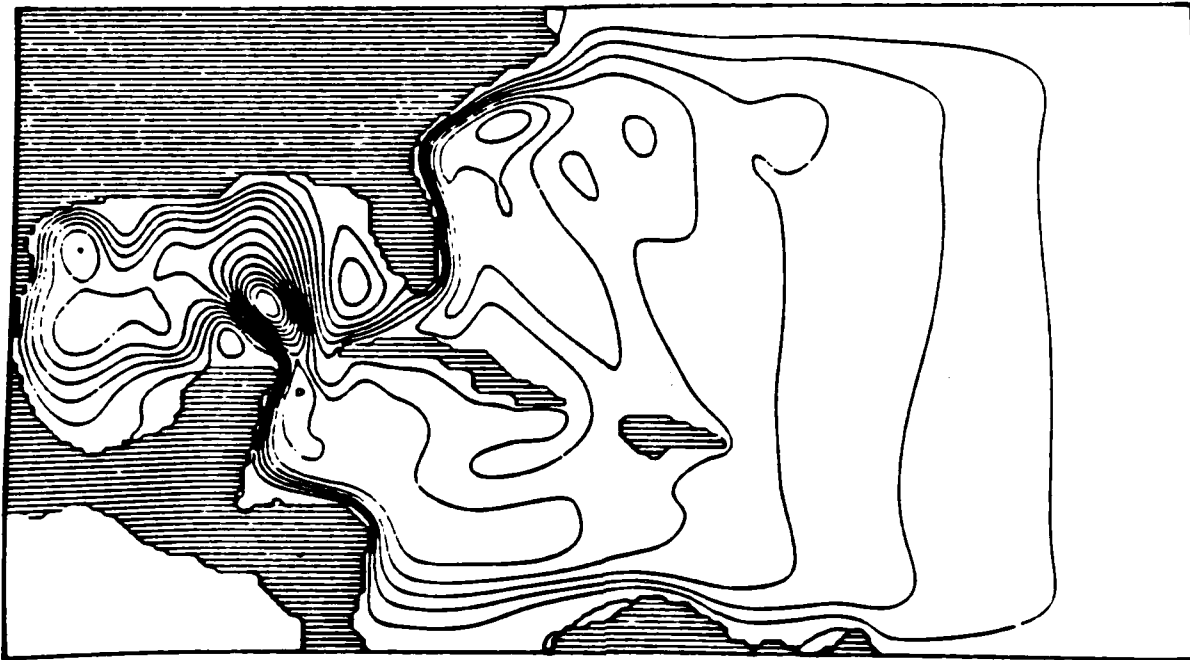


Figure 9. An instantaneous picture of the barotropic streamfunction in a limited area model of the southwestern North Atlantic including the Caribbean and Gulf of Mexico portions of the Gulf Stream system. Model resolution is  $1/4^\circ$  and the ocean is forced in the eastern part of the domain by a uniform wind stress curl. Flows across the northern and eastern boundaries could be specified in this model but have not in this calculation. Realistic Loop Current meandering and ring separation occur even in this simple barotropic case. Variability in the upstream flow may play a critical role in meandering of the Gulf Stream jet in the SYNOPS region.

PARTIAL SOLUTIONS FOR INERTIAL WESTERN  
BOUNDARY CURRENT WITH CONTINUOUS STRATIFICATION

Rui Xin Huang

Geophysical Fluid Dynamics Program  
P.O. Box 308  
Princeton University  
Princeton, New Jersey 08542

April, 1985.

## Abstract

A continuously stratified, diagnostic model of an inertial western boundary current provides a partial resolution to the puzzling problem pointed out by Blandford (1965) connected with multi-layer models. The model satisfies quite arbitrary upper boundary conditions on the vertical velocity, the western wall boundary condition,  $U = 0$ , and matches an interior ideal fluid thermocline solution with given potential vorticity functional  $q = F(B, \rho)$ , density and mass flux. The velocity condition along the lower boundary, however, is left open. Examples of inertial western boundary currents with continuous stratification are shown with and without a warm-core. The present model combined with a solution for an ideal fluid thermocline in the interior is a step forward in attempting to provide a complete solution for the circulation in a single basin.

## 1. Introduction

There have been many new models of the thermocline during the past few years. (see, for example, Rhines and Young, 1982; Luyten, Pedlosky and Stommel, 1983; Pedlosky and Young, 1983; Huang, 1984, 1985). Huang presented a method for solving the ideal fluid thermocline and current structures for a two-gyre basin with continuous stratification. However, the solution is incomplete, as the solution does not satisfy the important western boundary condition.

To close an ideal fluid thermocline model on the western boundary, there should be a western boundary current with continuous stratification. Within this narrow region the nonlinear advection terms and the Reynolds stress terms can be dynamically important. From a simple energy and potential vorticity budget analysis, frictional terms are dynamically important for a gyre circulation to be steady. However, frictional terms may not be important everywhere within the western boundary current.

Webster (1965) analyzed the surface-velocity measurements made during repeated GEK (geomagnetic electrokinetograph) crossings of the Florida current to estimate Reynolds stresses associated with the nontidal velocity fluctuations presented in the flow. As the northward flow  $\bar{v}$  increases offshore, the eddy momentum flux has found to be converging into the mean flow. The result was quite different from the intuitive expectation that lateral friction might tend to retard the Florida Current.

Schmitz and Niiler (1969) reexamined Webster's estimates and confirmed his conclusion. In addition, they found that the total energy flux integrated across the entire width of the current was not significantly different from zero within each cross section. Their conclusion was that although there was a region of strong energy transfer from eddy to mean flow, there was also a

wider region of energy transfer from mean flow to eddy over the other part of the current, resulting in no net energy gain nor loss. More recently, Brooks and Niiler (1977) made a more extended study on this problem. They came to the same conclusion that net energy conversion rates were dynamically unimportant.

Therefore, it is clear that Reynold stresses terms are dynamically unimportant in the overall energy balance for the Florida Current. The important point is that a simple constant diffusion coefficient approach cannot describe the Florida Current. In simple model it may be better to consider an ideal fluid model without the friction terms.

According to the measurements by Brooks and Niiler (1977), the relative vorticity within the Florida Current can be as big as  $-0.5f$  in the anticyclonic shear region and as big as  $f$  in the cyclonic shear region. Thus it is important to include the nonlinear advection terms for a western boundary current model. The question is whether a pure inertial western boundary current is possible for the southern half of the western boundary region. Charney (1955) and Morgan (1956) first formulated an inertial western boundary current for a reduced gravity model. The result was a reasonable fit with observations. Multi-layer models for an inertial western boundary current, however, are not successful and Blandford (1965) posed the interesting question: why is Charney's model with only one layer so successful while all multi-layer models breakdown? Though Robinson (1965) and coworkers claimed the existence of solutions for inertial western boundary currents with continuous stratification, the Taylor expansion procedure they used might not be appropriate away from the southern region where  $v$  is very small. So far the question posed by Blandford remains unanswered, and a concrete procedure of matching an interior ideal fluid thermocline with a pure



inertial western boundary current remain to be explored.

Welander (1983) presented a similarity solution for a continuously stratified inertial boundary current. The solution raised the hope of solving the inertial boundary current for general cases. His solution, however, is limited by the assumption of similarity. Among other things, the solution requires unrealistically strong upwelling on the surface.

Recently, Luyten and Stommel (1983) reexamined the question posed by Blandford and came to the conclusion that the problem of matching an interior geostrophic flow with an inertial western boundary current is overdetermined. Thus, generally for a given interior flow there is no solution which can uniquely match the interior flow with the western boundary condition. They concluded that Gulf Stream has upstream influence.

In brief, Luyten and Stommel suggested that we have to let the interior solution be self-adjusting to have a pure inertial western boundary current. A obvious question is whether some other boundary condition can be sacrificed and still have a inertial western boundary current still exist. As discussed in the Appendix A, one possible reason for separation is setting  $(u,v) = 0$  below the interface in a layer model. If the lower boundary velocity condition is relaxed, there can be many possible solutions for a given interior solution.

So far no ideal fluid thermocline solution with continuous stratification has been found that satisfies the lower boundary velocity condition. From physical point of view, the ideal fluid thermocline model may not be valid all the way to the bottom. It is also unlikely that there should be a unique isopycnal which separates the upper moving part of the ocean from the stagnant abyss.

Therefore, in the present model we basically ignore the velocity condition

along the lower boundary. We are more interested in finding some partial solutions which satisfy the upper and lateral boundary conditions.

The present model satisfies the following important boundary conditions:

- 1) At the western boundary  $U = 0$ .
- 2) On the upper boundary  $W = w_e$ , as arbitrarily specified boundary condition.
- 3) At the eastern boundary the inertial boundary current matches the interior flow with given density, potential vorticity distribution, and westward geostrophic mass flux.

By relaxing the velocity condition at the lower boundary, in contrast to no consistent solution for multi-layer models, there are an infinite number of solutions for a given interior solution. Each of these solution satisfies the same eastern, western, and upper ( $W=w_e$ ) boundary conditions. Different solutions correspond to different density conditions at the southern boundary and different northward velocity distribution given on the upper surface.

In brief, there are an infinite number of solutions for an ideal fluid model which satisfy the most important boundary conditions both for the interior and the southern half of the western boundary region. An entire gyre circulation, however, cannot be described by an ideal fluid model. From simple energy and potential vorticity balance consideration, there should be a region where the diffusion/friction terms are important and the air-sea interaction/vertical convection and other processes determine water mass properties before water leaves the western boundary region and joins the interior. Rhines (1984) discussed this pinching region in detail.

In a sense, if a pure inertial western boundary current can be formed within the southern half of the western boundary, then the only appropriate candidate of this pinching region will be the north-west corner. That is an important reason why we should try to solve a pure inertial model for the

upstream part of the western boundary current.

## 2. Basic Equations

It is assumed that the ocean is steady and incompressible and without dissipation. The Boussinesq and  $\beta$ -plane approximations are assumed. By standard boundary layer arguments we deduce that the flow parallel to the boundary is geostrophic, while the force balance in the other direction involves inertial terms. Therefore, the basic equations are;

$$-fv = -Px \quad (1)$$

$$uv_x + vv_y + wv_z + fu = -Py \quad (2)$$

$$P_z = -\rho g \quad (3)$$

$$u\rho_x + v\rho_y + w\rho_z = 0 \quad (4)$$

$$u_x + v_y + w_z = 0 \quad (5)$$

For this system there are two first integrals

$$\vec{u} \cdot \nabla q = 0 \quad (6)$$

where  $q$  is the potential vorticity

$$q = (f + v_x)\rho_z - v_z\rho_x \quad (7)$$

and

$$\vec{u} \cdot \nabla B = 0 \quad (8)$$

where  $B$  is the Bernoulli functional

$$B = p + \rho g z + v^2/2 \quad (9)$$

Because a streamline is a curve in a three-dimensional space, it can be described by two parameters. These two parameters can be  $q$  and  $B$ , for example. That means there is a functional relationship between  $\rho$  and  $(B, q)$ , namely  $\rho = \rho(B, q)$  or equivalently

$$q = F(B, \rho) \quad (10)$$

There is a simple relation between the velocity vector and all these conservative quantities. From (4) and (8), the velocity vector can be written as

$$\vec{u} = a \cdot \nabla \rho \times \nabla B \quad (11)$$

Where  $a$  is a constant factor which can be found either from (1) for the  $v$ -component or by solving (2) and (4) for the  $u$ - and  $w$ - components. Multiplying (1) by  $\partial p / \partial z$  and adding terms  $V(V_{x\rho z} - V_{z\rho x})$  on both sides, this factor is found to be  $1/q$ , where  $q$  is the potential vorticity. Thus (11) can be rewritten as

$$\vec{u} q = \nabla \rho \times \nabla B \quad (12)$$

Needler first proved (12) in the simpler case of an ideal fluid with no advective nonlinear terms, but the result is much more general.

Attempts were made to classify the equation system (1,2,3,4,5). This system, however, is degenerate as discussed in Huang (1984), and its mathematical properties are largely unknown. In Appendix B the conservation relation (6), (8) and relation (12) are proved to be true for more general case with inertial term included in (1). The corresponding system of equations has been classified as a non-strict hyperbolic quasilinear system (Huang, 1984). Streamlines are triple characteristics, and the  $z$ -axis is a double characteristic for this system.

### 3. Boundary Value Problem for the initial western boundary current with continuous stratification.

Assuming that the potential vorticity functional relation (10) is given, the integration procedure can be divided into two steps:

(i) Determination of boundary conditions on the sea surface with the following equations:

$$P + \frac{v^2}{2} = B \quad (13)$$

$$B_x \rho_y - B_y \rho_x = -wq \quad (14)$$

$$-fV = -P_x \quad (15)$$

Given  $w_e = w(x, y)$  and  $q = q(B, \rho)$ , if one specifies any one variable among  $(B, p, \rho, v)$ , the above system can be solved for the rest of the unknowns.

ii) Marching downward with

$$\rho_z = \frac{q(B, \rho) - g\rho_x^2/f}{(f + v_x)} \quad (16)$$

$$B_z = zg\rho_z - vg\rho_x/f \quad (17)$$

$$v_z = -g\rho_x/f \quad (18)$$

$u$  and  $w$  can be obtained from (12).

The solution has to satisfy other boundary conditions.

1) The eastern boundary condition.

$$v \rightarrow 0, \rho_s \rightarrow \rho_{se}, \rho_x \rightarrow 0 \quad \text{at } x = x_e \quad (19)$$

$$q = q(B, \rho) \text{ is given} \quad (20)$$

Generally the eastern boundary condition is put at  $x \rightarrow \infty$ . For a numerical integration, however, it is convenient to start from a finite eastern boundary.

2) The upper boundary condition. To initiate the upper surface field two quantities should be given. The natural choice is specifying  $w = w_e$  as the Ekman pumping velocity. For the interior ocean specifying  $w = w_e$  has proved

to be both reasonable and convenient (Huang, 1985). For the western boundary region the vertical velocity on the upper surface can be affected by both the lateral and bottom boundary conditions, and the dynamical role of the Ekman pumping velocity,  $w_e$  is uncertain. In most similarity solution  $w_e$  is strongly limited by the similarity assumption. In the similarity solution of inertial western boundary current by Welander (1983) there is a very strong upwelling. In the present model, however,  $w_e$  can be arbitrarily specified as one upper boundary condition.

A possible choice for the second upper boundary condition is specifying  $\rho = \rho_S$  as the density pumping down from the mixed layer, as has been done for the interior ocean (Huang, 1985). However, within the western boundary region the strong current must interact with the mixed layer, thus a simple one-layer mixed layer cannot give an appropriate value of  $\rho_S$ . Assuming  $\rho_S$  is given, then starting from the eastern/southern boundaries, the Bernoulli functional  $B$  can be found by integrating (14) along its characteristic  $\rho_S = \text{constant}$ . The next step is integrating

$$P + \frac{P_x^2}{2f^2} = B(x) \quad (20)$$

along each  $y = \text{const.}$  line and finding  $p$  and  $v$ . This first-order ordinary differential equation is highly nonlinear. For the present case of an inertial boundary current, the initial value problem with  $p(x_e) \sim B(x_e)$ ,  $dp/dx|_{x_e} \sim 0$  is very sensible to the initial condition. It is easy to prove that for stable stratification  $V_x > -f$  holds. As  $\rho_S$  is given arbitrarily, however, there is no guarantee that the above constraint can be met.

The difficulty of handling this ill-posed boundary value problem for nonlinear equation (20) can be overcome by the following approach. From the

discussion of western boundary condition  $B$  is constant along the western wall. Therefore, for any given value of  $y$ ,  $B$  is given on both the eastern and western boundaries. The problem is finding  $v(x)$ ,  $B(x)$  which satisfy

$$\frac{v^2}{2} + f \int_{x_0}^x v dx = B(x) \quad (21)$$

$$B(X_0) = B_w, B(X_e) = B_e \quad (22)$$

$$V(X_e) = 0 \quad (23)$$

Obviously, this is an underdetermined problem.

The simplest choice is

$$V(X) = V_0 (1 - X/X_e)^\alpha \quad (24)$$

where  $\alpha > 1$  to simulate the real case in ocean. Therefore

$$B(x) = B_e + V_0 (1 - x/x_e)^{\alpha+1} \left[ \frac{V_0}{2} (1 - x/x_e)^{\alpha-1} - \frac{fx_e}{\alpha+1} \right] \quad (25)$$

$$V_0 = \frac{fx_e}{\alpha+1} - \left[ \left( \frac{fx_e}{\alpha+1} \right)^2 - 2(B_e - B_w) \right]^{1/2} \quad (26)$$

To guarantee the existence of such solutions

$$\left( \frac{fx_e}{\alpha+1} \right)^2 > 2(B_e - B_w) \quad (27)$$

For such solution the relative vorticity satisfies

$$|V_X| < \frac{\alpha}{\alpha+1} f \quad (28)$$

on the sea surface. Thus the solution is valid at least near the upper surface.

Combination of solution in forms of (24) or others can also be applied. The point is that there are infinite number of solutions depending on the upper boundary condition.

The sea surface density can be computed from integrating (14) along



characteristics  $B=\text{const.}$  For simple case with  $w_e \approx 0$ ,  $\rho$  is constant along the  $B$ -constant lines.

3) The southern boundary condition. Both  $\rho_s$  and  $V_s$  are specified along the southern boundary (on the upper surface).

To guarantee that  $\rho_x$  is continuous in the interior, the density and the Bernoulli functional distribution around the east-southern corner should satisfy.

$$\left. \frac{dB}{d\rho} \right|_{\text{along } x \text{ axis}} = \left. \frac{dB}{d\rho} \right|_{\text{along } y \text{ axis}} \quad (29)$$

Although there may not be a water mass exchange across the southern boundary within the interior ocean, if the zero-Ekman-pumping line is a latitude circle and  $\rho_s = \text{const.}$  along this line (Huang, 1985); there can be water mass flux cross that line within the boundary current zone. This mass flux, however, must be determined from the overall dynamical balance of the entire basin circulation.

#### 4. The Western Boundary Condition

Assume that the ideal fluid model applies up to the western wall, thus

$$u = 0 \text{ at } x = x_w \quad (30)$$

A sufficient condition is

$$\rho = \rho_0 \text{ at } x = x_w \quad (31)$$

Condition (31) implies a further constraint on the solution.

From (15), by setting  $\rho_z = 0$

$$q = g\rho_x^2/f > 0 \text{ at } x = x_w \quad (32)$$

Since fluid in western boundary current comes from the interior where  $q$  should be always non-positive. Thus along the western wall

$$\rho = \rho_b, \rho_x = 0, q = 0, B = B_w \quad (38)$$

where  $\rho_b$  is the density for the abyss. Notice that  $p$  and  $v$  can vary along the western wall, though  $B$  is a constant there.

It is interesting to notice that an ideal fluid thermocline model can easily satisfy the  $u=0$  boundary condition by specifying  $\rho_s = \rho_b$  and  $q=0$  on the western wall (Huang, 1985). Although in such model the Bernoulli functional does not include the kinetic energy term and the potential vorticity does not include the relative vorticity. Therefore, the downstream velocity variation has no connection with the downstream pressure gradient. As Webster (1961) points out, the downstream pressure gradient is important to the energetics of the Florida Current because there is a simple Bernoulli function conservation law. It is, thus important to include the velocity term in the Bernoulli functional.

In comparison, it is interesting to note that a single moving layer model of wind-driven circulation cannot satisfy the western boundary condition  $u=0$  without including the non-linear advection terms. Furthermore, it is much harder to apply multi-layer models in simulating the wind-driven circulation

for a stratified ocean.

A similar density boundary condition applies to the eastern boundary (Killworth, 1983; Huang, 1985). By assuming shadow zones, Luyten, Pedlosky and Stommel successfully applied a multi-layer model up to the eastern wall. Pedlosky (1983) later relaxed the  $u = 0$  condition by assuming the existence of upwelling/downwelling near the eastern wall. These approaches cannot apply to the western boundary current, simply because  $u > 0$  implies separation and it is commonly known that pure inertial boundary current cannot exist for regions of  $u > 0$ .

If a multi-layer model is applied to the analysis of inertial western boundary currents, the interface might cross the upper surface. In such case the potential vorticity for layer model,  $q = (f + \zeta)/D$  is infinite along the outcropping edge. Luyten, Pedlosky and Stommel included this infinity in their potential vorticity figure. This infinity singularity makes the multi-layer model very hard to handle analytically. Strictly, potential vorticity for a layer model is not necessarily infinite on the edge of the outcropping line. There the other term from the horizontal density gradient should compensate,  $q = (f + \zeta)/D - \rho \partial^2 \chi / \partial x^2 = \infty - \infty$ .

The constant density condition along the western wall is only a sufficient condition. This condition renders the integrating procedure very easy by guaranteeing  $u = 0$  at  $X = X_w$ . In the real ocean observations show cold water piled up along the western wall, thus this assumption isn't too bad.

##### 5) The lower boundary condition.

There is no velocity condition at the lower boundary with the present model. Considering the fact that even for the interior no solution has been found which satisfies velocity condition at the lower-boundary, this choice seems reasonable.

Though the potential vorticity functional form used here guarantees density to be homogeneous in the interior abyss, the downward-marching procedure for an elliptic or hyperbolic-elliptic composite equation yields a very noisy solution once the integration gets down below the first few hundred meters. Therefore, our examples here are only some partial solutions. These solutions, hopefully give some typical structure for inertial western boundary current with continuous stratification.

## 4. An inertial western boundary current with no warm core

In principle the potential vorticity functional form can be fairly arbitrary. For example, an easy choice would be  $q = F(\rho)$  as used by Welander (1983). However, as pointed out in Huang (1985), such a functional form corresponds to an unreasonable circulation in the interior. Therefore, in our example, the potential vorticity form is adapted from Huang (1985)

$$q = F_1 = -a_1(\rho - \rho_1) - b_1(B_1 - B) \quad 1.026 < \rho < 1.027$$

$$= F_2 = -a_2\rho - b_2(B_2 - B) + b_3(B_3 - B)(B_4 + B) \quad 1.0275 < \rho < 1.028$$

$$= F_3 = -a_3(1.0285 - \rho) \quad 1.0280 < \rho < 1.0285$$

between these regions the potential vorticity functional is matched through smooth transitional regions

$$F = d_1 F_1 + (1 - d_1) F_2 \quad 1.027 < \rho < 1.0275$$

$$\text{where } d_1 = ((1.0275 - \rho)/0.0005)^3$$

$$\text{and } F = d_2 F_2 + (1 - d_2) F_3 \quad 1.028 < \rho < 1.0285$$

$$\text{where } d_2 = ((1.0285 - \rho)/0.0005)^3$$

This form of potential vorticity is an idealization from the GEOSECS western section and gives a reasonably good circulation pattern for a subtropical basin. Fig. 1 shows, for example, the potential vorticity contours along the western boundary and through the center of the gyre. For the details the reader is referred to the aforementioned paper.

Along the eastern boundary the Bernoulli functional is given

$$B_e = 0.000003y(1 - 2.5 \times 10^{-7}y)$$

which corresponds to a  $u$ -velocity linearly varied from zero on the north end to  $-7$  cm/sec on the southern end.

As a simple choice, density distribution along the eastern boundary is linearly proportional to the Bernoulli functional. This gives an upper surface density pattern with warm, light water on the north and cold, dense water on

the south. This kind of density pattern corresponds roughly to the observed structure at 300-400 meter depth from the GEOSECS Western section.

Because the role and the magnitude of Ekman pumping within the western boundary is uncertain,  $w_e = 0$  is used in the following example. Though any reasonably given  $w_e = w_e(x,y)$  can be used. This is also consistent with our simplified matching condition along the eastern boundary that  $v=0$  and  $B, \rho$  tend to the given interior distribution.

In the calculation, a simple  $\beta$ -plane approximation is assumed, thus

$$f = f_0 + \beta(y-y_0)$$

where  $f_0 = 6.16 \times 10^{-5}/s$

$$\beta = 1.79 \times 10^{-11}/s/m$$

$$y_0 = 1000 \text{ km}$$

The western boundary current is studied within a rectangular region with  $x = [0,300] \text{ Km}$ ,  $Y = [0,2000] \text{ Km}$ .

Along the southern boundary the flow condition is not given directly. Instead,  $B_w$  is specified and  $\alpha$  is chosen.  $B_w = -0.5$  and  $\alpha = 3$ , along the southern boundary. The density distribution along the southern boundary satisfies two conditions:

i)  $\rho_x = 0$  at  $x = x_w$ .

ii)  $\frac{dB}{d\rho} \Big|_{x \rightarrow x_e} = \frac{dB}{d\rho} \Big|_{y \rightarrow 0}$ .

For convenience, we choose

$$\rho = \rho_0 - \alpha x^2 \quad 0 \leq x \leq x_m$$

$$\rho = kB \quad X_M \leq X \leq X_e$$

At  $x = x_m$ ,  $\rho$  and  $d\rho/dx$  are continuous.

To find a better velocity profile  $\alpha$  is linearly decreased from 3 on the southern boundary to 2 on the northern boundary.

The first step is calculating the  $(B,V)$  field on the sea surface, using (24), (25), and (26). Then the density field is calculated by (14).

The second step is marching downward using (15), (16) and (17).  $z$ -coordinate is treated as a time-like coordinate. A Heun scheme with respect to  $z$ , and a central difference scheme with respect to  $x$  are used in the integration. (See Appendix C). In calculation  $\Delta x = 7500$  m,  $\Delta y = 50000$  m and  $\Delta z = 4$  m are used.

The calculated result is shown in Fig. 2-4. The potential density  $\sigma_\theta$  and  $v$ -velocity profiles are shown in Fig. 2 on the upper surface and at depth  $z = -300$  m and  $z = -600$  m (these depths correspond to roughly  $-400$  m,  $-700$  m, and  $-1000$  m in the Western Atlantic Ocean). The meridional sections for  $\sigma_\theta$  and  $v$ -velocity along the northern boundary, through the center of the gyre, and along the southern boundary are shown in Fig. 3. The depth contours for the  $\sigma_\theta = 28.35$  isopycnal surface is shown in Fig. 4.

The potential density patterns produced by this model fit reasonably well with many observations in the North Atlantic Ocean (c.f. Worthington, 1954), through the present model is very idealized. For example,  $\rho_x = 0$  along the western wall, thus  $v_z = 0$  there as required by our idealized assumption. As a result  $v$ -velocity is undamped along the whole depth. This is, of course, only true for such an idealized model. In a more realistic model with eddy diffusivity, this high velocity zone can be removed by eddy-mean flow interaction. The density along the western wall has been fixed to correspond to the abyssal density. This is also a very idealized assumption. In real oceans there is very cold dense water on the western boundary. In this sense,  $\rho = \rho_b$  is a crude, but reasonable assumption, though it is very idealized. As pointed above, all these idealized features will be modified by friction and diffusion near the western wall in the real ocean. Finally, the

specific form of upper surface velocity is oversimplified. This form does not include the cyclonic shear zone in the Florida Current. A more realistic velocity profile is studied in connection with the warm core structure of the Gulf Stream in the next section.



5. An example of the warm-core structure in an inertial western boundary current.

It is well known that the Gulf Stream appears as a warm current which transports warm water northward along the western boundary. The warm core feature can be seen from either the sea surface temperature maps or longitudinal hydrographic temperature (or density) sections. Blandford (1965) was among those few people who attempted to model this phenomenon with simple analytical models. Blandford's two-moving-layer model, however, was unsuccessful.

Therefore, in an attempt to find an inertial western boundary current which can match to a given interior thermocline solution, our diagnostic model in the previous sections is applied to a rectangular box with  $x = (0, 400 \text{ km})$  and  $y = (0, 1650 \text{ km})$ .

The eastern boundary conditions are specified from an interior solution, as described in Huang (1985). Therefore, the potential vorticity functional is the same as in previous section. The sea surface density is a second polynomial of the non-dimensional northward coordinate

$$\rho_s = 1.026 + (0.0002 + 0.0003 Y)Y \quad 0 \leq Y \leq 1$$

The Bernoulli functional (the sea surface pressure) along the eastern boundary of our box can be found from the corresponding interior solution by integrating a first-order differential equation

$$\frac{dp_s}{dx} = -\rho_s w_e F(\rho_s, p_s)$$

$$p_s(0, y) = 0$$

This equation should be integrated from the eastern wall to the western boundary. Because  $F(\rho_s, p_s)$  is a linear function, this equation can be easily integrated in analytical form and gives the Bernoulli functional along the

eastern boundary of our box as a matching boundary condition for the inertial western boundary current.

Therefore, the matching boundary condition for the inertial western boundary current is fixed along the eastern boundary which is chosen as  $X_e = 400$  km in the present example. Note that  $V$  is not zero at  $X = X_e$ . Actually,  $V_e$  has a small, negative value along the eastern boundary.

As the upper boundary condition,  $w_e = 0$  within the box is chosen for convenience. Along the southern boundary we can specify  $\rho_s$  quite arbitrary. Again, the northward velocity distribution over the entire upper surface is specified in some analytical form. As long as  $v$  is specified, the density distribution over the whole upper surface is determined by  $\rho = \rho(B)$ , as in the previous section.

The present case is much more complicated than the previous case because of the existence of a warm core. For example, the northward velocity attains a local maximum off the western boundary. Both the  $V$  distribution over the upper surface, and the  $\rho_s$  distribution along the southern boundary are written in piece-wise continuous parameter form and adjusted such that the flow field within the first few hundred meters below the sea surface is smooth.

It is obvious that there are infinite number of solutions each of them satisfying the same matching condition along the eastern boundary. Fig. 5 a,b, shows the northward velocity and density on the upper surface for one realization. The corresponding field at  $z = -160$ m is shown in Fig. 5c,d). As shown in Appendix A the corresponding systems of equations is a hyperbolic-elliptical composite system. Thus in the downward-marching process the error generally increases exponentially. This problem is more severe near the place where the information from the eastern boundary and

the southern boundary merges. This can be seen as some small bumps in the northward velocity contours at  $z = -160\text{m}$ . Nevertheless, Fig. 5 shows clearly how the north-south density gradient switches sign within the top 100-200m.

The flow field is quite smooth away from the southern boundary. two longitudinal sections, through the center of the box and along the northern boundary, are shown in Fig. 6. The corresponding density sections show distinctly a warm core structure which is not unlike many observations from the Gulf Stream. It is of interest to look at the potential vorticity contours for two sections in Fig. 6b,c. The low potential vorticity plateau is the most eminent feature in these two sections. Recently, R. Watts, M. Hall and their colleagues have conducted in-situ velocity measurements for the Gulf Stream. It would be of interest to compare their result with the present model.

The northward velocity, as expected, does not satisfy a lower boundary condition. As seen from Fig.c,f, the velocity field is quite different from observation. This a disadvantage of the present model. Since there are infinite number of solutions corresponding to different upper boundary conditions, there is still a possibility of finding some solutions which have reasonable velocity structure.

## 6. Conclusion

It is well known that the ideal fluid thermocline model provides an infinite number of solutions for the interior of a basin (see, for example, Rhines and Young, 1982; Huang, 1985). It has been shown here that by relaxing the velocity condition at the lower boundary, there are also an infinite number of possible solutions for the southern half of the western boundary region.

By relaxing the velocity condition at the lower boundary, our diagnostic model successfully matches with the most important upper and lateral boundary conditions. Most importantly, our model satisfies all matching conditions at the eastern boundary. The computed results are very similar to observations from the Gulf Stream.

The constant density condition along the western wall is only a sufficient condition, chosen for convenience. This condition could be relaxed in the future.

The proper velocity condition at the lower boundary is still uncertain. Corresponding boundary value problems in the density coordinate are currently studied which might lead to a final conclusion about the puzzling problem of an inertial western boundary current.

Though the final solution is still obscure, the large structure of western boundary currents becomes more clear. We look forward to the time when the interior solution can match with some reasonable boundary currents.

**Acknowledgments**

The author is indebted to Dr. G. Flierl who pointed out a mistake in an early manuscript. Drs. K. Bryan and P. Niiler have given many helpful suggestions.

## References

- Blandford, R., 1965: Inertial flow in the Gulf Stream. Tellus, 17, 69-76.
- Brooks, I.H., and P.P. Niiler, 1977: Energetics of the Florida Current. J. of Mar. Res., 35, 163-191.
- Charney, J.G., 1955: The Gulf Stream as an inertial boundary layer. Proc. Natl. Acad. Sci., 41, 731-740.
- Huang, R.X., 1984: The thermocline and current structure in subtropical/subpolar basins. Ph.D. Thesis. MIT/WHOI, WHOI-84-42.
- Huang, R.X., 1985: Exact solution for the ideal fluid thermocline with continuous stratification. (submitted to J. Phys. Oceanogr.)
- Korn, G.A., and T.M. Korn, 1968: Mathematical Handbook. McGraw-Hill Book Company, New York, 1130pp.
- Luyten, J., J. Pedlosky and H. Stommel, 1983: The ventilated thermocline, J. Phys. Oceanogr., 13, 292-309.
- Luyten, J. and H. Stommel, 1984: Upstream effects of the Gulf Stream on the mid-ocean thermocline. (submitted to Progress in Oceanography).
- Mesinger, F., and A. Arakawa, 1976: Numerical methods used in atmospheric models. GAPP Publication Series No. 14, WMO/ICSJ Joint Organizing Committee, 64pp.
- Morgan, G.W., 1956: On the wind-driven ocean circulation. Tellus, 8, pp. 301-320.
- Needler, G.T., 1983: On determining the velocity from the density field including a closed form, Ocean Modelling, 38, pp 3-5. (unpublished manuscript).
- Pedlosky, J. and W.R. Young, 1983: Ventilation, potential vorticity homogenization and the structure of the ocean circulation. J. Phys. Oceanogr., 13.
- Rhines, P.B., and W.R. Young, 1982: A theory of the wind-driven circulation. I: Mid-ocean gyres, J. Mar. Res., 40(Suppl.), 559-596.
- Rhines, P.B., 1984. A discussion of wind-driven circulation: the role of "gyration", preprint (submitted to J. Phys. Oceanogr.)
- Robinson, A.R., 1965: A three-dimensional model of inertial currents in a variable-density ocean. J. Fluid Mech., 21, 211-223.
- Schmitz, W.J., Jr., and P.P. Niiler, 1969: A note on the kinetic energy exchange between fluctuations and mean flow in the surface layer of the Florida Current. Tellus, 21, 814-819.

- Spiegel, S.L., and A.R. Robinson, 1968: On the existence and structure of inertial boundary current in a stratified ocean. J. Fluid Mech., 32, 569-607.
- Webster, F., 1965: Measurements of eddy fluxes of momentum in the surface layer of the Gulf Stream. Tellus, 21, 239-245.
- Welander, P., 1971: Some exact solution to the equations describing an ideal fluid thermocline. J. Mar. Res., 29, 60-68.
- Welander, P., 1983: Similarity solution for a stratified inertial boundary current. J. Phys. Oceanogr., 13, 2117-2120.
- Worthington, L.V., 1954. Three detailed cross-sections of the Gulf Stream. Tellus, 6, 116-123.

Appendix A  
Inertial Western Boundary Current Problem in Density Coordinate

Introducing the density anomaly

$$s = 1 - \rho/\rho_0$$

the governing equations (1-5) can be transformed to the new coordinates  $(x, y, s)$  in which  $z$  is a dependent variable (Robinson, 1965)

$$-fv + \Pi_x = 0 \quad (A-1)$$

$$uv_x + vv_y + fu + \Pi_y = 0 \quad (A-2)$$

$$\Pi_s + gz = 0 \quad (A-3)$$

$$(uz_s)_x + (Vz_s)_y = 0 \quad (A-4)$$

$$w = uz_x + Vz_y \quad (A-5)$$

where the Montgomery streamfunction  $\Pi = p/\rho_0 - gsz$  plays the same role as the pressure does in a Cartesian coordinates. From (A-4) a streamfunction can be defined

$$\psi_x = Vz_s, \psi_y = uz_s \quad (A-6)$$

There are two conservation quantities for this equation system

$$f + V_x = Z_s P(\psi, s) \quad (A-7)$$

$$\Pi + V^2/2 = B(\psi, s) \quad (A-8)$$

since (A-8) can be reversed and a relation  $\psi = \psi(B, s)$  can be substituted into (A-7) thus

$$f + v_x = Z_s P(B, s) \quad (A-9)$$

1) Separation of inertial western boundary current.

Let us begin by examining Charney's model. From the cross-stream momentum balance

$$fv = g'D^2x$$

by multiplying  $D$  on both sides and introducing the streamfunction  $\psi_x = Dv$  we get

$$f\psi_x = 1/2 g'D^2x$$



Integrate from  $x = 0$  to  $x = \infty$  and put  $\psi|_{x=0} = 0$ , thus

$$g'/2D_0^2 = g'/2D_\infty^2 - f\psi_\infty \quad (\text{A-10})$$

where  $\psi_\infty$  is connected to  $D_\infty$  by integrating the geostrophy relation, thus

$$D_0^2 = D_\infty^2 - f \int_{y_0}^y \frac{1}{f} \frac{d}{dy} D_\infty^2 dy \quad (\text{A-11})$$

For a given  $D_\infty = D_\infty(y)$ , there is a critical latitude where the right-hand-side is zero, meaning the separation of the western boundary current. For example, if  $D_\infty = af$  ( $a$  is a constant), then the separation appears at latitude where  $f=2f_0$ . Therefore, for a subtropical gyre with its southern boundary at  $10^\circ$ - $15^\circ$ N, the "Gulf Stream" should separate from the coast around  $20^\circ$ - $30^\circ$ N. That is not the real case. Though a different  $D_\infty(y)$  gives quite different separation latitude, integrand in (A-11) indicates that for small  $f_0$ , the contribution from low latitude is large and the separation cannot be too far away from  $y=y_0$ .

In many numerical simulations the strong western boundary currents tend to overshoot the "separation latitude". Therefore, what the Charney model predicts for a separation might not be the whole story of separation.

One possible cause of this apparent puzzle is the lower boundary condition. Layer models assume an absolutely stagnant abyssal water. The real ocean, however, has a continuous stratification and a continuous velocity field. For example, if a deeper interface  $S_2$  is chosen such that  $D_\infty$  is double. Because the velocity in the abyss is slow, the vertically integrated streamfunction  $\psi_\infty$  only increases slightly.  $g'$  for the new case should be slightly reduced. However, from (A-10) it is easy to see that now the separation latitude is much higher.

The separation problem can be seen more clearly in the density coordinate (Niiler, private communication). Multiplying (A-1) by  $Z_\theta$  and using

(A-6), (A-3)

$$f\psi_x = - \frac{\Pi_{ss}}{g} \Pi_x$$

Notice that

$$\int_0^\infty \int_{s_1}^{s_2} \psi_x dx ds = \int_{s_1}^{s_2} \psi_\infty ds$$

$$\int_0^\infty \int_{s_1}^{s_2} \Pi_{ss} \Pi_x dx dO = - \int_0^\infty \Pi_s \Pi_x \Big|_{s_1} dx - \frac{1}{2} \int_{s_1}^{s_2} \Pi_s^2 ds \Big|_0^\infty$$

where the fact that at the sea surface  $s_2 = s_2(X)$ ,  $\Pi_s = -gz = 0$  has been used. If we assume  $v = 0$  at  $s = s_1$ , then

$$- f \int_{s_1}^{s_2} \psi_\infty ds + \frac{g^2}{2} \int_{s_1}^{s_2} Z_\infty^2 ds = \frac{g^2}{2} Z_0^2 ds \quad (A-12)$$

By definition  $\int_{s_1}^{s_2} \psi_\infty ds$  is the total income mass flux from the interior ocean, which is relatively insensitive to the choice of  $s_1$ . Equation (A-12) is very similar to (A-10). This equation determines the latitude where  $\int_{s_1}^{s_2} Z_0^2 ds = 0$  meaning the total separation from the western boundary.

As  $s_1$  decreases, however, the second term increases very fast. thus the total separation latitude can be postponed to much higher latitude.

## 2) Boundary value problem for inertial western boundary current

Assuming  $P(B,S)$  is specified from the interior solution, the original equation system is reduced to

$$Z_s = \frac{V_x + f}{P, (B, s)} \quad (A-13)$$

$$V_s = - \frac{g}{f} Z_x \quad (A-14)$$

$$B_s = - gZ - VV_s \quad (A-15)$$

This is a third-order partial differential equation system for three dependent variables (Z,V,B) and two independent variables (x,s). The northward coordinate y comes into this system only implicitly, through  $f = f(y)$  and the boundary conditions which will be explained later.

A very popular assumption is  $P(B,s) = P(s)$ , and  $P(s) > 0$  for any stable case. Then (A-13) and (A-14) can combine to give rise a single equation for V

$$V_{xx} + \frac{fP(s)}{g} V_{ss} = 0 \quad (A-16)$$

It is an elliptical equation with variable coefficient for general cases.

There are many well-known properties for this kind of elliptical equation. For example, V attains its maximum and minimum value only along the boundary.

By transform to the density coordinate, we turn a problem of non-linear equations with fixed boundary into a problem of a linear equation with free boundary. Fortunately, by specifying an initial guess distribution of V over the sea surface, the upper boundary  $s = s(x)$  can be determined by the procedure in section 3,  $s-s(B)$ .

The boundary condition at  $x=0$  becomes a non-linear boundary condition. From (A-2),  $u \neq 0$  at  $x=0$  implies that  $B=B(s)$  is independent of y. As a result  $B=B(s)$  is the same for different latitudinal sections. This boundary condition can be transformed

$$-g \frac{f + V_x}{P(s)} + (VV_s)_s = \frac{+dB(s)}{ds^2} \quad \text{at } x = 0 \quad (A-17)$$

At  $x \rightarrow \infty$ ,  $V \rightarrow 0$  in order to match the interior solution. At  $s=s_1$ , the lower boundary, the boundary condition is not clear. Of course  $V \rightarrow 0$  as  $s \rightarrow s_1$ , is a convenient choice. However, as discussed above, this boundary condition may not give a realistic solution without involving with the separation problem.

It seems possible to find a solution after specify  $V=V(x)$  along the upper free boundary. The corresponding solution should satisfy the lateral boundary conditions and some lower boundary condition.

After the  $v$ -field have been calculated, the  $Z$  and  $B$  functions can be easily calculated by downward integration.

For general case when  $p$  depends on both  $B$  and  $S$ , equation system (A-13,14,15) is a third-order quasi-linear system which characteristic equation is

$$\phi_s \left( \phi_s^2 + \frac{g}{fP(B,s)} \phi_x^2 \right) = 0$$

It is a hyperbolic-elliptical composite system. Though there is no strict mathematical proof for any well-posed boundary value problem for this system, it seems reasonable to pose the same kind of boundary value problem as the case when  $P$  is only a function of  $s$ .

AD-A162 506

PROCEEDINGS OF THE GULF STREAM WORKSHOP HELD AT WEST  
GREENWICH RHODE ISLA (U) RHODE ISLAND UNIV KINGSTON  
GRADUATE SCHOOL OF OCEANOGRAPHY D R WATTS APR 85

5/7

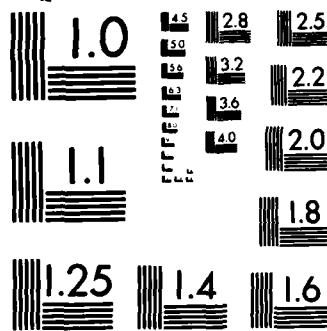
UNCLASSIFIED

N00014-85-G-0322

F/G 8/3

NL





MICROCOPY RESOLUTION TEST CHART  
NATIONAL BUREAU OF STANDARDS-1963-A

## APPENDIX B

For general cases of inertial boundary current, nonlinear advection terms in both horizontal momentum equations should be retained. Thus (1) becomes

$$uu_x + vu_y + wu_z - fv = -p_x \quad (B-1)$$

there are two first integrals

$$\vec{u} \cdot \nabla B = 0 \quad (B.2)$$

$$\vec{u} \cdot \nabla q = 0 \quad (B.3)$$

where

$$B = p + \rho g z + (u^2 + v^2)/2 \quad (B.4)$$

$$q = [f + (v_x - u_y)]\rho_z + (u_z\rho_y - v_z\rho_x) \quad (B.5)$$

are the Bernoulli functional and the potential vorticity. The velocity mass vector can also be related to  $q$ ,  $B$ , and  $\rho$  in the following way

$$\vec{u}q = \nabla\rho \times \nabla B \quad (B.6)$$

The partial differential equation system for this general cases of inertial boundary current has been classified as a non-strict hyperbolic system (Huang, 1984). Streamlines are triple characteristics and  $z$ -axis is double characteristics. However, the mathematical property of this system is largely unknown.

## APPENDIX C

Equation system (15,16,17) is solved with a Heun scheme with respect to  $z$  (Mesinger and Arakawc, 1976). Using vector notation, this system can be written as

$$\frac{dU}{dz} = f(U, Z) ; U = U(Z) \quad (C-1)$$

Thus

$$\begin{aligned} U^{(n+1)*} &= U^{(n)} + \Delta Z \cdot f^{(n)}, \\ U^{(n+1)} &= U^{(n)} + 0.5\Delta Z \cdot (f^{(n+1)} + f^{(n+1)*}) \end{aligned} \quad (C-2)$$

where

$$f^{(n+1)*} = f(U^{(n+1)*}, (n+1)\Delta Z)$$

For calculation of  $x$ -derivatives a second order scheme with smoothing (Korn and Korn, 1968) is used

$$\partial v / \partial x|_{i,j} = (-2V(i-2,j) - V(i-1,j) + V(i+1,j) + 2V(i+2,j)) / 10\Delta x$$

$\partial \rho / \partial x$  is treated similarly.

Because there is no  $y$ -derivatives, this integration can be done for each  $y = \text{const.}$  section independently.



## FIGURE CAPTIONS

- Fig. 1. Potential vorticity contours (in units of  $10^{-13}/\text{cm}/\text{sec}$ ) at two sections of an ideal fluid thermcline model for a subtropical basin. a) Meridional section along the western boundary. b) Longitudinal section through the center of the gyre.
- Fig. 2. Density and  $v$ -velocity contours for an inertial western boundary current with continuous stratification at different depth:  $\sigma_\theta$  at  $z = 0$  (a);  $-300$  m (c);  $-600$  m (e).  $v$  cm/sec at  $z = 0$  (b);  $-300$  m (d);  $-600$  m (f).
- Fig. 3. Meridional sections of density and  $v$ -velocity contours.  $\sigma_\theta$  at northern boundary (a); through the center (c); southern boundary (e).  $v$ (cm/s) at northern boundary (b); through the center (d); southern boundary (f).
- Fig. 4. Depth of the  $\sigma_\theta = 28.35$  isopycnal surface, in unit of hundred meters.
- Fig. 5. Velocity and density contours for an inertial western boundary current with warm core. Northward velocity (cm/sec) at  $z=0$  (a);  $z = -160$ m (b) density at  $z = 0$  (c);  $z = -160$ m. the warm core is seen in the middle of the upper surface density contour map.
- Fig. 6. Density ( $\sigma_\theta$ ), potential vorticity ( $10^{-13}/\text{cm}/\text{sec}$ ), and northward velocity (cm/sec) at two longitudinal sections. Density structure through the center a) and along the northern boundary d) shows the warm core on the top layer clearly. Potential vorticity contours through the center b) and along the northern boundary e) show the low potential vorticity core on the east. Northward velocity through the center c) and along the northern boundary f).

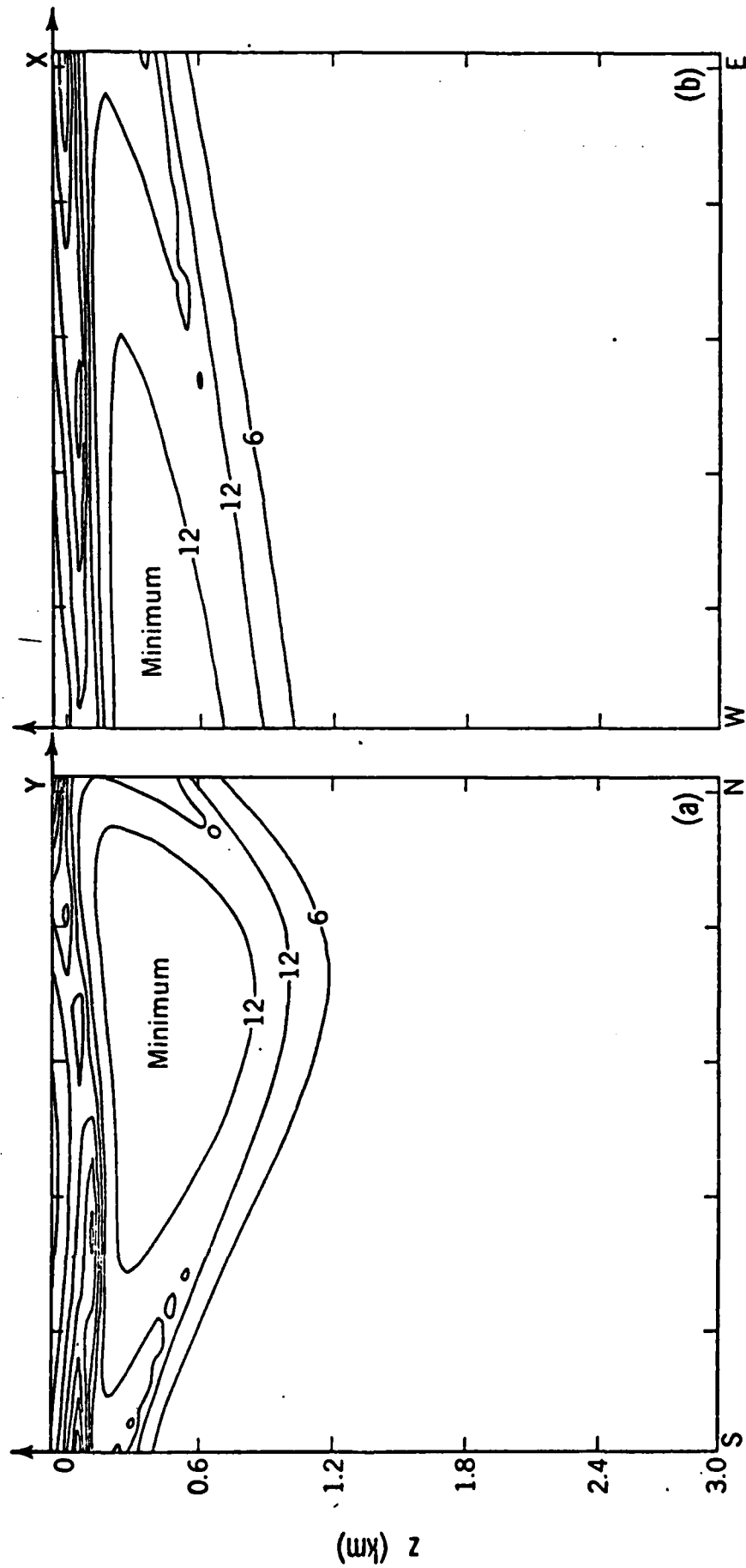


Fig. 1.

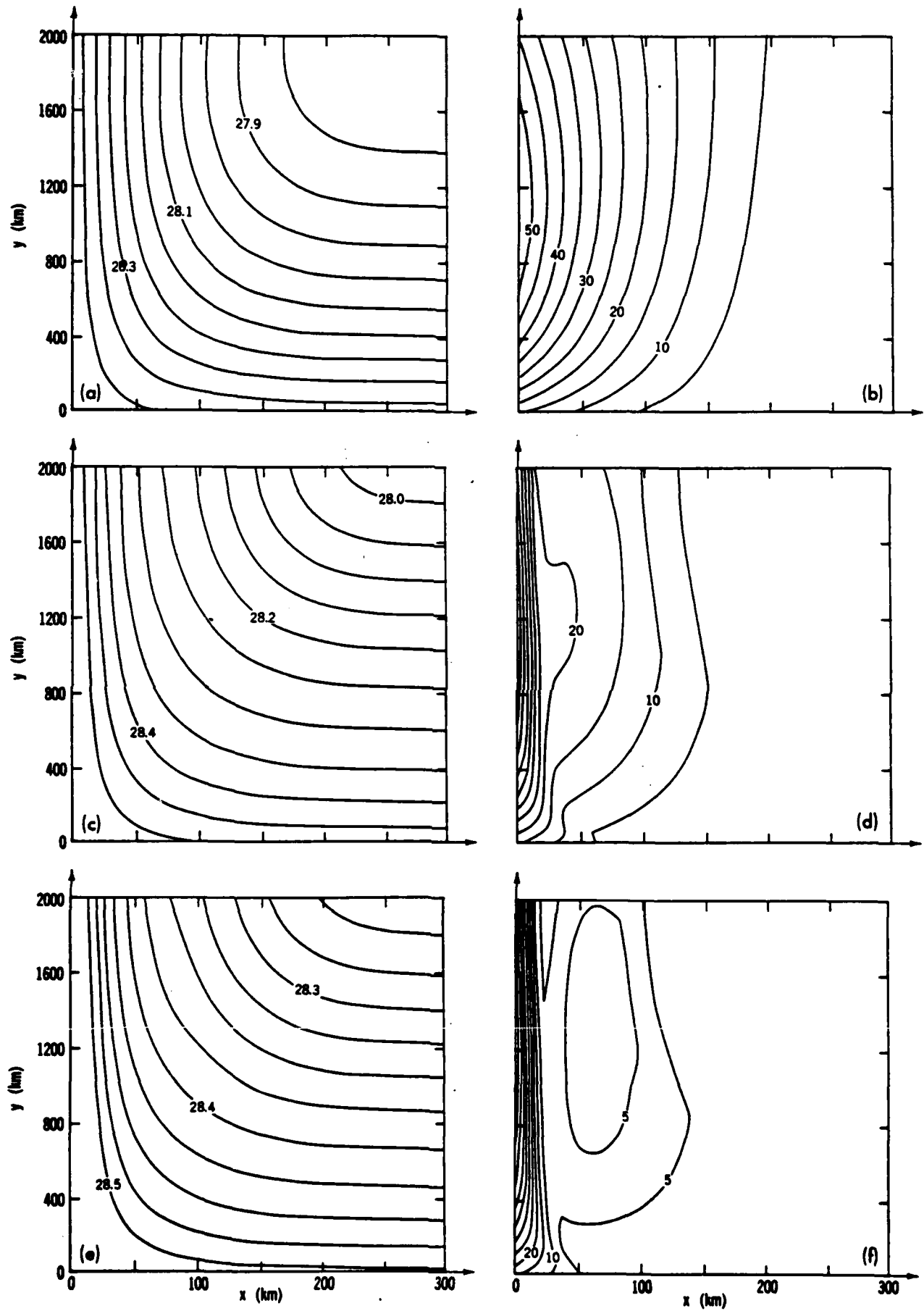


Fig.2

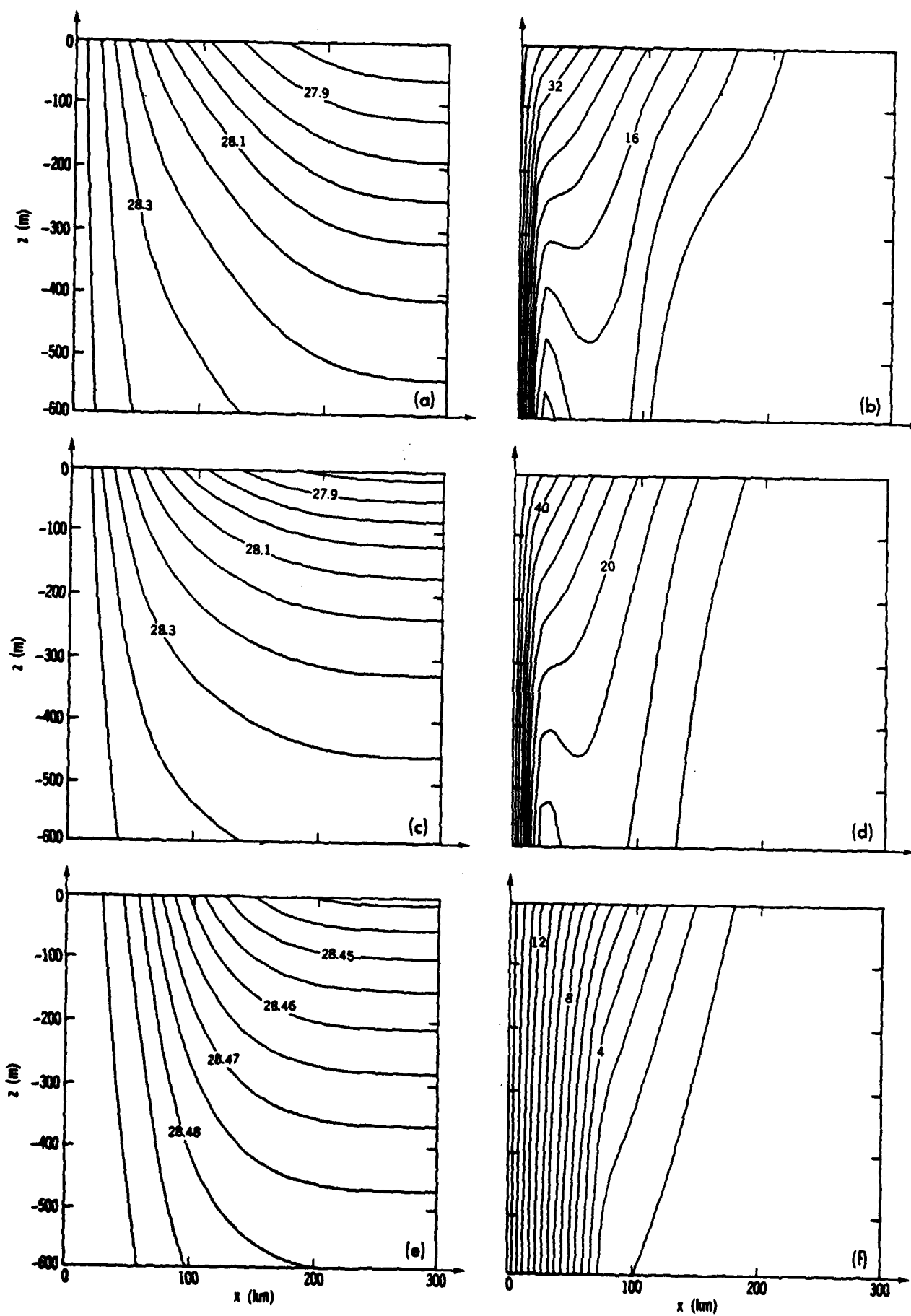


Fig.3

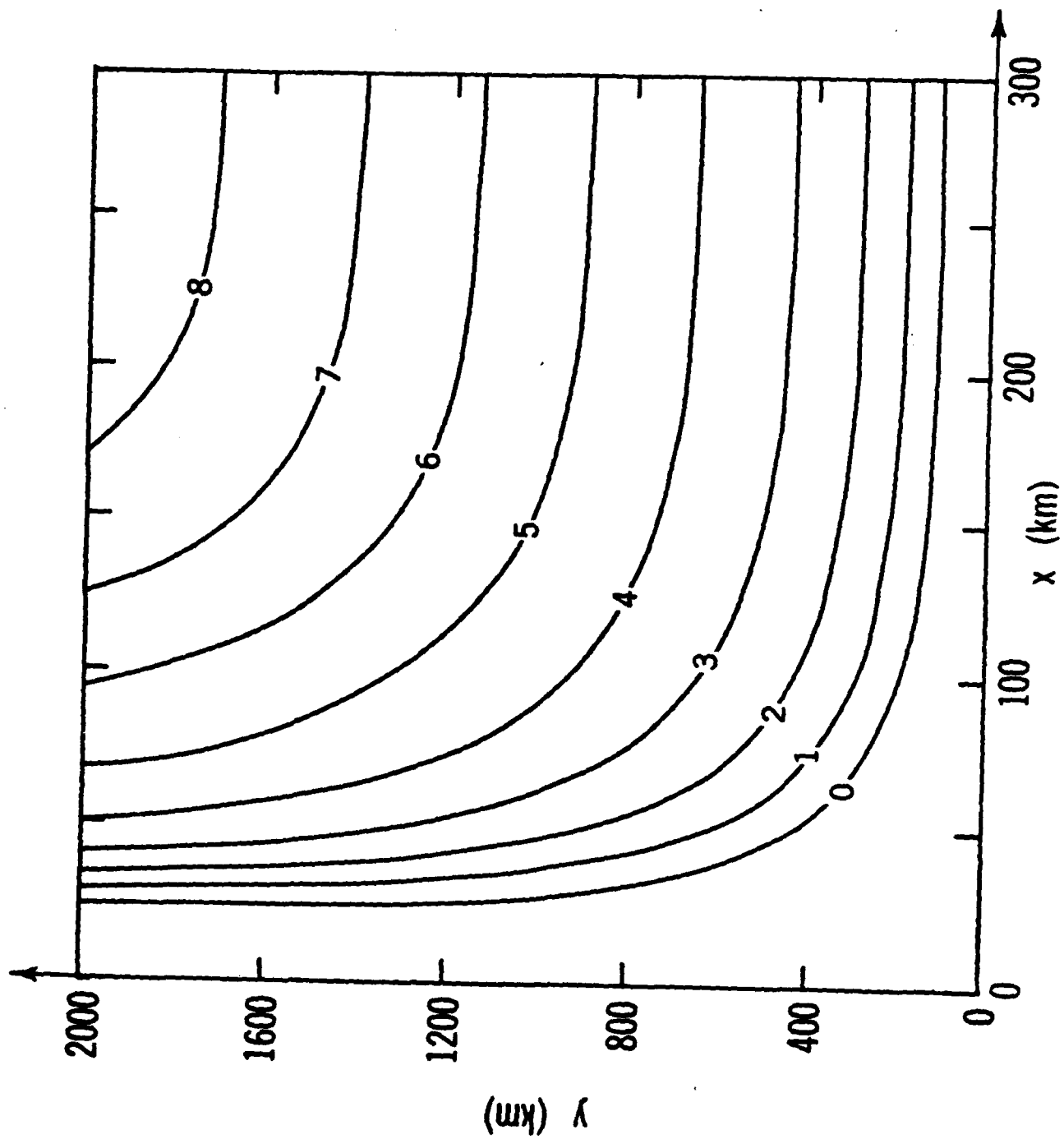
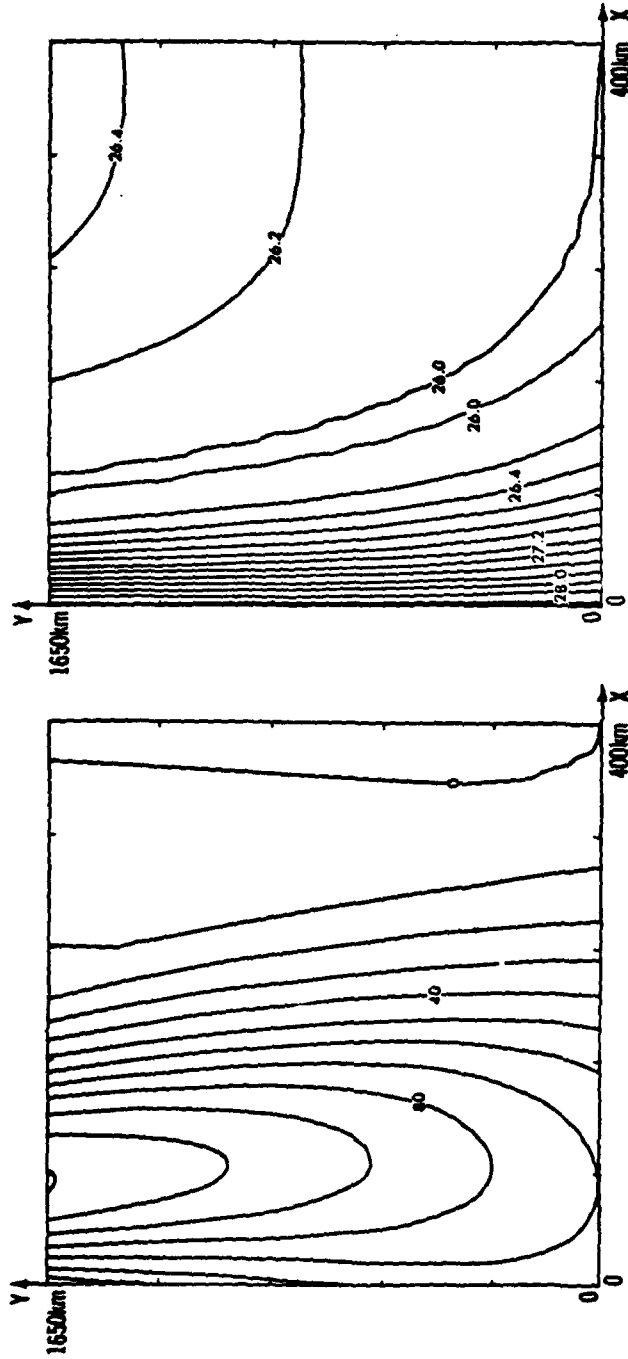
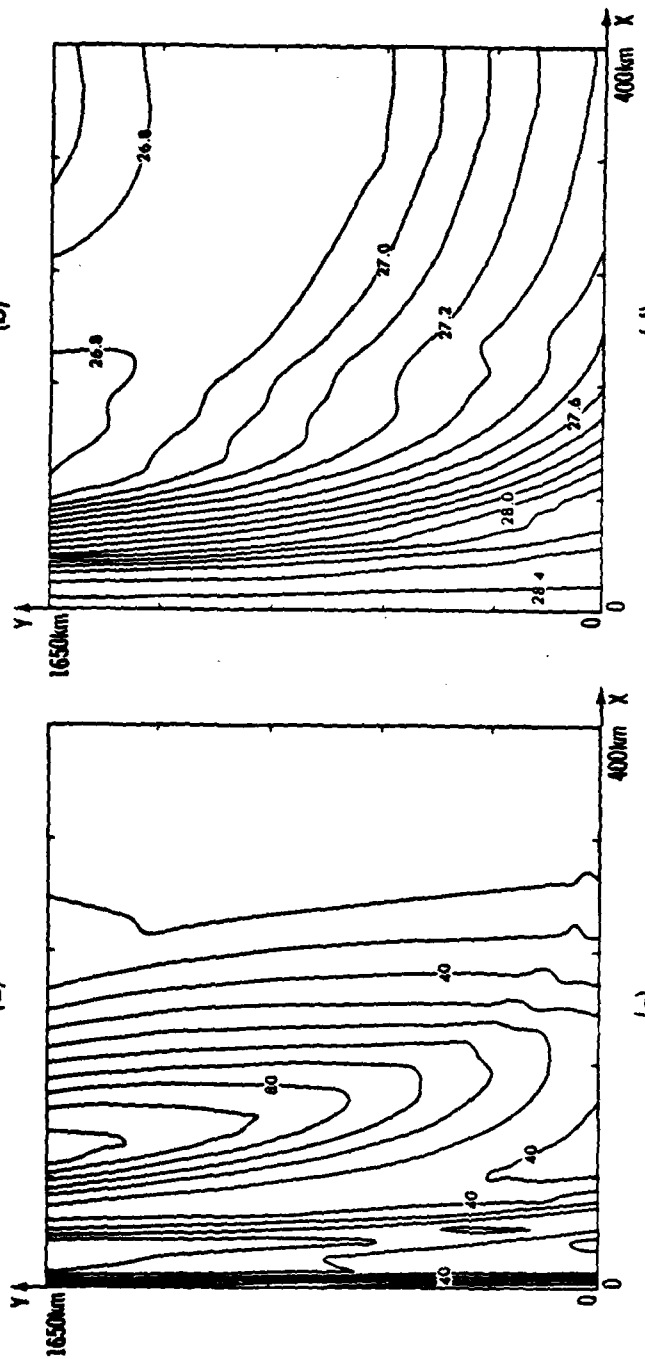


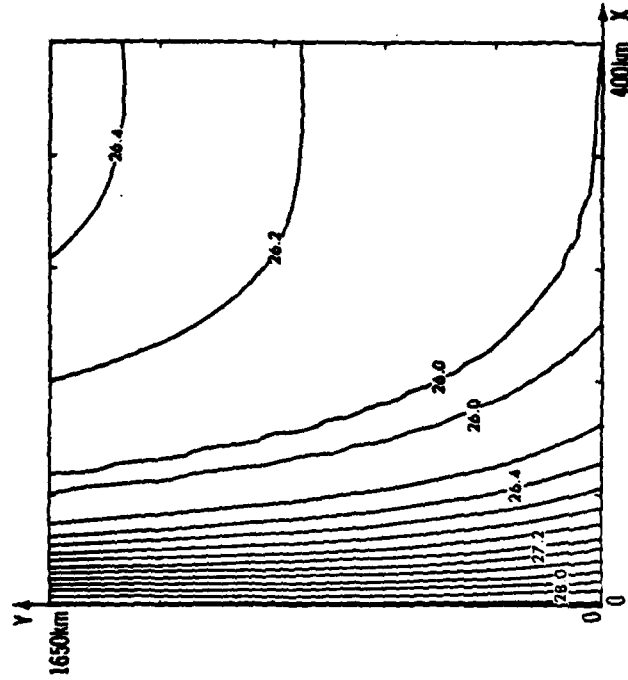
Fig. 4



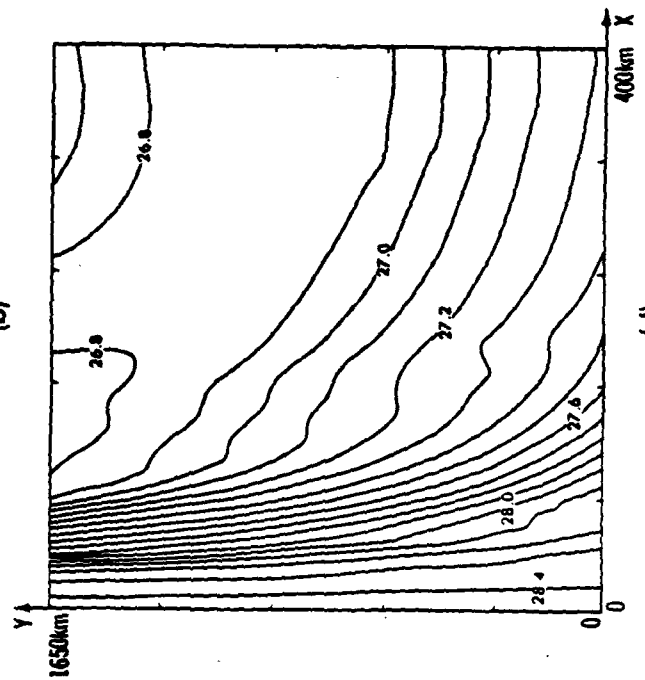
(a)



(b)



(c)



(d)

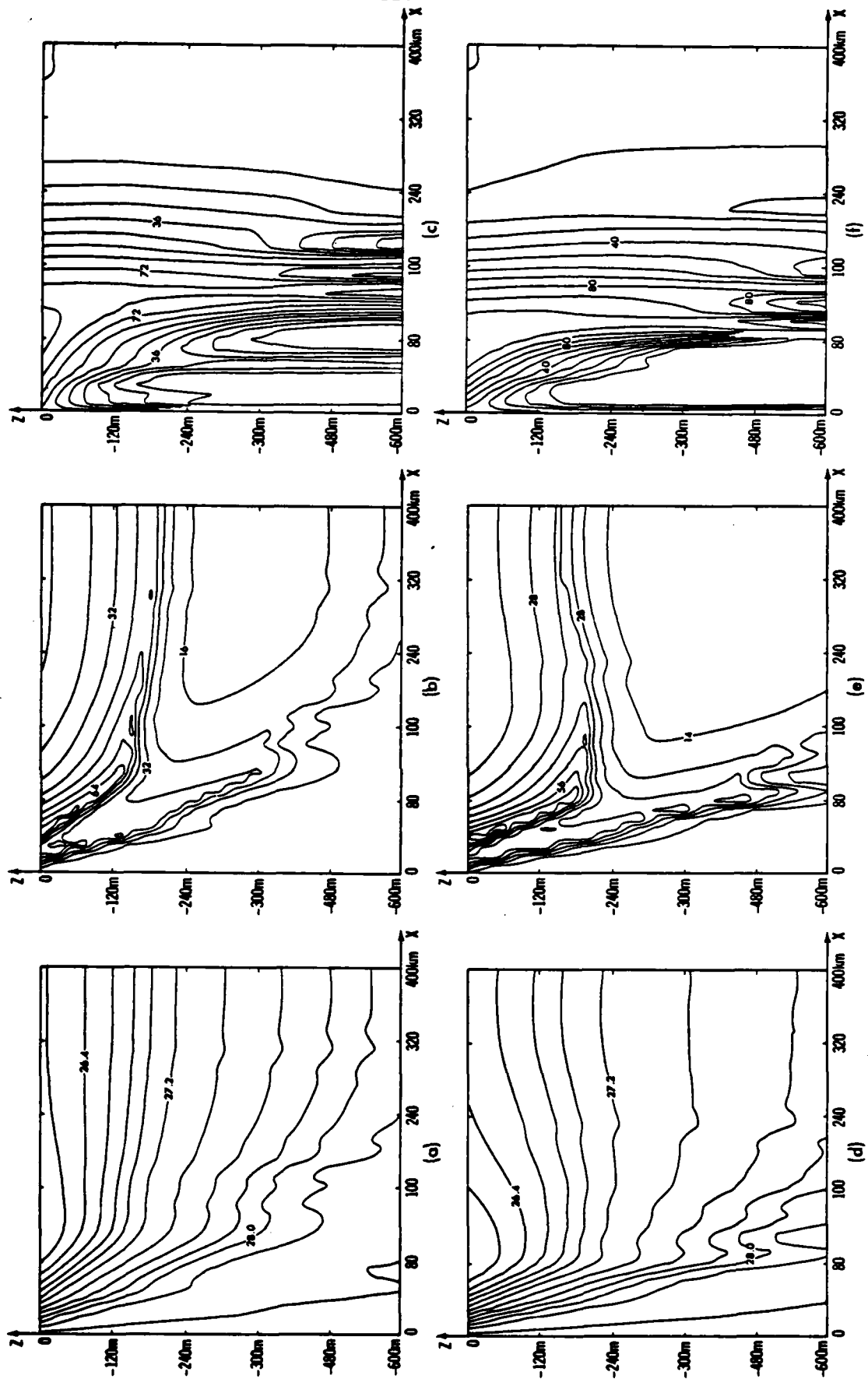


Fig. 6

TIME SCALES AND STRUCTURE OF TOPOGRAPHIC ROSSBY WAVES  
AND MEANDERS IN THE DEEP GULF STREAM

W.E. Johns  
Rosenstiel School of Marine and Atmospheric Science  
University of Miami  
Miami, Florida 33149

D.R. Watts  
Graduate School of Oceanography  
University of Rhode Island  
Narragansett, Rhode Island 02882

June 1985



## Abstract

During July-November 1982, current and temperature records were collected from six current meters spanning the lower 2000 m of the water column on two moorings in the Gulf Stream northeast of Cape Hatteras, N.C. Frequency domain EOF analysis of the velocity cross-spectra reveals that there are two kinematically distinct wave processes present in the subinertial range, identifiable as topographic Rossby and meander associated motions, which are energetically dominant at periods longer than and shorter than 14 days, respectively.

Simultaneous thermocline depth measurements obtained using inverted echo sounders show that the low frequency topographic Rossby wave motions are uncoupled with near surface displacements of the Gulf Stream path, but that cross-stream velocity fluctuations in the 14 day and 5 day period bands are associated with vertically coherent meanders of the Gulf Stream temperature front.

## I. Objectives and Observations

During July-November 1982, 135-day records were obtained from an array of three inverted echo sounders (IES) and six current meters deployed in the Gulf Stream 150 km northeast of Cape Hatteras, N.C. These measurements supplement an earlier data set collected during 1979-80 in this same region (Johns and Watts, 1985; hereafter JW85), but

were designed to effectively sample a larger extent of the deep water column than had been done previously. It was hoped that by combining measurements of the variation in the depth of the main thermocline (using IESs) together with deep current meter observations one could determine whether meanders extend coherently to the bottom in this region, and if so, begin to examine in more detail their kinematics and vertical structure.

The IES/current meter array was placed within the historical envelope of meandering of the Gulf Stream in a region where meanders are known to exhibit rapid spatial growth, yet where the lateral excursions of the path are still small enough that a limited array could be expected to continuously monitor variations within the current. The instrument locations are shown in Figure 1. Current meters were placed at levels of 500, 1000, and 1500-2000 m off the bottom on each of two moorings, designated sites 4 and 5. All current meters were of the vector-averaging type (VACMs). The two moorings were spaced approximately 30 km apart, forming a cross-stream pair. This spacing was chosen to be less than the internal Rossby deformation radius ( $\sim 35$  km), based in part on the relatively weak coherence observed over a 50 km cross-stream separation in the earlier current meter records (sites 2 and 3, Fig. 1). The IES sites were chosen to monitor fluctuations in the depth of the main thermocline, associated with the meandering of the path of the Gulf Stream, as described in Watts and Johns (1982). IES measurements were taken directly at the two current meter sites 4 and 5, with an additional IES placed approximately 25 km offshore of site 5 to ensure good tracking of the Gulf Stream. The notation used for the

current meter sites is a two-digit format, where the first number stands for the mooring number (4 or 5) and the second number denotes the current meter's position down from the top of that mooring (1 to 3). For example, site 42 is on mooring 4 and is second from the top.

The velocity and temperature time series at each of the current meter sites are shown in Figure 2. All of the data records have been low-pass filtered with a 24-hour half-width Gaussian window, and then subsampled at 12-hour intervals. Thermocline displacement records obtained from IES measurements at moorings 4 and 5 are shown in Figure 3. Table 1 summarizes the current meter mooring locations, and the means and variances of the current and temperature records.

The velocity and temperature time series (Figure 2) exhibit variability on time scales ranging from a few days to about one month. For the most part, the velocity fluctuations appear to be highly coherent vertically, and several events occur in the records which can be traced horizontally between moorings 4 and 5. At least two of the more energetic events (near Aug. 25 and Oct. 15) are bottom-intensified, although the true vertical structure of the fluctuations is somewhat obscured by the mean flow. For example, the event during mid- to late July, which appears nearly barotropic, is actually rather strongly bottom-intensified at mooring 5 after removing the mean vertical shear. During these events, current reversals at the upslope site (mooring 4) tend to lead those at the downslope site (mooring 5) by a few to several days.

## II. Mean Currents and Energy Spectra

### Mean Currents

The mean currents at sites are illustrated in Figure 4, together with the means obtained from the earlier records at site 1 (a 6-month record), site 2 (a 12-month record), and site 3 (a 9-month record) during the 1979-80 deployments. The most completely instrumented level is at 1000 m off the bottom, for which the mean currents are indicated in Figure 4 by solid vectors. A comparison with simultaneous thermocline depth measurements from the IESs shows that site 4 is moored almost directly beneath the mean location of the Gulf Stream's north wall ( $15^{\circ}\text{C}$  at 200 m), whereas mooring 5 is farther offshore within the body of the Gulf Stream. However, at the actual current meter depths  $>1200$  m, both of the moorings are in the cyclonic shear zone of the deep Gulf Stream, due to the offshore tilt of the Gulf Stream's velocity structure with depth. In view of the relatively short duration of the records, there is remarkable consistency between the measurement periods. At each of the three moorings in  $\sim 3000$  m water depth (moorings 1, 3 and 4) the mean current 1000 m off the bottom is veered to the right of the mean surface path ( $\sim 050^{\circ}\text{T}$ ), whereas at mooring 2 in 3700 m water depth the mean current 1000 m off the bottom is approximately colinear with the surface mean path. At mooring 5, in 3400 m water depth, the veering 1000 m off the bottom is intermediate between these extremes. Cast in the local downstream frame, this offshore turning of the mean flow vectors suggests an inflow to the Gulf

Stream which decreases systematically in strength in the offshore direction from a speed of about  $3-4 \text{ cm sec}^{-1}$  near the northern edge of the Gulf Stream. The observed clockwise veering of the mean flow vectors with depth on moorings 4 and 5 further suggests that the inflow component is nearly barotropic, when subtracted from the vertically-sheared downstream component. These observations are consistent with Halkin and Rossby's (1985) 3-year average of "Pegasus" measurements here, showing a statistically-significant, nearly depth-independent northern inflow of approximately  $5 \text{ cm/sec}$ . If integrated over depth and over a  $100 \text{ km}$  segment of the path this  $3-5 \text{ cm sec}^{-1}$  inflow yields a transport of  $10-15 \times 10^6 \text{ m}^3 \text{ sec}^{-1}$ , which implies that a significant fraction, if not most, of the observed rate of increase in transport of the Gulf Stream in this region (Knauss, 1969) is entering from the north. Halkin and Rossby's (1965) estimate of  $10.4 \times 10^6 \text{ m}^3 \text{ sec}^{-1}$  per  $100 \text{ km}$  segment of the path entering in the upper  $2000 \text{ m}$  is, in fact, roughly twice their estimate of the transport within this same depth range entering the Gulf Stream from the recirculation region to the south.

#### Kinetic Energy Spectra

To examine the structure of the fluctuating currents, kinetic energy spectra were computed by breaking up the records into 48-day segments, removing the mean, windowing with a Hanning (cosine) window in the time domain, Fourier transforming, and ensemble averaging. Segments were overlapped by 24 days (i.e. 50%). The resulting adjacent spectral estimates at periods of 48d, 24d, 16d, etc. have effective bandwidths of

0.0312 c.p.d. and are overlapped in the frequency domain by 33% (i.e. adjacent estimates are 67% independent). All additional spectral and cross-spectral quantities were computed in a similar manner. Some of these estimates (discussed later) have been averaged over two frequency bands to improve the reliability of estimates. These two-band-averaged estimates are centered at periods of 32, 14, 8.8, 6.4, 5.1, and 4.2 days, and are nominally 83% independent. Much of the subsequent analysis in sections 3 and 4 deals with these six basic frequency bands spanning periods from 4 to 48 days.

Figure 5 illustrates the vertical distribution of kinetic energy at moorings 4 and 5. Both sites are characterized by an increase in kinetic energy with depth for periods longer than about 16 days. Near period of 14 days, however, the structure changes. The kinetic energy in the 4 to 14 day period band at mooring 4 decreases with depth, and at mooring 5 it is nearly equal at the uppermost and deeper levels, with a curious minimum appearing at the intermediate level. At both sites there is an obvious spectral 'bulge' near periods of 5 days at the upper levels which does not, however, appear at deeper levels. Aside from this, the spectra are rather featureless, except for the notably small spectral slopes occurring at low-frequencies. In fact, at the deepest levels on moorings 4 and 5 the kinetic energy is actually larger at the 24 day period than at the 48 day period. This low-frequency behavior is typical of current records taken on the continental slope and rise (c.f. Thompson and Luyten, 1976), as distinguished from the "red" structure observed in open ocean, flat-bottom regions where the kinetic energy is dominated by longer time scales, approximately 100 days (Richman, Wunch,

and Hogg, 1977). Beginning near periods of 12-16 days and continuing to the 4 day period, all of the kinetic energy spectra fall off rapidly, with spectral slopes of  $f^{-2}$  to  $f^{-3}$ .

### III. Velocity Structure

To examine in more detail the structure of the velocity field we performed a frequency-domain, complex eigenvector (EOF) analysis on the current records (Groves and Hannan, 1968; Wallace and Dickinson, 1972). This analysis technique provides an efficient way to objectively analyze the complete body of simultaneous cross-spectral information for contributions from various wave structures.

In our earlier analysis of deep current meter records here (JW85) we found that the velocity fluctuations exhibited a consistent change in orientation with frequency: at low-frequencies (periods >10 days) the fluctuations were aligned nearly along the isobaths, whereas at higher frequencies the fluctuations were oriented essentially across-stream. Figure 6 illustrates the principal axes of variance from the earlier records (moorings 1-3), together with those from the new records, in two frequency bands. We suggested in JW85 that the cross-stream orientation is a signature of deep meander variability, and that the along-isobath flow at low-frequencies is a manifestation of topographic Rossby wave variability. The following frequency-domain EOF analysis was designed to further test these hypotheses.

For any given frequency band, the cross-spectra between all possible pairs of  $n$  measured physical variables can be represented as an  $n \times n$  Hermitian matrix: the diagonal elements are (real) auto-spectral estimates obtained by crossing each variable with itself, and the off-diagonal elements are (complex) cross-spectral estimates between pairs of variables. This cross-spectral matrix may be diagonalized to a linear combination of  $n$  orthogonal eigenvectors with weights  $\lambda_i$  (the associated eigenvalues) which determine the fraction of the cross-spectral variance explained by the  $i^{\text{th}}$  eigenvector, or mode (Wallace and Dickinson, 1972).

Prior to diagonalization, the cross-spectral matrix is normalized by dividing each element by the product of the square root of the variance associated with each member of that pair. This is known as coherence normalization, which effectively non-dimensionalizes the matrix (when variables with different physical units are used), and also has the advantage of giving equal weight to the measurements at each site. Otherwise the results are dominated by the few largest (most energetic) elements.

This procedure has been applied to the vector velocity time series at moorings 4 and 5. Temperature variations are considered separately in the next section, where they are compared with the simultaneous thermocline displacement records. There are a total of 12 velocity variables, i.e. east and north components measured at six locations. EOFs were computed for each of the six frequency bands centered at



periods of 32, 14, 8.8, 6.4, 5.1, and 4.2 days. For each frequency band, there result 12 complex eigenvectors  $\tilde{e}_i$ :

$$\tilde{e}_i = [\tilde{u}_1^2, \tilde{u}_2^2, \dots, \tilde{u}_{12}^2]$$

which express the variance of velocity components and relative phase differences between velocity components for each mode. The fractional variance accounted for by the  $i^{\text{th}}$  mode is:

$$\lambda_i / \sum \langle u_j u_j \rangle$$

determined by the size of the  $i^{\text{th}}$  eigenvalue relative to the trace (total normalized variance,  $n$ ) of the matrix.

The statistical significance of modes obtained by the EOF decomposition depends on the observed distribution of the  $\lambda_i$  relative to the standard probability distribution for  $\lambda_i$  based on a noise hypothesis, i.e. that of uncorrelated variables. Priesendorfer (1981) presents a comprehensive set of tables of the probability distributions for eigenvalues of random covariance matrices, as a function of  $n$ , the order of the matrix (number of variables), and  $p$ , the number of degrees of freedom associated with the matrix elements. The "noise" eigenvalue distribution for  $(p,n)=(12,12)$  is shown in Figure 7, where it is compared with the observed eigenvalue distribution (each two-band-averaged estimate has approximately 12 degrees of freedom).

All 1<sup>st</sup> modes contain significant variance at the 95% level, as does the 2nd mode in the 8.8 day band. The remaining modes are insignificant.

The basic quantities which describe a given mode are a) the magnitude of  $u$  and  $v$  at each site, b) the phase between  $u$  and  $v$  at each site, and c) the relative phase between velocity components at different sites. These quantities are graphically represented in terms of velocity hodographs for each mode, shown in Figure 8. The algebraic details are included in Appendix A. For any given mode, this representation allows vertical and horizontal phase variations over the array to be expressed concisely in terms of the relative phase of the principal, or major axis, velocity component.

In the 32 day band, the 1<sup>st</sup> mode describes bottom-intensified fluctuations which are oriented along the bathymetry and are nearly in-phase vertically. The motion has a cyclonic rotary tendency (i.e.  $u$  leads  $v$ ), but becomes increasingly transverse with depth. There is a large energy variation apparent in the array, with about three times more kinetic energy accounted for by this mode at site 5 than at site 4. Importantly, there is an average phase offset of approximately  $60^\circ$  between moorings 4 and 5, such that fluctuations lead (occur earlier) at site 4.

In the 14 day band, the 1<sup>st</sup> mode describes fluctuations which are now oriented in the NW-SE quadrant, more nearly perpendicular to the mean direction of the path of the Gulf Stream. The fluctuations are in-phase vertically and are essentially barotropic, with perhaps a small

baroclinic tendency. At each site  $u$  and  $v$  are nearly out-of-phase, except at the deepest level on mooring 5 where the fluctuations are purely anticyclonic ( $v$  leads  $u$  by  $90^\circ$ ) and the orientation is skewed N-S. This suggests that the fluctuations are weakly coupled vertically in deep layers at mooring 5. For this mode there is a much smaller (insignificant) average cross-stream offset of  $\sim 12^\circ$  between moorings 4 and 5.

At shorter periods, the cross-stream orientation continues to be dominant, however the mode structures become generally noisier and there are often irregular variations in orientation and phase over the array. For example, in both the 8.8 and 6.4 day bands the cross-stream, vertically in-phase motion shows up strongly at one mooring but not at the other, and in the 4.2 day band the variance is dominated by cross-stream, horizontally in-phase motion at the upper levels but not at depth. In the 5.1 day band the cross-stream, transverse variability does occur as a coherent mode throughout the array.

The variability at sites 4 and 5 may be summarized in terms of a transition from bottom-intensified flow oriented along the bathymetry at low-frequency, to essentially barotropic flow oriented in the NW-SE (cross-stream) direction at higher frequencies. The two coherent wave structures are further distinguished by the fact that the 32 day period fluctuations exhibit a significant phase lag over the  $\sim 30$  km cross-stream separation between sites, but that the cross-stream fluctuations at higher frequencies (periods of 14 days and 5 days) are nearly in-phase across the Stream. The 32 day period fluctuations are

characterized by offshore propagation, while the in-phase variability at higher frequencies suggests wavefronts oriented in the cross-stream plane, implying alongstream propagation. These results are consistent with our earlier findings (JW85), which indicated offshore phase propagation at low frequencies and downstream phase propagation for periods shorter than approximately 10 days.

The vertical structure, horizontal phase variation, and transverse character of the low-frequency fluctuations are very consistent with the kinematics and dispersion of topographic Rossby waves (TRWs). Rhines' (1970) linear topographic wave model showed that in the presence of both stratification and significant bottom slope the structure of low-frequency wave motions is bottom-intensified, with vertical structure of the form  $\cosh(\kappa Nz/f)$ , where  $\kappa = (k^2 + l^2)^{1/2}$  is the horizontal wavenumber,  $N$  is the Brunt-Vaisala frequency,  $f$  is the Coriolis parameter, and  $z$  is measured upward from the bottom ( $z = -H$ ). The frequency of this mode is given approximately by  $\omega = \Gamma N \sin \theta$ , where  $\Gamma$  is the bottom slope and  $\theta$  is the angle between the wavenumber vector and upslope. The fluid velocity is in the plane of the wavefronts, so that in the low-frequency limit the velocity fluctuations should be transverse along the isobaths and in the high-frequency limit the fluctuations should be transverse up- and downslope. Observationally, the variance ellipses and wavenumber vectors are very nearly perpendicular (Thompson, 1977). For typical regional values  $\Gamma = 10^{-2}$  and  $N = 10^{-3} \text{ sec}^{-1}$ , the shortest period to be expected is about  $2\pi/\Gamma N \approx 8$  days.

Thompson and Luyten (1976) showed previously that Rhines' (1970) model could accurately predict the orientation of the major axis of low-frequency variance ellipses at Site D (39°10'N, 70°W) as a function of frequency. Also, from the "Rise Array" data (Luyten, 1977), Thompson (1977) obtained good agreement between the model predictions and observed phase propagation of motions with periods from 8 to 32 days. Independently, Hogg (1981) analyzed the "Rise Array" data using EOFs and found that the horizontal phase variations and vertical energy decay away from the bottom were well described by a simple topographic wave propagating offshore and refracting slowly in response to changes in depth, bottom slope, and stratification. A summary of TRW properties estimated by these authors is given in Table 2.

At sites 4 and 5, the mean orientation of the 1st mode ellipses in the 32 day band is 15°T, just about exactly parallel to our estimate of the orientation of the mean bathymetry here (15°T and 20°T, respectively). The theoretical prediction for a 32 day period topographic wave in the presence of bottom slope and stratification ( $\Gamma, N$ ) = ( $10^{-2}, 10^{-3} \text{ sec}^{-1}$ ) is a clockwise rotation of  $\theta = \sin^{-1}(\omega/\Gamma N) = 13^\circ$  relative to the isobaths. Although small, this characteristic rotation does not seem to be present in these records. It is worth noting though that the direction of the isobaths in this region is sufficiently irregular over small scales that accurate estimates of the dynamically-significant topography are rather difficult to make, especially at site 5 (see Figure 3). For bottom-trapped waves the ellipse orientation of 15° implies a wavenumber vector pointing along 105°T, which is approximately 30° off the line joining sites 4 and 5

(138°). The 60° average phase offset between these sites therefore implies a phase speed  $c = 7.0 \text{ km day}^{-1}$  and wavelength  $\lambda = 225 \text{ km}$ . These estimates compare favorably with the 7-8  $\text{km day}^{-1}$  phase speeds and 0(250 km) wavelengths for 32 day period TRWs reported in Table 2, all of which were estimated from measurements taken in regions with similar ( $\Gamma$ ,  $N$ ).

The vertical decay scale of the motion has been estimated from our observations by a least square fit of the 1<sup>st</sup> mode principal axis velocity component amplitudes to the theoretical vertical structure  $V = V_0 \cosh(\alpha z)$ . The decay scale,  $\alpha$ , obtained in this way is  $0.43 \text{ km}^{-1}$  for site 4 and  $0.37 \text{ km}^{-1}$  for site 5. These estimates are somewhat larger than, but comparable to, the theoretical decay scale  $\alpha = \kappa N/f \approx 0.33 \text{ km}^{-1}$ , based on the estimated 225 km wavelength.

The 32 day period motions are therefore consistent with the properties of topographic Rossby waves, the single exception being the lack of a characteristic clockwise rotation of the wavefronts relative to the isobaths. Despite the uncertainties in the topography, it seems plausible that this discrepancy is real and that the absence of the characteristic rotation could indicate the superposition of a coherent, cross-isobath motion similar to what is observed at higher frequencies, but which is energetically much weaker than the TRW signal at low-frequencies. This impression is also given by the counterclockwise rotation of the low-frequency variance ellipses with height at moorings 4 and 5 (Fig. 6).

From earlier work we know that Gulf Stream meanders in this region are energetic over a range of periods from 4 days to at least 50 days (Watts and Johns, 1982; Halliwell and Mooers, 1983). Since TRWs have a high-frequency cut-off near 8 days, one would expect a meander-associated variability to emerge at periods shorter than about 8 days. In fact, the EOF analysis suggests that this transition occurs at significantly longer periods, around 14 days. It is important to note that for 14 day period motions the TRW theory predicts a 25-30° clockwise rotation of the principal axes relative to the bathymetry, whereas the observed rotation is much larger than this, >90°. This abrupt transition to a cross-stream orientation suggests that the higher-frequency fluctuations are associated with coherent lateral shifts of the Gulf Stream's path. In the next section we examine the vertical coherence and structure of the temperature field to test whether the cross-stream EOF velocity modes found in the 14 and 5 day period bands are, in fact, associated with vertically coherent meanders of the Gulf Stream temperature front. Secondly, we wish to examine the nature of the vertical coupling, if any, between the low-frequency bottom-intensified motions and near-surface displacements of the Gulf Stream path.

#### IV. Temperature Structure

Vertical displacements of the main thermocline at sites 4 and 5 are highly coherent and in-phase for periods longer than about 4 days (not shown), and are associated with rms lateral displacements of the Gulf

Stream path here of 10-15 km (Watts and Johns, 1982). The mean depth of the 15° isotherm (Z15) at site 4 is 150 m, so, as mentioned previously, mooring 4 lies nearly beneath the record-mean position of the Gulf Stream's north wall. At site 5 approximately 25 km offshore of the record-mean north wall position, the mean Z15 is 400 m.

Figure 9 shows the coherence and phase between thermocline (15°C isotherm) depth fluctuations at sites 4 and 5 and temperature fluctuations at each level on moorings 4 and 5. The results are divided into four frequency bands (24-48 days, 12-16 days, 6-10 days, and 4-5 days) based on the results of the EOF analysis. Also shown in Figure 9 are the rms vertical displacement fields in each of these frequency bands. At each current meter site the rms vertical displacement in a given frequency band is obtained by dividing the standard deviation of in-situ temperature within that same band by the local vertical potential temperature gradient,  $\bar{\theta}_z$  ( $\pm 15\%$ ), calculated from available "Pegasus" data (H. T. Rossby, personal communication).

Near the northern edge of the Gulf Stream (site 4), the coherence between thermocline displacements and temperature fluctuations at the uppermost level (1420 m) is significant in all frequency bands. Below this, at depths  $>2000$  m, the coherence becomes insignificant in the 24-48 day band, but remains significant in each of the other frequency bands. What is immediately striking is the high coherence in the 12-16 day band throughout the entire water column. The coherence in the 4-5 day band is also quite high, relative to the significance level, and is considerably larger than in the 6-10 day band.



The phase estimates are consistently positive (20 to 40°) in the two lowest bands and consistently negative (-5 to -25°) in the two highest bands. However, only the (positive) phase estimates in the 12-16 day band are significantly different from zero at the 95% level (due to the high coherence), implying that in this frequency band, vertical displacements in the lower layer tend to lead those at the thermocline level.

At mooring 4 there is an obvious bottom-intensification in the 24-48 day band, with rms vertical displacements increasing by a factor of approximately 3/2 between the thermocline and ~2500 m depth (500 m off the bottom). This corroborates the bottom-intensification observed in the 24-48 day velocity eigenfunction, as would be expected for motions which are in approximate geostrophic balance. In each of the higher frequency bands the vertical displacement field becomes essentially barotropic.

Farther offshore, at mooring 5, temperature fluctuations are also significantly correlated with thermocline displacements at the uppermost level (1230 m), but below this the vertical decay of the coherence function in all frequency bands is more rapid than at mooring 4. The low-frequency vertical displacements at the two deepest levels, again bottom-intensified, are totally incoherent with displacements at the thermocline level. Similarly, in the 12-16 day band, the vertical coherence is insignificant below 2000 m, remarkably different from that observed at mooring 4. Interestingly, there is evidence for bottom-

intensification at periods as short as 6-10 days, which may imply an increased TRW influence at shorter periods in the deeper waters here.

Our earlier results (JW85) showed a similar offshore decrease of vertical coherence for fluctuations with periods less than about 16 days, but in contrast to these measurements showed significant vertical coherence of the low-frequency (24-48 day period) temperature field across the Gulf Stream. We point out, however, that the low-frequency cross-spectra between near-surface path displacements and deep temperatures in the earlier records were dominated by a single, large-amplitude meander apparently forced by interaction between the Gulf Stream and a warm core ring (Cornillon, 1982), whereas the present records did not contain such an energetic low-frequency event. The correct interpretation may be simply that when large meanders do occur they extend coherently to the bottom, but that normally the low-frequency signals in deep water associated with evolving, small-amplitude meanders in this region are effectively masked by the energetic topographic wave variability. In any case, the low-frequency statistics are obviously not yet stationary and require further measurement.

The kinematics of the organized, one- to two-week time-scale meandering motions may be understood by examining the phase relationship between the fluctuating velocity and temperature fields. At each of the current meter sites the coherence between temperature and cross-stream (positive northwest) velocity, shown in Figure 10, is peaked near the 5-day period and typically shows a secondary maximum near the 14-day

period. The phase between temperature and cross-stream velocity is consistently positive (i.e. such that temperature leads), and is very near  $90^\circ$ , except at the deeper levels on mooring 5 where the phase estimates are considerably noisier and some tend toward  $180^\circ$ . In JW85 we discussed the significance of this phase relationship for propagating meanders and showed that in deep layers there exists an approximate three-term balance between local rate of change of temperature, cross-stream advection of temperature, and vertical advection of temperature, with the first two being of like sign. Thus, on average, vertical advection of temperature balances the sum of local rate of change and cross-stream advection of temperature. Kinematically this requires  $|w/v| > |T_y/T_z|$ , so that parcel trajectories in the cross-stream plane are inclined at angles steeper than the mean cross-stream slope of the isotherms. Physically, onshore displacements of the deep front are brought about by downward and offshore advection of the isotherms, whereas offshore displacements are brought about by upward and onshore advection of the isotherms. The meandering of the Gulf Stream thermal front is therefore a strongly three-dimensional process in which vertical advection of heat is of leading order.

## V. Conclusions

Based on our observations to date we offer the following summarization of the variability. At levels shallower than  $\sim 1500$  m, temperature variations in all frequency bands are dominated by spatially-coherent displacements of the thermal structure, associated with the meandering of the path of the Gulf Stream. However, at low

frequencies (periods of 24 to 48 days), the meander-dominated regime in the upper layer gives way to an essentially uncoupled TRW variability below about 2000 m. This would seem to imply that the topographic waves are not being forced locally but are propagating into the area along rays from a source region farther downstream. We are unaware of any direct observations of topographic wave forcing by the Gulf Stream, however, aside from being the logical energy source for these disturbances, there is mounting indirect evidence that these waves can be forced by large meanders (Hogg, 1981) and also by Gulf Stream rings (Louis and Smith, 1944).

At periodicities shorter than approximately 16 days, deep front displacements at depths  $\geq 2000$  m are coherent with near-surface path displacements near the northern edge of the Gulf Stream, and in the 14 day and 5 day period bands these displacements are associated with spatially-coherent, cross-stream velocity fluctuations. Farther offshore within the Gulf Stream, however, the temperature field is generally weakly coherent vertically, and in certain bands (e.g. at periods of 14 days and 4 days) the velocity eigenfunctions also indicate a weak vertical coupling there. This suggests that the deep meandering motions have relatively short cross-stream scales, of the order of a deformation radius ( $\sim 35$  km) or less. The vertically-coherent, organized motion does not occur near the center of the deep jet, but rather is found near the northern edge of the current, under the region of maximum baroclinicity. Longer-term measurements combining IES and current meter instrumentation are planned to refine the present observations and to provide a detailed description of the regional energetics.

## APPENDIX

## EOF Velocity Hodographs

At each site, the EOF analysis yields velocity modes which are defined by the velocity variance contained in each component,  $(\hat{u}^2, \hat{v}^2)$ , and the relative phase of velocity components,  $(\phi_u, \phi_v)$ . The velocity fluctuation described by a given mode may be written:

$$u = \hat{u} \sin(\theta + \phi_u)$$

$$v = \hat{v} \sin(\theta + \phi_v)$$

where  $\theta = \omega t$ . The major and minor axes of the velocity hodograph are found by defining the quantity  $w = (u^2 + v^2)^{1/2}$  and searching for the maximum and minimum of  $w$ , or  $w^2$ , as a function of  $\theta$ :

$$w^2 = a^2 \cos^2 \theta + b^2 \sin^2 \theta + 2c^2 \cos \theta \sin \theta$$

where

$$a^2 = (\hat{u}^2 \sin^2 \phi_u + \hat{v}^2 \sin^2 \phi_v)$$

$$b^2 = (\hat{u}^2 \cos^2 \phi_u + \hat{v}^2 \cos^2 \phi_v)$$

$$c^2 = 2(\hat{u}^2 \cos \phi_u \sin \phi_u + \hat{v}^2 \cos \phi_v \sin \phi_v)$$

$$dw^2/d\theta = 0 = -a^2 \cos \theta \sin \theta + b^2 \cos \theta \sin \theta + c^2 (\cos^2 \theta - \sin^2 \theta)$$

Therefore,

$$\tan^2 \theta + [(a^2 - b^2)/c^2] \tan \theta - 1 = 0$$

The  $\theta$  values which maximize/minimize  $w^2$  are found by applying the quadratic formula, viz.

$$\theta_{\max, \min} = \tan^{-1} [-B/2 \pm \sqrt{B^2 + 4/2}],$$

where  $B = (a^2 - b^2)/c^2$ . The relative phase of the major axis velocity component is  $\theta_{\max}$ , and the major and minor axes of the velocity hodograph are obtained by substituting these  $\theta$  roots into the expression for  $w$ . Finally, the geographic orientation of the major axis is given by:

$$\text{Orientation} = \tan^{-1} [v(\theta_{\max})/u(\theta_{\max})].$$

## References

- Cornillon, P., The edge of the Gulf Stream: satellite versus inverted echo sounder determinations, EOS Trans. AGU, 63, 363, 1982.
- Groves, G.W., and E.J. Hannan, Time series regression of sea level on weather, Rev. Geophys., 6, 129-174, 1968.
- Halkin, D., and H.T. Rossby, Structure and transport of the Gulf Stream at 73°W, J. Phys. Oceanogr., (submitted), 1985.
- Halliwel, G.R. Jr., and C.N.K. Mooers, Meanders of the Gulf Stream downstream from Cape Hatteras 1975-78, J. Phys. Oceanogr., 13(7), 1275-1292, 1983.
- Hogg, N.G., Topographic waves along 70W on the Continental Rise, J. Mar. Res., 39(4), 627-649, 1981.
- Johns, W.E., and D.R. Watts, Gulf Stream meanders: Observations on the deep currents, J. Geophys. Res., 90(3), 4819-4832, 1985.
- Knauss, J.A., A note on the transport of the Gulf Stream, Frederick C. Fuglister Sixtieth Anniversary Volume, Deep-Sea Res., 16 (supplement), 117-123, 1969.
- Louis, J.P., and P.C. Smith, The development of the barotropic radiation field of an eddy over a slope, J. Phys. Oceanogr., 12, 56-73, 1982.
- Luyten, J.R., Scales of motion in the deep Gulf Stream and across the Continental Rise, J. Mar. Res., 35, 49-74, 1977.
- Priesendorfer, R.W., Cumulative probability tables for eigenvalues of random covariance matrices, SIO Ref. Series 81-2, Scripps Inst. of Ocean., La Jolla, Calif., 1981.
- Rhines, P.B., Edge-, bottom-, and Rossby waves in a rotating stratified fluid, Geophysical Fluid Dynamics, 1, 273-302, 1970.

- Richman, J.G., C. Wunsch, and N.G. Hogg, Space and time scales of mesoscale motions in the western North Atlantic, Rev. of Geophys. Space Phys., 15, 385-420, 1977.
- Thompson, R.O.R.Y., and J.R. Luyten, Evidence for bottom-trapped topographic Rossby waves from single moorings, Deep-Sea Res., 23, 629-635, 1976.
- Thompson, R.O.R.Y., Observations of Rossby waves near Site D, Prog. in Oceanogr., 7, 1-28, 1977.
- Wallace, J.M., and R.E. Dickinson, Empirical orthogonal representation of time series in the frequency domain. Part I: Theoretical considerations, Jour. Appl. Meteor., 11, 887-892, 1972.
- Watts, D.R., and W.E. Johns, Gulf Stream meanders: Observations on propagation and growth, J. Geophys. Res., 87, 9467- 9476, 1982.



Table 1. Mooring statistics.

Year-Site	Latitude	Longitude	Duration (d)	Bottom Depth (m)	CM Depth (m)	Temp (°C)		U (cm/s)		V (cm/s)	
						Mean	$\sigma$	Mean	$\sigma$	Mean	$\sigma$
79-1	35°51.3'	73°50.2'	185	3070	1955	3.640	.058	4.2	3.8	-0.3	5.8
79-21	35°55.7'	73°13.7'	101	3690	2685	3.038	.073	2.5	2.7	1.6	4.7
80-21	35°55.8'	73°13.7'	241	3680	2665	3.127	.094	4.1	4.2	3.6	5.1
80-22	35°55.8'	73°13.7'	241	3680	3170	2.194	.066	0.6	3.4	0.8	2.8
80-3	36°18.0'	73°37.0'	241	3070	2060	3.489	.073	2.2	3.5	-1.2	5.6
82-41	36°10.0'	73°45.8'	135	3050	1420	3.916	.041	4.1	4.4	-4.0	6.0
82-42	36°10.0'	73°45.8'	135	3050	1955	3.565	.060	2.4	3.2	-1.6	5.8
82-43	36°10.0'	73°45.8'	135	3050	2490	2.997	.061	0.3	2.8	-3.2	6.4
82-51	35°57.3'	73°31.8'	135	3390	1230	4.215	.096	9.9	4.4	4.2	6.2
82-52	35°57.3'	73°31.8'	135	3390	2295	3.362	.064	4.8	4.2	1.4	7.0
82-53	35°57.3'	73°31.8'	135	3390	2830	2.753	.096	2.0	4.3	-0.3	8.0

Table 2. Observed topographic Rossby wave dispersion parameters on the western North Atlantic continental rise: period (T), wavelength ( $\lambda$ ), phase speed (c), and angle ( $\theta$ ) between the wavenumber vector and downslope direction. An asterisk indicates the principal axis angle relative to the isobaths, when the wavenumber direction was unknown.

<u>T (d)</u>	<u><math>\lambda</math>(km)</u>	<u>c (km/d)</u>	<u><math>\theta</math>(deg)</u>	<u>Reference</u>
32	230	7	15	Thompson (1977) site 'S'
	270	8	11	Thompson (1977) "Rise"
	-	-	13*	Thompson & Luyten (1976) site 'D'
16	290	18	16	"
	160	10	27	
	160	10	10*	
10.7	140	13	27	"
	240	22	34	
	130	12	32*	
8	190	24	49	"
	160	20	47	
	90	11	35*	

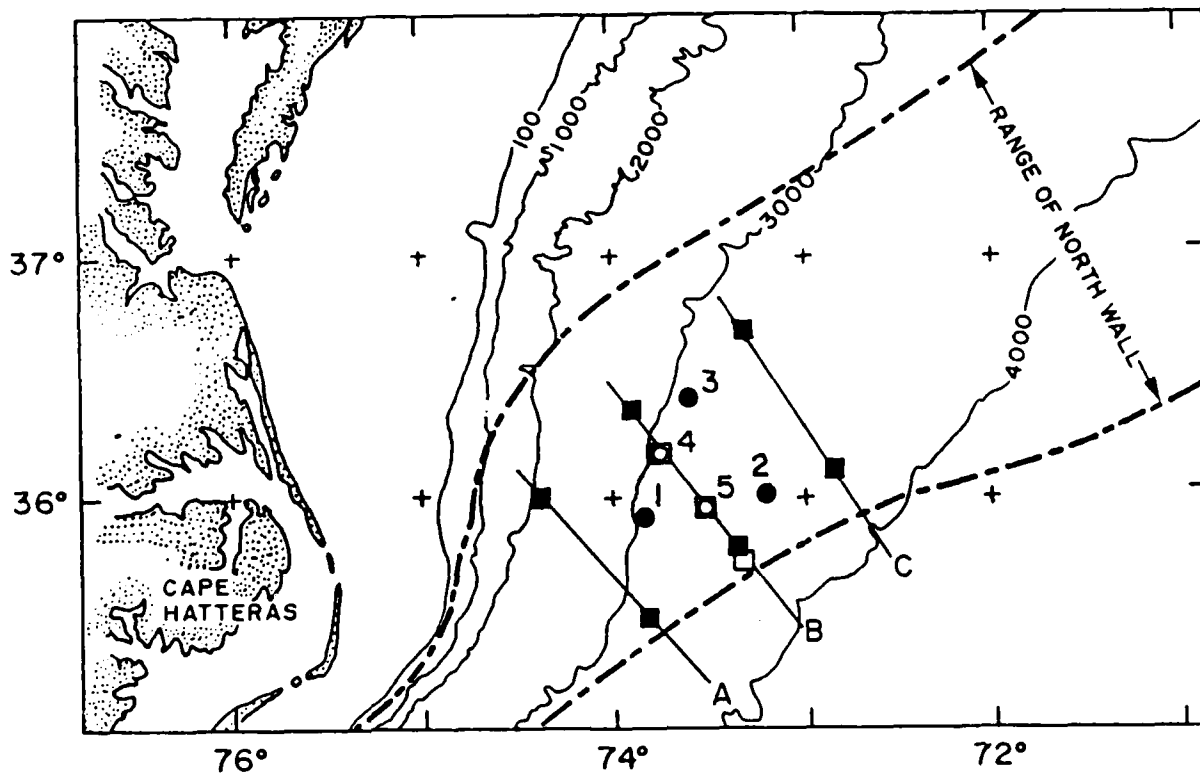


Figure 1. Survey area. Squares indicate the IES locations, and circles indicate the current meter mooring locations. Closed symbols designate the 1979-80 deployments; open symbols designate the 1982 deployments. The historical envelope of the north wall location is indicated by the bold dashed lines.

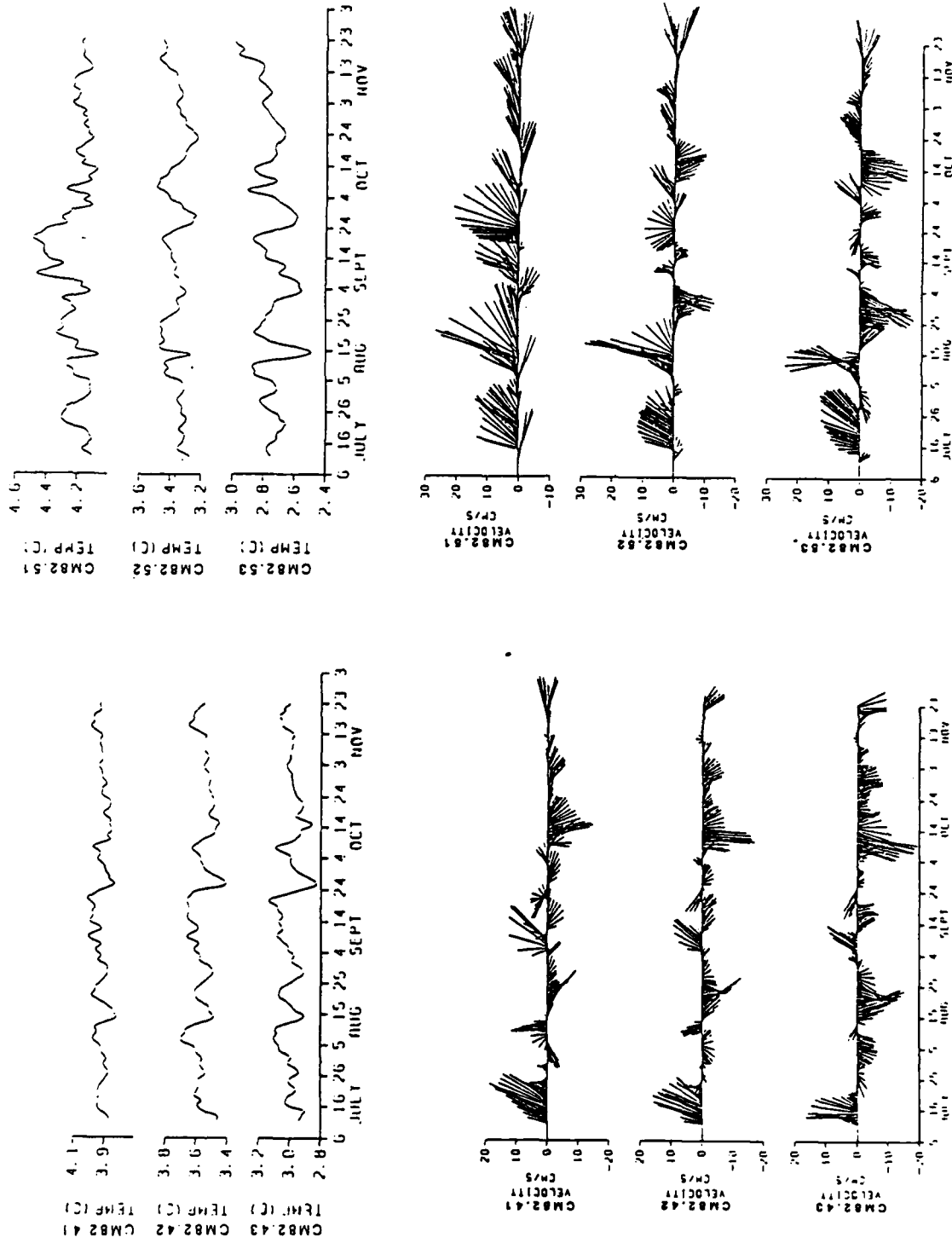


Figure 2. Time series of temperature and velocity (stick plots, with north up) at each of the current meter sites: mooring 4 (left) and mooring 5 (right).

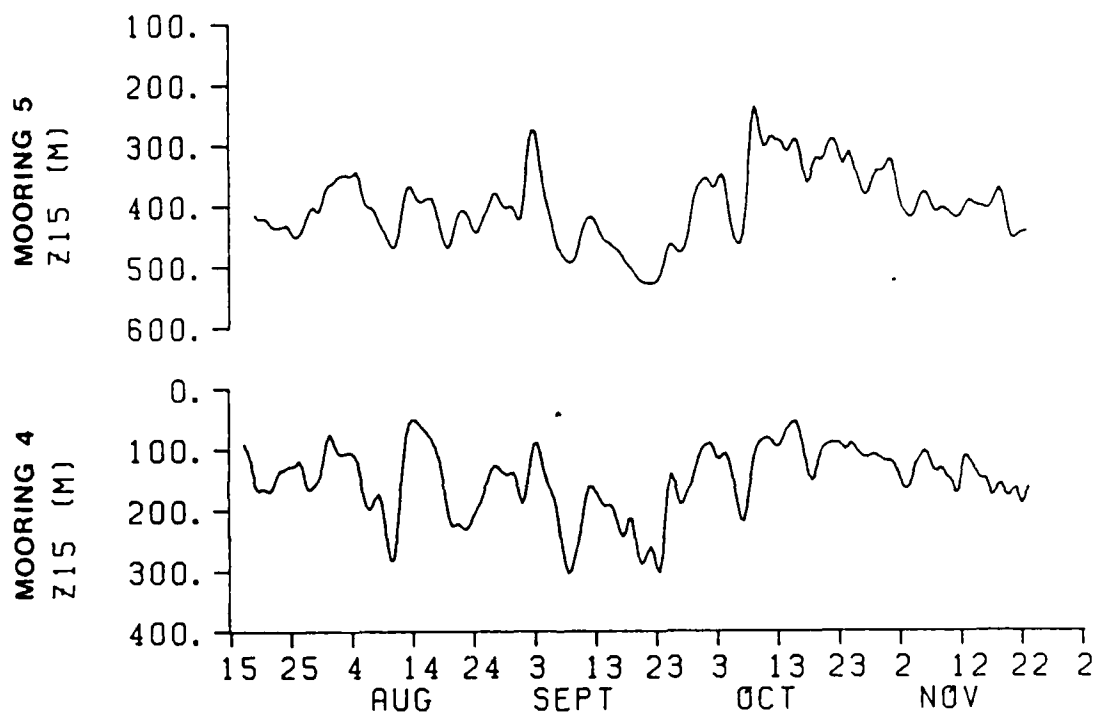


Figure 3. Time series of 15° isotherm depth (Z15) at moorings 4 and 5.

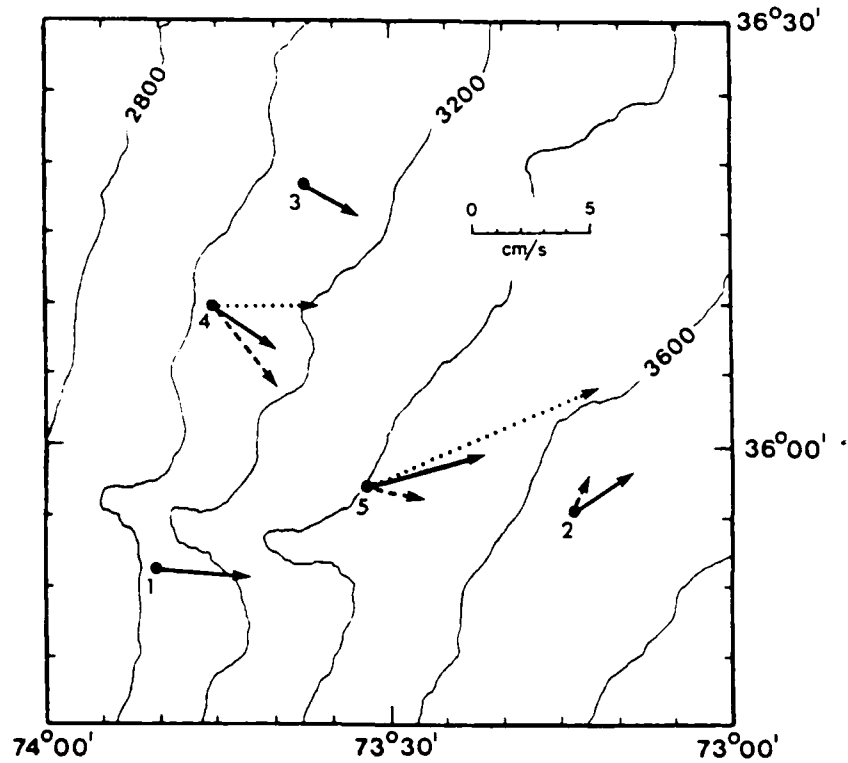


Figure 4. Mean currents. Solid vectors indicate the means at 1000m off the bottom, dashed vectors indicate the means at 500m off the bottom, and dotted vectors indicate the means at the shallowest levels (1500m off the bottom at site 4 and 2000m off the bottom at site 5).

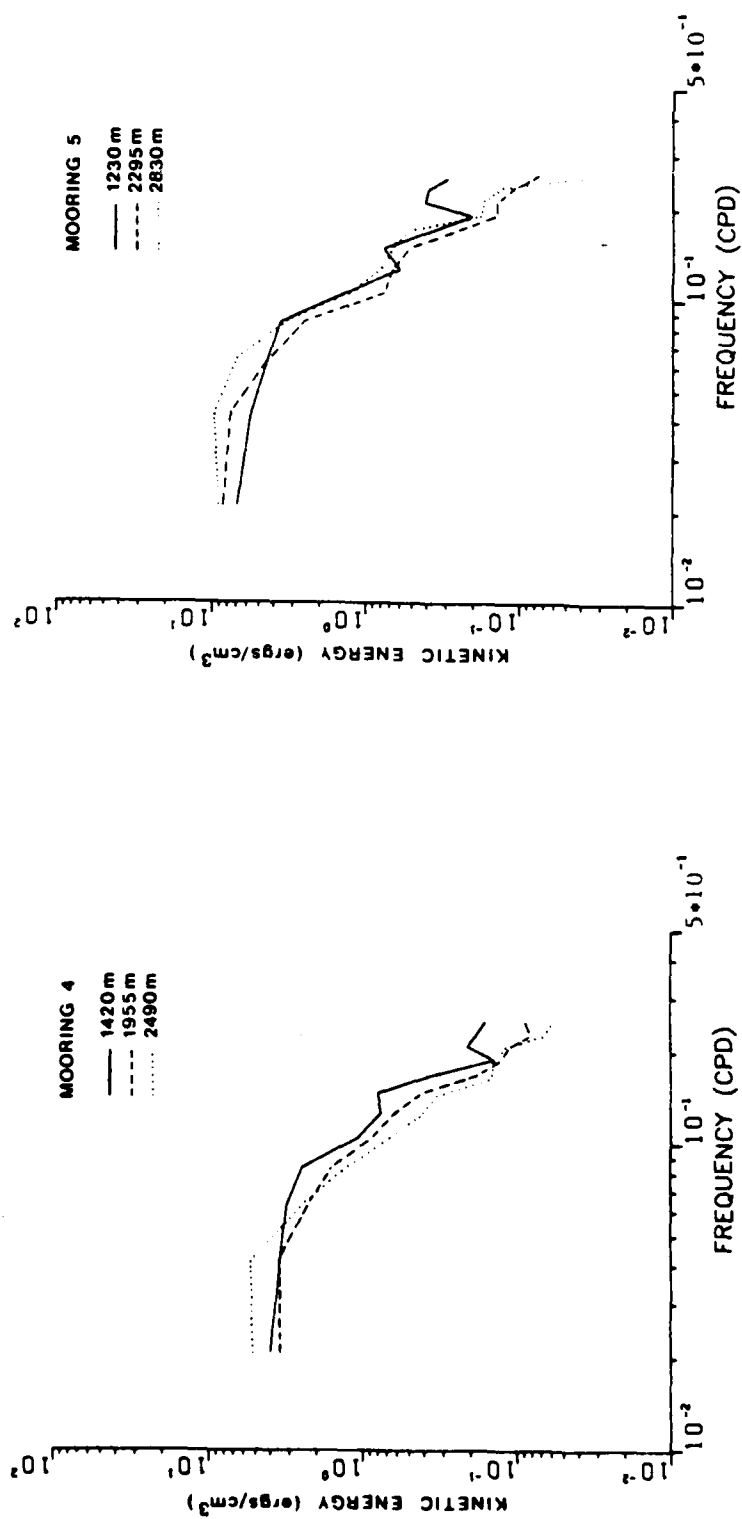


Figure 5. Eddy kinetic energy spectra versus depth at moorings 4 and 5.

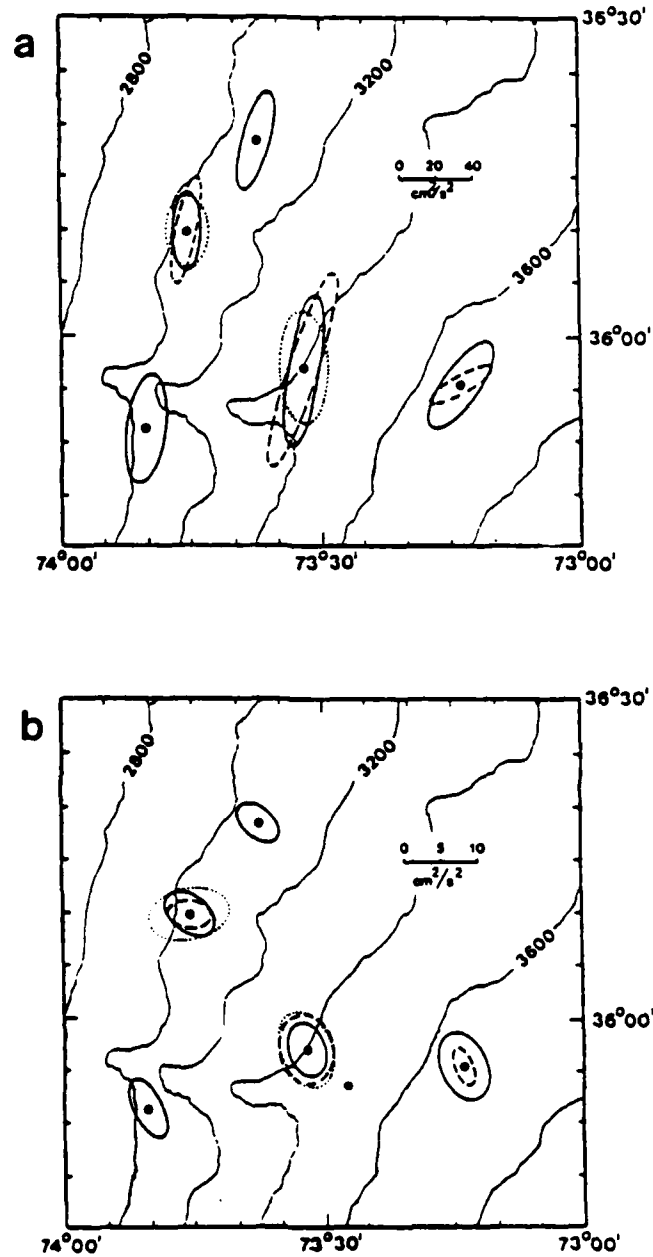


Figure 6. Rotary variance ellipses for each of the current meter sites: a) 12-48 day band, and b) 4-10 day band. Solid ellipses indicate sites at 1000m off the bottom, dashed ellipses at 500m off the bottom, and dotted ellipses at the shallowest levels (1500m off the bottom at site 4 and 2000m off the bottom at site 5).



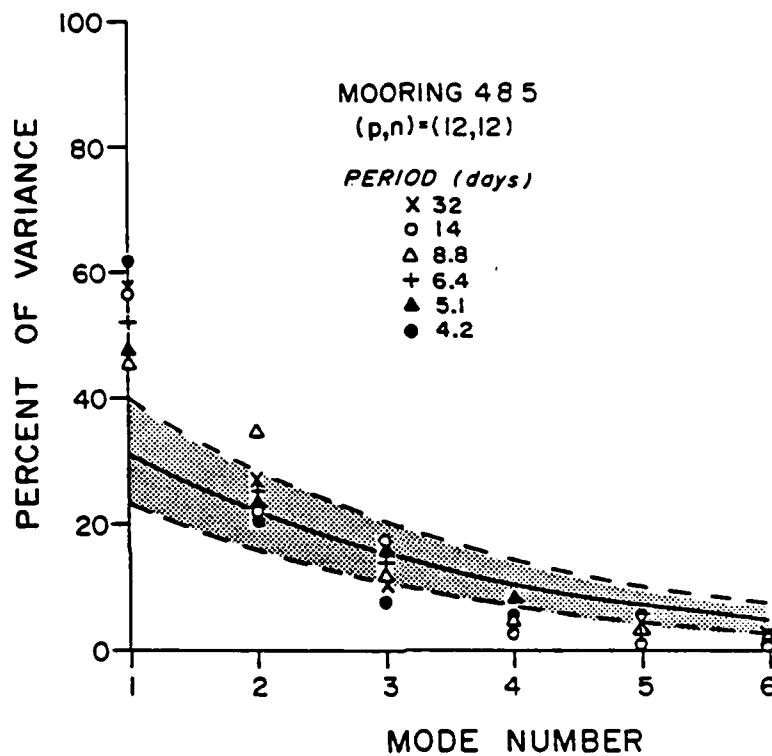


Figure 7. Percent variance explained by successive EOF modes at moorings 4 and 5. The symbols designate modes in different frequency bands, as shown. The solid line indicates the "noise" eigenvalue distribution for 12 degrees of freedom, and the shaded area indicates the 5% to 95% confidence intervals of this distribution.

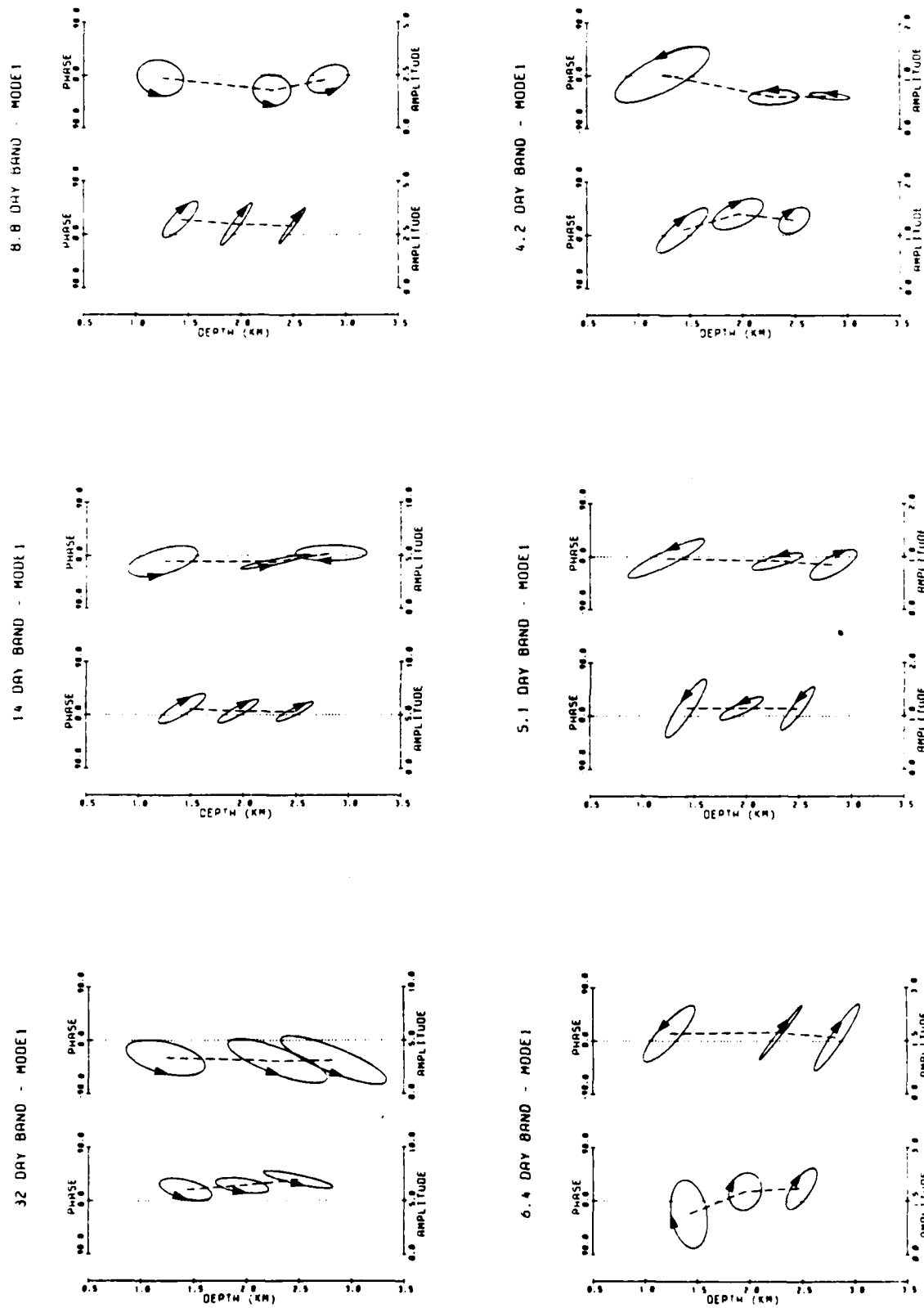
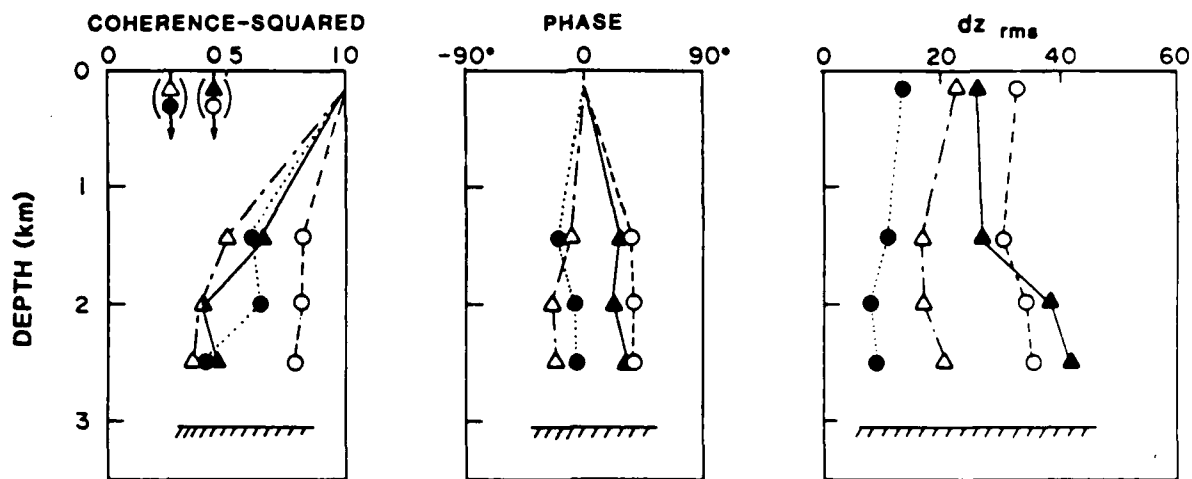


Figure 8. Structure of first EOF modes. Each frame illustrates the velocity hodographs at mooring 4 (left) and mooring 5 (right), within a particular frequency band. The geographical orientation and eccentricity of the velocity ellipse are displayed in the "plan view" sense, with north up and east to the right. The phase of the major axis velocity component at a site is indicated by the position of the center of the ellipse

## MOORING 4



## MOORING 5

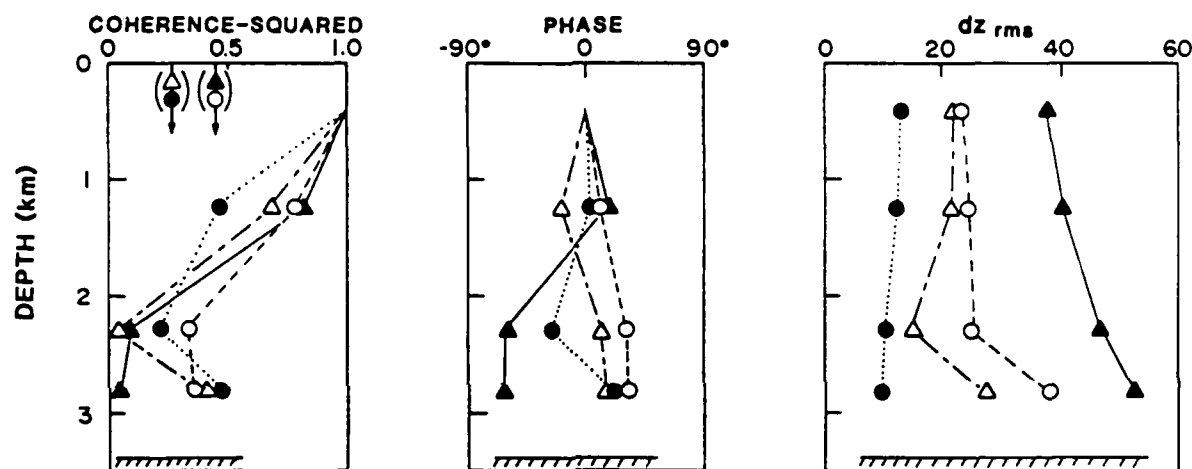


Figure 9. Coherence-squared and phase between thermocline depth fluctuations and temperature fluctuations at each level on moorings 4 and 5, and r.m.s. vertical displacement amplitudes. Each symbol represents a different period band:  $\blacktriangle$ , 24-48 days;  $\circ$ , 12-16 days;  $\triangle$ , 6-10 days;  $\bullet$ , 4-5 days. The 95% confidence level for non-zero coherence-squared in the 24-48 day and 12-16 day bands is 0.45; in the two higher bands (with greater bandwidth) it is 0.27, as indicated by arrows.

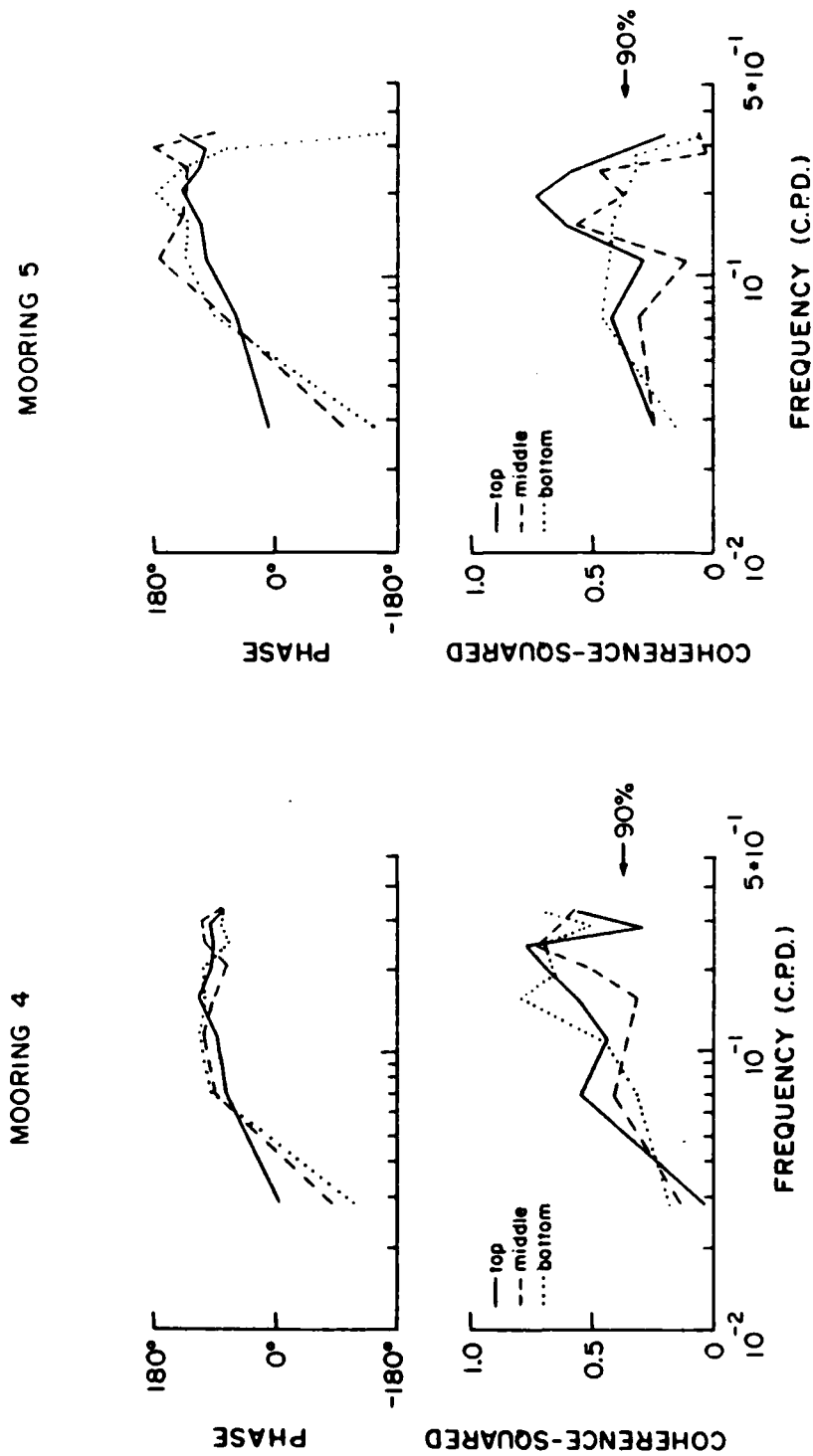


Figure 10. Coherence-squared and phase between temperature and cross-stream velocity at moorings 4 and 5.

## Boundary-forced Nonlinear Radiation: Numerical Experiments

P. Malanotte-Rizzoli, MIT, Cambridge, Mass.

D.B. Haidvogel, NCAR, Boulder, Colorado

An important, unsolved question for the Gulf Stream system is its interaction with the mesoscale oceanic eddy field. From the experimental evidence accumulated in experiments like MODE and POLYMODE important questions emerge not yet adequately treated even in the context of simple theoretical models. One of these questions concerns the possible generation mechanism of the mesoscale eddy field and, in the limit of high-amplitude radiation, the formation of ring-like structures from an eastward meandering jet, like those observed to emerge from the Gulf Stream.

This question is related to the general problem of radiation of mesoscale energy from a meandering current, which was studied by several authors. Flierl et al. (1975) examined the behavior of semi-infinite domains driven by boundary forcing, using the linear barotropic vorticity equation on the  $\beta$ -plane. Pedlosky (1977) treated the same problem with a 2-layer quasi-geostrophic model including a mean current. The basic result of these studies is that in the quiescent ocean the far field can transmit energy radiated by the northern boundary only if the latter has a westward phase speed.

All these models are however linear. Nonlinear effects may be expected to modify the above results, as indicated by numerical experiments carried out with fully nonlinear models in which mesoscale radiation is observed to be excited and radiate away from an eastward-moving jet (Holland, 1978; Ikeda, 1981; Ikeda & Apel, 1981).

In a successive work (P. Malanotte-Rizzoli, 1984) the above problem was

idealized in the context of a fully nonlinear, although simple, model in which again the meandering current was idealized as a moving northern boundary. The model is the quasi-geostrophic equivalent barotropic potential vorticity equation in a zonal channel over variable topography which allows for free, nonlinear wave solutions in different parameter ranges. One of these solutions is in the range of high nonlinearity and has a monopole shape, with closed recirculation regions, like Gulf Stream rings (Fig. 1).

The problem of boundary forced nonlinear radiation was then thoroughly examined in the weakly nonlinear parameter range. Nonlinearity allows for the production of radiation in the interior field through a resonance mechanism. The resonant equilibrium forced solutions obey a forced Korteweg-de Vries (KdV) equation and admit, for a specific choice of forcing, two equilibrium amplitudes.

Two further effects of nonlinearity were demonstrated analytically. First, in the limit of high nonlinearity, and for long wave radiation, the resonant interior response excited by an eastward-moving boundary has a cross-channel structure very different from that allowed by the corresponding linear model. This structure is oscillatory, i.e. radiating, near the northern boundary (Fig. 2a,b,c). For sufficiently high nonlinearity, this excited eddy will have closed recirculation regions and may detach from the boundary itself, propagating away from it like Gulf Stream rings (Fig. 3) (P. Malanotte-Rizzoli, 1984).

Second, allowing for a slow time modulation of the northern boundary wave, the resonant interior response obeys a time-dependent forced KdV equation. An initial condition corresponding to the steady equilibrium solution evolves with soliton production in the region directly affected by

the forcing. The interior response undergoes in the long time scale a nonlinear, deterministic cascade process producing nonlinear radiation of shorter wavelength, i.e. smaller nonlinear eddies. When the small nonlinear eddies emerge from the region directly affected by the forcing, they propagate as free nonlinear radiation. For a westward-propagating northern boundary wave, the smaller nonlinear eddies have a backward propagation, i.e. they move eastward (P. Malanotte-Rizzoli, 1984).

To confirm and extend the above analytical results to more realistic and complex circumstances, numerical experiments have been initiated using a numerical code for the equivalent barotropic, quasi-geostrophic potential vorticity equation in the zonal channel over variable relief. The code has periodic boundary conditions and uses Fourier expansion techniques in the along-channel direction and finite-differences in cross-channel direction, thus allowing the investigation of boundary forced problems.

The goal of this first set of experiments is to reproduce some of the analytical results previously discussed. In all the following experiments the relief  $h(y) = -2.2y + 2.2y^2$  is used. First, the boundary-forced equilibrium response is simulated as given by the analytical theory (P. Malanotte-Rizzoli, 1984) in the weakly nonlinear case. The cross-channel structure of the forced equilibrium solution corresponds to the lowest westward-propagating eigenmode over the above topography.

The equilibrium response is  $\psi_0 = A \operatorname{sech}^2(Bx)$  at initial time  $t = 0$ , centered at the center of the zonal channel, 25 units long and 1 unit wide. Being weakly nonlinear, we choose  $A = 10^{-2}$ , and  $B = 0.2$ . The northern boundary condition, imposed upon the  $O(\epsilon)$  solution, where  $\epsilon$  = Rossby number, is:

$$\psi_{\text{boundary}} = A_b \operatorname{sech}^4[B(x-ct)]$$

where  $A_b = \mathcal{O}(\epsilon)$  with respect to  $\nu_0$ . As  $\epsilon = 10^{-4}$  in the present experiment, this implies  $A_b = 10^{-4}$ .  $C = C_0 + \epsilon C_1$ , with  $C_0 \approx -0.11$  evaluated solving the zero-order eigenvalue problem and  $C_1$  evaluated from the analytical theory, is the westward phase speed of the northern boundary wave. Figure 4 shows the equilibrium forced solution (stream function left panel, vorticity, right panel) at initial time  $t = 0$  and  $t = 120$ , after almost one complete turn-over of the zonal channel. Notice that the plot has a ratio 1:2 of north-south to east-west length scales. The equilibrium wave propagates with no essential change of shape.

Always for the lowest westward going mode, initial value problems were solved in which the interior field is identically zero at the initial time. Thus the interior response is excited by the northern boundary forcing, the amplitude of which is progressively increased to observe the increasing effects of nonlinearity. Figure (5a,b,c) shows the results of the very weakly nonlinear experiment, with a boundary forcing function

$$f_{\text{boundary}} = A_b \operatorname{sech}^4 [B(x-ct)] ,$$

where  $B = 0.2$ , the same value for all the following experiments. In Fig. 5  $A_b = 0.01$ ; thus the observed evolution is dominated by dispersion. The interior forced eddy grows, but develops immediately a negative lobe trailing behind the primary, boundary forced positive lobe. At  $t = 100$  the negative low has the same amplitude as the boundary forced positive one. At each time, plots are shown for the streamfunction (upper panel) and vorticity (lower panel). Notice that the plots are now on a scale 10:1 in along channel direction.

In Fig (6a,b,c) the nonlinearity is increased. The boundary forcing function has the same shape but  $A_b = 0.0625$ . Initially, as the interior field is zero, dispersion dominates and the same tendency is observed for



the formation of the negative, dispersive lobe trailing the boundary forcing, positive one. Nonlinearity is however sufficiently strong to begin to balance dispersion as soon as the interior field has reached a sufficient amplitude. The negative, dispersive lobe thus never grows after the initial stage (Fig. 6b,  $t = 100$ ) and actually shrinks by the end of the experiment, after almost one turn-around of the channel. Nonlinearity and dispersion eventually balance each other and the interior forced response reaches an eddy pattern which propagates without essential change of shape: in this experiment we have excited the equilibrium boundary forced interior solution.

In the experiment of Fig. 7, the boundary wave amplitude is  $A_b = 0.09$ . Nonlinearity is now sufficiently important not only to excite the interior eddy shown in Fig. 6, but also to dominate dispersion almost immediately. An interior nonlinear cascade is now observed, for which the main interior boundary forced eddy breaks down into smaller, nonlinear eddies (all positive) which break off and propagate eastward. We are now in a sufficiently nonlinear regime obeying a time-dependent KdV dynamics and leading to the production of nonlinear radiation of shorter wavelength propagating backward. This result is in agreement with the results of the analytical theory previously summarized. Notice that the purely linear, dispersive response under the same boundary forcing produces an interior evolution (not shown) identical to that shown in Fig. 5.

A few numerical experiments have now been carried out for the eastward-propagating modes. In the next figure (8) the lowest eastward propagating solution is studied over the same topography, with the aim of first reproducing the free nonlinear wave. However, with the same width for the initial interior field  $\psi_0 = A \operatorname{sech}^2(Bx)$ , with  $B = 0.2$ , the eddy is so

elongated in the zonal channel that dispersion is practically zero. The amplitude  $A = 10^{-2}$  is still too big for such a small dispersion. In fact with  $B = 0.2$ , the above initial condition, allowed to evolve in the purely linear system (not shown) propagates eastward with essentially no change in shape over almost one turn-around of the channel, i.e. the wave is practically dispersionless.

Thus, instead of reducing the amplitude to almost insignificant values, we have increased dispersion, making the initial wave rounder. This also allows a decrease in the channel length, which in the next experiment is 10 to a width of 1.

The next figure (8) shows the evolution of the initial condition

$$\psi = A \operatorname{sech}^2 [B(x-ct)] \phi_{1E}(y)$$

with  $B = 0.6$  ;  $A = 0.01$  corresponding to the lowest eastward-going eigenmode over the same relief. Notice that even though dispersion is now greater, it still is not sufficient to balance nonlinearity in the initial phase of the evolution (at  $t = 0$ , Fig 8a, the eddy width is about 1/3 of the channel, while the westward propagating eddy of the previous figures is as wide as the channel). Thus initially nonlinearity dominates producing steepening on the forward face of the eddy (Fig. 8b). As this becomes rounder, dispersion also increases until a balance is reached: the eddy reaches a fairly round pattern which propagates without changing shape over the topographic "valley".

Future experiments will concentrate upon the eastward propagating modes and boundary forcing as most relevant for Gulf Stream related problems. First the effects of boundary forcing will be investigated in exciting an interior field starting from zero initial condition with focus on the change of the interior cross-channel structure with increasing nonlinearity (i.e.

amplitude of the boundary forcing). The final goal is to carry out a series of experiments with realistic and complex interior responses, and for the purely linear, dispersive case versus increasing values of the nonlinearity. Then the energetics of the interior field will be thoroughly studied with various diagnostic measurements (for instance energy and momentum fluxes) to explore the difference in the radiation properties of the far field.

## FIGURE CAPTIONS

Figure 1: High amplitude monopole solution, radially symmetric, over quadratic relief  $h(y) = y^2/2$  in the reference frame  $(\psi_0 + C_0 y)$ , moving with the ring, where  $C_0 = -1$ .

Figure 2: a) Relief  $h(y) = -2.2y + 3y^2$  in the zonal channel  $0 \leq y \leq 1$ .

b) Linear or weakly nonlinear interior response, resonantly excited by forcing at the northern boundary.

c) Interior response in the highly nonlinear case (Rossby number  $\mathcal{E} \rightarrow 1$ ) under the same northern boundary forcing.

Figure 3: Resonantly excited equilibrium nonlinear response under the northern boundary forcing  $f_b = \text{sech}^4[B(x-ct)]$  over the relief

$h(y) = 2.2y + 2.2y^2$ . Lowest westward propagating wave

$$\psi = \psi_0 + \delta_1^2 \psi_1, \text{ with } \delta_1^2 = L_{NS}^2 / L_{EW}^2.$$

$$\psi_0 = A \text{sech}^2[B(x-ct)] \phi_1(y); \quad B = 2; A = -2; \text{ Rossby number } \mathcal{E} = \delta_1^2 \approx 1.$$

Figure 4: Boundary forced equilibrium response in the weakly nonlinear case. Rossby number  $\mathcal{E} = 10^{-2}$ . Lowest westward moving mode over

$h(y) = -2.2y + 2.2y^2$ . The above response corresponds to the analytical equilibrium resonant solution of the weakly nonlinear problem. Left panel: streamfunction at  $t = 0, 120$ . Right panel: vorticity at the same times.

Figure 5: Excitation of the interior response from zero initial condition

in the very weakly nonlinear, dispersion-dominated regime. Boundary forcing

$$f_b = A_b \operatorname{sech}^4 [B(x-ct)] \text{ with } B = 0.2; A_b = 10^{-2}.$$

a)  $t = 10$ ; b)  $t = 50$ ; c)  $t = 100$ . Upper panel: streamfunction; lower panel: vorticity.

Figure 6: Excitation of the interior response under the same condition as Fig 5. Here  $A_b = 0.0625$ . a)  $t = 50$ ; b)  $t = 100$ ; c)  $t = 150$ .

Figure 7: Excitation of the interior response under the same conditions as Fig. 5. Here  $A_b = 0.09$ . All the fields shown are for the streamfunction a)  $t = 10$ ; b)  $t = 30$ ; c)  $t = 50$ ; d)  $t = 70$ ; e)  $t = 90$ ; f)  $t = 100$ .

Figure 8: Free, eastward moving interior solution over the same relief.

Initial condition at  $t = 0$ :  $\psi = A \operatorname{sech}^2 [B(x-L/2)] \phi_{1E}(y)$

where  $L$  = channel length;  $\phi_{1E}$  is the lowest eastward moving mode;

$A = -0.01$ ;  $B = 0.6$ .

a)  $t = 0$ ; b)  $t = 50$ ; c)  $t = 200$ ; d)  $t = 400$ ; e)  $t = 500$ ; f)  $t = 600$ .

Every panel shows streamfunction (upper) and vorticity (lower).

## REFERENCES

Flierl, G.R., V.M. Kamenkovich and A.R. Robinson, 1975: Gulf Stream meandering and Gulf Stream rings. Dynamics and the Analysis of MODE-1. Unpublished manuscript, MODE Dynamics Group, MIT, 43-135.

Holland, W.R., 1978: The role of mesoscale eddies in the general circulation of the ocean: numerical experiments using a quasi-geostrophic model. J. Phys. Oceanogr., 8, 363-392.

Ikeda, M., 1981: Meanders and detached eddies of a strong eastward-flowing jet using a two layer quasi-geostrophic model. J. Phys. Oceanogr., 11, 525-540.

Ikeda, M. and J.R. Apel, 1981: Mesoscale eddies detached from spatially growing meanders in an eastward-flowing oceanic jet using a two-layer quasi-geostrophic model. J. Phys. Oceanogr., 11, 1638-1661.

Malanotte -Rizzoli, P., 1984: Boundary forced nonlinear planetary radiation. J. Phys. Oceanogr., 14, 1032-1046.

Pedlosky, J., 1977: On the radiation of mesoscale energy in the mid-ocean. Deep-Sea Res., 24, 591-600.

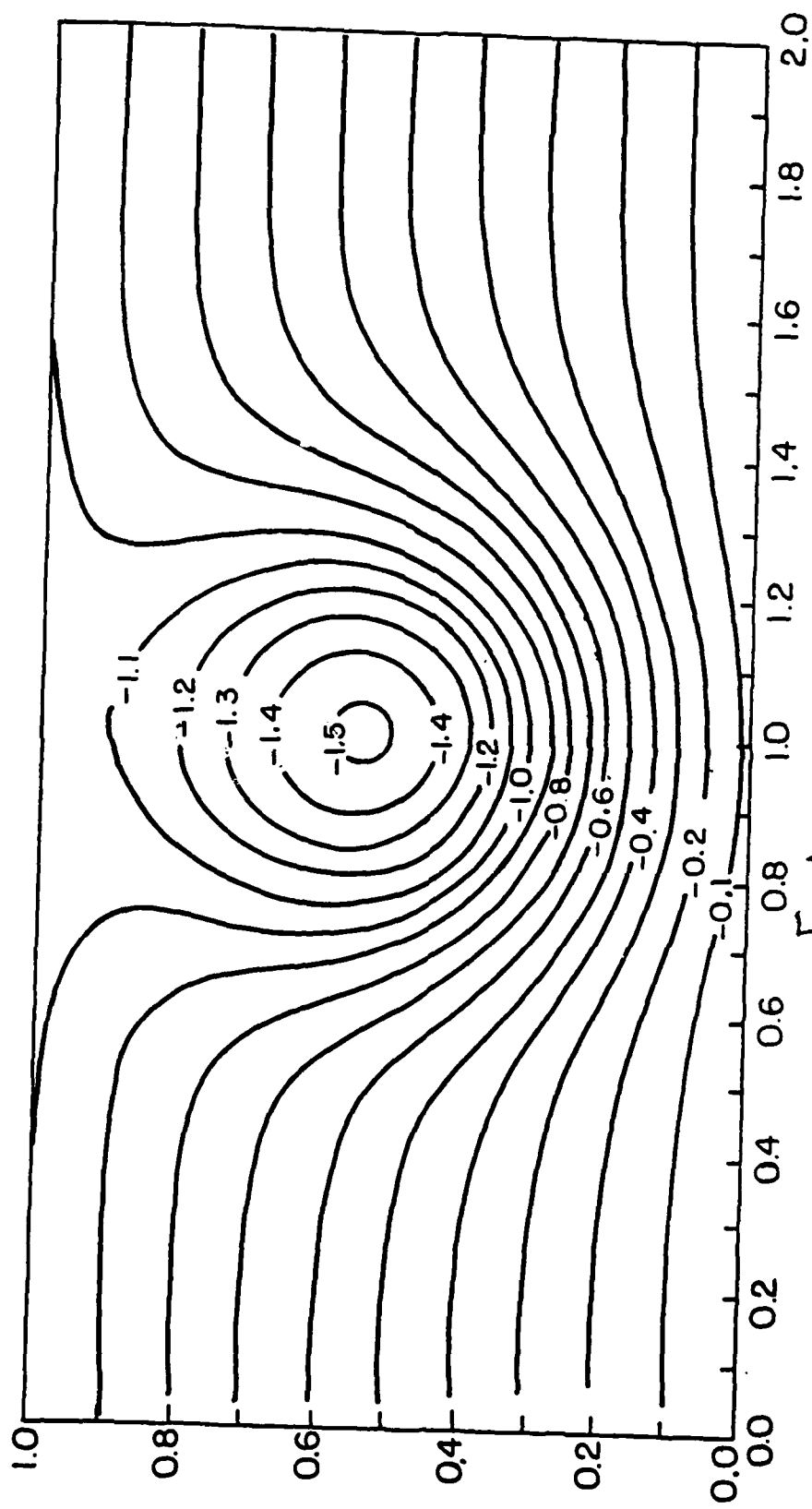


Fig 1

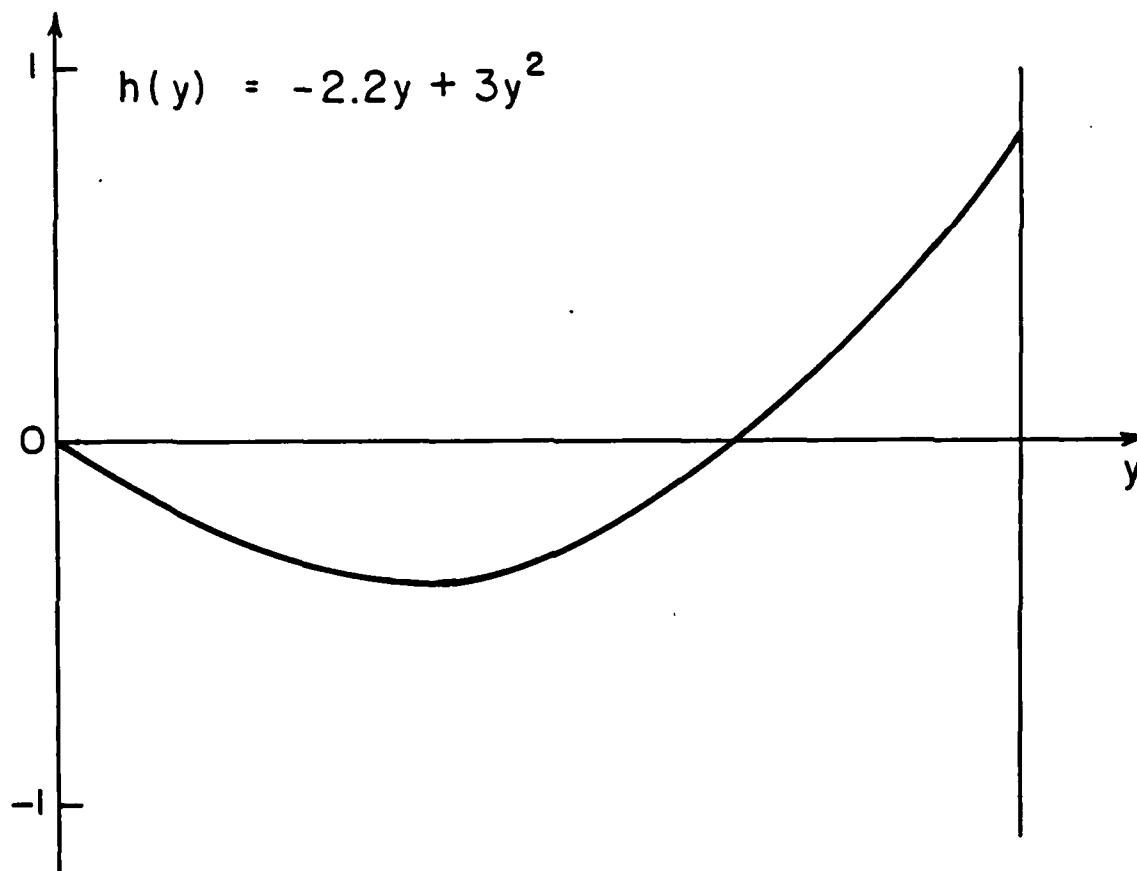


Fig 2a



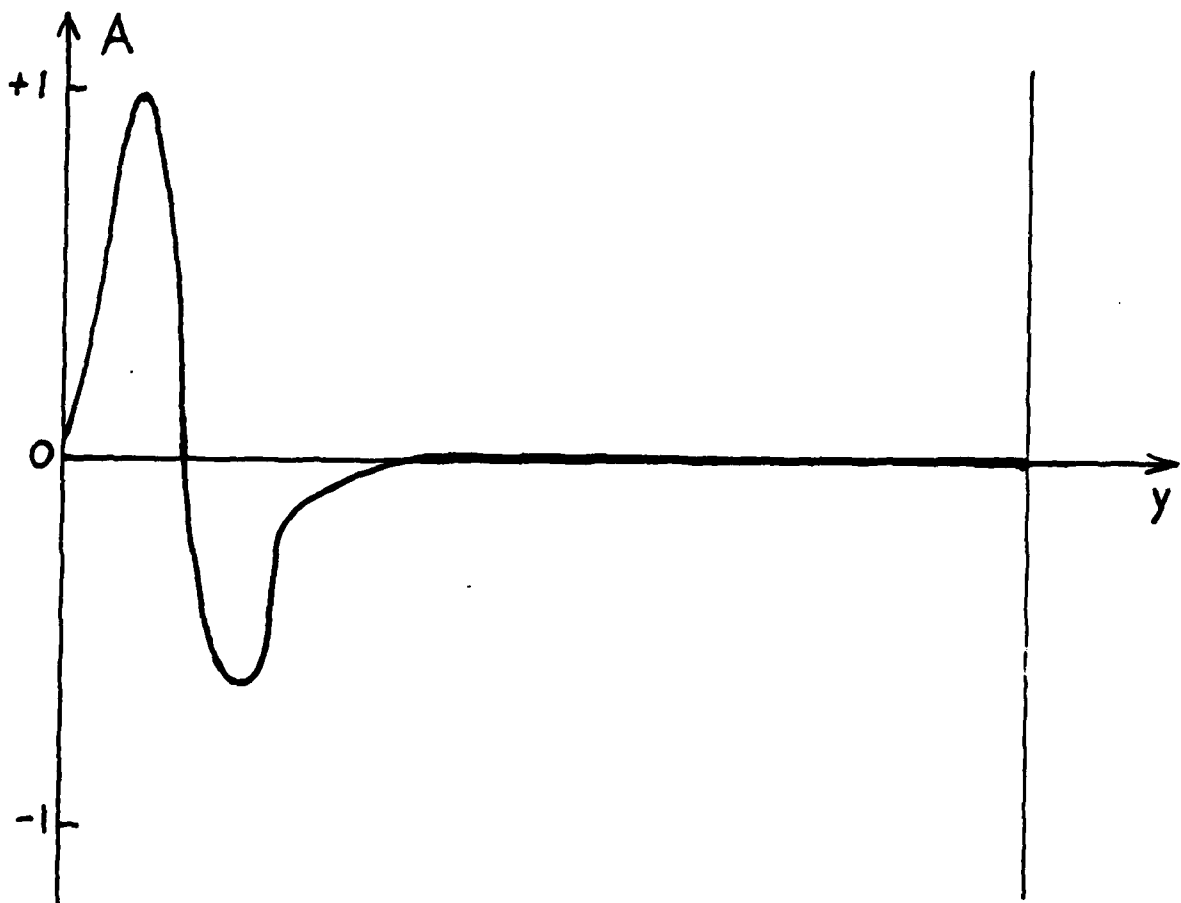


Fig 2b

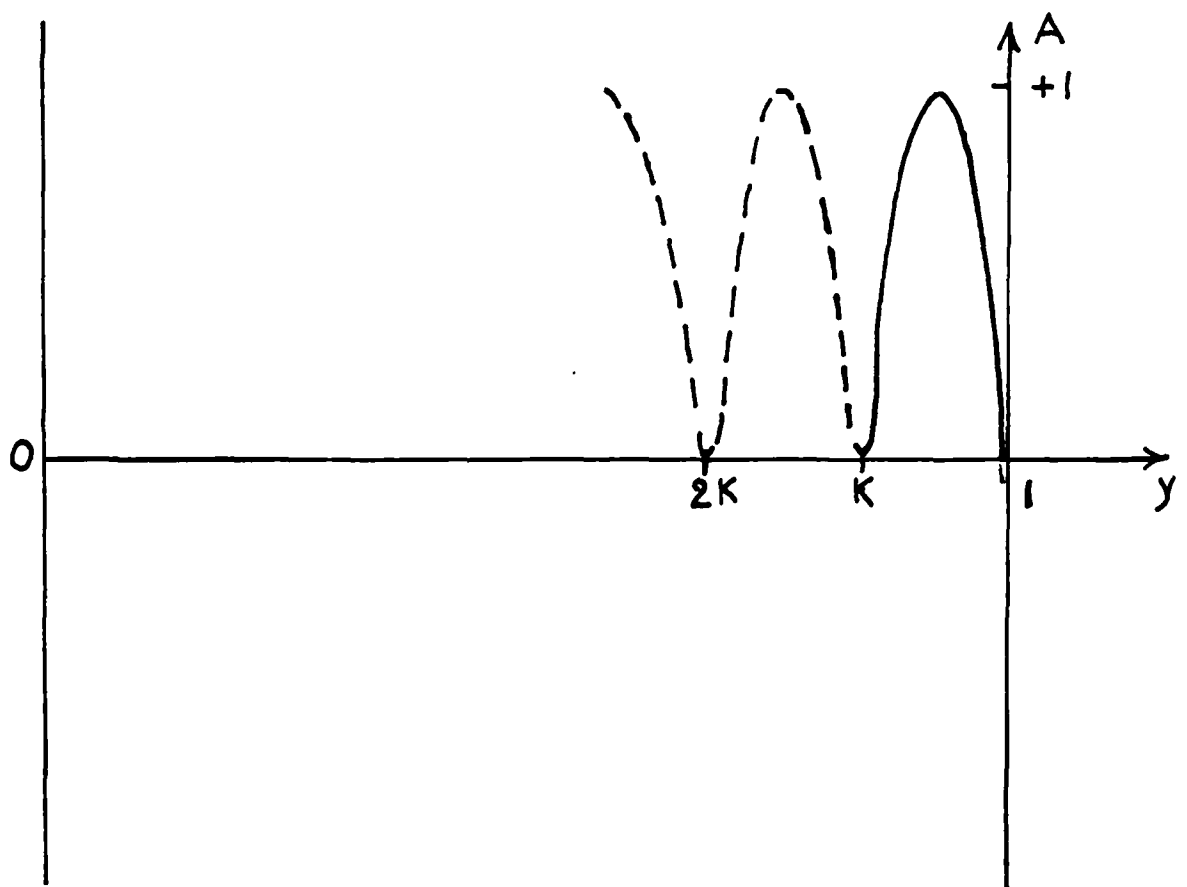


Fig 2c

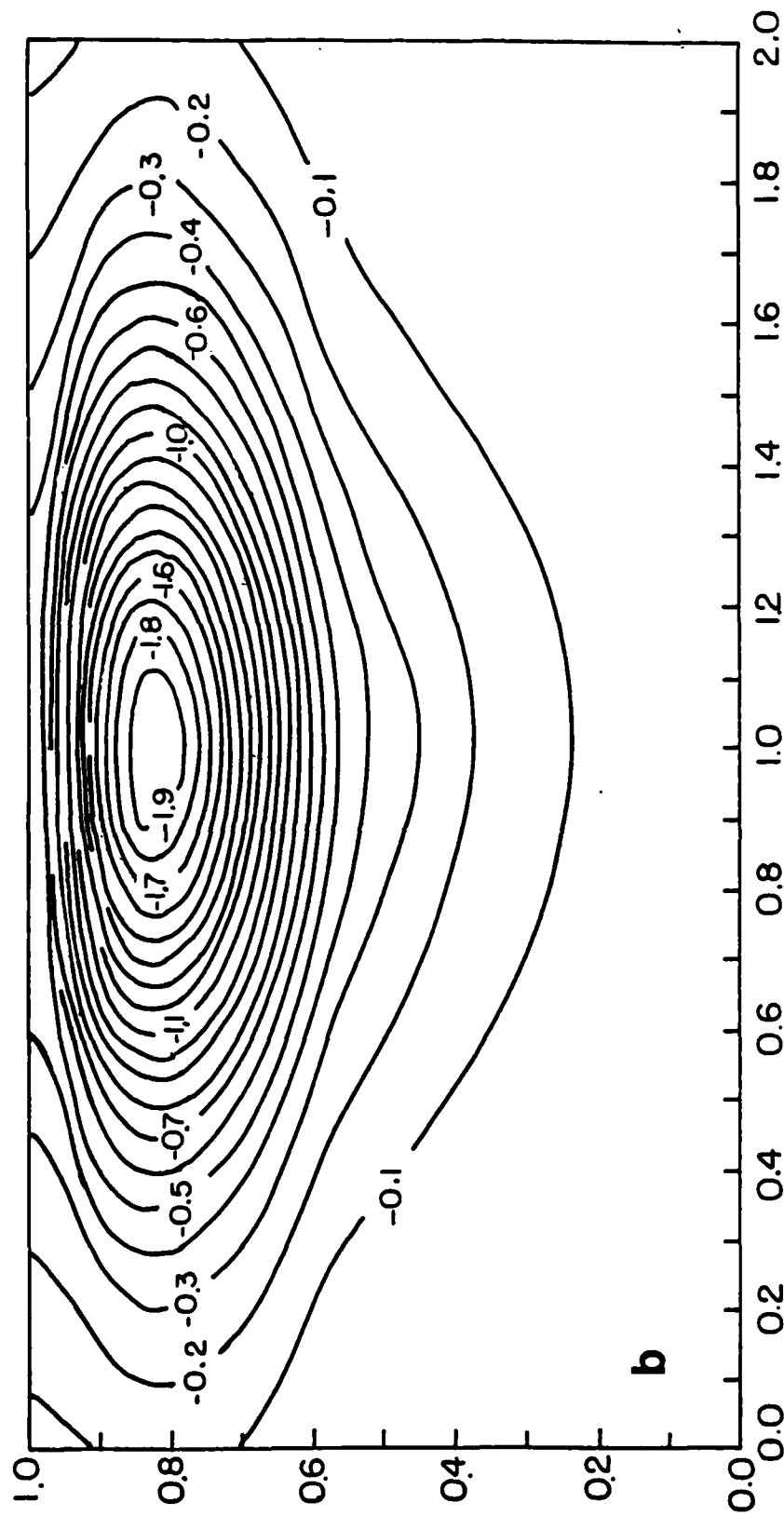
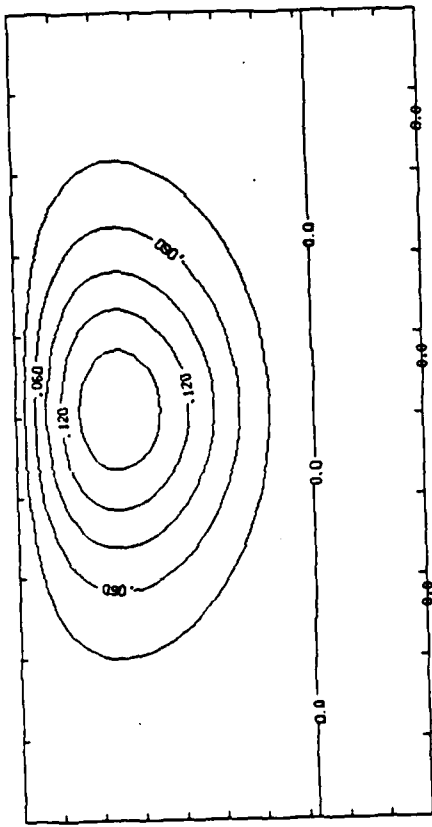


Fig 3

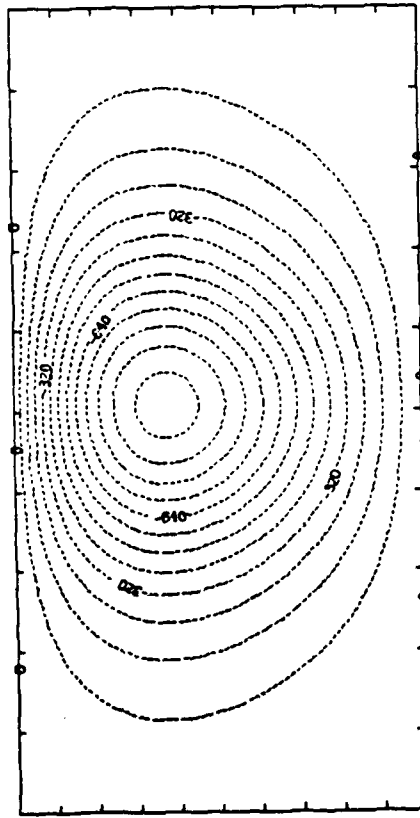
$\nabla^2 \psi - \alpha \psi$

$\psi$



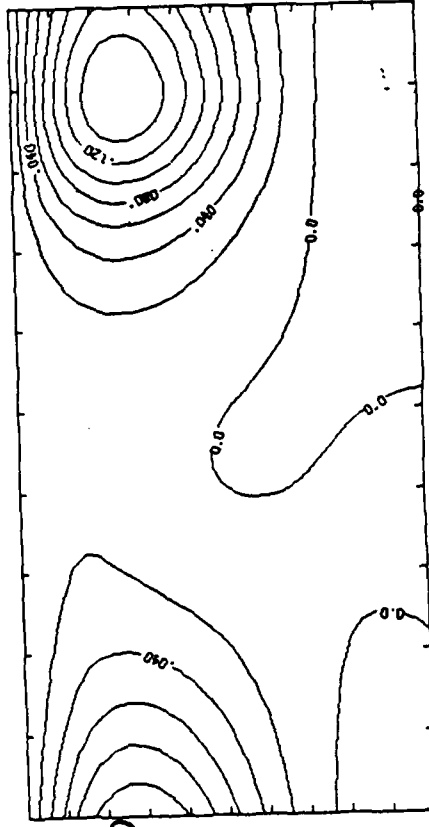
$T=0$

CONTOUR FROM 0.8000E+00 TO 0.1500E+01 PT(13,31) = -0.2585E-03  
CONTOUR INTERVAL OF 0.2000E+01



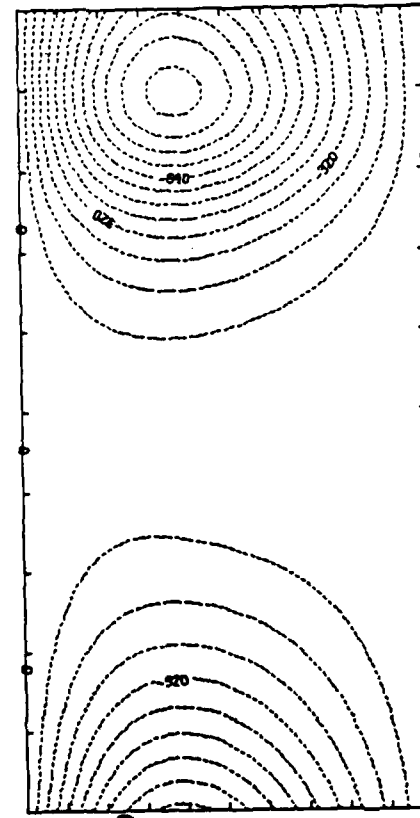
$T=0$

CONTOUR FROM -0.2585E-03 TO 0.1500E+01 PT(13,31) = -0.2585E-03  
CONTOUR INTERVAL OF 0.2000E+01



$T=120$

CONTOUR FROM 0.8000E+00 TO 0.1500E+01 PT(13,31) = -0.2585E-03  
CONTOUR INTERVAL OF 0.2000E+01



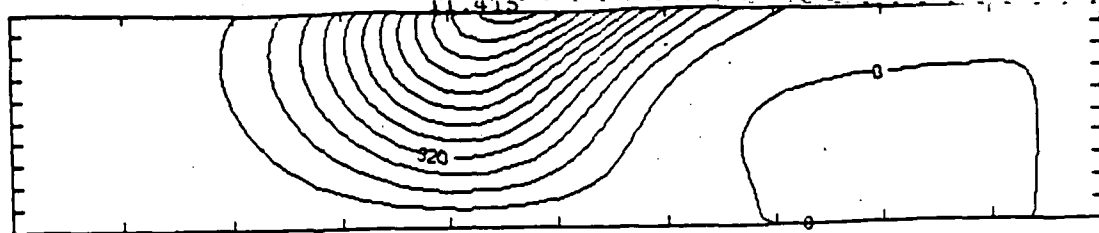
$T=120$

CONTOUR FROM -0.2585E-03 TO 0.1500E+01 PT(13,31) = -0.2585E-03  
CONTOUR INTERVAL OF 0.2000E+01

Fig 4

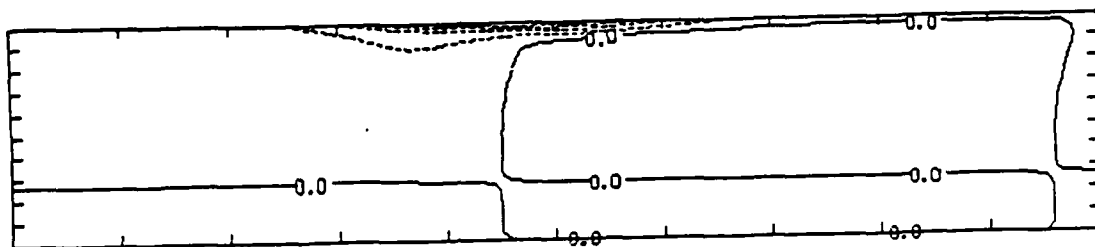
$\psi$

$T=10$



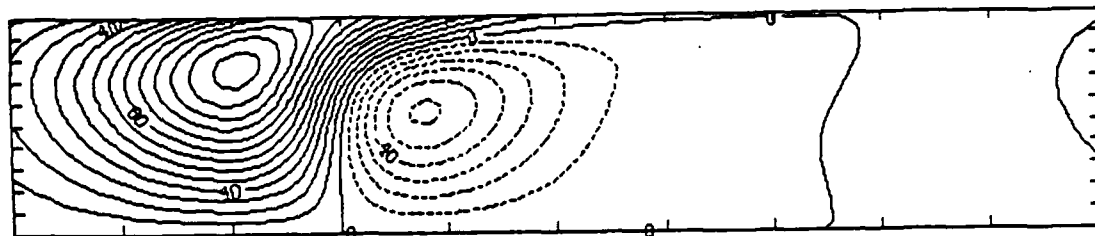
CONTOUR FROM 0.0000E+00 TO 0.9600E-02 CONTOUR INTERVAL OF 0.8000E-03 PT(3,3)= 0.47713E-05 LABELS SCALED BY 0.1000E+08

$\psi^2 - d\psi$

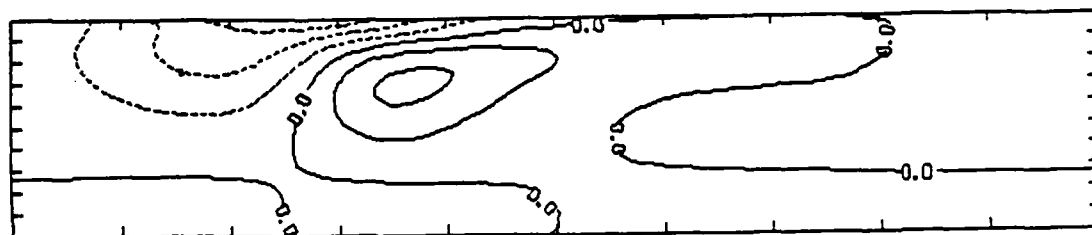


CONTOUR FROM -0.25000 TO 0.0000E+00 CONTOUR INTERVAL OF 0.5000E-01 PT(3,3)= 0.15190E-04

$T=50$

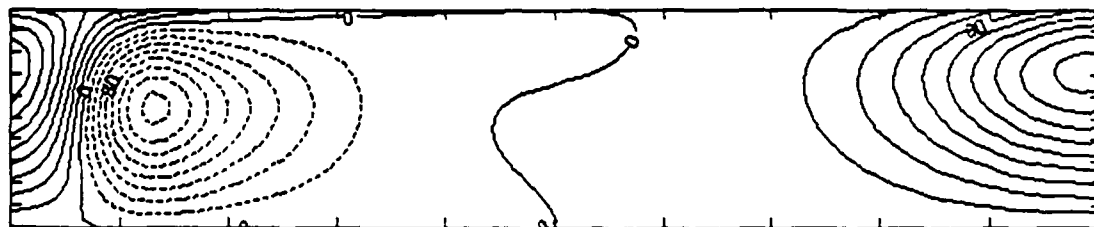


CONTOUR FROM -0.8000E-02 TO 0.1500E-01 CONTOUR INTERVAL OF 0.1000E-02 PT(3,3)= 0.97845E-03 LABELS SCALED BY 10000

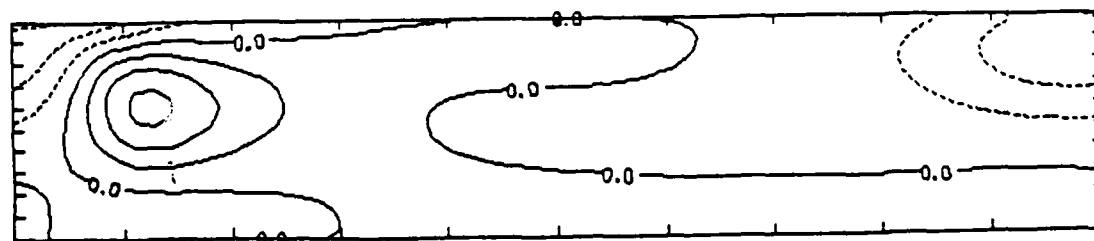


CONTOUR FROM -0.28000 TO 0.14000 CONTOUR INTERVAL OF 0.7000E-01 PT(3,3)= 0.19188E-02

$T=100$



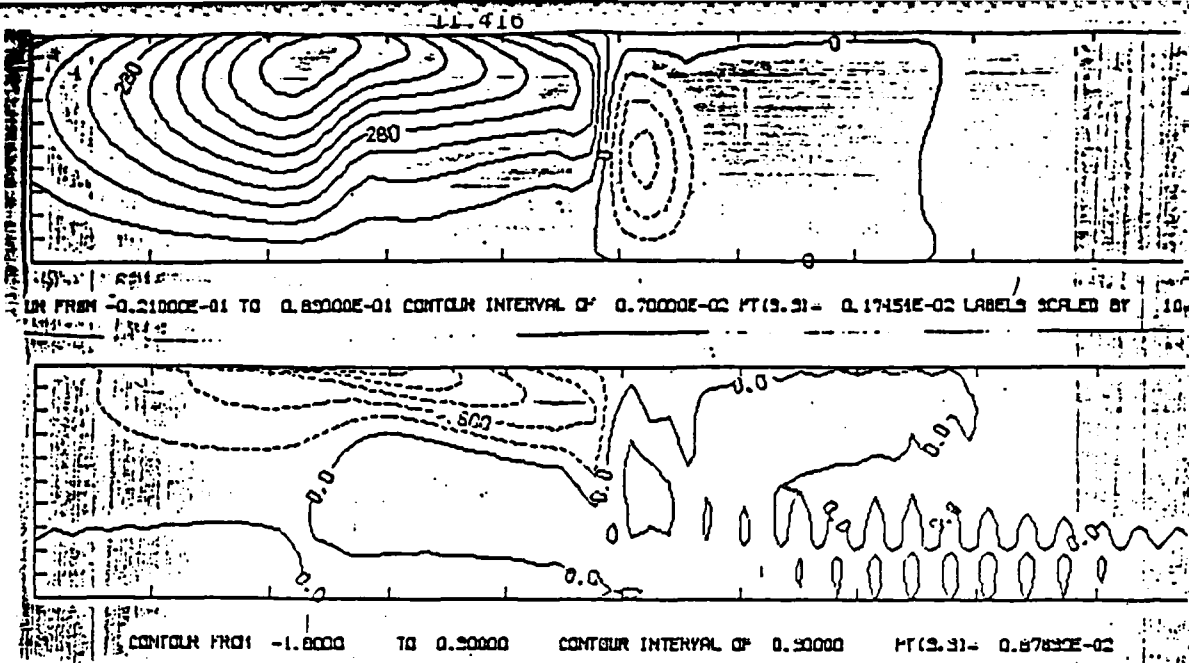
CONTOUR FROM -0.1800E-01 TO 0.1800E-01 CONTOUR INTERVAL OF 0.2000E-02 PT(3,3)= 0.12558E-02 LABELS SCALED BY 10000



CONTOUR FROM -0.27000 TO 0.27000 CONTOUR INTERVAL OF 0.9000E-01 PT(3,3)= -0.12843E-03

Fig 5

$\nabla^2 \psi - \alpha \psi$   
 T=50  
 (a)



T=100

(b)

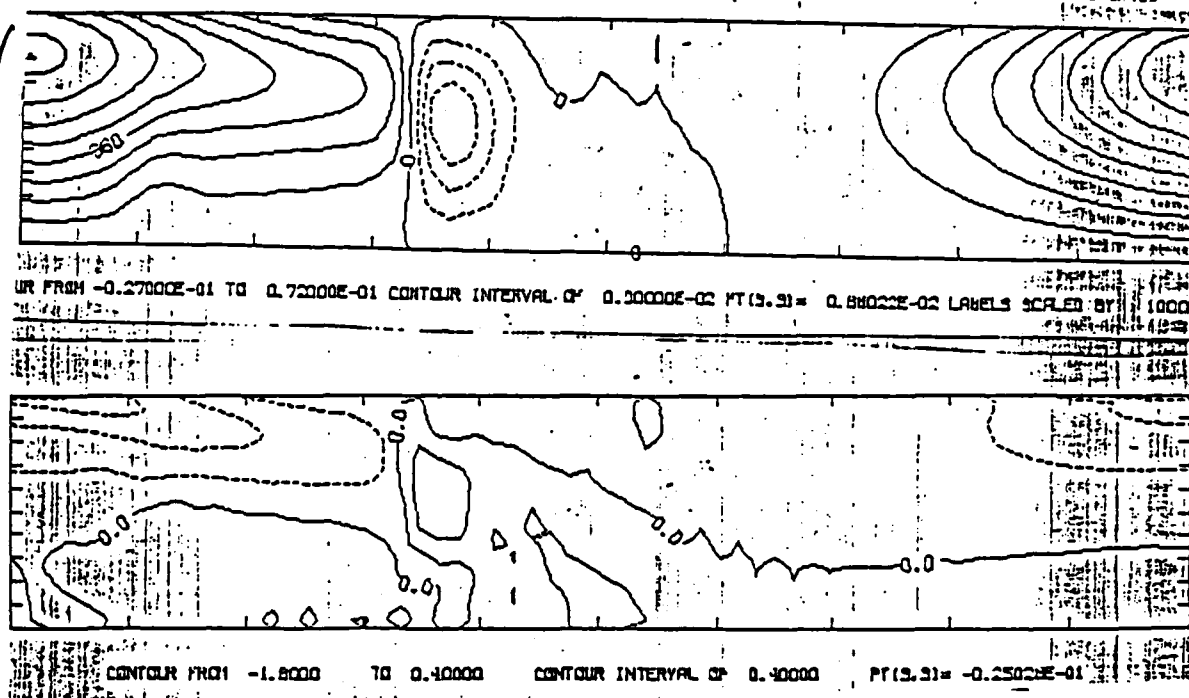


Fig 6

T=150

(c)

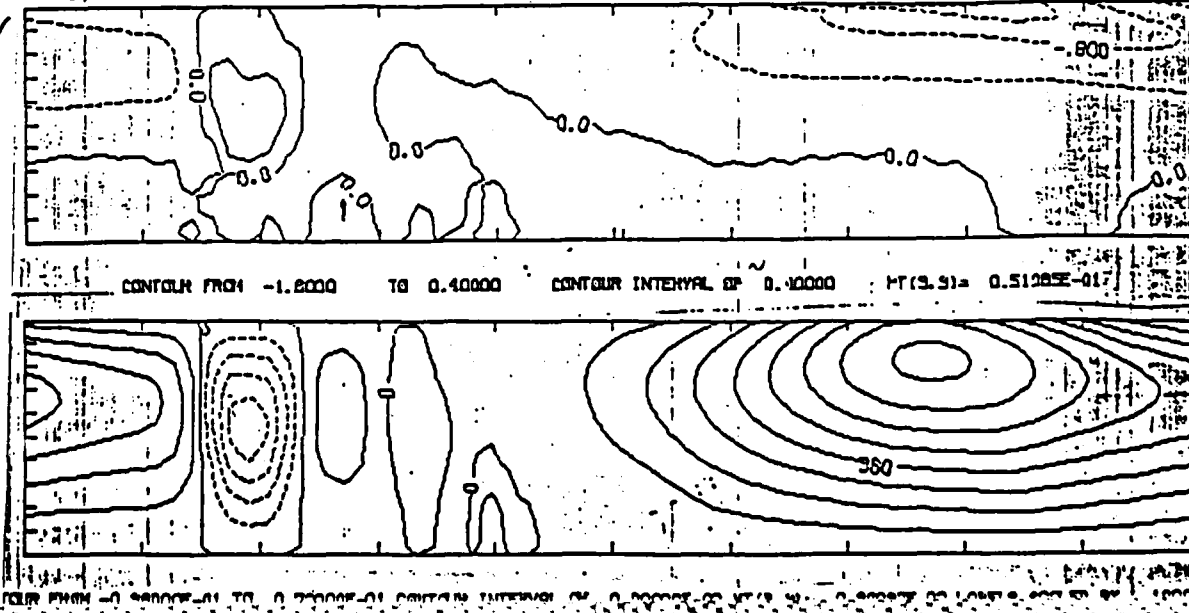
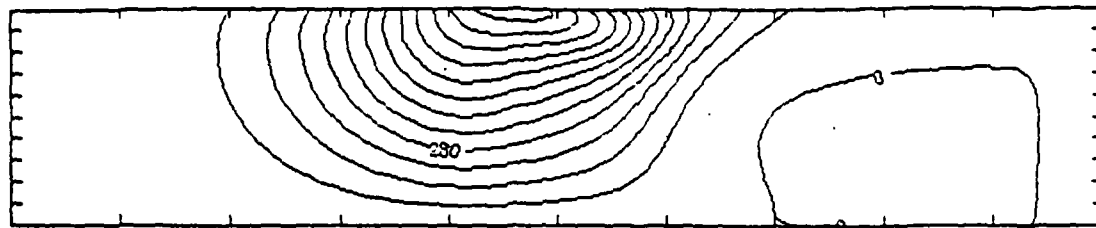


Fig 7 -  $\gamma$

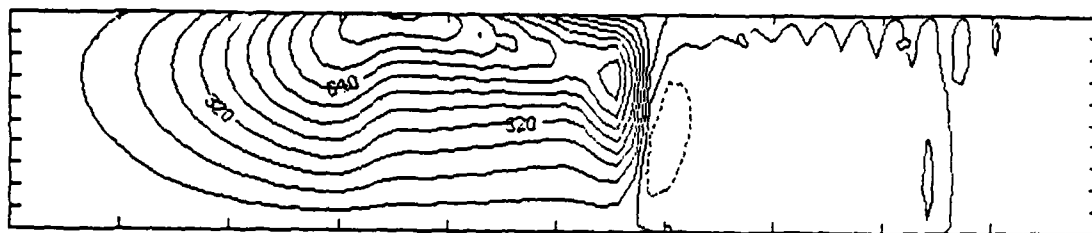
II.417

T=10  
(a)



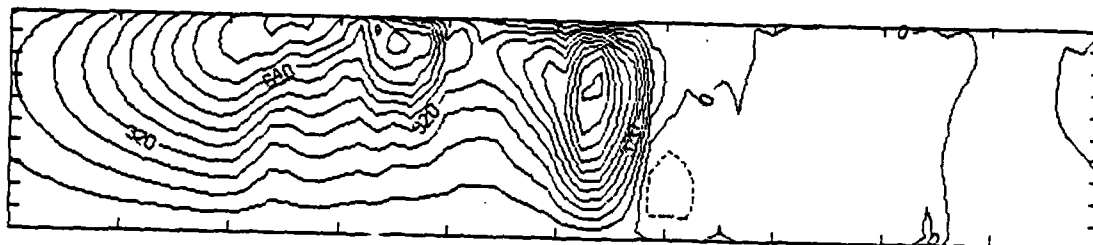
CONTOUR FROM 0.00000E+00 TO 0.84000E-01 CONTOUR INTERVAL OF 0.70000E-02 FT (3.3) = 0.42777E-04 LABELS SCALED BY 10000.

T=30  
(b)



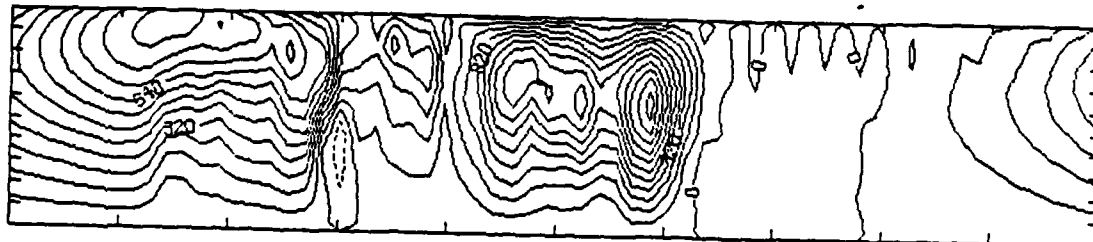
CONTOUR FROM -0.80000E-02 TO 0.80000E-01 CONTOUR INTERVAL OF 0.80000E-02 FT (3.3) = 0.48082E-03 LABELS SCALED BY 10000.

T=50  
(c)



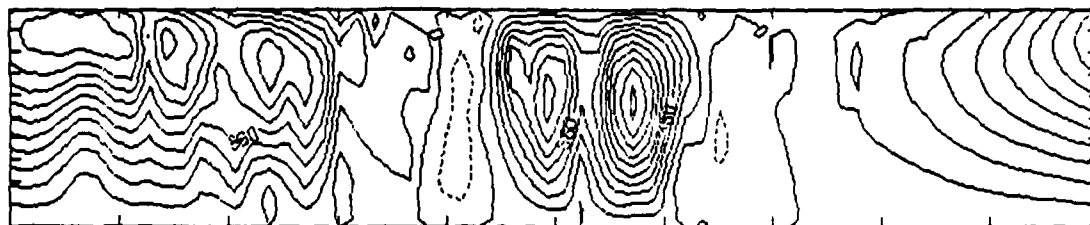
CONTOUR FROM -0.80000E-02 TO 0.80000E-01 CONTOUR INTERVAL OF 0.80000E-02 FT (3.3) = 0.21108E-02 LABELS SCALED BY 10000.

T=70  
(d)



CONTOUR FROM -0.80000E-02 TO 0.80000E-01 CONTOUR INTERVAL OF 0.80000E-02 FT (3.3) = 0.47123E-02 LABELS SCALED BY 10000.

T=90  
(e)



CONTOUR FROM -0.90000E-02 TO 0.90000E-01 CONTOUR INTERVAL OF 0.90000E-02 FT (3.3) = 0.61423E-02 LABELS SCALED BY 10000.

T=100  
(f)



CONTOUR FROM -0.90000E-02 TO 0.90000E-01 CONTOUR INTERVAL OF 0.90000E-02 FT (3.3) = 0.23240E-02 LABELS SCALED BY 10000.

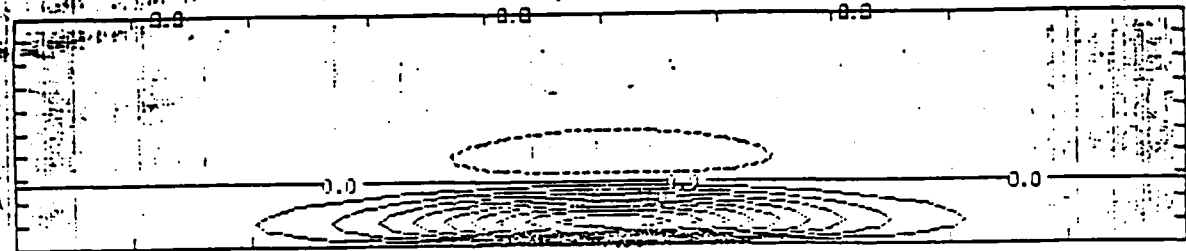
11.418

$T=0$   
(a)

$\nabla^2 \psi - \psi$

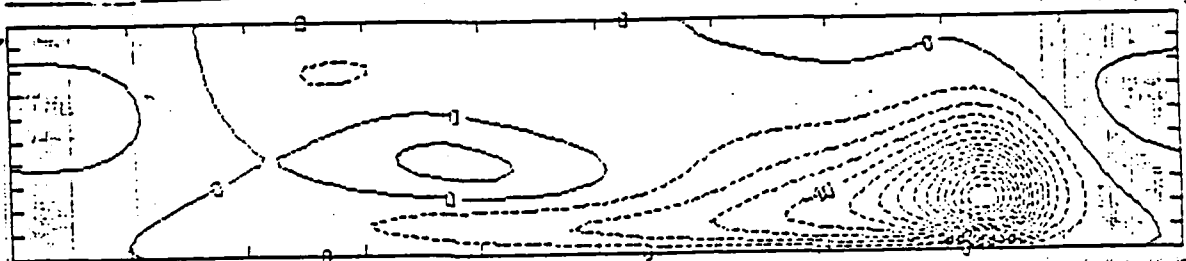
Fig 8

CONTOUR FROM -0.20000E-02 TO 0.00000E+00 CONTOUR INTERVAL OF 0.50000E-03 PT(3,3) = -0.24112E-04 LABELS SCALED BY 0.10000E+01

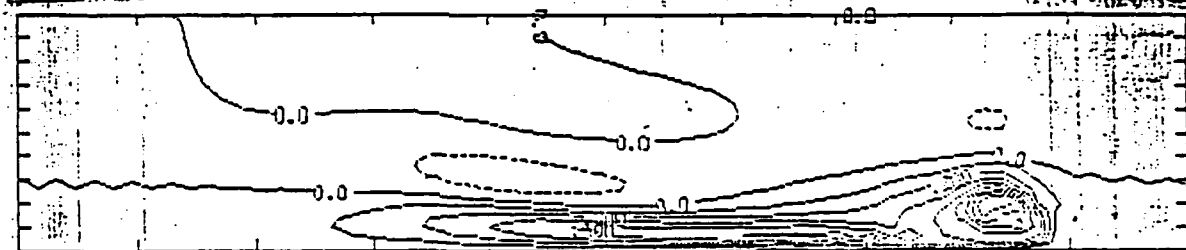


CONTOUR FROM -0.10000 TO 0.30000 CONTOUR INTERVAL OF 0.10000 PT(3,3) = 0.12457E-01

$T=50$   
(b)

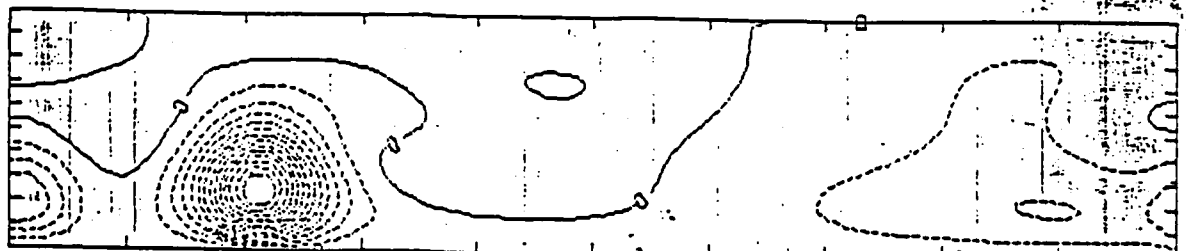


CONTOUR FROM -0.14000E-01 TO 0.10000E-02 CONTOUR INTERVAL OF 0.10000E-02 PT(3,3) = 0.37795E-04 LABELS SCALED BY 0.10000E+01

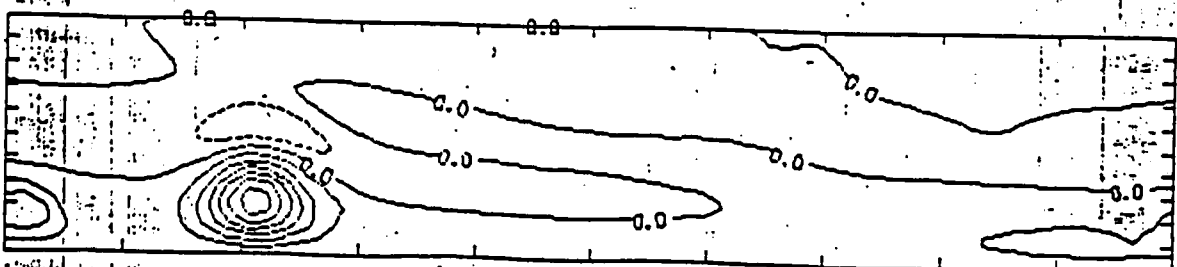


CONTOUR FROM -0.10000 TO 0.50000 CONTOUR INTERVAL OF 0.10000 PT(3,3) = 0.56955E-02

$T=200$   
(c)



CONTOUR FROM -0.12000E-01 TO 0.10000E-02 CONTOUR INTERVAL OF 0.10000E-02 PT(3,3) = -0.18706E-02 LABELS SCALED BY 0.10000E+01

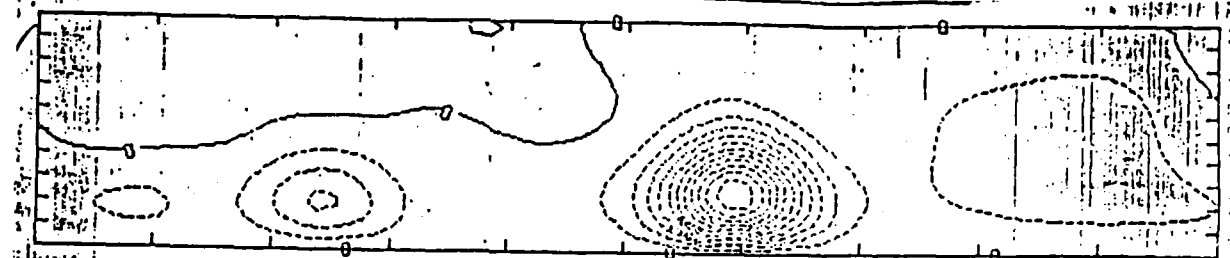


CONTOUR FROM -0.10000 TO 0.50000 CONTOUR INTERVAL OF 0.10000 PT(3,3) = 0.56955E-02

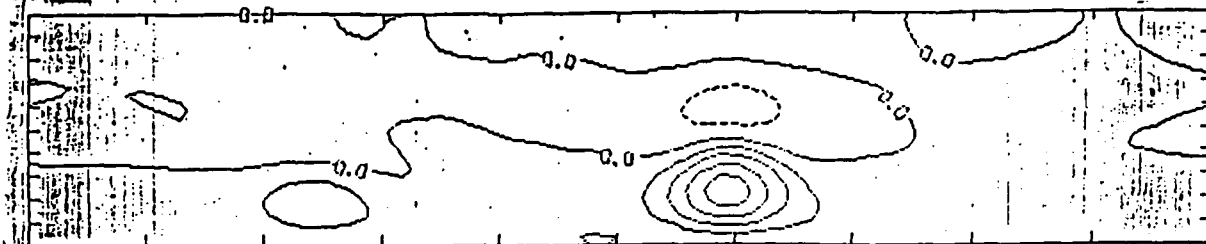


$\psi$   
 $F=400$ 

(d)

 $\nabla^2 \psi - \Delta \psi$ 
Fig 8  
(cont'd)

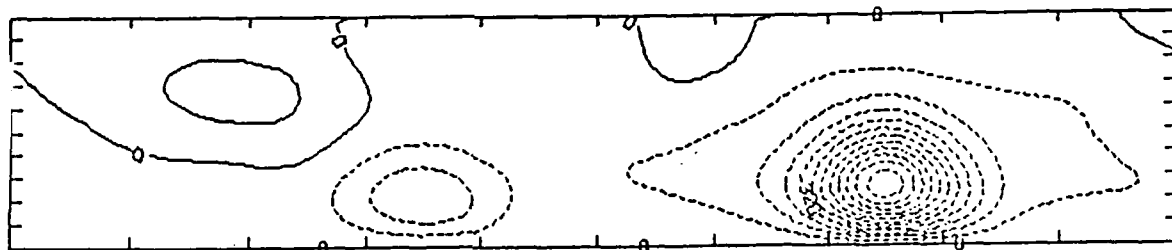
FROM -0.22000E-02 TO 0.00000E+00 CONTOUR INTERVAL OF 0.00000E-03 PT(5,3) = -0.44307E-03 LABELS SCALED BY 0.10000



CONTOUR FROM -0.10000 TO 0.10000 CONTOUR INTERVAL OF 0.10000 PT(5,3) = 0.99102E-01

 $F=500$ 

(e)



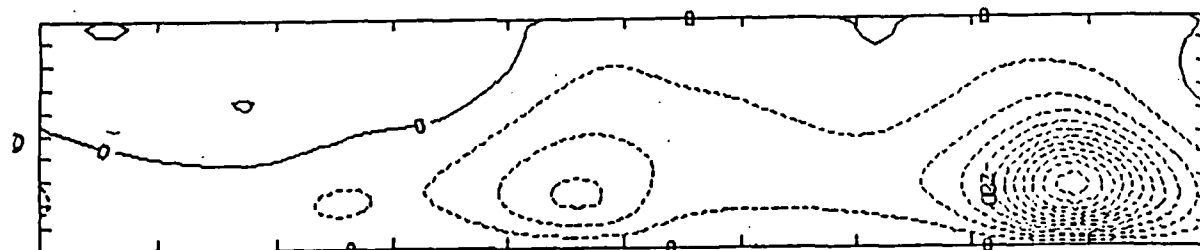
FROM -0.88000E-02 TO 0.80000E-03 CONTOUR INTERVAL OF 0.80000E-03 PT(5,3) = -0.55147E-03 LABELS SCALED BY 0.10000E+0



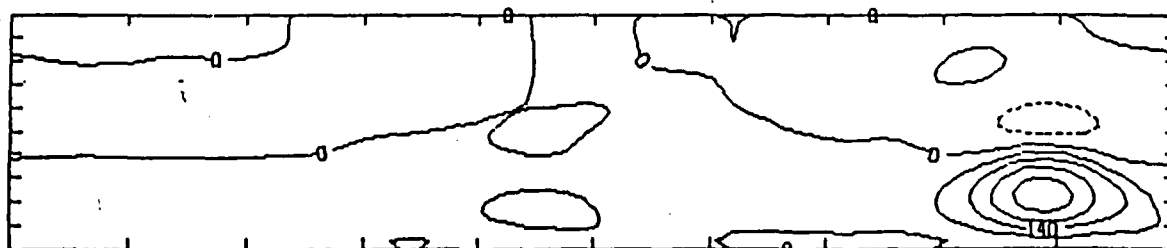
FROM -0.80000E-01 TO 0.52000 CONTOUR INTERVAL OF 0.80000E-01 PT(5,3) = 0.20721E-01 LABELS SCALED BY 1000.0

 $F=600$ 

(f)



FROM -0.77000E-02 TO 0.70000E-03 CONTOUR INTERVAL OF 0.70000E-03 PT(5,3) = -0.24522E-03 LABELS SCALED BY 0.10000E



# OPTIMAL ESTIMATION AND THE KALMAN FILTER FOR NUMERICAL OCEAN FORECAST MODELING

Robert N. Miller  
Department of Mathematics  
Tulane University  
New Orleans, LA

## I. Introduction.

As ocean models improve, assimilation of data with the help of models becomes increasingly important. Models such as the Harvard Open Ocean Model (Miller, Robinson and Haidvogel, 1983) are now beyond the testing phase and are being used for synoptic analysis (see, e.g., Robinson and Leslie, 1985; Robinson *et al.*, 1984). Future data assimilation schemes must be designed for use with increasingly sophisticated and computationally complex numerical models, as well as a variety of data sources and distributions.

The most common data assimilation technique used in numerical weather prediction today is optimal interpolation (hereafter OI; see, e.g., Rutherford (1972); Lorenc (1981)). In OI, a correction to the forecast is computed as a linear function of the difference between the forecast and the observed data. The matrix which defines this linear function is determined by the forecast error covariance. The covariance matrix is usually determined by fitting some functional form to the observed forecast error structure.

The Kalman filter is similar to OI; the difference is that in the Kalman filter, the covariance matrix is updated each step, using the forecast model and knowledge of its error characteristics. The application of the Kalman filter to numerical weather prediction has been investigated by Cohn (1982), Dee *et al.* (1985), Ghil *et al.* (1981) and Ghil *et al.* (1983). The updating of the covariance matrix is the major obstacle to practical implementation of the Kalman filter because of its considerable demands on computing resources.

## II. Some Results from a Pilot Study

The Kalman filter was applied to the one dimensional linearized barotropic potential vorticity equation:

$$\psi_{xxt} + U\psi_{xxx} + \psi_x = 0.$$

Experiments were performed with periodic boundary conditions, and with "open" boundary conditions, i.e.,  $\psi$  prescribed at both endpoints of the domain, and  $\psi_x$  prescribed at the inflow point.

The natural difference scheme to choose is the upwind difference scheme relative to the advection. If the advection speed  $U$  is positive, then there will in general be phase propagation of Rossby waves in both directions, which has the effect of rendering the resulting difference scheme unconditionally unstable. In this study the unstable scheme was retained in order to determine whether the Kalman filter can provide stable forecasts of an unstable system. Figure 1 shows the growth of

the error variance in the uncorrected system, i.e., without updating.

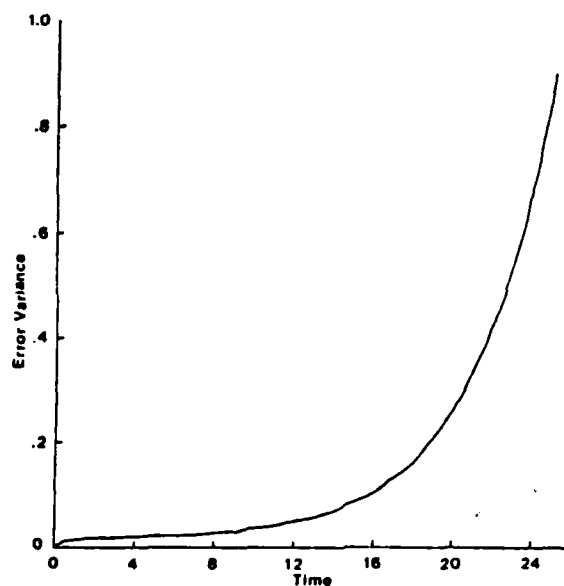


Figure 1. Evolution of expected error variance without updating.

Figure 2 shows the asymptotic form of the error variance as a function of space in an experiment in which the forecast is updated at 1 point (there are 19 points, total) every 4 time steps (there are 32 time steps per period of the fastest wave). This pattern is quite stable; it changes very little once it is set up. This is the sparsest observing scheme tested; even with this scheme, the pattern of forecasts remains stable.

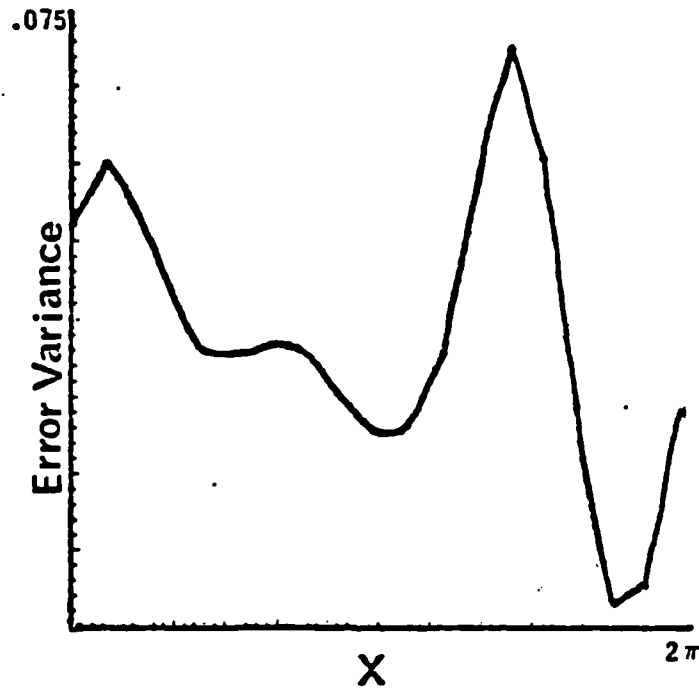


Figure 2. Asymptotic form of error variance as a function of space. The forecast is updated every four steps by one data point at the center of the domain.

Figure 3 illustrates an experiment in which observations in the form of  $\psi_x$  instead of  $\psi$  were provided ("velocity" instead of "streamfunction"). The behavior of the error variance is quite similar to an experiment (not shown) in which  $\psi$  was provided at the same points with the same frequency.

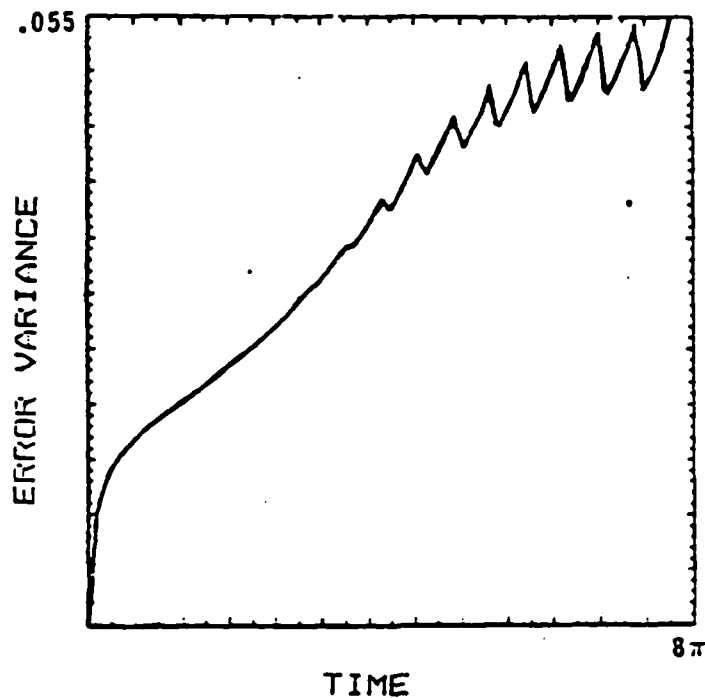


Figure 3. Error variance averaged over four points upstream of the data point vs time. Data in the form of  $\psi_x$  is introduced at two points every four time steps.

Figure 4 shows a realization of a boundary value problem simulation. The dashed curve represents the reference field. The error bars are derived from the diagonal of the error covariance matrix. In this simulation, data is relatively plentiful: the forecast is updated at 4 interior points each time step. The greatest uncertainty is at the boundaries: note the size of the error bars. The important thing to notice is that the large errors are confined to a neighborhood of the boundary. A detailed description of the pilot study may be found in Miller(1985)

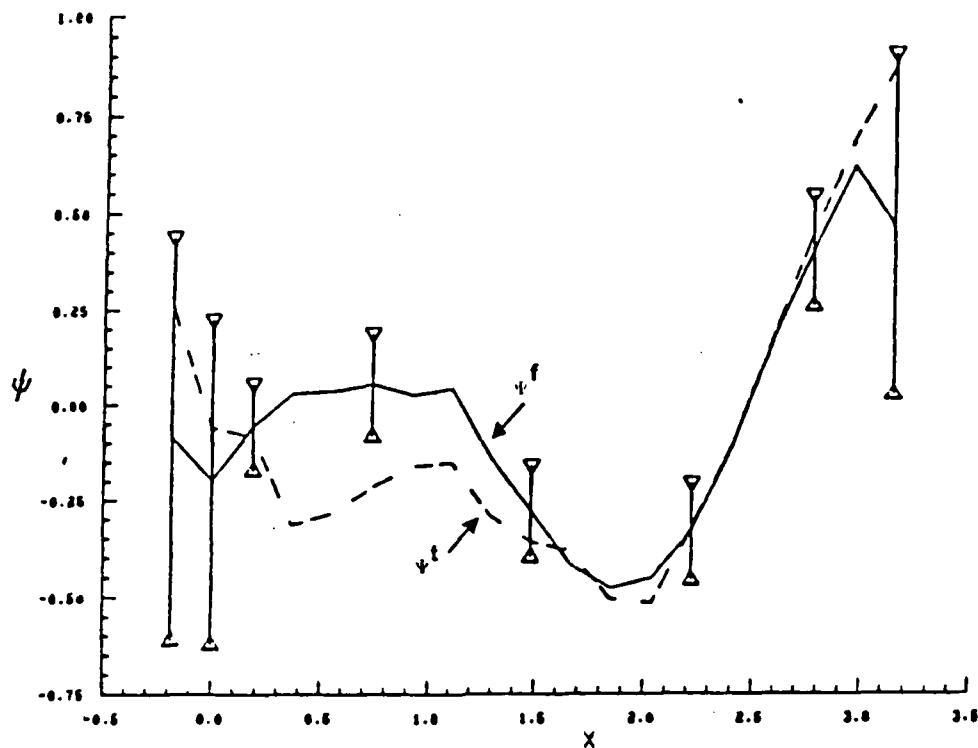


Figure 4. Comparison of forecast ( $\psi^f$ ) with reference field  $\psi^t$ . Error bars are one standard deviation in width.

### III. Questions About Practical Implementation

The foremost question is whether or not the Kalman filter can be used as a practical tool for oceanographic data assimilation, given computing resources available currently and in the near future. The full Kalman filter presents considerable demands on available computing resources, and it is therefore reasonable to seek appropriate simplifications. So far, the only quantitative estimates in this context of the practical demands of the Kalman filter on computing resources are those of Parrish and Cohn (1985), who applied the Kalman filter to the linearized shallow water equations in two space dimensions. The two dimensional grids they used were similar in size to those grids used in current ocean models. For all but the coarsest grid used in that study, the covariance matrix was assumed to have a banded structure. This is equivalent to assuming a finite correlation distance. Such an assumption is a common feature of OI schemes. In cases in which the full covariance matrix could be calculated, the assumption of bandedness did not make a significant difference. The resource utilization in Parrish and Cohn's experiments is summarized in Table 1. These numbers indicate that the demand on computing resources may not be as severe as had been previously supposed.

TABLE 1

TIME IN CPU SECONDS ON NMC CYBER 205 FOR UPDATING OF FORECAST  
ERROR COVARIANCE

BANDWIDTH	GRID SIZE		
	20x21	40x41	60x61
1	.11(93)	.27(154)	.52(178)
3	.48(94)	1.10(153)	2.15(176)
5	1.05(93)	2.51(156)	
7	1.84(93)		
full	3.24(89)		

(Numbers in parentheses are calculated speeds in megaflops; the maximum speed of the CYBER 205 is 200 megaflops. From Parrish and Cohn(1985))

Other simplifying strategies besides the sparse matrix assumption may prove fruitful. It may be possible to exploit homogeneity of the forecast error field, i.e., there may be broad regions in space where the covariance pattern does not vary much from point to point. There is also strong evidence that inhomogeneous error covariance fields reflect only inhomogeneities in data density.

It may also be feasible to exploit the usually rapid convergence of the error covariance matrix to its asymptotic form. Perhaps the updating of the covariance matrix can be turned on and off in response to changing conditions. In this case, it would be necessary to find some method to provide a signal to resume updating of the covariance matrix until a new steady covariance matrix is reached.

Results from the pilot study indicate that simplifications of the covariance matrix based on sparseness assumptions or on homogeneity assumptions may not be appropriate for quasigeostrophic prediction models. Figure 5 illustrates the error correlation matrix (i.e., the covariance matrix normalized so that the error in each variable has unit variance) of a typical boundary value problem run. In this figure, each column appears as a curve, with the diagonal element plotted at the point (0,1). This covariance matrix appears neither sparse nor homogeneous. If the matrix were sparse, each curve would decay to zero near the origin. If the correlations were homogeneous, the curves would be tightly clustered about a few representative correlation patterns. Ultimately, appropriate simplifications for the case of a quasigeostrophic prediction model will only be determined by experiment.

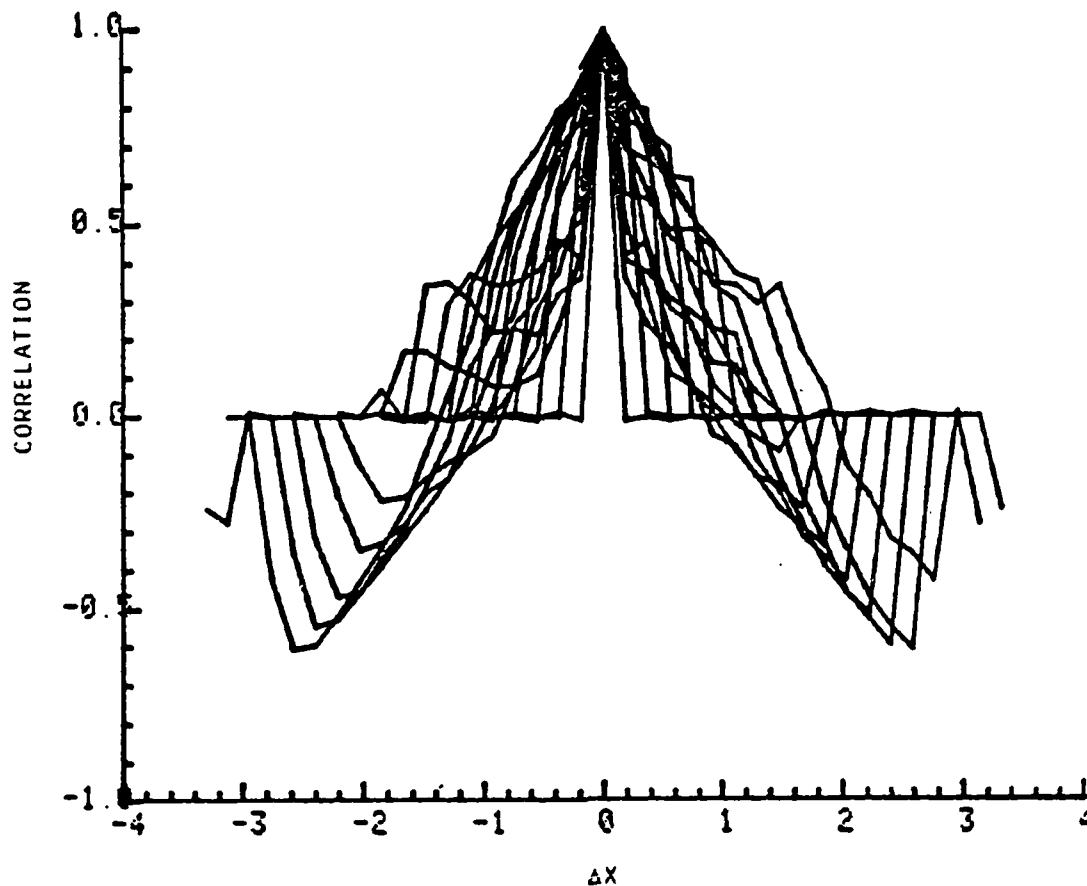


Figure 5. Analysis error covariance, normalized. Each curve represents a column of the covariance matrix with the diagonal element plotted at (0,1).

#### ACKNOWLEDGMENTS

The author is pleased to acknowledge the helpful advice, criticism and discussion provided by Michael Ghil and Stephen Cohn during the course of this project. This work was supported by Office of Naval Research Contract Number N00014-83-K-0488.

#### REFERENCES

Cohn, S. E., 1982: Methods of sequential estimation for determining initial data in numerical weather prediction. Doctoral dissertation, Department of Mathematics, New York University; published as Courant Institute of Mathematical Sciences report CI-6-82, New York University, New York, New York. 183 pp.

Dee, D. P., S. E. Cohn and M. Ghil, 1985. An efficient algorithm for estimating noise covariances in distributed systems. IEEE Trans. Autom.



Control AC-30, no. 11. in press.

Ghil, M., S. E. Cohn, J. Tavantzis, K. Bube and E. Isaacson, 1981: Applications of estimation theory to numerical weather prediction. in: Bengtsson, Ghil and Kallen (eds.), Dynamic Meteorology: Data Assimilation Methods. Applied Mathematical Sciences series vol. 36, Springer-Verlag, New York. 330 pp.

Ghil, M., S. E. Cohn and A. Dalcher, 1983: Applications of sequential estimation to data assimilation. in: the World Climate Research Programme, WCRP Publ. Ser. No. 1., vol. II, WMO-ICSU, Geneva, Switzerland, pp. 341-356.

Lorenc, A., 1981: A global three dimensional multivariate statistical interpolation scheme. Mon. Wea. Rev. 109, 701-721.

Miller, R. N., 1985: Toward the application of the Kalman filter to regional open ocean modeling. J. Phys. Oceanogr., to appear.

Miller, R. N., A. R. Robinson and D. B. Haidvogel, 1983: A baroclinic quasigeostrophic open ocean model. J. Comput. Phys. 50, 38-70.

Parrish, D. F. and S. E. Cohn, 1985: A Kalman filter for a two-dimensional shallow water model: formulation and preliminary experiments. Office note 304, National Meteorological Center, Washington, D.C., 20233.

Robinson, A. R. and W. G. Leslie, 1985: Estimation and prediction of oceanic eddy fields. Prog. Oceanogr. 14, 485-510.

Robinson, A. R., J. A. Carton, C. N. K. Mooers, L. J. Walstad, E. F. Carter, M. M. Rienecker, J. A. Smith and W. G. Leslie, 1984: A real time dynamical forecast of ocean synoptic mesoscale eddies. Nature 309, 781-783.

Rutherford, I. D., 1972: Data assimilation by statistical interpolation of forecast error fields. J. Atmos. Sci. 29, 809-815.

OCEANOGRAPHIC PLANS FOR ANALYSIS OF GEOSAT DATA  
DURING THE NW ATLANTIC REGIONAL ENERGETICS EXPERIMENT (REX)

Jim L. Mitchell  
NORDA Code 321  
NSTL, MS 39529

## INTRODUCTION

The oceanographic utility of data from the U.S. Navy GEOSAT satellite is the focus of several ongoing projects at the Naval Ocean Research and Development Activity (NORDA). The NORDA Accelerated Research Initiative in Satellite Altimetry is a basic research project sponsored by the Office of Naval Research with emphasis on an understanding of oceanic mesoscale dynamics and energetics in the Gulf Stream during the NW Atlantic Regional Energetics Experiment (REX). The GEOSAT Ocean Applications Program, an applied program sponsored by the Office of the Oceanographer of the Navy, has as a major objective the near realtime analysis of altimeter topography, winds, and waves with emphasis on Naval applications of these data initially in the NW Atlantic (Lybanon, 1984). Both programs have as a long-range goal the assimilation of satellite altimeter derived topography into eddy-resolving numerical models. This paper and companion papers by J.D. Thompson and Z.R. Hallock describe both plans for (and in the case of the modelling effort some initial results from) the REX.

## OVERVIEW OF REX

The basic objective of the NW Atlantic REX (Mitchell et al., 1985) is an understanding of Gulf Stream and associated ring dynamics and energetics in the vicinity of the New England Seamounts. This objective will be accomplished via the concurrent application of the following:

1. Satellite altimetry collected from the U.S. Navy GEOSAT
2. Field program based upon time series collected from bottom moored Inverted Echo Sounders (IES) and Pressure Gauges (PG) as well as classical hydrography and periodic AXBT surveys (see companion paper by Z.R. Hallock),
3. Regional Eddy-Resolving Numerical Modelling providing numerical simulations for assimilation studies, sensitivity studies, and experiment design (see companion paper by J.D. Thompson).

## U.S. NAVY GEOSAT: THE SATELLITE

As described in Mitchell and Hallock (1984), the GEOSAT satellite consists of an improved SEASAT single-frequency (13.5 GHz) altimeter mounted on a modified GEOS-C bus (see figure 1). Major improvements over SEASAT altimeter design are:

1. Use of a low power TWT
2. Improved instrumental noise floor of  $\pm 2$  cm as opposed to  $\pm 3.5$  cm for SEASAT (for range data averaged to one point per second)
3. Enhanced ability to maintain track over land and ice terrain.

The satellite configuration is gravity-gradient stabilized in attitude (as opposed to the active thruster stabilization used for SEASAT). This had been a potential cause for concern; however, recent experience with incoming GEOSAT data indicates that the attitude determination accuracy of the system is more than adequate for alleviating any error in range due to off-nadir pointing angles of the satellite.

A shortcoming of GEOSAT design is the lack of an onboard boresighted radiometer for high spatial resolution water vapor range correction. During the initial 18-month geodetic portion of the mission long wavelength water vapor range corrections will be provided by Fleet Numerical Oceanographic Center (FNOC) analysis fields (as was done for one of SEASAT's water vapor range corrections). During the follow-on GEOSAT-Exact Repeat Mission (GEOSAT-ERM; see later section) water vapor range corrections will be provided both by FNOC and, at much higher spatial resolution, by the Special Sensor Microwave Imager (SSM/I) onboard the next DMSP satellite slated for launch in late 1985 (though these radiometer corrections will, of course, not be boresighted with GEOSAT). It is anticipated that, statistically, unknown water vapor range errors may account for somewhat less than 10 cm rms global variability in observed altimeter range. In fact, power spectral analysis of SEASAT SMMR water vapor range corrections indicate that at wavelengths shorter than 600 km water vapor range corrections typically are less a few centimeters (though in specific cases unknown water vapor range corrections could be as large as 30-40 cm, e.g., when crossing an atmospheric front).

The accuracy with which the altimeter system can determine sea level depends upon both the precision of the range measurement (distance from the spacecraft to the sea surface) and the accuracy of the orbit determination (distance from the spacecraft to the center of mass of the Earth). Table 1 summarizes the RMS contributions to sea level of the various error sources (Born, 1984). Note the improvement in orbit determination accuracy which is possible with GEOSAT flying in a collinear or exact repeat orbit during the GEOSAT-Exact Repeat Mission (GEOSAT-ERM, see later section). By comparison to GEOSAT, the present level of accuracy associated with the released SEASAT Geophysical Data



# **ALTIMETER HEIGHT MEASUREMENT ERROR BUDGETS FOR FUTURE SATELLITE MISSIONS**

(BORN, 1984)

ERROR SOURCE	UNCERTAINTY (CM, $1\sigma$ )			
	GEOSAT GEODETTIC MISSION	ERM	TOPEX	WAVELENGTH OF ERROR (km)
ALTIMETER				
INSTRUMENT NOISE	<6.0	<6.0	3.5	MANY DAYS
BIAS DRIFT	2.0	2.0	2.0	20,000
TIME TAG	0.2	0.2	0.2	200-1000
TRACKER BIAS	2.0	2.0	0.5	
MEDIA				
E.M. BIAS	2.0	2.0	2.0	200-1000
SKEWNESS	1.0	1.0	1.0	200-1000
TROPOSPHERE-DRY	0.7	0.7	0.7	1000
TROPOSPHERE-WET	6.0	6.0	1.2	200
IONOSPHERE	4.0	4.0	1.3	1000
RSS (INST. AND MEDIA)	<10.0	<10.0	5.0	
ORBIT				
GRAVITY	140.0	50	10.0	>10,000
GM (MASS OF EARTH)	2.0	2.0	2.0	
ATMOSPHERIC DRAG	20.0	10.0	1.0	
TROPOSPHERE	1.0	1.0	1.0	
SOLAR RADIATION PRESSURE	15.0	5.0	1.0	
EARTH ALBEDO	2.0	1.0	1.0	
EARTH AND OCEAN TIDES	1.0	1.0	1.0	
STATION COORDINATES	25.0	10.0	5.0	
STATION AND SPACECRAFT CLOCKS	10.0	10.0	1.0	
HIGHER ORDER IONOSPHERE	5.0	5.0	5.0	
RSS (TOTAL)	<145.0	<54.0	13.6	

TABLE 1

Records (GDR) is about 1.5 meters (most of this error due to orbit determination inaccuracy). Fortunately for mesoscale work, the very long wavelengths (of the order of the circumference of the orbit) associated with orbit determination error render this large error source a relatively minor problem. Removal of a linear trend from the range data over track segments of the order of several thousand kilometers is sufficient to remove the bulk of residual orbit error provided the orbit can be determined to a level of accuracy of 10 meters or better (about the level of orbit determination accuracy which has been realized for the GEOS-3 system). On the other hand, the basin scale circulation to be observed with TOPEX requires the ability to observe topographic gradients of the order of 10 centimeters over spatial scales of 10,000 km.

#### U.S. NAVY GEOSAT: ORBITS AND MISSIONS

Following a successful launch from Vandenberg AFB on 12 March 1985, the U.S. Navy GEOSAT is presently returning altimetric measurements of the range from the satellite to the ocean surface as collected from a SEASAT-like orbit with an altitude of approximately 790 km and an inclination of 108 degrees. The nodal period of the present orbit is approximately 6040 seconds. This near 3-day repeat orbit results in the accumulation of a globally uniform grid of groundtracks separated by 932 km at the equator in approximately 3 days. Unlike SEASAT's final orbit, the present GEOSAT orbit is not exactly collinear, hence the accumulation of groundtracks results in a second globally uniform grid of groundtracks separated by 108 km at the equator after 372 orbits or approximately 24 days. This non-repeat pattern continues for a 6-month period with the end result being the accumulation of a global pattern of groundtracks separated by approximately 5 km at the equator. Three independent sets of this global grid will be collected during the initial 18-months of the GEOSAT mission. Data which is presently being returned from the satellite is exceptionally noise free (ie., the range measurement appears to be very precise) and, where tracks can be compared with SEASAT, the GEOSAT altimeter system appears to represent a significant improvement over the earlier system.

The primary objective of these data is computation of a global mean sea surface via the minimization of range differences at crossover points to be used as an approximation to the marine geoid for U.S. military navigational systems. Because of the strategic utility of the sea level data collected during this first 18-months, which constitute the Geodetic Mission for GEOSAT, altimeter measured ranges are classified SECRET. A by-product of the crossover point computation will be the compilation of global crossover point rms variability. This variability information will be unclassified and will thus provide much useful information to the research community on global topographic variability.

During the initial 18-month "geodetic" mission the major oceanographic focus of the GEOSAT topographic studies will be in the NW Atlantic (see figure 2) where an accurate geoid is available for the computation of topography (ie., sea level minus the geoid). These topographic

"residuals" are being computed at the Naval Ocean Research and Development Activity (NORDA) within a few hours of the playback of altimeter range data to the single ground station at the Applied Physics Laboratory (APL) of Johns Hopkins University. Data received at NORDA from APL consists of satellite range, wind speed, and significant wave height along with spacecraft clock time tags. At NORDA these so-called Sensor Data Records (SDR) are edited, averaged, and combined with sets of orbital elements in order to geographically locate the data points as well as to determine the height of the satellite relative to the center of mass of the Earth. Differences are computed between the altimeter observed sea level and the local geoid in the area shown in figure 2. Subsequently, a linear trend is removed independently from each pass of satellite data over the area. These detrended residuals are taken as a measure of ocean topography along each track. Very preliminary comparison of these residuals with satellite infrared imagery, as well as with an initial set of AXBT underflights which were collected in late May, 1985, indicate that the satellite can easily observe mesoscale topography over the NW Atlantic. Since the geoid used in the computation of these residuals is classified, the residuals themselves (which represent the difference between two classified data sets) are unclassified (GEOSAT Data Releasability Procedures Memorandum, 1984).

#### GEOSAT-EXACT REPEAT MISSION (GEOSAT-ERM)

Despite the relative ease with which topographic residuals are being computed in the NW Atlantic using GEOSAT altimeter data, good residuals can only be computed in relatively few areas of the global oceans (due to the unavailability of good geoid information). The global utility of an altimeter system to observe the oceanic mesoscale can best be realized by flying the satellite in a collinear or exact repeat orbit. Since the groundtracks laid down by the satellite repeat (within a few kilometers) on some known and uniform interval of time, differences in observed sea level from one pass to the next can be described in terms of temporal fluctuations in the topography along that particular track. Mitchell (1983) proposed that GEOSAT be placed in such an orbit at the end of its nominal 18-month mission. Plans are now proceeding within the GEOSAT Project to place the satellite in a collinear orbit during the Fall of 1986. A particular 17-day exact repeat orbit has been selected so as to alleviate security issues which have arisen over the open release of GEOSAT range data. At present, plans call for all GEOSAT range data collected during the GEOSAT-ERM to be unclassified. Of course, this will greatly enhance the utility of these data to the research community. The collinear orbit of the GEOSAT-ERM lays down a globally uniform grid of 244 orbits with spacing of 164 km at equator. The time difference between adjacent tracks is 3 days (the time difference between exact repeats being approximately 17 days). The pattern of groundtracks laid down in the NW Atlantic during the GEOSAT-ERM is shown in Figure 3. Note should be given to the somewhat inadequate crosstrack resolution of this grid of data for resolving mesoscale structure. Spatial resolution along track will be 7 km in a one sea level point per second averaged data stream. At present, plans call for the collection of at least 2 years of data from this collinear

SYNOPS Program are intended to overlap.

#### THE REX AND GEOSAT

Data from GEOSAT, most particularly topographic residuals, play a major role as input to the NW Atlantic Regional Energetics Experiment. The REX addresses several important questions regarding the mesoscale circulation in the region of figure 2 particularly:

1. What are the pertinent space and time scales of Gulf Stream fluctuations near the New England Seamounts?
2. What is the relative importance of barotropic and low-order baroclinic fluctuations in the region?
3. How is mesoscale vertical structure influenced by interaction with bathymetry?
4. What are the typical energy partitions within the region?

Such ambitious questions can not be addressed with satellite data alone. Thus, REX involves in addition an extensive field program and numerical model development effort which are discussed in the following companion papers by Hallock and Thompson.

## REFERENCES

Born, G.H. 1984. Private Communication.

Lybanon, M. 1984. GEOSAT Ocean Applications Program (GOAP) Initial Data Processing and Analysis System Test and Evaluation Plan. NORDA Technical Note 270. Naval Ocean Research and Development Activity, NSTL, Mississippi 39529.

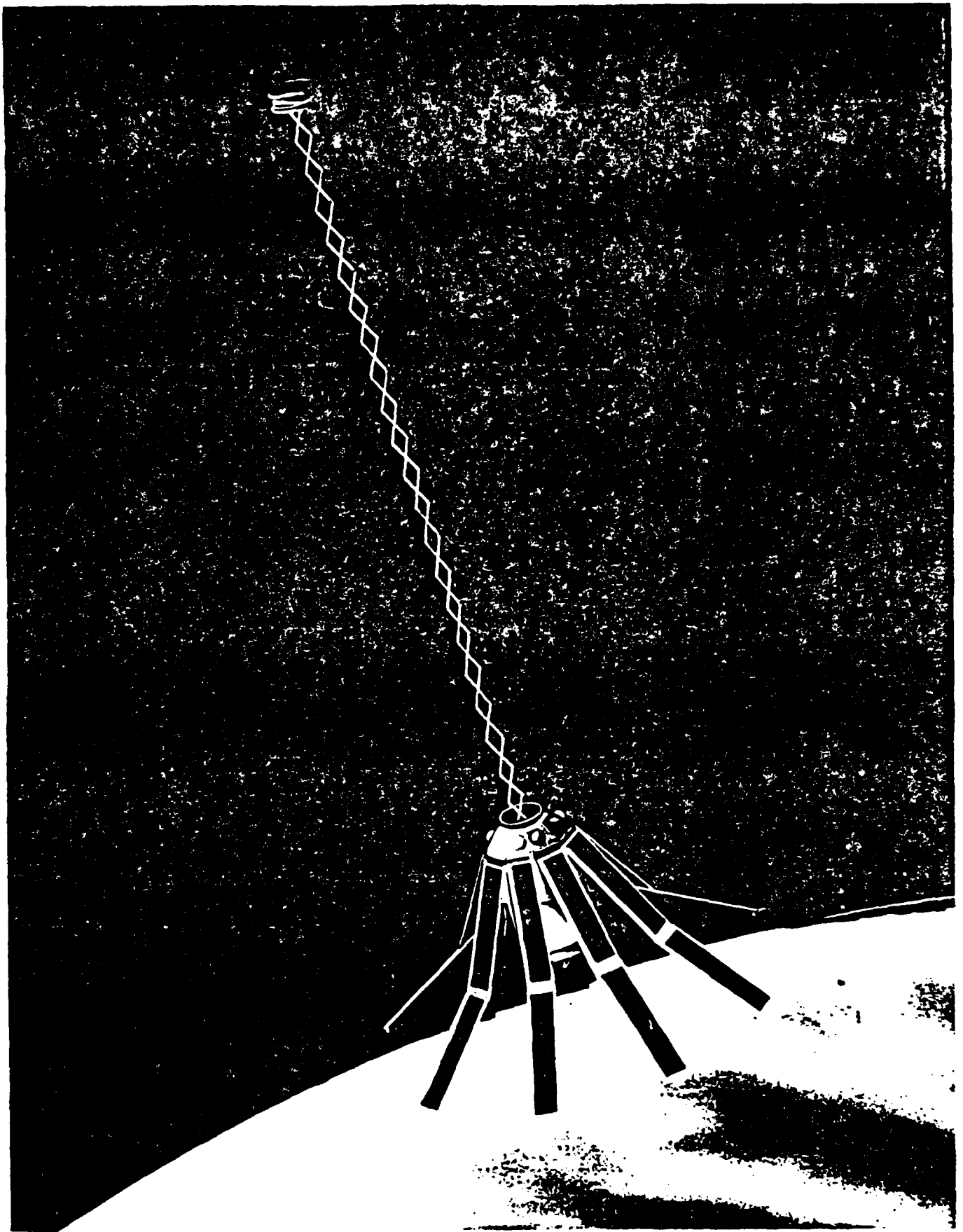
Mitchell, J.L. 1983. A Position Paper: Mesoscale Oceanography from GEOSAT. NORDA Technical Note 226. Naval Ocean Research and Development Activity, NSTL, Mississippi 39529.

Mitchell, J.L. and Hallock, Z.R. 1984. Plans for Oceanography from the U.S. Navy GEOSAT. In Proceedings of the Pacific Congress on Marine Technology (PACON '84), held April 24-27, 1984 at Honolulu, Hawaii.

Mitchell, J.L., Hallock, Z.R., and Thompson, J.D. 1985. The REX and the U.S. Navy GEOSAT. Naval Research Reviews. In Press.



Figure 1-- Artist's concept of the flight-configured U.S. Navy GEOSAT. Attitude stabilization is provided via the extended boom on the modified GEOS-C bus. The one-meter diameter altimeter antennna dish is located underneath the spacecraft.



A PAINTING OF THE GEOSAT-A SATELLITE. EXECUTED BY APL ARTIST ROGER SIMMONS

### GEOSAT-A RADAR ALTIMETER SPACECRAFT

OFFICE OF THE CHIEF OF NAVAL OPERATIONS/OFFICE OF NAVAL RESEARCH  
THE JOHNS HOPKINS UNIVERSITY/APPLIED PHYSICS LABORATORY  
SEPTEMBER 1982

Figure 2-- The NW Atlantic REX region with contoured bathymetry. NORDA arrays of IES/PG's will be located in regions 2 and 3, far downstream of the recent University of Rhode Island array in region 1. The mean axis of the Gulf Stream is shown as the dashed line through the region. The domain in which GEOSAT topography will be available during the 18-month geodetic mission is outlined.

— REGION OF AVAILABLE  
TOPOGRAPHIC RESIDUALS  
FROM GEOSAT

----- GULF STREAM AXIS

(1) URI IES ARRAY  
(2,3) NORDA IES ARRAYS

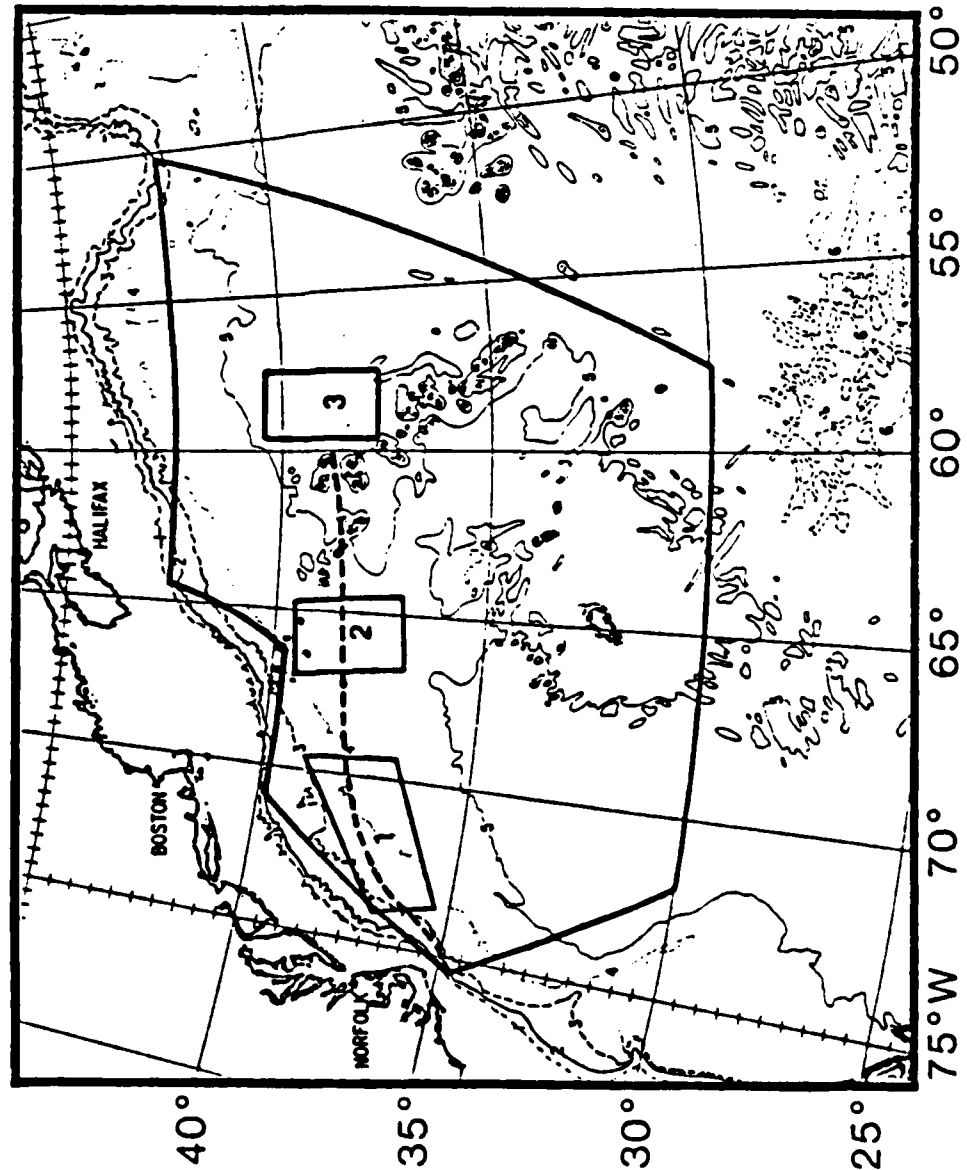


Figure 3-- Pattern of groundtracks in the NW Atlantic along which sea surface topographic fluctuations will be measured during the GEOSAT-ERM. During this two-year mission, global sea surface topographic fluctuations will be collected in a 17-day repeat cycle (i.e., every 17th day the satellite will overfly a given groundtrack). The background sea surface temperature image is from recent NOAA polar orbiter IR data. Contrasts in the image have been enhanced at NORDA, using a two-dimensional, digital filter which results in a relief-like effect, with warmer areas being higher than colder areas. Though the correlation between sea surface temperature and topography is not one-to-one, the image is liberally used to depict the depressions and elevations associated with three cold core rings and a Gulf Stream meander.



SENSING

Scales of Variability of the Gulf Stream Front  
Based on AVHRR Imagery and Related Topics

Christopher N.K. Mooers  
 Department of Oceanography  
 Naval Postgraduate School  
 Monterey, California, 93943

From several years of weekly charts of the surface locus of the Gulf Stream front based on AVHRR satellite imagery, Halliwell and Mooers (1979, 1984) found the following:

- 1) correlation scales for Gulf Stream front
  - temporal, 2 weeks
  - spatial, 80 km,
- 2) rms amplitude of the Gulf Stream frontal position increased from about 25 to 80 km in the first 1,000 km downstream of Cape Hatteras,
- 3) the dominant Gulf Stream meanders had wavelengths of ca. 320 km, periods of 6 to 8 wks, downstream propagation speeds of ca. 6 to 8 cm/s, a downstream group speed of ca. 17 cm s<sup>-1</sup>, and a downstream spatial growth rate of ca.  $3.2 \times 10^{-3}$  km<sup>-1</sup>,
- 4) long period (4 mos to at least 4 yrs) standing meanders with nodes at Cape Hatteras and 600 km farther downstream, and
- 5) the Gulf Stream frontal position, and the number and intensity of warm-core eddies shed by the Stream, varied interannually.

These points, and others, are illustrated with the attached figures from Halliwell and Mooers (1979, 1984). This data source also provided useful statistical information on the number and the trajectories of warm core eddies and on the interactions of warm core eddies with the shelf/slope front.

Over the past three years, the OPTOMA (Ocean Prediction Through Observation, Modeling, and Analysis) Program, a joint NPS/Harvard project, conducted in the California Current System (CCS) (Mooers and Robinson, 1984; Robinson, et al., 1984; Rienecker, et al, 1985; Smith, et al, 1985) and sponsored by ONR, has studied some of the data assimilation issues posed for SYNOPS.

For example, considerable experience has been gained in mapping quasi-synoptic realizations of the mass field, initialization and verification of a dynamical (QG) model with objectively analyzed fields, and otherwise conducting real-time ocean prediction experiments. One of the challenges still outstanding is effective utilization of AVHRR imagery in the data assimilation scheme used by OPTOMA. One step is to place the corrected, digital data for SST into a regular grid. Another is to make use of this data in an upper (mixed) layer model, and possibly coupled mixed layer and mesoscale eddy models. Yet another is to make use of pattern recognition to relate SST patterns to synoptic/mesoscale phenomena. Finally, there is the possibility of deriving surface motion fields from changes in successive images.

It would seem interesting and important to explore using available data sets (aircraft and ships-of-opportunity, XBTs, satellite remote sensing (AVHRR, altimetry, etc.), research data) to nowcast a time series of synoptic maps of Gulf Stream fields. Some variation of statistical objective analysis would be used until there is a proven dynamical model to be used as well. Initially, a domain 1,000 km by 500 km centered on the mean Gulf Stream axis has been chosen for nowcasting. For this task, the adequacy of "operational" temperature profile data sources available through FNOG is now being assessed. A preliminary assessment of available data for 1984 is summarized in the attached table and figure; it appears promising. (A similar approach is planned with NMCs SST retrievals from AVHRR imagery.) The availability of a time series of O.A.'d maps would facilitate studies in 4-D data assimilation and the study of dynamical questions associated with the Gulf Stream and the synoptic/mesoscale eddy field. Also, it would be of interest to examine the relationship between the large scale space-time variability of the wind stress curl field and the location of the Gulf Stream path.



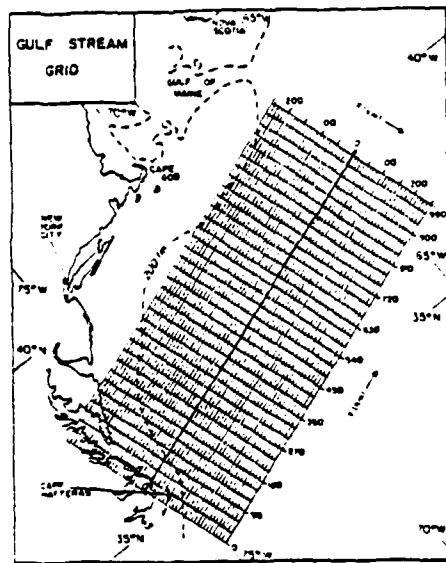


FIG. 1. The Gulf Stream grid.

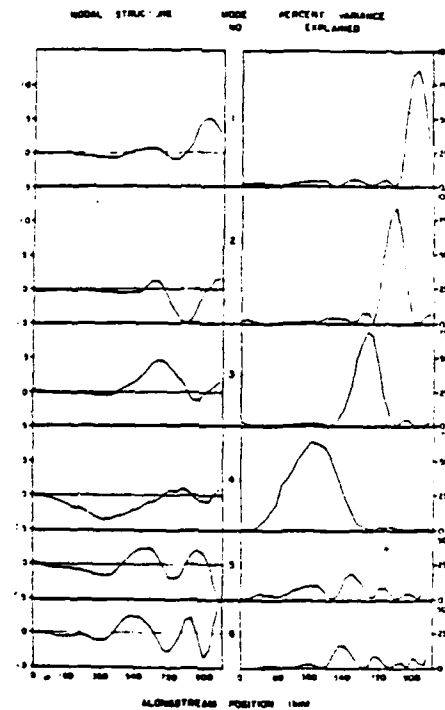


FIG. 4. The modal structure of, and percent variance explained by, the first six EOF modes in the time domain of the surface front.

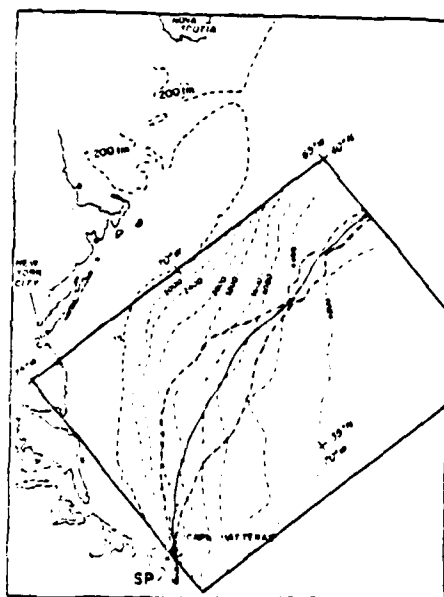


FIG. 8. Mean position, standard deviation envelope, and extreme position envelope of EOF Mode 4. SP is the separation point.

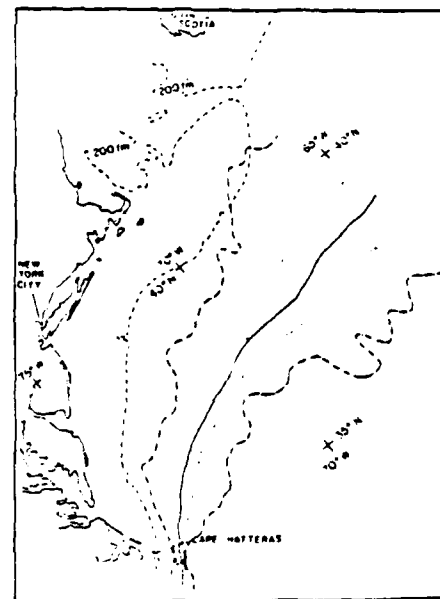


FIG. 10. Mean position (solid line), standard deviation envelope (dotted line), and extreme position envelope (dash-dot line) of the propagating meander time series.

REPRODUCED BY PERMISSION OF THE NATIONAL OCEANOGRAPHIC SOCIETY

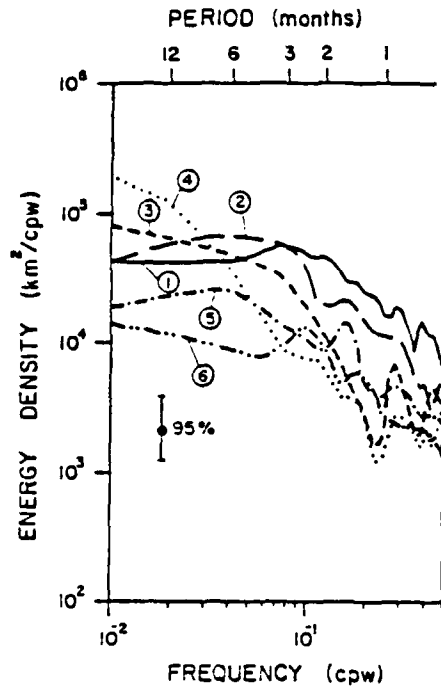


FIG. 5. Autospectra of the first six EOF modes in the time domain. The 95% confidence band is shown.

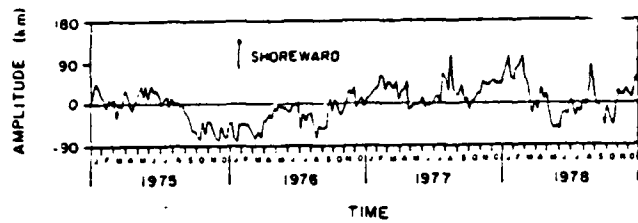


FIG. 9. Time-varying amplitude of EOF Mode 4 at its antinode,  $y = 390$  km.

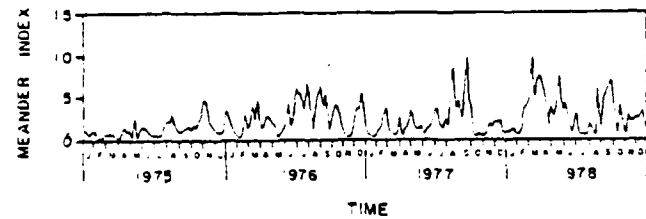
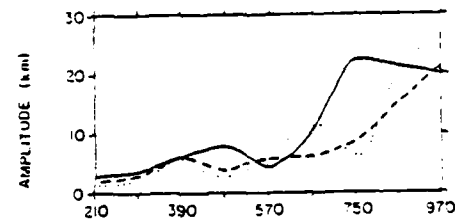


FIG. 15. Gulf Stream propagating meander amplitude index.



— 4.0-4.5 cpw  
 --- 5.2-5.8 cpw  
 ..... 6.5-8.5 cpw

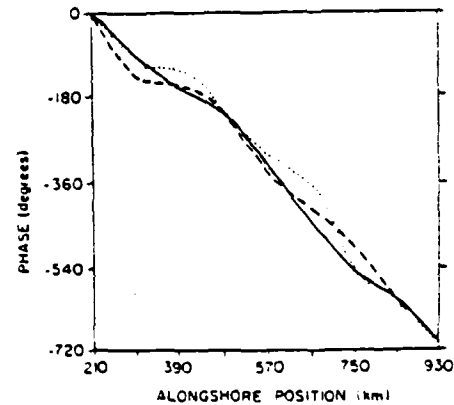


FIG. 13. Amplitude and phase of the most significant frequency domain EOFs for three frequency bands of the propagating meander time series.

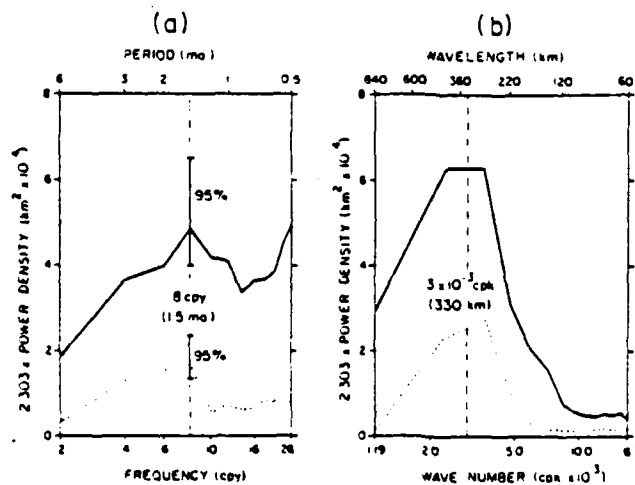


FIG. 12. Distribution of total variance of the propagating meander time series in the frequency and wavenumber domains: (a)  $2.303 \times \text{frequency} \times \text{energy density}$ , (b)  $2.303 \times \text{wavenumber} \times \text{energy density}$ . The solid lines are total variance, and the dotted lines are the propagating wave variance. The variance within a specified frequency or wavenumber band equals the area beneath the appropriate curve. The most energetic frequency and wavenumber are marked by the vertical dashed lines.

REPRODUCED AT GOVERNMENT EXPENSE

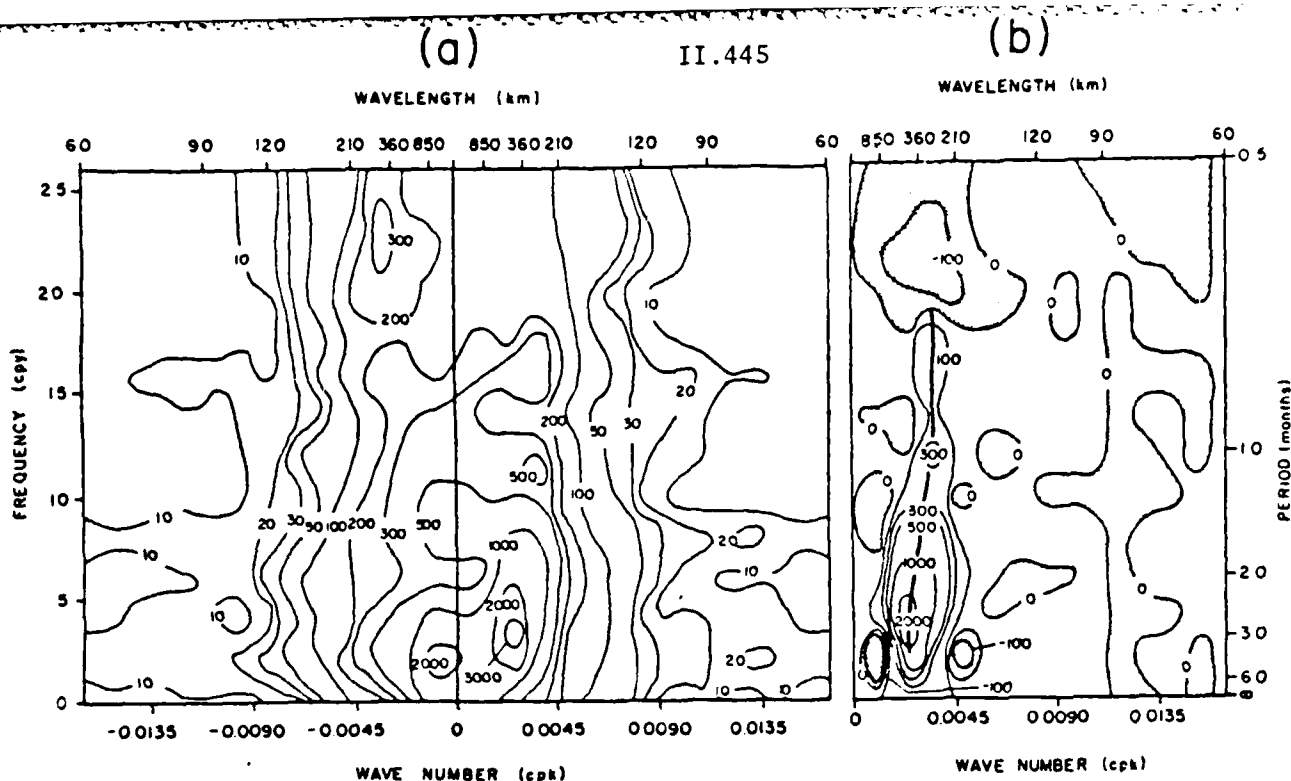


FIG. 11. Wavenumber-frequency autospectra of the propagating meander time series ( $240 \leq y \leq 990$  km): (a) Total autospectrum; (b) propagating wave autospectrum. The maximum ridge in the propagating autospectrum is shown by the thick line. Contours are in  $\text{km}^2 \text{cpw}^{-1} \text{cpk}^{-1} \times 10^{-3}$ .

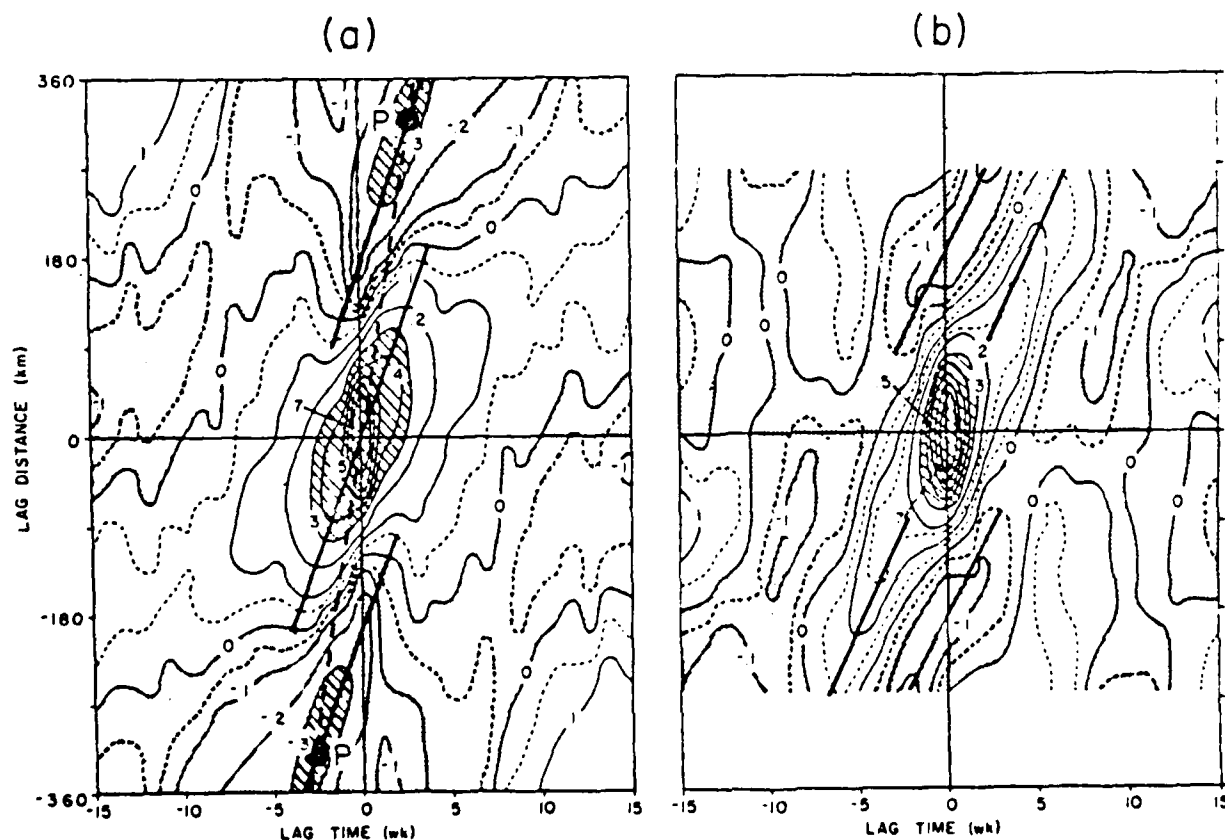


FIG. 14. Space-time autocorrelation functions of the propagating meander time series: (a)  $240 \leq y \leq 690$  km; (b)  $690 \leq y \leq 990$  km. Phase speed is equal to the slope of the thick solid lines and group speed is equal to the slope of the thick dashed lines. Correlation minima are indicated by the points P. Regions with correlation magnitude  $> 0.3$  are cross-hatched to enhance ridges and troughs.

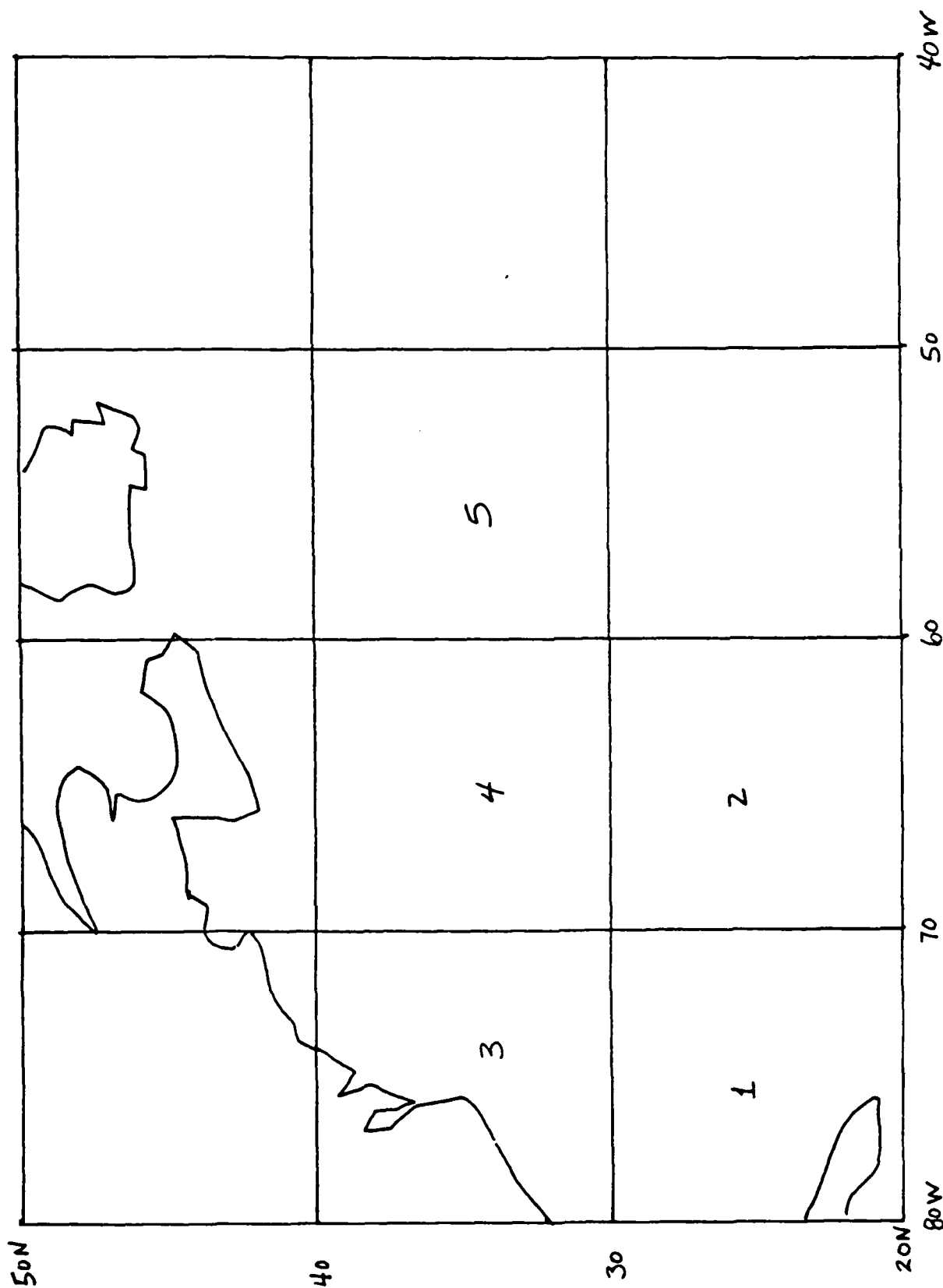
## 1984 FNOC/XBT SUMMARY (UNCLASSIFIED &amp; CONFIDENTIAL SOURCES)

TIME FRAME	GLOBAL TOTAL XBT'S	Approximate # of XBT's in Area					
		1	2	3	4	5	$\Sigma$
01-15 Jan	959	9	0	20	10	1	40
16-31 Jan	1287	20	6	19	4	0	50
01-15 Feb	1495	10	15	40	20	0	85
16-29 Feb	1267	1	12	13	2	1	30
01-15 Mar	1252	5	2	5	1	1	15
16-31 Mar	1163	35	1	5	5	0	45
		<u>80</u>	<u>36</u>	<u>102</u>	<u>42</u>	<u>3</u>	<u>265</u>
01-15 Apr	1112	10	1	20	15	5	51
16-30 Apr	1089	1	0	25	2	15	43
01-15 May	1467	25	0	15	0	0	40
06-31 May	1568	15	5	15	15	8	58
01-15 Jun	1302	22	8	30	20	0	80
16-30 Jun	1304	27	5	15	15	1	63
		<u>100</u>	<u>19</u>	<u>120</u>	<u>67</u>	<u>29</u>	<u>335</u>
01-15 Jul	1199	20	5	15	15	6	61
16-31 Jul	1282	12	5	20	5	5	47
01-15 Aug	1319	15	7	22	9	7	60
16-31 Aug	1386	15	15	45	3	3	81
01-15 Sep	1078	2	10	20	10	1	43
16-30 Sep	965	0	3	20	3	1	27
		<u>64</u>	<u>45</u>	<u>142</u>	<u>45</u>	<u>23</u>	<u>319</u>
01-15 Oct	1366	10	0	20	10	10	50
16-31 Oct	1467	5	1	20	3	7	36
01-15 Nov	1231	2	1	25	1	0	32
16-30 Nov	884	0	3	0	3	2	8
01-15 Dec	952	0	2	3	0	0	5
16-31 Dec	768	10	0	10	0	1	21
		<u>27</u>	<u>7</u>	<u>78</u>	<u>17</u>	<u>20</u>	<u>152</u>
GRAND TOTAL		271	107	442	171	75	1071

Two wk. period

Mean 41  
Std. Dev. 24

Two Week #'s	Mean	Std. Dev.
Area 1	11.3	9.5
2	4.5	4.5
3	18.4	10.2
4	7.1	6.4
5	3.1	3.9



REFERENCES

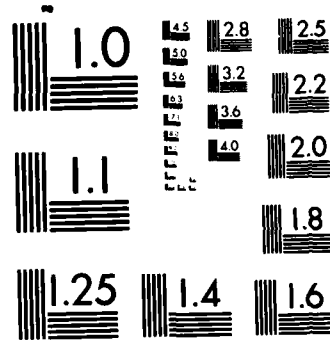
- Halliwel, G.R. and C.N.K. Mooers (1979), The Space-Time Structure and Variability of the Shelf Water-Slope Water and Gulf Stream Surface Temperature Fronts and Associated Warm-Core Eddies, JGR, 84:7707-7725,
- Halliwel, G.R. and C.N.K. Mooers (1983), Meanders of the Gulf Stream Downstream of Cape Hatteras, 1975 through 1978, JPO, 13:1275-1292.
- Mooers, C.N.K. and A.R. Robinson (1984), Turbulent Jets and Eddies in the California Current and Inferred Cross-Shore Transports, SCIENCE, 223:51-53.
- Robinson, A.R., C.N.K. Mooers, J.A. Carton, L.J. Walstad, E.F. Carter, M.M. Rienecker, J.A. Smith, and W.G. Leslie (1984), A Real Time Dynamical Forecast of Ocean Synoptic/Mesoscale Eddies, NATURE, 309:781-783.
- Rienecker, M.M., C.N.K. Mooers, D.E. Hagan, and A.R. Robinson (1985), A Cool Anomaly Off Northern California: An Investigation Using IR Imagery and In Situ Data, JGR, 90:4807-4818.
- Smith, J.A., C.N.K. Mooers, and A.R. Robinson (1985), Estimation of Quasi-Geostrophic Modal Amplitudes from XBT/CTD Survey Data. Journal of Atmospheric and Oceanic Technology, In Press.

UNCLASSIFIED

N00014-85-G-0322

NL

NL



MICROCOPY RESOLUTION TEST CHART  
NATIONAL BUREAU OF STANDARDS-1963-A



PROTOTYPE DATA ASSIMILATION  
IN THE GULF STREAM REGION

BY

Nadia Pinardi

Michael A. Spall

Harvard University  
Center for Earth and Planetary Physics  
Cambridge, Massachusetts

to appear in Proceedings of  
ONR Workshop on the Gulf Stream  
Narragansett, Rhode Island

April 1985

The goal of this research is to set up the Harvard Descriptive-Predictive System in the Gulf Stream region (Robinson, 1985). This would allow for study of important phenomena such as local dynamics and energetics of meander and ring formation processes, the influence of boundary forcing such as the upper mixed layer and bottom topography, and the physics of eddy-mean flow interactions. The Harvard Open Ocean Model is a baroclinic, quasigeostrophic (QG) model (Miller, Robinson, 1983) (see Figure 1). Forecasts consist of initializing the model from available data sets. Since the model is open domain, the forcing at the boundaries consistent with observations has also to be imposed. Knowledge of the important physical and dynamical processes may be gained by analyzing the model forecasts. Those portions of the observations not reproduced by the model may be attributed to inaccurate initialization or/and reference fields and inadequate model physics. Phenomenon successfully modelled may be analyzed using local energy and vorticity analysis and variation of model parameters to determine the important physics of the events.

The Gulf Stream region contains important physics on a wide range of spatial and temporal scales. At the large space scales are the stream meandering, deep undercurrent variations, and air-sea interactions. Intermediate scales include warm and cold rings, mesoscale eddies, warm water outbreaks and localized topographic forcing. Each of these phenomena may be important to the dynamics of the region. The domain shown in Figure 2 was chosen to be large enough to include these events yet still retain fine horizontal resolution (15 km, higher resolution in the future will be used). Contained within the domain are the New England seamounts, the nodal point at 70°W, and regions of active ring-stream interaction and ring formation processes.

In the absence of large data sets it is still desirable to be able to conduct data assimilation experiments in the Gulf Stream region. Lacking

data below the surface, we have begun preliminary work utilizing feature models (Figure 3) to initialize the descriptive-predictive system. We use remote sensing (IR) to locate the surface signature of major phenomena in the region, such as the Gulf Stream northern edge and warm and cold rings. Analytical models derived from historical data sets are then used to extend these surface signatures into the deep water. A thin jet model (Niiler and Robinson, 1967) defines the velocity structure of the stream. Analytic expressions for the warm and cold rings are chosen to match typical velocity structures (Olsen, 1980). This approach allows for prototype data assimilation experiments with direct comparison with sea surface IR observations. Satellite IR and QG streamfunction utilizing the feature model initialization method is shown in Figure 4 for Nov. 23, 1984.

Preliminary work has been done initializing the model using Rafos float data. The Rafos floats are placed in the stream and, remaining on a prescribed isopycnal, return location and depth as a function of time. Utilizing this data and the thin jet model it is possible to derive a stream axis position and hence a streamfunction field. Shown in Figure 5 is the float track, inferred axis position, and QG streamfunction for Rafos float 22. A preliminary experiment has been done initializing the field with float 16 and forecasting ahead 9 days to float 17. The forecast streamfunction is shown in Figure 6. The general tendency of the stream has been reproduced but the slight dip is seen too far to the east.

A data assimilation experiment has been done for the IR data set of Nov. 23 to Dec. 19, 1984. The QG model was initialized from observations on Nov. 23, which include two existing rings, and forced at the boundaries with the data shown in Figure 7. The model domain is centered at 29 N, 59.5 W and rotated 20° CCW. After initialization the flow undergoes two major types of

adjustment. First the feature models locally adjust themselves to become consistent with the model physics. Adjustment of the motionless near field is also necessary because this is not in balance with the features. It is hoped that the near field adjustment takes place rapidly so as to minimize the shortcomings of the feature model initialization procedure. As we see in Figure 8, the forecast stream interacts with the existing warm ring, the meander then deepens and pinches off a cold ring after 12 days. The cold ring size and location are consistent with later IR images but seems to develop between 5 and 14 days too early.

Local energy and vorticity analysis has been carried out to interpret dynamically the detachment of the cold core ring in the model forecast of Figure 7. The consistent quasigeostrophic kinetic and available gravitational energy equations are written in Figure 9 together with the subdomain chosen for the local analysis. The equations are explained in Pinardi and Robinson (1985) and the reader is referred to it for completeness. Figures 10 to 13 show maps of the terms in the vorticity equation (see Figure 1) and in the energy equations.

The preliminary dynamical analysis of cold core ring formation process at 300 m of depth indicates that:

- a) • Vorticity is mostly thermal at this level  $[(\sigma\psi_z)_z]$ 
  - Advective vorticity flux divergences are at intermediate scales ( $\sim 50$  km)
  - Multipolar structure of the divergence of vorticity fluxes along the meridional southward propagating part of the meander. Mixed meridional jet instability?

- 3-D enstrophy cascade in the neck of the cutting meander at breakoff time, due to overlapping advective flux divergences  $(\vec{v} \cdot \nabla (\nabla^2 \psi))$  of the same sign as  $\vec{v} \cdot \nabla (\sigma \psi_z)_z$ .
- b) • Advective flux  $(\Delta F_K, \Delta F_A)$  and pressure work  $(\delta f_\pi, \delta F_\pi)$  divergence are all important
- In the neck, at breakoff time,  $\Delta F_\pi$  and  $\delta f_\pi$  dominant over  $\Delta F_K$ .
- Strong divergence of radiative fluxes  $(\Delta F_\pi, \delta f_\pi)$  in the region of pinching
- In the jet associated with the newly formed ring we have a  $\Delta F_K$  and  $\Delta F_\pi$  balance
- The buoyancy work and  $\Delta F_A$  decrease A.G.E. in the deepening meander and neck: net  $A \rightarrow K$  conversion.

In the rectified stream strong radiative flux divergences propagate energy downstream.

The Harvard descriptive-predictive system has been set up for data assimilation in the Gulf Stream region. Utilizing feature models for initialization, forecasts have been done from both Rafos float and satellite IR data sets. The preliminary results are very encouraging. The next step which needs to be taken is improvement of the existing feature models to match the historical data sets better. More complete model initializations including a larger domain, all observed rings, and the sea surface temperature are being carried out. On a longer time scale an open ocean dynamical model retaining more complete physics should be developed to determine the range of validity of the quasigeostrophic dynamics in this region.

References

Joyce, T.M., 1984, J.P. V. 14, p. 936.

Niiler, Robinson, 1967, Tellus XIX, V. 4, p. 601.

Olson, D.B., 1980, JPO, V. 10, p. 514.

Miller, Robinson, Haidvogel, J.C.P. vol. 50, N. 1, 1983, p. 38.

Pinardi, Robinson, 1985, "Quasigeostrophic energetics in open ocean regions",  
submitted to DAO.

Robinson, 1985, "Data assimilation, mesoscale dynamics and dynamical forecasting",  
to appear in the Proceedings of ONR Workshop on the Gulf Stream.

Fig 1

OPEN BOUNDARIES QUASIGEOSTROPHIC  
MODEL

$$\frac{\partial}{\partial t} \nabla^2 \psi + \frac{\partial}{\partial t} \Gamma^2 (\bar{\sigma} \psi_z)_z = -\alpha \vec{U} \cdot \nabla \nabla^2 \psi - \vec{U} \cdot \nabla \Gamma^2 (\bar{\sigma} \psi_z)_z - \beta \vec{U} \cdot \nabla \psi$$

B.C.  $q = \nabla^2 \psi + \Gamma^2 (\bar{\sigma} \psi_z)_z$  at inflow points $\psi$  along the boundaries $\psi_z$  top and bottom horizontal boundariesI.C.  $\psi$  at each level $\psi_z$  top and bottomPARAMETERS : $\frac{\rho_0}{\rho} = \text{Shapiro filter}$ 

$$\Gamma^2 = \frac{\rho_0^2 d^2}{N_0^2 H^2} \quad \alpha = t_0 \frac{U_0}{d} \quad \beta = \beta_0 \text{ to } d \quad \bar{\sigma} = \frac{N_0^2}{N^2(z)}$$

$$f_0 = 2\Omega \sin \theta_0 \quad \beta_0 = \frac{2\Omega \cos \theta_0}{a} ; \theta_0 = \text{central basin latitude}$$

$a = \text{radius of the earth}$

 $d = \text{horizontal length scale}$  $H = \text{vertical length scale}$  $t_0 = \text{time scale such that } \frac{1}{f_0 t_0} \ll 1$  $N_0^2 = \text{mid. thermocline}$ 

Brunt Vaisala frequency

 $N^2(z)$  climatological Brunt Vaisala frequency profile for the region.

FIGURE 2 THE GULF STREAM REGION

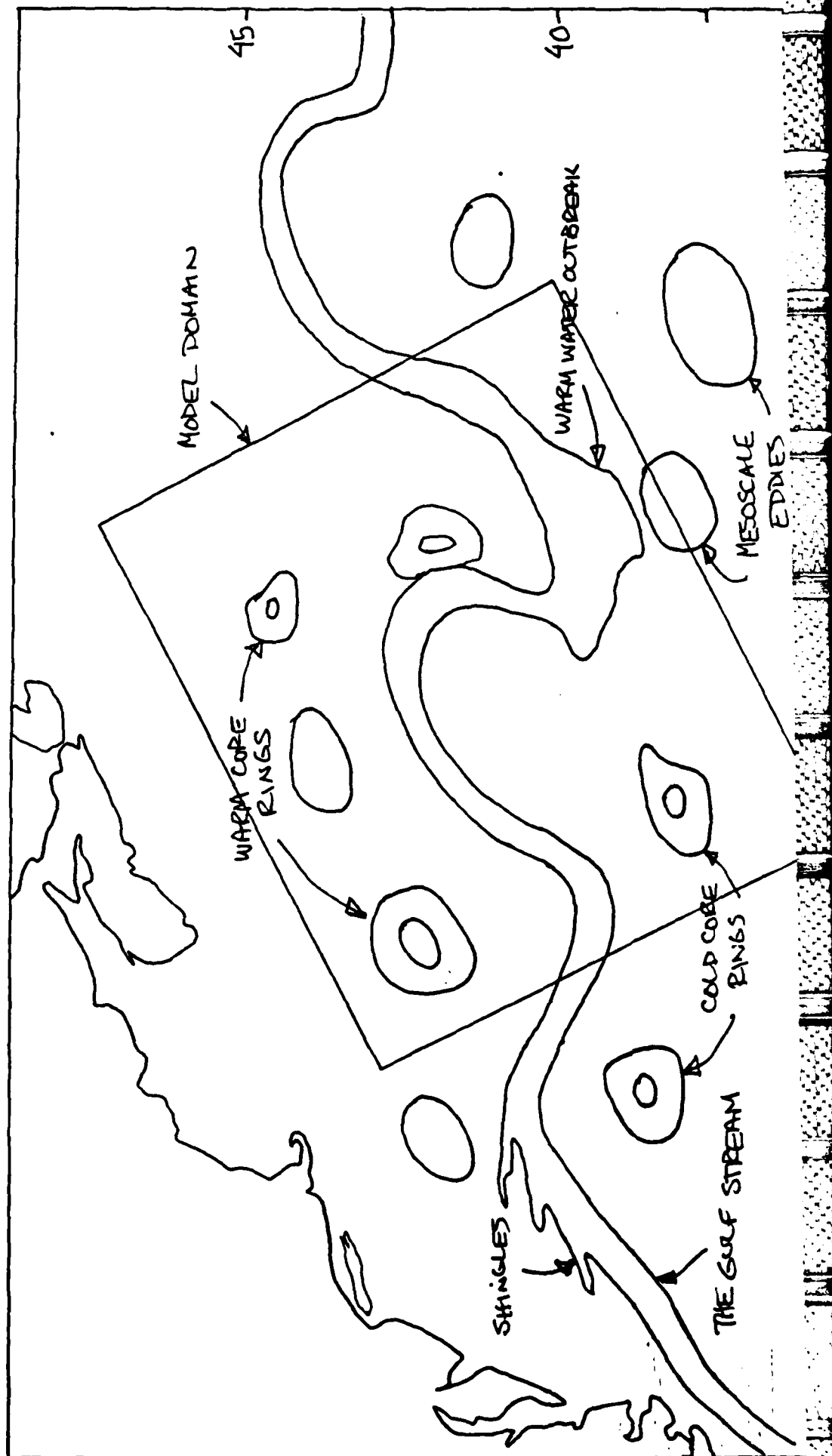
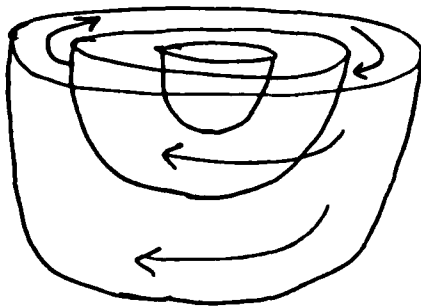




# FIGURE 3

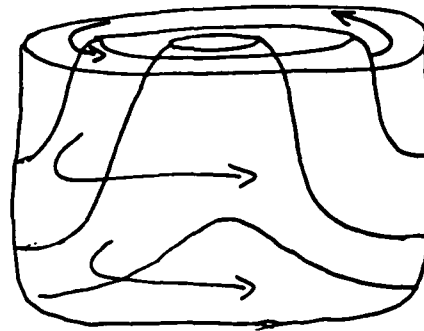
## FEATURE MODELS



WARM RING

$$\begin{aligned} z < d_{\max} & \quad V = r * V_{\max} / r_{\max} \\ r < r_{\max} \\ z > d_{\max} & \quad V = 0 \\ r > r_{\max} \end{aligned}$$

$$\begin{aligned} V_{\max} &= 150 \text{ cm/s} \\ r_{\max} &= 100 \text{ km} \\ d_{\max} &= 400 \text{ m} \end{aligned}$$

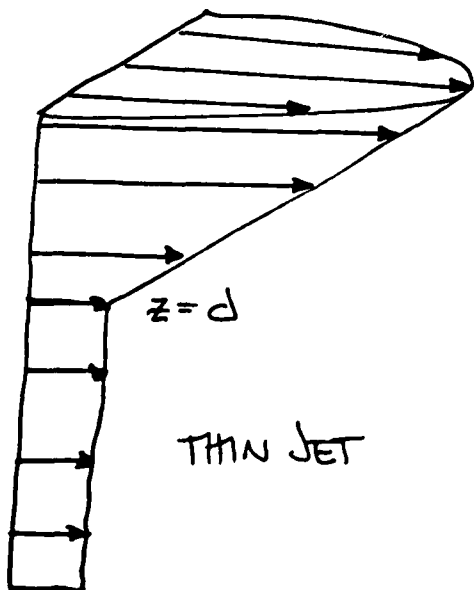


COLD RING

$$\begin{aligned} z < d_{\max} & \quad V = r * V_{\max} / r_{\max} \\ r < r_0 & \\ r_0 < r < r_{\max} & \quad V = \exp(-3(1-r/r_0)) \end{aligned}$$

$$\begin{aligned} z > d_{\max} & \\ r > r_{\max} & \quad V = 0 \end{aligned}$$

$$\begin{aligned} V_{\max} &= 150 \text{ cm/s} \\ r_0 &= 40 \text{ km} \\ r_{\max} &= 100 \text{ km} \\ d_{\max} &= 400 \text{ m} \end{aligned}$$

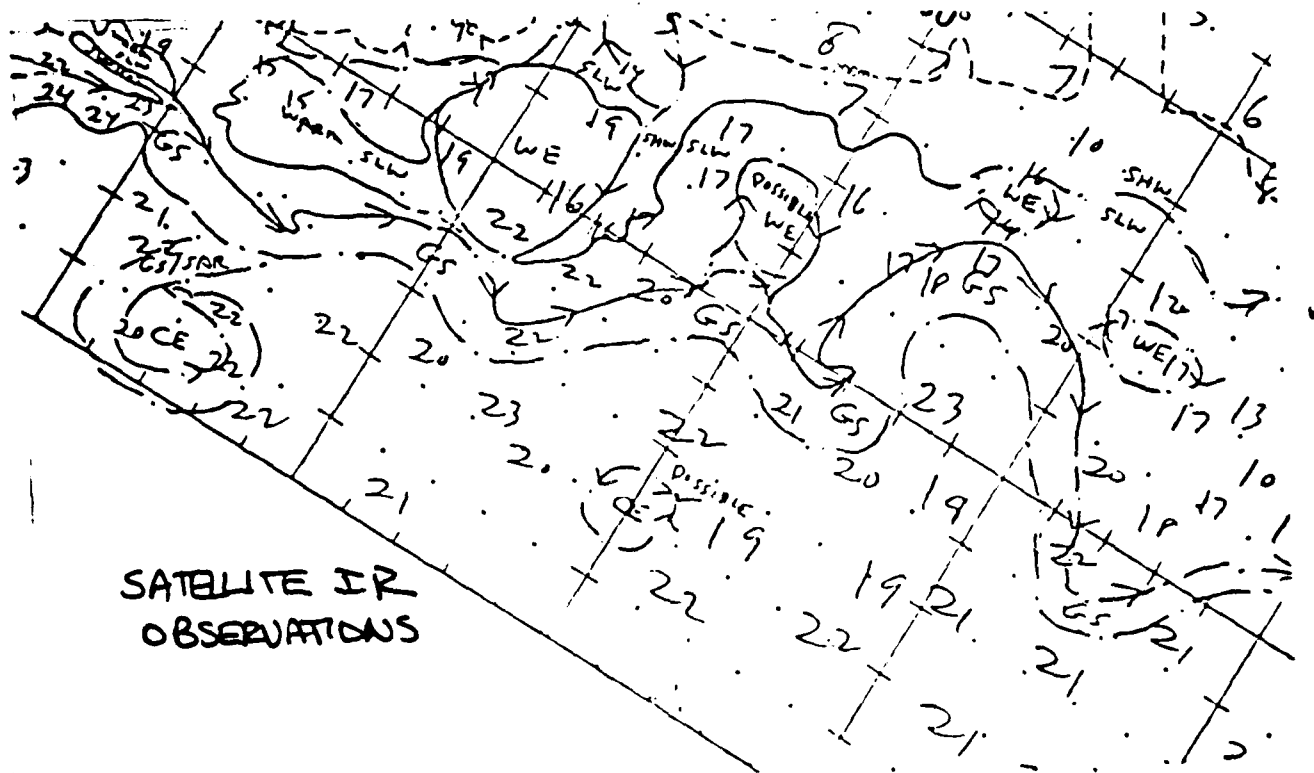


THIN JET

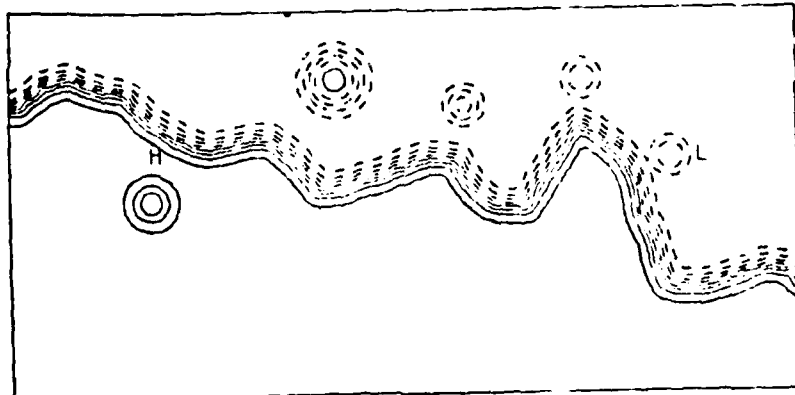
$$V = V_{\text{axis}} \exp(-\eta^2/g_0)$$

$$\begin{aligned} V_{\text{axis}} &= V_B + (V_T - V_B) \left( \frac{d-z}{d} \right) & z < d \\ &V_B & z > d \end{aligned}$$

$$\begin{aligned} V_T &= 200 \text{ cm/s} \\ V_B &= 5 \text{ cm/s} \\ d &= 1000 \text{ m} \\ g_0 &= 160 \text{ km}^2 \end{aligned}$$



SATELLITE IR  
OBSERVATIONS

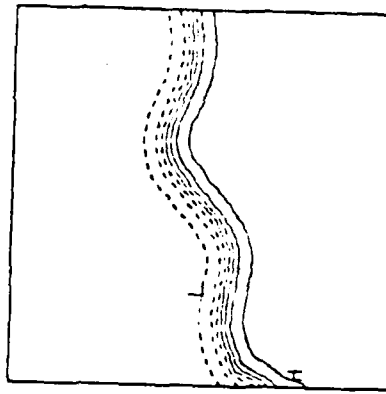


Q6 STREAMFUNCTION

INITIALIZATION WITH FEATURE MODELS

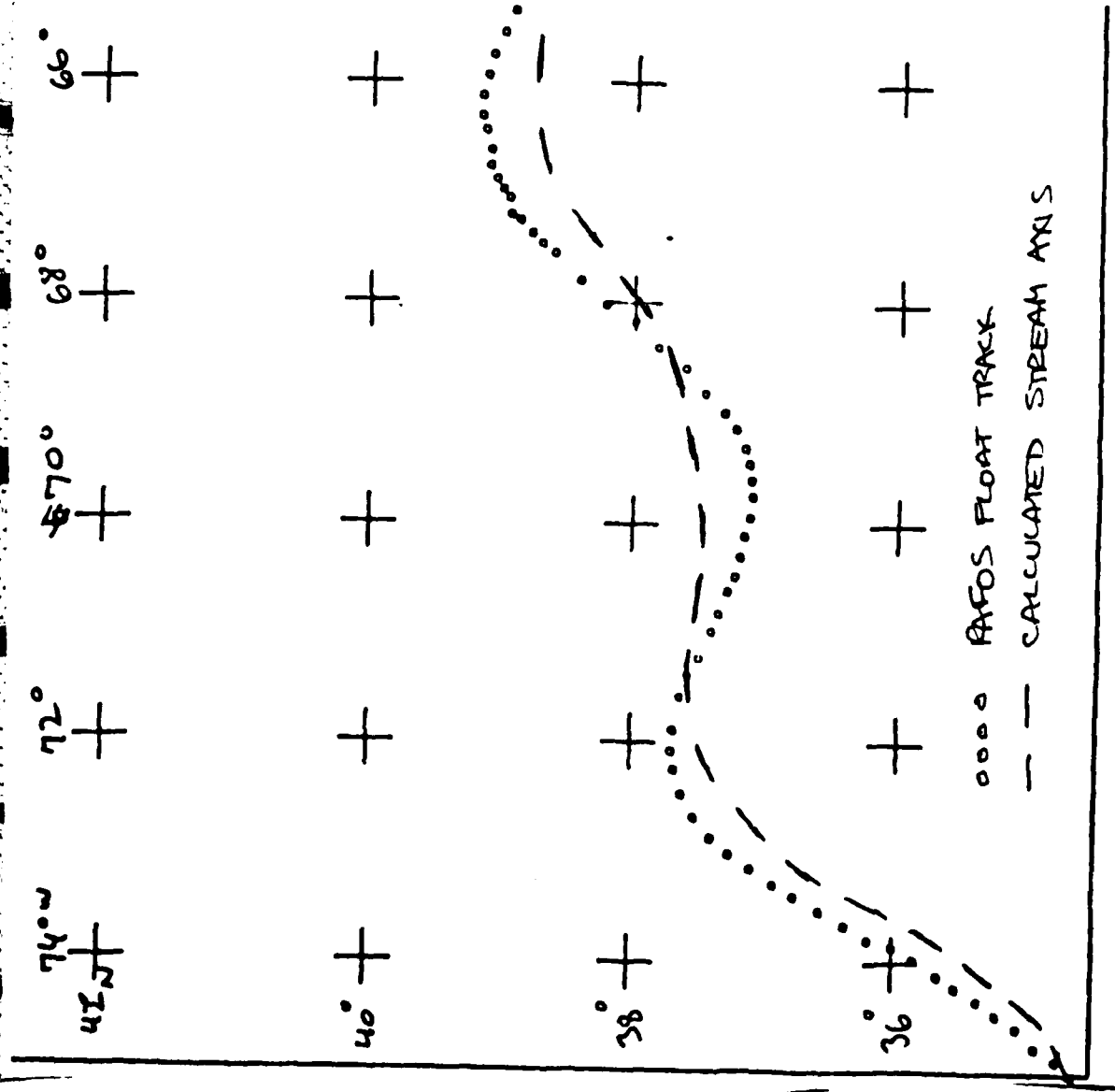
FIGURE 4

II.459



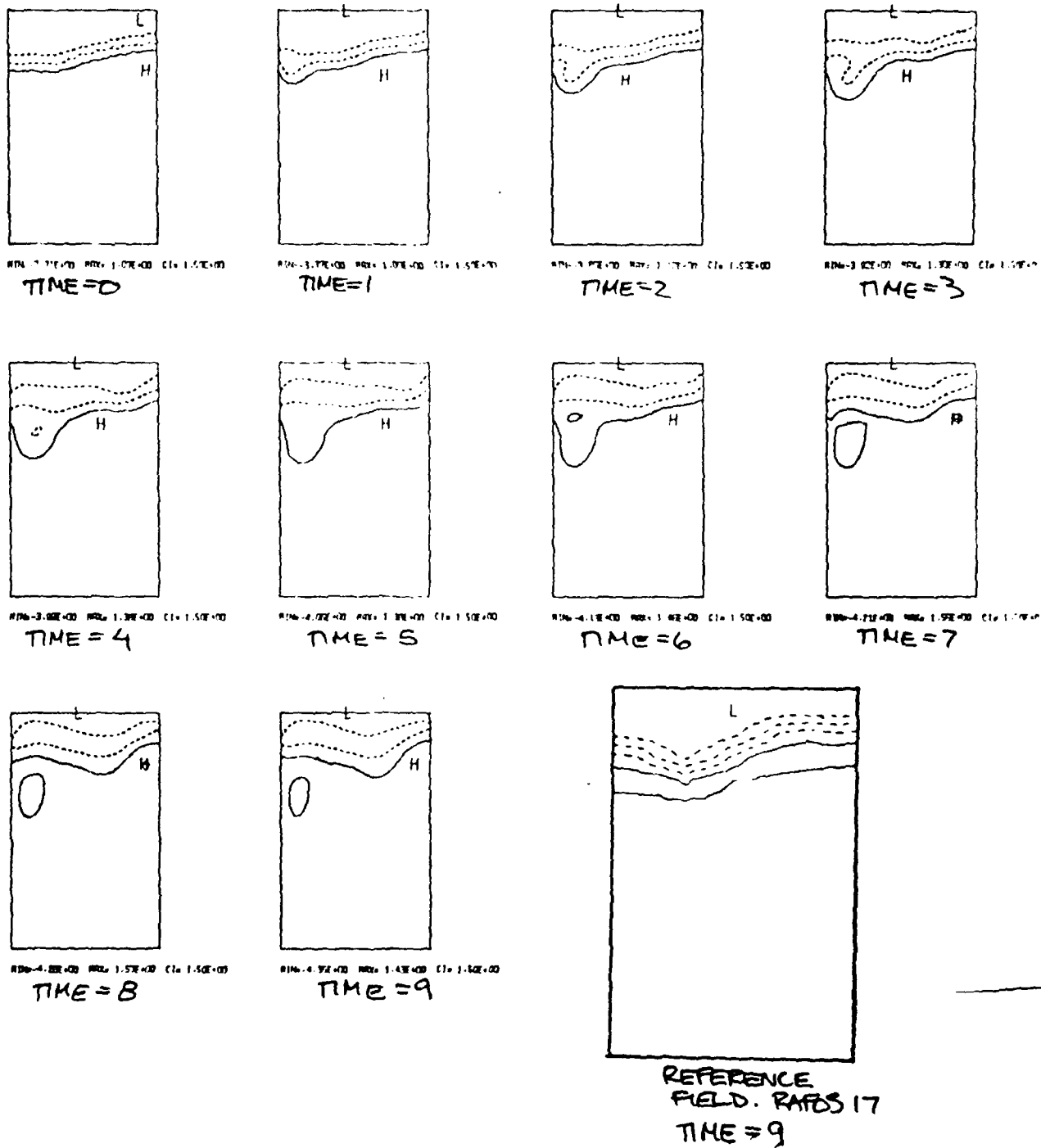
MIN=3.00E+00 MAX=3.10E+00 CI=1.00E+00

Q6 STREAMFUNCTION



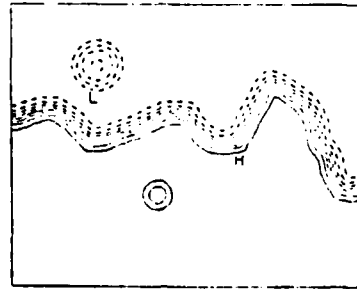
RAFOs FLOAT INITIALIZATION

FIGURE 5

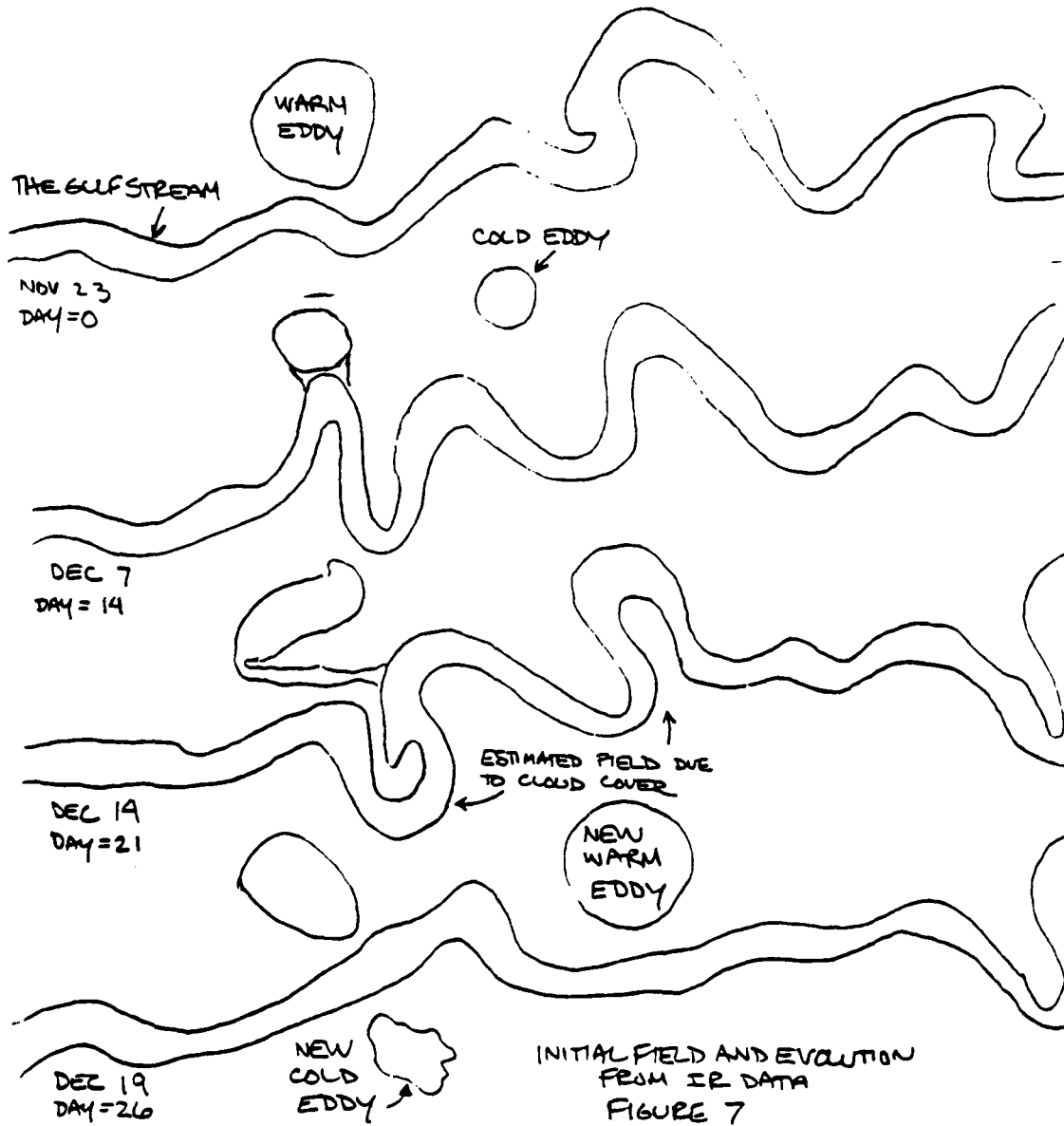


RAFS FLOAT FORECAST STREAMFUNCTION AT 700m

FIGURE 6



INITIAL  
QG STREAMFUNCTION



03:46:36

30-MAR-85

II.462

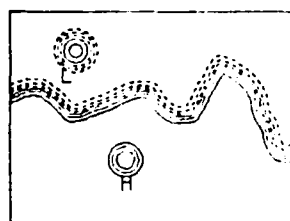
DAY

0.000 TO

13.5

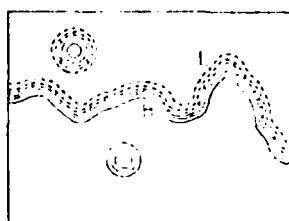
3/28/85 NEW G.S. WITH 200 CM/SEC UPPER LAYER MAX.VEL AND 5 B.L.  
 GAMMA=1.411 AVERAGE BOTTOM DEPTH 4500 DX=15.KM. I.R. DATA

STREAMFUNCTION AT 300. M  
 EVERY 1. DAYS



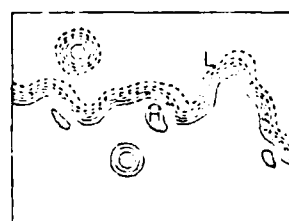
MIN=-3.54E+00 MAX=2.60E+00 CI=1.00E+00

TIME=0



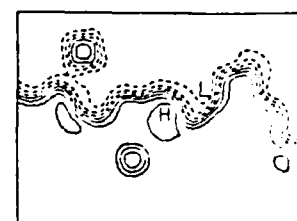
MIN=-3.60E+00 MAX=2.74E+00 CI=1.00E+00

TIME=1



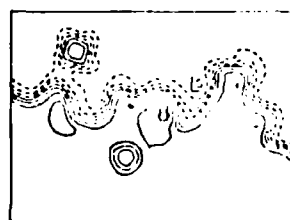
MIN=-3.70E+00 MAX=3.42E+00 CI=1.00E+00

TIME=2



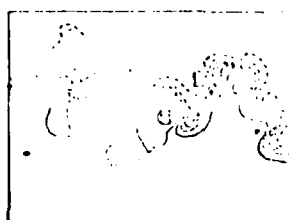
MIN=-3.77E+00 MAX=3.85E+00 CI=1.00E+00

TIME=3



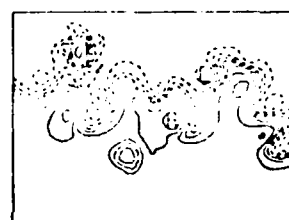
MIN=-4.09E+00 MAX=4.23E+00 CI=1.00E+00

TIME=4



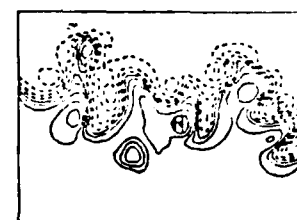
MIN=-4.47E+00 MAX=4.57E+00 CI=1.00E+00

TIME=5



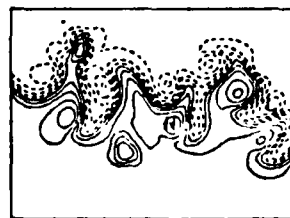
MIN=-4.67E+00 MAX=4.84E+00 CI=1.00E+00

TIME=6



MIN=-5.24E+00 MAX=5.03E+00 CI=1.00E+00

TIME=7



MIN=-5.75E+00 MAX=5.37E+00 CI=1.00E+00

TIME=8



MIN=-6.21E+00 MAX=5.18E+00 CI=1.00E+00

TIME=9



MIN=-6.82E+00 MAX=5.34E+00 CI=1.00E+00

TIME=10



MIN=-7.38E+00 MAX=5.38E+00 CI=1.00E+00

TIME=11

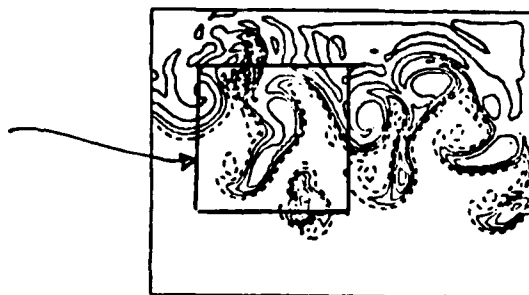


MIN=-7.88E+00 MAX=5.18E+00 CI=1.00E+00

TIME=12

SATELLITE IR FORECAST EXPERIMENT

FIGURE 8

DOMAIN OF  
ANALYSIS

100-5.122-01 100-5.74-01 100-5.402-01

QUASIGEOSTROPHIC KINETIC AND AVAILABLE GRAVITATIONAL  
ENERGY EQUATIONS

$$\frac{\partial}{\partial t} K = -\nabla \cdot (\vec{U}_g K) + \nabla \cdot (p_g \nabla p_{gt} + p_g \vec{U}_g \cdot \nabla \vec{\nabla} p_g + \beta p_g^2 \hat{z}) - (p_g \omega_a) + p_c$$

$$\dot{K} = \Delta F_K + \underbrace{\Delta F_\pi^t + \Delta F_\pi^\omega + \Delta F_\pi^\beta}_{\Delta F_\pi} + \delta p_\pi - t$$

$$\frac{\partial}{\partial t} A = -\nabla \cdot (\vec{U}_g A) - p_{gz} \omega_a$$

$$\dot{A} = \Delta F_A + b$$

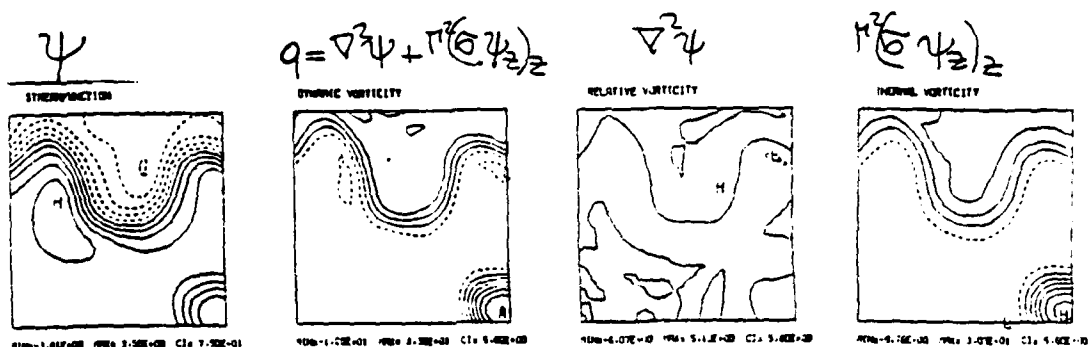
$p_g$  = geostrophic stream function

$$\vec{U}_g = \vec{\nabla} p_g \times \hat{k} \quad K = \frac{u_g^2 + v_g^2}{2} \quad A = \frac{\sigma \pi^2 (p_{gz})^2}{2}$$

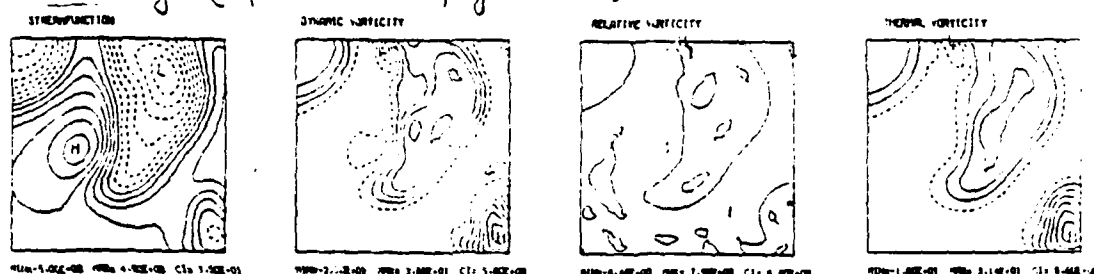
$$\omega_a = \text{ageostrophic vertical velocity} = -\frac{\partial}{\partial t} \left( \frac{\sigma \pi^2 p_{gz}}{2} \right) - \vec{U}_g \cdot \nabla (\sigma \pi^2 p_g)$$

Fig 10 II.464

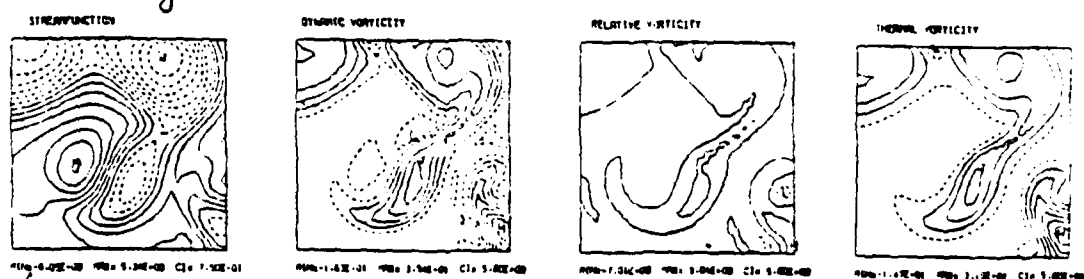
## VORTICITY ANALYSIS OF RING FORMATION PROCESS



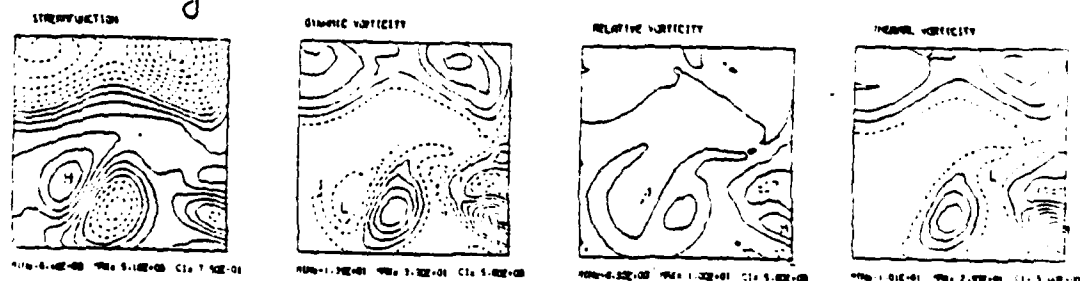
t = 5 days (after start of forecast)



t = 9 days



t = 11 days



t = 13 days



Fig 11

## VORTICITY DYNAMICS ANALYSIS

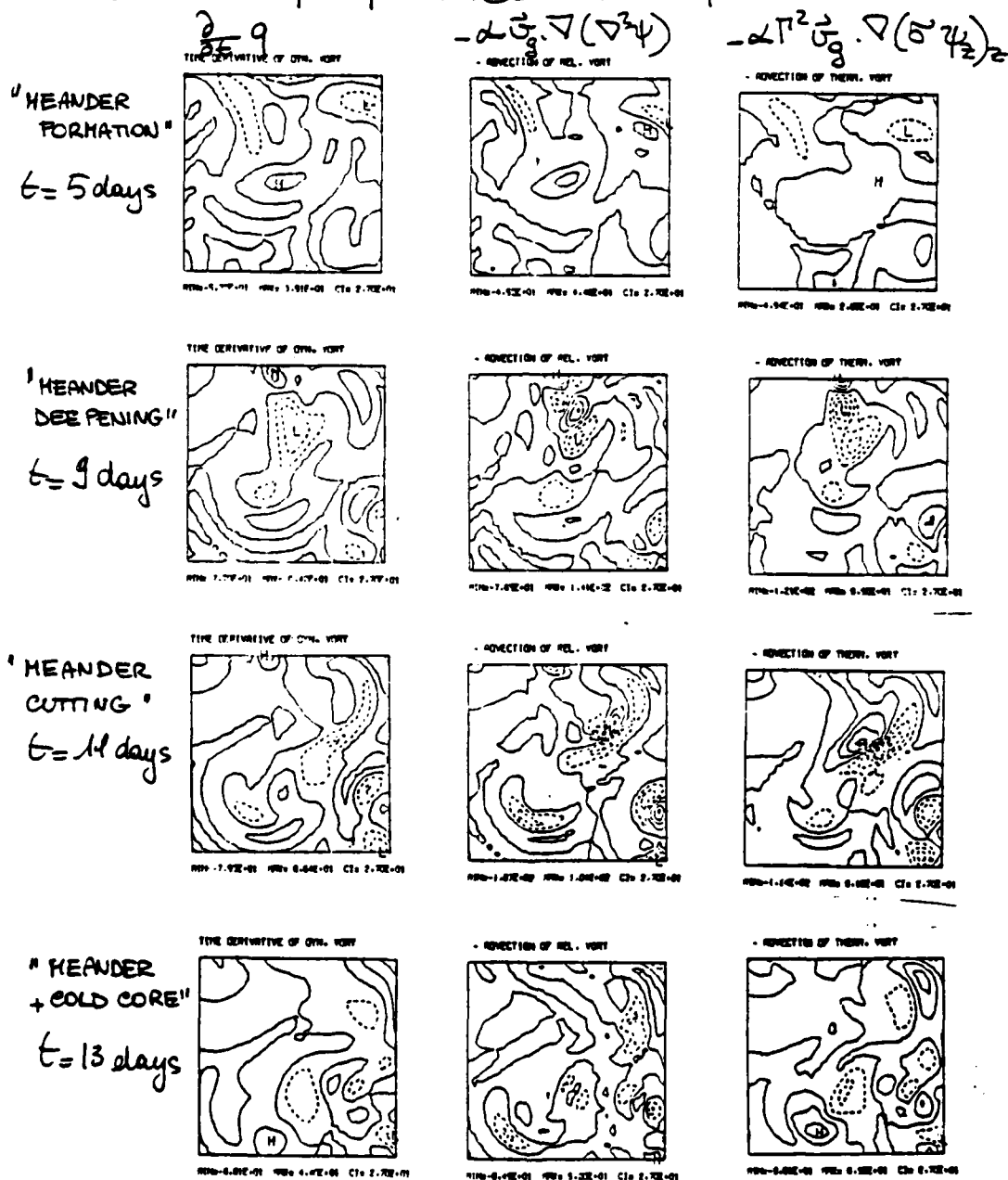
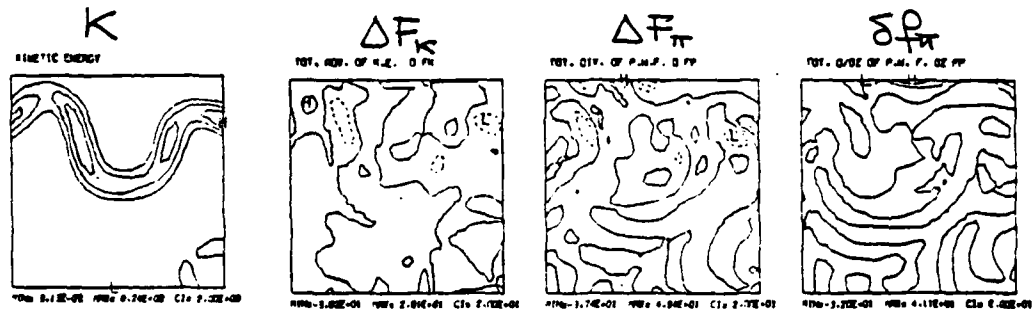
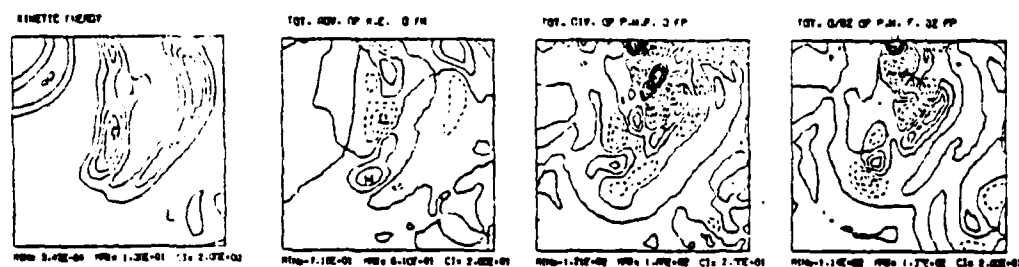


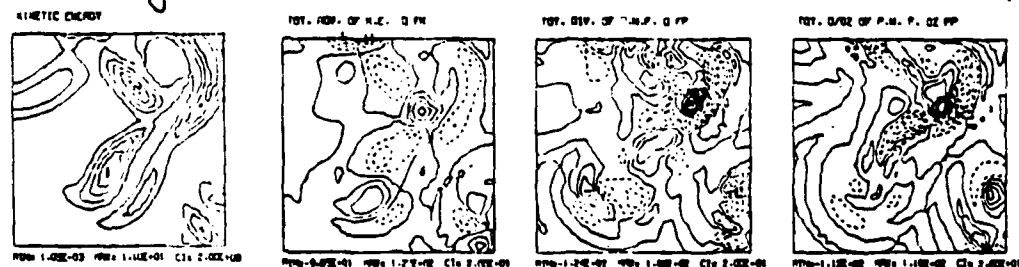
Fig 12  
KINETIC ENERGY DYNAMICS



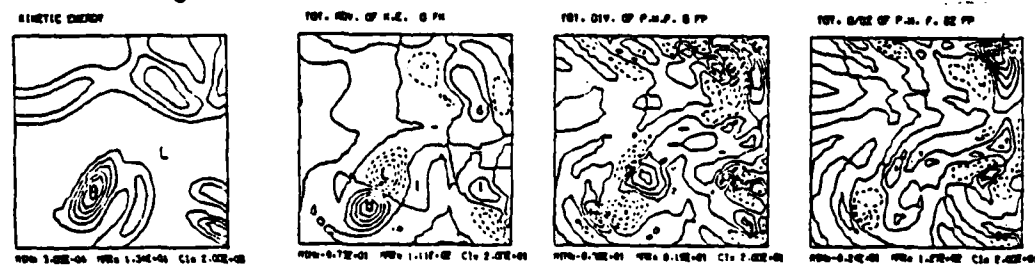
$t=5$  days



$t=9$  days

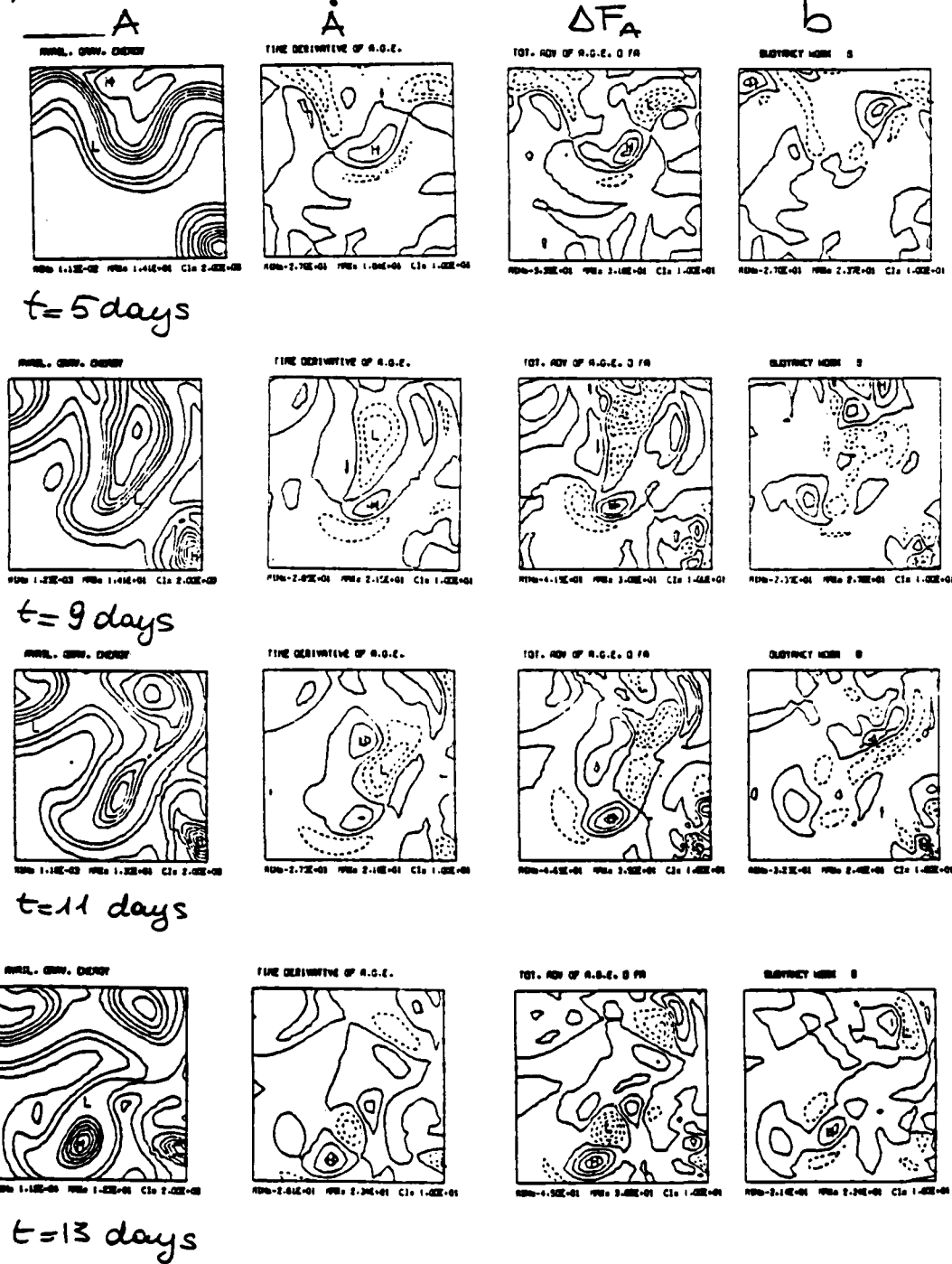


$t=11$  days



$t=13$  days

Fig 13  
AVAILABLE GRAVITATIONAL ENERGY DYNAMICS



Theoretical and Numerical Studies of  
Gulf Stream Ring Formation

by

L.J. Pratt  
(University of Rhode Island)

Abstract

A combination of theoretical and numerical tools are described for use in studying highly nonlinear mesoscale wave propagation problems in the ocean. In particular, the problem of Gulf Stream ring generation is focused upon and some preliminary calculations involving a simple one and a half layer model jet are presented. Analytic solutions for the path of the Stream using a 'long wave' theory show that, apart from simple meandering, the path can execute cycloidal meanders (in which the path folds back upon itself) and may even close upon itself to form an eddy. For moderate length disturbances, numerical integrations using the method of contour dynamics are able to reproduce the initial phases of the 'pinching off' process whereby meanders form rings. For isolated (non periodic) disturbances, it is found that one- and two-lobe meanders tend not to form rings, whereas three-lobed disturbances form rings more easily.

Introduction

The train of events which leads to the birth of a Gulf Stream ring or ring-like eddy is extremely involved. The commonly held scenario starts with a small disturbance in the path of the Stream growing to a

large amplitude meander through some type of infinitesimal instability. Strongly nonlinear effects then intervene, causing the large meander to steepen and fold back on itself. Eventually a segment of the Stream is pinched off and a ring is born. Of course, the picture is clouded by external influences such as older rings. The plan here is to concentrate on understanding the stage of evolution which begins with a finite amplitude meander and ends with the birth of a ring. At the start, external influences such as seamounts and exterior rings will be neglected, although these effects may be addressed later. The immediate questions to be addressed are as follows:

- 1) Are there preconditions that foretell the birth of a ring. It is well-known that all meanders do not form rings; what are the characteristics of the meanders that do form rings?
- 2) In terms of dynamics, what are the simplest conditions under which rings form; What are the essential ingredients?
- 3) What determines the area and volume of "pinched-off" fluid in a ring and what is the associated cross-stream heat flux?

Secondary questions include:

- 4) How do exterior rings interact with the Stream and how important are exterior rings to the ring formation process?
- 5) How do the New England Seamounts influence the generation of new rings?

#### Preliminary Results

Preliminary work has begun on a hierarchy of deductive Gulf Stream

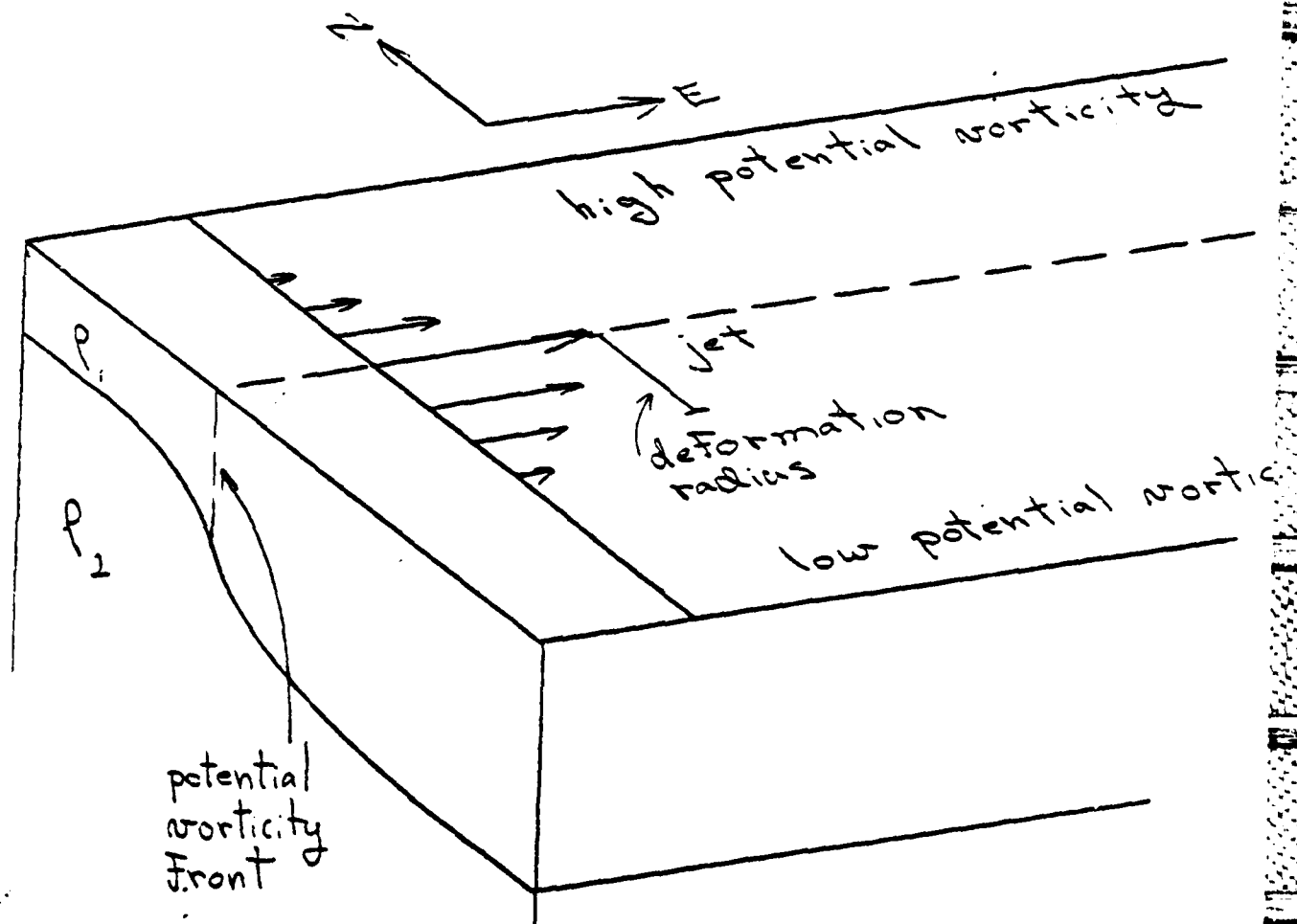


Figure 1. Sketch of model  $1\frac{1}{2}$ -layer jet. The eastward flowing jet is formed about a potential vorticity front in the upper layer.

models, the simplest of which is sketched in Figure 1. A quasi-geostrophic jet flowing from west to east is formed in the upper layer of a reduced gravity model. Along the centerline of the jet  $y=L(x,t)$  lies a potential vorticity front dividing low potential vorticity fluid in the south from high potential vorticity fluid in the north. (Potential vorticity fronts are a main feature of the potential vorticity distribution in the intense upper levels of the Gulf Stream (Hall, 1985)). Present studies concentrate on disturbances in the path of the jet from its equilibrium path  $L=\text{constant}$ .

In the study of formation of rings and other quasi-turbulent features the classical approach is to follow disturbances of initially small amplitude as they grow due to hydrodynamic instability. The approach used in the preliminary work is based on an entirely different philosophy. Instead of focusing on initial disturbances with small amplitude, one considers initial disturbances of large wavelength (or, more precisely, of curvature small compared to the Rossby radius of deformation). The advantage is that these "long wave" disturbances can often be described using closed form analytic solutions which are valid regardless of the disturbance amplitude. Thus, the strong nonlinearity which is essential to ring formation can be dealt with at the start. Even if closed form solutions cannot be found, the disturbance can often be studied using a nonlinear "path" equation - a considerable simplification over the full quasi-geostrophic potential vorticity equation.

For the model shown in Figure 1a the "long-wave" approximation gives the following equation for the position  $L(x,t)$  of the jet centerline

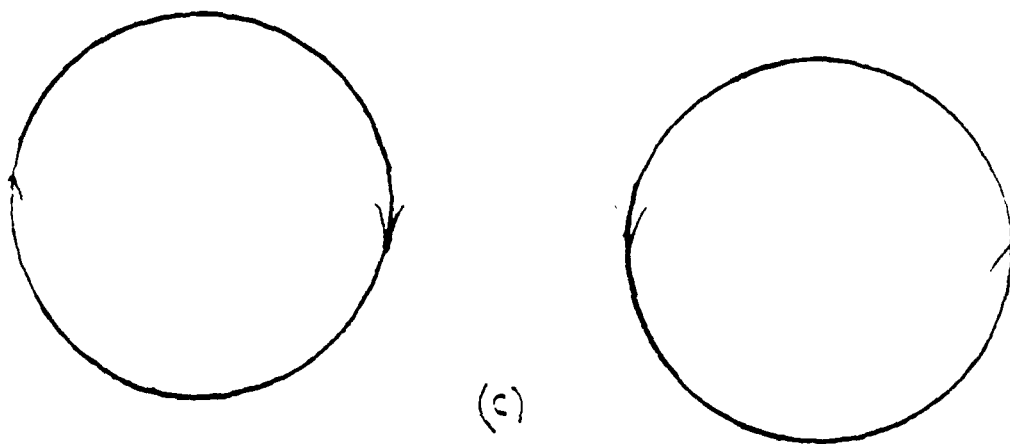
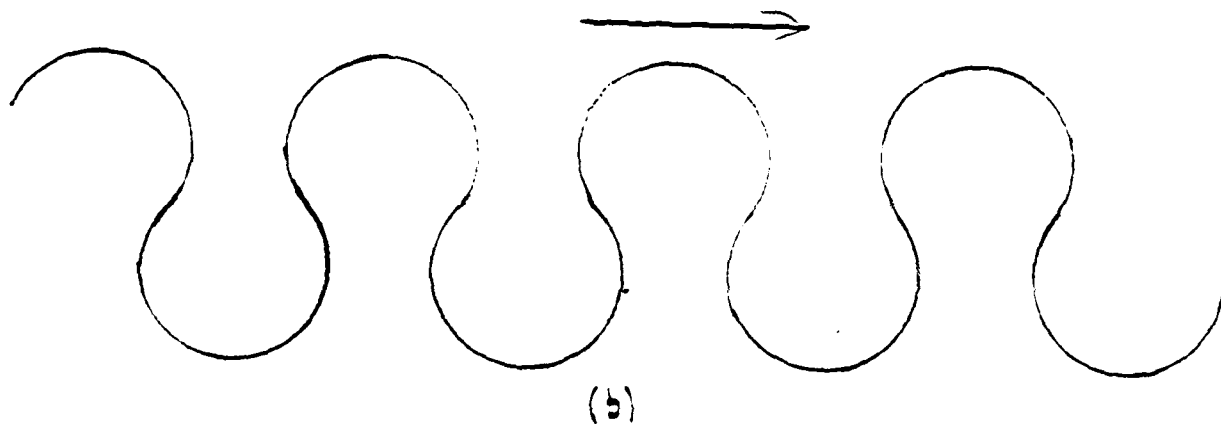
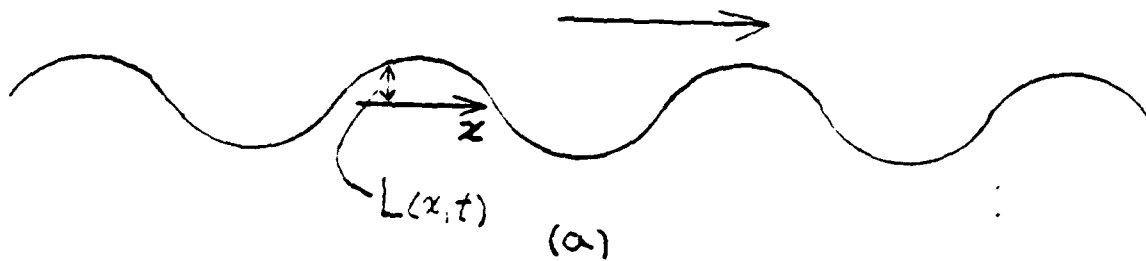
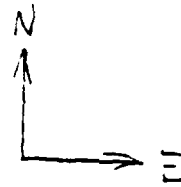


Figure 2. Special solutions to the path equation: (a) eastward propagating meanders (b) eastward propagating cycloids (c) circular warm and cold core eddies.



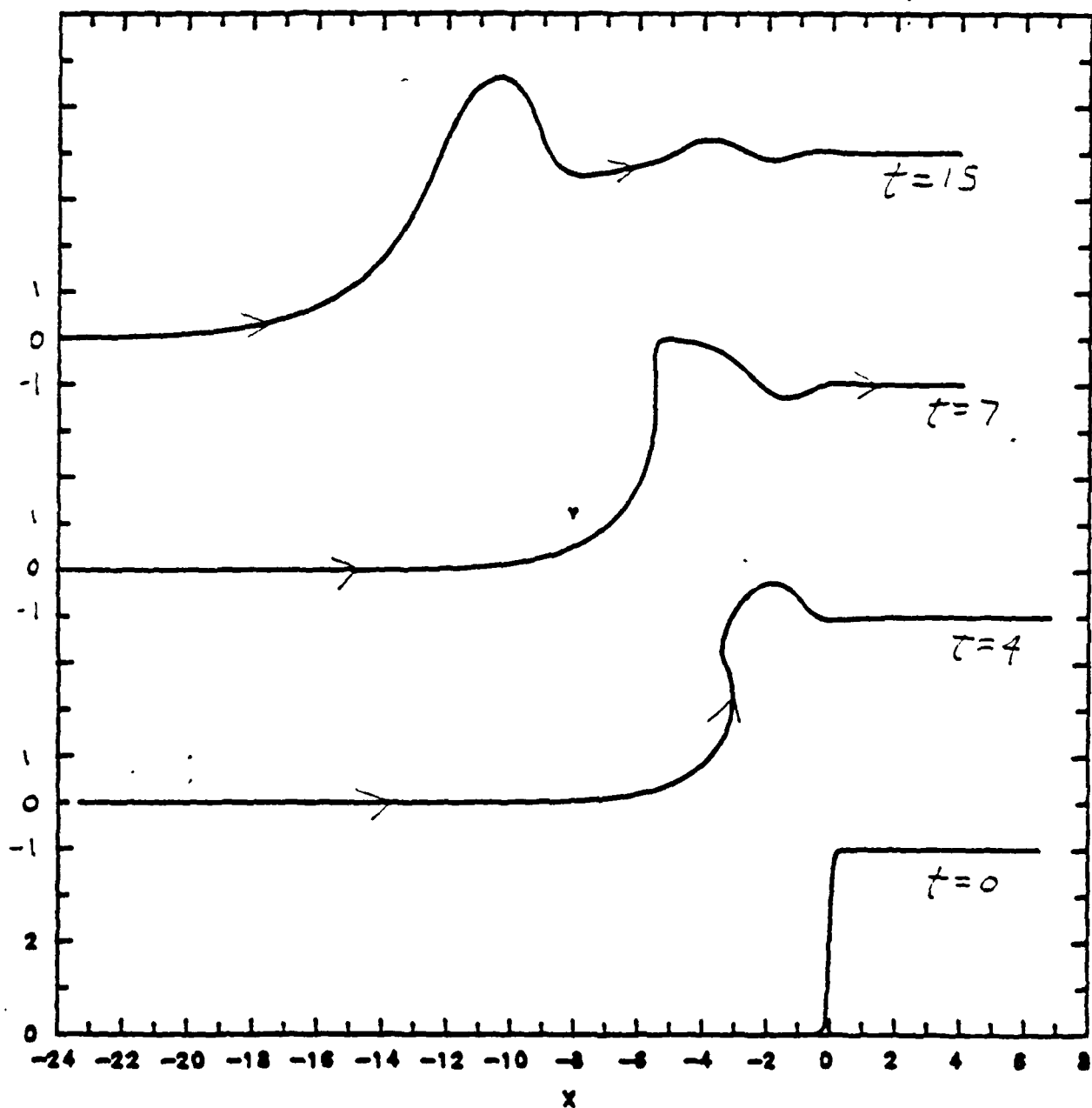
$$L_t - \frac{L_{xxx}}{2(1+L_x^2)^{3/2}} + \frac{2L_{xx}^2 L_x}{3(1+L_x^2)^{5/2}} = 0 \quad (1)$$

This equation is derived in Pratt and Stern (1985) and is valid as long as the curvature of the jet is small relative to the deformation radius. Some special solutions to (1) have been found and are sketched in Figure 2a-c. The first (Fig. 2a) is a meandering solution with the meanders propagating to the east. The second (Fig. 2b) is also a meandering solution except that the meanders fold back on one another, forming a "cycloid". The third (Fig. 1d) is a stationary circular ring-like eddy which may have either a cold or warm core. This sequence of solutions suggests that ring formation may be a feature of more general solutions to (1); however further work is required to answer this question.

Of course Gulf Stream meanders may develop large curvatures, in which case equation (1) is no longer valid. In this case the evolution of the jet path can be solved for using the method of contour dynamics, a numerical method in which one follows Lagrangian points on the jet centerline. Contour dynamics provides an algorithm which is computationally simpler than a full-blown finite difference model, often allowing more insight into specific dynamical processes. Also, the method is ideally suited to problems in which a contour (i.e. the jet centerline) folds back on itself or undergoes other complicated distortions. The method has been used successfully by Stern and Pratt (1985) to examine large-amplitude disturbances of vorticity fronts.

Preliminary calculations using contour dynamics have been made in

Figure 3. Evolution of the potential vorticity front from a 'step' profile in which the latitude of front  $L(x,0) = 0$  for  $(x < 0)$  and  $L(x,0) = 4$  deformation radii for  $(x > 0)$ . The scales  $x$  and  $L$  are given in deformation radii.



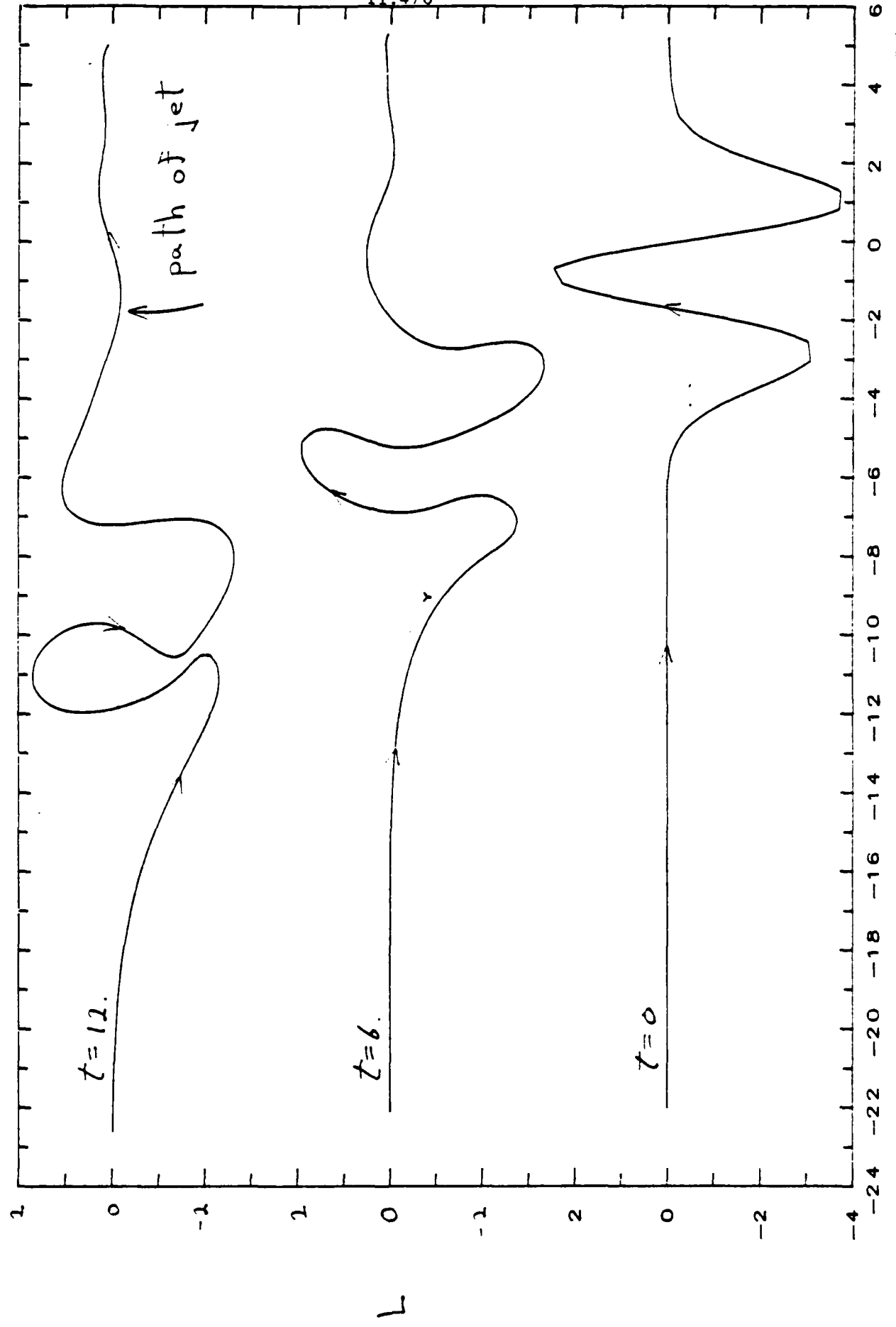
which the evolution of the path of the jet is followed from various types of initial shapes. For isolated initial disturbances consisting of one or two meanders, it has been found that rings do not occur unless unrealistically large amplitudes are introduced. For example, consider the initial state in which the jet path changes abruptly from one latitude to a slightly higher latitude. Figure 3 shows the evolution of the path from this shape up to time  $t = 15$ . (For visual convenience, this and all remaining figures have been drawn in a frame of reference moving to the west at unit speed. In a stationary frame the disturbances would move west.) Although 'wave breaking' occurs (the jet folds back upon itself) at  $t = 4$ , the jet later unfolds ( $t = 7$ ) and disperses ( $t = 15$ ).

Ring-like features are observed for moderate amplitudes if more structure is allowed in the initial disturbance. Consider the three-lobed meander shown at  $t = 0$  in Figure 4. The center lobe evolves into a rounded blob of anticyclonic fluid which begins to pinch off at  $t = 12$ . Figure 5 shows another such blob in detail as it pinches off forming a warm core ring-like eddy. The computation has been stopped at the point where grazing contact between different segments of front has occurred. Further integration requires the mild dynamical assumption that the 'chimney' of the ring be erased, so that the jet path evolves as a multiply connected contour.

### Discussion

The results of numerical integrations using contour dynamics suggest

Figure 4. Evolution of the path of the potential vorticity front from the 3-lobed initial disturbance shown at  $t = 0$ .



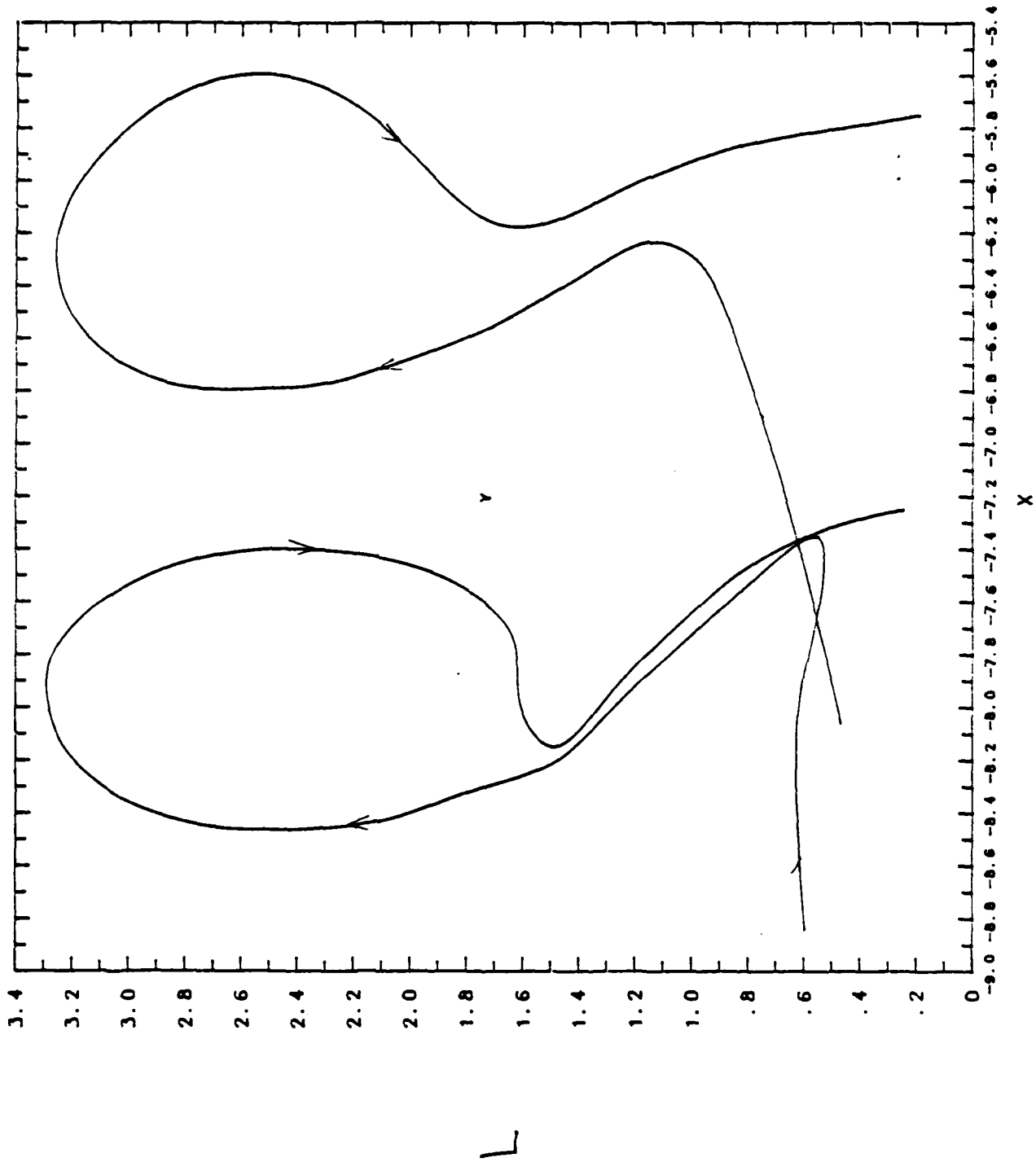


Figure 5. Detailed view of detaching warm core ring.

that ring-like eddies can form due to simple vortex induction and shearing effects. Other factors such as the beta effect or the presence of other rings do not appear to be essential (although they may certainly be important in the Gulf Stream). Further efforts are required to determine why certain types of initial disturbances form rings and why others do not. It is hoped that studies of solutions to the path equation (1) may help develop insight along these lines.

#### REFERENCES

- Hall, M.M. (1985) 'Horizontal and Vertical Structure of Velocity, Potential Vorticity, and Energy in the Gulf Stream', Ph.D. Thesis, MIT/WHOI, WHOI-85-16.
- Pratt, L.J. and M.E. Stern (1985) 'Dynamics of Potential Vorticity Fronts and Ring Formation' (in preparation).
- Stern, M.E. and L.J. Pratt (1985) 'Dynamics of Vorticity Fronts', Submitted to J. Fluid Mech.

GULF STREAM TOMOGRAPHY:  
PRELIMINARY RESULTS FROM AN EXPERIMENT

John L. Spiesberger and Robert C. Spindel

Department of Ocean Engineering  
Woods Hole Oceanographic Institution  
Woods Hole, Massachusetts 02543

## ABSTRACT

In October 1984, an acoustic tomography experiment was carried out near the Gulf Stream. A bottom mounted acoustic source (center frequency 400 Hz) transmitted signals having 10 ms resolution to three bottom mounted receivers at ranges between 20 and 50 km. The experiment was designed to determine whether steep ray paths could be observed after reflecting from the rough surface and bottom, and to determine whether such rays can be used for tomography. Strong ray arrivals (about 30 to 40 dB signal-to-noise ratios) were observed at all three receivers, even during the onset of hurricane conditions. Preliminary inversions compare favorably with CTD measurements taken during the experiment.



## I. INTRODUCTION

A numerical simulation of a bottom mounted tomographic array beneath the Gulf Stream revealed the capability of mapping significant features of the Gulf Stream<sup>1</sup>. It is simpler and less expensive to mount tomographic instruments on the bottom than to suspend them at mid-depth on moorings. However, when the instruments are bottom mounted and are separated by about 20 km, the ray paths are steep and reflect from the wavy surface. Also, there is some interaction between the acoustic signal and the bottom near the instruments which may or may not degrade the received signals. Previous observations of surface and bottom reflected paths have been made in tomographic experiments<sup>2</sup>, but these reflected paths grazed the boundaries at small angles (between zero and about three degrees). It was not known whether steeper ray paths (20 degrees) would attenuate or complicate the multipath records to the extent where tomographic inversions would be impossible. Hence, the present experiment was done to determine the feasibility of using bottom mounted instruments and steep ray paths for tomographic reconstruction of the ocean. (The experiment was not designed to provide accurate reconstructions of the Gulf Stream region.)

The inversion procedure relates the measured travel times of the acoustic signals to the sound-speed or current field. The relation is nonlinear and so a linear approximation is made<sup>3</sup>. The linear approximation is accurate for steep ray paths subject to the variability of the Gulf Stream<sup>4</sup>. It is simpler to understand the results of linear inversions than of nonlinear inversions<sup>5</sup>.

The experiment is described in Section II. Some of the data are discussed in Section III. The identification of the observed arrivals is discussed in Section IV. A preliminary inversion of the sound speed field from

the acoustic travel times is presented in Section V. A discussion follows in Section VI.

## II. EXPERIMENT DESCRIPTION

An acoustic source and three acoustic receivers were placed about one meter above the bottom on the continental slope near Cape Hatteras (Fig. 1). The receivers to the north and east of the source (denoted  $R_{\text{north}}$  and  $R_{\text{east}}$ ) were about 20 km from the source. The south receiver ( $R_{\text{south}}$ ) was about 50 km from the source. The water depth is about 3.5 km and the instruments were placed under the climatological position of the Gulf Stream.

The acoustic source is peak power limited, so it is necessary to transmit a large time-bandwidth signal and use pulse compression techniques so that the signal can be reliably detected at the receivers. A 400 Hz carrier was phase modulated by a 5.11 s linear maximal shift register sequence. Forty-two consecutive sequences were sent so the transmission duration was  $42 \times 5.11 = 215$  s. The bandwidth of the transmission was about 100 Hz. This signal is equivalent to transmission of a single pulse having a resolution of 0.01 s. The signal processing gain was about 43 dB. The expected peak signal-to-noise ratio at 20 km range is about +44 dB (Table I). Details of similar processing schemes can be found elsewhere<sup>6-8</sup>.

The source was turned on at four hour intervals on odd yeardays (1 January is day one). These transmissions were intended to extend for a two-month period. However, due to an unfortunate hardware failure in the source, data was obtained only on yeardays 285 and 287.

Eight CTD stations were taken to the bottom between the acoustic instruments on yeardays 282 and 283.

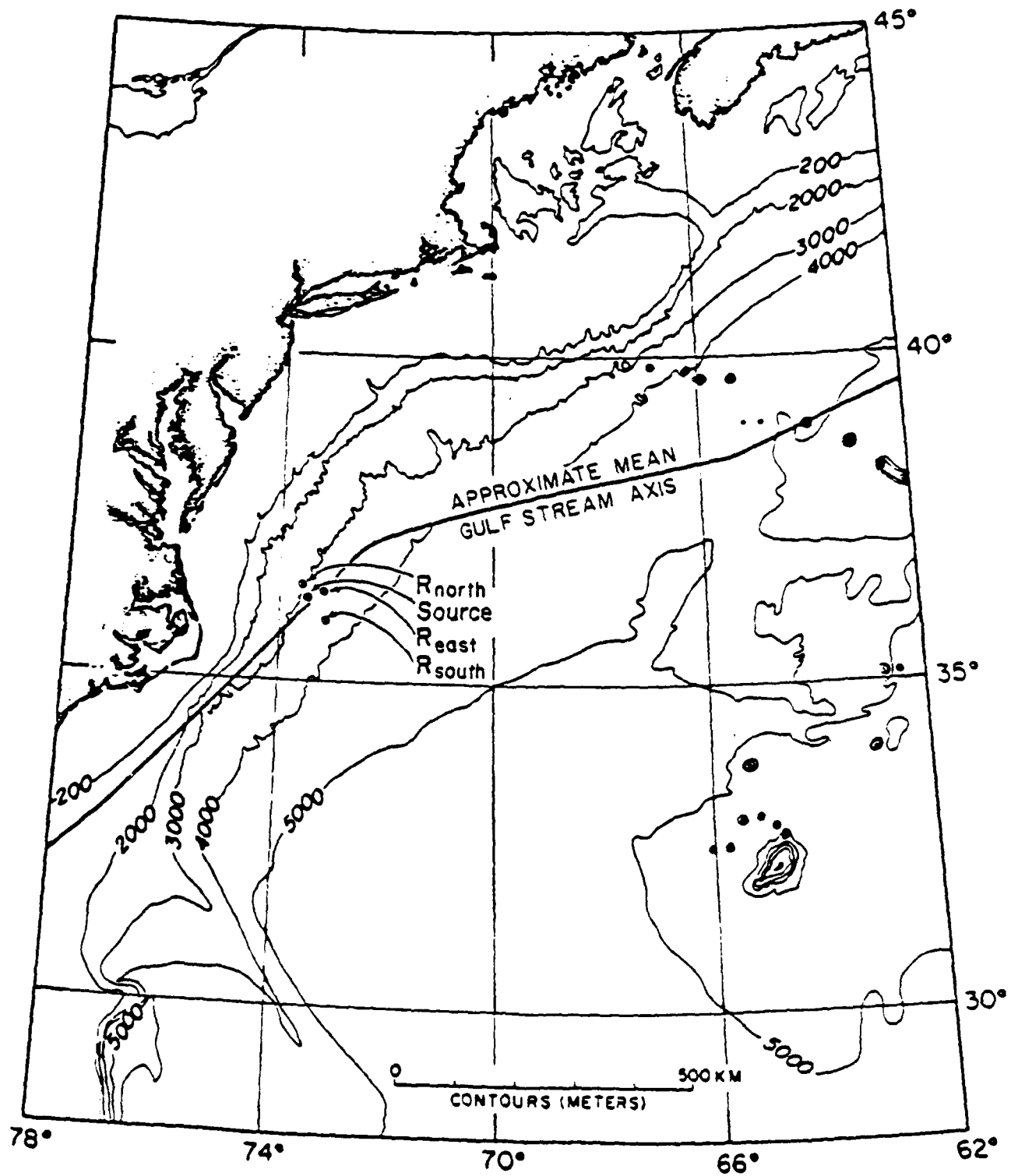


Fig. 1. The location of the tomography experiment.

Source level re 1 $\mu$ Pa at 1 m	+186 dB
Spherical spreading loss at 20 km	- 86
In-situ absorption at 400 Hz at .02 dB/km	- 0.4
Noise in a 1 Hz band at 400 Hz	- 70
Additional noise in a 100 Hz band	- 20
Surface scattering loss for 1 reflection	- 8
Pulse compression and coherent averaging for 3 min	<u>+ 43</u>
Approximate peak signal-to-noise ratio	+ 44 dB

Table I. The calculation of the received signal-to-noise ratio. The calculations are made for a ray which reflects once from the surface at an angle of about 20 degrees with respect to the horizontal in a sea with an r.m.s. surface roughness of 1.2 m.

### III. THE DATA

Some of the processed data are shown in Fig. 2 for the north receiver. The largest arrival is about +43 dB above the noise level as expected. The other signals originate from nonlinearities in the power amplifier located in the source. The other data at this receiver and at the east receiver look like that shown in Fig. 2. During yearday 285 and 287, a hurricane was moving into the area and the surface was not calm.

The amplitudes of the signals do not fluctuate as do multipath arrivals at long ranges in the ocean. At long ranges (order 1000 km) at 400 Hz, the internal wave field scatters the sound so that the amplitude is unsteady<sup>9</sup>. Evidently, at 20 km range and for this geometry, geometric optics is applicable and therefore the amplitude is steady.

There are two prominent arrivals at the south receiver.

### IV. IDENTIFICATION

A reference sound speed profile is constructed by averaging 195 historical hydrographic stations (Fig. 3). These stations were not measured during this tomography experiment. The stations consist of both Slope and Sargasso sea waters.

The theoretical arrival times of the rays at each receiver compare well with the measured times (not shown). The rays are identified by  $\pm N(U, L)$ , where rays leaving the source upwards (downwards) take the positive (negative) sign, and the total number of turning points plus reflections is  $N$ . The total number of surface and bottom reflections is given by  $U$  and  $L$ , respectively.

The prominent arrival observed at the north and east receiver is classified as +1 (1,0). It is from a ray which leaves the source at about 17 degrees

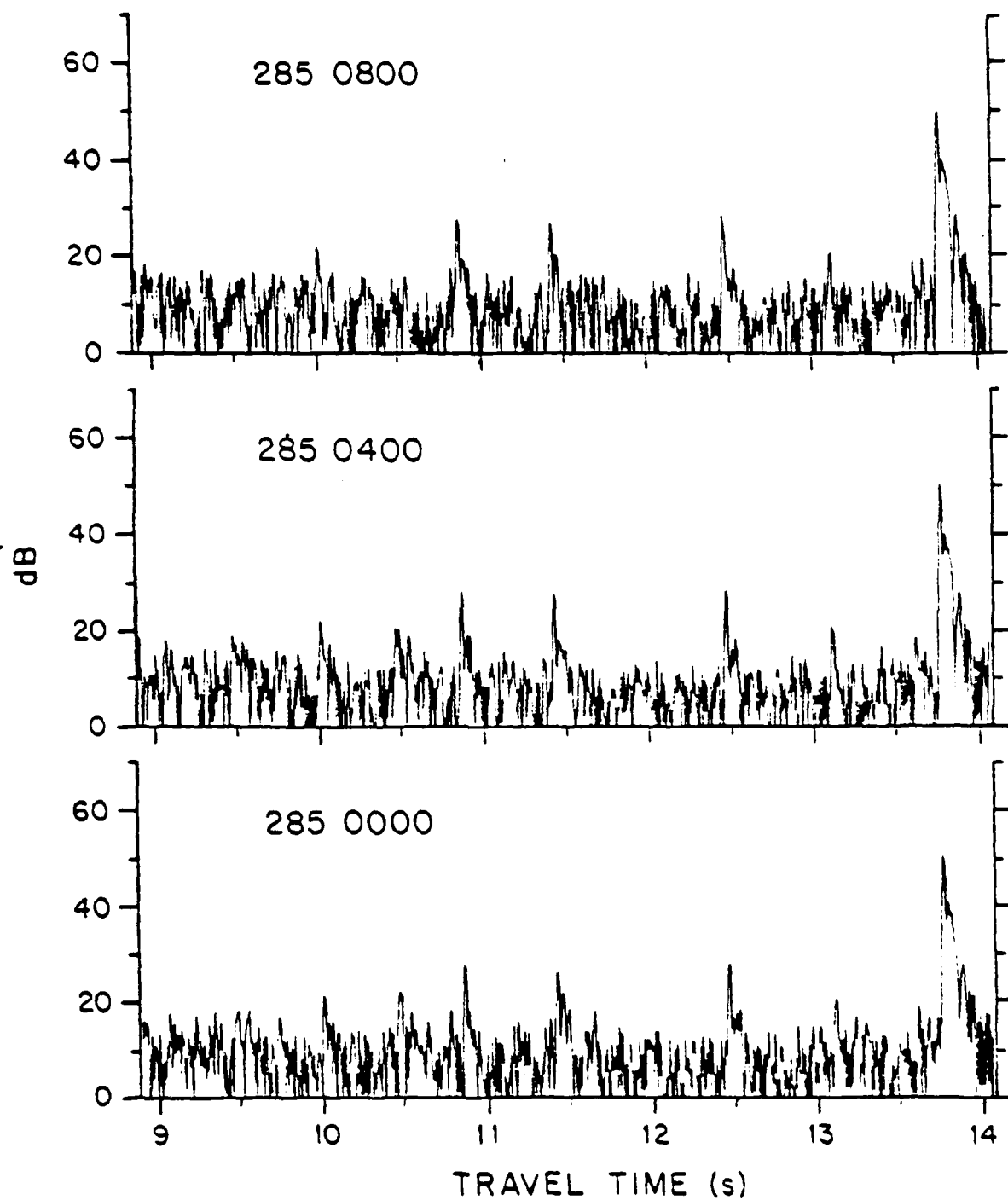


Fig. 2. The amplitudes of three records at the north receiver on yearday 285, 1984 at the indicated hour (GMT).

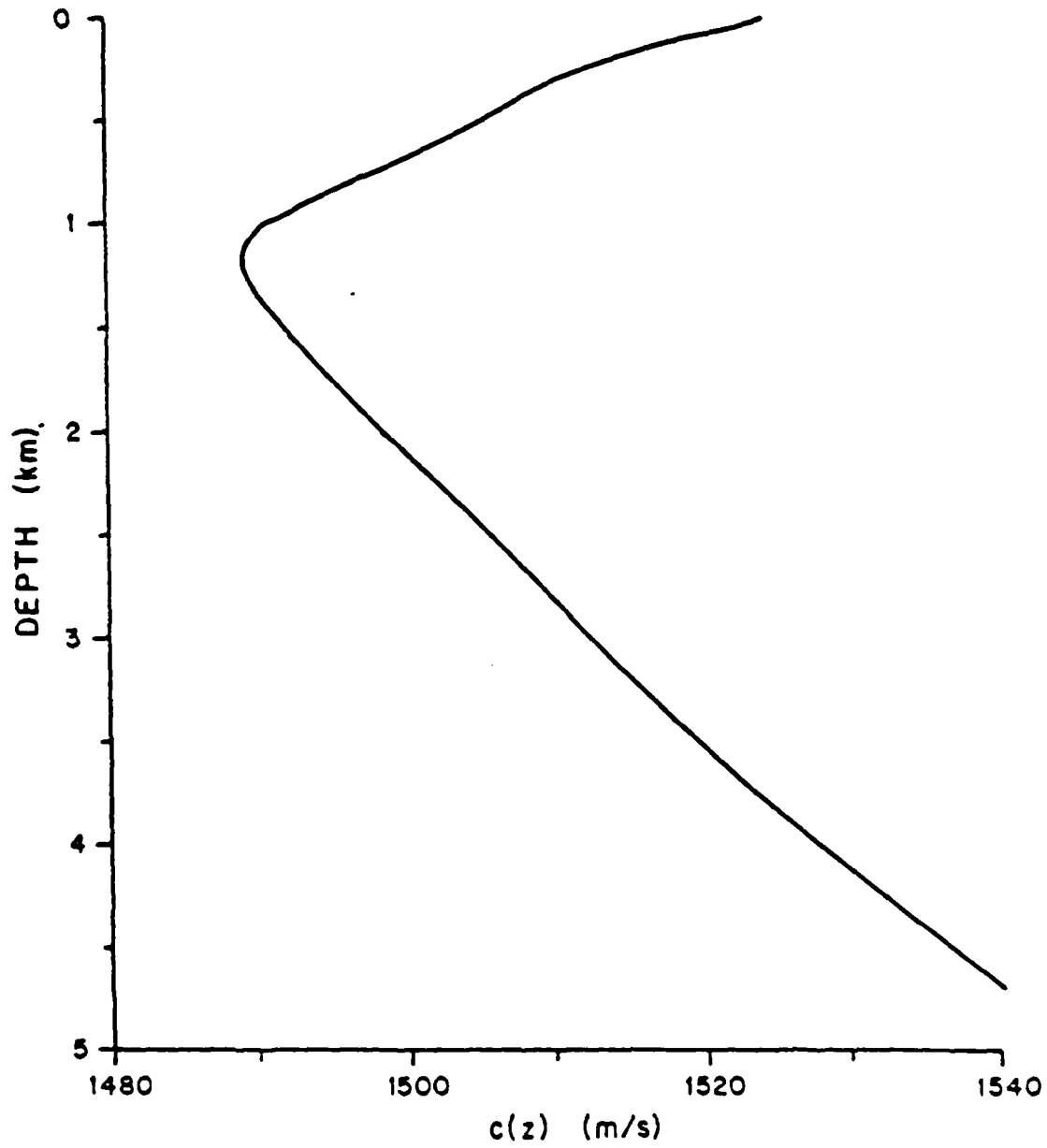


Fig. 3 The reference sound speed profile.

with respect to the horizontal. Because the ray is steep, the inclination remains near 17 degrees throughout the water column (Fig. 4). There are three prominent arrivals at the south receiver classified +1 (0,0) and +3 (2,1). The inclination angles of the +1 (0,0) and +3 (2,1) rays are about 6 and 15 degrees, respectively.

The purpose of this experiment was to determine whether the steep ray paths which interact with the rough surface and bottom could be used to construct tomographic maps. The arrivals are stable, resolvable, and identifiable, so they can be used for tomographic constructions.

## V. PRELIMINARY INVERSIONS

The travel times of the rays computed through the reference profile (Fig. 3) are denoted  $T_0$ . The measured travel times are denoted  $T_1$ . The differences,

$$\delta T_1 = T_1 - T_0, \quad (1)$$

are the data used for the inversion. The  $\delta T_1$  are of order 0.1 s (Fig. 5). Corrections due to clock drifts in the instruments have been made. The contributions to  $\delta T_1$  are principally due to:

- a) Variations of the sound-slowness (inverse sound speed) profile from the reference profile.
- b) Uncertainties in the distances between the instruments.

The travel time variations due to a) are of order  $0.1 \text{ s}^4$ . To reduce errors due to b), the tomographic instruments were acoustically surveyed from the ship with the aid of LORAN-C. The surveying technique leads to a range error of about 0.2 km, which translates to a travel time uncertainty of 0.13 s.



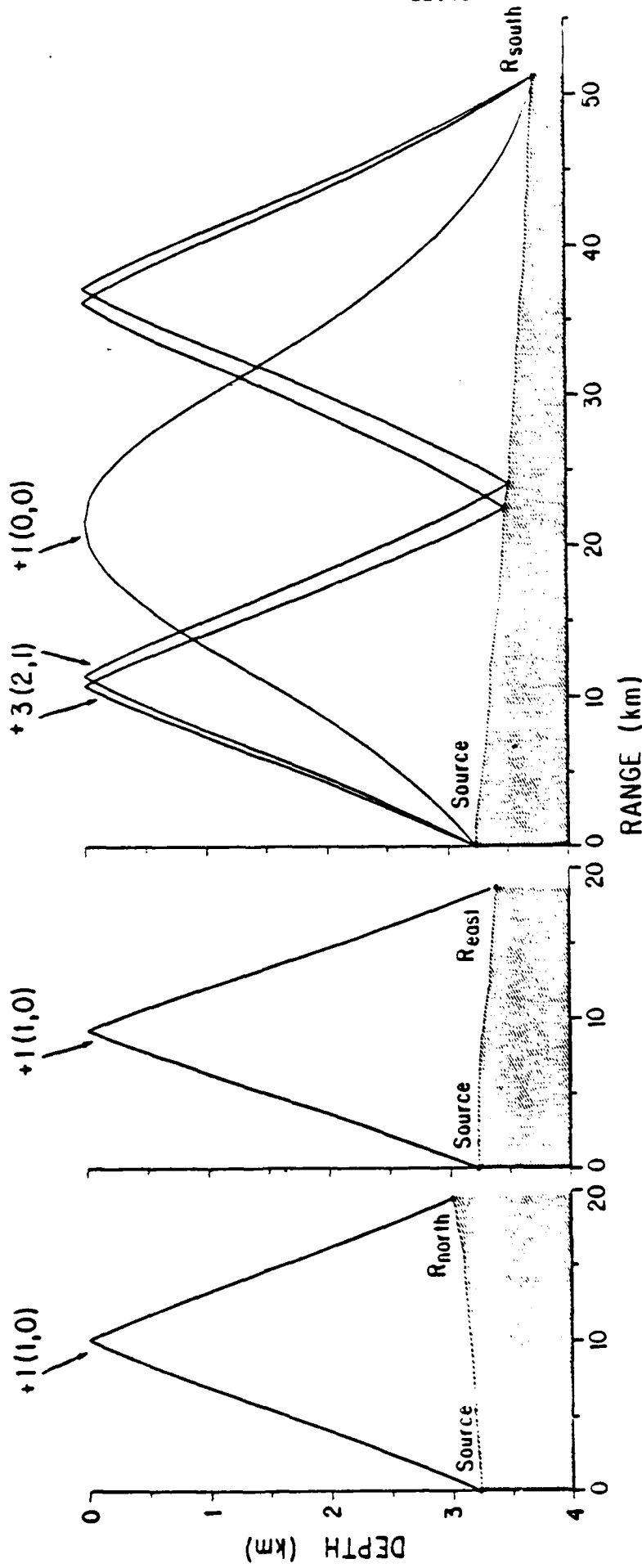


Fig. 4. The reference ray paths.

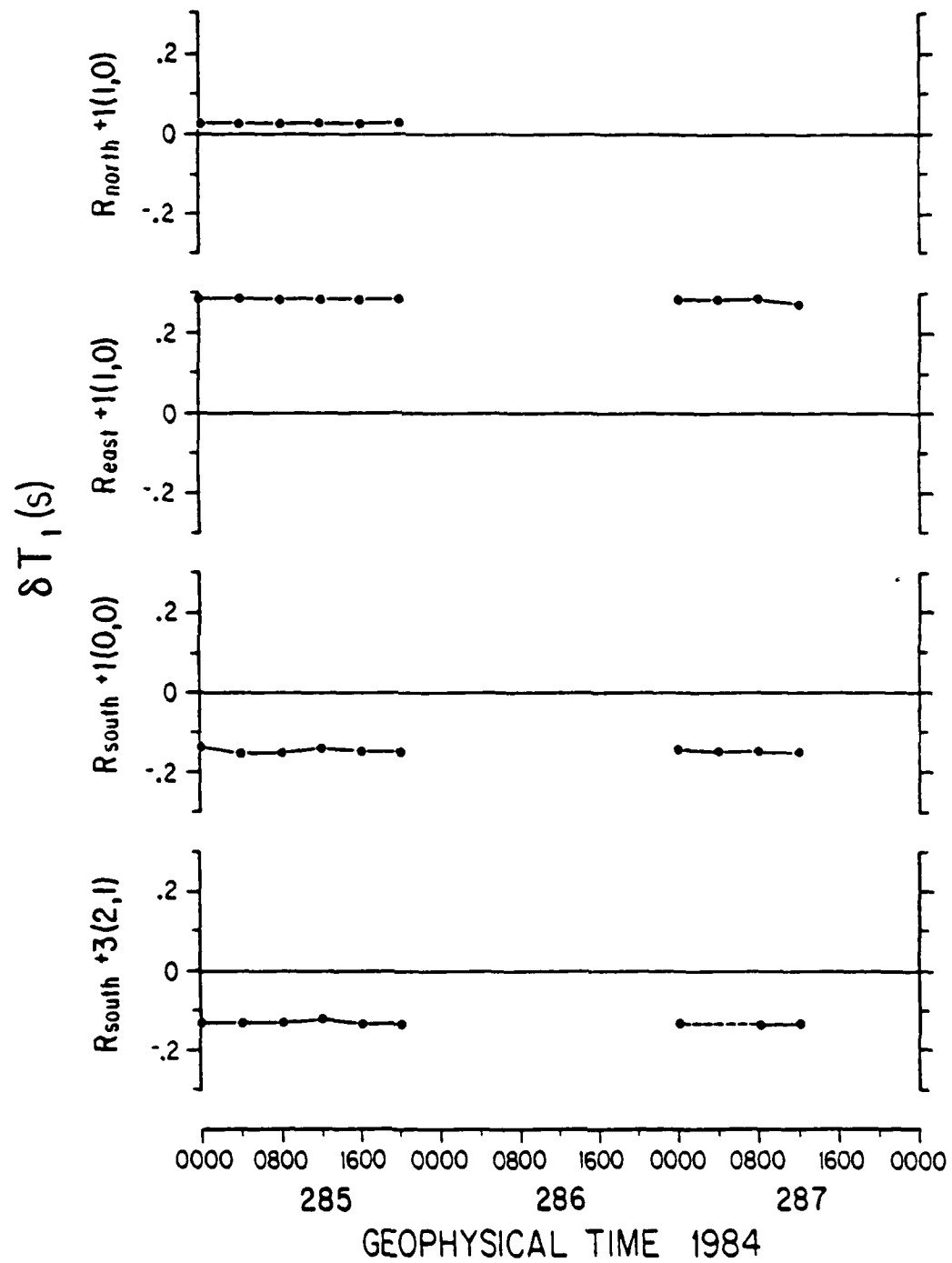


Fig. 5. The data (dots) used for the geophysical inversion. The dashed line indicates a gap.

The relation between the data and models of the sound-slowness (hereafter S.S.) and instrument separation is nonlinear<sup>3,4,10</sup>. However, a good linear approximation for  $\delta T_1$  due to S.S. is

$$\delta T_1 \cong \tilde{\delta T}_2 = \int_{r_0} ds \, \delta n, \quad (2)$$

where  $r_0$  is the reference ray path,  $ds$  is an increment of arc on the path, and  $\delta n$  is the change of S.S. relative to the reference profile<sup>4</sup>. A linear approximation between  $\delta T_1$  and the instrument location can also be made<sup>10</sup>.

A Wiener filter is used to reconstruct the sound speed field from the acoustic travel times (Fig. 5) by methods previously described<sup>10</sup>. The inversions here are preliminary and may or may not be significantly improved. The model is not significantly different from the reference profile at one standard deviation (Fig. 6). The model is also consistent with the CTD measurements. A satellite photograph (courtesy Peter Cornillon) of the sea surface temperature shows the Gulf Stream front to the north of the tomographic array (not shown), which implies that Sargasso sea water surrounds the instruments. Since the Sargasso waters are warmer (acoustically faster) than the reference profile, the inversion results are qualitatively consistent with the satellite measurement.

## VI. DISCUSSION AND PLANS

This experiment demonstrated the feasibility of using bottom-mounted tomographic instruments to generate tomographic maps of the Gulf Stream region.

Our plan is to determine how well the fluxes and gradients of mass, heat momentum, and vorticity can be measured using reciprocal transmissions for various instrument configurations (not exclusively bottom mounted). The goal

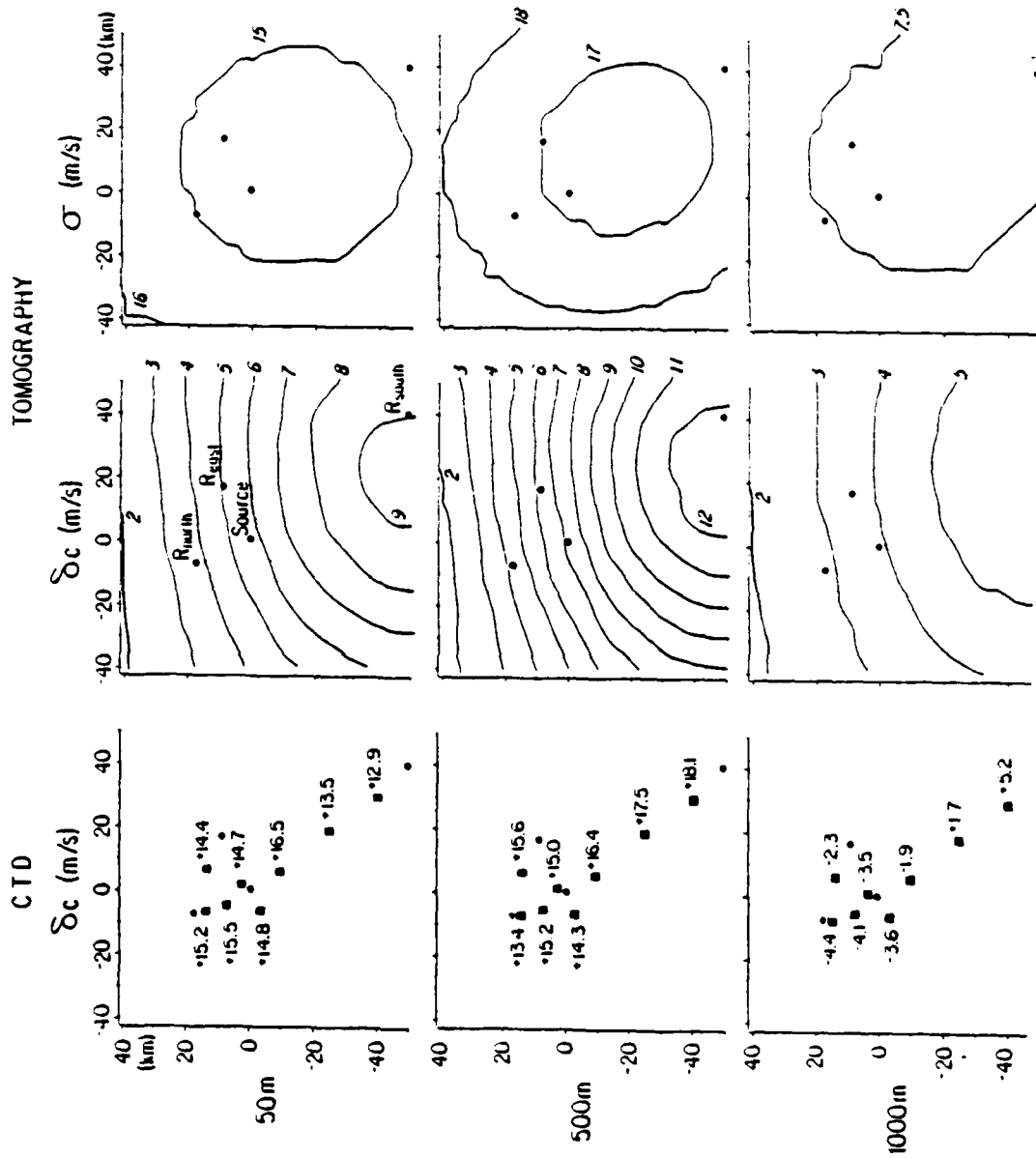


Fig. 6. The preliminary acoustic inversion for day 285 hour 0000 (GMT) is compared with some results from the CTD survey (left column, squares). The contour interval for the acoustic inversion is 1 m/s. The error bars (right column) indicate one standard deviation. The horizontal axis is positive to the east. The origin of the coordinate system is located at the acoustic source located at  $36^{\circ} 15.22'N$  and  $13^{\circ} 28.15'W$ .

of these numerical simulations and experiments is to better understand the dynamics of the Gulf Stream. Two questions of interest are:

- a) How and where does the Gulf Stream region dissipate the vorticity which was added to the surface layer over the North Atlantic gyre?
- b) How does the Gulf Stream radiate mesoscale energy into the Atlantic?

#### ACKNOWLEDGEMENTS

We thank Stephen Liberatore and Frederick Schuler for their work on the electronics in the source and the receiver. We also are grateful to Paul Boutin and John Kemp for the design and handling of the instruments at sea and on shore, and to Maxine Jones for her programming work. This work is supported by the Office of Naval Research under Contract N00014-84-C-0278.

## REFERENCES

1. P. Malanotte-Rizzoli, B. Cornuelle, and D. Haidvogel, "Gulf Stream acoustic tomography modelling simulations," *Ocean Modelling*, 46, 1982.
2. J. Spiesberger, T. Birdsall, K. Metzger, R. Knox, C. Spofford, and R. Spindel, "Measurements of Gulf Stream meandering and evidence of seasonal thermocline development using long-range acoustic transmissions," *J. Phys. Ocean.*, 13(10), pp 1836-1846, 1983.
3. J.L. Spiesberger and P. Worcester, "Perturbations in travel time and ray geometry due to mesoscale disturbances: a comparison of exact and approximate calculations," *J. Acoust. Soc. Am.* 74(1), pp 219-225, 1983.
4. J.L. Spiesberger, P. Rizzoli, and E. Welsh, "Travel time and geometry of steep acoustic rays subject to Gulf Stream variability," *J. Acoust. Soc. Am.*, in press.
5. R. Parker, "Understanding inverse theory," *Ann. Rev. Earth Planet. Sci.*, 5, pp 35-64, 1977.
6. S.W. Golomb, Shift Register Sequences (Holden-Day, San Francisco, 1967), Chaps. 3 and 4.
7. J.L. Spiesberger, R. Spindel, and K. Metzger, "Stability and identification of ocean acoustic multipaths," *J. Acoust. Soc. Am.* 67(6), pp 2011-2017, 1980.
8. K. Metzger, "Signal processing equipment and techniques for use in measuring ocean acoustic multipath structures," Cooley Electronics Laboratory Technical Report No. 231, The University of Michigan, Ann Arbor, Michigan, December 1983.
9. S.M. Flatte, R. Dashen, W. Munk, K. Watson, and F. Zachariasen, Sound transmission through a fluctuating ocean, (Cambridge University Press, 1979).
10. B.C. Cornuelle, "Inverse methods and results from the 1981 ocean acoustic tomography experiment," Ph.D. thesis, Massachusetts Institute of Technology/Woods Hole Oceanographic Institution, 1983.

Numerical Modelling and Assimilation of Altimeter Data  
in the Gulf Stream System: Recent Results

by

J. Dana Thompson, H.E. Hurlburt and John Kindle  
Ocean Dynamics and Prediction Branch, Code 323  
Naval Ocean Research and Development Activity  
National Space Technology Laboratories  
Mississippi

Abstract

The dynamics of portions of the Gulf Stream System (GSS) have been studied via numerical integrations, comparisons with in-situ and remotely-sensed data, and simplified analytical models. In the southern portion of the GSS we have simulated and explained the dynamics of many consistently observed features of the Gulf of Mexico Loop Current, including its northward penetration, westward bending, large amplitude meandering, quasi-periodic generation of warm-core anticyclonic rings, and the production of a cyclone-anticyclone pair in the western Gulf. A simple potential vorticity-conserving model can account for the size of the shed eddies, the eddy-shedding period, and the westward eddy drift. Detailed regional and basin-wide eddy-mean energetics indicate that barotropic, baroclinic, and mixed-instabilities can exist in this portion of the GSS. However, the basic warm-core ring generation process is dominated by a barotropic instability and is well simulated by a single vertical mode, reduced-gravity model.

More recent modelling work has concentrated on the dynamics of the Gulf Stream downstream from Cape Hatteras. There the generation of deep flow by instabilities of the Gulf Stream can provide a mechanism whereby the New England Seamount Chain influences the mean path of the Stream, the amplitude of its meanders, and the distribution of the eddies in the vicinity of the seamounts, even when the Gulf Stream does not directly impinge on the topography. The dynamics of this process closely parallel those in the Gulf of Mexico. However, a single vertical mode reduced-gravity model and a two-layer model with small-amplitude topography consistent with the quasi-geostrophic assumption give results quite different and less realistic than those from the two-layer primitive equation model with full topography.

Having established the basic validity of the numerical model, we have applied it to the assimilation of sea surface height information from a satellite-borne altimeter. Three studies on sampling strategies, geoid error and initialization, and the dynamic conversion of surface to subsurface information were undertaken for the Gulf of Mexico model. Because of the important similarities between the dynamics of the Loop Current and those of the Gulf Stream downstream of Cape Hatteras results from those studies can be applied to the assimilation of GEOSAT data in the upcoming REX and SYNOP experiments in the NW Atlantic.

## 1. Introduction

In the next decade oceanographers will organize and participate in several exciting and ambitious programs, inspired in part by the rapidly emerging technologies of satellite remote sensing, new in-situ instrumentation, a new generation of numerical ocean models, and a new class of supercomputers. These programs will be part of a larger effort to monitor, understand, and predict the ocean and atmosphere on many time and space scales. Obvious practical applications of this work will encompass climate studies, naval operations, and commercial activities. In the near future at least one of these programs will include a concerted attempt to predict the evolution of some part of the Gulf Stream System (GSS). Before addressing that task, we are obliged to examine the prediction problem in light of our basic understanding of Gulf Stream dynamics and the potential of present and future observing systems. While it is possible to make very accurate predictions of some ocean parameters (tides, for example) with little or no basic understanding of ocean dynamics or physics, for most elements of ocean prediction, where we lack adequate observing systems and historical data, our knowledge of ocean dynamics is critical for efficient use of very limited resources.

There are many types of ocean prediction and several classes of phenomena for which predictions are desirable. As noted by Hurlburt (1984) and shown in Table 1, one means of distinguishing various classes of ocean processes is their response to atmospheric forcing. Each class has its own particular requirements for (1) accuracy of the initial state, (2) time scales for skillful forecasts, (3) modeling strategy, (4) data types, and (5) data acquisition and sampling strategies. For the most part predictions related to the GSS, at least those related to Gulf Stream meandering and eddy shedding, are identified with Class 2. This class is most sensitive to initial conditions, not directly related to atmospheric forcing, and subject to contamination by errors in boundary conditions over time scales comparable to that needed to propagate information across the forecast domain.

We have been involved in the Class 2 prediction problem for the GSS through our work on the Gulf of Mexico and more recently on the Gulf Stream downstream of Cape Hatteras. Our strategy for both regions has consisted of



the following basic steps: (1) Develop the simplest model of the system which has some hope of simulating the consistently observed features. (2) Using the best-known forcing functions and boundary conditions available, drive the model to statistical equilibrium. Perturb the forcing functions and boundary conditions to explore the full range of possible model response. (3) Compare model results with observations, noting what processes exhibit close agreement and substantial disagreement. (4) Explain the models results in terms of basic dynamics. Can a simple analytical model account for the observations? (5) Once the numerical model has been validated, use it to make predictions of features yet to be observed and for developing techniques to improve the utilization and collection of observational data. This paper is a brief description of how we have used this strategy in the study of the dynamics and predictability of the GSS.

## 2. GSS Modelling - South

In the southern portion of the GSS the Loop Current enters through the Yucatan Straits and traces an anticyclonic path which may extend almost to the Mississippi Delta before turning southward and exiting through the Florida Straits. The Loop Current volume transport is approximately  $30 \times 10^6 \text{ m}^3 \text{ sec}^{-1}$  and eventually becomes a principal component of the Gulf Stream. Maximum geostrophic surface currents in the Loop can exceed  $150 \text{ cm sec}^{-1}$  and the dynamic height change across the stream can be greater than 75 cm, easily detectable by a satellite altimeter. Large anticyclones, also termed rings, having diameters larger than 300 km have been observed to break off from the Loop Current and are believed to move into the western Gulf. Elliott (1979) has estimated the mean westward drift speed after break-off to be about  $2.4 \text{ cm sec}^{-1}$ , although recent observations suggest the speed of eddy drift can be quite variable. Fig. 1b, from near-synoptic hydrographic data by Leipper (1970), shows the Loop Current and a large anticyclonic ring about to be shed from it. Much earlier, Ichiye (1962) suggested that detached Loop Current eddies could drift across the Gulf and maintain an anticyclonic circulation in the western basin. Sturges and Blaha (1976) proposed that wind stress curl might drive a mean anticyclonic gyre in the western Gulf.

The Loop Current was once thought to penetrate into the Gulf during the spring and summer, shed an anticyclone during late summer and fall and exhibit minimum penetration in the winter. This cycle was believed to be due to seasonal variations in the flow through the Yucatan Straits (Cochrane, 1965). New oceanographic and satellite data have shown that the eddy shedding period ranges from eight to fifteen months (Molinari, 1980) and that the earlier interpretation of a dominant seasonal cycle was due to a bias in the data set (Molinari et al., 1977). Results from low-order vertical mode primitive equation numerical models of Hurlburt and Thompson (1980), henceforth referred to as HT, show that approximately an annual period of eddy shedding can occur with no variations in the inflow transport and that for realistic constant values of inflow transport the mean period between major eddy breakoff is about ten months. The model Loop Current spontaneously and regularly shed eddies with realistic diameter, amplitude, and speed of propagation. Agreement between model and observations and the theoretical basis for Loop Current penetration, the size of the rings, the rate of shedding, and the westward translation speed are discussed in terms of momentum and potential vorticity conservation and Rossby wave dynamics in HT. An energetics analysis of model experiments exhibiting baroclinic and/or barotropic instability is provided in Hurlburt and Thompson (1982).

The first semi-implicit eddy-resolving primitive equation model retaining realistic geometry and bottom topography for any deep ocean basin was developed for the Gulf of Mexico by Wallcraft (1984), who extended the rectangular-basin model of HT to include an irregular coastline. A two-layer, hydrodynamic version of the model on a beta-plane was driven from rest to statistical equilibrium by steady inflow through the Yucatan Straits and exactly compensated by outflow through the Florida Straits. Fig. 1a shows a snapshot from a model experiment described in Hurlburt (1984) near the same phase of eddy shedding as found by Leipper (1970). A benchmark experiment using a similar model is discussed below. Model parameters for the present benchmark experiment are given in Table 2. The principal difference between this experiment and the one described by Hurlburt (1984) is the vertical distribution of volume transport through the Yucatan Straits. By allowing a larger fraction of the total transport to be carried by the deep flow we have found more consistent agreement between model and observations, both in terms of the size of the anticyclones and the amplitude of the fluctuating component

of the dynamic sea surface height. Existing data on the long-term vertical distribution of transport through the Yucatan Straits is inadequate to validate any particular choice of transport forcing within a rather wide range in each layer although the total transport value of  $30 \times 10^6 \text{ cm}^3 \text{ sec}^{-1}$  is well accepted as a mean.

Fig. 2 shows a sequence of dynamic sea surface height anomaly maps (height above an initial uniform level) for the benchmark experiment following spin-up to statistical equilibrium. The first five panels are snapshots every 30 days from Day 1450 to Day 1570, while the last panel is Day 1890, during the subsequent shedding cycle. Once the Loop has penetrated sufficiently far into the Gulf it becomes barotropically unstable and rapidly sheds an anticyclone (Day 1450 - Day 1540). During this period an anticyclone shed in the previous cycle impinges on the western Gulf, distorts its shape rapidly as it decays, and evolves to a small, residual anticyclone in the northwestern Gulf by Day 1540. In the eastern Gulf the development of a cold intrusion and a closed cyclonic circulation on the east side of the Loop is evident between Days 1510 and 1540. This feature is often seen in satellite imagery and has been directly observed from shipboard hydrographic data (Vukovich, 1982). The rate of shedding of large anticyclones from the Loop Current in this experiment is 316 days. The shed anticyclone drifts toward the southwest at about  $4 \text{ cm sec}^{-1}$ . As the main ring drifts into the central and western Gulf a weak cyclonic circulation develops to its west and northwest. This is a precursor of the cyclone/anticyclone pair found in the observations and in other numerical experiments.

The model, driven by realistic forcing to statistical equilibrium, is capable of producing dynamic sea surfaces which can be compared with both altimeter and in-situ data. Moreover, one can combine the model results, in-situ data, and the altimeter data for an optimal estimation of both the dynamic heights and the geoid (Wunsch and Gaposhkin, 1980; Marshall, 1984). Thompson (1985) has compared in detail (1) the mean dynamic height and variability of the sea surface in the Gulf as determined by Maul and Herman (1985) from hydrographic data and the correlation of temperature and salinity in the deep waters of the Gulf, (2) the mean sea surface and its variability as determined from GEOS-3 and SEASAT altimeter crossover data presented by Marsh et al. (1984), henceforth termed MC, and (3) the mean sea surface height

and variability as determined from the numerical model after reaching statistical equilibrium.

The variability of the sea surface from altimeter crossover differences as determined by MC and from the numerical model are shown in Fig. 3a and 3b respectively. In the eastern Gulf the sea surface height variability amplitude and approximate position were very similar for model, altimeter, and in-situ data (not shown). However, in the central Gulf, while the model variability map and the altimeter map agreed very well, indicating a ridge of high variability extending from the Loop Current toward the southwestern Gulf, they both differed substantially from the map determined from the in-situ data. The existence of the ridge of high variability towards the southwest in the model and in the altimeter data supports the hypothesis that eddies shed from the Loop Current do drift southwestwards. This result has important implications for the fate of materials transported by the Gulf circulation and the role of anticyclones in the circulation of the western Gulf. However, the fact that this ridge does not appear in the in-situ data is very disconcerting. This is not merely a minor discrepancy in interpretation or analysis procedure and has considerable dynamical significance. The reasons for these discrepancies are presently being investigated.

Because of the close agreement between model sea surface variability and that observed from altimeters, the dynamical consistency of the results with auxiliary data such as drifter trajectories in shed eddies (Kirwan, 1983 and personal communication), and the evaluation of the model through comparison with synoptic observations, we conclude that the model is sufficiently realistic so that we can begin to use it as a tool for studying how to use altimeter data for ocean monitoring and prediction in the GSS.

### 3. Altimeter Data and the GSS

Once the validity of the model was established by comparisons with in-situ and altimeter data we were able to employ it in the study of predictability of Gulf circulation using altimetrically derived sea surface heights. As part of the ONR Special Focus Program on Ocean Dynamics from Altimetry at NORDA three studies have been conducted using various versions of the Gulf of Mexico model: (1) geoid error and initialization, (2) conversion of surface to subsurface information, and (3) sampling strategies using a

single nadir-beam altimeter. The latter two experiments used the rectangular-domain, idealized Gulf of Mexico geometry.

In the first study the experiment described previously was used as a benchmark and compared with results from four experiments in which the model was initialized with fields modified from archived benchmark data. The experiments differed only in the initialization fields. Each experiment was integrated for 100 days and inflow transport remained constant throughout the integration. The experiments were initialized geostrophically (1) with the exact sea surface and pycnocline height fields, (2) with only the exact sea surface heights and the pycnocline assumed to exactly compensate such that the deep flow vanished, (3) just as in (2) but with a geoid error component added, and (4) just as in (3) except the the geoid error model included an additional contribution in strong geoid gradient regions. The experiments are outlined in more detail and reported in Thompson (1985).

The results of the experiments are summarized in Fig. 4, where the normalized RMS error of the FSA, PHA, and the lower-layer pressure is plotted. The normalization factor is the RMS variability of each field from the benchmark case. The lower layer pressure field is the most difficult field to predict from initial knowledge of the free surface only. At the initial time the NRMS error of P2 for Experiment 2 is 100% and increases to over 120% before gradually decreasing to less than 40% by the end of the period.

In Experiments 1 and 2 we dealt with perfectly known sea surface height information. In Experiments 3 and 4 we have focused on errors likely to be introduced by uncertainties in the geoid on small spatial scales, comparable to the length scale of seamounts or, more generally, the scale of very rapid changes in geoid height associated with strong bottom slopes. These errors may prove very difficult to remove from the sea surface height signal, particularly because they may be correlated with dynamic ocean processes over the same scales. In Experiment 3 the error field is represented as random noise with a Normal probability distribution function, a zero mean, and a standard deviation of  $\pm 5$  cm. The range of variation over the domain is  $>34$  cm. The error field is uncorrelated over the .2 degree model grid. Experiment 4 contains an error field that reflects the fact that geoid error are likely to be larger on the small scale in the vicinity of strong geoid gradients such as the Campeche escarpment, where the geoid gradient approaches a meter in 10 km. The range of variation in this case is  $>47$  cm and the impact of the strong

gradient areas on the error field is especially large in the southwestern Gulf.

From the sequence of four numerical experiments we found that even when only the sea surface height information was provided to the numerical model at the initial time, the forecasts of FSA, PHA and even deep pressure were superior to persistence or climatology over the 100 day forecast period. We also found that noise in the initial field, at least on the amplitude and scales of that used in the experiments, did not seriously degrade the forecasts. This occurred despite the obvious excitation of growing waves on the Loop Current and in the western Gulf.

While the preceding experiments were instructive, they did not provide a comprehensive view of how well altimeter data might be utilized in different dynamical regimes. Hurlburt (1985) has examined this problem in the context of converting well-observed surface altimeter data into subsurface information. This was done for a variety of dynamical regimes with (1) barotropic, baroclinic, mixed, and episodic instabilities, (2) flat bottoms or large amplitude topography, (3) relatively vigorous or gentle exchanges of energy between the layers, (4) major time scales which are short ( $\sim 60$  days), long ( $\sim 1$  year) or both, and (5) unstable currents and isolated eddies. In all cases the pattern of the deep pressure field is much different from that of the current-related variations in the sea surface elevations and sometimes not obviously related to it. Given only the free surface elevation (simulated altimeter data) from the true model solution, the model was able to reconstruct the deep pressure field even in situations with energetic shallow and deep circulations, baroclinic instability, and a vigorous vertical exchange of energy. However, in such experiments the frequency of updating for the free surface was critical. In this study the maximum update interval that allowed successful dynamic surface to subsurface transfer was about half the shortest major time scale (SMTS), which is 50 to 60 days in the experiments with baroclinic instability (Fig. 5).

Without knowledge of the deep pressure field, numerical predictions of the surface pressure field and the depth of the pycnocline were typically better than climatology for  $1/4$  to  $1/2$  the SMTS, but with successful dynamic surface to subsurface transfer, forecasts without updating were better than climatology for the SMTS or more. The time scale for predictive skill is substantially longer than the maximum update interval permitted because the

update interval must be short enough to allow decreasing error in the deep pressure field from one free surface update to the next until the error asymptotes at some acceptable level, approximately 30 to 50% in these results. Forecasts of isolated eddies demonstrated predictive skill for three months or more even when the subsurface initial state was unknown.

In the third study Kindle (1985) utilized the one-layer reduced-gravity model of the Gulf of Mexico to study the spatial and temporal sampling problem associated with a single nadir-beam altimeter. The two previous studies assumed data was available over the entire domain at a given time rather than along narrow swaths staggered in time. The simulated data were obtained by flying an imaginary altimeter over the model ocean and sampling the sea surface in a manner similar to a real altimeter, (see Fig. 6). The numerical model was geostrophically initialized using the asynoptic data which are assumed to be valid at the mid-point of the observing period. Fig 7a shows the RMS errors of the forecasts generated using only the data from the ascending tracks for each of the three periods (72, 36, and 24 days) of the exactly repeating satellite tracks. Fig. 7b demonstrates that if the descending tracks data are used, the RMS error can be significantly different. Surprisingly, in the descending track forecast the error decays more rapidly even though the initial value of the RMS error is substantially greater than the representation based on the ascending track observations. Fig 7c shows the results of applying an intermittent updating scheme during the nowcast period in order to reduce the effects of asynopticity. The numerical nowcast is initialized with the asynoptic data (Fig 6a,b,c) at the beginning of the observing period and the data are reinserted into the numerical solution 4 tracks at a time (i.e. every 12 days) until Day 0 of the forecast. No data is inserted into the model during the forecast. The results demonstrate that the asynopticity of the 72 day repeat track observations were reduced so effectively that the forecast was just as accurate as the one using the 24 day repeat track data. A similar experiment using the descending track data (not shown) exhibited virtually identical results.

The essence of Kindle's study is that the sampling trade-off between track spacing and repeat period may not be as difficult a dilemma as once thought. The interaction between synoptic altimeter data and a hydrodynamic numerical model indicates that both adequate spatial and temporal resolution may be possible with a single nadir-beam altimeter. The observations form the

basis of the model initialization and, in turn, the model 'corrects' the asynoptic of the data. The result is an accurate nowcast which, for highly asynoptic data, would not have been possible without the use of the model. A sampling strategy should favor spatial resolution and resolve the important dynamic features; the inherent asynoptic of the measurements can be reduced by applying an initialization/updating scheme to the numerical nowcast.

#### 4. GSS Modelling - North

We have begun to employ the strategy used for modelling the southern portion of the GSS to the northern portion downstream of Cape Hatteras. Recently, Thompson and Hurlburt (1982) and Hurlburt and Thompson (1984), both henceforth referred to as HTG, have developed a primitive equation model of the Gulf Stream including bottom topography. In the HTG study the model domain extended from Cape Hatteras to the Grand Banks. The domain was rotated 28 degrees counterclockwise from zonal. To avoid unknown specification of open boundary segments the model domain was closed except for an inflow port at Cape Hatteras and an outflow port roughly at the mean position of the Gulf Stream as it passes south of the Grand Banks. In all of the experiments reported the flow of the Gulf Stream was confined to the upper layer of the model. Thus this work departs significantly from other studies of flow over topography in that the flow is not directly forced to impinge on the topography. Here, any flow in the lower layer must be driven from above due to pressure fluctuations associated with the active upper ocean. Any influence of the seamount chain on the path of the Gulf Stream must be a back interaction driven by the upper ocean.

Five numerical experiments were conducted. All but one used two active layers, the minimum allowing baroclinic instability and both a thermocline and bottom topography. One experiment used a reduced gravity model with an active upper layer and a lower layer infinitely deep and at rest. The other experiments were identical except for the bottom topography used. In experiment 3 a Gaussian ridge with maximum height of 2500 m was added across the channel with an e-folding half-width of 50 km. For the seamount experiments a set of four Gaussian seamounts with an amplitude of 2500 m for Experiment 4 and 500 m for Experiment 5 were aligned across the channel with the same e-folding half width as for the ridge. The seamounts were spaced



200 km apart. The separation and the diameter of the seamounts is substantially greater than for the real seamounts, a compromise dictated by the affordable grid resolution and the desired domain size. The diameter (radius) of the real (model) seamounts is comparable to the baroclinic radius of deformation.

The five numerical experiments were integrated from rest for seven years. Approximately four years were required to reach statistical equilibrium and another three years were added for a stable, long time series. Results of the modelling study can be briefly summarized as follows:

1. The model NESC was found to have a substantial influence on the Gulf Stream even when the Stream did not directly impinge on the topography.
2. Results from the reduced-gravity model were quite unrealistic, suggesting that addition of the barotropic mode, which yielded a more realistic GS, is critical to modelling the GS in this region.
3. Warm core ring generation was enhanced by the NESC. Prolific generation of warm core rings occurs immediately upstream of the NESC with a frequency of about 2/year.
4. When compared to the flat bottom experiment, the NESC increased both baroclinic and barotropic instabilities as measured by the rate of transfer of mean potential to eddy potential energy and mean kinetic to eddy kinetic energy.
5. Maximum EKE in the large seamount experiment exceeds  $2000 \text{ cm}^2/\text{sec}^2$  in the upper layer and  $130 \text{ cm}^2/\text{sec}^2$  in the lower layer. These values are comparable to observations but located too near Cape Hatteras in the model.
6. Maximum sea height variability  $>35 \text{ cm}$  was found in the large amplitude seamount experiment, comparable to that observed by Douglas et al. (1983) and MC from altimeter data from GEOS-3 and SEASAT. Location of the maximum was upstream of the seamounts however, unlike the observations.

Thus using a limited-domain model with open boundary conditions we have shown that the NESC can have a significant influence on the GS mean path and its eddy statistics. We clearly showed that baroclinic instability of the Gulf Stream could generate deep mean flows which interacted with the bottom topography and in turn influenced the upper ocean circulation. However, to answer a broader range of questions, for example how the large scale topography might influence the mean path and the eddy statistics, a much larger domain is required. This is certainly required before we can continue our strategy of developing the models to the point where the same model/data comparisons and altimeter studies we have done for the Gulf of Mexico can be done for the REX and SYNOP region. At the same time we must not sacrifice the eddy resolving capability of the model. Thus a realistic numerical model of the GSS is expensive, both in manpower for model development and in actual computer time. In some respects this expense must be considered in the same category as ship time or mooring costs. Great care and forethought must be taken to insure that the model is as efficient as possible while choosing research problems which have some chance of success with limited computer resources. Therefore, in proposing experiments in modelling the GSS it is important to determine what problems are "doable" on present and near-future computers.

The domains for our proposed experiments are shown in Fig. 8. Domain A includes the Gulf Stream and its principal recirculation region but does not encompass the Gulf of Mexico, the Caribbean, and part of the North Atlantic. However, this domain closely parallels Holland's (1982) QG domain and should provide a good benchmark for assessing the differences between the PE and QG models and the influence of large scale topography. Domain B, while bigger, will be more costly and is of more limited use in terms of possible experiments. It will, however, allow us to evaluate the limitations of Domain A for studying the GSS and should provide some useful information on the role of the Caribbean and the Gulf of Mexico in modulating the transport in the Gulf Stream under time-varying wind forcing. We have chosen the southern latitude of Domain B based on some numerical experiments from Dr. George Heburn of our group using a coarse grid (one and one-half degree by one and one-quarter degree) one-active-layer reduced gravity world ocean model driven by climatological monthly mean winds. In Fig. 9a the solution for the interface deviation after nearly five years of integration is shown while in

Fig. 9b a no-slip barrier has been placed at 9N. While there are some differences in the details, the basic circulation of the Gulf Stream at mid-latitudes remains unchanged. We have developed an eddy-resolving (.2 degree) spherical geometry, arbitrary n-layer primitive equation, semi-implicit model for the North Atlantic. The first version of the model, with a flat bottom and two layers and driven by a simple zonal wind is now being run on the newly-installed Cray-XMP 12 at the Naval Research Laboratory. We are presently involved in adding more realistic wind forcing and bottom topography.

In the immediate future there are a wide range of scientific issues that form the basis for research on the GSS. Some of those issues are directly amenable to observational study while others will require more theoretical effort. It seems clear however that for the foreseeable future observational efforts in the GSS should be coupled with a serious, stably-funded modelling program. The models will provide valuable guidance in determining sampling strategies, in interpreting field data from sparse observational networks, and in generating new hypotheses for field testing. In some instances, for example in the utilization of altimeter data for ocean forecasting, the models will be critical for data assimilation in space and time.

There are at least three areas of GSS research which are timely and of critical concern: First, while numerical models have become more realistic, there are still some serious discrepancies between model simulations and the sparse observations. This is partly a modelling problem and partly a problem with data density. The models have failed to simultaneously account for both the mean path of the Gulf Stream and its penetration far into the interior of the North Atlantic and for the high energy levels in the deep water downstream of the NESC at 55W, where long time series from moored current meters are available. This is especially perplexing since abyssal eddy kinetic energies along 152 E near the Kuroshio Extension are a factor of 2 to possibly a factor of 5 lower than those at similar depths in the analogous part of the Gulf Stream (Schmitz et al., 1982). What is unique about the GSS which yields such high abyssal EKE? What is lacking in the models which prevents them from generating such energies far away from the western boundary?

A second question involves the importance of topographic control on the dynamics and statistics of the Gulf Stream downstream of Cape Hatteras. Increasing observational evidence and our modelling work suggest an important role for the continental shelf and slope as well as the obvious topographic

anomalies such as the NESC in influencing the Gulf Stream. However, most of the existing models of the GSS either utilize a flat-bottom model or, by using the QG assumption, require the topography to be of small amplitude. Our work has shown that the small amplitude seamount results are qualitatively different from those for the large-amplitude case. An additional concern associated with the topography is the determination of whether or not the Gulf Stream penetrates to the bottom after it leaves Cape Hatteras. Direct current meter observations along the continental slope are often contaminated by low-frequency topographic Rossby waves, making it difficult to determine the relationship between deep fluctuations and meanders of the Gulf Stream (Bryden, 1982). How are these waves generated and can a model account for them? Hogg(1981) traced the origin of the TRWs observed near 70W back to a generation region near 38N and 68W. This is at the northern end of the NESC. Is it possible that meanders of the GS, interacting with the seamounts might be the trigger for these waves? Another aspect of the topographic influence is related to ring generation, movement, and decay. Our work clearly indicates that warm core ring generation efficiency is increased by the seamounts and that eddy activity in the deep water in the vicinity of the seamounts was increased compared to the flat bottom experiment. It is also quite evident in the observations that the continental shelf and slope influence the movement and decay of the rings.

The third scientific issue is related to the measurement of various statistical quantities, both from the models and in the observations. We have evaluated the complete energetics budget for our model experiments and can map each term in the kinetic and potential energy equations, both for the means and for the fluctuations. This is much easier to do in the models than in the observations. The best that can be done observationally is to monitor some of the terms in the energy equations, estimate the magnitude of the energy reservoirs, and make educated guesses at the total picture. By subsampling the model with "imaginary" current meters, IESs, altimeters, etc. and recomputing certain energetic quantities that one might observe in the ocean, then comparing them to the "true" solutions from the full model output, we can begin to make statements about how sensitive eddy-mean calculations are to record length, resolution of the measurements, and error contamination. This should aid the design of new observational programs as well as improve our efforts to compare models and observations. Other quantities, such as mass

transport, relative and potential vorticity, vertical velocity, sea surface height, and Lagrangian drifter statistics are readily obtained from the model. Much work still needs to be done on the optimum means for intercomparing models and oceanic data and on standardizing the rules for determining when a model realistically compares with the observations.

### References

Bryden, H.S., 1982: Review of Gulf Stream measurements in the region south of New England. Proceedings: Workshop on Gulf Stream Structure and Variability, Office of Naval Research, Ed. J.M. Bane, Jr., Univ. of N.C., Chapel Hill. 48-59.

Cochrane, J.D., 1965: The Yucatan Current and equatorial currents of the western Atlantic, Unpublished report, Dept. of Oceanography, Texas A&M University, Ref. (65-17T), 20-27.

Douglas, B.C., R.E. Cheney, and R.W. Agreen, 1983: Eddy energy of the Northwest Atlantic and Gulf of Mexico determined from GEOS-3 altimetry. J. Geophys. Res., 88, 9595-9604.

Elliott, B.A., 1979: Anticyclonic rings and the energetics of the circulation of the Gulf of Mexico. Ph.D. Thesis, Dept. of Oceanography, Texas A&M University, 188 pp.

Hogg, N.G., 1971: Topographic waves along 70W on the continental rise. J. Mar. Res., 39, 627-649.

Holland, W.R., 1982: Simulation of North Atlantic variability. Proceedings: Workshop on Gulf Stream Structure and Variability, Office of Naval Research, Ed. J.M. Bane, Jr., Univ. of N.C., Chapel Hill. 114-126.

Hurlburt, H.E., 1984: The potential for ocean prediction and the role of altimeter data. Mar. Geod., 8, 17-66.

\_\_\_\_\_, and J.D. Thompson, 1980: A numerical study of Loop Current intrusions and eddy shedding. J. Phys. Oceanogr., 10, 1611-1651.

\_\_\_\_\_, and J.D. Thompson, 1982: The dynamics of the Loop Current and shed eddies in a numerical model of the Gulf of Mexico. Hydrodynamics of Semi-enclosed Seas, edited by J.C.J. Nihoul, Elsevier, Amsterdam, 243-298.

\_\_\_\_\_, 1985: Dynamic transfer of simulated altimeter data into subsurface information by a numerical ocean model. JGR Oceans Special Issue on Remote Sensing of the Ocean and Troposphere (to appear).

Ichiye, T., 1962: Circulation and water mass distribution in the Gulf of Mexico, Geofisica Internacional (Mexico City), 2, 47-76.

Kindle, J.C., 1985: Sampling strategies and model assimilation of altimetric data for ocean monitoring and prediction. JGR Oceans Special Issue on Remote Sensing of the Ocean and Troposphere (to appear).

Kirwan, A.D., Jr., W.J. Merrell, Jr., J.K. Lewis, and R.E. Whitaker, 1984: Lagrangian observations of an anticyclonic ring in the western Gulf of Mexico, J. Geophys. Res., 89, 3417-3424.

Leipper, D.F., 1970: A sequence of current patterns in the Gulf of Mexico, J. Geophys. Res., 75, 637-657.

Marsh, J.G., R.E. Cheney, J.J. McCarthy and T.V. Martin, 1984: Regional mean sea surfaces based upon GEOS-3 and SEASAT altimeter data. Mar. Geod., 8, 385-402.

Marshall, J.C., 1985: Sea-surface topography determination and geoid improvement from satellite altimetry. J. Phys. Oceanogr., to appear.

Maul, G.A. and A. Herman, 1985: Mean dynamic topography of the Gulf of Mexico with application to satellite altimetry. Marine Geodesy (to appear).

Molinari, R.L., 1980: Current variability and its relation to sea-surface topography in the Caribbean Sea and the Gulf of Mexico. Mar. Geod., 3, 409-436.

\_\_\_\_\_, S.R. Baig, D.W. Behringer, G.A. Maul and R. Legeckis, 1977: Winter intrusions of the Loop Current. Science, 198, 505-507.

Schmitz, W.J., Jr., P.P. Niiler, R.L. Bernstein, and W.R. Holland, 1982: Recent Long-term moored instrument observations in the western North Pacific. J. Geophys. Res., 87, 9425-9440.

Sturges, W.A., and J.P. Blaha, 1976: A western boundary current in the Gulf of Mexico, Science, 192, 367-369.

Thompson, J.D., and H.E. Hurlburt, 1982: A numerical study of the influence of the New England Seamount Chain on the Gulf Stream: Preliminary results. Proceedings: Workshop on Gulf Stream Structure and Variability, Office of Naval Research, Ed. J.M. Bane, Jr., Univ. of N.C., Chapel Hill. 346-362.

\_\_\_\_\_, 1985: Altimeter data and geoid error in mesoscale ocean prediction: Some results from a primitive equation model. JGR Oceans Special Issue on Remote Sensing of the Ocean and Troposphere (to appear).

Wallcraft, A.J., and J.D. Thompson, 1984: Ocean modelling and drifters, 1984 Drifting Buoy Workshop: Proceedings, Marine Technology Society, Gulf Coast Section, 81-98.

Wunsch, C., and E.M. Gaposchkin, 1980: On using satellite altimetry to determine the general circulation of the oceans with application to geoid improvement. Rev. Geophys. Space Phys., 18, 725-745.

Table 1

Classes of oceanic response to atmospheric forcing where predictive skill is feasible.

Class	Implications	Examples
1. Strong, rapid ( $< 1$ wk) and direct	<p>A. short-range forecasts limited by the time scale for atmospheric predictive skill</p> <p>R. less sensitive to errors in the initial state; more sensitive to errors in the forcing functions</p>	<p>surface mixed layers, surface and some internal waves, Ekman drift currents, some coastal and equatorial processes such as upwelling (in some cases), coastal storm surges, and the onset of some equatorial and coastal waves</p>
2. Slow (weeks to months) and indirect	<p>A. long-range forecasts (potentially a month or more)</p> <p>B. more sensitive to errors in the initial state, less sensitive to errors in the forcing functions</p> <p>C. statistical properties of features and ensembles may be predicted by skillful simulation</p> <p>D. prediction of individual features requires oceanographic data. Altimeter data are the most promising operational source now on the horizon</p>	<p>mesoscale eddies, meandering currents, some frontal positions, features caused by mesoscale flow instabilities.</p>
3. Slow (weeks to years) but direct (i.e. integrated response)	<p>A. long-range forecasts</p> <p>B. sensitive to errors in atmospheric forcing functions on long time scales (e.g. monthly means); but less sensitive to errors on short time scales (e.g. daily fluctuations)</p> <p>C. nowcasting and forecasting are potentially feasible without good oceanic data by means of simulations that use appropriate ocean circulation models</p>	<p>El Niño, much of the tropical ocean circulation (in the Atlantic, Pacific, and Indian Oceans), equatorial waves, part of the large-scale ocean circulation, features such as gyres directly driven by persistent or repeated patterns in the wind, often in conjunction with geometric constraints, e.g. most of the circulation features in the Mediterranean Sea with scales <math>&gt; 100</math> km.</p>

11.512



Table 2

Model Parameters for Benchmark Experiment

A	$300 \text{ m}^2 \text{ sec}^{-1}$	$\beta$	$2 \times 10^{-11} \text{ m}^{-1} \text{ s}^{-1}$
$C_B$	$2 \times 10^{-3}$	$\rho$	$10^{-3} \text{ kg m}^{-3}$
$f_0$	$5 \times 10^{-5} \text{ s}^{-1}$	$\tau$	0
$g$	$9.8 \text{ m sec}^{-2}$	$\Delta x, \Delta y$	$.2^\circ$
$g'$	$.03(H_1 + H_2)/H_2 \text{ m}^2 \text{ s}^{-2}$	$H_1, H_2$	200 m, 3400 m
Upper/Lower Layer Inflow Volume Transport			20/10 $\text{m}^3 \text{ s}^{-1}$

### Figure Legends

Fig. 1: (a) Instantaneous view of the interface deviation in a two-layer simulation of the Gulf of Mexico driven from rest to statistical equilibrium solely by inflow through the Yucatan Straits. The contour interval is 25 m, with solid contours representing downward deviations. (b) Depth of the 22° C isothermal surface, 4-18 August 1966 (Alaminos cruise 66-A-11), from Leipper (1970). The contour interval is 25 m. (From Hurlburt, 1984)

Fig. 2: Snapshots of the sea surface height anomaly (FSA) for Experiment 1 at (a) Day 1450, (b) Day 1480, (c) Day 1510, (d) Day 1540, (e) Day 1570 and (f) Day 1890.

Fig. 3: (a) ~~The mean sea surface and (b)~~ sea surface variability in the Gulf of Mexico computed from all SEASAT and GEOS-3 crossover data (from Marsh et al., 1984), (b) Sea surface height variability over 3 eddy-shedding cycles for the benchmark numerical experiment in statistical equilibrium.

Fig. 4: Normalized RMS error in percent for (a) FSA, (b) PHA, and (c) P2 for Experiments 1-4 for the 100 day forecast period. Values normalized by RMS variability of each field from the benchmark experiment.

Fig. 5: Normalized RMS error versus time for forecasts of the free surface elevation anomaly,  $\eta$ , the pycnocline depth anomaly,  $h_1'$  and the deep pressure field anomaly,  $p_2$ . The forecasts were initialized at day 1080 and had an update interval of (a) 40 days and (b) 30 days. The true model solution is aperiodic with 57 days as the most prominent period and with baroclinic instability dominating the behavior. Note the dramatic decrease in error when the update interval is reduced from 40 to 30 days. The error for a forecast of climatology (the temporal mean of the solution) is 50% for  $\eta$  and  $h_1'$  and 99% for  $p_2$ . From Hurlburt (1985, JGR - Oceans, to appear).

Figure 6: Asynoptic sampling along simulated altimeter tracks of the Gulf of Mexico numerical solution. The repeat periods are: 72 days (a, b); 36 days (c, d); and 24 days (e, f). In (a)-(c) are depicted sampling along ascending tracks while (d)-(e) are the descending track observations. Dashed straight lines denote positions of tracks during the first half of the observing period, and solid lines show the most recent half of the repeat period. The most recent track (Day 1200 of simulation) is a solid line with an adjacent dashed line to the east. All other adjacent tracks are separated by 3 days (from Kindle, 1985).

Fig. 7: (a) Normalized RMS error vs. time of predictions initialized with ascending track observations: (1) 72-day repeat; (2) 36-day repeat; (3) 24-day repeat. Negative days denote nowcast period while positive days indicate forecast. (b) Normalized RMS error vs. time of forecasts in which the nowcasts were initialized with asynoptic observations from the 72-day repeat period: (1) initialized with ascending data (same as (a)-1); (2) initialized with descending track observations. (c) Normalized RMS error vs. time of forecasts for three track periods (same as in (a)); nowcast is initialized at the beginning of the observation period and updated every 12 days. Only

observations from ascending tracks are used. Repeat periods are identical to (a). (from Kindle, 1985)

Fig. 8: The two domains for the numerical experiments. Free-slip boundary conditions are used on the open ocean boundary segments and the irregular coastlines are included in both domains.

Fig. 9: Interface deviation from a one-layer reduced gravity model of the world ocean driven by monthly mean climatological winds. Grid spacing is one and one-half degrees zonally and one and one-quarter meridionally. Although after five years of integration the model has still not reached statistical equilibrium, the main features of the North Atlantic are readily seen. In (a) the entire North Atlantic is shown. In (b) a solid free-slip wall was placed at 9N. From work by Heburn (personal communication).

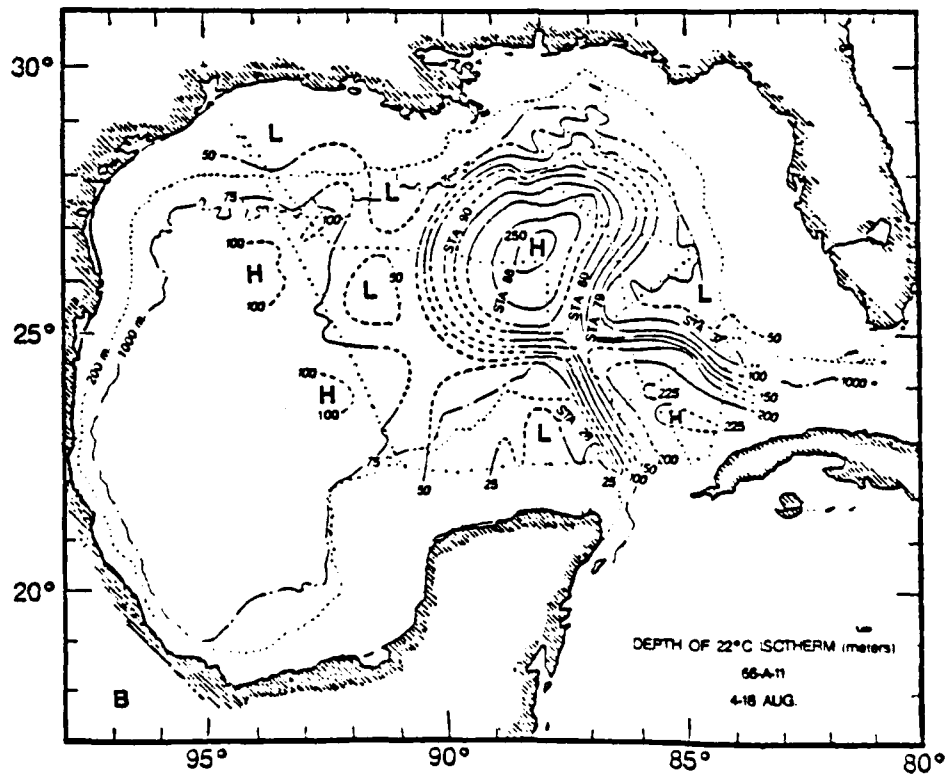
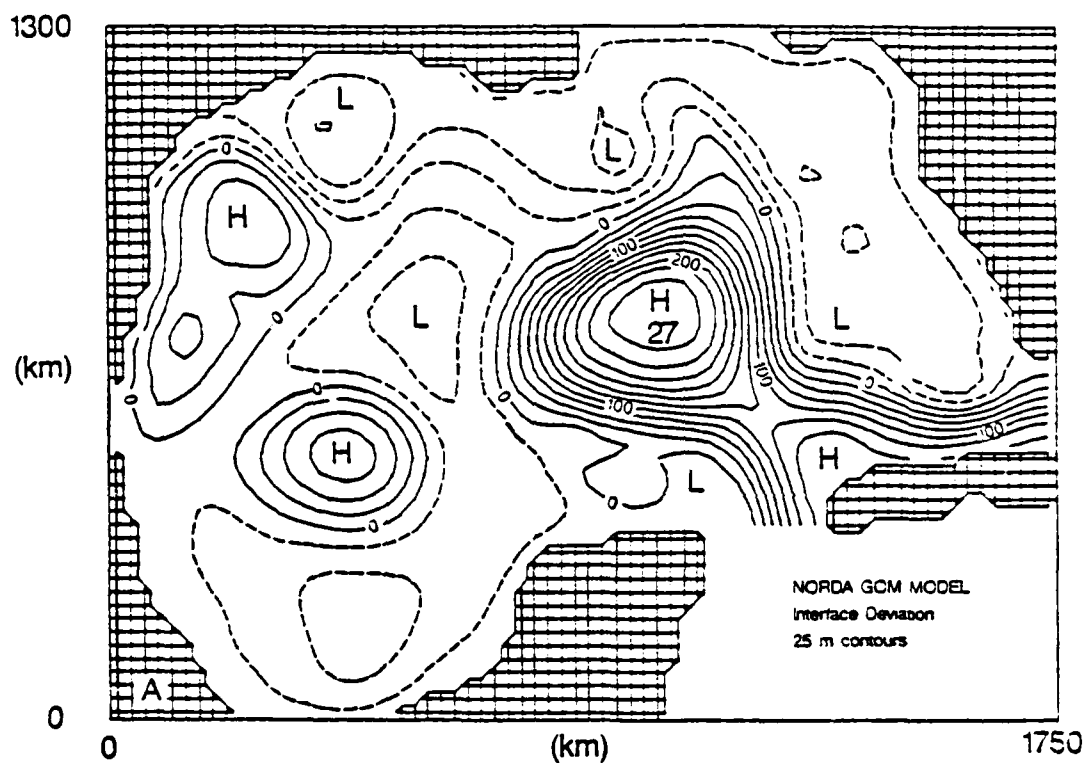


Figure 1

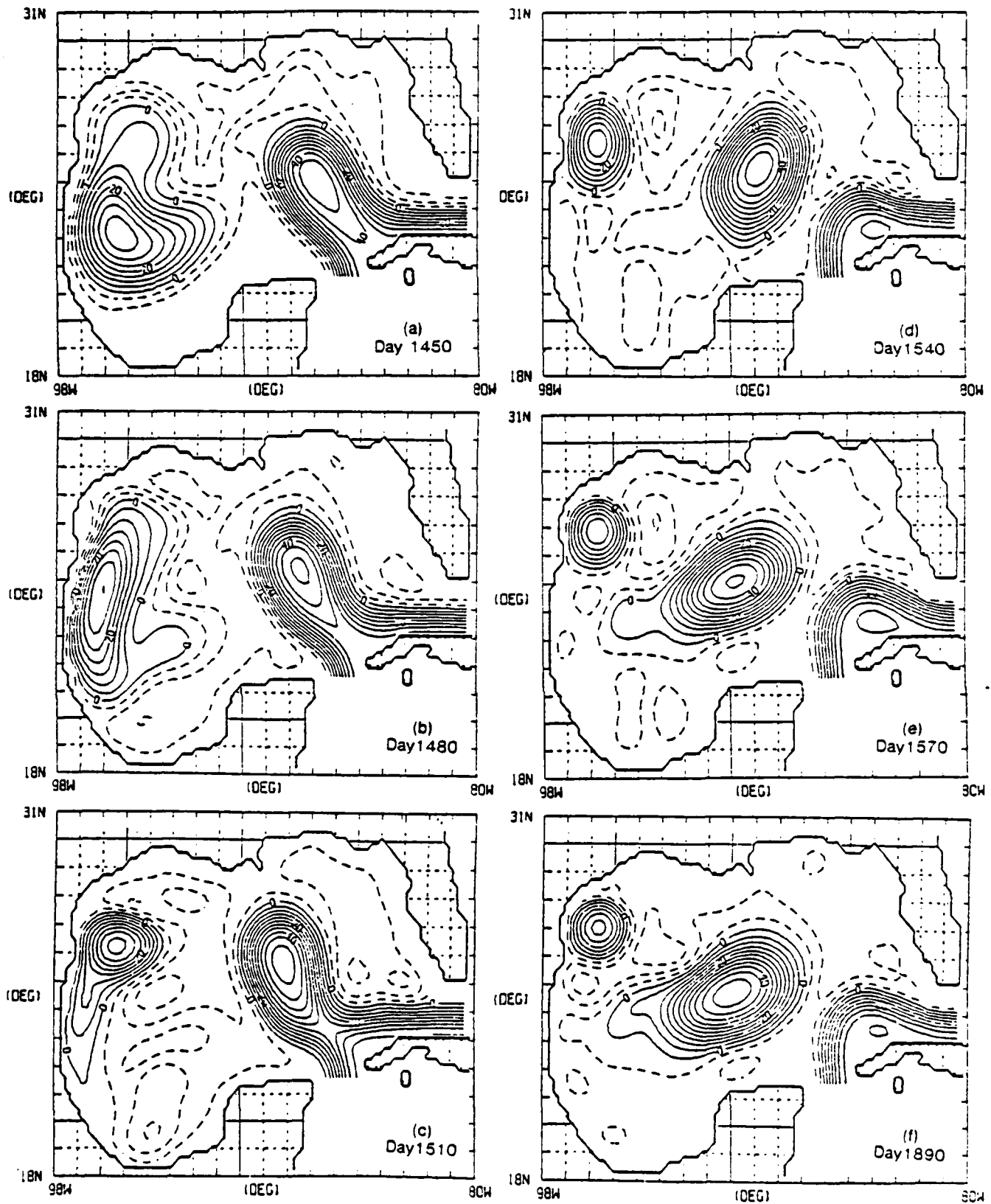


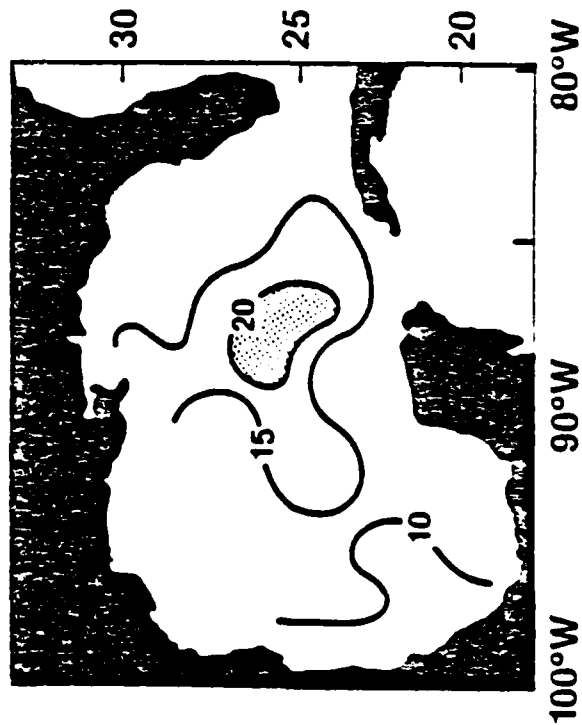
Figure 2



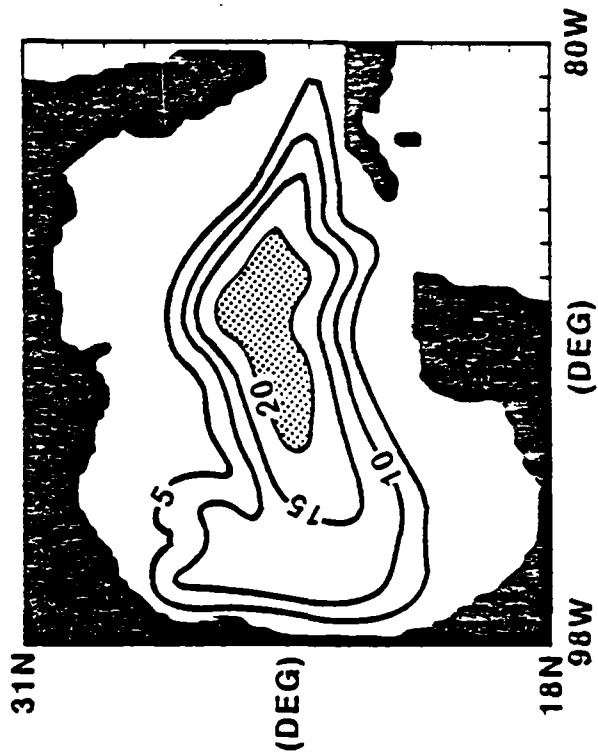
# NAVAL OCEAN RESEARCH AND DEVELOPMENT ACTIVITY

LA62-1

SEA SURFACE VARIABILITY FROM  
GEOS-3 AND SEASAT CROSS-OVERS (CM)  
(From Marsh, et al., 1984)



SEA SURFACE VARIABILITY (CM)  
FROM NORDA MODEL



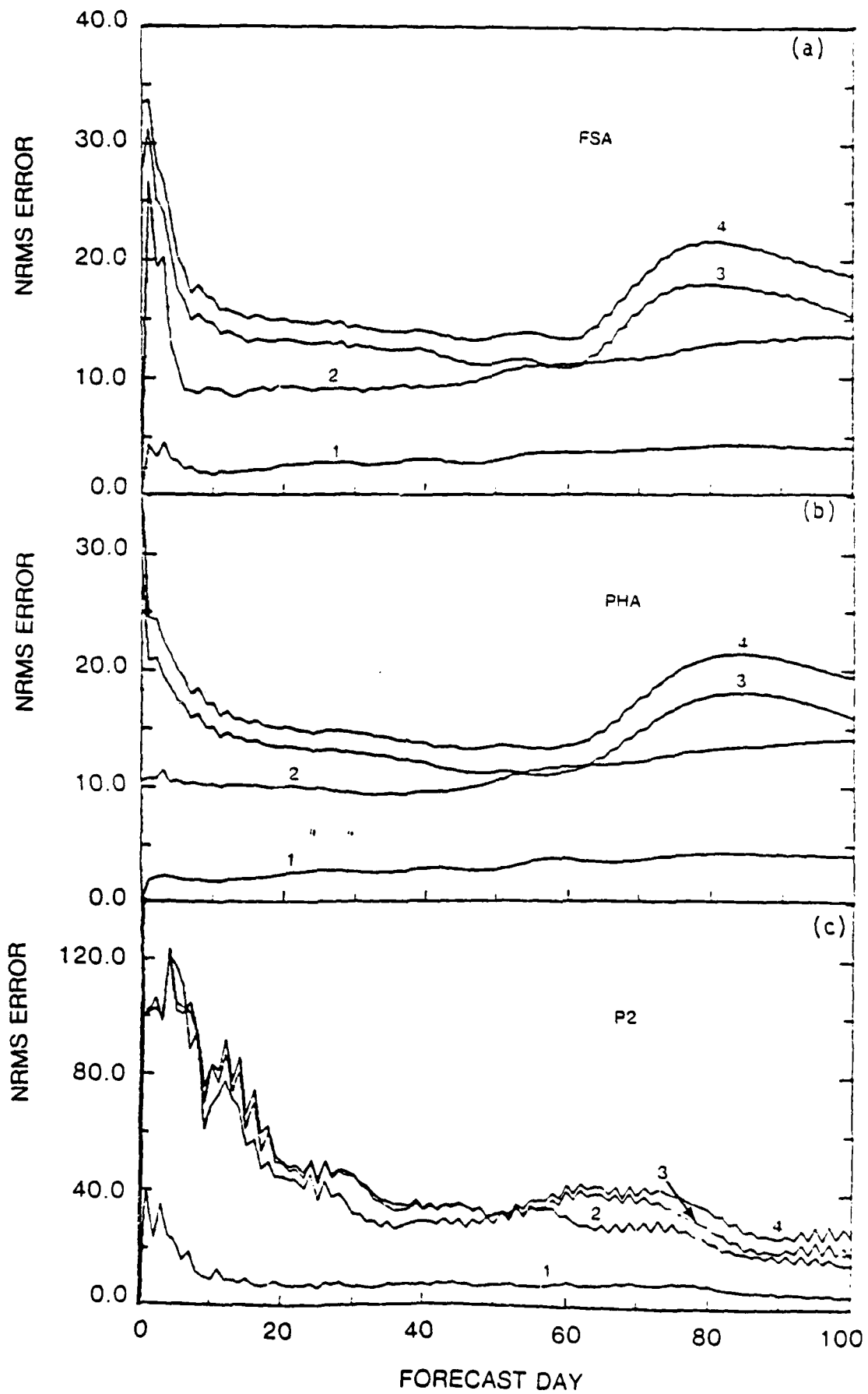


Figure 4

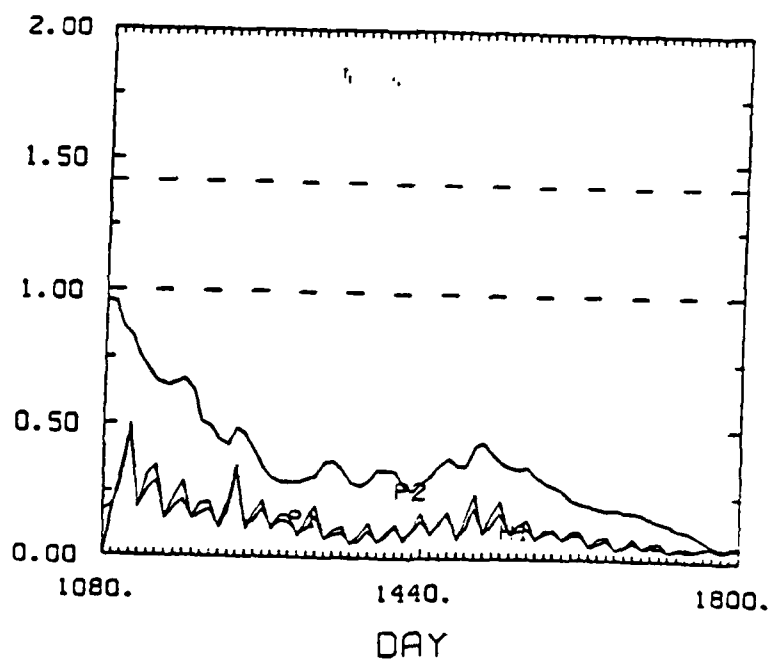
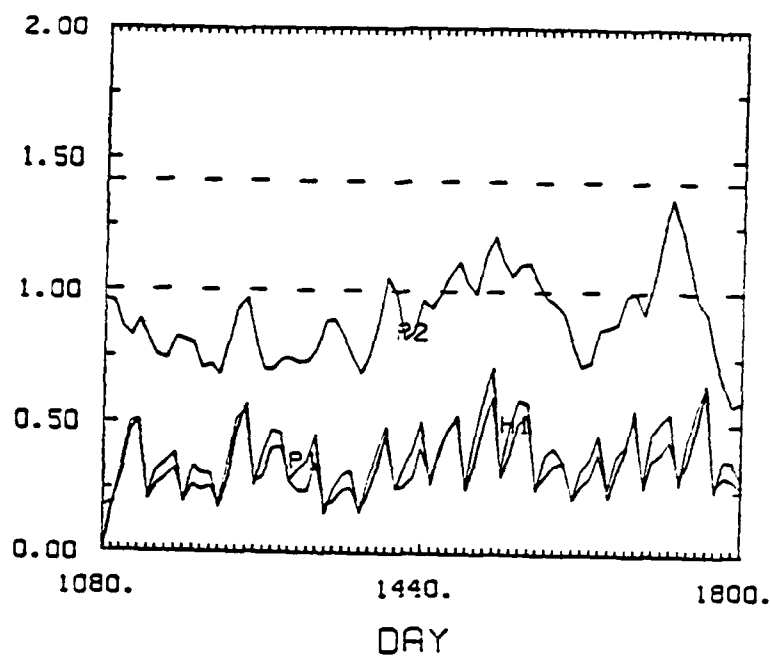


Figure 5



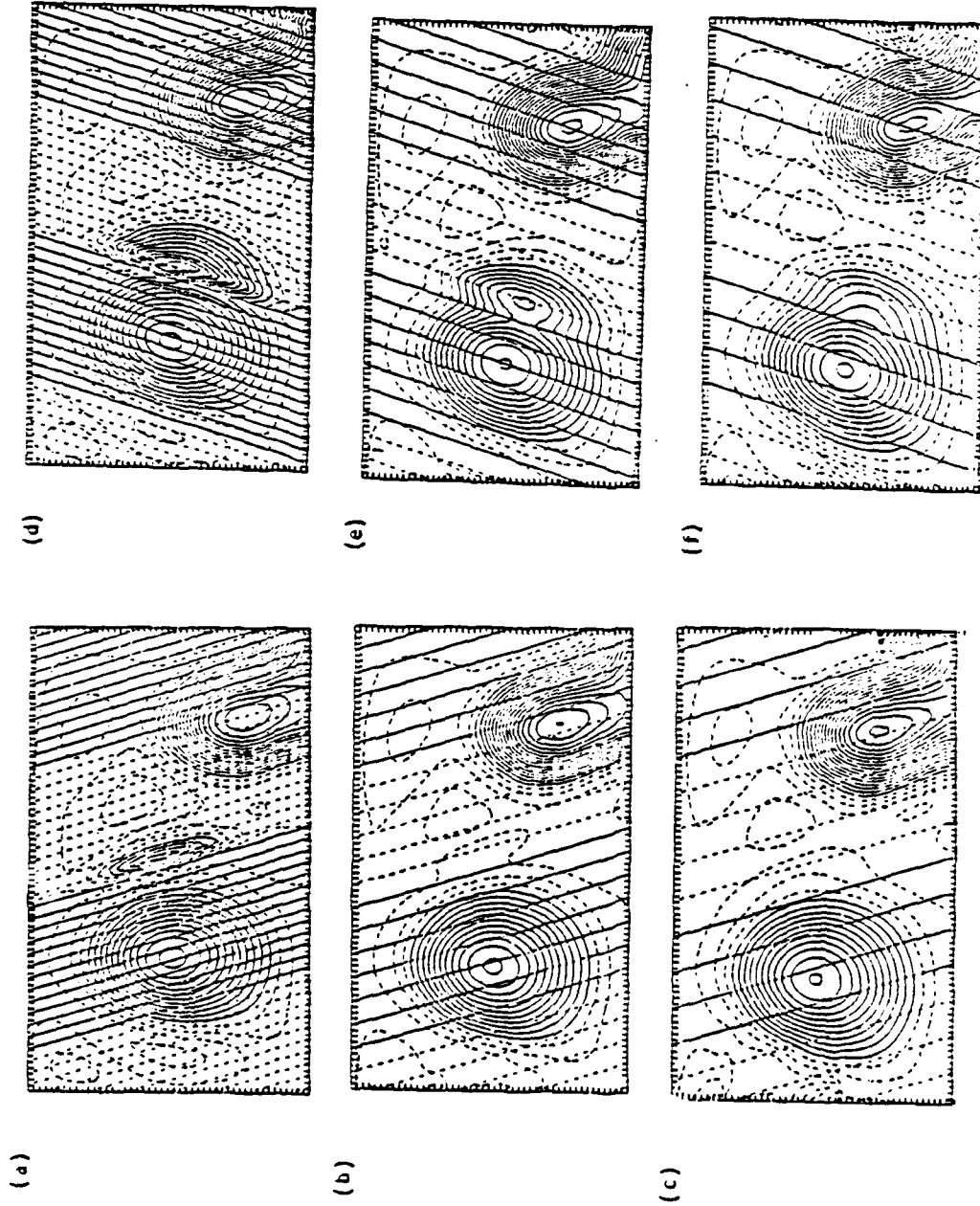


Figure 6

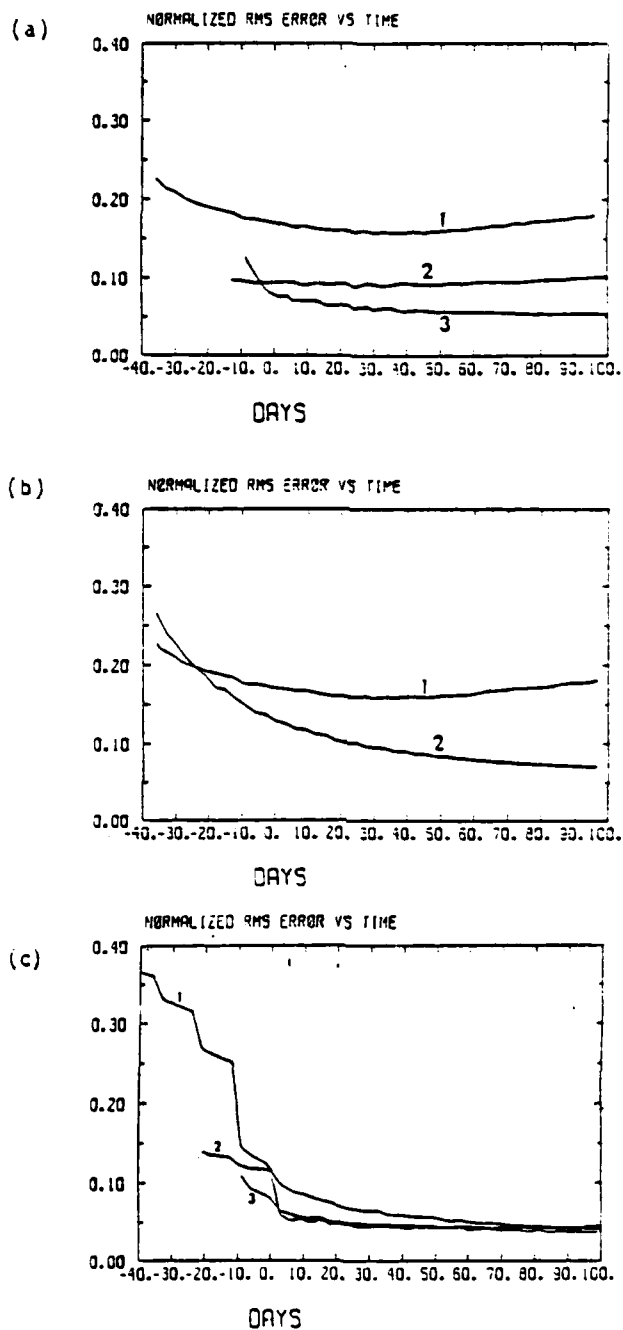


Figure 7

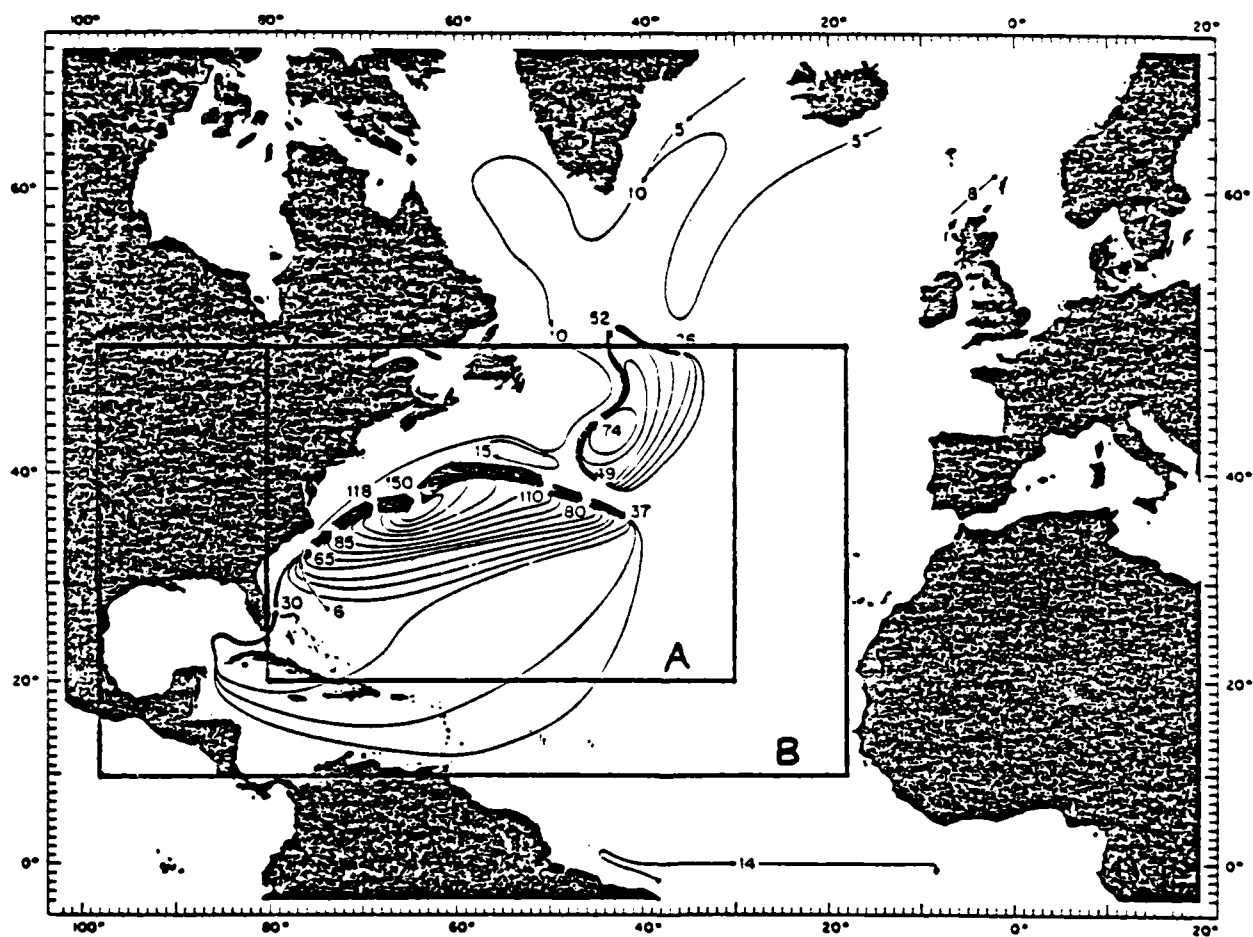


Figure 8

INTERFACE DEVIATION WOPEN-N.ATL 11111.10101  
 DAY = 1800 DH = 10.0 (M) LAYER = 1

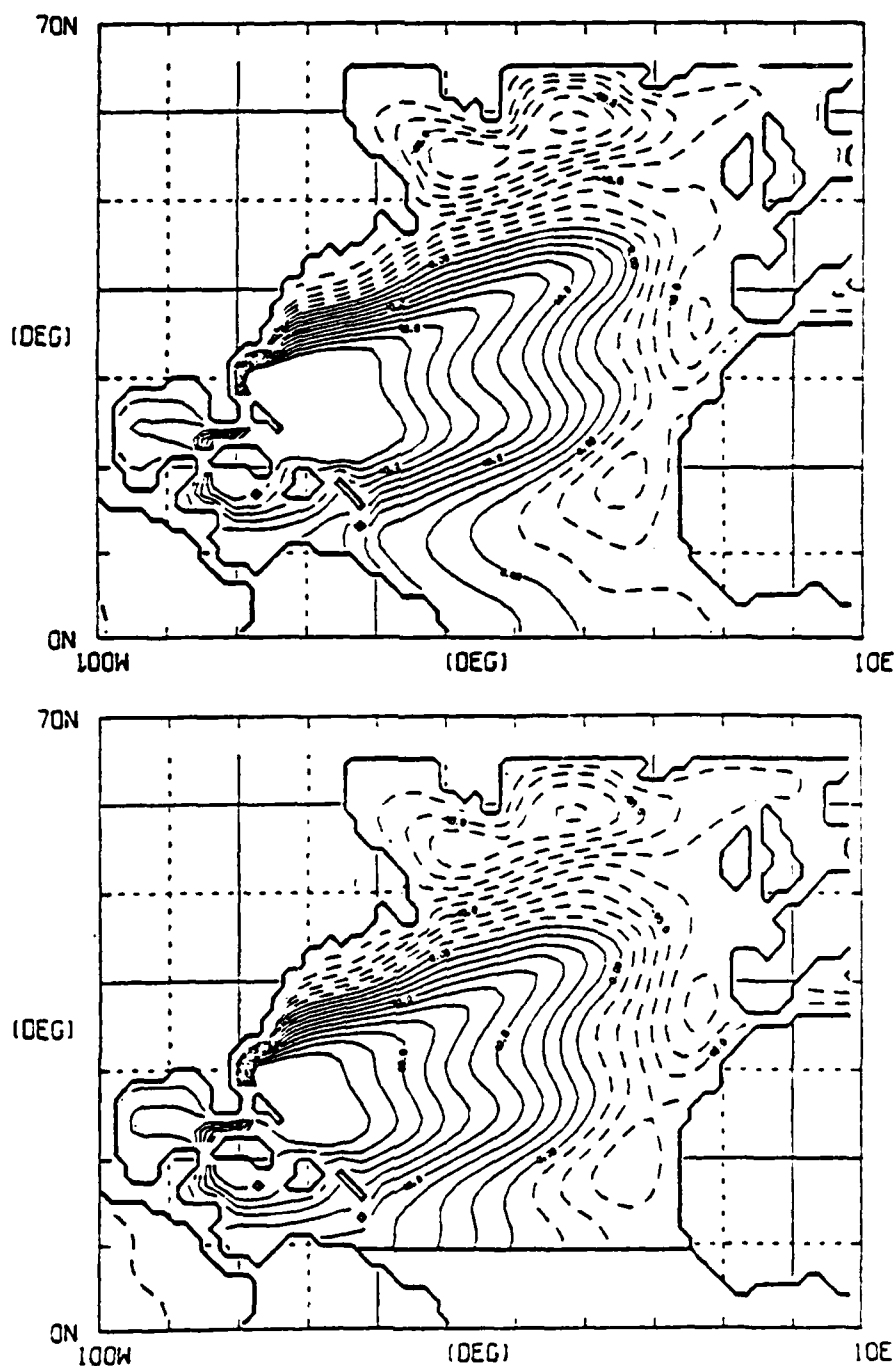


Figure 9

# OBJECTIVE ANALYSIS OF THE GULF STREAM THERMAL FRONT FROM INVERTED ECHO SOUNDERS

D. Randolph Watts and Karen L. Tracey  
Graduate School of Oceanography  
University of Rhode Island  
Narragansett, RI 02882

## ABSTRACT

Objective maps of the Gulf Stream thermocline depth ( $12^{\circ}\text{C}$  isotherm) field northeast of Cape Hatteras have been produced for January-June 1984. To apply objective mapping to the Gulf Stream thermal front, the input data is first treated to remove the mean field and normalize the perturbation field variance. The space time correlation function is estimated from all IES measurement-pairs available since 1979. The observations show the correlation function  $\rho$  to be isotropic at zero time lag. The peak of  $\rho$  remains symmetric at non-zero time lags, but decays slowly as it moves downstream at 12 km/day. The observed correlation function is approximated as:

$$\rho(x', y', t') = \exp(-|t'|/T_0) \exp(-r/A) \cos(\pi r/2B)$$
 where  $r^2 = (x'-ct)^2 + (y')^2$ ,  $T_0 = 9.3$  days,  $A = 391$  km,  $B = 171$  km, and  $c = 12$  km/day.

Thermocline depth maps reveal that the Gulf Stream is nearly 100 km north of its historical mean position during 1984. The accuracy of the objective mapping is confirmed by comparisons with AXBT surveys and current meter measurements.

During the period January-June 1984 an array of 18 inverted echo sounders (IES) has monitored thermocline depth variations within the Gulf Stream. The instruments were located on six sections, in an approximately rectangular grid 130 km across-stream by 360 km downstream (Figure 1). In addition, current meter moorings as well as IES were located at five of the western sites. During earlier years, subsets of these sections and sites have also been occupied. The IES measurements have been calibrated to  $Z_{12} = 12^{\circ}\text{C}$  isotherm depth records

and 24-hour low-pass filtered (Watts and Johns, 1982). Objective maps of the thermocline ( $Z_{12}$ ) field in the array region have been produced at daily intervals from these records. The boxed region in Figure 1, oriented  $064^\circ\text{T}$ , is the region being mapped.

In order to apply objective mapping techniques suitable for isotropic homogenous perturbation fields (Carter, 1983) to the Gulf Stream thermal front, special treatment of the input dataset is first required to remove the mean field and normalize the perturbation field variance. These are restored after the objective analysis to obtain the true  $Z_{12}$  field. The flow chart in Figure 2 illustrates the processing steps and inputs/outputs, which are described in the following paragraphs.

To represent the mean field, we approximated the cross-stream thermocline profile by an asymmetric tanh-like function of cross-stream distance  $y$  of the form:

$$\bar{Z}(y) = Z_{\text{INFL}} + \left[ \frac{Z_B - Z_A}{1 + \frac{1}{D}} \right] \left[ \frac{1 - e^{\frac{-2(y - c)}{A}}}{1 + D e^{\frac{-2(y - c)}{A}}} \right] \quad (1)$$

where  $Z_{\text{INFL}} = 350$  m,  $Z_A = 100$  m,  $Z_B = 850$  m,  $D = 2.0$ ,  $A = 40$  km and  $C = 25$  km. The agreement between  $\bar{Z}(y)$  and the observed mean profile, measured by several XBT surveys in this region, was within 5 m for the steeply sloping portion of the thermocline and within 20 m at the northern and southern edges. The mean field was assumed not to vary in

the downstream direction (Figure 3) and was subtracted from the measured  $Z_{12}$ 's at each IES site. For example, at the  $j$ th IES site located at  $y_j$ , the de-measured field is  $Z_{12}'_j = Z_{12} - \bar{Z}(y_j)$ .

Objective analysis also requires uniform variance throughout the region being mapped. The variance of our data however varied systematically, related to the proximity of the sites to the mean north wall location. Higher variance was located near the mean Gulf Stream center as a result of the steep thermocline slope in that region. Lower variance was found both to the north and south where the thermocline slope was much reduced. We approximated the variance field,  $\sigma(y)$ , as the first derivative of the mean field, scaled to agree in magnitude with the observed variance. Figure 3 shows the variance in plan view, with the variance of the central ridge about three times that at the edges. The de-measured data was normalized by this field [e.g.  $\xi_j = Z_{12}'_j / \sigma(y_j)$  for the  $j$ th site] before use as input to the objective analysis.

The remaining essential input to the objective analysis is the space/time correlation function  $\rho(x',y',t')$ , where primes indicate lag distances in space/time. To estimate  $\rho(x',y',t')$ , we combined data from all previous IES deployment-pairs in the Gulf Stream to estimate the average correlation function  $\hat{\rho}(x',y',t')$ , for all  $(x',y')$  spatial separations and time lags  $t'$  from -16 to +16 days. Fifty-three individual instruments, from 1979 to 1984 in six deployment periods, were used and all the pair separations are plotted in Figure 4. To

check for anisotropy of  $\rho$ , we first identified cross-stream and along-stream IES pairs and separately calculated their correlation functions. These were averaged in 10 km bins and are shown in Figure 5 versus distance. At zero time lag the observations show  $\rho$  to be remarkably isotropic, since the functional shapes for instruments spaced in either direction are indistinguishable. Consequently we can approximate  $\rho = \hat{\rho}(r)$ . Figure 6 shows the observed correlation function in plan view for time lags out to 10 days. These have been smoothed by a 50 km Gaussian weighted low-pass filter. At non-zero time lag the peak of the observed correlation function moves downstream at 12 km/day, decays slowly (e.g., exceeding 0.7 at  $t' = 6$  days), and maintains its symmetric shape.

We can approximate  $\rho$  by the functional form:

$$\rho(x', y', t') = \exp(-|t'|/T_0) \exp(-r/A) \cos(\pi r/2B) \quad (2)$$

where  $r^2 = (x' - ct')^2 + (y')^2$ ,  $T_0 = 9.3$  days,  $A = 391$  km,  $B = 171$  km, and  $c = 12$  km/day. Figure 6 also shows the idealized function for the same time lags as the observed function. We chose this function such that the temporal decay rate of the central peak is similar to the observed values. The spatial decay rate is exactly the same as that observed for zero time lag; thus the idealized function at zero time lag (upper left corner) is another view of  $\hat{\rho}(r)$ , which was already shown in Figure 5. The decay rates of both functions remain similar out to



4 days time lag, but the observed correlations decay more slowly than the idealized function for the longer time lags.

For each output grid point, the objective mapping technique selects, from all the input data within a specified maximum time lag ( $T$ ) and radial distance ( $R$ ), the number of points ( $N$ ) which have the highest  $\rho$ . The output fields shown in Figures 7 and 8 result from specifying  $N = 9$ ,  $T = \pm 4$  days,  $R = 120$  km, and using the idealized  $\rho$  with an assumed noise level ( $E$ ) of 0.05. This set of parameters ( $N$ ,  $T$ ,  $R$ ,  $E$ ,  $\rho$ ) was chosen to minimize the estimated error field. However, the mapping appears to be very robust, in the sense that it is not sensitive to any of these parameters. When we allowed the parameters to vary within the following ranges  $4 \leq N \leq 9$ ,  $80 \leq R \leq 120$ ,  $0 \leq |T| \leq 8$ ,  $0.01 \leq E \leq 0.1$ , the error field changed by less than 2% within the array area and by about 6% for the extrapolated region outside.

An important output of the objective mapping includes the estimated error fields. The error field (percent variance),  $\epsilon(x,y)$ , is shown in Figure 7 along with the error-bar field,  $e(x,y)$ , which is obtained by renormalizing by the variance field:  $e(x,y) = \sigma(y) \cdot [\epsilon(x,y)]^{1/2}$ . In general, the error estimates are less than 10% within the array area. Higher variance  $\sigma(y)$  near the mean Gulf Stream center results in a slight ridge of the error-bar field even though  $\epsilon(x,y)$  is low.

The main output of the objective analysis is the perturbation field  $\hat{\xi}(x,y)$  on a full grid of points (20 km grid spacing) within the 200 km

by 400 km mapping region shown in Figure 1. By renormalizing the perturbation field,  $\hat{\xi}(x,y)$ , by the variance and restoring the mean, thermocline depth maps are obtained [i.e.,  $\hat{Z}(x,y) = \hat{\xi}(x,y) \cdot \sigma(y) + \bar{Z}(y)$ ]. The two fields  $\hat{\xi}(x,y)$  and  $\hat{Z}_{1,2}(x,y)$  are shown in Figure 8 for the period January-June 1984 at five day increments. Meanders of 350 km wavelength are the dominant features propagating through the array. For example, from 21 January to 5 February, two meander crests are clearly seen moving downstream in the perturbation field and the 12°C isotherm depth maps. During much of the time period from mid-February to mid-April, the Gulf Stream is nearly 100 km north of its historical mean position. (Note that  $Z_{1,2}$  at 300 m corresponds closely to  $Z_1$  at 200 m, the traditional 'north wall' indicator.)

Additional data collected during this time period confirm the accuracy of the objective mapping shown in Figure 8. Current meter records obtained along the western two sections showed that the current was flowing to the northwest between 20 - 25 April (shown elsewhere in these Proceedings by Bane and Watts, 1985). Figure 9 compares the objective mapped  $\hat{Z}_{1,2}$  field for 1 June with an AXBT survey flown in the same region by John Bane on the same date. Both maps agree well at the IES sites and within the unshaded portion of the objective map. The small differences do not appear to exceed the error estimates of Figure 7, and are probably due to the contouring routines.

We envision many uses for these objective maps of the Gulf Stream thermocline field. They should be particularly well suited for

comparisons with our current meter array measurements and with satellite imagery and Rafos float tracks, as well as to test numerical models of the Gulf Stream path evolution.

REFERENCES

- Bane, John M. and D. Randolph Watts, Recent current measurements in the Gulf Stream downstream from Cape Hatteras, Gulf Stream Workshop April 1985, Proceedings, University of Rhode Island, 1985.
- Carter, Everett F., The statistics and dynamics of ocean eddies, Ph.D. Thesis, Harvard University, 1983.
- Watts, D. Randolph and William E. Johns, Gulf Stream meanders: observations on propagation and growth, J. Geophys. Res. 87 9467-9476, 1982.

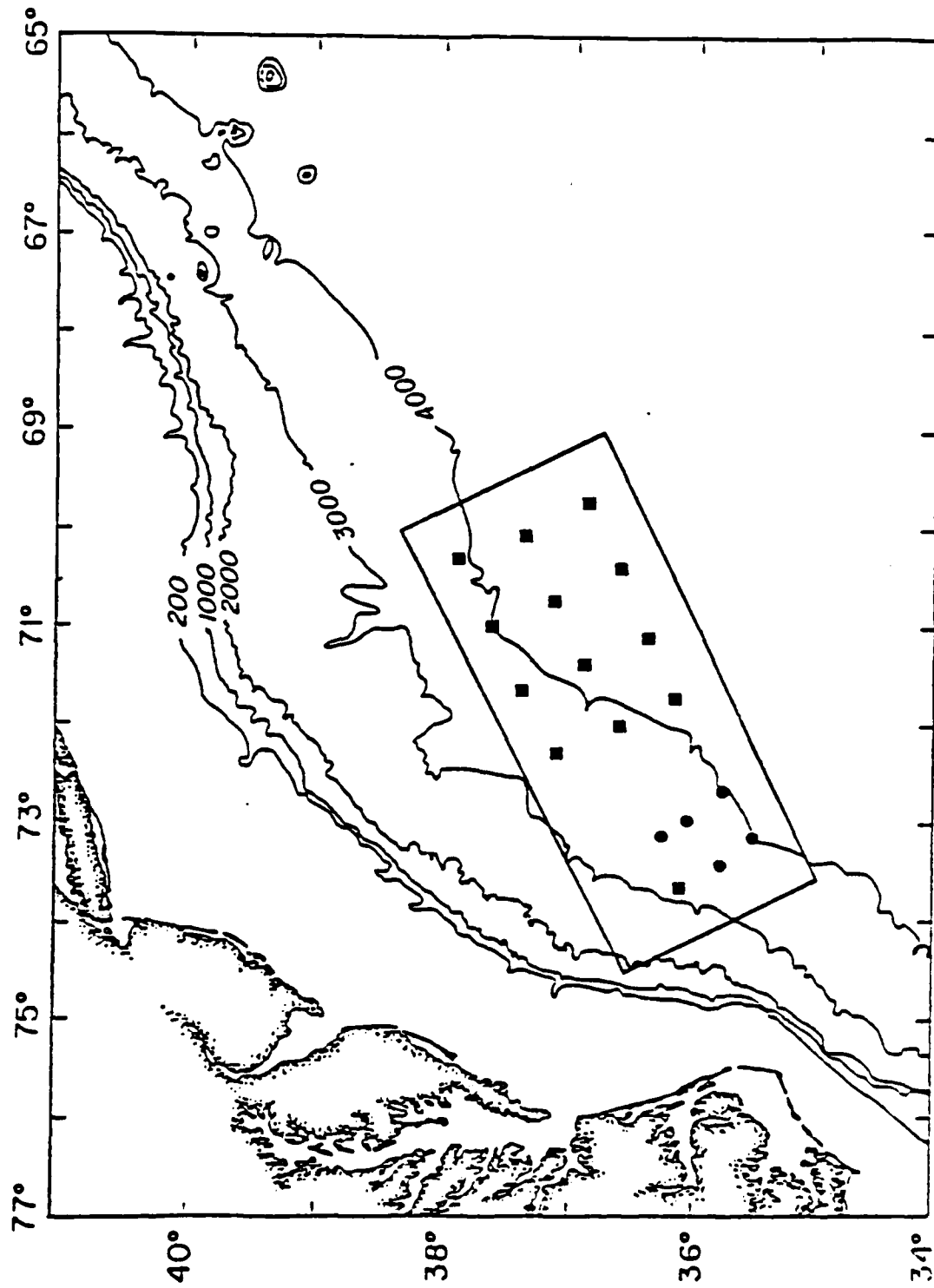


Figure 1. Array showing IES sites (boxes and circles) during 1984. Current meter moorings as well as IESSs were located at the sites shown by the solid circles. The boxed region is the region being mapped by objective analysis.

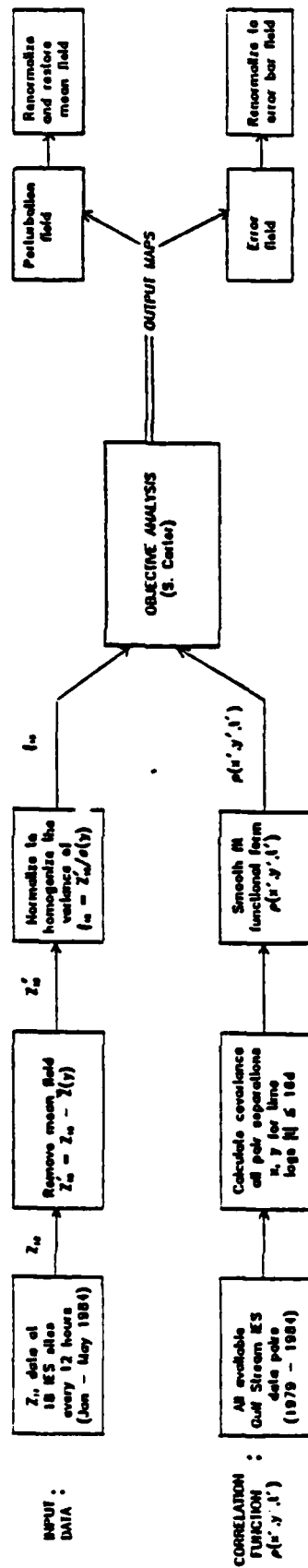


Figure 2. Flowchart of the objective mapping processing steps. Inputs are the data measurements and the correlation function. Outputs are the perturbation and 12°C isotherm depth maps and the error fields.

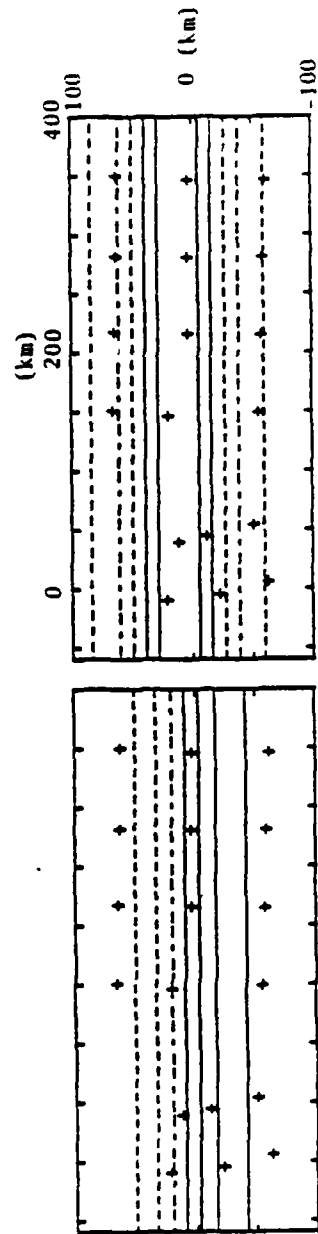


Figure 3. Mean field  $\bar{Z}(y)$  of Equation 1 contoured in plan view (left). Contour interval is 100 m with the dashed region shallower than 500 m. Root-mean-square variance field  $\sigma(y)$  contoured in plan view (right). Contour interval is 25 m with the dashed region  $\leq 150$  m rms. IES sites are shown by the '+'s.

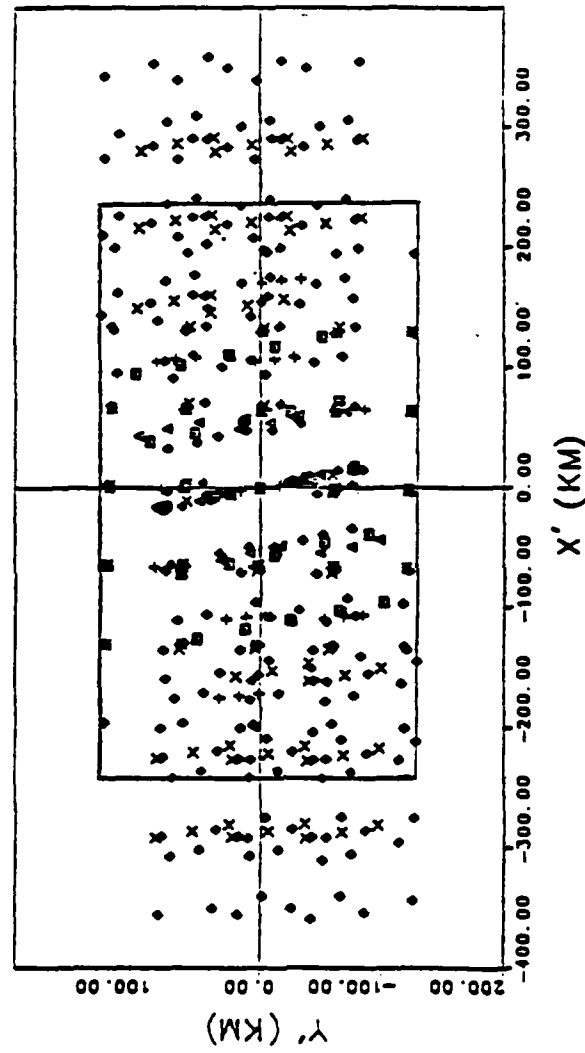


Figure 4. Plot of all IES pair separations ( $x', y'$ ) with a different symbol used to represent each deployment period. The center box corresponds to the region for which the smoothed  $\rho(x', y', t')$  is contoured in Figure 6.



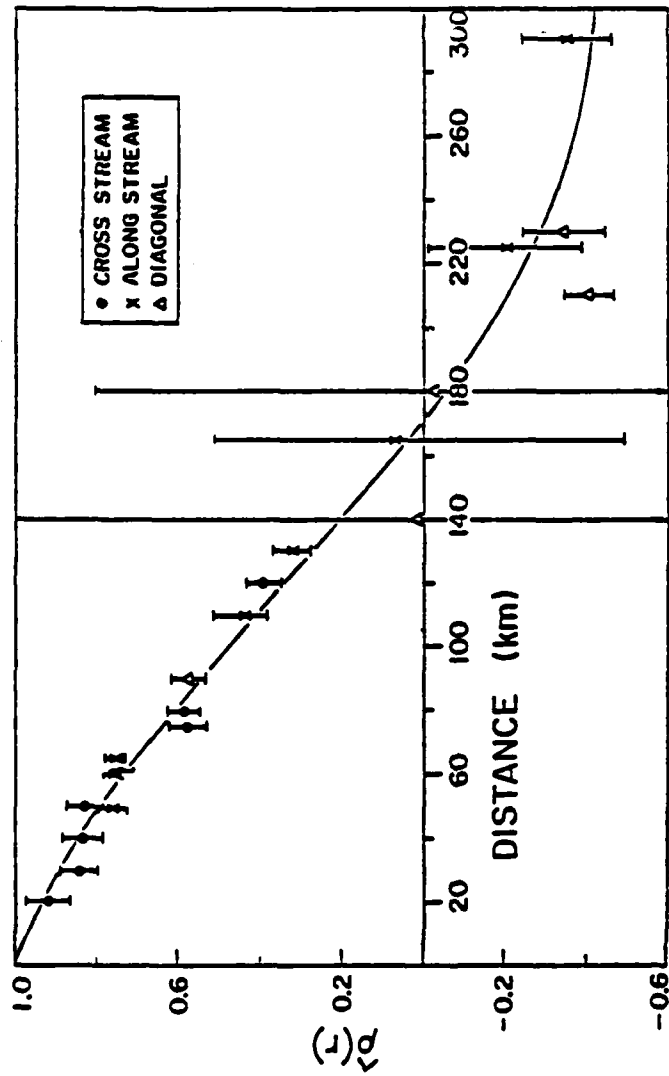


Figure 5. Correlation functions for cross-stream, along-stream, and diagonal IES pairs versus distance. The solid curve through the values is the idealized  $\rho(x',y',t')$  of Equation 2 at zero time lag (see text).

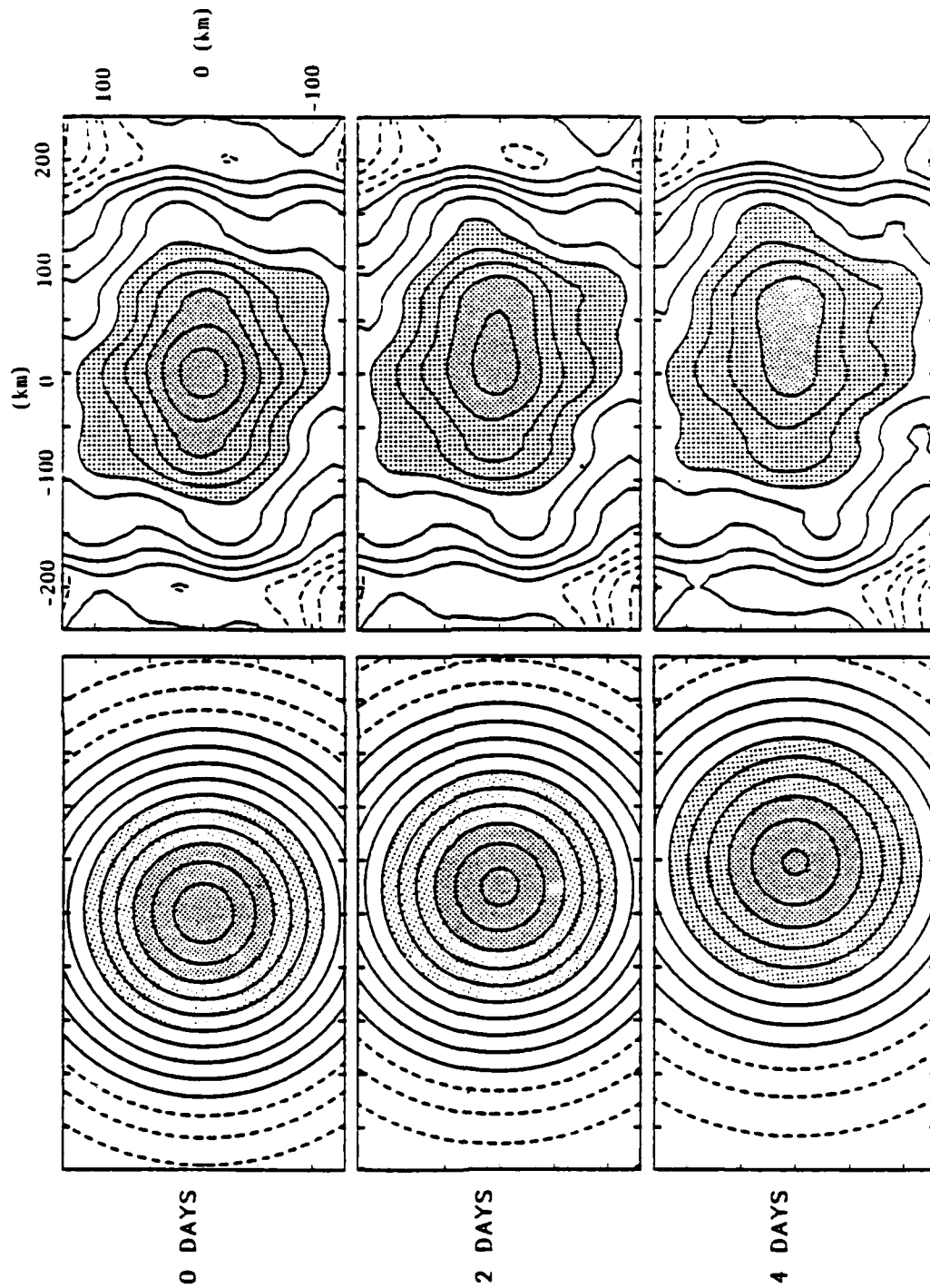


Figure 6. Idealized (left) and observed (right) correlation functions  $\rho(x', y', t')$ , contoured in plan view for the time lags shown, from 0 to 10 days in 2 day steps. For negative time lags, note that  $\rho$  is implicitly given by the symmetry relation  $\rho(-x', -y', -t') = \rho(x', y', t')$ . Contour interval is 0.1 and negative contours are dashed. Darker shading indicates  $\rho \geq 0.7$ ; lighter shading indicates  $\rho \geq 0.4$ .

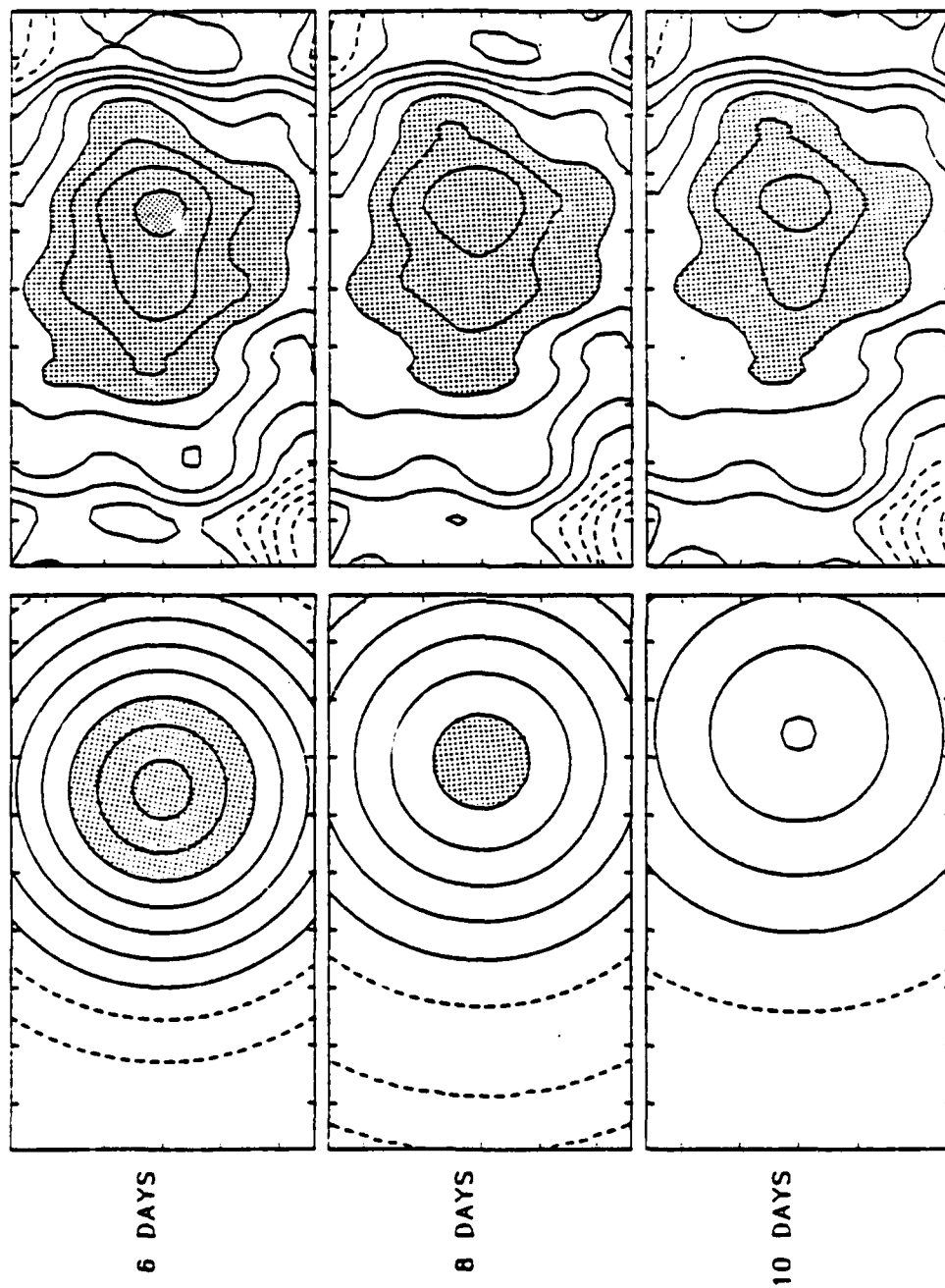


Figure 6. Continued

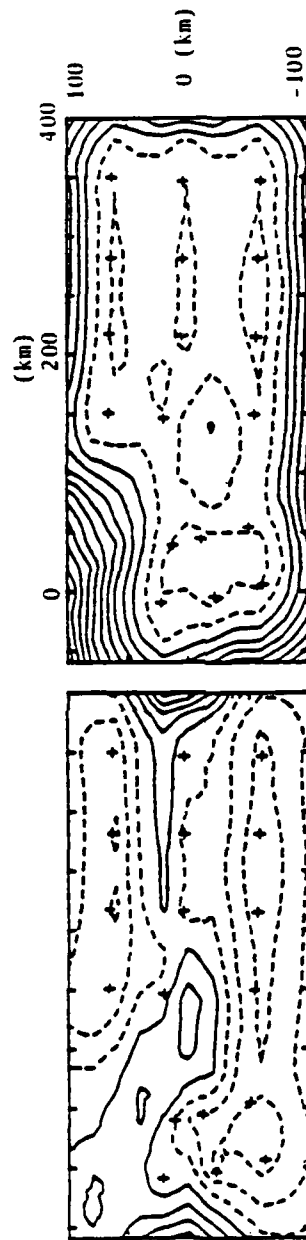


Figure 7. The error (% variance) field  $e(x,y)$  is shown at right with contour interval of 5% and the dashed region corresponding to <15% error. The renormalized error-bar field  $e(x,y)$  is shown at the left with contour interval of 10 m and the dashed region corresponding to errors <50 m.

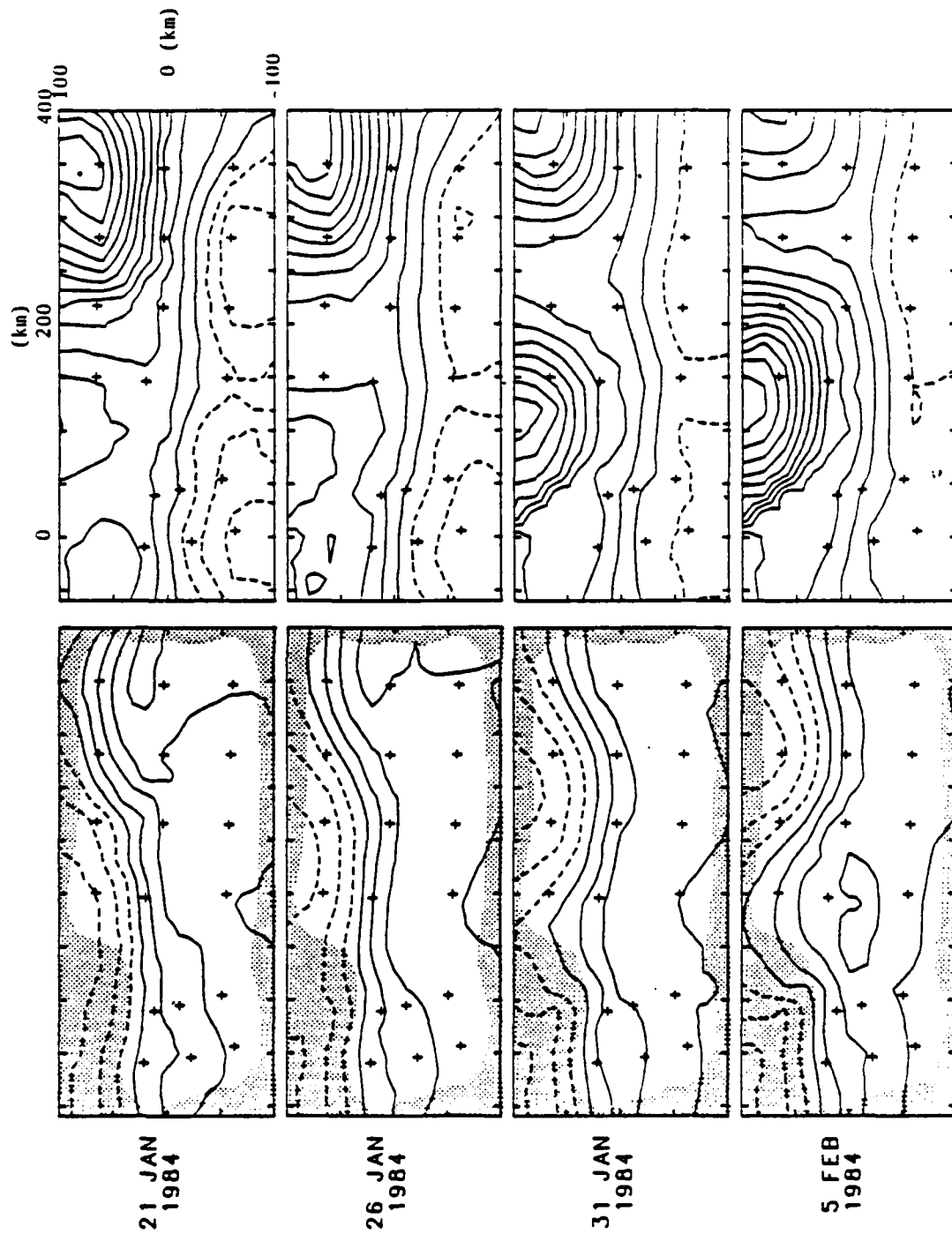


Figure 8. The 12°C isotherm surface  $\hat{Z}_{12}(x,y)$  (left) and perturbation field  $\hat{\xi}(x,y)$  (right). Contour interval of the perturbation field is 0.5 with the dashed region corresponding to negative values. The 12°C isotherm surface is contoured at 100 m intervals and depths shallower than 500 m are dashed. The shaded area corresponds to regions of  $\geq 15\%$  estimated error from the error maps shown in Figure 7.

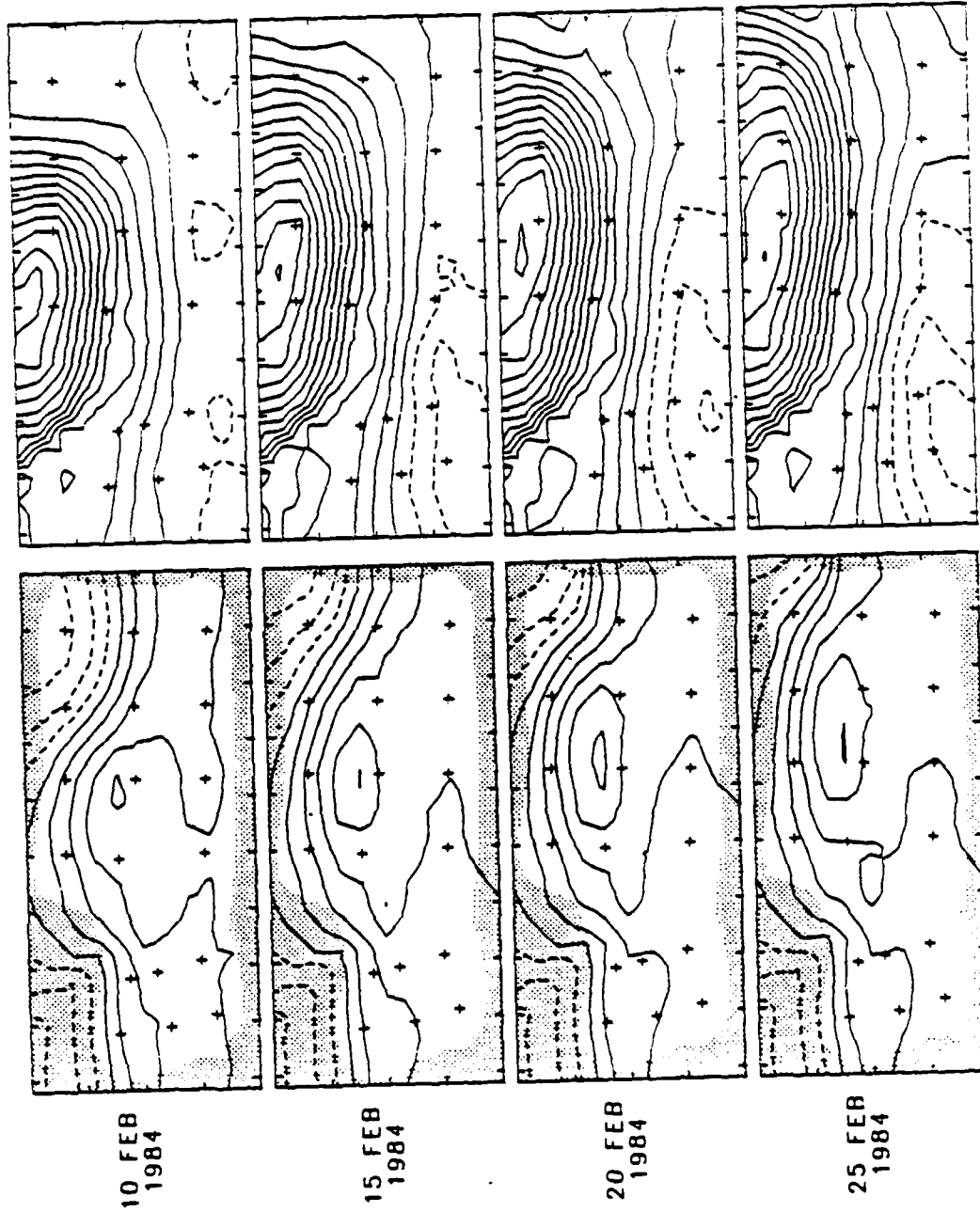


Figure 8. Continued

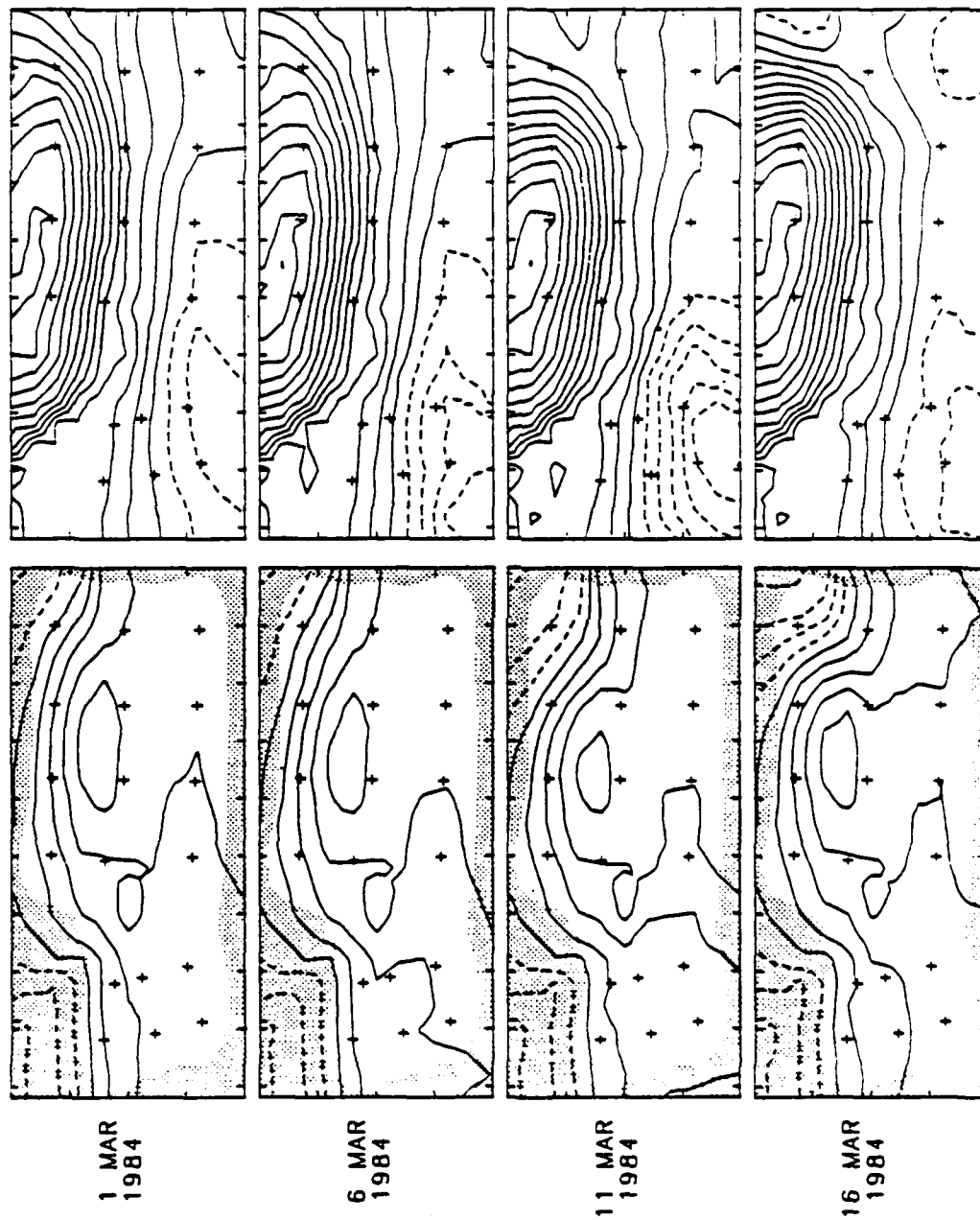


Figure 8. Continued

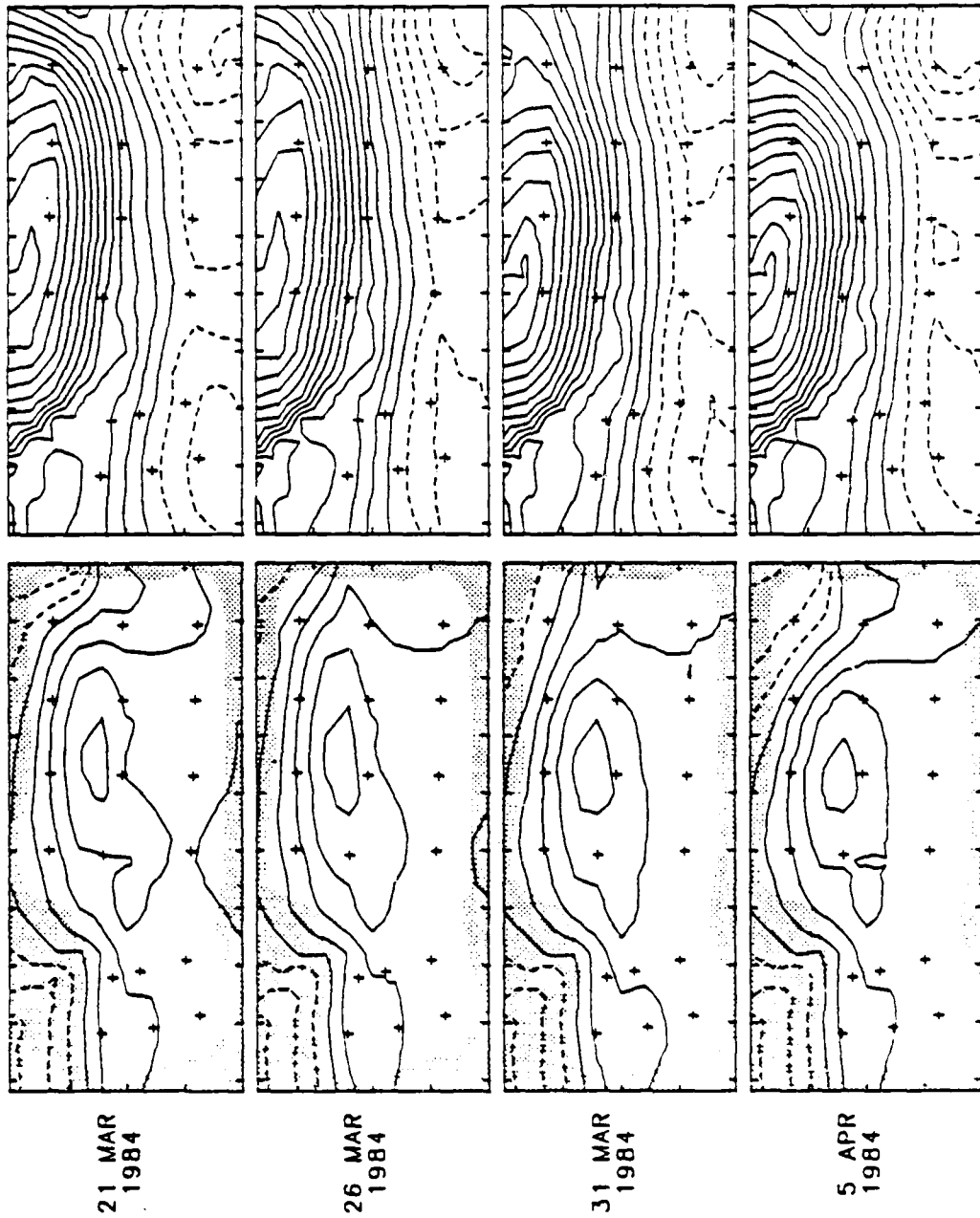


Figure 8. Continued



AD-A162 586

PROCEEDINGS OF THE GULF STREAM WORKSHOP HELD AT WEST  
GREENWICH RHODE ISLA (U) RHODE ISLAND UNIV KINGSTON  
GRADUATE SCHOOL OF OCEANOGRAPHY D R WATTS APR 85

777

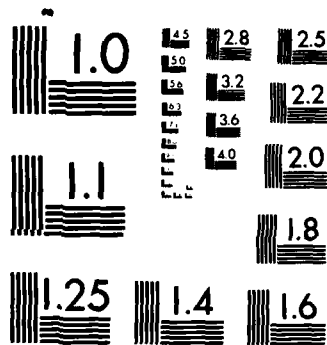
UNCLASSIFIED

N00014-85-G-0322

F/G 8/3

NL





MICROCOPY RESOLUTION TEST CHART  
NATIONAL BUREAU OF STANDARDS-1963-A

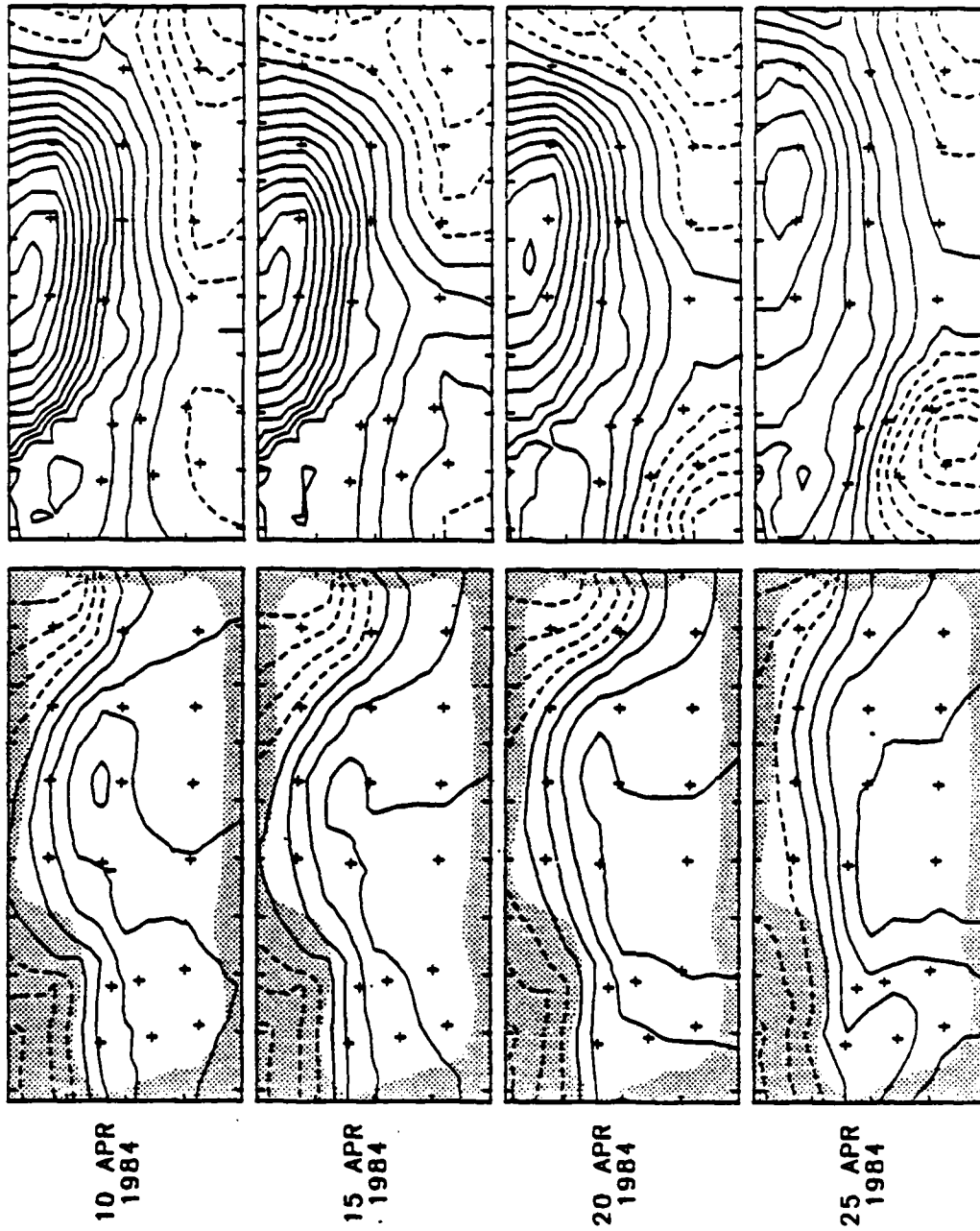


Figure 8. Continued

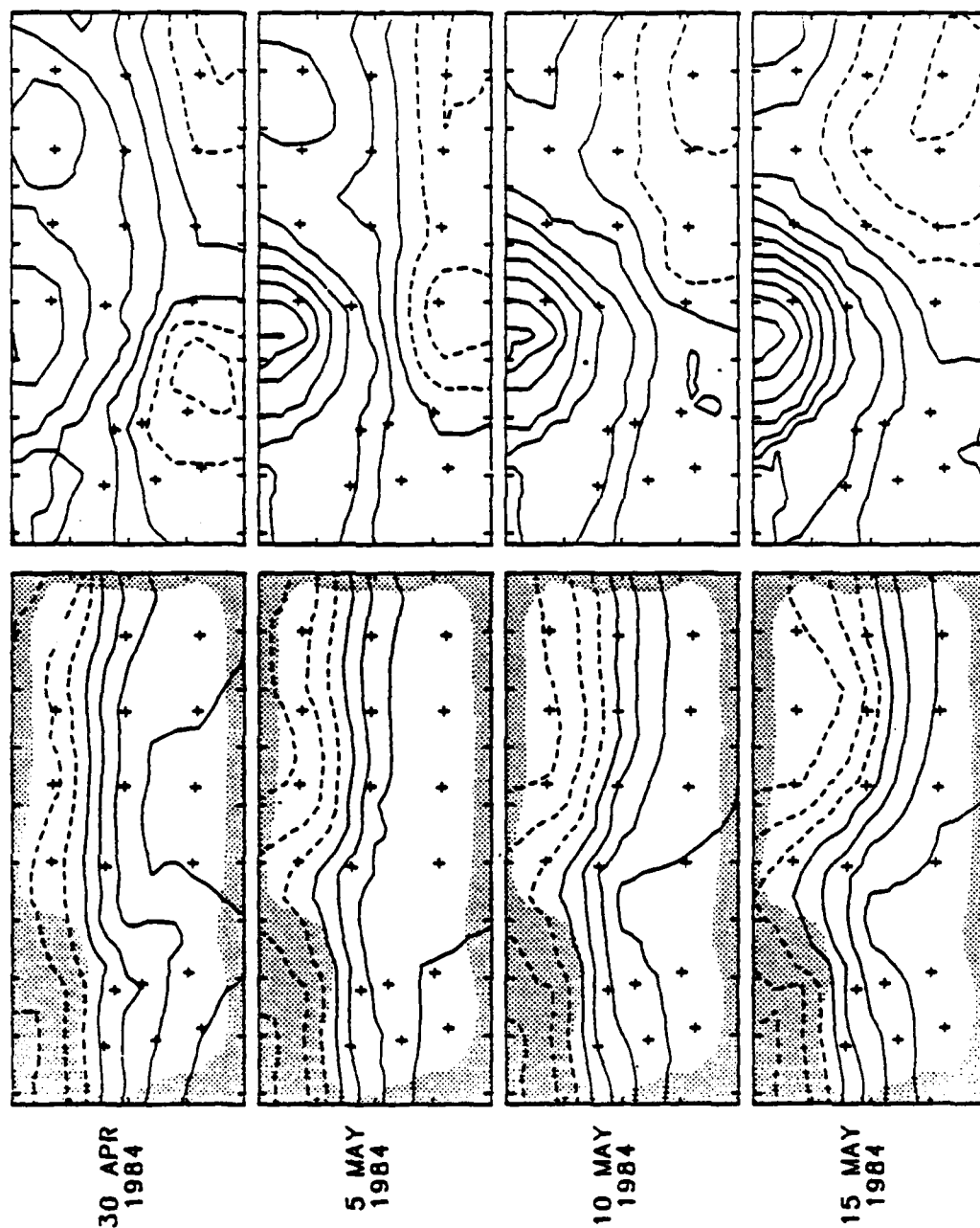


Figure 8. Continued

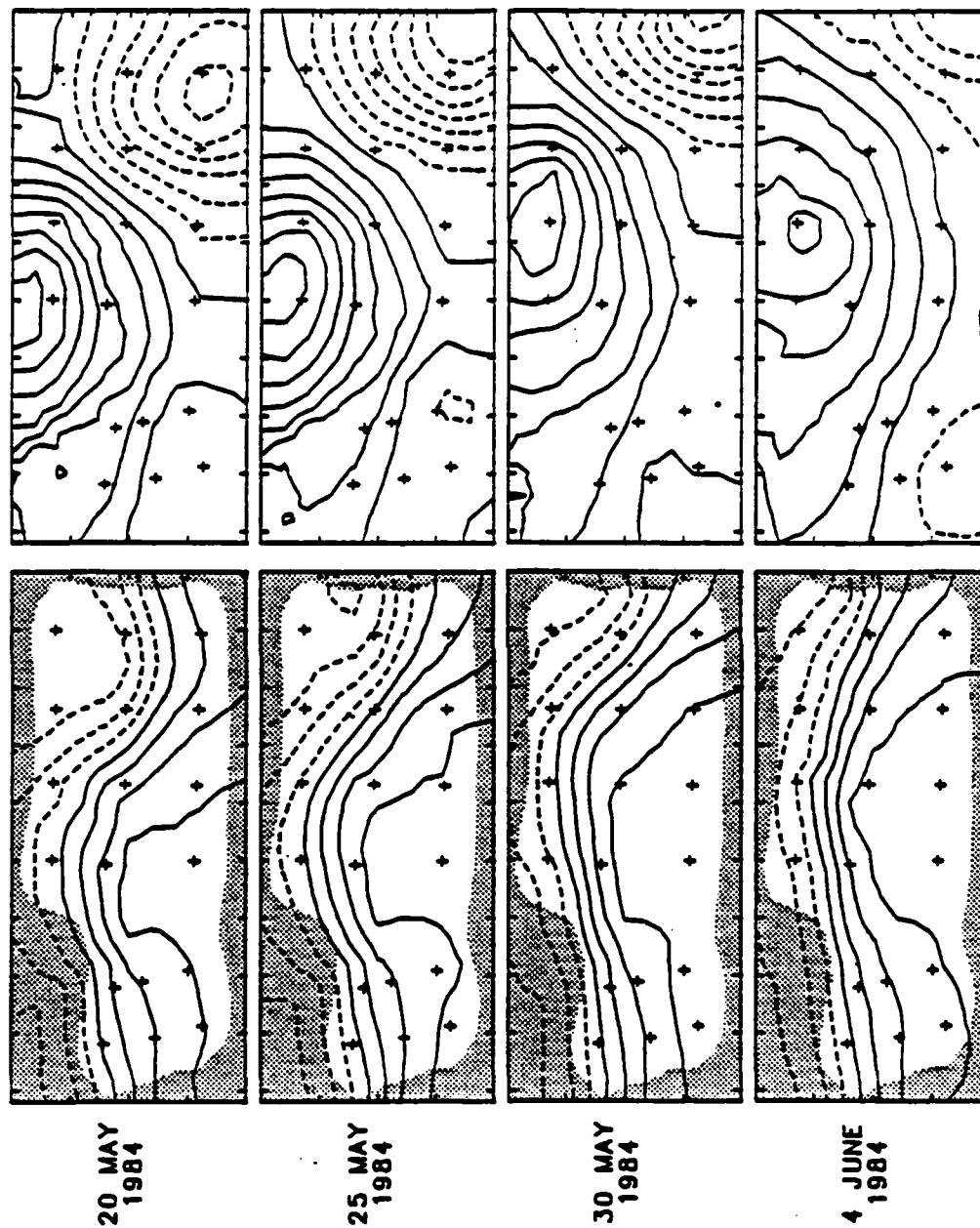
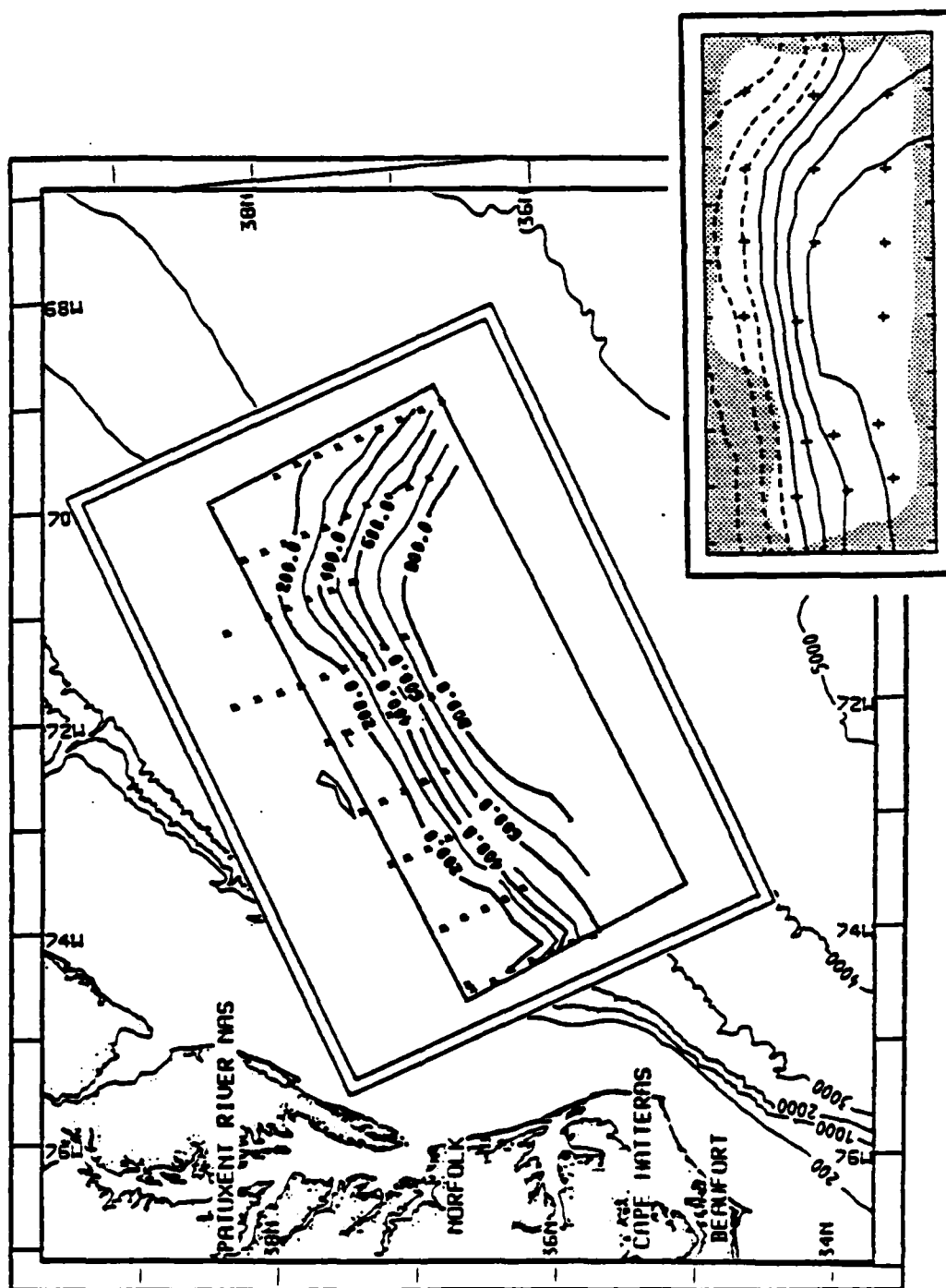


Figure 8. Continued



**Figure 9. The 12°C isotherm depths from the AXBT survey on 1 June 1984. The inner box designates the portion of this survey which we have mapped by objective analysis of the IES data (lower right).**

Unclassified

SECURITY CLASSIFICATION OF THIS PAGE

AD-A162506

REPORT DOCUMENTATION PAGE				
1a. REPORT SECURITY CLASSIFICATION Unclassified		1b. RESTRICTIVE MARKINGS None		
2a. SECURITY CLASSIFICATION AUTHORITY		3. DISTRIBUTION/AVAILABILITY OF REPORT Unlimited distribution		
2b. DECLASSIFICATION/DOWNGRADING SCHEDULE				
4. PERFORMING ORGANIZATION REPORT NUMBER(S) None		5. MONITORING ORGANIZATION REPORT NUMBER(S)		
6a. NAME OF PERFORMING ORGANIZATION University of Rhode Island	6b. OFFICE SYMBOL (If applicable)	7a. NAME OF MONITORING ORGANIZATION Office of Naval Research		
6c. ADDRESS (City, State, and ZIP Code) Graduate School of Oceanography Kingston, RI 02881		7b. ADDRESS (City, State, and ZIP Code) 800 North Quincy Street Arlington, VA 22217		
8a. NAME OF FUNDING/SPONSORING ORGANIZATION	8b. OFFICE SYMBOL (If applicable)	9. PROCUREMENT INSTRUMENT IDENTIFICATION NUMBER N00014-85-G-0322		
8c. ADDRESS (City, State, and ZIP Code)		10. SOURCE OF FUNDING NUMBERS		
		PROGRAM ELEMENT NO.	PROJECT NO.	TASK NO.
		WORK UNIT ACCESSION NO.		
11. TITLE (Include Security Classification) Gulf Stream Workshop Proceedings				
12. PERSONAL AUTHOR(S) D. Randolph Watts, ed.				
13a. TYPE OF REPORT Workshop Proceedings		13b. TIME COVERED FROM TO	14. DATE OF REPORT (Year, Month, Day) 1985 April	15. PAGE COUNT 581
16. SUPPLEMENTARY NOTATION				
17. COSATI CODES			18. SUBJECT TERMS (Continue on reverse if necessary and identify by block number)	
FIELD	GROUP	SUB-GROUP		
Oceanography			Gulf Stream, circulation, synoptic scale variability, field observations, numerical modelling, prediction, SYNOPSIS	
19. ABSTRACT (Continue on reverse if necessary and identify by block number)				
<p>In recent years, studies of the fundamental physical processes governing the Gulf Stream structure and variability have benefited from great advances in observational and theoretical techniques. The U.S. Office of Naval Research is sponsoring a special-focus program entitled "SYNOPSIS" (Synoptic Ocean Prediction) to advance our physical understanding of ocean regions of high synoptic-scale variability and develop predictive capabilities for these phenomena. The Gulf Stream region where meanders grow to exhibit large amplitude is the chosen study area. In order to exchange ideas among researchers representing the rapidly developing specialties in Gulf Stream studies and to stimulate cooperative research efforts, a Gulf Stream Workshop was hosted by the University of Rhode Island at the Alton Jones Conference Center on 23-26 April 1985 under ONR Grant N00014-85-G-0322. These PROCEEDINGS contain (a) a summary of the Workshop results and recommendations and (b) the scientific papers associated with five keynote addresses plus 25 oral and poster presentations.</p>				
20. DISTRIBUTION/AVAILABILITY OF ABSTRACT <input checked="" type="checkbox"/> UNCLASSIFIED/UNLIMITED <input type="checkbox"/> SAME AS RPT. <input type="checkbox"/> DTIC USERS			21. ABSTRACT SECURITY CLASSIFICATION Unclassified	
22a. NAME OF RESPONSIBLE INDIVIDUAL Dr. Thomas Curtin		22b. TELEPHONE (Include Area Code) 202-696-4112		22c. OFFICE SYMBOL Code 1122P.O.

DD FORM 1473, 34 MAR

33 APR edition may be used until exhausted.  
All other editions are obsolete.

SECURITY CLASSIFICATION OF THIS PAGE

Unclassified

**END**

**FILMED**

---

*2-86*

**DTIC**